COMPUTER AIDED RELIABILITY BASED HYDRO-STRUCTURAL RESPONSE ANALYSIS OF TENSION LEG PLATFORMS

Pratul Chandra Chatterjee B.Tech.(Hons.)

THIS THESIS IS SUBMITTED FOR THE DEGREE OF
DOCTOR OF PHILOSOPHY

DEPARTMENT
OF
NAVAL ARCHITECTURE AND OCEAN ENGINEERING

UNIVERSITY OF GLASGOW

ProQuest LLC.
789 East Eisenhower Parkway
P.O. Box 1346
Ann Arbor, MI 48106 – 1346

DECLARATION

Except where reference is made to the work of others,
this thesis is believed to be original.

ACKNOWLEDGEMENTS

I am grateful to the University of Glasgow and the Committee of Vice Chancellors and Principals for their financial support which enabled the work presented in this thesis.

I wish to express my deepest gratitude to Professor D. Faulkner, Head of Department, and Dr. P.K. Das, Lecturer, of the Department of Naval Architecture and Ocean Engineering for their advice and timely encouragement throughout the duration of my research.

I would like to thank Mr. J. Taylor of Computing Service and Ms. Y. Mather of Mechanical Engineering Department for their invaluable help.

I would like to take this opportunity to thank all the staff in the Department of Naval Architecture and Ocean Engineering who in one way or another helped me in producing this work.

I am grateful for the moral support and encouragement from my father, uncle and aunt at home in India.

Finally, I am forever indebted to my nearest friend, Dr. Keya Nag for her patience and invaluable support throughout my study.

CONTENTS

CHAPTER 2 EQUIVALENT FORCES FROM ENVIRONMENTAL LOADING

THESIS LAYOUT

The thesis is arranged into seven chapters each of which has its own tables, figures and references. The references are numbered and organised alphabetically. The numbering system for equations, tables, figures and references starts with the chapter number in front. The equation numbers are shown in round brackets whereas the reference numbers are given in square brackets.

The word processing application used to prepare all chapters is Microsoft Word for Windows (version 6). However, several other software packages on different hardware platforms are involved in the preparation of this thesis. A number of tables and figures from spreadsheet, drawing and painting applications are directly inserted into the main text with the help of a new technology called OLE (Object Linking and Embedding) in the PC Windows environment. But it is still difficult to import objects in the 'landscape' orientation unless a powerful publishing package is used. As a consequence, a number of figures are placed at the end of each chapter.

SUMMARY

The TLP technology has gained credibility with the offshore industry and the associated engineering community. The TLP concept covers a number of areas where there is a great need for research. The developments associated with the TLP technology are briefly reviewed in Chapter 1. For numerical demonstrations, a TLP model is selected which was originally chosen by the Derived Loads Committee I.2 of the 1985 ISSC. The principal particulars of the ISSC TLP are discussed in detail.

Some important design parameters that influence significantly the configuration of TLPs are outlined in Chapter 1. A complete global analysis of a TLP includes many analytical and empirical methods where some of them are fairly standard but some other may not be well defined. The problem areas involved in the analysis and the future trends in design are also discussed.

Chapter 2 examines different components of the environmental loading. Second order effects are included. Drift forces are estimated from simplified analytical solutions. The calculation of external forces described in Chapter 2 are used in the next chapters. Some closed-form expressions are derived that are particularly important for transforming complicated external forces into equivalent nodal loads. A step-by-step procedure combining transformation matrices and results from standard load cases is proposed which deals with complex member loads on a 3-D beam, arbitrarily oriented in space.

Chapter 3 describes the development of a rigid body motion analysis program, RBRA. The dynamic equation of motion which takes account of all six rigid body degrees of freedom and the associated coefficient matrices are discussed. A solution technique is proposed which is found quite effective to estimate the linearised rigid body responses. The results from RBRA are compared with the published results from 17 organisations who have used boundary element formulations and diffraction-radiation analysis for their calculations.

Chapter 4 discusses the development of a computer program, DCATLP which can bring hydrodynamic and structural aspects together in the dynamic coupled analysis of a TLP. The TLP is modelled as a 3-D frame structure with internal hinges to account for the hull-tether connections. However, main particulars of a TLP are not enough for any structural analysis. For numerical demonstration, the ISSC TLP components are designed realistically with stiffeners to estimate their scantlings.

In DCATLP, the global mass and stiffness matrices are stored in skyline arrays. The dynamic equilibrium equations are solved in the time domain. The non-linear time integration algorithm belongs to the Newmark-β family but it is a modification and combination of a number of existing algorithms. DCATLP can calculate internal member forces in each beam element under the action of environmental loading. The structural displacements, velocities and accelerations at each and every FE node are calculated. The static, quasi-static and dynamic components of the environmental forces are applied simultaneously in DCATLP to include the inertia effects. A different type of model for the ISSC TLP is developed in LUSAS where tethers are replaced by linear springs at each corner. Responses of two different ISSC TLP models (one for DCATLP and the other for LUSAS) under sinusoidal loads are compared. The structural and hydrodynamic responses of the ISSC TLP in a peak storm event are also presented.

Chapter 5 presents a step-by-step calculation procedure to find failure probabilities of TLP column structures after assigning appropriate coefficients of variation to the strength and load variables. The calculation of longitudinal and hoop stresses from maximum axial compression, torsion, shear forces, bending moments and hydrodynamic pressure is also shown. The uncertainty modelling is mainly based on the previous work carried out in the author's Department. The failure surfaces for TLP columns are formulated according to API Bulletin 2U and the Model Code of TLP RCC. The chapter also describes some improvements achieved in developing a program BCCNNV, based on the AFOSM method. The program is sufficiently accurate for non-normal correlated variables and it is validated by considering a few classic cases.

The main objective in Chapter 6 is to carry out a detailed FE analysis of a part of a TLP structure with the help of the results obtained from a 3-D beam element based global analysis. One ring only stiffened and three orthogonally stiffened cylinders, similar to TLP columns are modelled in LUSAS to compare the numerical predictions with the experimental results available from other researchers' work. To get an initial 'feel' for the structure, the buckling loads of the FE models are estimated by eigenvalue buckling analyses. The author also attempts to capture the post-buckling phase of the FE models through rigorous non-linear FE analyses.

Chapter 7 contains the final discussion and conclusions and ends with some recommendations for future research work.

LIST OF SYMBOLS

A	=	Cross-sectional area of the element
A_n	=	$J_n'^2(kr) + Y_n'^2(kr)$
A_p	=	Projected area of the object in the wind force calculation
A_s	=	Cross-sectional area of one stringer stiffener in a TLP column (or cylinder)
A_{sh}	=	Shear area of a stiffened circular cross-section with two vertical planes of symmetry
A_{sy}	=	Shear area of a stiffened circular cross-section about its local y axis
A_{sz}	=	Shear area of a stiffened circular cross-section about its local z axis
A_t	=	Material cross-sectional area of tethers in one corner
A_{wp}	=	Waterplane area of one corner column
α_i	=	Sensitivity factors
α_d	=	Phase lag of diffraction force
α_R	=	Rayleigh Mass Damping Coefficient (also RMDC in MYSTRO plots)
$\alpha_E, \beta_E, \gamma_E$	=	Eulerian transformation angles
$[B]$	=	Global damping matrix
$[B_r]$	=	Rigid body (6×6) non-linear damping matrix
$[B_{rl}]$	=	Rigid body (6×6) linearised damping matrix
b_a	=	Actual width of shell of a TLP column (or cylinder) in the circumferential direction
b_{Dl}	=	Damping in a SDF system
b_e	=	Effective width of shell of a TLP column (or cylinder) in the circumferential direction
b_p	=	Breadth of pontoon
β	=	Reliability or safety index

β_R	=	Rayleigh Stiffness Damping Coefficient (also RSDC in MYSTRO plots)
β_N	=	Newmark β parameter
C_a	=	Added mass coefficient (= C_m-1)
C_{aX}, C_{aY}, C_{aZ}	=	Added mass coefficients in global X, Y and Z directions
C_D	=	Drag coefficient
C'_D	=	Drag coefficient of an oscillating cylinder in calm water
C_m	=	Inertia coefficient
C_s	=	Shape coefficient in the wind force calculation
C_X, C_Y, C_Z	=	Direction cosines in the global co-ordinates
$C_0, \cdots C_n$	=	Arbitrary constants
d	=	Water depth
d_f	=	Draft
D	=	Width or diameter of the element
d_{cl}	=	Distance between column centres
d_p	=	Depth of pontoon
dl	=	Incremental length of the element
Δ	=	Displacement of the platform
δ_N	=	Newmark δ parameter
δT	=	Change in tether tension
$\delta\{X\}$	=	Incremental global joint displacement vector
$\{E\}$	=	Twelve internal resisting forces in local co-ordinates (i.e. member-end reactions)
E_Y	=	Modulus of elasticity
f(x, t)	=	Member force per unit length
f_a	=	Applied stress due to axial compression
f_b	=	Applied stress due to bending moment
$\bar{f}_D$	=	Time average of viscous drift force due to current
f_{hoop}	=	Total applied stress in the hoop direction

f_{long}	=	Total applied stress in the longitudinal direction
f_{θ}	=	Applied stress due to hydrodynamic pressure
f_s	=	Applied stress due to shear force
f_{tq}	=	Applied stress due to torsional moment
$\overline{F}_{fs}$	=	Time average of viscous drift force due to free surface
F_{FKx}	=	Horizontal Froude-Krylov force on a pontoon element
F_{FKy}	=	Vertical Froude-Krylov force on a pontoon element
$f_{MF}(t)$	=	Diffraction force per unit length of a vertical cylinder according to MacCamy and Fuchs theory
$f_{MI}(t)$	=	Inertia force per unit length of a vertical cylinder according to the Morison equation
$f_{MD}(t)$	=	Drag force per unit length of a vertical cylinder according to the Morison equation
$f_{Mx_w}(t)$	=	Component of the normal force per unit length along x_w according to Borgman
$\{F_r\}$	=	Rigid body (6×1) external forces
F_{sc}	=	Second order correction force
$F_{wn}(t)$	=	Instantaneous wind force
$\overline{F}_{21}$	=	Time average of second-order wave elevation potential drift force
$\overline{F}_{22}$	=	Time average of second-order velocity head potential drift force
$\overline{F}_2^-$	=	Time average of second-order drift force
$F_2^-(t)$	=	Second-order instantaneous drift force
$F_2^+(t)$	=	Second-order high frequency springing force
ϕ_{yaw}	=	Horizontal angle of rotation due to yaw motion
$\{\Phi_b\}$	=	Eigenvectors for calculating buckling mode shapes by subspace iteration
g	=	Acceleration due to gravity
$g(x_1, x_2, \cdots\cdots, x_n)$	=	Performance or state function (in short $g(\cdot)$)
$\{G\}$	=	Array for storing temporary variables

G_s	=	Shear modulus
$\overline{GM}_R$	=	Metacentric height for roll motion
$\overline{GM}_P$	=	Metacentric height for pitch motion
H	=	Wave height
H_{wn}	=	International reference height in wind velocity calculation (= 10 m)
η_{ai}, η_{aj}	=	Amplitude of i or j component (regular) of random waves
I_{xx}	=	Roll mass moment of inertia of the platform
I_y	=	Second moment of inertia about local y axis
I_{yy}	=	Pitch mass moment of inertia of the platform
I_z	=	Second moment of inertia about local z axis
I_{zz}	=	Yaw mass moment of inertia of the platform
J_x	=	Polar moment of inertia about local x axis
$J'_n(kr)$	=	Derivative with respect to 'kr' of Bessel function of the first kind and of order n
k	=	Wave number
$[K]$	=	Global stiffness matrix
$[K_\sigma]$	=	Global stress stiffness matrix
$[K^*]$	=	Global effective stiffness matrix
$\left[K_l^e\right]$	=	Beam element stiffness matrix in local co-ordinates
$\left[K_g^e\right]$	=	Contribution of $[K_e]$ in global co-ordinates
$[K_L]$	=	Lower triangular matrix decomposed from $[K^*]$
$[K_U]$	=	Upper triangular matrix decomposed from $[K^*]$
$[K_{rh}]$	=	Rigid body (6×6) hydrostatic stiffness matrix
$[K_{rt}]$	=	Rigid body (6×6) tether stiffness matrix
k_{DI}	=	Stiffness of a SDF system
L	=	Length of the element
l_p	=	Length of pontoon

L_t	=	Length of tethers
L_w	=	Wave length
$\{\lambda_b\}$	=	Eigenvalues in the buckling calculations by subspace iteration
$[M]$	=	Global mass matrix
$[M_{rp}]$	=	Rigid body (6×6) physical mass matrix
$[M_{ra}]$	=	Rigid body (6×6) added mass matrix
M_{acv}	=	Heave added mass of a vertical column
$[M^e_{pl}]$	=	Beam element physical mass matrix in local co-ordinates
$[M^e_{pg}]$	=	Contribution of $[M^e_{pl}]$ in global co-ordinates
$[M^e_{ag}]$	=	Element added mass matrix in global co-ordinates
m_{Dl}	=	Mass of a SDF system
μ_{x_i}	=	Mean of *i*-th design variable
N_s	=	Number of stringers in a TLP column (or cylinder)
n_{wn}	=	Exponent between 7 and 13 for wind velocity calculation
υ	=	Kinematic viscosity
P_f	=	Probability of failure
p_d	=	Dynamic pressure
$P_i(t)$	=	Equivalent force or moment at the ends of a 2D beam
$\overline{P}^{\pm}_{ij}$, $\overline{Q}^{\pm}_{ij}$	=	Normalised even and odd components of second-order forces
Q_a	=	Ratio of the effective area to the actual area
$Q_M(t)$	=	Total Morison force over the whole element length
θ	=	Wave direction with respect to global X axis
θ_t	=	Tether inclination angle with the upright position of the platform
R_{cl}	=	Radius to centreline of shell of a TLP column (or cylinder)
R_o	=	Outside radius of a TLP column (or cylinder)

r	=	Radius of the element
$[RM]$	=	Eulerian transformation matrix
R_e	=	Reynold's number
$R_i(t)$	=	Fixed-end force or moment at the ends of a 2D beam
$R_{y_i}(t)$	=	Fixed-end force or moment at the ends of a 3D beam under the action of external load in the local y direction
ρ	=	Mass density of water (= 1025 kg/m^3)
ρ_a	=	Mass density of air (= 1.203 kg/m^3)
ρ_s	=	Mass density of the structural element
SWL	=	Still water level
σ_{x_i}	=	Standard deviation of *i*-th design variable
t	=	Time
t_s	=	Thickness of shell of a TLP column (or cylinder)
T	=	Wave period
T_0	=	Initial tension or pretension in one corner
$[T_r]$	=	Transformation matrix for element mass and stiffness matrices
$[\hat{T}_r]$	=	Submatrix within $[T_r]$
T_{ii}, δ_{ii}	=	Amplitude and phase of the quadratic transfer function (QTF)
$[\Gamma]$	=	Correlation matrix with coefficients Γ_{ij}
u_p	=	Horizontal instantaneous water particle velocity
u_{pa}	=	Amplitude of u_p
$\dot{u}_p$	=	Horizontal instantaneous water particle acceleration
u_s	=	Velocity of the structure in the context
$\dot{u}_s$	=	Acceleration of the structure in the context
u_{x_w}, u_{y_w}, u_{z_w}	=	Components along wave axes of the normal (to the element axis) velocity
$v(x, t)$	=	Displacement function
V	=	Volume of the element

V_c	=	Current velocity
$V_{z_{wn}}$	=	Wind velocity at the height of interest
$V_{H_{wn}}$	=	Wind velocity at the international reference height
V_{wnt}	=	Total wind velocity
V_{wns}	=	Sustained component of wind velocity
V_{wng}	=	Gust component of wind velocity
v_p	=	Vertical instantaneous water particle velocity
$\dot{v}_p$	=	Vertical instantaneous water particle acceleration
$\{W(t)\}$	=	Global equivalent joint load vector
$\{W^*\}$	=	Modified global equivalent joint load vector
$\{W_A(t)\}$	=	Equivalent joint load vector at the node A
ω	=	Wave circular frequency (= $2\pi/T$)
ω_n	=	Natural frequency
ω_f	=	Forcing frequency
$x_1, x_2, \cdots\cdots, x_n$	=	Actual design variables
$(x_1^*, x_2^*, \cdots\cdots, x_n^*)$	=	The most probable failure point
X_m	=	Model uncertainty factor
X_0	=	Horizontal offset of the platform in global X direction
$\{X\}$	=	Global joint displacement vector
$\{\dot{X}\}$	=	Global joint velocity vector
$\{\ddot{X}\}$	=	Global joint acceleration vector
$\{X_g^e\}$	=	Twelve displacement values at the end-nodes of a beam element in global co-ordinates
$\{X_l^e\}$	=	Twelve displacement values at the end-nodes of a beam element in local co-ordinates
x_{Dl}	=	Displacement of a SDF system
x_{Dlc}	=	Damped free vibration part of x_{Dl}
x_{Dlp}	=	Forced vibration part of x_{Dl}
x_{Dla}	=	Amplitude of x_{Dl}

$\dot{x}_{Dl}$	=	Velocity of a SDF system
$\dot{x}_{Dla}$	=	Amplitude of $\dot{x}_{Dl}$
$\ddot{x}_{Dl}$	=	Acceleration of a SDF system
x_s	=	Displacement of the structure in the context
x, y, z	=	Local Cartesian co-ordinates
x_j, y_j, z_j	=	Midpoint local co-ordinates of the jth. division of the element
X, Y, Z	=	Global Cartesian co-ordinates
x_w, y_w, z_w	=	Wave Cartesian co-ordinates
ξ_d	=	Modal damping ratio
$\{\ddot{X}_r\}$	=	Rigid body (6×1) acceleration
$\{\dot{X}_r\}$	=	Rigid body (6×1) velocity
$\{X_r\}$	=	Rigid body (6×1) displacement
$\{X_{ra}\}$	=	Amplitude of rigid body (6×1) displacement
$\{\dot{X}_{ra}\}$	=	Amplitude of rigid body (6×1) velocity
$y_1, y_2, \cdots\cdots, y_n$	=	Transformed uncorrelated orthogonal variables
ψ_c	=	Angle involving V_c and u_{pa} in the viscous drift calculation due to current
$\psi_i(x)$	=	Shape function
$Y_n'(kr)$	=	Derivative with respect to 'kr' of Bessel function of the second kind and of order n
z_{wn}	=	Height of interest in wind velocity calculation
Z_s	=	Set-down of the platform when away from its upright position
Z_{sm}	=	Safety margin

N.B. Symbols not listed here have local definitions.

CHAPTER 1

INTRODUCTION

1.1 GENERAL

The most accessible and economically attractive offshore oil reserves are already in production. A new generation of petroleum reserves is waiting to be developed in far deeper waters. It is possible for mobile drilling rigs to explore these deep water fields but it is beyond the technical feasibility for traditional fixed production platforms. Moreover, the conventional fixed platforms become progressively expensive with increasing water depths even if they are feasible.

The Tension Leg Platform (TLP) provides a promising solution to the future development of the new deep water reserves. But the TLP technology is still evolving and the offshore industries have just started along the learning curve of how best to implement and use the capabilities of such technology in the near future.

TLPs stand different from other offshore oil production platforms because of their unique characteristics. This motivated the author to start the work which is presented in this thesis. This interest in TLPs finally helped the author in developing some computational tools to assist the TLP designers in future. This thesis illustrates these computational tools along with the associated analysis methodologies. But the author's work does not involve any conventional laboratory experiment primarily because he is interested in engineering software development and thus he devoted his time to numerical modelling and finite element 'experiments'. However, results from numerical modelling have been compared with appropriate experiments done elsewhere if test data are available.

1.2 A FEW WORDS ABOUT TLPS IN SERVICE

TLPs have developed from a scientific concept to a widely accepted engineering solution for deepwater oil and gas field development. The process has been similar to that for most innovations, in that time is needed for confidence to build. A milestone project to investigate the application of a TLP to the offshore energy industry was initiated in 1973. With sponsorship from 17 oil companies the Deep Oil Technology constructed a 635 tonne version (about 1/3 scale) of a triangular TLP. It was successfully tested off the coast of California during 1974 and 1975. This demonstration was important since it helped the industry to assess the validity of the analytical methods used to design the model. The test program showed that oil field equipment and personnel can function effectively on a TLP deck subjected to the test conditions.

The first TLP from Deep Oil Technology is known as TLP-X1. It was on station for a

three month period in 58 m (190 feet) of water on the seaward side of Santa Catalina Island, California. Its design features together with the test program, instrumentation and lessons derived from analysis of the data acquired are described in a magazine article [1.3]. Additional and more extensive tests were carried out in 1978 with an array of risers connected to the seabed.

1.2.1 The Hutton TLP

The Hutton TLP is probably one of the most talked about structures in existence. The Hutton Field was discovered in 1973 but development was deferred because economic prospects were unclear at that time. The oil industry was working to solve the problem of how to produce oil and gas from very deep water by developing sea-floor production systems. Conoco recognised [1.21] that there would still be a need for above-water deck space for machinery and the men to operate and maintain it and the TLP concept would enable operations as much like those on conventional bottom-fixed platforms as possible. In August 1980, the development plan of a TLP production platform was approved by the Hutton license group.

Over one and a half million man-hours of engineering were spent in completing the design of the Hutton TLP. It was a first-of-kind project but the main objective was not innovation but business-as-usual oil production. The project's guiding principle was to err on the side of over- rather than under-design.

The Hutton deck is a grillage of plate girders which span the tops of the columns and provide support for three levels of outfitting. The hull is a six column semisubmersible-like structure providing buoyancy. The tethers are multi-part thick walled drill pipes. They were installed from the mooring tunnels inside the corner columns. There are various publications on different features of the Hutton TLP and it is unnecessary to reproduce them here. However, there will be discussions as appropriate on existing TLPs in service in other sections of this thesis.

1.2.2 The Jolliet TLWP

The Jolliet Tension Leg Wellhead Platform (TLWP) was installed during 1989 in 536 m (1760 feet) water in Green Canyon Block 184 in the Gulf of Mexico. It was the world's deepest production platform before the installation of the Auger TLP. The oil field is about 100 miles from shore on a steep slope where the water depth varies from 275 m to 640 m over the four miles breadth of the Block. As the discovery was being delineated, the perceived centre of the reservoir, the best location for the production platform, kept migrating to deeper water from 427 m initially to 536 m. A major

feature of a TLP is that cost is not very dependent on increasing water depth. The use of a TLP concept in the Jolliet Field allowed this depth change accommodation for optimum platform location in the middle of detailed structural engineering studies without affecting the resulting fabrication and installation schedule.

The Hutton experience was, like many first-of-kind projects, more expensive than planned and perhaps, more conservative than required [1.21]. Even before Hutton was installed research was underway to enable new designs to benefit from the learning curve. Faulkner et al [1.10] were carrying out experiments and analyses of orthogonally stiffened cylindrical shells to support changes in design practices to enable considerable weight and cost benefits. The Jolliet TLWP hull design uses this improved know-how.

One-piece foundation template and twelve one-piece buoyant thin walled tendons with side entry connectors at both the foundation and the hull are the striking features of Jolliet. All the wells were drilled before the TLWP was installed and consequently, there is no drilling riser on Jolliet.

1.2.3 The Snorre TLP

The Snorre Field located on the Norwegian North Sea about 95 miles west of Floro was discovered by Saga Petroleum in 1979. A unique field development plan uses a TLP and a subsea production facility for the first phase of production. The TLP was installed in May 1992 and the installation process involved a series of complex and weather dependent operations [1.27]. The second phase of development may involve relocation of the TLP after 14 years of service.

The steel hull of the Snorre TLP has four columns. The pontoons are square with a bilge radius of 2 metres. The deck configuration employs both trusses and plate girders as required for safety, ventilation and other design issues. The mooring system is a close cousin of the Hutton system, comprising four tethers per corner, installed through mooring tunnels in the columns. But the tethers are partially buoyant, thin walled tubulars. The Snorre TLP is based on four separate concrete foundation templates, installed on the sea-bed in 310 metres of water in the summer of 1991.

1.2.4 The Auger TLP

Shell's Auger TLP was installed in a record breaking 872 m (2860 feet) of water in February 1994. The Field is located on Garden Banks Block 426 in the Gulf of

Mexico. The total development cost for Auger, including TLP fabrication, installation, facilities, pipelines, drilling and well completion is $1.2B [1.8].

The TLP has the capability to support 32 wells, although only 14 wells are anticipated to be drilled initially. The TLP is held on location by a combination of an eight-point lateral mooring system (LMS) and 12 tethers latched into the foundation templates. The unique aspect of Auger centres around the drilling system [1.26]. It has a fixed drilling rig and free standing individual seafloor wellheads. The LMS is used to position the drilling rig over any individual well.

The Auger TLP design is accomplished by a number of computer programs. Shell's TLP_SIZE is one of them which uses a combination of hydrostatic equilibrium, simple storm response analysis and extrapolations from previous designs to establish payload specifications. It does a gross simplification of detailed analyses but it has been found to be an extremely useful tool [1.26] with a fast rate of convergence during conceptual and preliminary design.

The Auger hull consists of four cylindrical columns connected by four rectangular pontoons. The 22.5 m (74 feet) diameter columns are orthogonally stiffened with a 10.4 m (34 feet) inner shell stiffened circumferentially. The pontoons are 8.5 m (28 feet) tall by 10.7 m (35 feet) wide boxes, made up of orthogonally stiffened flat plates. The deck is an open truss design [1.8] covering an approximate area of 8360 m^2.The LMS is an eight-point catenary mooring system comprising 5-inch diameter wire, chain, linear winches, submerged buoys and anchors. The twelve tethers are 0.66 m (26 inch) diameter, 3.3 cm (1.3 inch) thick steel tubulars attached externally on the hull near keel level.

Auger is a learning experience for Shell and other organisations involved. Schott et al [1.26] expect that all experiences with Auger, both negative and positive, would help to reduce the cost and cycle time associated in construction of Shell's second generation Mars TLP.

1.2.5 The Heidrun TLP

The Heidrun TLP is proposed for the Haltenbanken Field in the Norwegian Sea, approximately 175 km off the coast of Mid-Norway in a water depth of 350 m [1.31]. Conoco and Statoil have decided to construct a concrete hull for Heidrun which would make the TLP significantly different from the others in service. The selection of concrete is based on various criteria. The case study [1.31] comparing steel and

concrete hulls shows that a significant difference exists in the maximum tether load for the two types of hull. The steel hull produces 1.5 times greater tether load. The advantages of employing concrete in the hull construction is discussed in Section 1.6.1.

The reduced tether loads on the Heidrun concrete hull are mainly because of the lower overall centre of gravity achieved by its large mass and deep draft. This places the centre of gravity closer to the centre of environmental loading and in turn reduces the platform over-turning moment that must be resisted by the tethers. Like Jolliet, Heidrun is going for 12 one-piece neutrally buoyant tubular steel tethers with wall thickness of 3.8 cm [1.2]. The concrete hull will have four columns of 24.5 m diameter. The pontoons will be square in section with 13.4 m width.

1.3 THE ISSC TLP

It is not possible to explain the analysis methodologies unless a typical TLP configuration is available for numerical modelling. Chapters 3, 4 and 5 present the reliability based hydro-structural design concepts with a 'theoretical TLP' as an example. The model was initially proposed by Boom and Tan [1.5]. They carried out Model tests in the Netherlands Ship Model Basin. Their test results are available both in regular and irregular seas. The same TLP model (see Table 1.1) was chosen by the ISSC Derived Loads Committee I.2 in 1985 for a case study to judge the applicability of different compliant system packages available [1.28]. The TLP model (better known as ISSC TLP) has a relatively simple hull configuration. The configuration came from some elementary design considerations. Details such as cross bracings were left out since they were not expected to produce significant hydrodynamic effects. The platform has symmetry about two orthogonal vertical planes. The square deck is supported by four circular columns which are interconnected by submerged rectangular pontoons (Fig. 1.1).

One main reason behind this selection was to avoid any company specific TLP in service. For validation and complex modelling a general purpose software, LUSAS [1.20] is used in this thesis under an academic research agreement. The author's Department is involved in many other TLP related activities and thus to avoid any confusion regarding the software license, TLPs in service are not selected here for numerical modelling.

The author was initially interested in comparing his results with published ones from various sources. Ref. [1.25] and [1.28] present diffraction/ radiation analysis based

results from 17 organisations. In fact, that is another reason for selecting the ISSC TLP for different numerical demonstrations.

Table 1.1 Particulars of the ISSC TLP [1.28]

Spacing between column centres	86.25 m
Column radius	8.44 m
Pontoon width	7.5 m
Pontoon height	10.5 m
Draft	35.0 m
Displacement	54.5×10^6 kg
Total mass	40.5×10^6 kg
Total tether pretension	137.34 MN
Longitudinal metacentric height	6.00 m
Transverse metacentric height	6.00 m
Roll mass moment of inertia	82.37×10^9 kg m^2
Pitch moment of inertia	82.37×10^9 kg m^2
Yaw moment of inertia	98.07×10^9 kg m^2
Vertical position of CG above keel	38.0 m
Length of mooring tethers	415.0 m
Vertical stiffness of combined tethers	813.0 MN/m
Roll and pitch effective stiffness	1501.0 GN/radian

1.4 CONFIGURATION AND PROPORTIONS

The main reason behind the success of TLPs is the restrained heave motion of the platform which enables drilling and production capabilities similar to those of conventional fixed platforms. The main well flow control valves (i.e. 'christmas tree') can be located at the TLP's deck level. This arrangement is superior to subsea well developments because of its simpler connections from seabed wellheads and convenient well system access. Subsea developments obviously have a place in the deep water areas, but they do not provide a 'catch-all' solution. The budget allocations are much higher for the subsea wells. Oil recovery factors are only 70% of that for platform wells [1.17] and subsea wells are shut sooner because of high maintenance costs.

The TLPs which have been designed to date are for quite different missions and therefore have different dimensions and other features. Some of the characteristics are also different for new innovation and design evolution. But some dominant factors influence all designs in the same way [1.6]. This section presents an account of useful information about these design factors and also provides background which is useful for discussions and relevant explanations in the next chapters of this thesis.

1.4.1 Number of Columns

A TLP hull can be seen as a 'column-stabilised' floating structure, quite similar to the semisubmersible drill rigs. Deep Oil Technology's TLP-X1 was a triangular deck with three columns. But the use of four columns appears to be a firm trend after the installation of the Hutton TLP.

A three column TLP is more difficult to build. The advantage of a three-legged TLP might be in equalising tendon loads without restoring to precise tendon lengths, because it is a determinate structure (like a three-legged stool). However, this feature is not particularly important in deep water since there is enough stretch in the tendons to ensure equalisation if four or more tendon sets are used [1.15].

On very large TLPs it may be desirable to increase the number of columns and provide intermediate supports for the deck truss. If the number of columns in a large TLP is more than four, it will definitely lead to a lighter deck construction but there may not be any savings in the total weight of the platform. The 6-column Hutton TLP is compared with the 4-column Auger TLP to indicate the impact of this approach.

Table 1.2 Effect of Number of Columns on Hull and Deck Weight

Weight in tons	Hutton	Auger
Fixed Payload	11500	11500
Hull Weight	20500	18200
Deck Structure	7500	10000
Hull and Deck	28000	28200

The 'fixed payload' is the same for both TLPs. But the comparison does not show any clear advantage from the standpoint of weight since the hull is heavier but the deck is lighter for more number of columns. However, in this context it should be emphasised that Auger differs significantly from Hutton in a number of ways. Auger has been installed with a more efficient design and better technology whereas Hutton is the first

TLP. Problems arose in many facets of the Hutton project as designers addressed first-of-a-kind components, unfamiliar service requirements and an absence of specific acceptance criteria.

1.4.2 Column Spacing

Column spacing depends on the deck size and the deck design is governed by the equipment layouts and well bay size. A change in column spacing affects a number of important factors.

- Free-floating stability of the TLP during pre-service conditions increases with a greater column spacing.
- An increase in column spacing can reduce the wave peak enhancement under the TLP. This can reduce freeboard because the 'minimum air gap' controls the freeboard requirement.
- A larger column spacing will increase fabrication costs substantially. The weight of the structure will increase with a heavier deck and more expensive pontoons because of their additional length.
- But an optimum column spacing should provide enough clearance between the production risers and the pontoons in order to avoid pontoon-riser interference in extreme storm conditions.
- The construction and installation process can impose limitations on a column spacing decision. The building dock has to accommodate the hull structure within its width. If the hull and deck are to be built separately and joined afloat, column spacing must account for the breadth of a transport barge sufficient to carry the deck.

1.4.3 Column and Pontoon Configuration

To a first order selection of column and pontoon, sizes will be governed by hydrostatic and hydrodynamic principles and not by strength criteria. So the application of the structural codes usually occurs after some preliminary sizing based on hydrodynamics and hydrostatics.

The TLP concept originally evolved from the semisubmersible drilling vessel but TLP column and pontoon proportions have distinctive features. The displacement assigned to the columns is appreciably larger than that of a semisubmersible. Horton et al [1.16] have studied optimum hull proportions for three-column TLPs and shown that the

preferred ratio of column displacement to the total displacement is about 0.7. This ratio turns out to be reasonable for TLPs with other numbers of columns.

Fairly low ratios of the column length to diameter are selected in the present trend of TLP design so that the columns can provide adequate bending and shear strength without diagonal bracing members to provide truss support of the global structure. This also enhances internal and external inspectability and avoids additional complexity of small-to-large member junctions.

The pontoons provide an effective structural tie between the columns at the lower end. The variations in column/pontoon volume ratio have dramatic effects on the tether tension. Grant, et al [1.11] have mentioned that an optimum proportion of column and pontoon would minimise the tether pretension (and thus hull displacement) and the tether design loads, and maximise tether fatigue life. In order to achieve this target, it is important to select a proper ratio of column and pontoon volume which results in an effective cancellation of forces between the two at desired wave periods. Larger pontoons will increase the heave cancellation period and the heave motion response for lower wave periods (also at heave resonance). Pitch motion is also increased. Small pontoons will increase the heave response for higher periods [1.12]. Similar effects were observed by Almeland et al [1.1] in the case of Snorre TLP. A low displacement ratio (pontoon displacement / total displacement) was found to give less tether force for lower wave periods, important for fatigue, while a higher displacement ratio was more favourable for extreme loads. A displacement ratio, close to 0.29, was decided to be the optimum solution for the Snorre TLP. Horton [1.15] also recommends in general, a displacement ratio equal to about 0.3, based on an extensive hydrodynamic analysis.

It is difficult to comment on the choice of pontoon cross-section shape. The pontoons are usually rectangular, constructed of orthogonally stiffened panels with web frames and longitudinal stringers, much like a small tankship hull. But the Jolliet TLWP selected a circular cross section and the Hutton and Snorre TLPs selected a rectangular section with generously rounded corners. The Auger TLP has chosen a sharp-edged square pontoon cross-section. As an argument, it can be said that Auger has lower 'relative design wave height' than the others because it is both a fairly large platform and is to be located in the Gulf of Mexico, where the waves are not as large as in the North Sea. So the hydrodynamics involved, does not impose restrictions on a straight-forward, relatively simpler sharp-edged construction of pontoons.

1.4.4 Tether Pretension

The mooring system of a TLP is a relatively new structural concept, common to all TLP designs and it seems to be the most critical element of the platform. The difference between excess buoyancy and platform weight (i.e. 'pretension') yields a restoring force to resist the steady horizontal environmental forces, thereby limiting offset and setdown. Tethers experience tension variations throughout their design life. But the tether tension must not go beyond the tensile capacity of the tether or drop down to zero as a result of extreme storm waves. So the pretension magnitude is very important. If it is too high, the tethers may reach the maximum limit value and high mean tension is critical for fatigue failures. But if the pretension is too low, the minimum tether tension can drop down to zero due to dynamic response and the tether will be slack. Although momentarily slack tethers do not necessarily produce failure [1.11], the situation is unreliable since the impulsive stresses which follow the slacking can be high and the tether behaviour becomes uncertain and difficult to predict [1.23]. Mercier, et al [1.21] mention that substantial snatch loads for a four-legged TLP will only occur if two adjacent legs are to go slack simultaneously. This may lead to failure and should be avoided. Moreover, some bottom connectors of tethers cannot operate without tension.

So an optimum selection of the tether pretension ratio (total tether pretension / total displacement) is essential. The chosen pretension ratio varies from 0.23 to 0.27 for the first three TLPs to date.

1.4.5 Operational Draft

The choice of operational draft is governed by the maximum and minimum tether tension, maximum offset and minimum wave gap. It is also influenced by structural requirements and pre-service conditions. Increased draft will reduce heave and increase pitch motion when the mass and VCG are fixed [1.12]. In this case the net effect will lead to an increase in the tether tension. Conversely, for the reduced draft the effect of increased heave motion will be higher than the reduction in pitch, and it will again increase dynamic tether tension. If the draft is too small, the pontoons will have insufficient submergence and the tether tension becomes difficult to predict. Operational draft also controls hull steel weight and its centre, thus influencing pre-service draft and stability. Grant et al [1.11] have found that the minimum operational draft that would satisfy in-place performance criteria, should be typically optimum.

1.4.6 Deck Clearance

The minimum air gap or clearance between the deck and a wave crest is an important parameter in the design. The minimum air gap is a result of TLP set down, caused by horizontal offset, and maximum wave crest height. The maximum wave crest height can be found from a detail analysis giving a wave crest enhancement factor (wave height with diffraction effects / wave height) which results from the blockage effect on large TLP columns. Wave asymmetry, column wave run-up and tide must also be taken into account when calculating the total wave crest. The deck clearance has an effect on the vertical position of the centre of gravity and in turn on the maximum and minimum tether tensions. The overturning moment caused by wind forces increases with the deck elevation. Usually a higher deck has adverse effects on tether tension responses.

The designer can either provide a minimum deck clearance or allow for wave impact on portions of the deck, hull or lower appurtenances. In the second choice, the designer must have confidence in the accuracy of the wave crest elevation and the contact should be localised. The deck bottom should be designed for the anticipated local and global wave slamming forces [1.4]. In the present trend of design, usually a minimum deck clearance is preferred. Almeland et al [1.1] reported that the Snorre design criteria required a 1.5 m air gap between the wave crest and the underside of the deck during the 100-year storm event. Both calculations and model tests showed that the wave enhancement factor would be significant, as much as 1.5, for sea states having a peak period of about 12 seconds. So required freeboard for Snorre was set at 27 m.

1.5 PROBLEM AREAS INVOLVED IN A TLP GLOBAL ANALYSIS

The large scale production of papers on elements of TLP analysis is one of the impressive consequences of the TLP innovation. But it is unfortunate that many articles only provide beautiful panel model figures of TLP column/ pontoon nodes and response RAOs. They hardly mention the main assumptions involved in the analysis. A few years back, Shell, Amoco and Exxon undertook analyses of a given TLP configuration to predict maximum and minimum tether tensions in an extreme design storm in the Gulf of Mexico [1.14]. Although the participants had close interactions and in some cases they used the same method of analysis, differences in the results were observed. But detail explanations regarding the underlying assumptions and the causes of variation in the results have made the paper different from many others.

The TLP global analysis is very important in setting the TLP configuration. The method of analysis selected by a designer depends on the availability of computational tools, current stage of design and the degree of accuracy required. At the preliminary level of design, the Morison equation based models can be used but they are generally found to be poor for computing TLP pitch/heave response and it is well accepted that the large diameter, inertia load dominated TLP columns require diffraction effects to be handled adequately. So the first-order wave loads can be calculated based on McCamy-Fuchs theory for the columns and the Morison equation for the pontoons. But for more reliable results, in many cases a hybrid computing model is used which accounts for both diffraction/radiation theory and the Morison equation. This implies that added mass, potential damping and wave drift coefficients are computed by a panel type of linear diffraction/radiation program and then transferred to the Morison program. In many cases it may not be straight-forward to replace or supplement Morison-type hydrodynamic models with data obtained from radiation/diffraction analysis. Natvig, et al [1.22] have explained that they used both a panel and a space frame model for the same TLP hull and had to make use of a special program to transfer all radiation and diffraction data derived from a wetted surface discretisation of the hull to the Morison equation. In this way, the hydrodynamic analysis can account for potential forces as well as viscous forces.

At the early stages of configuration development, frequency domain techniques are usually employed. The most significant limitation of them is that all non-linearities in the equations of motion must be ignored or replaced by linear approximations. However, the frequency domain techniques have the advantage of simplifying the computations and the frequency domain input and output are often more convenient and useful for the designer. But the fully coupled time domain simulation of TLP motions is valuable for determining the maximum offset and tendon tensions due to extreme storm conditions where the linear assumptions break down.

In general, a complete global analysis of a TLP includes many analytical and empirical methods. Some of them are fairly standard but some other may not be well defined and universally accepted methodologies since there is no clear analytical solution. Since they depend on past experience or experimental evidence, they do give some indication of the relative uncertainties involved in the final results. Some recently identified problem areas are discussed below.

1.5.1 Nonlinear Resonant Excitations

Nonlinear resonant excitations have been widely observed in model tests but not yet

easily or well modelled by analytical means. The 'Springing' phenomenon appears to arise from high frequency excitations attributed to nonlinear sum-frequency interactions of the wave frequencies. Second-order hydrodynamic theories establish Quadratic Transfer Functions (QTF) to predict some of these loads but the programs are not readily available and the resulting response is particularly sensitive to damping, causing uncertainties in the results [1.1]. It may be speculated that an increased platform natural period would tend to increase the springing effect on the extreme response, but it would reduce the effect on the fatigue response. This follows from the springing response as seen at the double wave frequency [1.12].

The slowly varying wave drift force covers a wide frequency band. So the high period resonant degrees of freedom, i.e., surge, sway and yaw are excited by the dynamic part of the wave drift. Wind gust forcing is slowly varying and it affects the motion in much the same way as the wave drift but with less effect. The magnitude of the total slowly varying force is generally small, but the damping is usually low because potential damping is virtually zero in the high period range and the viscous drag is also small if there is no current. So the estimation of damping is very important. Due to the contribution of the low frequency resonance, the resulting surge motion is broad banded.

There is another phenomenon, often referred to as 'ringing' which is not yet fully understood and verified. It appears as a transient response in model test data. This excitation is likely to be due to impulsive loadings from large wave crests which are not accounted for by perturbation theories [1.14].

Even the advanced nonlinear second-order diffraction theories can only account for a portion of these nonlinear resonant excitations. So there is a great need for research in this area.

1.5.2 Tethers in Deep Water

Recently, many attempts have been taken to look in some detail at TLP designs for 3000 feet water depth and beyond. With increasing water depth, the current loading on tethers will cause sagging which will reduce the axial stiffness and increase the natural period. In most cases, TLP designers want to keep the natural periods in heave, roll and pitch under four seconds to avoid resonant excitations from the first-order wave loads. If the natural periods are within the wave period range, the fatigue life of tethers becomes more critical. In order to reduce the response at resonance, the natural periods can be reduced by increasing the tether stiffness. So in deep water, the tether

size will be governed by the stiffness requirement rather than the strength and it is this requirement that has limited the use of wire strand in composites as TLP tethers [1.15].

The suspended weight of TLP tethers in very deep water is of such concern that much research and development effort has been expended to create 'near-buoyant' designs. Existing tether designs have achieved this by using large diameter, heavy-walled tubulars that must resist combined hydrostatic and axial loads. Design against collapse in very deep water results in structural elements that can be difficult to fabricate and install.

As water depth increases, the assumption that the tethers can be modelled as linear springs in the hull analysis becomes less accurate. Davies, et al [1.7] have given a method which would result in a more efficient hull design and in significant savings over one based on a customary frequency-domain response analysis model using linear springs. They have suggested a time-domain coupled-model simulation to generate data needed for spring characterisation of the tethers over the entire range of frequencies. With increasing water depth a coupled analysis becomes essential because it is difficult to prescribe sensible boundary conditions at the top of the tethers. These are actually quite complex orbital paths which are strongly influenced by the effects of set-down.

1.5.3 Tether Fatigue

API RP 2T [1.4] recommends that the tether components be designed for a life of 10 times the design service life. This is mainly because of a large amount of uncertainty involved in the tether fatigue which is one of the significant design considerations of TLPs. Tethers have a high mean tension and experience tension variations throughout their design life. In addition, most tethers have welds which have a lower fatigue strength than the base metal. Most designs also incorporate connectors which may result in additional stress concentrations. A TLP in 3000 feet of water with twelve tethers and a connector every 80 feet will have approximately 450 connectors and 900 circumferential butt welds to connect the connectors to the base pipe. If a tether has 100 square inches of cross sectional area and one inch long welds, there will be about 90 thousand cubic inches of weld metal in all the tethers. So large scale testing is the only way to find a fatigue curve and the corresponding scatter band of the weld and connector profiles in the tethers. Fowler, et al [1.9] describes the development of a machine which can test full scale sections of tethers to fatigue loadings similar to those seen in service.

The main innovative features of the Jolliet TLWP can be seen in its twelve one-piece tethers with side-entry connectors at both the foundation and the hull. The results of fatigue and fracture mechanics analyses showed the largest circumferential defect that could be left in the tethers during fabrication was 0.185 inch deep by 1.75 inches long [1.13]. This sized defect could be tolerated by the tethers without failure over the life of the project. The analysis defined a critical size (0.625 inch deep by 5.0 inches long) and if a defect ever grew to this critical size, the tether should be replaced. Hein, et al [1.13] describes the development and the first use of the Jolliet TLWP tether inspection system with a capability of detecting one-half of the originally assumed installed defect size. The results of the inspection show no flaw indication detected in any tether that exceeds the half "trigger" size defect, proving the value of the extra care in the on-land fabrication of the tethers.

But the present trend in design seems to provide a conservative estimate of tether fatigue. Large scale testing and further research should be necessary to eliminate uncertainties in this area.

1.6 FUTURE TRENDS IN DESIGN

Oil from deep water does not command a higher sales price than oil from beneath shallow water or on land. The economics of oil prospects from deep water are less attractive because of the present oil price. But economic challenges often stimulate innovative approaches to enable developments to go ahead. Several researchers and experts are working in various parts of the world to develop new techniques in deep water technology. Quite a number of these researches are related to TLPs since the TLP concept seems feasible for future missions in greater water depths. A few interesting topics are described here.

1.6.1 Concrete TLPs

It is difficult to predict various aspects of the future fleet of TLPs, but it is clear that concrete is gaining more favour as a promising material of construction after the final selection of a concrete TLP on the Heidrun field. A number of advantages offered by concrete, over steel are briefly noted below [1.21], [1.12]:

- Concrete is essentially immune to the marine environment and is almost maintenance free.
- Concrete fabrication processes are well established in ocean industries since twenty or so concrete gravity type platforms have been already installed on the

seabed in the North Sea. A concrete TLP can be built in a similar way.

- The construction time due to the combination of dry dock and inshore slipforming for a concrete TLP is approximately half as compared to a steel unit.
- The concrete version of a steel TLP would have significantly deeper draft and larger displacement. The hydrodynamic responses of a concrete platform are expected to be favoured by designers because of the deep draft and low centre of gravity as indicated in Section 1.2.5.
- A concrete hull results in a simpler design with fewer structural elements and smooth surfaces without the local stiffening found in steel hulls.
- Concrete structures have ample reserve strength against external pressures and adequate fatigue life. Reserve for fatigue is an advantage because of greater uncertainty with welded steel!

So it is expected that concrete is likely to compete more effectively with steel for larger size platforms. But the limiting water depths for tow-out in many locations around the world can be a problem for the development of deep draft concrete TLPs. Hannus et al [1.12] find that the natural periods of a concrete hull are markedly higher than those of the equivalent steel hull. But they show that a concrete hull TLP can have acceptable fatigue life even at natural periods of about 5 seconds. However, this topic needs further investigations with various concrete hull forms.

Conoco and Norwegian Contractors undertook a case study on the feasibility of using floating structures for deep sea oil production in the Norwegian Barents Sea. Karsan et al [1.18] report that initially six potential floating system configurations are identified and finally a five column TLP (four corner columns and one central column for riser protection) is selected by using the Analytical Hierarchy Process for further study. Tension cable fendering system is a new feature of this proposed concrete TLP since the area of interest lies in the Sub-Arctic location of the Northern Barents Sea where interactions with large icebergs and waves are expected. But the TLP would differ significantly from a "No Ice TLP" in terms of costs.

1.6.2 STLP and HRP

A TLP in very deep water means that the tethers must be very long and progressively more expensive. TLP foundations and the tether system will also become more difficult and expensive to install in great water depths. The Single Tension Leg

Platform (STLP) concept came up in order to limit the cost of the mooring system. The STLP has a centrally located tether (or tether cluster) that restricts heave like a conventional TLP but allows compliant response in pitch and roll. The recent Heave-Restrained Platform (HRP) concept goes another step ahead to combine the roles of well risers and tethers. An auxiliary spread mooring plays a key role in stress management for the tie-back components by tightly restricting offsets. A well systems-centred design approach is followed to permit the most effective drilling and production operations [1.30]. Several advantages are claimed for this novel concept :

- Well conductors provide excellent anchor piles for a HRP. They penetrate many times the depth required to secure piles.
- A reduction in deck size is possible because the deck is efficiently supported by the central column. In addition, the riser/tether tensions combine the mooring tensions with riser tensioning duty.
- Dual casing of a riser/tether should be safe to encounter abnormal pressure of fluids in very deep water operations. The outer casing will be there mainly for corrosion and mechanical protection. Moreover, the two casings together can provide enough steel cross sectional area to moor the platform in the heave restrained mode.
- The drilling rig for HRP can be stationary because the lateral mooring system not only limits horizontal motion but also replaces the rig skidding system necessary for bringing the platform vertically over the sea floor well during drilling and workover operations.

But some other crucial factors should be verified to ensure the suitability of the platform.

- The HRP depends even more heavily than the STLP on its spread mooring system to limit platform offset so that large riser angles and moments at the seabed are prevented.
- The HRP configuration is very sensitive to changes in draft with increasing draft beneficial to reducing pitch response.
- Double-walled risers provide a means for safety containing the fluid pressures expected but the resulting heavy riser sections require large riser top-end tension loads that must be accommodated by robust deck structures and additional platform buoyancy.

- Direct wave loading is greatly reduced by the moonpool arrangement but platform pitch and roll motions can impose significant bending moments on the top of the riser/tether strings.

Recently a family of Seastar TLPs have been developed and patented by Atlantia Corporation [1.19]. They come from a similar innovative concept like HRP and STLP. A Seastar TLP will have a single surface-piercing column which results in reduced environmental loading. The construction cost is expected to be low enough to develop marginal fields. The primary reasons for low cost are that it would contain less steel and can be competitively fabricated and installed. Tethers will be attached to three submerged corner columns to suppress all vertical motions like those in conventional TLPs. Perhaps this type of configuration design will offer economical opportunities to develop deepwater oil and gas fields in future.

1.6.3 New Method of Installation

The conventional installation technique controls a TLP configuration in several ways. The installation methods proposed to date, usually rely on using an offshore deck and hull mating operation. The hull-deck mating is done in sheltered sites where water depth is shallow but adequate for this type of operation. The hull is usually ballasted down to deeper draft, leaving minimum freeboard necessary for the deck carrying barge to transfer the load. In this operation, the deck goes from a hogging to a sagging condition and the hull has to withstand heavy hydrostatic pressure for its unusual draft. The mated hull and deck are subsequently towed out to the final installation site. But the mated hull and deck form a top heavy floating structure that requires adequate stability reserve for the tow-out. The stability required in the floating condition controls hull column spacing and diameter. This is important because the free-floating stability requirement in tow-out condition may lead to a TLP configuration which may not be the optimum one for the long-term, in-place conditions. Rajabi et al [1.24] propose a new method of installation that will allow the deck modules to be installed on the Module Support Frame (MSF) of the hull in the final installation site after securing the hull with all tethers.

The new method of installation is particularly suitable in the Gulf of Mexico. The conventional deck-hull mating at an intermediate site may be adversely affected by the narrow weather window in the Gulf of Mexico. The operation requires a costly temporary mooring system which cannot be used readily for other purposes. From a schedule standpoint, any delay in the deck fabrication will postpone the TLP hull deployment timing, resulting in an overall schedule delay. The proposed method of

installation eliminates these deficiencies. It extends the application of heavy lift Semi-Submersible Construction/Crane Vessel (SSCV) for foundation template setting, pile driving, tendon installation, crew accommodation and deck module setting in a cost effective way. But the modular deck approach may require longer hook-up and commissioning time offshore.

1.6.4 Titanium Stress Joint

Before the installation of the Hutton TLP, one significant problem found during the analysis was fatigue at the top and bottom end of the stiff tethers. The utilisation of a flex-joint is a way to accommodate the cyclic load. Nuclear submarines, missiles and bearings on helicopters that make it possible to change pitch of the blades during each rotation, use these joints. All TLP projects to date have adopted this flex-joint solution. Valenzuela [1.29] proposes a replacement of a flex-joint with a titanium stress joint and a collet connector for a number of prospective advantages. The titanium stress joint in the new tether system, has longer and better life than steel and has no moving parts. The collet connector provides easy latching and unlatching capabilities, specially for tether removal. The new solution is less expensive than the existing construction of a flex-joint. However, research is necessary in this field since Valenzuela [1.29] has analysed an isolated case in the Gulf of Mexico.

1.7 REFERENCES

[1.1] Almeland, B., Gaul, T.R., Pettersen, D.J. and Vogel, H.: "Snorre TLP Configuration and Analysis Technology", OTC 6622, 23th Annual Offshore Technology Conference, Houston, pp 577-586, 1991.

[1.2] Anonymous: "Heidrun Field Development Waiting for Go-ahead", Ocean Industry, pp. 53-56, July 1990.

[1.3] Anonymous: "New Platform Begins Offshore Test", The Oil and Gas Journal, pp 59-60, May 1975.

[1.4] API RP 2T : "Recommended Practice for Planning, Designing, and Constructing Tension Leg Platforms", American Petroleum Institute, 1987.

[1.5] Boom, de W.C. and Tan, S.G.: "The Wave Induced Motions of a Tension Leg Platform in Deep Water," OTC 4074, 13th Annual Offshore Technology Conference, Houston, pp. 89-98, 1981.

[1.6] Chatterjee, P.C.: 'Factors Influencing TLP Configuration', Departmental Report (No. NAOE-93-23), Department of Naval Architecture and Ocean Engineering, University of Glasgow, 1993.

[1.7] Davies, K.B. and Mungall, J.C.H.: "Methods for Coupled Analysis of TLP's", OTC 6567, 23th Annual Offshore Technology Conference, Houston, pp 57-68, 1991.

[1.8] Enze, C.R., Brasted, L.K., Arnold, P., Smith, J.S., Breaux, J.N. and Luyties, W.H.: "Auger TLP Design, Fabrication and Installation Overview", OTC 7615, 26th Annual Offshore Technology Conference, Houston, pp 379-387, 1994.

[1.9] Fowler, J.R., Long, J.R. and Albert, J.W.: "Full-Scale Fatigue Testing of TLP Tendons", OTC 6571, 23th Annual Offshore Technology Conference, Houston, pp 103-108, 1991.

[1.10] Faulkner, D., Birrell, N.D. and Stiansen, S.G.: "Development of a Reliability-Based Code for the Structure of Tension Leg Platforms", OTC 4648, 15th Annual Offshore Technology Conference, Houston, 1983.

[1.11] Grant, R.G., Sircar, S. and Nikodym, L.A.: "A Systematic Procedure for Developing Optimum TLP Configurations", OTC 6570, 23th Annual Offshore Technology Conference, Houston, pp 93-101, 1991.

[1.12] Hannus, H.G., Engebretsen, K.B. and Borresen, R.H.: "Concrete TLP's in Water Depths Beyond 3000 ft", OTC 6896, 24th Annual Offshore Technology Conference, Houston, pp 207-215, 1992.

[1.13] Hein, N.W. Jr., Warren, D.H., Saffrhan, R.W.: "Development and First Use of the Jolliet TLWP Tendon Inspection System", OTC 6886, 24th Annual Offshore Technology Conference, Houston, pp 121-128, 1992.

[1.14] Hodges, S.B., Chiu, H. and Kan, W.C.: "A Comparison of Methods for Predicting Extreme TLP Tendon Tensions", OTC 6887, 24th Annual Offshore Technology Conference, Houston, pp 129-138, 1992.

[1.15] Horton, E.: "Develop Configuration", Session 4, TLP Design Technology Seminar, OMAE and Petroleum Divisions of ASME, 1992.

[1.16] Horton, E.E., McCammon, L.B., Murtha, J.P. and Paulling, J.R.: "Optimization of Stable Platform Characteristics", Offshore Technology Conference, Houston, 1972.

[1.17] Hunter, A.: "Selection Process - Technology and Economics", Session 1, TLP Design Technology Seminar, OMAE and Petroleum Divisions of ASME, 1992.

[1.18] Karsan, D.I. and Borreson, R.: "Concrete TLP for Sub-Arctic Conditions", OTC 6569, 23th Annual Offshore Technology Conference, Houston, pp 85-

89, 1991.

[1.19] Kibbee, S.E., Chianis, J., Davies, K.B. and Sarwono, B.A.: "The Seastar Tension-Leg Platform", OTC 7535, 26th Annual Offshore Technology Conference, Houston, pp 243-256, 1994.

[1.20] LUSAS User Manual, Version 11.0, Finite Element Analysis Limited, 66 High Street, Surrey, 1990.

[1.21] Mercier, J.A., Birell, N.D., Chivvis, J.C. and Hunter A.F.: "Tension Leg Platforms - Progress and Prospects", SNAME Transactions, Vol. 99, pp 249-279, 1991.

[1.22] Natvig, B.J., Vogel, H.S. and Johnsen, O.: "TLP Global Motion Performance Analysis Procedures", OTC 6889, 24th Annual Offshore Technology Conference, Houston, pp 147-153, 1992.

[1.23] Prucz, Z. and Soong, T.T.: "Reliability and Safety of Tension Leg Platforms", Engineering Structures, Vol. 6, pp 142-149, 1984.

[1.24] Rajabi, F.D. and Kleinhans, J.W.: "A New Approach for TLP Installation in the Gulf of Mexico", OTC 6900, 24th Annual Offshore Technology Conference, Houston, pp 237-245, 1992.

[1.25] Report of Committee I.2: "Case study of a Tension Leg Platform", Proceedings of the Ninth International Ship and Offshore Structures Congress, Registro Italiano Navale, Genova, Vol. 1, pp. I.2-48-55, 1985.

[1.26] Schott, W.E. (III), Rodenbusch, G., Mercier, R.S. and Webb, C.M.: "Global Design and Analysis of the Auger Tension Leg Platform", OTC 7621, 26th Annual Offshore Technology Conference, Houston, pp 541-552, 1994.

[1.27] Skogvang, A.: "Snorre TLP - Offshore Verification Programme", BPP Seminar on Tensioned Buoyant Platforms, London, 1993.

[1.28] Taylor, R.E. and Jefferys, E.R.: "Variability of Hydrodynamic Load Predictions for a Tension Leg Platform", Ocean Engineering, Vol. 13, No. 5, pp. 449-490, 1986.

[1.29] Valenzuela, E.D.: "Titanium Stress Joint for a TLP Tendon System", OTC 6910, 24th Annual Offshore Technology Conference, Houston, pp 335-341, 1992.

[1.30] White, C.N., Goldsmith, R.G. and Triantafyllou, M.S.: "A TLP Reduces Costs and Eases Operations by "Well Systems-Centered" Design", OTC 6884, 24th Annual Offshore Technology Conference, Houston, pp 97-112,

1992.

[1.31] Wilson, T.J.: "Concrete Versus Steel for Tension Leg Platform Hulls", 5th International Conference on Deep Offshore Technology, Paper B1-f, Marbella, pp 75-89, October 1989.

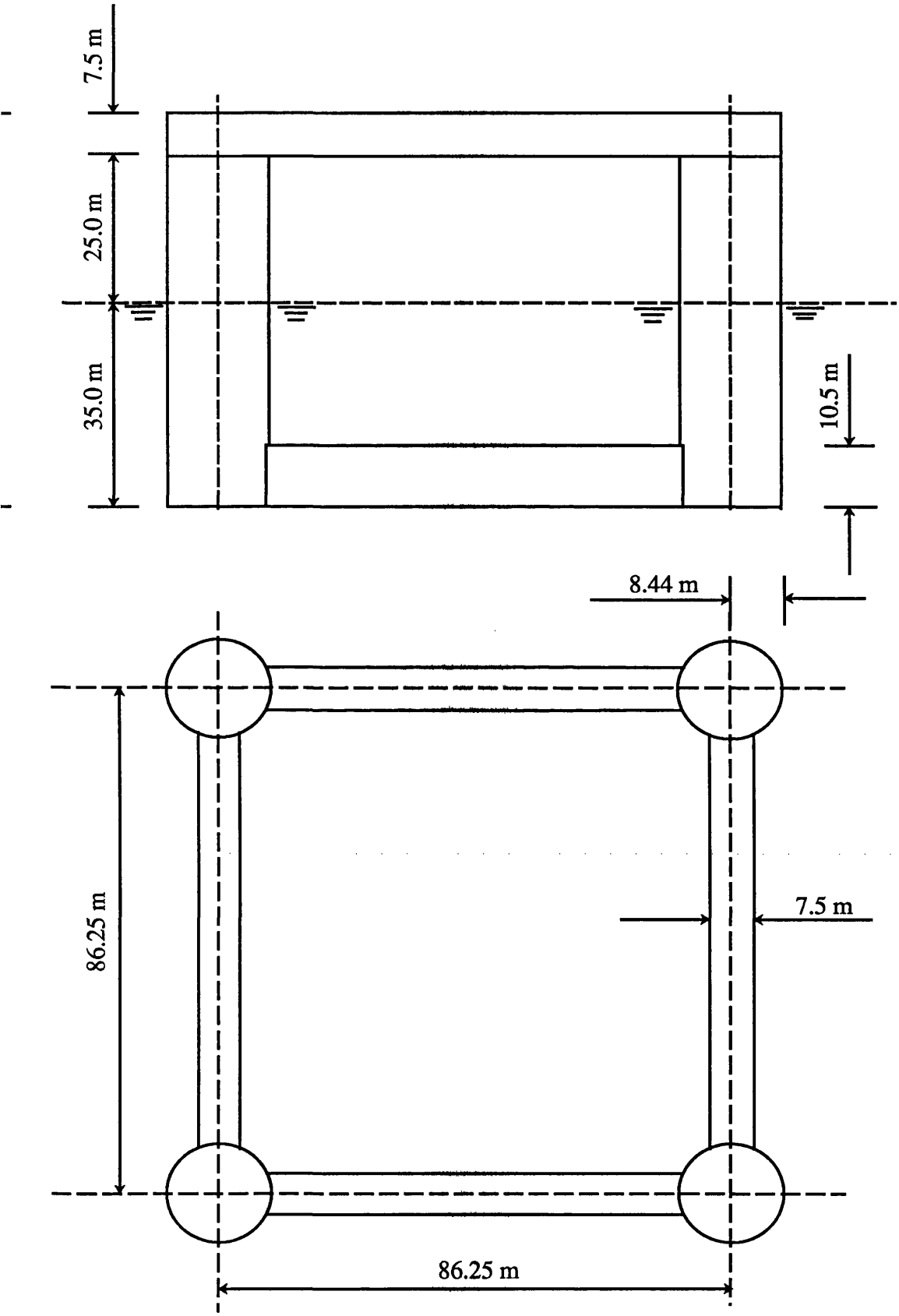

Fig. 1.1. Configuration of ISSC TLP

CHAPTER 2

EQUIVALENT FORCES FROM ENVIRONMENTAL LOADING

2.1 INTRODUCTION

This thesis is not aimed at designing the structural components of the ISSC TLP, described in Chapter 1. Rather I want to demonstrate the importance of a hydro-structural analysis that would help us to start with better scantlings and / or geometry of TLP components in the next design stage. The ISSC TLP will serve as an example in the numerical modelling. But a design process also involves external loading acting on the design structure. Therefore, design environmental conditions in the numerical demonstration are to be set in order to find the capability of the main structural components to withstand most severe combinations of extreme environmental loads.

Unfortunately, several idealisations and assumptions are necessary to model complicated structures as well as external loads in the ocean environment. A space frame type of structure for TLPs is preferred in this work for a number of reasons. Chapters 4 and 6 will discuss them in more detail. A frame type model is relatively simple and computationally efficient but still the environmental loads are to be placed appropriately on its nodes. This chapter deals with the environmental loading scheme and the equivalent load calculations. The contents of this chapter are very general in nature, not specifically for the ISSC TLP.

2.2 SPACE FRAME STRUCTURES

There are various books available, even from the fifties, which deal with framed structures, made up of many elements. In many cases attention is appropriately paid to formulate various matrices relating to framed structures. But when modelling external loads discussions are often limited to concentrated joint loads and uniformly distributed loads. In the case of other types of member loads, the previous trend was to use engineering handbooks. Even today, besides concentrated and uniformly distributed loads, only a few standard types can be handled adequately by general-purpose finite element software. Here it will be shown that a few sets of equations can be derived through algebraic manipulations from member loads of a very general nature acting on three-dimensional beams and the derived equations can be programmed easily for use as a 'black box' later on. This academic exercise is essential because water wave forces do not follow any standard pattern. However, some closed-form expressions are 'achieved' which would offer a number of advantages in the finite element beam analysis. These expressions are certainly capable of minimising computational time since equivalent nodal forces can be immediately calculated in the case of a large element instead of subdividing the element and then summing up individual contributions from each subdivision. In addition, closed-form expressions can be very

helpful to anyone who does not want to get into the complexities in understanding the interaction of offshore structures with the environmental loading.

Before the 'computer age', most constructions used to be idealised by means of a model composed of straight members. For calculation purposes, a structure used to be modelled as a three-dimensional frame with beams interconnected in different ways. So beam elements used to have a wide range of applications. Even today it is very difficult to avoid a space frame formulation of the structural system, especially when global responses are required. A complete finite element model of an offshore structure using higher order, multi-node elements can be time consuming and computationally very expensive. A proper implementation of the boundary conditions can offer a reasonable solution to the problem of calculating structural responses and the stress resultants acting in the members of the structure even when they are modelled as beam elements. The global responses and stress resultant values can be utilised in a local analysis where the structure is modelled in a relatively sophisticated way using complex finite elements. Murotsu et al [2.20] have analysed a complete semi-submersible platform as a three-dimensional framework by the combination of a plastic node method and a matrix method before performing their reliability analysis. Natvig et al [2.21] have described a space frame model of a TLP hull which was specially formulated so that a panel model for radiation and diffraction analysis could be generated directly from that space frame.

2.2.1 Conventional FE Analysis

The conventional analysis of an indeterminate structural system is achieved by superimposing the solution of the restrained structure under the action of applied disturbances, and the solution of the restrained structure for joint displacements. The artificial restraining actions in the structure vanish when a linear function of the solutions for the application of unit values of the possible joint displacements is combined with the solution for the applied loads. However, the combination of these solutions of the restrained structure must yield the true support reactions acting on the indeterminate structure.

Let us consider the dynamic equation of motion for a multiple-degree-of-freedom (MDOF) system:

$$M]\{\ddot{X}\} + [B]\{\dot{X}\} + [K]\{X\} = \{W(t)\} \qquad (2.1)$$

Each element in the joint load matrix, $\{W(t)\}$ may be the sum of two types of joint load: (a) applied joint load and (b) equivalent joint load. Any load applied externally to

a joint or a 'node' of a structure is classified as an applied joint load. The joint actions which result from the loading of the members of the restrained structure along their length are referred to as equivalent joint loads. Since the analysis procedure assumes all joints restrained, the reactions developed at the ends of the members are simply fixed end moments and fixed end shears. The equivalent joint loads appearing at the end of a member are equal in magnitude and opposite in direction to these fixed end moments and shears. In other words, a fixed end moment or shear can be transformed into an equivalent joint load by simply reversing its sign. The fixed end actions for the more common loading conditions of a prismatic member and a few loading conditions of particular non-prismatic beam elements can be found in available engineering handbooks. A general loading on structural members can be converted into equivalent joint loads by one of several techniques of structural mechanics. Here, the Bernoulli-Euler theory is used to obtain closed-form expressions of equivalent joint loads where the structural members are subjected to complicated wave loading.

2.2.2 Shape Functions of Bernoulli-Euler Beams

It is necessary to reproduce the shape functions of a Bernoulli-Euler beam because they will be used extensively in the next sections. In Fig. 2.1, the transverse deflections of a uniform beam element of length L, mass density ρ_s, elastic modulus E, cross-sectional area A and moment of inertia I, are shown. The displacement function is assumed as:

$$v(x,t) = \sum_{i=1}^{4} \psi_i(x) v_i(t) \tag{2.2}$$

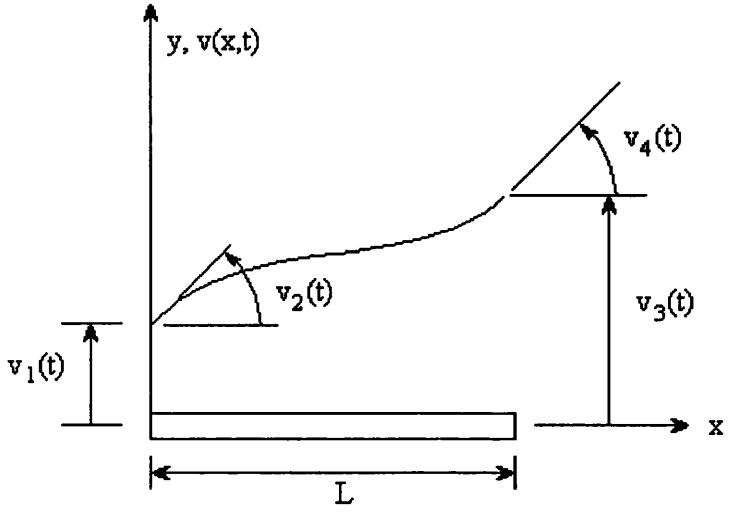

Fig. 2.1. The Transverse Deflections of Bernoulli-Euler Beam

where the shape functions, $\psi_i(x)$ satisfy the following boundary conditions:

$$\psi_1(0) = 1, \quad \psi_1'(0) = \psi_1(L) = \psi_1'(L) = 0 \tag{2.3a}$$

$$\psi_2'(0) = 1, \quad \psi_2(0) = \psi_2(L) = \psi_2'(L) = 0 \tag{2.3b}$$

$$\psi_3(L) = 1, \quad \psi_3(0) = \psi_3'(0) = \psi_3'(L) = 0 \tag{2.3c}$$

$$\psi_4'(L) = 1, \quad \psi_4(0) = \psi_4'(0) = \psi_4(L) = 0 \tag{2.3d}$$

The general solution to Eq.(2.2) for a uniform beam is a cubic polynomial:

$$v(x) = c_1 + c_2\left(\frac{x}{L}\right) + c_3\left(\frac{x}{L}\right)^2 + c_4\left(\frac{x}{L}\right)^3 \tag{2.4}$$

The term (x/L) is used so that all constant terms in the equation will have the same dimensions. Substituting the four sets of boundary conditions in Eqs.(2.3) into Eq.(2.4), the following shape functions are obtained:

$$\psi_1 = 1 - 3\left(\frac{x}{L}\right)^2 + 2\left(\frac{x}{L}\right)^3 \tag{2.5a}$$

$$\psi_2 = x - 2L\left(\frac{x}{L}\right)^2 + L\left(\frac{x}{L}\right)^3 \tag{2.5b}$$

$$\psi_3 = 3\left(\frac{x}{L}\right)^2 - 2\left(\frac{x}{L}\right)^3 \tag{2.5c}$$

$$\psi_4 = -L\left(\frac{x}{L}\right)^2 + L\left(\frac{x}{L}\right)^3 \tag{2.5d}$$

2.3 ANALYTICAL FIRST-ORDER DIFFRACTION FORCE

In diffraction theory, wave forces are calculated from the integration of total water pressure field around a body. The method is appropriate when the body is large relative to the water motion amplitude so that viscous forces are relatively unimportant and the body is sufficiently large relative to the wavelength to modify the wave field through diffraction and radiation. An analytic solution to the linear diffraction problem is possible for a fixed vertical circular cylinder extending from the sea-bed and piercing the free surface. The problem was initially solved by Havelock [2.12] for the deep-water case and extended by MacCamy and Fuchs [2.17] for intermediate depths. A significant practical advantage of the MacCamy and Fuchs' solution is that, while it accounts for the diffraction effects in an analytical form, it can be applied for any ratio of wave length to column diameter [2.2]. Although the solution is valid for a circular cylinder resting on the sea bed, it can be applied with sufficient accuracy in practice for

the calculation of wave inertia forces on floating columns of a platform [2.1]. This analytic solution seems to have a great practical value since 'panel and sources' methods are avoided, although the results are comparable. The equivalent forces on 3-D beams from this analytical diffraction force are derived here and discussed in detail because they are used in Chapter 4 to calculate inertia forces on TLP columns.

According to the MacCamy and Fuchs' theory is , the net force in the direction of wave propagation per unit axial length of the cylinder is given by:

$$f_{MF}(t) = \frac{2\rho g H}{k}\frac{\cosh k(y_w + d)}{\cosh kd}\frac{1}{\sqrt{A(kr)}}\cos(kx_w - \omega t + \alpha_d) \qquad (2.6)$$

where

$$A(kr) = J_1'^2(kr) + Y_1'^2(kr) \qquad (2.7)$$

and

$$\alpha_d = \tan^{-1}\left(\frac{J_1'(kr)}{Y_1'(kr)}\right) \qquad (2.8)$$

The wave axes x_w and y_w are chosen such that x_w is positive in the direction of wave propagation and y_w is positive upward, measured from the SWL. The third wave axis, z_w is the transverse axis in the horizontal plane. If we consider the centre of gravity of the structure as the origin of the global XYZ axes system, and if we fix the origin of the wave axes system on the SWL, directly below or above (depending on the structure under consideration) the CG position (Fig. 2.2), a simple relation can be found between the two axes systems:

$$x_w = X\cos\theta + Y\sin\theta \qquad (2.9)$$

$$y_w = Z \pm h \qquad (2.10)$$

In Fig. 2.2, it is shown that y_w is equal to (Z+h). In the deep-water case we can replace the hyperbolic term in Eq.(2.6) by $\exp(ky_w)$, since:

$$\lim_{d\to\infty}\frac{\cosh k(y_w + d)}{\cosh kd} = \exp(ky_w) \qquad (2.11)$$

Substituting Eq.(2.9), (2.10) and (2.11) into Eq.(2.6):

$$f_{MF}(t) = \frac{2\rho g H}{k}\exp\{k(Z \pm h)\}\frac{1}{\sqrt{A(kr)}}\cos\{k(X\cos\theta + Y\sin\theta) - \omega t + \alpha_d\} \qquad (2.12)$$

So all the terms in Eq.(2.12) are shown in the global co-ordinates. If we define:

$$G_{MF}(t) = \frac{2\rho g H}{k}\exp(\pm kh)\frac{1}{\sqrt{A(kr)}}\cos\{k(X\cos\theta + Y\sin\theta) - \omega t + \alpha_d\} \qquad (2.13)$$

Eq.(2.12) will be simplified because $G_{MF}(t)$ does not depend on the global Z co-ordinates. Thus,

$$f_{MF}(t) = G_{MF}(t)\exp(kZ) \tag{2.14}$$

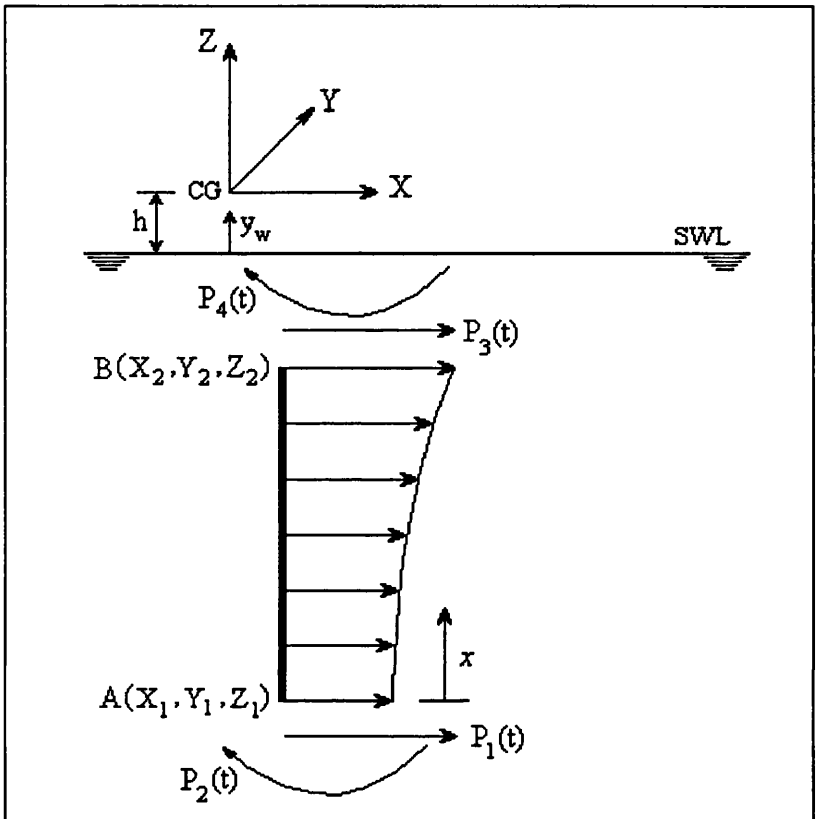

Fig. 2.2. The Global and Local Coordinates of Beam AB

In Fig. 2.2, a portion of a vertical circular cylinder is presented as a beam element. The global Z co-ordinate of the beam has the following relation with its local x co-ordinate:

$$Z = Z_1 + x \quad \text{where} \quad Z_1 \le Z \le Z_2 \tag{2.15}$$

So the net horizontal force per unit length in Eq.(2.14) can be finally written as:

$$f_{MF}(t) = G_{MF}(t)\exp(kZ_1)\exp(kx) \tag{2.16}$$

2.3.1 Equivalent Nodal Diffraction Forces and Moments

For Bernoulli-Euler beams:

$$P_i(t) = \int_0^L f(x,t)\psi_i(x)dx \tag{2.17}$$

To find out the equivalent forces and moments acting at the ends of AB, the following

results are used which can be obtained by applying the method of 'integration by parts':

$$\int_0^L x e^{kx}\,dx = \frac{Le^{kL}}{k} - \frac{e^{kL}}{k^2} + \frac{1}{k^2} \tag{2.18a}$$

$$\int_0^L x^2 e^{kx}\,dx = \frac{L^2e^{kL}}{k} - \frac{2Le^{kL}}{k^2} + \frac{2e^{kL}}{k^3} - \frac{2}{k^3} \tag{2.18b}$$

$$\int_0^L x^3 e^{kx}\,dx = \frac{L^3e^{kL}}{k} - \frac{3L^2e^{kL}}{k^2} + \frac{6Le^{kL}}{k^3} - \frac{6e^{kL}}{k^4} + \frac{6}{k^4} \tag{2.18c}$$

$P_1(t)$ is found by substituting Eq.(2.16) and (2.5a) into Eq.(2.17):

$$P_1(t) = \int_0^L G_{MF}(t)\exp(kZ_1)\exp(kx)\left[1 - 3\left(\frac{x}{L}\right)^2 + 2\left(\frac{x}{L}\right)^3\right]dx \tag{2.19}$$

After simplification,

$$P_1(t) = G_{MF}(t)\exp(kZ_1)\left[\int_0^L e^{kx}\,dx - \frac{3}{L^2}\int_0^L x^2e^{kx}\,dx + \frac{2}{L^3}\int_0^L x^3e^{kx}\,dx\right] \tag{2.20}$$

The results from Eqs.(2.18) are substituted into Eq.(2.20). Thus,

$$P_1(t) = G_{MF}(t)\exp(kZ_1)\left[\frac{6}{L^2k^3}\left(e^{kL}+1\right) - \frac{12}{L^3k^4}\left(e^{kL}-1\right) - \frac{1}{k}\right] \tag{2.21a}$$

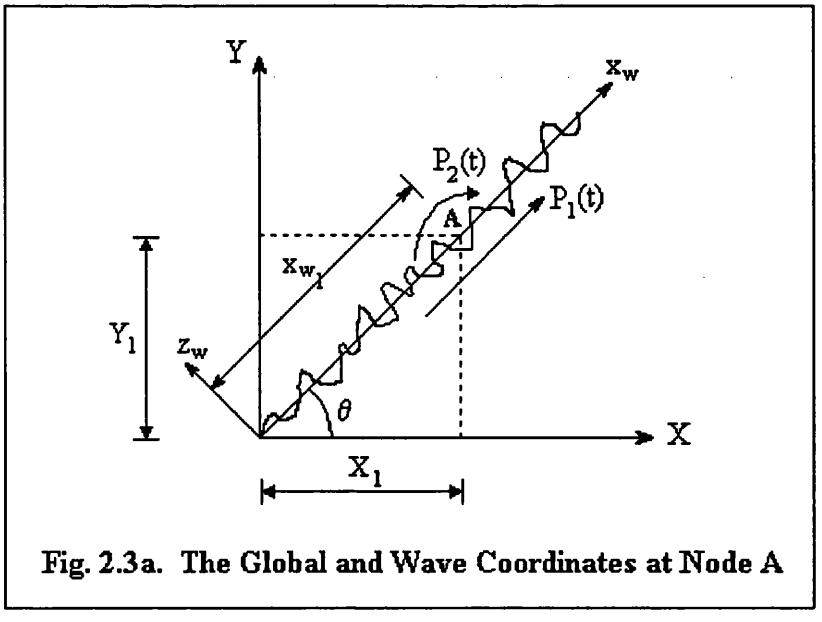

Fig. 2.3a. The Global and Wave Coordinates at Node A

Eq.(2.21a) is the closed-form expression for the equivalent shear force acting at the node A of the beam element. Similarly, the other three equivalent forces are found:

$$P_2(t) = G_{MF}(t)\exp(kZ_1)\left[\frac{2}{Lk^3}\left(e^{kL}+2\right) - \frac{6}{L^2k^4}\left(e^{kL}-1\right) + \frac{1}{k^2}\right] \quad (2.21b)$$

$$P_3(t) = G_{MF}(t)\exp(kZ_1)\left[-\frac{6}{L^2k^3}\left(e^{kL}+1\right) + \frac{12}{L^3k^4}\left(e^{kL}-1\right) + \frac{e^{kL}}{k}\right] \quad (2.21c)$$

$$P_4(t) = G_{MF}(t)\exp(kZ_1)\left[\frac{2}{Lk^3}\left(2e^{kL}+1\right) - \frac{6}{L^2k^4}\left(e^{kL}-1\right) - \frac{e^{kL}}{k^2}\right] \quad (2.21d)$$

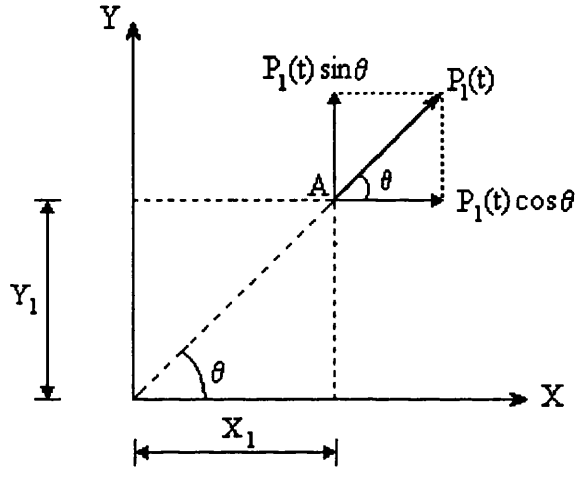

Fig. 2.3b. The Global Components of Equivalent Nodal Force at A

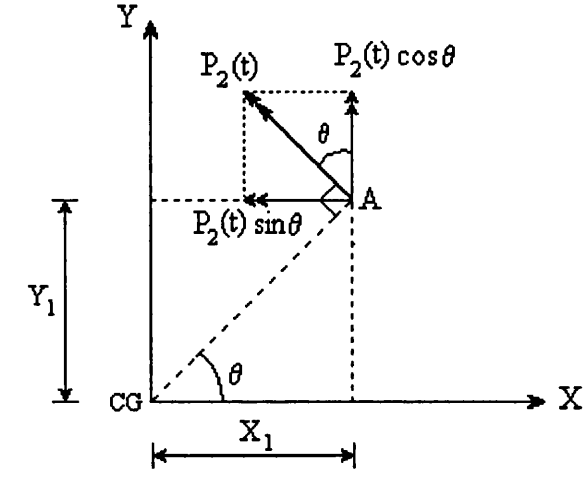

Fig. 2.3c. The Global Components of Equivalent Nodal Moment at A

The equivalent global load vector, {W(t)}is formed from Figs. 2.3:

$$\{W_A(t)\} = \begin{Bmatrix} P_1(t)\cos\theta \\ P_1(t)\sin\theta \\ 0 \\ -P_2(t)\sin\theta \\ P_2(t)\cos\theta \\ 0 \end{Bmatrix} \tag{2.22a}$$

Figs. 2.3 explain the situation at the node A. But $\{W_B(t)\}$ is formulated easily by replacing $P_1(t)$ and $P_2(t)$ by $P_3(t)$ and $P_4(t)$, respectively in Eq.(2.22a).

$$\{W_B(t)\} = \begin{Bmatrix} P_3(t)\cos\theta \\ P_3(t)\sin\theta \\ 0 \\ -P_4(t)\sin\theta \\ P_4(t)\cos\theta \\ 0 \end{Bmatrix} \tag{2.22b}$$

The global joint load vector $\{W(t)\}$ is generated by summing the contributions from each node.

2.4 REVISED FORM OF MORISON EQUATION

The Morison equation was developed by Morison, O'Brien, Johnson and Schaaf [2.19] for describing the horizontal wave forces acting on a vertical pile which extends from the seabed through the free surface. When the characteristic dimensions of the submerged structures are less than 20% of the wave length under consideration, diffraction effects become unimportant. So this most widely accepted approach to the calculation of wave forces can be used which is based on the assumption that the wave force can be expressed as the linear sum of a drag force, due to the velocity of the water flowing past the structure, and an inertia force, due to the acceleration of water. The standard form of Morison equation assumes that the structure, which is experiencing the forces, is rigid.

$$f_{MI}(t) + f_{MD}(t) = C_m\rho A\dot{u}_p + \tfrac{1}{2}C_D\rho D|u_p|u_p \tag{2.23}$$

However, if the structure has a dynamic response or is a part of a floating body, its induced motions may be significant when compared with the water particle velocities and accelerations. A compliant structure like a TLP is free to move in waves. In these cases, the following form of the Morison equation can be used to account for the structural movement:

$$f_{MI}(t) + f_{MD}(t) = C_m\rho A\dot{u}_p - C_a\rho A\dot{u}_s + \tfrac{1}{2}C_D\rho D|u_p|u_p - \tfrac{1}{2}C'_D\rho D|u_s|u_s \tag{2.24}$$

This form is known as the independent flow fields model and is obtained as the linear superposition of two independent flow fields, a far field due to the wave motion and relatively unaffected by the structure motion and a near field resulting from the structure motion. The values of C_m and C_D may be obtained from wave experiments while the coefficients C_a and C'_D are derived from the experiments of oscillating cylinder in calm water.

There is another way of writing the forces in terms of relative motion and single coefficients can be assumed to apply:

$$f_{MI}(t) + f_{MD}(t) = C_m\rho A(\dot{u}_p - \dot{u}_s) + \rho A\dot{u}_s + \tfrac{1}{2}C_D\rho D|u_p - u_s|(u_p - u_s) \quad (2.25)$$

This relative velocity model needs two coefficients less to determine than in Eq.(2.24). It has been extensively used in the past to evaluate stochastic dynamic response of offshore platforms [2.5].

Sometimes it is convenient to separate the inertia coefficient from the added mass term specially when they come from the diffraction-radiation theory. Therefore, a third alternative form of the modified Morison equation is:

$$f_{MI}(t) + f_{MD}(t) = C_m\rho A\dot{u}_p - C_a\rho A\dot{u}_s + \tfrac{1}{2}C_D\rho D|u_p - u_s|(u_p - u_s) \quad (2.26)$$

It is difficult to compare the appropriateness of the equations given above because the original Morison equation is empirical. Obviously the coefficients derived from one of these formulations can be justifiably used in the application of that form only.

Chapter 3 describes the results from a program RBRA (Rigid Body Response Analysis) where as Chapter 4 deals with DCATLP (Dynamic Coupled Analysis of Tension Leg Platforms). The Morison equation based RBRA originated from the initial phase of the author's work and quite simplified in nature. RBRA cannot handle equations where the structural motions and wave particle velocities are coupled. Therefore, it is necessary to simplify Eq.(2.26) for RBRA. However, DCATLP operates in time domain and calculates the wave-current-motion interaction force which is discussed in Section 2.7.2.

The following approximation was first used by Tasai, et al [2.29]:

$$\tfrac{1}{2}C_D\rho D|u_p - u_s|(u_p - u_s) + \tfrac{1}{2}C_D\rho D|u_s|u_s = \tfrac{1}{2}C_D\rho D|u_p|u_p \quad (2.27)$$

This approximation has an important consequence. It allows the calculation of wave forces based on water particle kinematics only. Referring to Eq.(2.1), the structural contributions can be handled separately. This simplification is used in RBRA and

described in Chapter 3.

2.4.1 Inertia Forces on a Vertical Cylinder

As indicated earlier, DCATLP in Chapter 4 calculates inertia forces from the MacCamy and Fuchs' theory but RBRA in Chapter 3 is based on the Morison equation only. Hence, it is necessary to find the equivalent forces for $f_{MI}(t)$ too.

Based on Airy's linear wave theory, the net inertia force in the direction of wave propagation per unit axial length of a vertical cylinder can be written as:

$$f_{MI}(t) = \tfrac{1}{2}C_m\rho gAHk\exp(ky_w)\sin(kx_w - \omega t) \qquad (2.28)$$

Eq.(2.9) and (2.10) can replace the terms involving the wave axis system.

$$f_{MI}(t) = \tfrac{1}{2}C_m\rho gAHk\exp\{k(Z \pm h)\}\sin\{k(X\cos\theta + Y\sin\theta) - \omega t\} \qquad (2.29)$$

If we again define:

$$G_{MI}(t) = \tfrac{1}{2}C_m\rho gAHk\exp(\pm kh)\sin\{k(X\cos\theta + Y\sin\theta) - \omega t\} \qquad (2.30)$$

then the terms in Eq.(2.29) which are independent of the global Z co-ordinate, can be isolated. Thus,

$$f_{MI}(t) = G_{MI}(t)\exp(kZ) \qquad (2.31)$$

Eq.(2.31) is identical to Eq.(2.14). Therefore, from the similarity, we can write directly the closed-form expressions of the equivalent nodal forces acting at the nodes of the beam element which is presenting the vertical cylinder submerged in water.

$$P_1(t) = G_{MI}(t)\exp(kZ_1)\left[\frac{6}{L^2k^3}\left(e^{kL}+1\right) - \frac{12}{L^3k^4}\left(e^{kL}-1\right) - \frac{1}{k}\right] \qquad (2.32a)$$

$$P_2(t) = G_{MI}(t)\exp(kZ_1)\left[\frac{2}{Lk^3}\left(e^{kL}+2\right) - \frac{6}{L^2k^4}\left(e^{kL}-1\right) + \frac{1}{k^2}\right] \qquad (2.32b)$$

$$P_3(t) = G_{MI}(t)\exp(kZ_1)\left[-\frac{6}{L^2k^3}\left(e^{kL}+1\right) + \frac{12}{L^3k^4}\left(e^{kL}-1\right) + \frac{e^{kL}}{k}\right] \qquad (2.32c)$$

$$P_4(t) = G_{MI}(t)\exp(kZ_1)\left[\frac{2}{Lk^3}\left(2e^{kL}+1\right) - \frac{6}{L^2k^4}\left(e^{kL}-1\right) - \frac{e^{kL}}{k^2}\right] \qquad (2.32d)$$

The joint load vectors $\{W_A(t)\}$ and $\{W_B(t)\}$ can be found straight from Eqs.(2.22).

2.4.2 Drag Forces on a Vertical Cylinder

If the structural velocity terms are uncoupled from water particle velocities, as

explained earlier, it is possible to find similar closed-form expressions for the equivalent nodal forces, even in the case of velocity squared non-linear drag forces acting on a vertical cylinder. Based on Airy's linear wave theory and from Eqs.(2.26) and (2.27):

$$f_{MD}(t) = \pm\tfrac{1}{8}C_D\rho gDH^2k\exp(2ky_w)\cos^2(kx_w - \omega t) \qquad (2.33)$$

The sign of Eq.(2.33) is the same as the sign of $\cos(kx_w - \omega t)$. In other words, if $\cos(kx_w - \omega t)$ is positive, $f_{MD}(t)$ will be positive. Eq.(2.33) is now written in the global co-ordinate format, using Eqs.(2.9) and (2.10)

$$f_{MD}(t) = \pm\tfrac{1}{8}C_D\rho gDH^2k\exp\{2k(Z \pm h)\}\cos^2\{k(X\cos\theta + Y\sin\theta) - \omega t\} \qquad (2.34)$$

For a vertical cylinder, the global X and Y co-ordinates are constant throughout its length. So almost all the terms in Eq.(2.34) do not depend on the global Z co-ordinate. If we again define:

$$G_{MD}(t) = \pm\tfrac{1}{8}C_D\rho gDH^2k\exp(\pm 2kh)\cos^2\{k(X\cos\theta + Y\sin\theta) - \omega t\} \qquad (2.35)$$

Eq.(2.34) takes up a simple form:

$$f_{MD}(t) = G_{MD}(t)\exp(2kZ) \qquad (2.36)$$

Eq.(2.36) is very similar to Eq.(2.31) and it is possible to take advantage of this similarity by replacing 'k' by '2k' in Eqs.(2.32) so that the closed-form expressions are obtained directly without involving integration.

$$P_1(t) = G_{MD}(t)\exp(2kZ_1)\left[\frac{3}{4L^2k^3}\left(e^{2kL}+1\right) - \frac{3}{4L^3k^4}\left(e^{2kL}-1\right) - \frac{1}{2k}\right] \qquad (2.37a)$$

$$P_2(t) = G_{MD}(t)\exp(2kZ_1)\left[\frac{1}{4Lk^3}\left(e^{2kL}+2\right) - \frac{3}{8L^2k^4}\left(e^{2kL}-1\right) + \frac{1}{4k^2}\right] \qquad (2.37b)$$

$$P_3(t) = G_{MD}(t)\exp(2kZ_1)\left[-\frac{3}{4L^2k^3}\left(e^{2kL}+1\right) + \frac{3}{4L^3k^4}\left(e^{2kL}-1\right) + \frac{e^{2kL}}{2k}\right] \qquad (2.37c)$$

$$P_4(t) = G_{MD}(t)\exp(2kZ_1)\left[\frac{1}{4Lk^3}\left(2e^{2kL}+1\right) - \frac{3}{8L^2k^4}\left(e^{2kL}-1\right) - \frac{e^{2kL}}{4k^2}\right] \qquad (2.37d)$$

2.5 A GENERAL APPROACH TO COMPLICATED MEMBER LOADS ON BEAMS

In this section a general way of handling complicated member loads on a beam element, arbitrarily oriented in space, is discussed. It is not possible to find the closed-form expressions of equivalent nodal vector in the most general case. But the following approach may offer a better understanding to the problem.

The beam element AB in Fig. 2.4 is divided into N equal parts. The equivalent load vector is found by superimposing the contributions of external loads acting on each division of the beam.

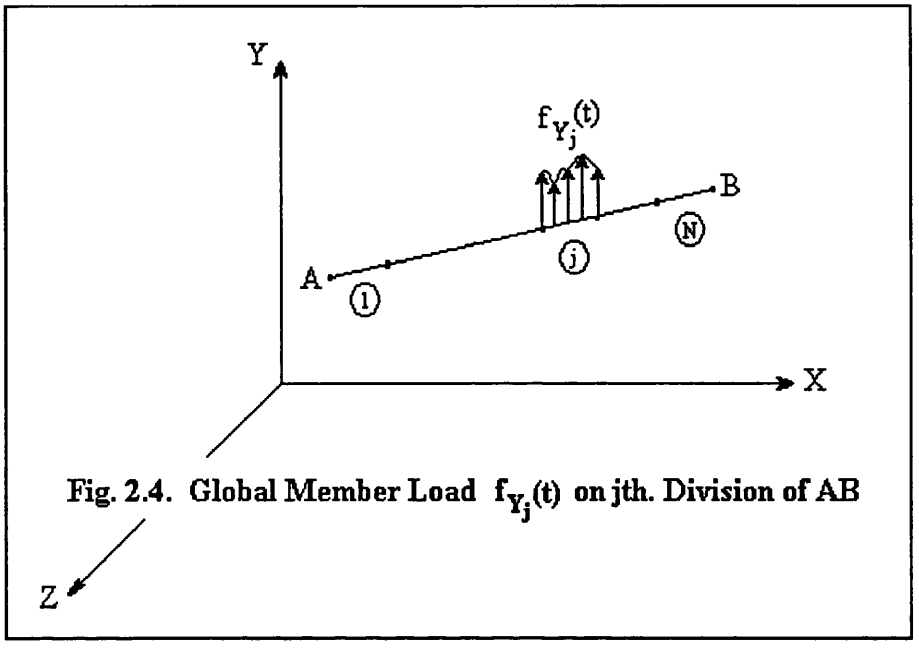

Fig. 2.4. Global Member Load $f_{Y_j}(t)$ on jth. Division of AB

Let us consider the local co-ordinates of the midpoint of the jth. division,

$$x_j = (j-1)\frac{L}{N} + \frac{1}{2}\frac{L}{N} = (j-\frac{1}{2})\frac{L}{N} \tag{2.38a}$$

$$y_j = 0 \tag{2.38b}$$

$$z_j = 0 \tag{2.38c}$$

The corresponding global co-ordinates are:

$$X_j = X_1 + \frac{(X_2 - X_1)(j-\frac{1}{2})}{N} \tag{2.39a}$$

$$Y_j = Y_1 + \frac{(Y_2 - Y_1)(j-\frac{1}{2})}{N} \tag{2.39b}$$

$$Z_j = Z_1 + \frac{(Z_2 - Z_1)(j-\frac{1}{2})}{N} \tag{2.39c}$$

The next step is to calculate the external load per unit length in the global X, Y and Z directions. It may be simple to specify the member load per unit length in the global directions in most cases but the computation is certainly difficult when ocean-wave forces on an offshore structure are under consideration. In the following section, an extension of the Morison equation is used to demonstrate the calculation involved to specify member load in the global directions.

2.5.1 Wave Forces on an Inclined Member

The formulation for an inclined cylinder [2.3] is based on the so-called independence principle. It states that the forces on the inclined cylinder can be decomposed into their normal and tangential components and the tangential component can be neglected. However, noting that the water particle motion in waves is orbital, the original Morison equation also neglects the tangential component of force on the vertical cylinder.

Using vector algebra, at first, the component of horizontal and vertical water particle velocities is found which is normal to the axis of the cylinder. This normal velocity component is then divided into three parts along the wave x_w, y_w, and z_w directions.

$$u_{x_w} = u_p - C_{x_w}(C_{x_w}u_p + C_{y_w}v_p) \tag{2.40a}$$

$$u_{y_w} = v_p - C_{y_w}(C_{x_w}u_p + C_{y_w}v_p) \tag{2.40b}$$

$$u_{z_w} = -C_{z_w}(C_{x_w}u_p + C_{y_w}v_p) \tag{2.40c}$$

The acceleration components along x_w, y_w, and z_w are obtained by differentiating Eqs.(2.40) with respect to time. The direction cosines in wave co-ordinates are to be calculated. It is better to find their relationship with the direction cosines in the global co-ordinates. From Fig. 2.4,

$$C_X = \frac{X_2 - X_1}{L} \tag{2.41a}$$

$$C_Y = \frac{Y_2 - Y_1}{L} \tag{2.41b}$$

$$C_Z = \frac{Z_2 - Z_1}{L} \tag{2.41c}$$

From Figs. 2.2 and 2.3a and with the help of Eq.(2.9) and (2.10):

$$C_{x_w} = C_X\cos\theta + C_Y\sin\theta \tag{2.42a}$$

$$C_{y_w} = C_Z \tag{2.42b}$$

$$C_{z_w} = C_Y\cos\theta - C_X\sin\theta \tag{2.42c}$$

Now the forces per unit length on a randomly oriented cylinder are calculated in the wave co-ordinate system from the following expressions:

$$f_{Mx_w}(t) = C_m\rho A\dot{u}_{x_w} + \tfrac{1}{2}C_D\rho D u_{x_w}\sqrt{u_{x_w}^2 + u_{y_w}^2 + u_{z_w}^2} \tag{2.43a}$$

$$f_{My_w}(t) = C_m\rho A\dot{u}_{y_w} + \tfrac{1}{2}C_D\rho D u_{y_w}\sqrt{u_{x_w}^2 + u_{y_w}^2 + u_{z_w}^2} \qquad (2.43b)$$

$$f_{Mz_w}(t) = C_m\rho A\dot{u}_{z_w} + \tfrac{1}{2}C_D\rho D u_{z_w}\sqrt{u_{x_w}^2 + u_{y_w}^2 + u_{z_w}^2} \qquad (2.43c)$$

Finally the hydrodynamic load per unit length in the global X, Y and Z directions can be found from the following interrelation:

$$f_{MX}(t) = f_{Mx_w}(t)\cos\theta - f_{Mz_w}(t)\sin\theta \qquad (2.44a)$$

$$f_{MY}(t) = f_{Mx_w}(t)\sin\theta + f_{Mz_w}(t)\cos\theta \qquad (2.44b)$$

$$f_{MZ}(t) = f_{My_w}(t) \qquad (2.44c)$$

2.5.2 Equivalent Joint Load Vector

In Section 2.5.1, $f_{MX}(t)$, $f_{MY}(t)$ and $f_{MZ}(t)$ are established as an example of member load components in the global axes system. It may be possible to specify member load directly or in a relatively easier way in other cases. But in the next step, it will be necessary to calculate the components of these forces in the local axes system. Harrison [2.11] has given the relations between two sets of concurrent orthogonal forces in equilibrium in matrix format. According to this Eulerian method, the force transformation matrix can be written as:

$$[RM] = \begin{bmatrix} -\cos\alpha_E\cos\beta_E & \sin\alpha_E\cos\gamma_E - \cos\alpha_E\sin\beta_E\sin\gamma_E & -\sin\alpha_E\sin\gamma_E - \cos\alpha_E\sin\beta_E\cos\gamma_E \\ -\sin\alpha_E\cos\beta_E & -\cos\alpha_E\cos\gamma_E - \sin\alpha_E\sin\beta_E\sin\gamma_E & \cos\alpha_E\sin\alpha_E - \sin\alpha_E\sin\beta_E\cos\gamma_E \\ \sin\beta_E & -\cos\beta_E\sin\gamma_E & -\cos\beta_E\cos\gamma_E \end{bmatrix} \qquad (2.45)$$

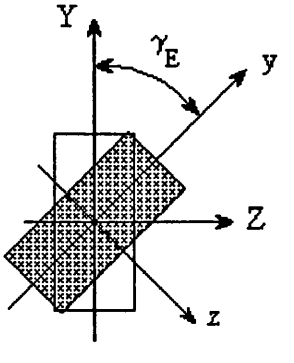

Fig. 2.5. The Rotational Angle γ_E about X Axis

The Eulerian transformation represented by the three rotations α_E, β_E and γ_E is the

most convenient way of dealing with the resolution of forces and moments in three dimensions. In visualising these rotations, one imagines that the global co-ordinate system has been moved to coincide with the end A of the beam element, AB. The sequence of rotations of α_E about the Z axis, then β_E about the Y axis and finally γ_E about the X axis are what is done to make the global co-ordinate system coincide with the local system. The final rotation γ is relevant only to members such as that in Fig. 2.5, which otherwise would not be bent about principal axes by the end moments. The angle γ_E is, in fact, the only one of the three angles needs to be given as an input. The other angles are evaluated from the element projections. So the coefficients in the matrix [RM] can be rewritten as:

$$RM(1,1) = \frac{-(X_2 - X_1)}{L} \tag{2.46a}$$

$$RM(2,1) = \frac{-(Y_2 - Y_1)}{L} \tag{2.46b}$$

$$RM(3,1) = \frac{-(Z_2 - Z_1)}{L} \tag{2.46c}$$

$$RM(1,2) = \frac{-(Y_2 - Y_1)\cos\gamma}{L_1} + \frac{(X_2 - X_1)(Z_2 - Z_1)\sin\gamma}{LL_1} \tag{2.46d}$$

$$RM(2,2) = \frac{-(X_2 - X_1)\cos\gamma}{L_1} + \frac{(Y_2 - Y_1)(Z_2 - Z_1)\sin\gamma}{LL_1} \tag{2.46e}$$

$$RM(3,2) = \frac{-L_1\sin\gamma}{L} \tag{2.46f}$$

$$RM(1,3) = \frac{-(Y_2 - Y_1)\sin\gamma}{L_1} + \frac{(X_2 - X_1)(Z_2 - Z_1)\cos\gamma}{LL_1} \tag{2.46g}$$

$$RM(2,3) = \frac{(X_2 - X_1)\sin\gamma}{L_1} + \frac{(Y_2 - Y_1)(Z_2 - Z_1)\cos\gamma}{LL_1} \tag{2.46h}$$

$$RM(3,3) = \frac{-L_1\cos\gamma}{L} \tag{2.46i}$$

With the help of [RM], it is possible to calculate the components of $f_X(t)$, $f_Y(t)$ and $f_Z(t)$ in the local axes. But Eq.(2.45) is actually the relationship between member-end actions and the external nodal loads. They are rather against each other to keep the equilibrium at the node. So a negative sign appears in the following equation:

$$\begin{Bmatrix} f_x(t) \\ f_y(t) \\ f_z(t) \end{Bmatrix} = -[RM]^{-1} \begin{Bmatrix} f_X(t) \\ f_Y(t) \\ f_Z(t) \end{Bmatrix} \tag{2.47}$$

In Fig. 2.6, a classic case is considered where a uniformly distributed load, f(t) of length c is acting on a beam element of length L, at a distance (=a) from the node A. The four fixed end reactions can be found from a standard engineering handbook:

$$R_1(t) = \frac{f(t)cb}{L} + \frac{\{R_2(t)+R_4(t)\}}{L} \tag{2.48a}$$

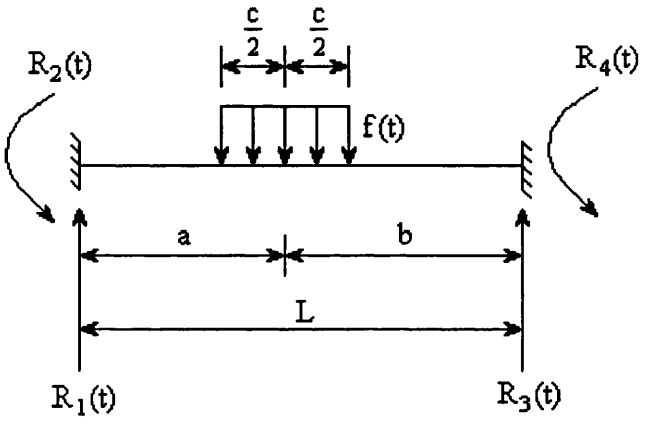

Fig. 2.6. Fixed-end Forces from UDL of Length c

$$R_2(t) = \frac{f(t)c}{12L^2}[c^2(L-3b)+12ab^2] \tag{2.48b}$$

$$R_3(t) = \frac{f(t)ca}{L} - \frac{\{R_2(t)+R_4(t)\}}{L} \tag{2.48c}$$

$$R_4(t) = -\frac{f(t)c}{12L^2}[c^2(L-3a)+12a^2b] \tag{2.48d}$$

If member loads per unit length acting at the midpoint of any division are approximated as uniform load over the division, a reasonable solution can be achieved with the help of Eqs.(2.48). The accuracy will depend on the number of divisions and the element length. Fig. 2.6 describes a two-dimensional case. In the case of a three-dimensional beam, arbitrarily oriented in space, the law of superposition will be assumed to formulate the twelve fixed-end reactions. The standard results from Eqs.(2.48) can be used in both local x-y and x-z planes. Let us use a subscript 'j' to specify the three member load components in Eq.(2.47), acting at the midpoint of the jth. division of the beam element. From Eq.(2.38) and Fig. 2.6:

$$a = (j-\frac{1}{2})\frac{L}{N},\ b = \frac{(N-j+\frac{1}{2})L}{N},\ c = \frac{L}{N} \tag{2.49}$$

The reactions corresponding to the member load component, $f_{y_j}(t)$ in the local y

direction are found by substituting Eq.(2.49) into Eqs.(2.48).

$$R_{y_1}(t) = \frac{f_{y_j}(t)(N-j+\frac{1}{2})L}{N^2}$$

$$+\frac{f_{y_j}(t)L}{4N^4}\{1-4(j-\tfrac{1}{2})(N-j+\tfrac{1}{2})\}(2j-N-1) \qquad (2.50a)$$

$$R_{y_2}(t) = \frac{f_{y_j}(t)L^2}{12N^4}\{N-3(N-j+\tfrac{1}{2}) + 12(N-j+\tfrac{1}{2})^2(j-\tfrac{1}{2})\} \qquad (2.50b)$$

$$R_{y_3}(t) = \frac{f_{y_j}(t)(j-\frac{1}{2})L}{N^2} - \frac{f_{y_j}(t)L}{4N^4}\{1-4(j-\tfrac{1}{2})(N-j+\tfrac{1}{2})\}(2j-N-1) \qquad (2.50c)$$

$$R_{y_4}(t) = -\frac{f_{y_j}(t)L^2}{12N^4}\{N-3(j-\tfrac{1}{2}) + 12(N-j+\tfrac{1}{2})(j-\tfrac{1}{2})^2\} \qquad (2.50d)$$

Similarly the reactions in the local x-z plane can be found after replacing $f_{y_j}(t)$ by $f_{z_j}(t)$ in Eqs.(2.50). With some careful attention paid to signs, the twelve fixed-end reactions can be written as:

$$E(1) = -f_{x_j}(t), \quad E(2) = -R_{y_1}(t), \quad E(3) = -R_{z_1}(t) \qquad (2.51a)$$

$$E(4) = 0, \quad E(5) = -R_{z_2}(t), \quad E(6) = -R_{y_2}(t) \qquad (2.51b)$$

$$E(7) = 0, \quad E(8) = -R_{y_3}(t), \quad E(9) = -R_{z_3}(t) \qquad (2.51c)$$

$$E(10) = 0, \quad E(11) = -R_{z_4}(t), \quad E(12) = -R_{y_4}(t) \qquad (2.51d)$$

In some cases the member load in the local x direction, $f_{x_j}(t)$ (tangential component of forces) is neglected. So E(1) will be zero when $f_{x_j}(t)$ is ignored. Combining Eqs.(2.50) and (2.51):

$$E(1) = -f_{x_j}(t) \qquad (2.52a)$$

$$E(2) = -\frac{f_{y_j}(t)(N-j+\frac{1}{2})L}{N^2} - \frac{f_{y_j}(t)L}{4N^4}\{1-4(j-\tfrac{1}{2})(N-j+\tfrac{1}{2})\}(2j-N-1) \qquad (2.52b)$$

$$E(3) = -\frac{f_{z_j}(t)(N-j+\frac{1}{2})L}{N^2} - \frac{f_{z_j}(t)L}{4N^4}\{1-4(j-\tfrac{1}{2})(N-j+\tfrac{1}{2})\}(2j-N-1) \qquad (2.52c)$$

$$E(4) = 0 \qquad (2.52d)$$

$$E(5) = -\frac{f_{z_j}(t)L^2}{12N^4}\{N-3(N-j+\tfrac{1}{2}) + 12(N-j+\tfrac{1}{2})^2(j-\tfrac{1}{2})\} \qquad (2.52e)$$

$$E(6) = -\frac{f_{y_j}(t)L^2}{12N^4}\{N-3(N-j+\tfrac{1}{2}) + 12(N-j+\tfrac{1}{2})^2(j-\tfrac{1}{2})\} \quad (2.52f)$$

$$E(7) = 0 \quad (2.52g)$$

$$E(8) = -\frac{f_{y_j}(t)(j-\tfrac{1}{2})L}{N^2} + \frac{f_{y_j}(t)L}{4N^4}\{1-4(j-\tfrac{1}{2})(N-j+\tfrac{1}{2})\}(2j-N-1) \quad (2.52h)$$

$$E(9) = -\frac{f_{z_j}(t)(j-\tfrac{1}{2})L}{N^2} + \frac{f_{z_j}(t)L}{4N^4}\{1-4(j-\tfrac{1}{2})(N-j+\tfrac{1}{2})\}(2j-N-1) \quad (2.52i)$$

$$E(10) = 0 \quad (2.52j)$$

$$E(11) = \frac{f_{z_j}(t)L^2}{12N^4}\{N-3(j-\tfrac{1}{2}) + 12(N-j+\tfrac{1}{2})(j-\tfrac{1}{2})^2\} \quad (2.52k)$$

$$E(12) = \frac{f_{y_j}(t)L^2}{12N^4}\{N-3(j-\tfrac{1}{2}) + 12(N-j+\tfrac{1}{2})(j-\tfrac{1}{2})^2\} \quad (2.52l)$$

Now the force transformation matrix [RM] can be used again to relate the twelve fixed-end reactions, {E} to the equivalent joint load vectors $\{W_A(t)\}$ and $\{W_B(t)\}$ in the global directions and to complete the computation procedure:

$$\begin{Bmatrix} W_A(1) \\ W_A(2) \\ W_A(3) \\ W_A(4) \\ W_A(5) \\ W_A(6) \\ W_B(1) \\ W_B(2) \\ W_B(3) \\ W_B(4) \\ W_B(5) \\ W_B(6) \end{Bmatrix} = \begin{bmatrix} [RM] & & & \\ & [RM] & & \\ & & [RM] & \\ & & & [RM] \end{bmatrix} \cdot \begin{Bmatrix} E(1) \\ E(2) \\ E(3) \\ E(4) \\ E(5) \\ E(6) \\ E(7) \\ E(8) \\ E(9) \\ E(10) \\ E(11) \\ E(12) \end{Bmatrix} \quad (2.53)$$

2.5.3 Numerical Verifications

Eqs.(2.52) appear in a complex form but they are suitable for programming purposes. Small FORTRAN subroutines are developed to check the important equations presented in Section 2.5.2. The external forces and the fixed-end reactions should

maintain the equilibrium at the nodes. So arbitrary values are assigned to the member load components and the equilibrium condition is verified.

The general step-by-step procedure in Section 2.5.2 is further verified by considering few classic cases where the reaction forces can be found from a standard engineering handbook. One of them is described below.

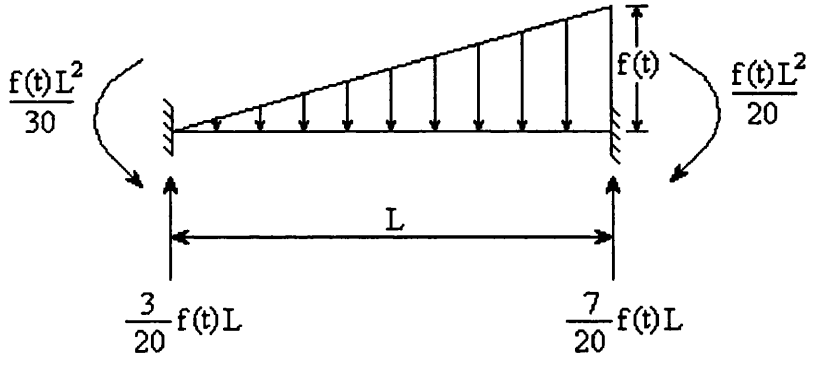

Fig. 2.7a. Fixed-end Forces for a Standard Triangular Loading

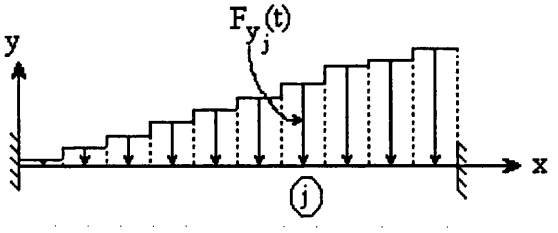

Fig. 2.7b. The Approximated Load Case

The hydrostatic loading is a typical example of triangularly distributed load on members. The 'exact' reaction forces and moments are shown in Fig. 2.7a. The beam is divided into 10 segments and the member load per unit length acting at the midpoint of each division is approximated as uniform load over the division. Fig. 2.7b shows the approximated load case. The fixed-end reactions are found by superimposing the contributions of external loads acting on each division of the beam. The values are shown in Table 2.1 where L = 30 units and f(t) = 20 units. The approximation is reasonable since the calculated values are very close to the 'exact' values in an ideal situation.

Table 2.1. The Contributions from Each Division of the Beam

Division No.	F_{y_j}	E(2)	E(6)	E(8)	E(12)
1	-1	2.9715	3.9225	0.0285	-0.2775
2	-3	8.4375	28.9125	0.5625	-5.2875
3	-5	12.6375	62.8125	2.3625	-21.1875
4	-7	15.0675	92.6625	5.9325	-50.1375
5	-9	15.5115	109.822	11.4885	-89.9775
6	-11	14.0415	109.973	18.9585	-134.227
7	-13	11.0175	93.1125	27.9825	-172.087
8	-15	7.0875	63.5625	37.9125	-188.438
9	-17	3.1875	29.9625	47.8125	-163.837
10	-19	0.5415	5.2725	56.4585	-74.5275
Total	-	90.501	600.015	209.499	-899.985
Theory	-	90	600	210	-900

2.6 ENVIRONMENTAL FACTORS COMMON TO RBRA AND DCATLP

Previous sections have illustrated the equivalent load calculations strategy. With that background, other components of the environmental loading will be discussed in the following sections. It should be noted that RBRA does not include anything beyond the Morison equation based wave forces. Therefore, it is necessary to distinguish clearly the external loading factors required in RBRA and DCATLP. Section 2.7 will discuss other environmental forces applicable to DCATLP only.

2.6.1 Acceleration Force and Added Mass Coefficients

In general the inertia and drag coefficients are determined experimentally. Several published literature are available with experimental values of these coefficients but the scatter in the results can make an appropriate selection quite difficult. The inertia coefficients are not required as input when the analytical diffraction solution (i.e. MacCamy-Fuchs theory) is used to calculate the inertia part of the wave force. This is one significant advantage of using the MacCamy and Fuchs' solution. But still added mass coefficients for columns, pontoons and tethers are required to generate the global mass matrix of the structure in DCATLP. DCATLP forms the global physical mass matrix from consistent element mass matrices and the added masses are then lumped onto the leading diagonal of the global physical mass matrix. However, RBRA forms the global mass matrix of (6x6) size by adding the physical and added mass matrices

and the calculation is relatively simple. But RBRA also requires the added mass coefficients.

At the simplest level C_a for columns can be taken as 1.0 but Taylor and Jefferys [2.30] provide more information in this respect from an axisymmetric finite element solution used by one of the participants in the ISSC case study. The added mass coefficient will be less than 1.0 because of three dimensional flow effects past the bottom of the columns. The finite element solution [2.30] suggests a value of 0.875. So for analysing the ISSC TLP C_a is taken as 0.875 although the interference effects among columns and pontoons cannot be included. When in line with the structure motion, the pontoon in-between fore and aft columns would tend to reduce the added mass value calculated by considering columns in isolation. But the pontoons perpendicular to the motion would probably increase the estimate but this compensating effect is likely to be small.

It is difficult to select C_a for the equivalent tether in each corner. An equivalent tether ideally should account for the interference effects in the tether group it represents. Etok and Kirk [2.10] have described a tensioned riser model (diameter = 0.66 m) of a TLP for dynamic analysis with $C_a = 1.0$. For equivalent tethers the same value is assumed in this study.

Taylor and Jefferys [2.30] have estimated the horizontal and vertical added mass coefficients for rectangular pontoons from Sarpkaya and Isaacson [2.25]. TLP Rule Case Committee [2.8] have recommended added mass coefficients for various cross-sectional shapes in the absence of any experimental data. But C_a values in these references are based on two dimensional flow. DnV [2.9] includes two modification factors for the corner radius and finite length of the rectangular member:

$$C_a = \frac{\pi}{4}\alpha k_l \left(\frac{d_p}{b_p}\right) k_r, \quad k_l = \frac{1}{1+(d_p / l_p)^2} \tag{2.54}$$

The coefficient α is to be found from a table and interpolations may be necessary. It is interesting to note that C_a is not defined with respect to any reference cross-sectional area of a circular cylinder. The added mass of the rectangular member in question can be simply found as the product of C_a in Eq.(2.54) and the enclosed volume of the member. The values of C_a for the ISSC TLP pontoons are given below from different references:

Table 2.2. Added Mass Coefficients for the ISSC TLP Pontoons

C_a	TLP RCC [2.8]	DnV [2.9]	Ref. [2.24], [2.30]
Horizontal	1.5944	1.5586	1.57
Vertical	0.9081	0.8976	0.91

C_a from DnV are less because k_l in Eq.(2.54) includes three dimensional flow effects. For DCATLP and RBRA, input is given based on the DnV formula. Added mass along the pontoon length is ignored.

2.6.2 Heave Added Mass of Columns

There is no simple formula for the heave added mass of TLP columns which works reasonably well in the wave frequency range. The heave added mass for columns cannot be ignored although the predominant contribution is usually from the pontoons. The heave added mass of a cylinder can be approximated from that of a disk with the same diameter as the cylinder in question.

$$M_{acv} = \frac{4}{3}\rho r^3 \tag{2.55}$$

The added mass of the cylinder is half of that for a thin circular disk because only the cylinder bottom is under water. But Eq.(2.55) does not take into account the aspect ratio of the cylinder. The effect of aspect ratio is significant and should be considered. Miller [2.18] gave allowance for the aspect ratio and the 3-D flow around the cylinder. In his method the cylinder is divided into strips lengthwise and added mass of all these rectangular strips are calculated. The method, strictly speaking, requires the added mass coefficients to be known for each rectangular strip but the average value of the aspect ratio of the strips can provide reasonable solution.

$$\text{Mean aspect ratio} = \frac{\pi r}{2d_f} \tag{2.56a}$$

$$M_{acv} = \frac{4}{3}\rho\pi r^3 k_\alpha k_\beta, \quad k_\beta = \frac{2}{\pi} \tag{2.56b}$$

Eq.(2.56) follows from Ref.[2.18]. k_α takes the effect of three dimensionality into account and depends on the mean value in Eq.(2.56a). As the draft decreases k_α approaches 1. DCATLP and RBRA use Eq.(2.56b) to calculate the vertical acceleration force acting on the platform.

2.6.3 Froude-Krylov Force on TLP Pontoons

Chakrabarti [2.5] has described a method for deriving the total force accounting for the fluid flow around the structure from the Froude-Krylov theory. The force on the structure in a particular direction is obtained by integrating the component of dynamic pressure in that direction over the submerged portion of the structure. Some coefficients are then used as multipliers to get the total force. These coefficients do not come from the Froude-Krylov theory and limit the applicability of this method in general. In this work, these coefficients are ignored because we are interested in calculating the dynamic pressure force only, not the total wave force acting on the pontoons from this method. The bright side of this method is in the closed-form expressions for dynamic pressure forces on a few submerged basic structures of symmetry which are obtained using the linear wave theory.

The water particle acceleration varies along the length of TLP pontoons depending on their orientation with wave direction. To apply the closed-form equations for Froude-Krylov Force, it is necessary to divide the pontoons into a number of segments so that the value of water particle acceleration can be assumed as constant over each segment. If a pontoon is divided into 'n' segments:

$$F_{FKx} = \frac{1}{n}\rho l_p b_p d_p \frac{\sinh(kd_p/2)}{(kd_p/2)} \frac{\sin(kb_p/2)}{(kb_p/2)} \dot{u}_p \qquad (2.57a)$$

Similarly, the total vertical force acting on the rectangular segment is given by:

$$F_{FKy} = \frac{1}{n}\rho l_p b_p d_p \frac{\sinh(kd_p/2)}{(kd_p/2)} \frac{\sin(kb_p/2)}{(kb_p/2)} \dot{v}_p \qquad (2.57b)$$

2.6.4 Dynamic Pressure and Buoyancy

A TLP works under excess buoyancy to keep its tethers under tension. In a typical TLP configuration columns may contribute 70% of the total displacement [2.13]. The dynamic buoyancy force from columns is very important. The linear wave theory is used throughout this study for estimating different components of environmental loading. The dynamic buoyancy from the columns are calculated by multiplying the area at the column base with the dynamic pressure at that level. The subsurface dynamic pressure is:

$$p_d = \rho g d_f + \frac{1}{2}\rho g H \exp(-kd_f)\cos(kx_w - \omega t) \qquad (2.58)$$

If d_f is taken up to the undisturbed instantaneous water level, the linear wave theory is violated. In this work, d_f is defined up to the still water level only. But it should be noted that this draft with respect to SWL increases when a TLP moves away from its

upright position because of the set-down effect. Although it is not possible to go up to the instantaneous free surface, DCATLP does consider the variation in d_f with time.

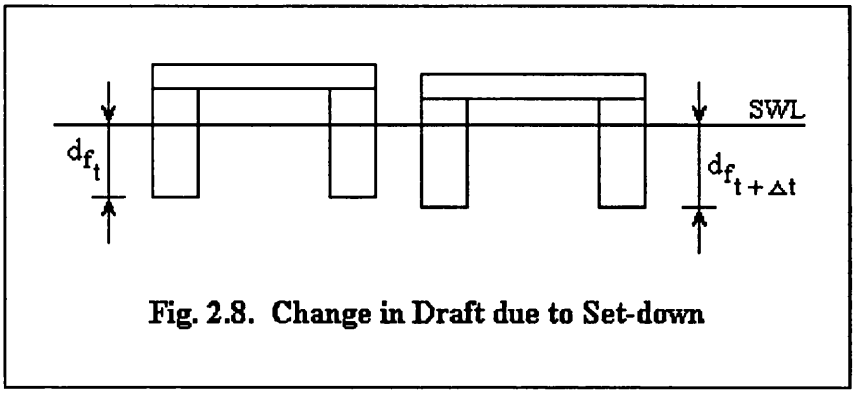

Fig. 2.8. Change in Draft due to Set-down

The added mass of TLP columns would change due to the variation in d_f. DCATLP takes into account the variation in added mass of the platform and the change in dynamic pressure with time.

As indicated earlier, RBRA cannot consider these added mass and draft variations like DCATLP. It is worth noting that DCATLP does not have any direct input regarding tension in the tethers. It calculates tether tension as a difference between variable buoyancy and platform weight. Therefore, the static term, $\rho g d_f$ in Eq.(2.58) is important for DCATLP. However, RBRA does not include $\rho g d_f$ while computing dynamic pressure because initial pretension in tethers is one of its direct input. This topic is discussed in detail in Chapter 3.

2.6.5 Drag coefficients

Drag coefficients depend on Reynolds' number, Keulegan-Carpenter number and surface roughness of the object. The recommended graphs for selecting C_D coefficients for circular cylinders in [2.8] and [2.9] are more or less similar. TLP RCC has suggested a proper upward adjustment of C_D to account for the surface roughness resulting from marine growth, fouling and other factors expected to occur during the life of the platform. For calculating drag coefficients for columns and tethers corresponding Reynolds numbers are to be estimated. For demonstration purpose the amplitude of horizontal water particle velocity is calculated at the middle of the submerged portion of columns and tethers.

$$u_{pa} = \frac{\pi H}{T} \exp(k y_w) \tag{2.59}$$

The Reynolds' number in a wave-current field is often defined as:

$$R_e = \frac{(u_{pa} + V_c)D}{\nu} \tag{2.60}$$

For the ISSC TLP, R_e at the middle of columns and tethers is 45.382E6 and 8.9E5 respectively. According to Eq.(2.60) there would be a variation in R_e over the length of the tethers. But C_D chosen here for both columns and tethers is 0.7 which includes an upward adjustment [2.8].

For rectangular pontoons C_D is calculated from the empirical formulae given in Ref. [2.9]. The skin friction along the length is ignored.

$$\left.\begin{array}{l} C_D \text{ along the length } = 0.0 \\ C_D \text{ in the transverse direction } = 2.0 \\ C_D \text{ in the vertical direction } = 1.7143 \end{array}\right\} \text{ for pontoons} \tag{2.61}$$

2.7 OTHER ENVIRONMENTAL FORCES FOR DCATLP ONLY

This section describes other environmental forces that can be accounted for while performing a dynamic analysis with DCATLP. The principle followed in this study is to utilise analytical closed-form solutions as far as possible to enhance the computational efficiency. The time domain algorithm and structural matrices involved in DCATLP are not straight-forward and demand high speed computational capabilities. So the loading side is kept relatively simple but sufficient.

2.7.1 Wind

TLP RCC [2.8], API RP 2T [2.1] and DnV [2.9] suggest different formulae for calculating wind velocity as a function of height above the SWL. The formulae are based on an average wind velocity at the international reference height of 10 m. The wind force relationship given in API RP 2T [2.1] takes into account the variable nature of the wind field and the wind-structure interaction. In the present analysis API RP 2T is followed for calculating the instantaneous wind force. The total wind speed can be written as a summation of a sustained component and a gust component:

$$V_{wnt} = V_{wns} + V_{wng} \tag{2.62}$$

The empirical power law formula can be used to find wind velocity at heights other than the international reference height:

$$\frac{V_{z_{wn}}}{V_{H_{wn}}} = \left(\frac{z_{wn}}{H_{wn}}\right)^{1/n_{wn}} \tag{2.63}$$

For numerical demonstration in Chapter 4, one hour average wind velocity at the reference height (i.e. 10 m) above the SWL is taken as 30 m / s. The gust component is ignored in the calculation because adequate site data is required to define this time varying function. The instantaneous wind force on each member of the TLP above the water line is calculated from the following equation [2.1]:

$$F_{wn}(t) = \frac{1}{2}\rho_a C_s A_p \left|V_{wns} + V_{wng} - u_s\right|\left(V_{wns} + V_{wng} - u_s\right) \qquad (2.64)$$

The shape coefficients taken are 0.5 and 1.0 for TLP columns and deck respectively. The exposed area of the deck structure has been estimated from the Hutton TLP configuration. The wind force on the deck structure would have a point of action above the deck elements shown in Fig. 2.9(a).

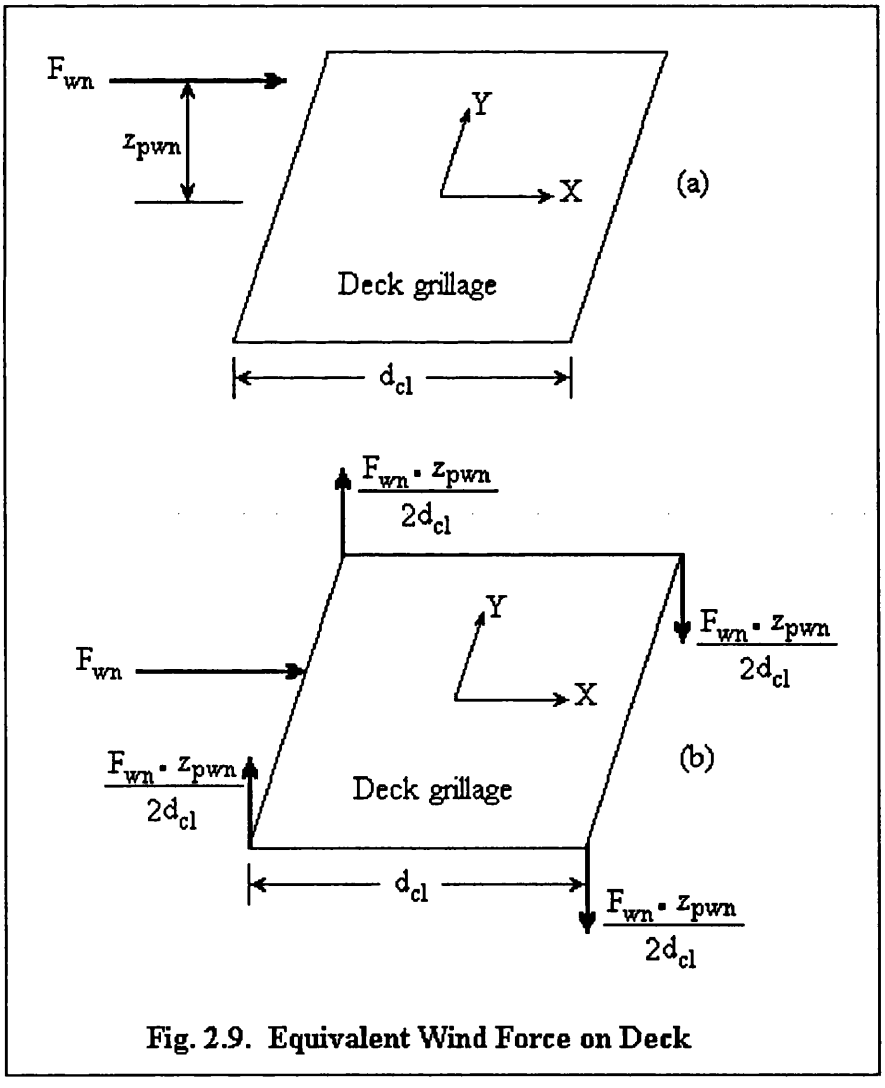

Fig. 2.9. Equivalent Wind Force on Deck

This complication can be solved by resolving the wind force into an equivalent force at the deck level and two adjusting couples taking care of the difference in height, z_{pwn}.

The deck grillage is not shown in Fig. 2.9. The figure considers a specific case where the wind velocity is along the global X axis. In more general case the couples in Fig. 2.9(b) would have a contribution from the Y-component of $F_{wn}(t)$. For wind force on columns, the column beam elements are considered individually. The wind force is assumed to be uniformly distributed along each element although force magnitude per element would be different depending on the height of interest above SWL.

2.7.2 Current

Three alternative forms of the modified Morison equation have been discussed in Section 2.4. If we consider one of those alternatives, Eq.(2.26), it would be further modified in the presence of current:

$$f_{MI}(t) + f_{MD}(t) = C_m\rho A\dot{u}_p - C_a\rho A\dot{u}_s + \tfrac{1}{2}C_D\rho D\left|u_p \pm V_c - u_s\right|(u_p \pm V_c - u_s) \qquad (2.65)$$

For TLP columns, the MacCamy-Fuchs analytical diffraction solution is used in DCATLP and for tethers the drag force is only of interest. So it is necessary to separate the inertia and drag components from Eq.(2.65). Hence, the drag force in the presence of waves and current is:

$$f_{MD}(t) = \tfrac{1}{2}C_D\rho D\left|u_p \pm V_c - u_s\right|(u_p \pm V_c - u_s) \qquad (2.66)$$

$f_{MD}(t)$ in Eq.(2.66) is also known as wave-current-motion interaction force. It is only possible to evaluate Eq.(2.66) directly in time domain. Several simplifications are required to transform Eq.(2.66) to a suitable form when calculations are done in frequency domain. But it is difficult to supply an appropriate value of C_D in Eq.(2.66). The test results in the presence of waves and current and specially in case of floating structures are almost non-existent. Considerable research is required to achieve insight into this most complex problem [2.5]. The force and structural displacements depend on the water particle kinematics as well as the velocity and acceleration of the structure itself. In numerical demonstrations in Chapter 4, "standard" drag coefficients are chosen for the absence of proper data and the effects are discussed.

2.7.2.1 Current profile

The current profile shown in Fig. 2.10 is used in Chapter 4 to model the current field.

Current	N. depth
1.30	1.00
0.85	0.95
0.85	0.90
0.85	0.80
0.85	0.50
0.61	0.05
0.54	0.02
0.49	0.01

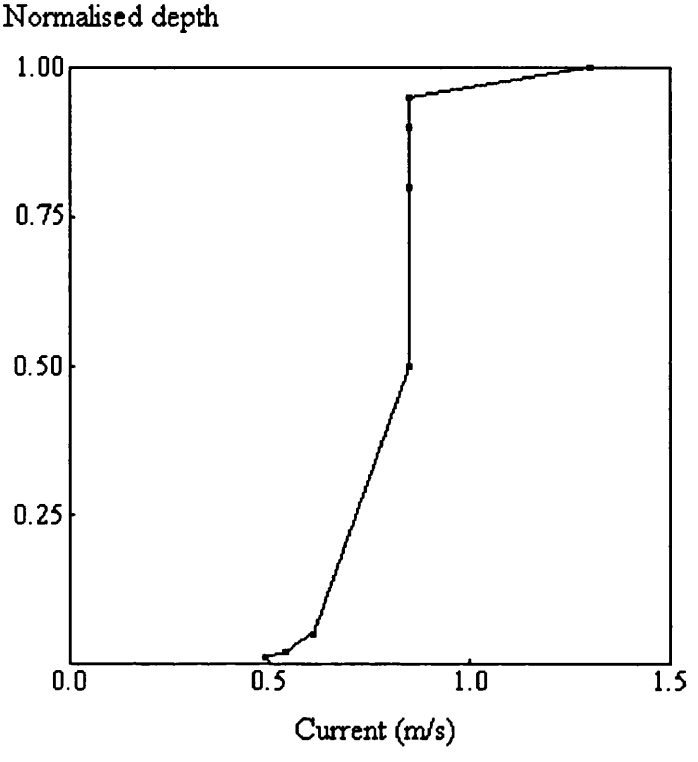

Fig. 2.10. Department of Energy (1990) Recommended Current Profile

2.7.3 Free Surface Boundary Condition

The basic assumption of the linear wave theory is that waves are of an infinitesimal amplitude, in which case linear homogeneous boundary conditions apply, both on the mean free surface and at the mean position of the platform. Employing the exact free surface boundary condition is still regrettably far from state-of-the-art within numerical hydrodynamics [2.22] and presently non-linearities are accounted for by a perturbation expansion in the velocity potential where the wave amplitude or the wave steepness usually plays the role of the perturbation parameter, and where the expansion is carried out only to second-order. This extension of linear theory has profound consequences in the occurrence of sum and difference frequency terms in bi-chromatic waves. DCATLP at present is not capable of dealing with these complex issues in numerical hydrodynamics. Some closed-form expressions (discussed later) are used to estimate these second-order effects.

2.7.4 Drift Forces

2.7.4.1 Wave drift

A TLP may experience another type of set-down effect. Because of the relatively large excursion of a TLP in surge and sway, the calculation of wave forces at its mean equilibrium position for the dynamic analysis, irrespective of its position during a wave cycle may be questioned. The results of calculating wave forces at a displaced position introduces a steady offset in the solution for both deterministic and stochastic wave fields [2.27]. DCATLP considers this complaint characteristics of TLPs. The external loading at the immediate future $(t+\Delta t)$ time station is determined with a set of assumed values of TLP responses. The next cycle of iteration starts with the computed values of responses in the previous iteration cycle so that the structure and the external forces together 'decide' the dynamic equilibrium position.

2.7.4.2 Steady viscous drift

There are two areas that may produce a non-zero mean viscous drift force. When current is present along with waves a mean drift force is generated from the drag force at any elevation of the cylinder. Several researchers [2.6], [2.4], [2.16] have developed different expressions for this steady drift force due to viscous flow. The following relations are from Ref. [2.6]:

$$\frac{\bar{f}_D}{\frac{1}{2}\rho D C_D u_{pa}^2} = \pm\left[\frac{1}{2}+\left(\frac{V_c}{u_{pa}}\right)^2\right] \quad \text{for} \quad \frac{|V_c|}{u_{pa}} \geq 1 \tag{2.67a}$$

$$\frac{\bar{f}_D}{\frac{1}{2}\rho D C_D u_{pa}^2} = \frac{1}{\pi}\left\{\left(\frac{V_c}{u_{pa}}\right)^2(2\psi_c-\pi) + 4\left(\frac{V_c}{u_{pa}}\right)\sin\psi_c + \left(\psi_c-\frac{\pi}{2}+\frac{1}{2}\sin 2\psi_c\right)\right\} \quad \text{for} \quad \frac{|V_c|}{u_{pa}} < \tag{2.67b}$$

where

$$\psi_c = \cos^{-1}\left(-\frac{V_c}{u_{pa}}\right) \quad 0 \leq \psi_c \leq \pi \tag{2.67c}$$

But Eq.(2.67) is not required here because DCATLP calculates wave-current-motion interaction force. Eq. (2.67) is important when the analysis is done in frequency domain. But the relative velocity model including current in time domain is a better solution for calculating viscous drift because it accounts for the variation within a wave cycle and it includes the structural motion.

The computation of first order effects is limited up to the still water level. Effects of current are usually present up to SWL. But there will be a mean drift at SWL from the changing free surface of waves. The linear wave theory is applicable for infinitesimal wave amplitudes and is valid up to SWL. It is not theoretically possible to use the expressions for water particle kinematics from the linear wave theory up to the free surface of a finite wave. Chakrabarti [2.7] recommended the form of velocity and (hence acceleration) which includes the free surface as:

$$u_p = \frac{gkH}{2\omega}\frac{\cosh k(y_w + d)}{\cosh k(d+\eta)}\cos(kx_w - \omega t) \tag{2.68}$$

Wheeler [2.31] has suggested 'stretching' formulae in finite water depth where the water particle kinematics are slightly different from Eq.(2.68). But water particle velocities have the same value at the wave crest and trough as in Eq.(2.68).

$$u_p = \frac{gkH}{2\omega}\frac{\cosh k(y_w + d)(d/(d+\eta))}{\cosh kd}\cos(kx_w - \omega t) \tag{2.69}$$

Chakrabarti [2.6] has utilised Eq.(2.69) to find the mean force from the free surface effect acting on a fixed vertical cylinder:

$$\frac{\bar{F}_{fs}}{\rho g C_D D/k^2} = \frac{(kH)^3}{12\pi}\left[\frac{1}{\sinh 2kd} + \frac{1}{2kd}\right] \tag{2.70}$$

The mean force is a function of the cube of wave height as opposed to the square of it for potential drift force. The integration has been carried out over the entire submerged length of the cylinder in Eq.(2.70) but it is important to note that the mean force is only due to the free surface variation. In the absence of free surface (i.e. without wave elevation) the integration would produce a zero mean. Eq.(2.70) is used in DCATLP to calculate viscous drift due to free surface effects at the still water level. Please note that the linear wave theory is used throughout this study with only one exception here (i.e. Eq.(2.69)). The author did not follow any 'stretching' formulae for calculating other forces for their mathematically unpleasant feature. They no longer satisfy the Laplace equation unless the term $(d+\eta)$ is treated as a constant in the differentiation of the velocity potential with respect to other variables.

Standing et al [2.28] have given a similar expression for the mean free surface force in of deep water case:

$$\frac{\bar{F}_{fs}}{\rho g C_D D/k^2} = \frac{(kH)^3}{12\pi} \tag{2.71}$$

However, the mean free surface force in Eq.(2.70) approaches zero as the water depth approaches infinity.

2.7.4.3 Steady potential drift

The first step in arriving at the slowly varying or steady drift is to compute the second order force in regular waves. The second order forces are obtained from the first and second order velocity potentials and the complete Bernoulli's equation. However, if the structure is allowed to move additional terms arise if the instantaneous position of the structure is taken into account. The final expression for second order force reduces to main five integrals and the steady drift force is obtained by averaging these integrals over a complete cycle of a regular wave. One of the five integrals [2.23] has a zero mean and does not contribute to the steady drift force. The other four components are:

I) Wave elevation drift force:- The contribution of first order relative wave elevation is usually larger than the other components. For a floating hemisphere [2.23] this one was about twice that of the total force having the same sign.

II) Velocity head drift force:- This is the contribution of the square of the first order velocity vector. For the hemisphere its magnitude was around the same as the total force but the direction was opposite.

III) Body motion drift force - The contribution of the product of the first order pressure gradient and first order motion amplitude is less important than the first two drift components. Body motion drift is zero when the structure is fixed.

IV) Rotational inertia drift force - It comes from the contribution of the vector product of first order motion and inertia force. This one is also less important and zero when the structure is fixed.

For a fixed vertical cylinder the first two drift components (i.e. I and II) can be obtained in a closed form [2.6], [2.17]. The derivation uses the total first order pressure including diffraction effects from the MacCamy-Fuchs theory. One of the main assumptions in formulating the closed-form equation for the wave elevation drift force is the hydrostatic decay of pressure from SWL to the free surface. The velocity head drift force is calculated from the pressure due to the velocity squared term in the Bernoulli's equation. In deep water case, the total of velocity head and wave elevation drift has the following form:

$$\frac{\bar{F}_{21} + \bar{F}_{22}}{\rho g H^2 r} = \frac{1}{\pi^2 (kr)^3} \sum_{n=0}^{\infty} \left[1 - \frac{n(n+1)}{(kr)^2} \right]^2 \frac{1}{A_n A_{n+1}} \qquad (2.72a)$$

where

$$A_n = J_n'^2(kr) + Y_n'^2(kr) \qquad (2.72b)$$

For large kr (>5.0) the asymptotic value given by Havelock [2.12] is:

$$\frac{\bar{F}_{21} + \bar{F}_{22}}{\rho g H^2 r} = \frac{1}{6} \tag{2.73}$$

while for small kr (<0.5) Standing et al [2.28] have given:

$$\frac{\bar{F}_{21} + \bar{F}_{22}}{\rho g H^2 r} = \frac{2}{3}(kr)^3 \tag{2.74}$$

2.7.4.4 Slowly varying wave drift and springing

Today it is widely appreciated that both low and high frequency responses will occur due to non-linear additions in the wave loading spectrum. And even though the relative magnitude of this resonant excitation is small, compared to first order wave frequency excitation, the corresponding damping levels are also small, leading to considerable dynamic amplification. For practical TLP design, high and low frequency resonant responses are both significant and must therefore be taken into account. The high frequency tension oscillation of the tethers is often called springing.

The slow oscillation is generated in two ways. If the structure is subjected to seiche or groundswell (of periods of the order of 25 to 120 seconds) the surge response is greatly magnified because of the low damping at the natural period in surge. Such long period wave of small amplitude and seiches may occur in nature. The low frequency forces on the structure also appear due to the difference in the neighbouring frequencies in the random ocean waves. The first step in high and low frequency response calculation is to compute the second order forces from the first and second order velocity potentials and the complete Bernoulli's equation. Assuming two frequency components, ω_i and ω_j present in the random wave, the total non-linear force arising from these frequencies having corresponding wave amplitudes of η_{ai} and η_{aj} is obtained as:

$$F_2^{\pm}(t) = \sum_{i=1}^{n}\sum_{j=1}^{n}\eta_{ai}\eta_{aj}\left[\bar{P}_{ij}^{\pm}\cos\left\{\left(\omega_i \pm \omega_j\right)t - \left(\delta_i \pm \delta_j\right)\right\}\right.$$
$$\left. + \bar{Q}_{ij}^{\pm}\sin\left\{\left(\omega_i \pm \omega_j\right)t - \left(\delta_i \pm \delta_j\right)\right\}\right] \tag{2.75}$$

where $\bar{P}_{ij}^{\pm}$ and $\bar{Q}_{ij}^{\pm}$ are the even and odd components of second order forces due to frequency components ω_i and ω_j. The bar indicates that these force components are normalised by the component wave amplitudes, η_{ai} and η_{aj}. The number of wave components in the random wave simulation is 'n'. The negative exponent refers to the drift force while the positive exponent gives the high frequency springing force. It is clear that in regular waves:

$$F_2^-(t) = 0 \tag{2.76a}$$

$$F_2^+(t) = \eta_{ai}^2 \left\{ \bar{P}_{ii}^+ \cos 2(\omega_i t - \delta_i) + \bar{Q}_{ii}^+ \sin 2(\omega_i t - \delta_i) \right\} \tag{2.76b}$$

So the low or difference frequency force is absent in regular waves but there is a constant or mean drift force as discussed earlier. The high or sum frequency force in regular waves appears at twice the regular wave frequency. The amplitude and phase of the Quadratic Transfer Function (QTF) with respect to the exciting force are:

$$T_{ii}^+ = \left[\left(\bar{P}_{ii}^+ \right)^2 + \left(\bar{Q}_{ii}^+ \right)^2 \right]^{1/2} \tag{2.77a}$$

$$\delta_{ii} = -\tan^{-1} \left(\frac{\bar{Q}_{ii}^+}{\bar{P}_{ii}^+} \right) \tag{2.77b}$$

Eqs.(2.76) may appear to be simple but it should be noted that it refers to the QTF in regular waves only. In practice, QTFs tend to vary fast both with respect to heading angle and frequency, increasing the computational burden enormously [2.22]. The calculation involves a 4-dimensional (bi-directional and bi-frequency) matrix of coefficients. At present QTFs are computed by a few specialised research institutions rather than by the offshore engineering industry since most of the available software require specialist knowledge of the codes both to model the structure adequately and to assess the results for accuracy. Such computer codes require a much finer panel mesh than a normal wave frequency analysis. Further, a fine panel mesh on the free surface in the area around the surface piercing part of the TLP is also required to evaluate the free surface integral. The QTF computations based on panel models are extremely computationally intensive [2.22].

At present in DCATLP high frequency force is neglected and low frequency force does not arise because the calculations are done in regular waves. But the analysis can be extended to account for irregular waves as discussed in more detail in Chapter 4. The high and low frequency forces can be neglected except close to resonance where due to low system damping they may contribute substantially to the overall response. A simplified method [2.5] for calculating the difference frequency force is to consider those frequencies only which are close to the natural frequencies of the system. The simplified expression is:

$$F_2^-(t) = \bar{F}_2^- \cos \omega_n t \tag{2.78}$$

where $\omega_n = \omega_i - \omega_j$. Since ω_i and ω_j are close to each other, $\bar{F}_2^-$ can be approximated from the steady drift force in regular waves at a frequency that is mean of the two frequencies ω_i and ω_j whose difference produces the natural frequency, ω_n.

2.7.5 Second Order Wave Correction Forces

At present the environmental loading module in DCATLP does calculations based on regular waves only. So slowly varying drift forces and high frequency springing forces are not included in the analysis. It is perhaps necessary to estimate the higher order forces left out. Incecik [2.14] has proposed a closed-form expression based on Ref. [2.15] which estimates second order dynamic, waterline and correction force for disturbance due to a vertical cylinder in regular waves. This time varying second order force appears at twice the regular wave frequency:

$$F_{sc} = \frac{1}{4}\rho g\pi H^2 kr^2\left[2-\frac{1}{2}\left(1-e^{-2kd_f}\right)\right]\sin(kx_w-\omega t)\cos(kx_w-\omega t) \qquad (2.79)$$

At present DCATLP uses this closed-form equation to add second order corrections in the environmental loading.

2.7.6 Tidal Variations

The water level changes due to the atmospheric tide, astronomical tide and storm surge. The change because of astronomical tide is usually treated independently from the occurrence of storm [2.26]. In the numerical demonstration in Chapter 4, the tidal variations are neglected. But there is no difficulty in including them in the analysis. If they are required the initial operating draft should be calculated and given as input to DCATLP. When the analysis starts in time domain all other factors such as tension variation in tethers, set-down effects would change accordingly with the initial operating draft.

2.8 CONCLUSIONS

The author has tried to combine some existing computational methods and techniques of structural mechanics to simplify the task of transferring complicated member loads to the corresponding nodes of beam elements. In the process, some closed-form expressions are formulated which can be very helpful to anyone who does not want to get into the complexity of the interaction of waves with the structure. There is an added advantage. The closed-form expressions are analytically integrated and simplified. So there is no need for any numerical integration which is always computationally expensive. There will be no subdivision of the element. So the expressions will considerably decrease the computer run time and storage requirements.

In the case of a beam, arbitrarily oriented in space, the full integration can only be carried out numerically. The computation procedure proposed here, will achieve a

reasonable solution depending on the number of divisions and the element length. The procedure can also deal with any other form of member loads in addition to forces from ocean waves. In fact, it can be easily programmed and stored as a separate module which will be utilised later by the actual analysis.

This chapter also provides a background of RBRA and DCATLP discussed later. Small Fortran subroutines have been developed based on the equations presented here. They will find their applications in one of the modules in RBRA and/or in DCATLP.

2.9 REFERENCES

[2.1] API RP 2T: "Recommended Practice for Planning, Designing, and Constructing Tension Leg Platforms", American Petroleum Institute, 1987.

[2.2] Armenis, D.Th., Angelopoulos, T.A. and Papanikas, D.G.: "Time Domain Simulation of the Dynamic Behaviour of a Tension Leg Platform", First International Offshore and Polar Engineering Conference, Edinburgh, pp 100-107, 1991.

[2.3] Borgman, L.E.: "Computation of the Ocean-Wave Forces on Inclined Cylinders", Journal of Geophysical Research, Transactions AGU, pp 885-888, 1958.

[2.4] Burns, G.E.: "Calculating Viscous Drift of a Tension Leg Platform", Proceedings of Second International Offshore Mechanics and Arctic Engineering Symposium, ASME, Houston, pp. 22-30, 1983.

[2.5] Chakrabarti, S.K.: "Hydrodynamics of Offshore Structures", Computational Mechanics Publications, pp. 232-243, 1987.

[2.6] Chakrabarti, S.K.: "Steady Drift Force on Vertical Cylinder - Viscous vs. Potential", Applied Ocean Research, Vol. 6, No. 2, 1984.

[2.7] Chakrabarti, S.K.: "Dynamics of Single Point Mooring in Deep Water (Discussion), Journal of Waterways, Harbours and Coastal Engineering Division, ASCE, Vol. 97, 1971.

[2.8] Conoco/ABS TLP Rule Case Committee: "Model Code for Structural Design of Tension Leg Platforms", New York, February 1984.

[2.9] Det norske Veritas: "Rules for Classification of Mobile Offshore Units," DnV, Oslo, Part 3, Chapter 1, Section 4, 1981.

[2.10] Etok, E.U. and Kirk, C.L.: "Random Dynamic Response of a Tethered

Buoyant Platform Production Riser", Dynamic Analysis of Offshore Structures Recent Developments, Edited by C.L. Kirk, Southampton, 1982.

[2.11] Harrison, H.B.: "Structural Analysis and Design: Some Mini-computer Applications", Pergamon Press, Sydney, Part 1, pp 113-123, 1979.

[2.12] Havelock, T.H.: "The Pressure of Water Waves on a Fixed Obstacle", Proceedings of Royal Society, London, Series A, pp 409-421, 1940.

[2.13] Horton, E.: "Develop Configuration", Session 4, TLP Design Technology Seminar, OMAE and Petroleum Divisions of ASME, 1992.

[2.14] Incecik, A.: "Design Aspects of the Hydrodynamic and Structural Loading on Floating Offshore Platforms under Wave Excitation", Ph.D. Thesis (No. NAOE-82-47), Department of Naval Architecture and Ocean Engineering, University of Glasgow, Glasgow, 1982.

[2.15] Lighthill, J.: "Waves and Hydrodynamic Loading", Opening Address-1, Proceedings BOSS 1979, London, 1979.

[2.16] Lundgren, H., Sand, S.E. and Kirkegaard, J.: "Drift Forces and Damping in Natural Sea States - a Critical Review of the Hydrodynamics of Floating Structures, Proceedings of Third International Conference on Behaviour of Offshore Structures, MIT, Boston, Vol. II, pp. 592-607, 1982.

[2.17] MacCamy, R.C. and Fuchs, R.A.: "Wave Forces on Piles: A Diffraction Theory", Technical Memo No. 69, US Army Corps of Engineers, Beach Erosion Board, 1954.

[2.18] Miller, N.S.: "Effect of Geometry and Dimensions on Natural Heaving Period", in 'Semi-submersibles and Tethered Buoyant Platforms - Some Design Considerations', Lecture Note for a Course on 26-30th September, 1977, Department of Naval Architecture and Ocean Engineering, University of Glasgow, Glasgow, 1977.

[2.19] Morison, J.R., O'Brien, M.P., Johnson, J.W. and Schaaf, S.A.: "The Force Exerted by Surface Wave on Piles", Petroleum Transactions, AIME, Vol. 189, pp 149-157, 1950.

[2.20] Murotsu, Y., Okada, H., Matsuda, A., Niho, O., Kobayashi, M. and Kaminaga, H.: "Application of the Structural Reliability Analysis System (STRELAS) to a Semi-submersible Platform", Offshore Mechanics and Arctic Engineering Conference, Vol. II, pp 209-217, 1992.

[2.21] Natvig, B.J., Vogel, H.S. and Johnsen, O.: "TLP Global Motion Performance Analysis Procedures", OTC 6889, 24th Annual Offshore Technology

Conference, Houston, pp 147-153, 1992.

[2.22] Natvig, B.J. and Teigen, P.: "Review of Hydrodynamic Challenges in TLP Design", International Journal of Offshore and Polar Engineering, Vol. 3, No. 4, pp. 241-249, 1993.

[2.23] Pinkster, J.A.: "Low Frequency Second Order Wave Exciting Forces on Floating Structures", Publication No. 650, Netherlands Ship Model Basin, Wageningen, 1981.

[2.24] Report of Committee I.2: "Case study of a Tension Leg Platform", Proceedings of the Ninth International Ship and Offshore Structures Congress, Registro Italiano Navale, Genova, Vol. 1, pp. I.2-48-55, 1985.

[2.25] Sarpkaya, T. and Isaacson, M.St.Q.: "Mechanics of Wave Forces on Offshore Structures", van Nostrand Reinhold, New York, 1981.

[2.26] Shin, Y.S., Xanthopoulos, E. and Unger, D.P.: "Extreme Value and Probability Density Function of Motion, Tether Tension and Load Effects on a North Sea Tension Leg Platform", Paper RCC(b) 16, 7 February 1983.

[2.27] Spanos, P.D. and Agarwal, V.K.: "Response of a Simple Tension Leg Platform Model to Wave Forces Calculated at Displaced Position, Journal of Energy Resources Technology, Transactions ASME, Vol. 106, pp. 437-443, 1984.

[2.28] Standing, R.G., Dacunha, N.M.C. and Matten, R.B.: "Mean Wave Drift Forces: Theory and Experiment", National Maritime Institute, Report No. R124, 1981.

[2.29] Tasai, et al: "A Study on the Motion of a Semi-submersible Catamaran Hull in Regular Waves", Journal of the Society of Naval Architects of West Japan, July 1970.

[2.30] Taylor, R.E. and Jefferys, E.R.: "Variability of Hydrodynamic Load Predictions for a Tension Leg Platform", Ocean Engineering, Vol. 13, No. 5, pp. 449-490, 1986.

[2.31] Wheeler, J.D.: "Method for Calculating Forces Produced by Irregular Waves", Proceedings of First Offshore Technology Conference, Houston, OTC 1006, 1969.

CHAPTER 3

RIGID BODY RESPONSE

3.1 INTRODUCTION

In reality a TLP is a continuous system with an infinite number of degrees of freedom and consequently, an infinite number of free vibration modes and frequencies. But as a starting point for research, the consideration of the platform as a rigid body with six degrees of freedom is often more convenient and useful for the researcher to realise the general characteristics and motion behaviour of the structure.

This chapter describes in brief the theoretical background behind developing a program RBRA (Rigid Body Response Analysis). This Morison equation based Fortran program originated from the initial phase of the author's work and quite simplified in nature. There were three important reasons behind the author's involvement in writing RBRA. First of all, he was interested in understanding the basic characteristics of TLPs through numerical calculations. Ref. [3.2] is an ideal example where simple hand calculations are demonstrated to illustrate the dynamic behaviour of a TLP. In fact, a number of results from RBRA have been checked by hand calculations and Mathematica [3.11]. Secondly, there are rigid body response results available from various sources [3.8], [3.9] on the ISSC TLP which is selected here as a demonstration model. It was of interest to compare those results with the output from a simple and straight-forward program such as RBRA. Thirdly, a program was required in a different research work with TLPs and multi-variate environmental modelling [3.7] for calculating force and response transfer functions quickly and efficiently. RBRA was tailored to meet that requirement.

3.2 BASIC ASSUMPTIONS

There are a number of assumptions behind the Morison equation based formulation used in RBRA to calculate motions in all six degrees of freedom. They are stated below:

1) The cylindrical columns and rectangular pontoons are assumed to have small ratios of cross-sectional dimension to length. These dimensions are assumed small when compared to incident wavelengths.

2) The motion amplitudes of the platform and waves are assumed to be small.

3) Wave forces on individual elements of the structure are computed as though other members were not present. In other words, hydrodynamic interference between members is ignored.

4) The forces associated with sinusoidal wave motions are computed

independently of the forces involving absolute motions of the structure.

5) The non-linear drag damping term is linearised by assuming an effective linear damping which would dissipate the same energy at resonance as the non-linear damping. The contribution of wave radiation effects to the damping terms is assumed to be negligibly small.

There are programs available [3.8] based on the diffraction analysis which can account for member interactions with incident waves and interaction due to adjacent members. Conversely, they do not consider drag forces or non-linear damping effects unless a hybrid computing model is used. Whatever might be the calculation technique, there are a few common steps involved in a conventional TLP motion response analysis:

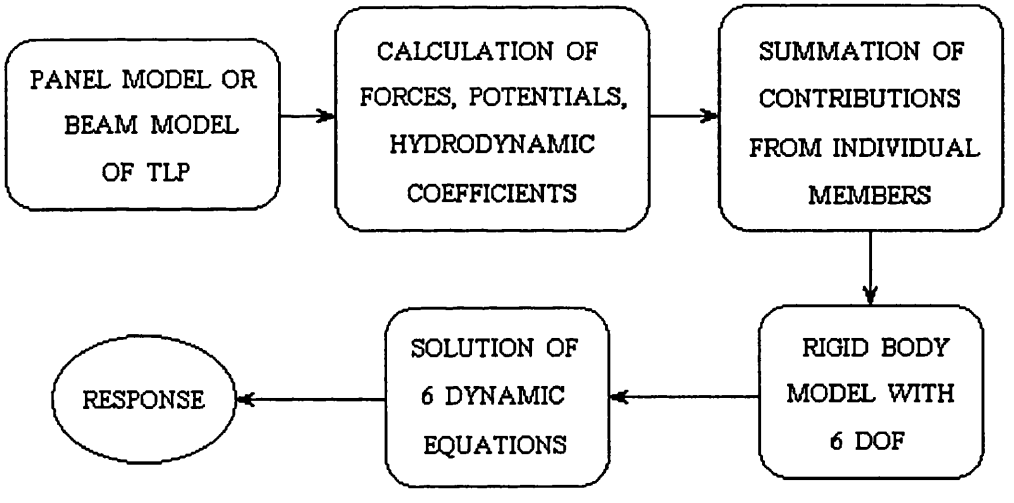

Fig. 3.1. Conventional Motion Response Analysis of TLPs

3.3 DYNAMIC EQUATION OF MOTION

The dynamic equation of rigid body motions in six degrees of freedom for a TLP can be written as:

$$\left([M_{rp}]+[M_{ra}]\right)\{\ddot{X}_r\} + [B_r]\left|\{\dot{X}_r\}\right|\{\dot{X}_r\} + \left([K_{rh}]+[K_{rt}]\right)\{X_r\} = \{F_r\} \quad (3.1)$$

The subscript 'r' is used to distinguish rigid body matrices from those used later in Chapter 4 to consider structural deformations. Eq.(3.1) is actually simplified by considering the relatively large magnitude of inertia force and the decay of wave particle velocities with water depth, which makes the drag damping term small for members with significant submergence below still water level [3.5].

Ref. [3.5] was quite helpful in the development of RBRA. In RBRA, the formulations

for the coefficients in the matrices on the left hand side of Eq.(3.1) are taken from Ref. [3.5]. In fact, Patel et al [3.6] were involved in implementing all these matrices in a motion response program called UCLRIG.

3.3.1 Physical Mass Matrix

$$[M_{rp}] = \begin{bmatrix} M_s & 0 & 0 & 0 & 0 & 0 \\ 0 & M_s & 0 & 0 & 0 & 0 \\ 0 & 0 & M_s & 0 & 0 & 0 \\ 0 & 0 & 0 & I_{xx} & I_{xy} & I_{xz} \\ 0 & 0 & 0 & I_{xy} & I_{yy} & I_{yz} \\ 0 & 0 & 0 & I_{xz} & I_{yz} & I_{zz} \end{bmatrix} \tag{3.2}$$

In RBRA it is not necessary to select the origin of the structural reference axes system at the centre of gravity of the structure. However, if the reference axes chosen are principal axes, the physical mass matrix becomes diagonal because the product of inertia terms (i.e. I_{xy}, I_{xz}, and I_{yz}) would be zero.

3.3.2 Added Mass Matrix

The added mass matrix, $[M_{ra}]$ is a symmetric matrix. For calculating its coefficients, the TLP is assumed to be a collection of circular cylinders and rectangular pontoons and the hydrodynamic interference between members is ignored. Hence, the added mass for each TLP member is evaluated separately. The main assumption in the added mass calculation is that only the acceleration component perpendicular to the longitudinal axis of a TLP member will have a significant added mass force. A generalised added mass matrix for a circular cylinder can be readily evaluated [3.5] when the cylinder end co-ordinates, diameter and applicable normal flow added mass coefficients are known. The added mass coefficients for the ISSC TLP have been discussed in Chapter 2.

3.3.3 Damping Matrix

The rigid body damping matrix $[B_r]$ for the structure is also evaluated as a sum of the contribution from each individual member. The main assumption is also the same as in the case of evaluating the rigid body added mass matrix. Only drag forces normal to the member longitudinal axis are assumed to be significant. But, unlike the added mass matrix, the non-linear velocity square proportionality generates an asymmetric damping matrix. As mentioned before, the matrix components are taken from Ref. [3.5].

3.3.4 Hydrostatic Stiffness Matrix

Contributions to the hydrostatic stiffness matrix $[K_{rh}]$ will only arise in the heave, roll and pitch degrees of freedom due to the buoyancy forces in the water plane cutting members of the hull. If, for member number, n, A_{wn} denotes the water plane area and x_{wc}, y_{wc} are the co-ordinates of that water plane area centroid, then the hydrostatic stiffness elements can be written as the following summations:

$$K_{rh}(3,3) = \rho g \sum A_{wn} \tag{3.3a}$$

$$K_{rh}(4,3) = \rho g \sum y_{wc} A_{wn} \tag{3.3b}$$

$$K_{rh}(5,3) = -\rho g \sum x_{wc} A_{wn} \tag{3.3c}$$

$$K_{rh}(5,4) = \rho g \sum A_{wn} x_{wc} y_{wc} \tag{3.3d}$$

$$K_{rh}(4,4) = \rho \Delta \overline{GM}_P \tag{3.3e}$$

$$K_{rh}(5,5) = \rho \Delta \overline{GM}_R \tag{3.3f}$$

where Δ is the vessel displacement and $\overline{GM}_R$, $\overline{GM}_P$ are meta-centric heights in roll and pitch respectively. All other stiffness terms in the matrix $[K_{rh}]$ are zero.

3.3.5 Tether Stiffness Matrix

The symmetric tether stiffness matrix is taken from Ref. [3.5]. The derivation assumes that each tether is weightless and perfectly elastic with a known tension and elastic stiffness. The tether being weightless is assumed to lie along a straight line joining the two co-ordinates. The platform is presumed to move through small displacements relative to the tether lengths involved. The tether stiffness in each corner is assumed to be equal and the vertical stiffness of combined tethers is given by their sum. The 'set down' effect is also ignored.

The formulation of $[K_{rt}]$ is simple and straight-forward. But the simple assumptions might be questionable depending on water depths and platform configurations. Different spring stiffnesses associated with the tethers are discussed in detail in Chapter 4. It is worth noting in this context that program DCATLP treats the tethers in a completely different way in order to explore the complicated nature of tether dynamics.

3.4 WAVE FORCE VECTOR

$\{F_r\}$ in Eq.(3.1) is the right hand side column vector of 6×1 dimension. The methods of calculating equivalent loads at nodes of a TLP member have been discussed in Chapter 2. RBRA only considers the Morison equation based wave forces. The inertia

and drag force calculations are briefly described in Section 2.4. Wave forces on each TLP member are found by using the techniques presented in Chapter 2. These forces are then summed to obtain the total member wave force. Taking moments of these elemental forces about a geometrically convenient point on the member, the point of action of the total member wave force is found. In the next step, member wave forces are summed in three global directions. In other words, the total surge, sway and heave forces are evaluated by summing the horizontal, transverse and vertical member wave forces respectively. These three forces in three global directions are the first three coefficients in the wave force vector $\{F_r\}$. The position and direction of action of a member wave force plays an important role in calculating the next three coefficients in $\{F_r\}$. The total roll, pitch and yaw moments are found by taking moments of these member wave forces about the centre of gravity of the structure.

3.5 SOLUTION OF THE EQUATION OF MOTION

Although the coefficient matrices in the equation of motion are programmed according to Patel, et al [3.5] but the solution procedure in RBRA is different from them. They [3.5] have used an iterative technique to account for the non-linear damping term. The first approximate diagonal linear damping matrix in their analysis was obtained by ignoring all non-diagonal terms in the total mass and stiffness matrices and assuming damping of 10% of critical. The equation of motion was then solved with the approximate damping values to obtain a better approximation for the displacement vector, $\{X_r\}$. They have found that the iteration is only significant in the vicinity of resonant frequencies.

The solution method in RBRA is not extra-ordinary but the author would like to point out that it does not come from any published literature. It is also an iterative technique since it is difficult to avoid iterations because of the non-linear drag damping term.

3.5.1 Wave Forces

As indicated before, the wave forces are computed independently of the forces involving structural motions. The wave force vector $\{F_r\}$ consists of six terms - three forces and three moments. First of all, it is necessary to linearise wave forces. Secondly, it is essential to find the linearised amplitudes of all six terms in $\{F_r\}$ (for a given wave direction) for calculating force and response RAOs. In order to do that the wave forces on the structure are calculated for a few wave cycles. Then six different sinusoidal curves are fitted to wave force data (one curve each for surge, sway, heave force and roll, pitch, yaw moment) and the amplitudes of these sinusoidal curves are taken as the linearised wave force amplitudes, $\{F_{ra}\}$. This process depends on wave

height, period and direction. If any one of these three factors is changed, the process must be repeated to find the new linearised wave force amplitudes. It should be noted that the sinusoidal curves are very close to the actual curves plotted by joining wave force data because the non-linear drag contribution is small. The curve fitting is tested and verified with the help of Mathematica [3.11].

3.5.2 The Iteration Technique

The iteration starts by replacing $[B_r]\{\dot{X}_r\}|\{\dot{X}_r\}$ with $[B_r]\{\dot{X}_r\}$! In other words, the following equation is solved instead of Eq.(3.1):

$$\left([M_{rp}]+[M_{ra}]\right)\{\ddot{X}_r\} + [B_r]\{\dot{X}_r\} + \left([K_{rh}]+[K_{rt}]\right)\{X_r\} = \{F_r\} \quad (3.4)$$

Eq.(3.4) is a linear equation and it can be solved directly. For a steady state solution the response will be sinusoidal if the forcing function is sinusoidal. It may be shown [3.1] that the response amplitudes can be calculated straight from the following equation:

$$\{X_{ra}\} = \frac{\{F_{ra}\}}{\left(-\left([M_{rp}]+[M_{ra}]\right)\omega^2 + j[B_r]\omega + \left([K_{rh}]+[K_{rt}]\right)\right)} \quad (3.5)$$

The denominator on the right hand side of Eq.(3.5) is called impedance matrix. Before talking about the solution of Eq.(3.5) it is necessary to examine the approximation in the first step of iteration. The approximation (i.e. replacing $[B_r]\{\dot{X}_r\}|\{\dot{X}_r\}$ with $[B_r]\{\dot{X}_r\}$) can be quite useful and the reason might be explained with the help of a simple example of two arbitrary constants:

$$(C_0 + jC_1)^{-1} = \frac{1}{C_0 + jC_1} = \frac{C_0}{C_0^2 + C_1^2} - j\frac{C_1}{C_0^2 + C_1^2} \quad (3.6)$$

where $C_0 + jC_1$ is a complex number. If C_1 is small compared to C_0 then a change in C_1 does not affect significantly the inverse of $C_0 + jC_1$. Similarly, if $[B_r]\omega$ is small compared to $\left(-\left([M_{rp}]+[M_{ra}]\right)\omega^2 + \left([K_{rh}]+[K_{rt}]\right)\right)$, the approximation in Eq.(3.5) would be close to the actual solution.

Approximate values of $\{X_r\}$ are obtained from the first iteration. The following equation is solved in the next iterations until required convergence is achieved:

$$\{X_{ra}\} = \frac{\{F_{ra}\}}{\left(-\left([M_{rp}]+[M_{ra}]\right)\omega^2 + j[B_{rl}]\omega + \left([K_{rh}]+[K_{rt}]\right)\right)} \quad (3.7)$$

Eq.(3.7) is very similar to Eq.(3.5) but with a difference in the drag damping term.

$[B_r]$ in Eq.(3.5) is replaced by $[B_{rl}]$ in Eq.(3.7) where the linearised formulation of $[B_{rl}]$ is based on the assumption of equal energy dissipation at resonance [3.5]:

$$[B_{rl}] = \frac{8}{3\pi}[B_r]\left|\{\dot{X}_{ra}\}\right| \tag{3.8}$$

Since the amplitudes of structural velocities are yet to be established in the iteration process, the following equation is used to approximate Eq.(3.8):

$$[B_{rl}] = \frac{8\omega}{3\pi}[B_r]\left|\{X_{ra}\}_{\text{last iteration}}\right| \tag{3.9}$$

It is found that the iteration is only significant in the vicinity of resonant frequencies.

3.5.3 Complex Matrix Inversion

It is important to note that it is not necessary to calculate the inverse of $\left(-\left([M_{rp}]+[M_{ra}]\right)\omega^2 + j[B_{rl}]\omega + \left([K_{rh}]+[K_{rt}]\right)\right)$ to find $\{X_r\}$. An equation of type [a]{X}={b}can be solved for {X} without inverting [a]. Usually the solution process is much faster when the inversion is avoided. Some advanced solution techniques would be discussed in Chapter 4 for a system of large number of equations. In RBRA, two powerful routines from Linpack Blas are used to solve Eqs.(3.5) and (3.7). The routines in Linpack Blas were developed in the University of New Mexico. The Fortran source codes of these routines are available free of charge if a request mail is sent to netlib@ukc.ac.uk.

Three routines (i.e. zgeco, zgesl and zgedi) in Linpack Blas are important while working with the complex impedance matrix in Eqs.(3.5) and (3.7). The routine, zgeco reduces a complex matrix to an upper triangular matrix and estimates the condition of the matrix. To avoid inversion zgeco should be followed by zgesl. However, the determinant and inverse of a complex matrix can be found if zgeco is followed by a different routine, zdedi.

These routines in Linpack Blas are excellent in speed and performance. The author has compared them with many others available from different sources (e.g. NAG library [3.10]). But the performance of the Linpack Blas routines has remained unmatched.

3.6 NUMERICAL RESULTS

One main reason for selecting the ISSC TLP configuration was to compare rigid body response results with those published in Refs. [3.9] and [3.8]. The published results in Refs. [3.9] and [3.8] are from 17 different organisations who have used boundary

element formulation and diffraction/ radiation analysis for their calculation. The results are presented for three wave heading angles. It is worth noting that the ISSC TLP has a square deck and consequently, two vertical planes of symmetry. Hence, it is not necessary to present sway and roll responses for waves heading at 0 and 45 degrees. In addition, there should not be any yaw motion for waves at 0 and 45 degrees. However, at 22.5 degree wave heading all six responses are required because they would be substantial and different.

Force and response RAOs calculated from RBRA are presented in Figs. 3.2-3.13 for waves at 0, 22.5 and 45 degrees. Please note that the formulations in RBRA are independent of any wave heading angle. Similar results for waves at a different angle can be calculated without any modification in the program [3.3].

Refs. [3.8] and [3.9] present the results in scattered diagrams based on the data obtained from 17 organisations. With the help of a digitiser, the upper and lower boundaries of diffraction analysis based results are captured in a data file since it is always difficult to compare results from scattered diagrams, especially when the data is not supplied in a table format. The diffraction upper and lower boundaries together with the Morison equation based results from RBRA are shown in Figs. 3.2-3.13.

Diffraction becomes increasingly important when the member diameter and wave length ratio is more than 0.2. Therefore, for the ISSC TLP, the Morison equation is not valid for wave periods less than 7 seconds. When the wave period is less than 7 seconds, the forces and moments are generally overestimated by RBRA as we can see in Figs. 3.2-3.13. Otherwise, the results from RBRA are in sufficiently good agreement with the published results [3.8], [3.9].

3.7 CLOSURE

The philosophy behind this research is to proceed from the simplest computational methods in the early stages of design to more accurate methods, after understanding the global behaviour of the structure. This issue has been discussed in more detail in Ref. [3.4].

Program RBRA has been successfully used in a different research work [3.7] for modelling multi-variate environmental data. One important feature of RBRA is that it can quickly and efficiently generate force and response RAOs. The square of the RAOs can be multiplied to a sea spectrum to generate the corresponding response spectrum. The Morison equation based models are generally found to be poor for computing

TLP pitch/heave responses and it is well accepted that the large diameter inertia load dominated TLP columns require diffraction effects to be handled adequately. So an immediate step to improve the analysis could be the application of McCamy-Fuchs' theory for the columns. For more reliable results many researchers are using hybrid computing models involving both diffraction/radiation theory and the Morison equation because they can account for potential forces as well as viscous forces.

The simplified formulations in RBRA have helped the author to gain an insight into the problem. DCATLP described in the next chapter has been developed from this background.

3.8 REFERENCES

[3.1] Barltrop, N.D.P. and Adams, A.J.: "Dynamics of Fixed Marine Structures", Butterworth-Heinemann Publication, 1991.

[3.2] Burns, G.E.: "Simplified Analysis of a Tension Leg Platform", Deep Offshore Technology Conference, Palma de Mallorca, vol. 2, pp. 182-196, 1981.

[3.3] Chatterjee, P.C., Das, P. K., Faulkner, D.: "A Simplified Method for Analysing TLP Responses for Reliability Based Component Design", Integrity of Offshore Structures, 5th. International Symposium, Glasgow, 1993.

[3.4] Chatterjee, P.C. and Das, P.K.: "Hydro-Structural Response Analysis of Tension Leg Platforms using LUSAS", LUSAS User Conference 1994, Cheltenham, UK.

[3.5] Patel, M.H. and Witz, J.A.: "Compliant Offshore Structures", Butterworth-Heinemann Publication, 1991.

[3.6] Patel, M.H. and Badi, M.N.M.: "A Calculation Method for the Wave Induced Motion Response of a Semisubmersible Vessel - Program Manual for UCLRIG, Department of Mechanical Engineering, University College London, Report No. OEG/80/6, July 1980.

[3.7] Prince-Wright, R.: "Statistical Models of Environmental Data for Marine Structure Design", Ph.D. Thesis (No. NAOE-93-26), Department of Naval Architecture and Ocean Engineering, University of Glasgow, Glasgow, 1993.

[3.8] Report of Committee I.2: "Case study of a Tension Leg Platform", Proceedings of the Ninth International Ship and Offshore Structures

Congress, Registro Italiano Navale, Genova, vol. 1, pp. I.2-48-55, 1985.

[3.9] Taylor, R.E. and Jefferys, E.R.: "Variability of Hydrodynamic Load Predictions for a Tension Leg Platform," Ocean Engineering, vol. 13, no. 5, pp. 449-490, 1986.

[3.10] The NAG Fortran Library Manual, Mark 14, The Numerical Algorithms Group Limited, Oxford, UK, April 1990.

[3.11] Wolfram, S.: "Mathematica - A System for Doing Mathematics by Computer", Second Edition, Addison-Wesley Publishing Co., California, 1991.

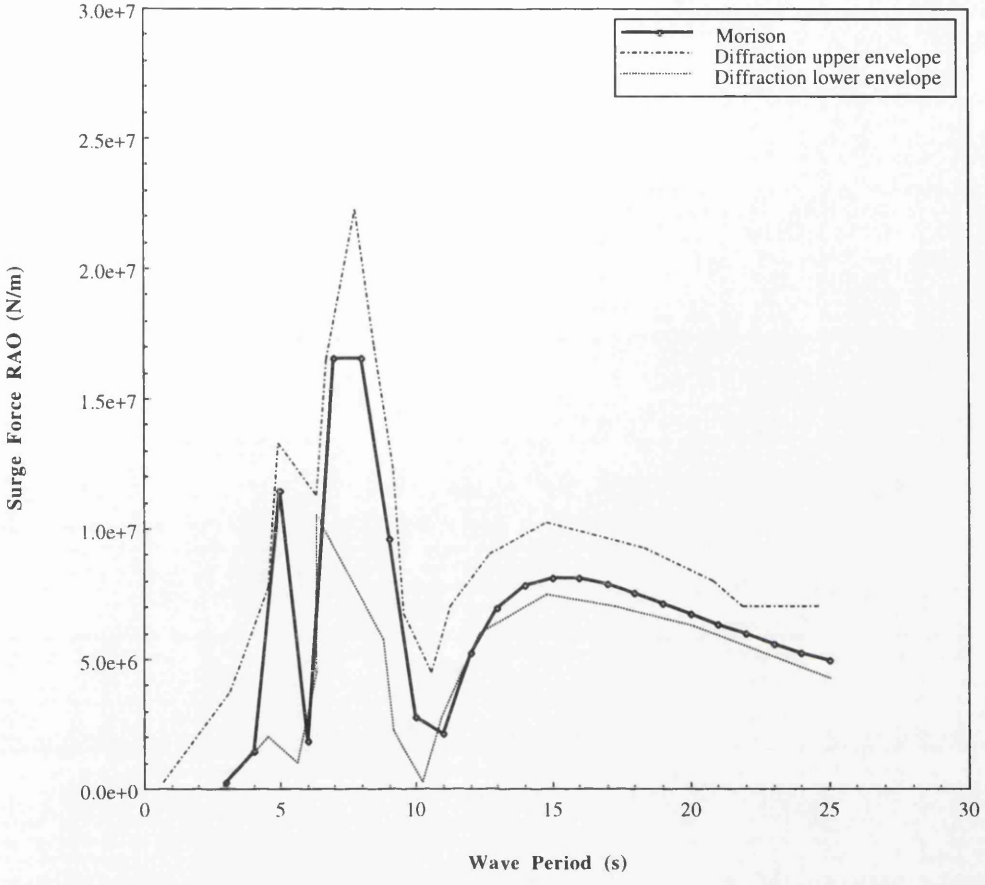

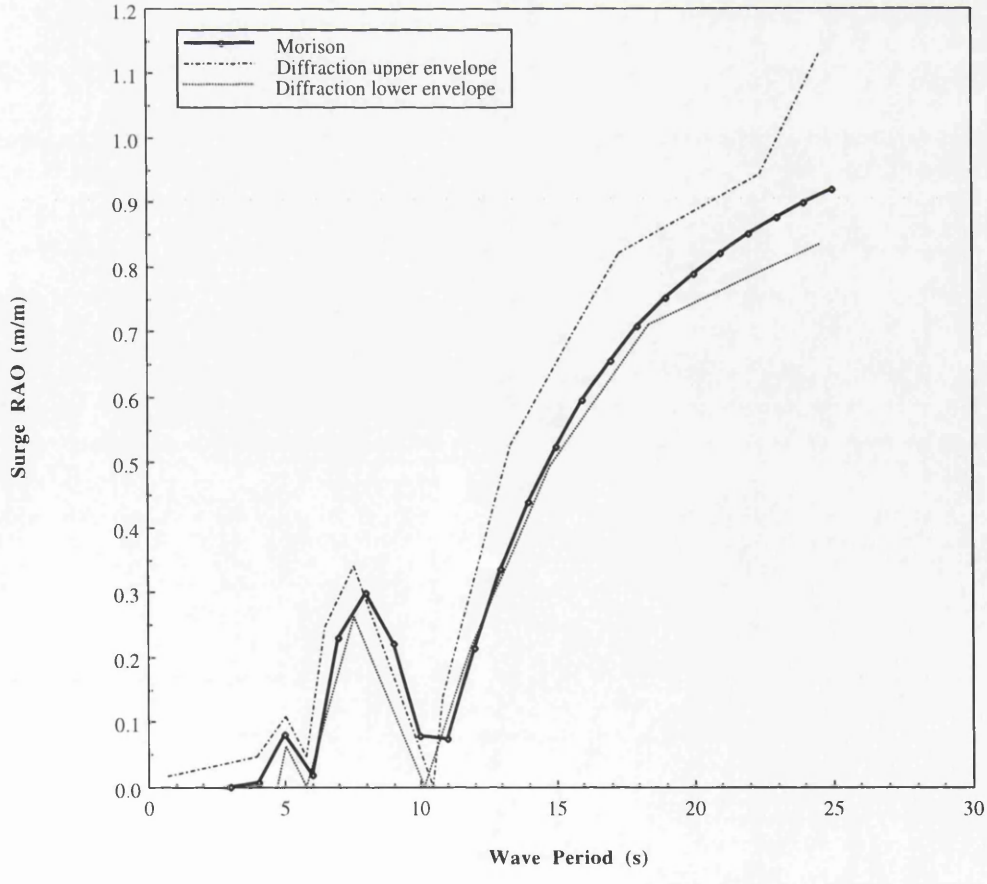

Fig. 3.2. Surge Force and Response RAOs for Waves at 0 deg.

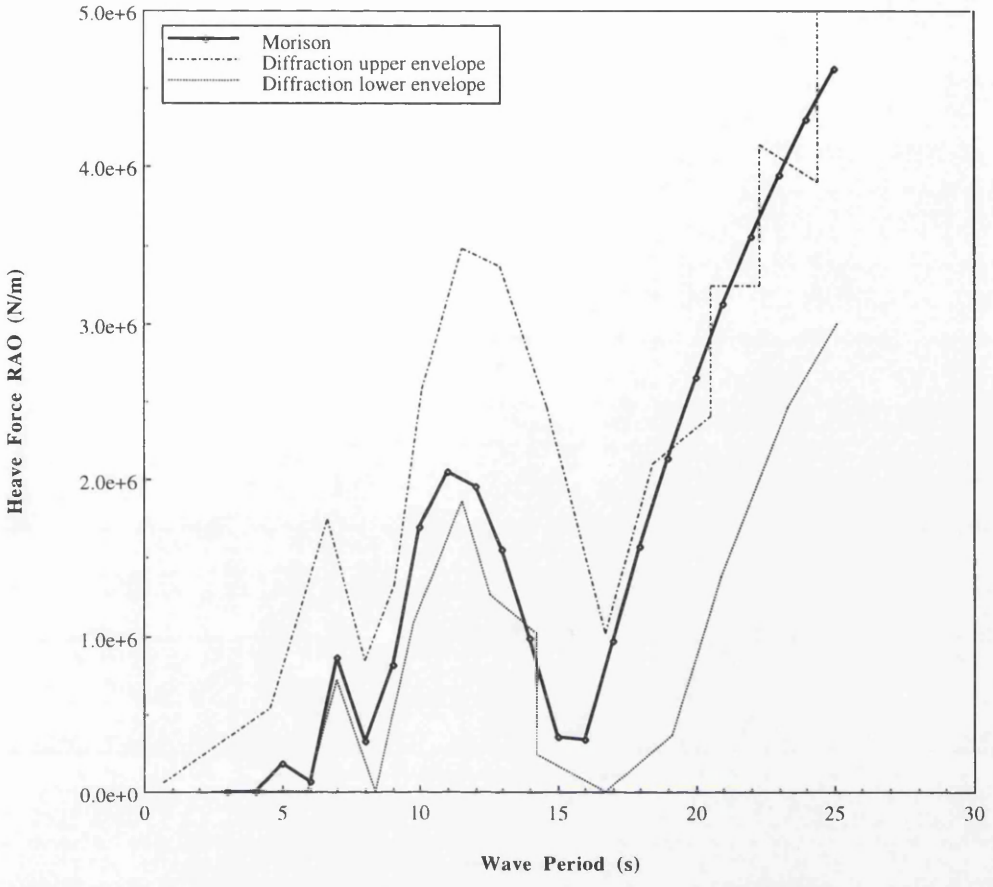

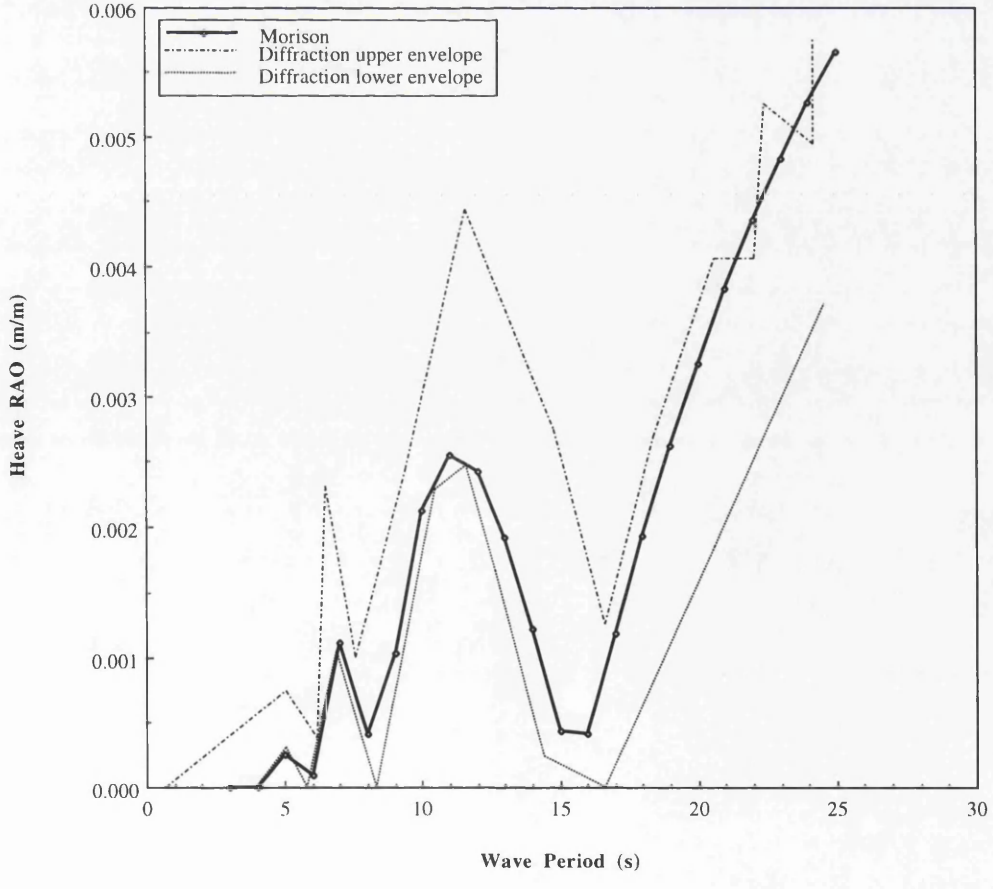

Fig. 3.3. Heave Force and Response RAOs for Waves at 0 deg.

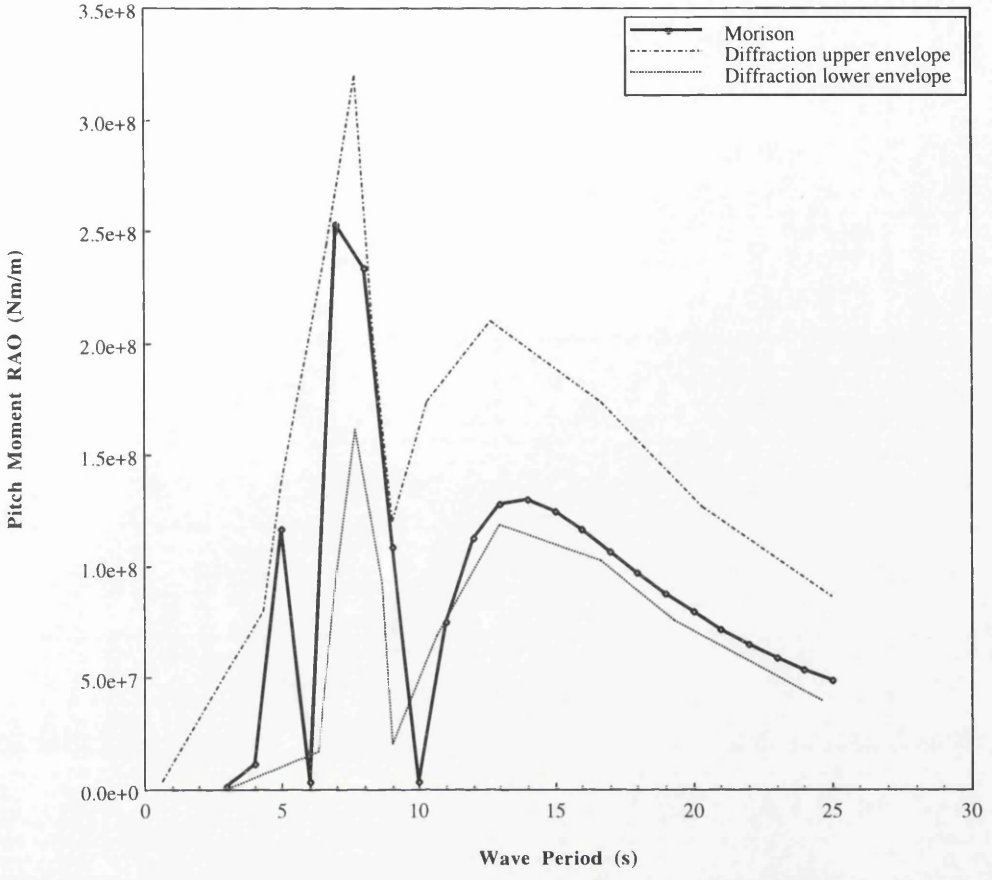

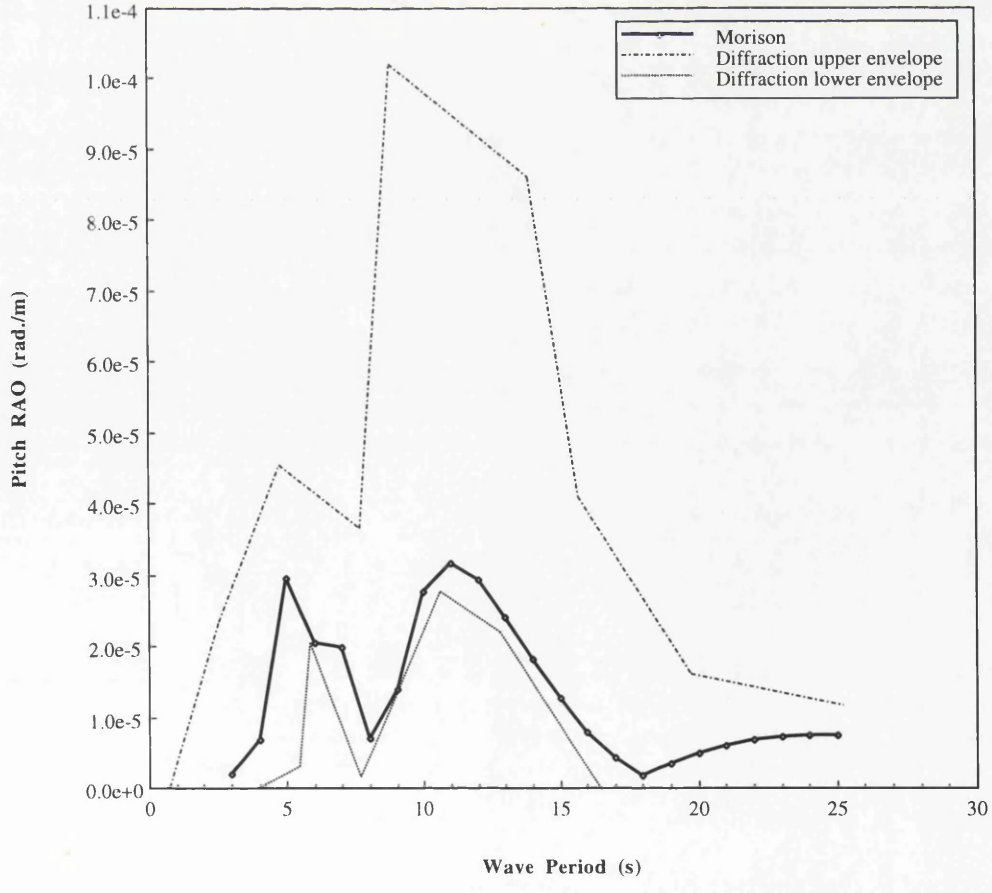

Fig. 3.4. Pitch Moment and Response RAOs for Waves at 0 deg.

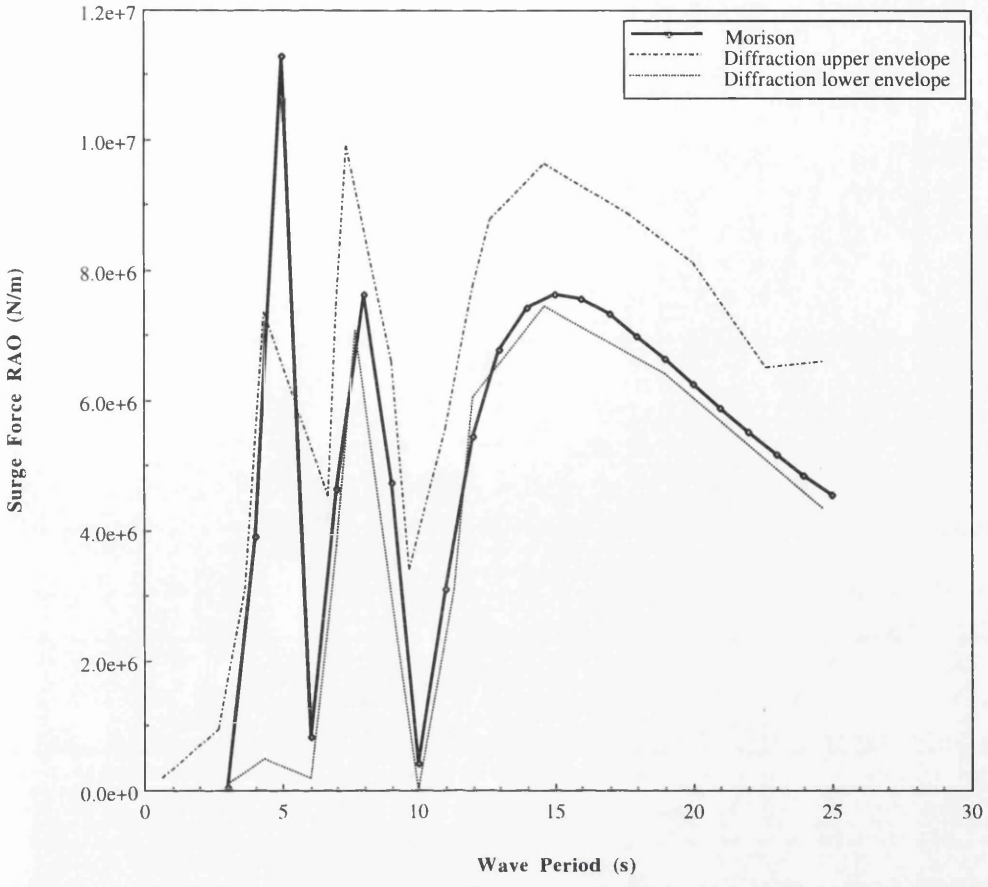

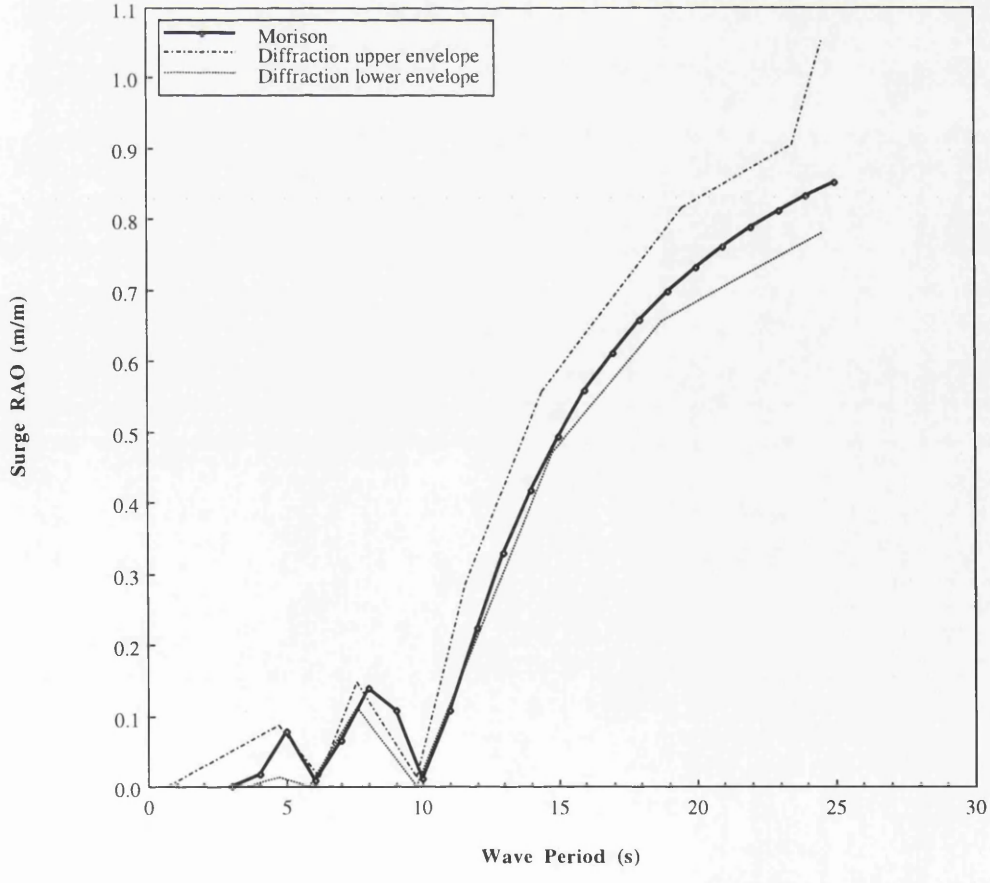

Fig. 3.5. Surge Force and Response RAOs for Waves at 22.5 deg.

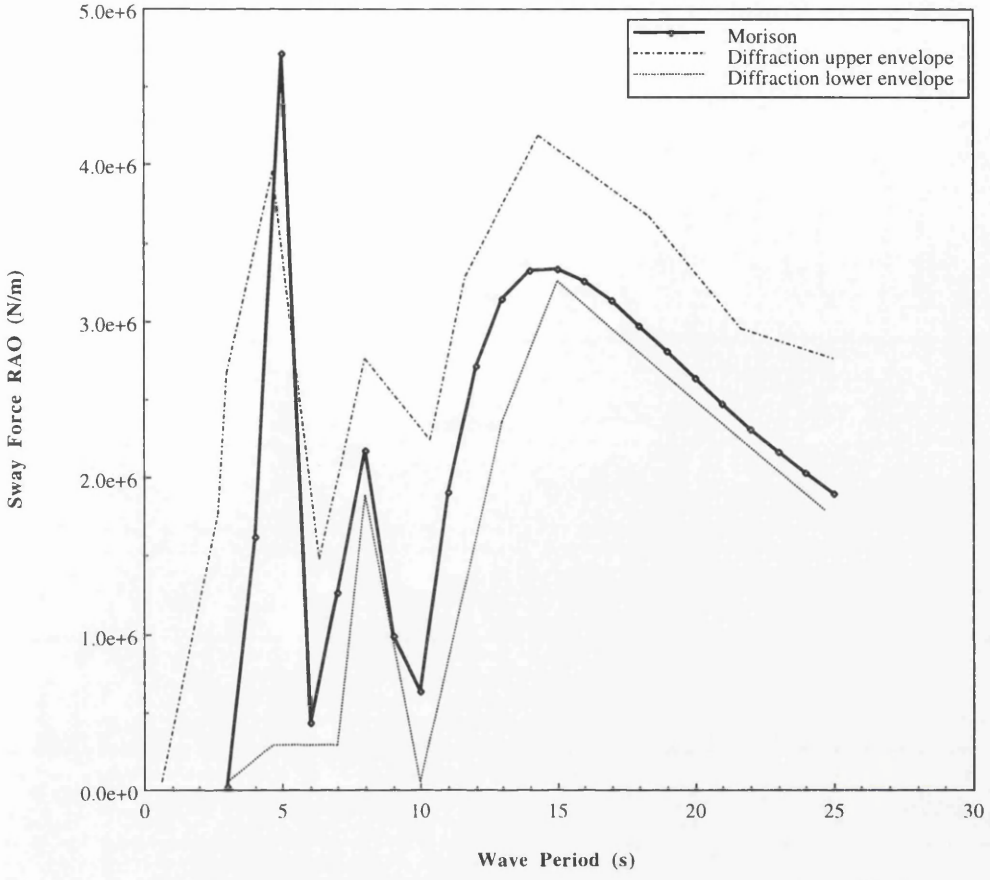

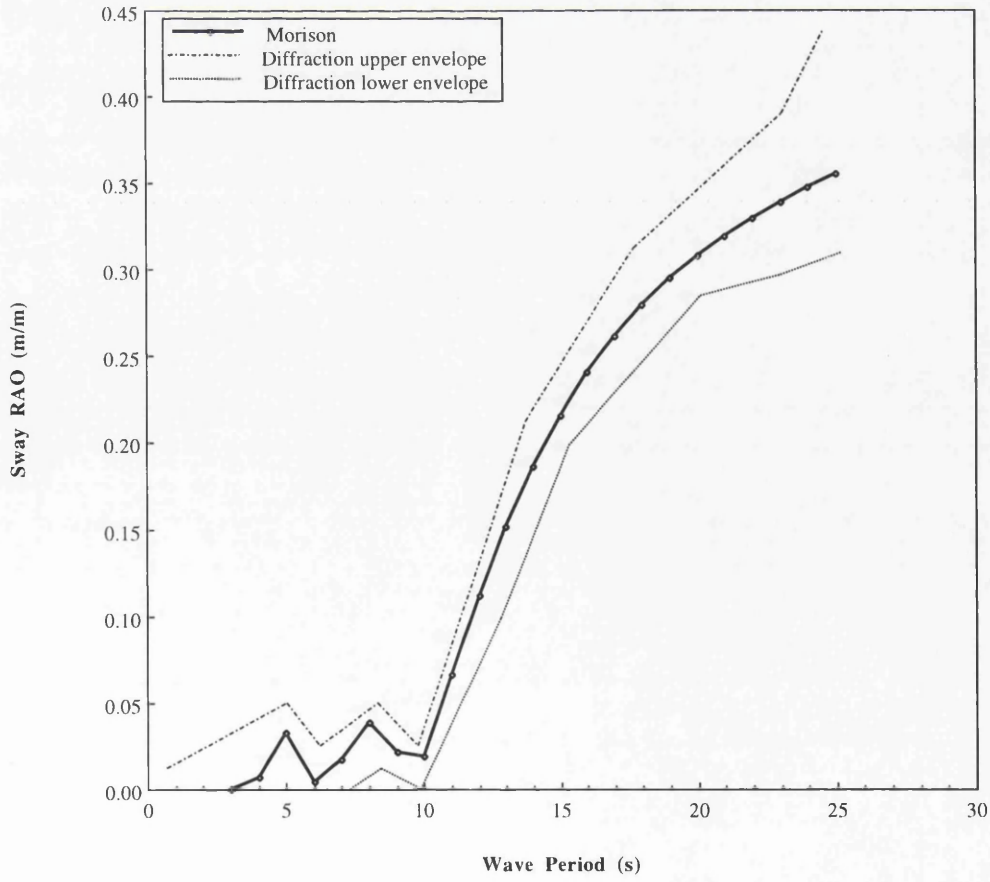

Fig. 3.6. Sway Force and Response RAOs for Waves at 22.5 deg.

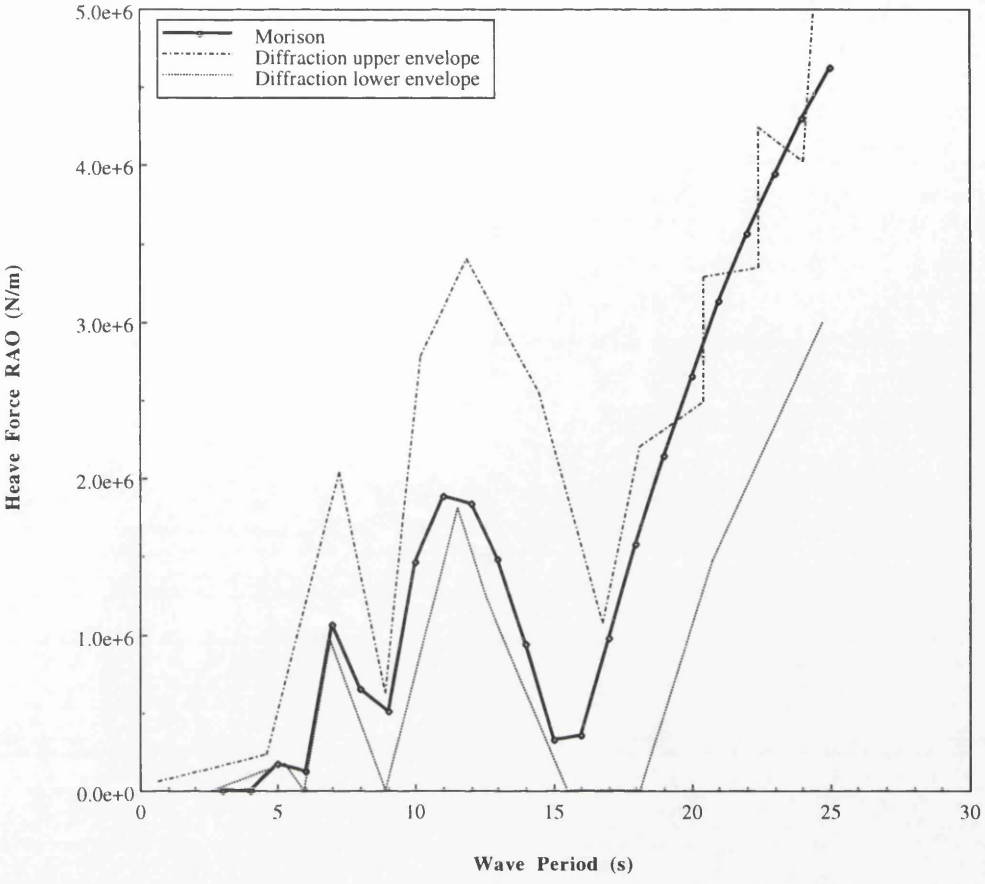

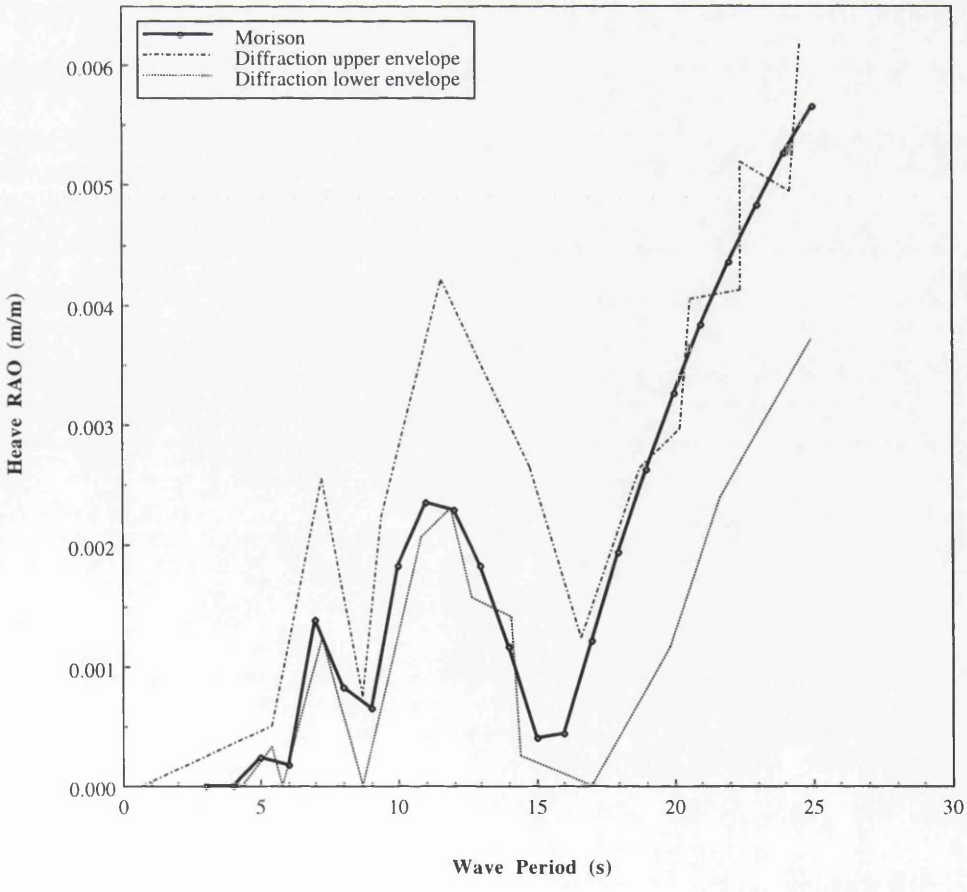

Fig. 3.7. Heave Force and Response RAOs for Waves at 22.5 deg.

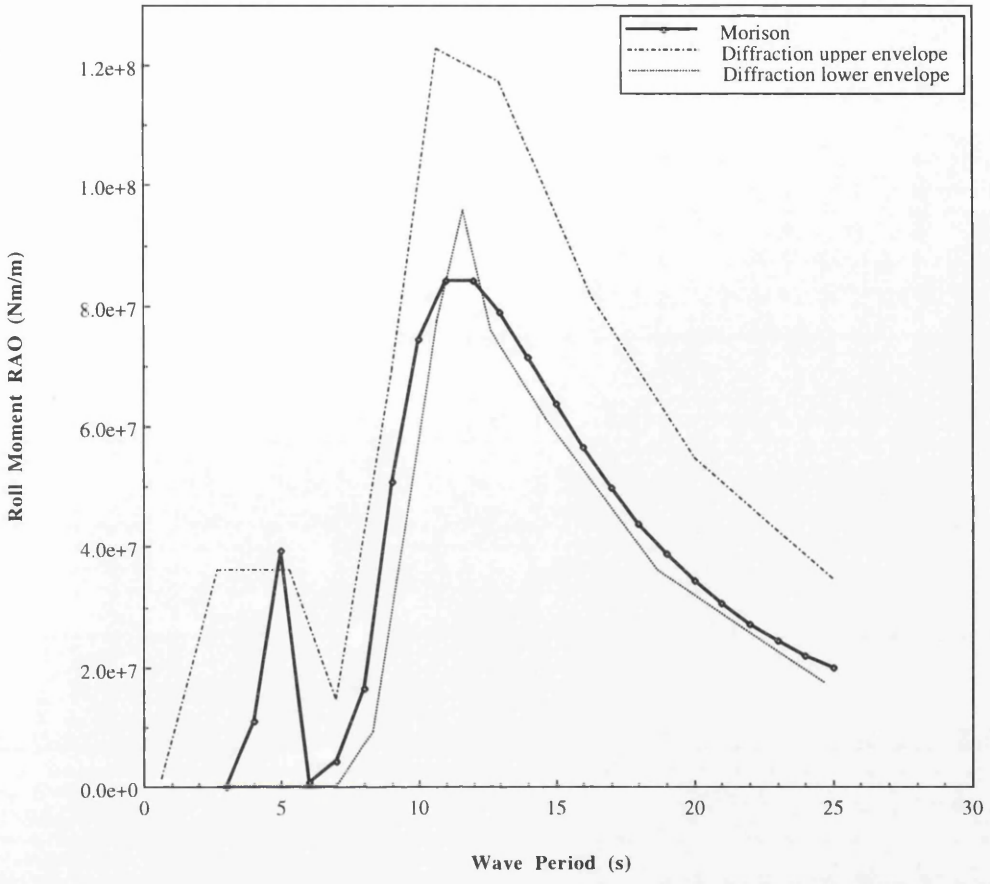

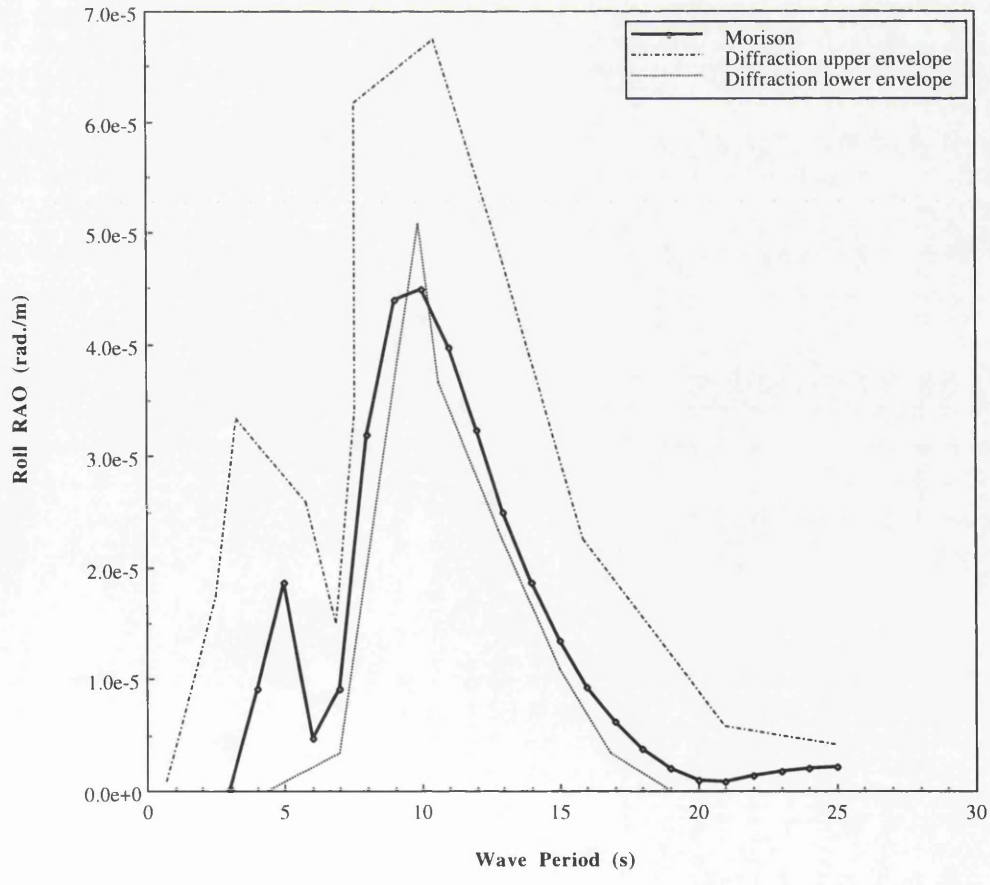

Fig. 3.8. Roll Moment and Response RAOs for Waves at 22.5 deg.

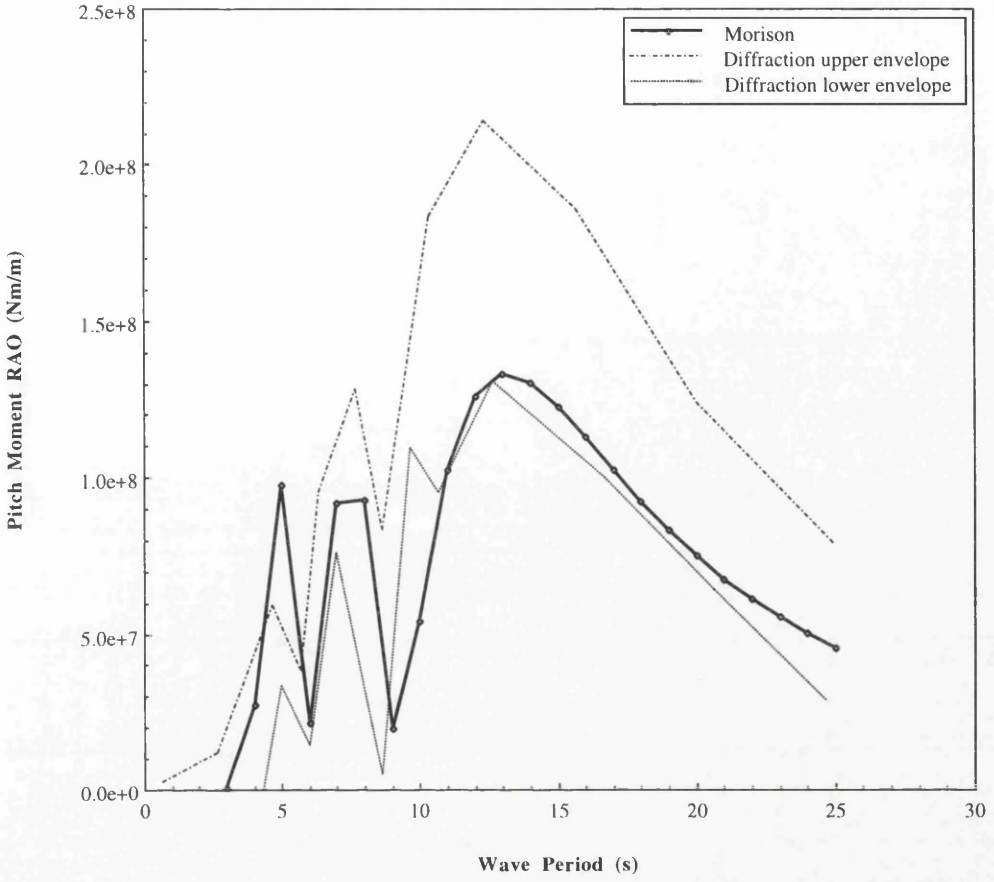

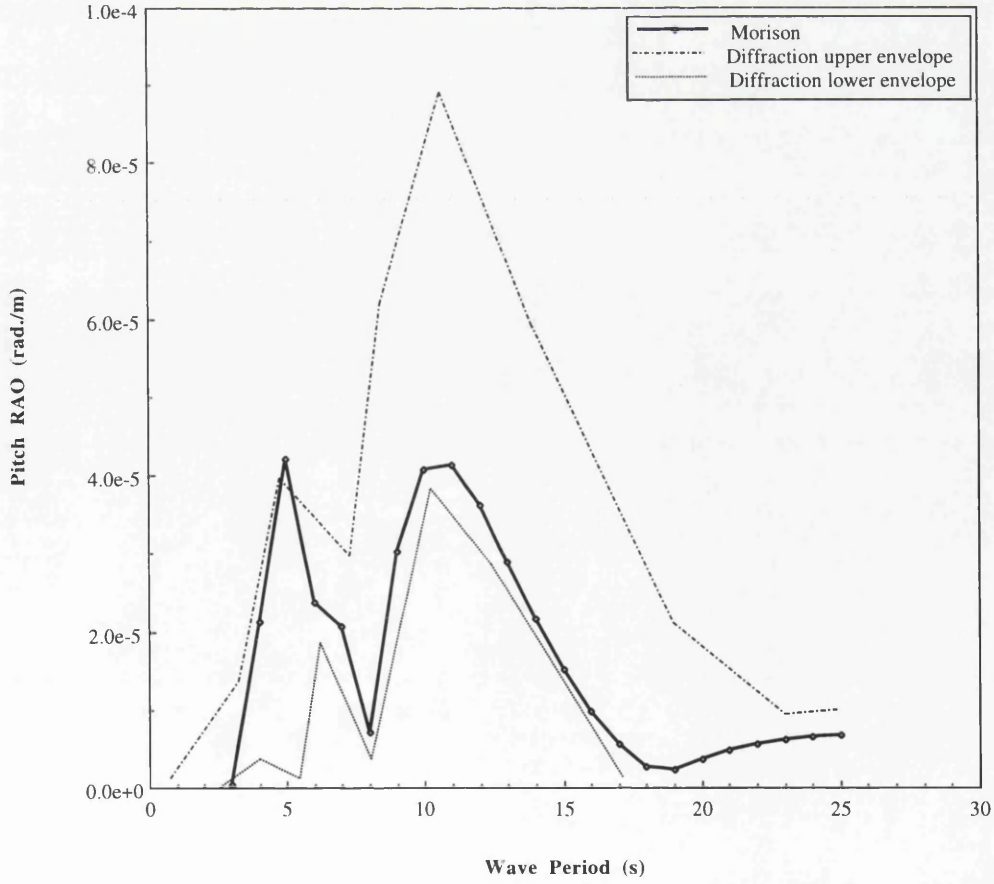

Fig. 3.9. Pitch Moment and Response RAOs for Waves at 22.5 deg.

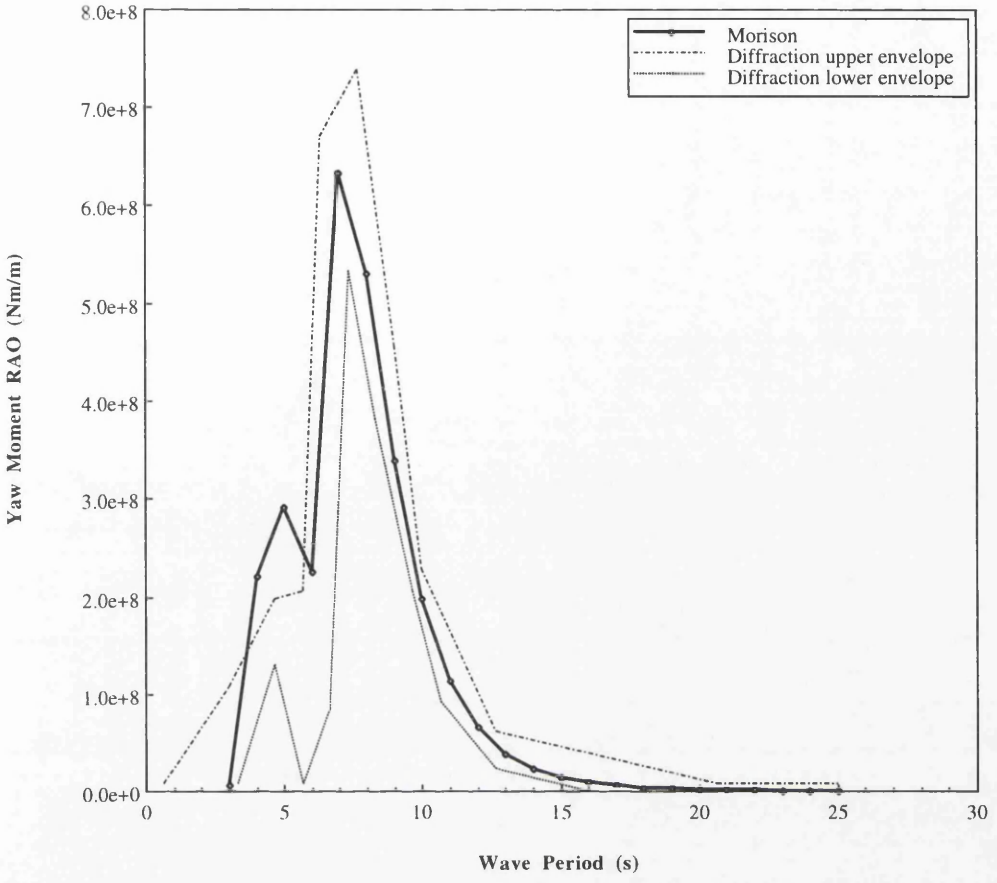

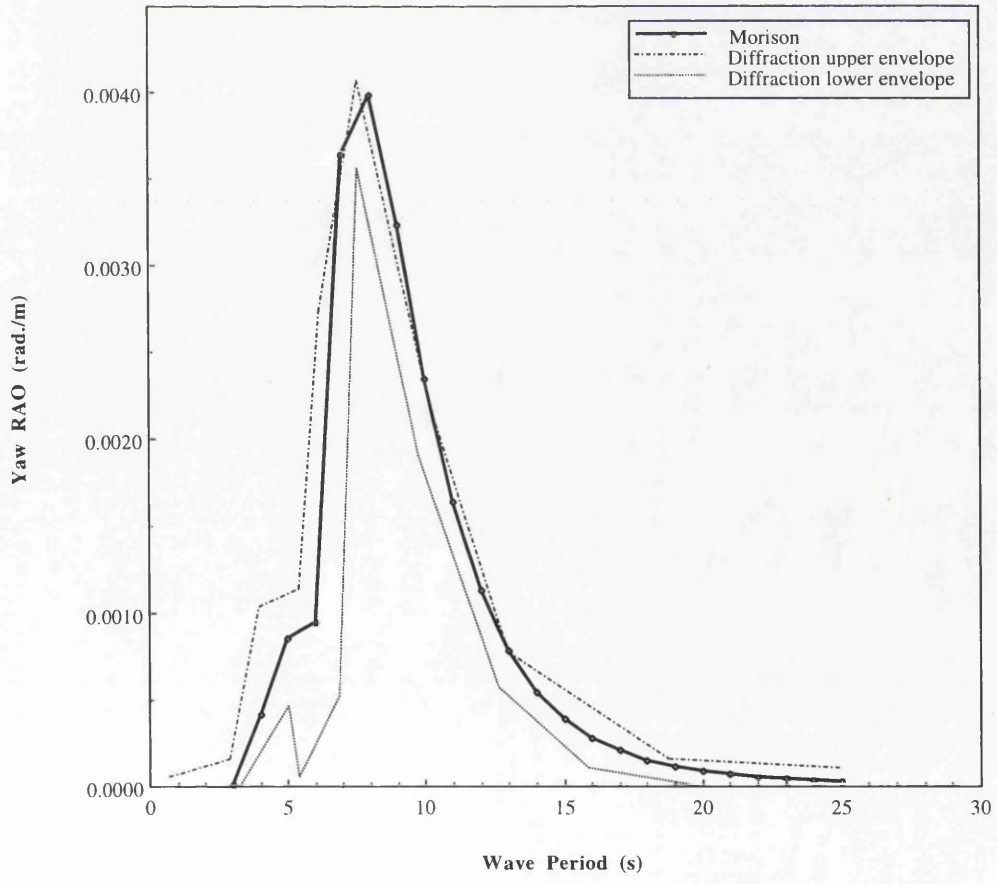

Fig. 3.10. Yaw Moment and Response RAOs for Waves at 22.5 deg.

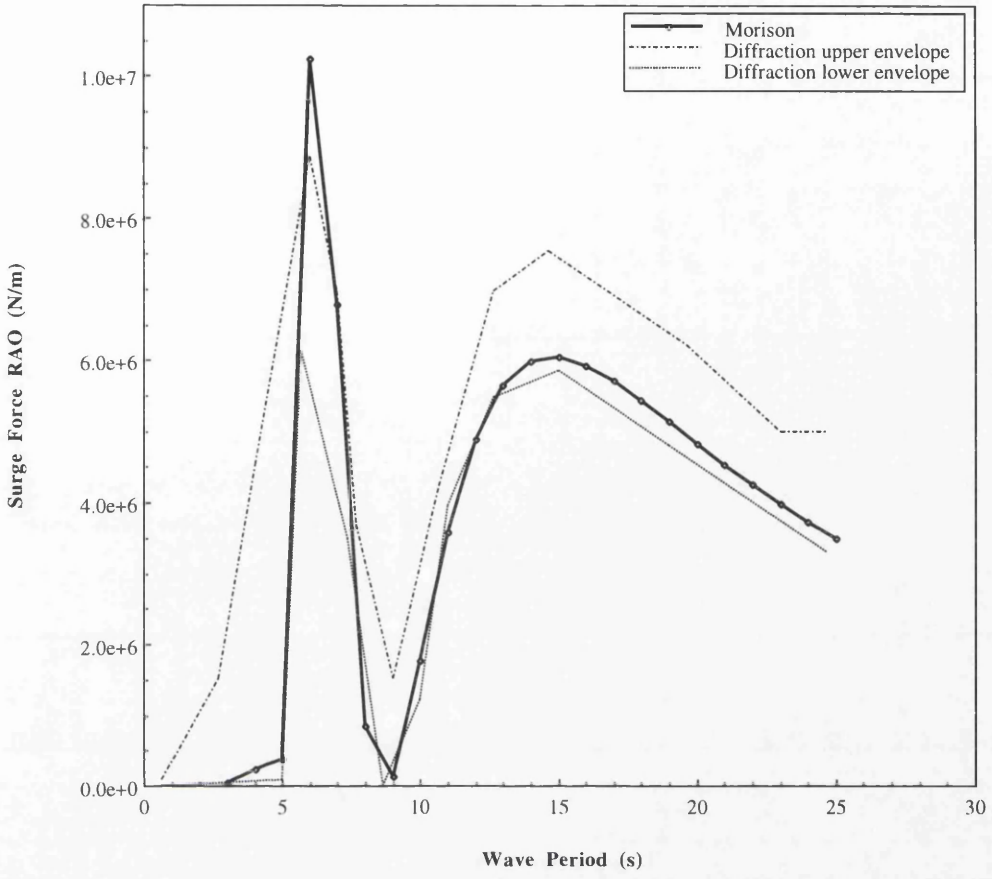

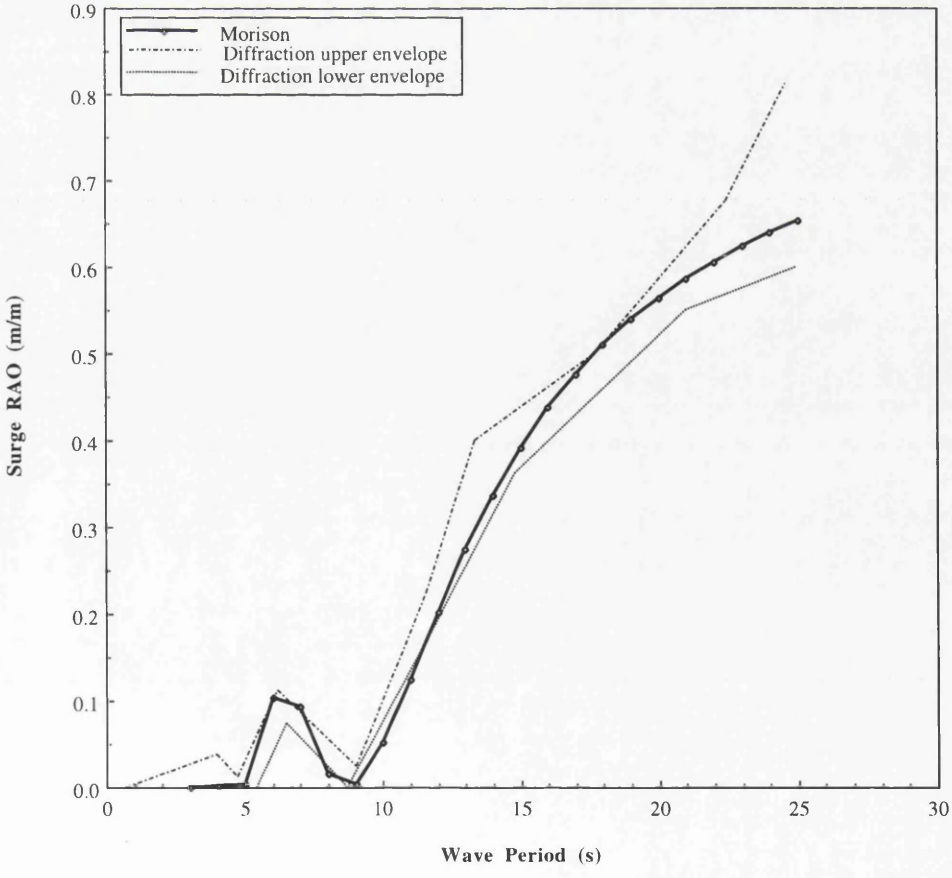

Fig. 3.11. Surge Force and Response RAOs for Waves at 45 deg.

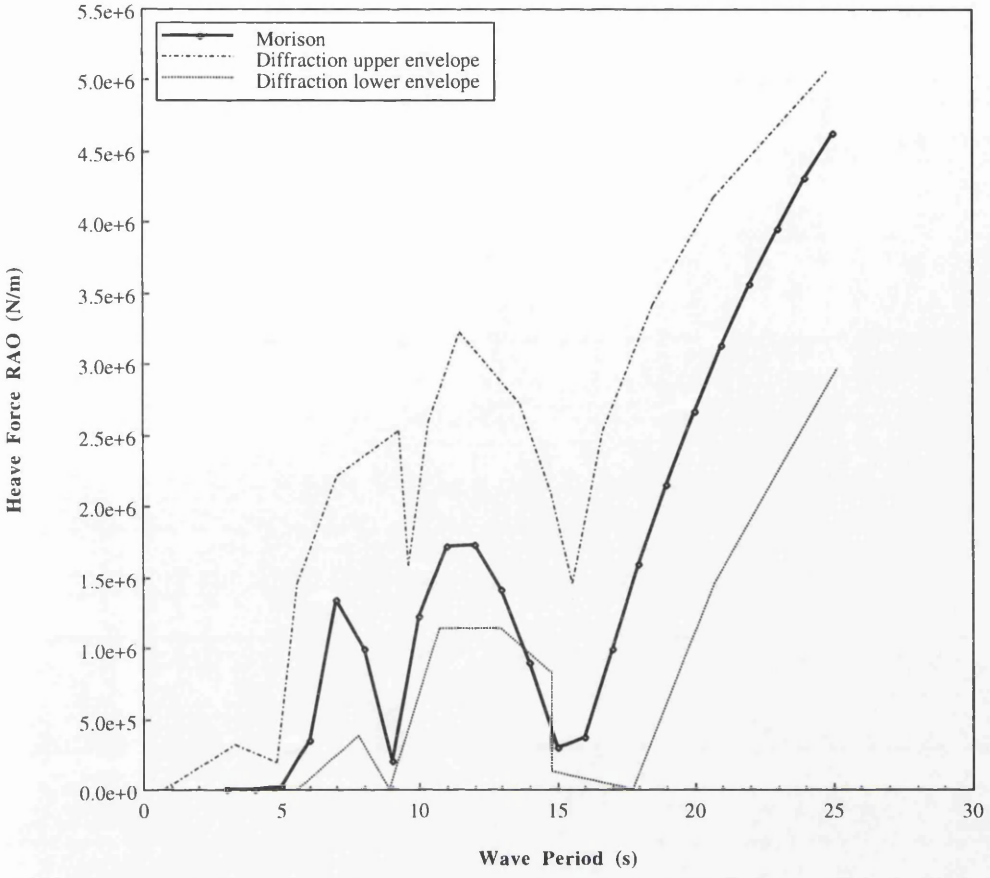

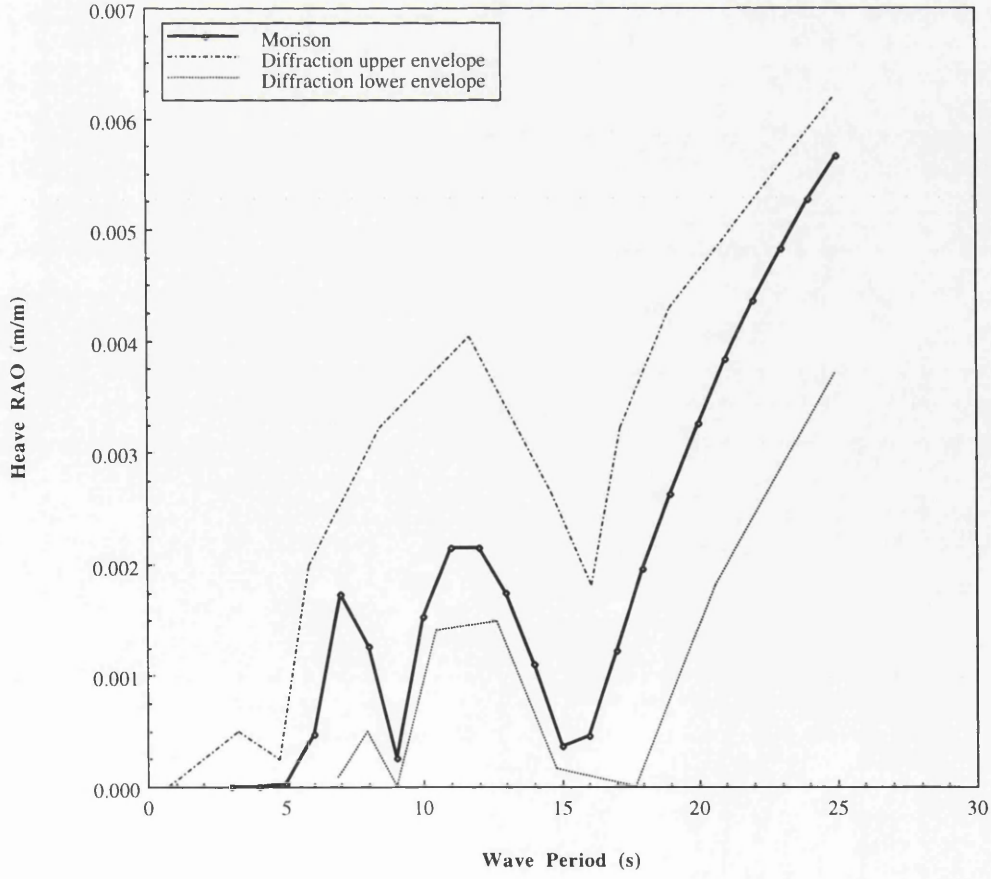

Fig. 3.12. Heave Force and Response RAOs for Waves at 45 deg.

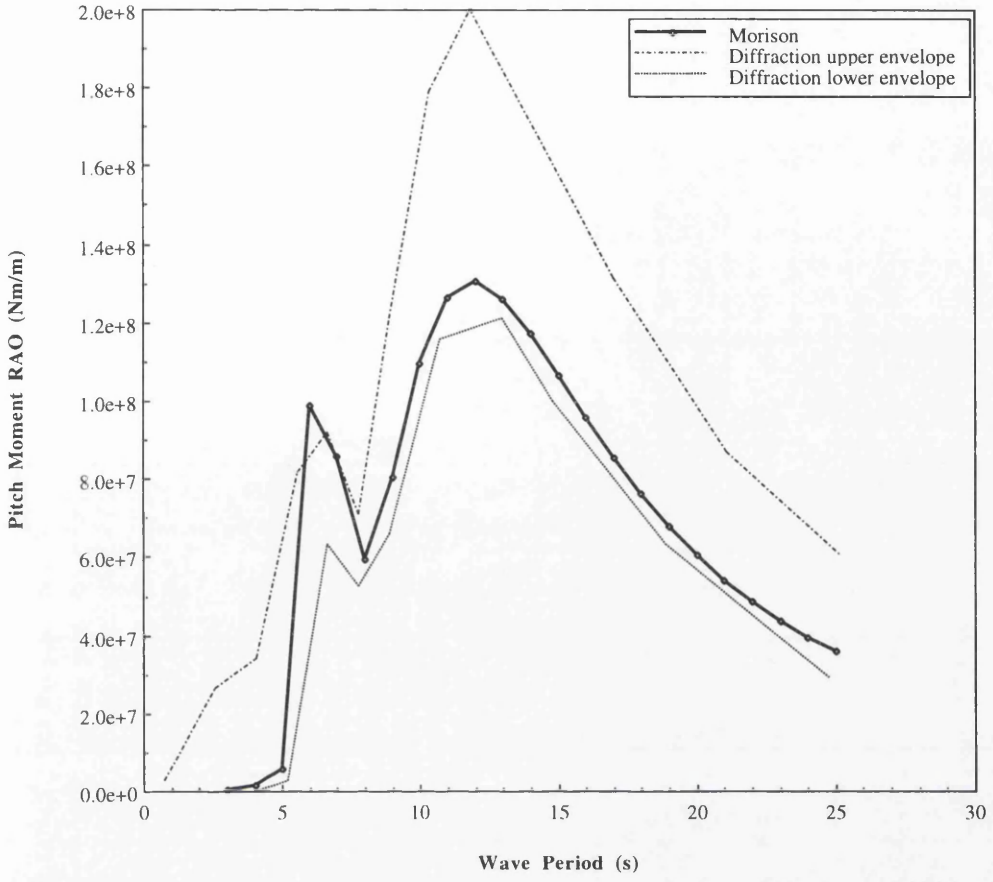

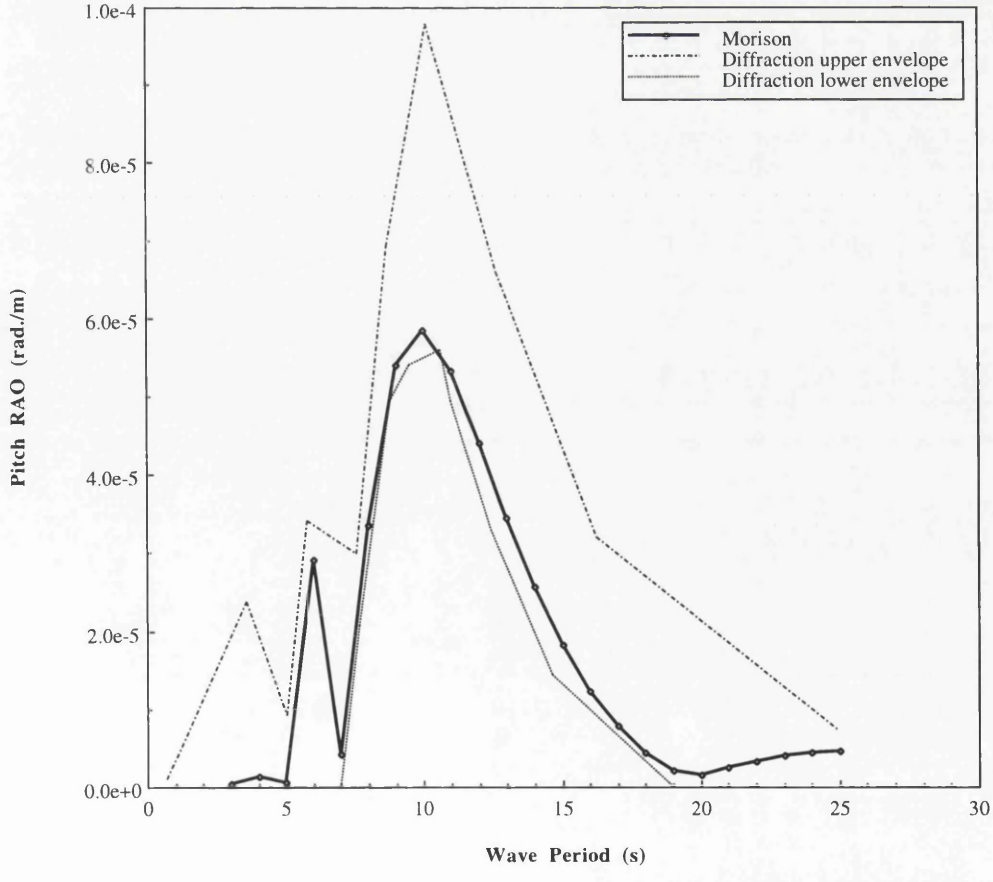

Fig. 3.13. Pitch Moment and Response RAOs for Waves at 45 deg.

CHAPTER 4

HYDRO-STRUCTURAL RESPONSE ANALYSIS

4.1 INTRODUCTION

This chapter describes the author's attempt to overcome the limitations of a conventional hydrodynamic analysis. The rigid body response calculations are suitable in establishing maximum motion amplitudes and related factors. But in the context of structural design, they are not quite helpful. The design process will inevitably demand a separate space frame analysis and that will involve transfer and modification of results from the rigid body hydrodynamic program. It is discussed later in detail that this 'migration' from the hydrodynamic domain might be complicated and decisions involved may vary depending on the TLP configuration. A hydro-structural analysis program is an ideal solution in this respect because it can take care of the data transfer 'internally'. Moreover, the solution process would be automatic and independent of the TLP configuration. The following sections present this hydro-structural analysis concept relating to TLPs.

4.2 STRUCTURAL CONFIGURATION OF ISSC TLP

Table 1.1 in Chapter 1 provides a complete set of data for conventional hydrodynamic calculations for the ISSC TLP. RBRA in Chapter 3 has used them to calculate the response RAOs. But the data in Table 1.1 are not enough for a hydro-structural analysis. There are several other pieces of information required for structural modelling of the members. Some important simplifications and assumptions are also necessary to establish the global structural model. It is worth noting that plate and shell elements are more appropriate in modelling continuum structures like TLPs. But a global model using higher-order multi-node elements can be time consuming and computationally very expensive. As a reasonable compromise, TLP components can be modelled as numerous 3-D beam elements. In this study there are two important structural simplifications. The tether group per corner is replaced by a hydrodynamically equivalent tether. The whole deck structure that may involve a number of deck layers in a 'real' TLP is modelled here as a single grillage of box girders.

4.2.1 TLP Member Scantlings

It is at first essential to design the columns, pontoons, deck girders and tethers to generate additional information necessary for structural analysis. Proper attention has been given to keep these designs very close to those used in practice. For the corner columns a typical design is available [4.11] where it was considered as an illustrative example for the purpose of demonstrating the applications of the new code. A parametric study was carried out there with a number of models with minor variations in different parameters. Our column for the ISSC TLP, shown in Table 4.1 is designed

from the "most desirable model" of the TLP Rule Case Committee. But it should be noted that the North Sea TLP in their study is significantly different from the ISSC one especially in terms of water depth.

Table 4.1. Design of Corner Columns from TLP RCC Model Code

Parameters	Unit	TLP RCC	ISSC TLP
Radius	mm	8840	8440
Shell thickness	mm	25.34	25
No. of stringers	-	60	60
Stringer web depth	mm	300	300
Stringer web thickness	mm	15	15
Stringer flange width	mm	189	189
Stringer flange thickness	mm	19	19
Ring frame spacing	mm	2200	2200

Lee [4.20] has considered the Hutton TLP and two other possible variations for system reliability analyses. The pontoons of the ISSC TLP (7.5 m x 10.5 m) and the Hutton TLP (8 m x 10.8 m) are very close in size. So the Hutton TLP is taken as a starting reference for the pontoon design. The thickness varies for bottom, side shell and deck plates of the Hutton pontoons. But here we will consider uniform thickness all around the pontoon as a starting point for design.

Table 4.2. Design of the ISSC TLP Pontoons

Pontoon Parameters	Dimension (mm)
Plate thickness (bottom, side and deck)	28
Stiffener (bottom, side and deck) spacing	750
Stiffener web depth	400
Stiffener web thickness	14
Stiffener flange width	150
Stiffener flange thickness	25

Fig. 4.1 shows the pontoon cross-section for numerical studies. Please note that TLP pontoons have generously rounded corners for hydrodynamic reasons [4.16] when they have rectangular sections. It is possible to include a corner radius in the analysis

but there is no information given in Ref. [4.31] in this context. So it is decided here to go for a rectangular section ignoring the effects of its hard corners. The stiffeners are also arranged accordingly so that they do not foul with any corner curvature given later in design.

Deck structure does not come under the main focus of this study. A simple grillage of box girders is assumed here as the deck. The scantlings of the deck girders (Fig. 4.2) are taken similar but less than those of the pontoons. The selection of scantlings is arbitrary but believed to be reasonable to start with.

Table 4.3. Design of the ISSC TLP Deck Girders

Deck Girder Parameters	Dimension (mm)
Breadth	7500
Height	7500
Plate thickness (bottom, side and deck)	20
Stiffener (bottom, side and deck) spacing	750
Stiffener web depth	350
Stiffener web thickness	14
Stiffener flange width	150
Stiffener flange thickness	20

Table 4.4 gives brief details about TLPs in service in relation to the ISSC TLP tether design. The Jolliet, Auger and Heidrun [4.1] TLPs have 12 tethers in total whereas Hutton and Snorre have 16. Jolliet, Snorre, Auger and Heidrun have thin-walled [4.23] tethers whereas Hutton, operating in much less water depth, has thick-walled tethers. The main particulars in Table 1.1 in Chapter 1 do not provide any information about tethers and risers. It rather suggests to replace tethers by the spring stiffness values given. In the original TLP Concept, tether and riser dynamics played little part. The tethers were conceived as being constructed of wire rope or possible drill pipe and sufficiently tensioned by the excess buoyancy of the platform as to prevent any significant departure from straight. It is possible to calculate the material area of the equivalent tether in each corner:

$$\frac{4E_Y A_t}{L_t} = 813 \text{ MN/m} \quad \Rightarrow \quad A_t = \frac{813 \times 10^6 \times 415}{4 \times 208 \times 10^9} = 0.40552 \text{ m}^2 \qquad (4.1)$$

This material area is very close to that adopted for Heidrun. Two designs are given in Table 4.4. The main difference comes in the total number of tethers. It is difficult to do a beam element based analysis with three tethers per corner. But the equivalent tether

concept is only for simplifying the calculations. It cannot form the basis of real and practical design of tethers.

It is worth noting that 'mass' and 'weight' have different roles in a dynamic analysis. If the system is neutrally buoyant, there is no resultant force in the vertical direction as a consequence of weight and buoyancy of the system. But it certainly does not suggest that a neutrally buoyant system will have no lateral dynamics. The lateral dynamics comes from the system mass and its added mass in the lateral direction. Tether lateral dynamics is important in certain load cases specially when loading frequencies are close to tether natural frequencies. But the principal particulars in Table 1.1 do not have any information regarding tether mass distribution. Tethers here are assumed to have the standard steel mass density (i.e. 7850 kg/m^3). When tether mass is included in the system it will have some contribution to the overall lateral dynamics. The TLP behaviour may differ significantly from the original massless spring concept.

4.3 TWO OTHER DIFFERENT MODELS OF ISSC TLP

4.3.1 Introduction to Other Models

Model_1 for rigid body analysis has been illustrated in Chapter 3 while explaining results from RBRA. In this chapter, two other models are created for the ISSC TLP. Table 4.5 briefly distinguishes the differences among these three models:

Table 4.5. Three Different Models of the ISSC TLP

Models	Deck	Hull	Tethers
Model_1	Platform mas	lumped at the CG	(6x6) restoring matrix
Model_2	Simple grillage	Beam elements	6 springs in each corner
Model_3	Simple grillage	Beam elements	Beam elements

Model_2 and Model_3 have the same three dimensional frame as their hull. But the modelling of tethers are different. Model_2 has six springs in each corner whereas Model_3 has ten beam elements in line representing each equivalent tether per corner. Sketches (i.e. not to scale) in Figs. 4.3-4.8 represent the beam element division of the hull. It is worth noting that more divisions will not necessarily increase the accuracy in the solution because many closed-form equations are used that take care of the length parameter. Consistent mass and stiffness matrices are used that do not depend significantly on the element length like lumped mass matrix formulation. These issues

are discussed in more detail in Section 4.5.3. The main objective is to establish a computational tool that can help a designer to go through the design 'loops' by reflecting the effects of changes in various design parameters. The aim is not to design the ISSC TLP itself. This TLP is just an example for numerical studies.

Please note that even in a rigid body motion response analysis 'stick' [4.25] or beam models are used for calculating the environmental loading but in the equation solving stage the system is considered as a lumped mass at its CG position (like Model_1 in Chapter 3). That is where the analysis stands different for Model_2 and Model_3. The number of equations solved in such cases depends on the number of nodes and associated boundary conditions.

Element number 82, 84, 86 and 88 actually represent column joints in Fig. 4.10. The rest of the elements are for equivalent tethers. Fig. 4.9 shows the corresponding nodes. Tether elements are for Model_3 only. It is important to discuss the origin and definition of column and pontoon joint elements in this context. These joint elements are beam elements with stronger sectional properties representing the columns and pontoons at their junctions. Fig. 4.11 explains the problem of line diagrams through the centre lines of structural members of finite width and height.

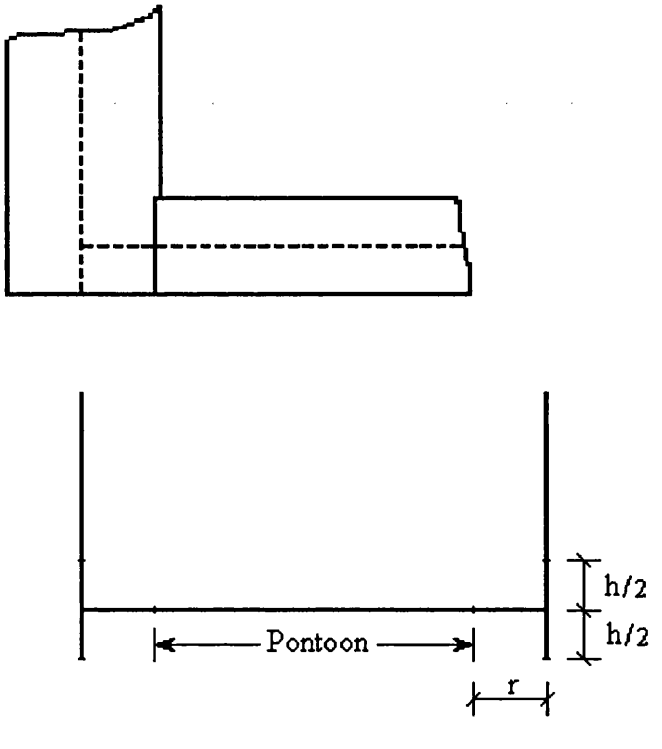

Fig. 4.11. Column and Pontoon Joint Elements

The symbols 'r' and 'h' stand for column radius and pontoon height respectively. A pontoon joint element is the one with length r (element 89-96 in Fig. 4.8) connected to the adjacent column. In reality they do not exist because of the width of columns. So pontoon joint elements are not subjected to external loads in this analysis. Similarly each column joint element (number 81-88 in Figs. 4.6 and 4.10) is of length h/2 and with stronger sectional properties because a column-pontoon node in reality has many additional stiffening members.

One of the main objectives in this study is to compare results with others. So it is necessary to follow the principal particulars in Table 1.1 in Chapter 1 as close as possible. Table 4.6 presents the adjustment done to keep the CG position of the hull at 38 m above keel according to Table 1.1. Table 4.6 also provides the mass density values in lb./ft^3. This calculation is done in a spreadsheet software and the initial values of mass densities are taken from Grant et al [4.16] Although the final values are higher than their typical mass density values, the proportions are roughly the same. This adjusting calculation has two constraints: the total mass and the CG position. Any spreadsheet software is extremely helpful in this context because it can instantly reflect the effects of any changes made.

For any finite element calculation specially with beam elements, the moment of inertia, rotatory inertia and material cross-sectional area of the element are very important. In fact they are the main items in the input data file. Table 4.7 presents the sectional properties of TLP members. Inertia and area values of tether elements are for Model_3 only.

4.3.2 Model_2 Developed in LUSAS

Model_2 is developed mainly for using it with a finite element package called LUSAS. LUSAS is from FEA Limited and it has many advanced computational capabilities. It can handle a wide range of non-linear problems and different types of complicated structures. The graphical interface of LUSAS, also known as MYSTRO is well equipped with hidden surface removal and 'slicing' algorithms and other advanced techniques required in a three-dimensional presentation of a complex finite element problem. But LUSAS cannot perform any interactive hydro-structural response calculation and there is no straight-forward way of including added mass of the structure in the analysis. LUSAS also does not offer any loading module for hydrodynamic calculations. The resources available in LUSAS are very general in nature.

However, it is not the correct way to represent roll, pitch and yaw stiffnesses by attaching rotational springs at the column base although it is suitable as a working model. If geometric stiffness is introduced, the model can be improved. But this is not always correct since roll will introduce an apparent side force on the pontoons. However, it is only the tow out condition that requires this refinement for a TLP.

Simple finite element programs that can only handle 'fixed' or 'free' support conditions are not suitable for TLPs. Only rotational and translational springs can define the boundary conditions of a TLP hull when tethers are excluded from the analysis. Fortunately LUSAS works with spring boundary conditions in three dimensions. It is possible in LUSAS to attach three linear translational and three linear rotational springs in one node. Other features of LUSAS will be discussed in more detail in Chapter 6.

Fig. 4.12 shows Model_2 for LUSAS. Six linear springs are attached to four end nodes (number 114-117 in Fig. 4.9). LUSAS has a library of various elements to be used for different types of finite element problems. The element type JSH4 [4.21] is selected to introduce additional mass (i.e. not structural mass) in Model_2. JSH4 elements are joint elements in true sense, unlike the column and pontoon joint elements mentioned before. A JSH4 element has six degrees of freedom. Different mass, stiffness and Rayleigh damping parameters can be specified in each degree of freedom. This capability of handling different mass, stiffness and Rayleigh damping parameters in different degrees of freedom actually allows the user to include added mass in the analysis because added mass is dependent on the direction of motion. The symbol 'Z' in Fig. 4.12 indicates the nodes where added mass has been lumped in all three directions. The springs shown at each column base in Fig. 4.12 look a bit clumsy because of their existence at the same place!

4.3.3 Surge and Sway Spring Constants for Model_2

In order to find the spring constants it is necessary to deal with different parameters governing the offset, set-down of the platform and the change in tether tension. The tethers are assumed to be straight at all times in this section to derive the spring constants for Model_2 although the curvature and lateral dynamics have been studied later in case of Model_3. The change in length due to the increase in tether tension is taken into account although the extensions are marginal. The tethers are generally slender pipe structures connected with the help of flex-joints to the hull and foundation at the top and bottom ends. The mathematical model here in this section considers 'ball and socket' connections at both ends of tethers.

In Fig. 4.13, F_X is the net force (i.e. resultant of platform inertia and external forces) in the global X direction. Only surge motion is considered to find out the corresponding spring constant. For sway the spring value would be the same. The tether in Fig. 4.13 is assumed to remain straight while rotating in a pendulum like motion about its lower end by an angle θ_t. The top end of the tether moves with the hull and its resulting

excursions are X_0 and Z_s in the horizontal and vertical directions respectively. At the offset position, the five unknown variables are: tether angle (θ_t), change in tether length (δL_t), offset (X_0), change in tether tension (δT) and set down (Z_s). They can be solved from the following five force balance and geometric constraint equations:

Geometry:

$$\cos\theta_t = \frac{L_t - Z_s}{L_t + \delta L_t} \tag{4.2}$$

$$\sin\theta_t = \frac{X_0}{L_t + \delta L_t} \tag{4.3}$$

Force:

$$F_X = (T_0 + \delta T)\sin\theta_t \tag{4.4}$$

$$T_0 + \rho g A_{wp} Z_s = (T_0 + \delta T)\cos\theta_t \tag{4.5}$$

Elasticity:

$$\delta L_t = \frac{L_t \delta T}{A_t E_Y} \tag{4.6}$$

When the value of δL_t is substituted from Eq. (4.6) to Eq. (4.2):

$$Z_s = L_t\{1 - (1 + \frac{\delta T}{A_t E_Y})\cos\theta_t\} \tag{4.7}$$

From Eq. (4.4):

$$\delta T = F_X \text{cosec}\,\theta_t - T_0 \tag{4.8}$$

From (4.4) and (4.5) and using (4.7) and (4.8):

$$F_X \cot\theta_t = T_0 + \rho g A_{wp} L_t [1 - \{1 + \frac{1}{A_t E_Y}(F_X \text{cosec}\,\theta_t - T_0)\}\cos\theta_t] \tag{4.9}$$

The parametric studies in Ref. [4.13] are partly utilised here to generate a new form of equation with only one unknown, θ_t and the equation can be solved numerically. But the aim is to find the surge spring constant which is F_X / X_0. So Eq.(4.4) is divided by Eq.(4.5):

$$F_X = (T_0 + \rho g A_{wp} Z_s)\tan\theta_t \tag{4.10}$$

Similarly dividing Eq.(4.3) by (4.2):

$$\tan\theta_t = \frac{X_0}{L_t - Z_s} \tag{4.11}$$

Finally, from Eq.(4.10) and (4.11):

$$\frac{F_X}{X_0} = \frac{(T_0 + \rho g A_{wp} Z_s)}{L_t - Z_s} \tag{4.12}$$

X_0 might be negative or positive in sign but Z_s is a positive quantity (ignoring stretch-up dynamics discussed later) whenever the platform moves from its upright position because the top of the tethers would tend to follow a circular arc. Eq.(4.12) ignores tether lateral dynamics and its curvature due to weight and current drag forces. But still the spring stiffness in Eq.(4.12) is non-linear in nature and it is difficult to use it in a linear dynamic analysis with LUSAS. So the effect of set-down is ignored:

$$\frac{F_X}{X_0} = \frac{T_0}{L_t} < \frac{(T_0 + \rho g A_{wp} Z_s)}{L_t - Z_s} \tag{4.13}$$

T_0 / L_t, the ideal spring stiffness value for small X_0 has been widely used in various published literature and design. But this ideal value is less than the one which is more close to real-life situation (i.e. Eq.(4.12)). But the alternative in this case (i.e. a non-linear dynamic analysis in LUSAS with non-linear large displacement beam elements) is rather complex and may not be necessary because the ideal spring stiffness may work within reasonable approximations. The numerical value for the ISSC TLP is:

$$\frac{F_X}{X_0} = \frac{T_0}{L_t} = \frac{1}{4} \times \frac{137.34 \times 10^6}{415} = 82735 \text{ N/m} \tag{4.14}$$

The factor 1/4 is for the spring at one column base, not for the whole platform. The ideal spring stiffness in Eq.(4.13) and (4.14) is used for the surge and sway modes of motion of Model_2.

4.3.4 Heave Spring Constant for Model_2

Heave spring stiffness in one corner is the sum of tether stiffness and hydrostatic stiffness. From Table 1.1,

$$\text{Heave stiffness} = \frac{813 \times 10^6}{4} + \rho g A_{wp} \tag{4.15a}$$

$$= 203.25 \times 10^6 + 1025 \times 9.81 \times \pi \times (8.44)^2 \tag{4.15b}$$

$$= 203.25 \times 10^6 + 2.25 \times 10^6 \tag{4.15c}$$

$$= 205.5 \times 10^6 \text{ N/m} \tag{4.15d}$$

The calculations are given in detail in Eq.(4.15) to show the proportion of tether stiffness and hydrostatic stiffness in one corner of the platform. For the ISSC TLP the hydrostatic stiffness is only 1.1% of the tether stiffness.

4.3.5 Roll and Pitch Spring Constants for Model_2

Roll or pitch spring constant is evaluated from the tether roll or pitch stiffness and hydrostatic stiffness, very similar to the heave stiffness. From Table 1.1,

$$\text{Roll stiffness} = \frac{1}{4} \times \left(1501 \times 10^9 + \Delta \times \overline{GM}_R\right) \quad (4.16a)$$

$$\text{Pitch stiffness} = \frac{1}{4} \times \left(1501 \times 10^9 + \Delta \times \overline{GM}_P\right) \quad (4.16b)$$

Here $\overline{GM}_R$ and $\overline{GM}_P$ are the same because the platform has symmetry in two orthogonal vertical planes. So,

$$\text{Roll or pitch stiffness} = \frac{1}{4} \times \left(1501 \times 10^9 + 54.5 \times 10^6 \times 9.81 \times 6.0\right) \quad (4.17a)$$

$$= 375250 \times 10^6 + 802 \times 10^6 \quad (4.17b)$$

$$= 376052 \times 10^6 \text{ N-m / radian} \quad (4.17c)$$

The hydrostatic stiffness contribution is negligible in this case.

4.3.6 Yaw Spring Constant for Model_2

The spring constant for yaw motion does not have any straight-forward expression like those for roll, pitch and heave motion. Fig. 4.14 shows the effect of yaw motion on the platform. If we assume ϕ_{yaw} is small, the set-down can be ignored. The restoring force can be written as $(T_0 + \delta T) \sin\theta_t$. For small angle the change in tether tension is also negligible. The restoring force can be approximated as:

$$(T_0 + \delta T) \sin\theta_t \approx T_0 \sin\theta_t \approx T_0\theta_t \approx T_0 \tan\theta_t \quad (4.18a)$$

$$T_0 \tan\theta_t = T_0 \phi_{yaw} d_{cl} \frac{\sqrt{2}}{2L_t} \quad (4.18b)$$

The yaw restoring moment can be written by multiplying the restoring force with the moment lever:

$$\text{Restoring moment} = T_0 \phi_{yaw} d_{cl} \frac{\sqrt{2}}{2L_t} d_{cl} \frac{\sqrt{2}}{2} = T_0 \phi_{yaw} \frac{d_{cl}^2}{2L_t} \quad (4.19a)$$

$$\text{So, yaw spring constant per corner} = \frac{T_0 d_{cl}^2}{2L_t} \quad (4.19b)$$

Please note that the platform here has a square deck. So the distance between column centres (d_{cl}) is the same in both longitudinal and transverse directions. For other TLPs with rectangular but not square decks, the expression for the yaw spring constant would be slightly different.

4.3.7 Natural Frequency Analysis and Mode Shapes of Model_2

LUSAS can perform large eigenvalue analysis for natural frequencies and linear structural buckling. Model_2 has 113 free nodes with six degrees of freedom per node.

So theoretically Model_2 has 678 natural frequencies and corresponding mode shapes. But the higher natural frequencies do not have any major role in structural dynamics of TLPs. The first 20 eigenvalues are extracted in LUSAS and six of them are identified as the rigid body mode shapes. MYSTRO, the powerful GUI (Graphical User Interface) for LUSAS, was helpful in identifying the mode shapes in Figs. 4.15-20. The boundary springs are intentionally omitted to maintain clarity in the plots. Table 4.8 compares the natural frequency values of Model_2 with simple hand calculations done by Boom and Tan [4.7].

Table 4.8. Natural Frequencies of Model_2

Modes of	Natura Period (s)		Spring Stiffness
Motion	Rigid Body [4.7]	Model_2	of Model_2
Surge	106	101.09	82735 N/m
Sway	106	101.09	82735 N/m
Heave	2	1.82	205.5 MN/m
Roll	2.1	1.44	376052 MNm/rad.
Pitch	2.1	1.44	376052 MNm/rad.
Yaw	86	59.87	307735 kNm/rad.

It is quite natural if the results from a large eigenvalue analysis are different from simple hand calculations. In fact that is not the main reason creating differences in Table 4.8. The added mass values assumed by Boom and Tan [4.7] are considerably larger than those used for Model_2. Table 4.9 provides a comparison. The added mass coefficients used in this study have been discussed in Chapter 3. It has been possible to give the total added mass in global X, Y and Z directions in Table 4.9 because LUSAS estimates the total mass of the system in three global directions. But the added mass moment of inertia values of Model_2 for roll, pitch and yaw are not known explicitly. For a rigid body analysis forces are finally summed up in global directions and moments are calculated from these forces and their 'levers' from a reference point (in many cases centre of gravity of the structure). But for a 3-D frame with special joint elements, the analysis technique is different. Each and every lumped added mass in a specific direction has its contribution to the corresponding mass moment of inertia but the total summation is not known explicitly.

Table 4.9. Added Mass Values Compared

Modes of	Adde Mass		Values in Kg
Motion	Rigid Body [4.7]	Model_2	for Model_2
Surge	1.0 Δ/g	0.8285 Δ/g	45.1523 x 10^6
Sway	1.0 Δ/g	0.8285 Δ/g	45.1523 x 10^6
Heave	0.7 Δ/g	0.4782 Δ/g	26.0632 x 10^6
Roll	1.0 I_{xx}	-	-
Pitch	1.0 I_{yy}	-	-
Yaw	1.35 I_{zz}	-	-

4.3.8 Complete Solution of Single Degree of Freedom System

It is important to review the motion characteristics of a Single Degree of Freedom (SDF) system before describing forces and responses of a Multiple Degrees of Freedom (MDF) system like a TLP. The derivations in this context are not given here. They can be found in any standard textbook of vibration (e.g. Mukhopadhyay [4.24]). Only a few equations that would be helpful in explaining the importance of damping in the analysis are given in this section:

$$m_{D1}\ddot{x}_{D1} + b_{D1}\dot{x}_{D1} + k_{D1}x_{D1} = F_0 \sin \omega_f t \tag{4.20}$$

Eq.(4.20) is the dynamic equilibrium equation of a SDF system acted upon by a force $F_0 \sin \omega_f t$. The subscript 'D1' stands for a SDF system. The complete solution of Eq.(4.20) consists of two parts, the complementary function and the particular integral. The complementary function here is the solution of the damped free vibration and can be assumed in the following form:

$$x_{D1c} = C_1 e^{\lambda_{sc} t} \tag{4.21}$$

The Substitution of Eq.(4.21) into (4.20) transforms a linear second order differential equation into a quadratic equation. Let us define:

$$n_s = \frac{b_{D1}}{2m_{D1}}, \quad p_s^2 = \frac{k_{D1}}{m_{D1}} \tag{4.22}$$

Now the solution can be written as:

$$\lambda_{sc} = -n_s \pm \sqrt{n_s^2 - p_s^2} \tag{4.23}$$

Three cases may arise but we will discuss only the underdamped system where $n_s < p_s$. Both roots are complex when n_s is less than p_s:

$$\lambda_{sc} = -n_s \pm i\sqrt{p_s^2 - n_s^2} \tag{4.24}$$

From the initial conditions:

$$x_{Dlc} = e^{-n_s t}\left(x_{Dla}\cos t\sqrt{p_s^2 - n_s^2} + \frac{n_s x_{Dla} + \dot{x}_{Dla}}{\sqrt{p_s^2 - n_s^2}}\sin t\sqrt{p_s^2 - n_s^2} \right) \tag{4.25}$$

The trial solution for the particular integral can be assumed as:

$$x_{Dlp} = C_2\cos\omega_f t + C_3\sin\omega_f t \tag{4.26}$$

Values of C_2 and C_3 can be found by substituting Eq.(4.26) into Eq.(4.20):

$$x_{Dlp} = \frac{-2F_0 n_s\omega_f / m_{Dl}}{\left(p_s^2 - \omega_f^2\right)^2 + \left(2n_s\omega_f\right)^2}\cos\omega_f t + \frac{F_0\left(p_s^2 - \omega_f^2\right)/m_{Dl}}{\left(p_s^2 - \omega_f^2\right)^2 + \left(2n_s\omega_f\right)^2}\sin\omega_f t \tag{4.27}$$

Defining ϕ_{Dl}:

$$\phi_{Dl} = \tan^{-1}\frac{2n_s\omega_f}{p_s^2 - \omega_f^2} \tag{4.28}$$

Eq.(4.27) now can be simplified to:

$$x_{Dlp} = \frac{F_0 / m_{Dl}}{\sqrt{\left(p_s^2 - \omega_f^2\right)^2 + \left(2n_s\omega_f\right)^2}}\sin(\omega_f t - \phi_{Dl}) \tag{4.29}$$

Now the complete solution comes from the summation of Eq.(4.29) and Eq.(4.25) as follows:

$$x_{Dl} = e^{-n_s t}\left(x_{Dla}\cos t\sqrt{p_s^2 - n_s^2} + \frac{n_s x_{Dla} + \dot{x}_{Dla}}{\sqrt{p_s^2 - n_s^2}}\sin t\sqrt{p_s^2 - n_s^2} \right) +$$

$$\frac{F_0 / m_{Dl}}{\sqrt{\left(p_s^2 - \omega_f^2\right)^2 + \left(2n_s\omega_f\right)^2}}\sin(\omega_f t - \phi_{Dl}) \tag{4.30}$$

The first term on the right hand side of Eq.(4.30) with a factor $e^{-n_s t}$ is for the free damped vibration. The other term with the same frequency as the disturbing force, represents forced vibration. The actual motion is a superposition of two simple harmonic motions, with different amplitudes, different frequencies and different phases. The resulting motion is somewhat irregular and complicated in nature. However, due to damping in the system the free vibration part vanishes after a short time and only the forced vibration part remains which is harmonic in nature. So the transient state of the oscillatory motion involves only the first few cycles.

In most of the solution techniques in the frequency domain, only the forced vibration

part can be taken into account. So the results from a frequency domain technique are usually linearised steady state solutions. But the situation would be different when the analysis is sought in the time domain. The author believes that there is a trend among researchers to consider only mass and stiffness matrices when simplified solutions are required in the time domain. The damping matrix is usually ignored because of its complicated nature. If we look back to Eq.(4.30), $e^{-n_s t}$ is 1.0 when damping is neglected. So the free vibration component would not decrease in an exponential manner and as a result, the actual motion would never converge to the steady state response of the system. For steady state response, it is essential that the free vibration part would die out in the course of time. So some form of damping should be present in the analysis, otherwise it would be confusing while explaining the results in connection with frequency domain solutions.

4.4. SINUSOIDAL LOADING AND RESPONSES

4.4.1 Introduction to DCATLP

A brief description of DCATLP is given here before comparing results with LUSAS. DCATLP (Dynamic Coupled Analysis of Tension Leg Platforms), is a non-linear program designed for 3-D time domain dynamic simulation of TLPs in deep water. It is written specifically as a research tool in which various modules can be changed or added to as desired. The main intention is to establish a direct link between global motion response analysis and local finite element or reliability based structural analysis and optimisation of TLP components (Fig. 4.21). The program is interactive in nature where the environmental loading is dependent on the nodal displacements and velocities. It is necessary to account for this dependence to ensure the compliant characteristics of TLPs.

It is not possible to solve this type of interactive problem in LUSAS with complicated environmental loading. But some form of validation is essential before employing a computer program for practical use. Several routines in DCATLP when developed, are checked with LUSAS in parallel by solving standard examples. But still that does not validate the final results from DCATLP. There are some results available from different organisations [4.31], [4.33] but their analyses were of a different nature. It is possible to get some impression about the magnitude of diffraction forces from those results but they are not enough for the validation, especially when the structural responses are concerned. Now-a-days 'well-tested' operating systems seem to have a number of bugs inside. After all, the programs are written in languages other than those we use in everyday life!

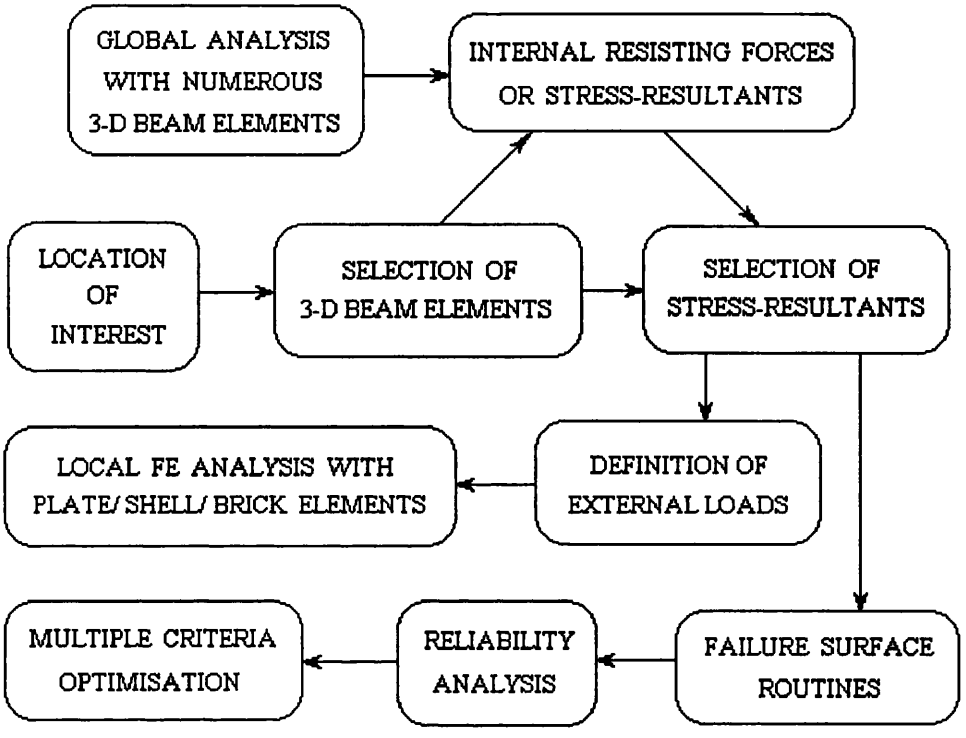

Fig. 4.21. The Ultimate Goal of DCATLP

The sole purpose of developing Model_2 for LUSAS is to compare its results with DCATLP. LUSAS cannot process interactive environmental loading but non-interactive (i.e. force magnitude is known beforehand) sinusoidal loading is not a problem. It is interesting to note that the resultant horizontal and vertical forces on a platform from a regular wave are nearly sinusoidal in nature. If we ignore the contribution of drag forces, the wave force in different locations of the platform can be visualised as time dependent sine or cosine curves. The summation of all sine curves with varying phase differences is also sinusoidal if their frequencies are identical. The following is a simple demonstration:

$$\sin(\omega t + C_1) + \sin(\omega t + C_2) = 2\sin\left(\frac{\omega t + C_1 + \omega t + C_2}{2}\right)\cdot\cos\left(\frac{\omega t + C_1 - \omega t - C_2}{2}\right)$$

$$= 2\sin\left(\omega t + \frac{C_1 + C_2}{2}\right)\cdot\cos\left(\frac{C_1 - C_2}{2}\right)$$

$$= C_3\sin(\omega t + C_4) \qquad (4.31a)$$

$$\text{where } C_3 = 2\cos\left(\frac{C_1 - C_2}{2}\right) \text{ and } C_4 = \frac{C_1 + C_2}{2} \qquad (4.31b)$$

So the resultant in Eq.(4.31b) is also sinusoidal with different phase. The most

probable maximum first order wave force in the surge direction on the ISSC TLP has been estimated by Prince-Wright [4.28] as 75.6 MN. In the following numerical examples the magnitude of the sinusoidal surge force is chosen nearly half of that most probable maximum first order wave force. The selection is arbitrary but believed to be reasonable because wave surge force of such magnitude (i.e. 40 MN) may occur often in practice. From 5 seconds to 20 seconds may be considered as the time period region of most ocean waves. The sinusoidal horizontal force in numerical examples is associated with three different time periods. Two of them are the lower bound (i.e. 5 s) and upper bound (i.e. 20 s) of the wave frequency region and the third period is just at the middle. The 12.5 seconds period is more important because of the energy associated in the wave spectra around this region. So the importance of damping in the analysis is demonstrated only in the case of sinusoidal load of 12.5 seconds period.

It has been already mentioned that Model_3 is only for DCATLP and it differs from Model_2 in the modelling of tethers. There is another important difference. LUSAS here is chosen to perform linear dynamic analysis in time domain. It forms the global mass and stiffness matrices of Model_2 only once and employs frontal techniques for the solution of dynamic equilibrium equations. On the other hand, DCATLP has to form the global mass and stiffness matrices of Model_3 in each time step for accuracy. One time step in DCATLP may involve a number of iterations whereas LUSAS does the linear calculations only once in each time step. A linear dynamic analysis is always faster when frontal or skyline methods are used. So the usefulness and efficiency of DCATLP may be questioned. If required results can be found in a linear analysis, there is no need for any further complex computation. Actually the formation of global stiffness and mass matrices in each time step is required for Model_3 because it includes the tethers. Fig. 4.13 may explain the problem. The global stiffness matrix is the summation of element stiffness matrices in the global directions. In the upright position, when the tethers are included in the system and there is no equivalent spring, the global stiffness matrix has no contribution from tethers that can produce horizontal restoring force simply because the tethers are standing vertical. The horizontal restoring force arises only when the tethers are inclined. But its magnitude varies with the tether inclination angle. So the initial global stiffness matrix when the platform has zero offset is of no value unless it is reformed with the change in the tether inclination angle. For Model_2 the problem does not arise. The horizontal restoring force from springs is zero when the offset is zero and linearly increases with the surge displacement. In a nutshell, if linear springs are not allowed in the modelling, a time-incremental-iterative approach cannot be avoided. The author accepts this negative feature of including tethers in the analysis. But the iterations and reformations of global

matrices can be justified if the analysis can capture some special characteristics of tethers. The tethers cannot remain straight when the platform is under hostile environment. Fig. 4.22 gives the explanation in detail:

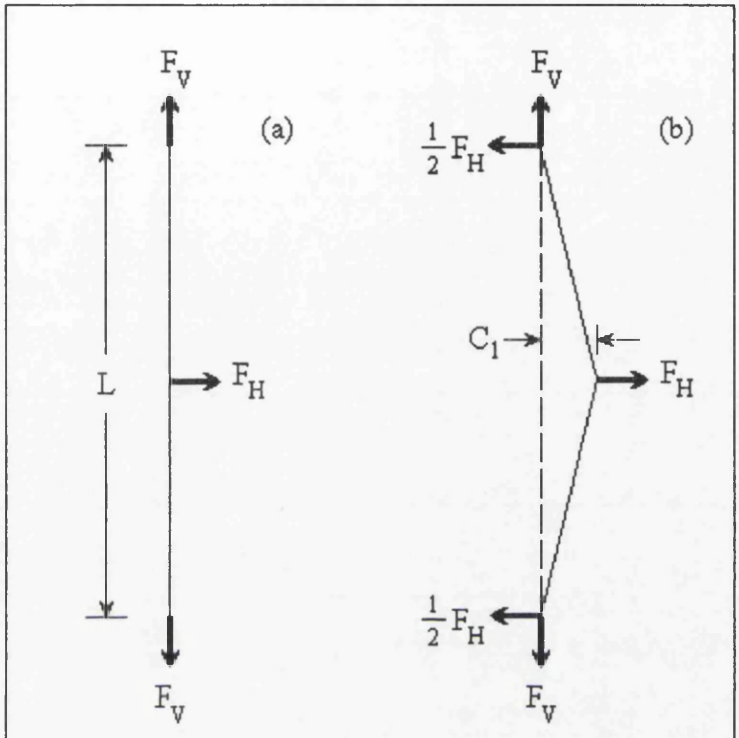

Figs. 4.22(a) and (b). A String under Tension

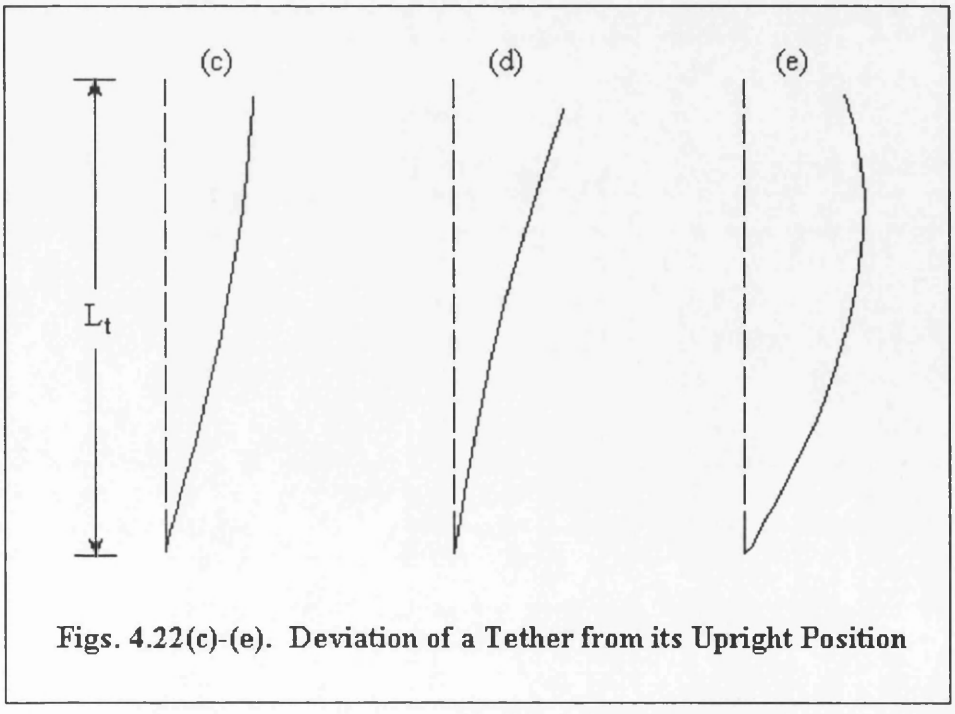

Figs. 4.22(c)-(e). Deviation of a Tether from its Upright Position

Fig. 4.22(a) presents a classic school physics question - "What is the magnitude of F_V that can keep the string straight when F_H is not zero?". The forces in the vertical direction do not have any component in the horizontal direction. So there would be a finite displacement C_1 whose magnitude would depend on the ratio of F_V and F_H. Similarly a large pretension in tethers cannot keep them straight. The locus of a tether-top is actually a complex orbital path strongly influenced by second-order effects like set-down [4.12] and the path can be found only in a coupled (i.e. platform-tether combination) analysis.

The horizontal current drag forces would cause bending as shown in Fig. 4.22(c). When the tethers are not neutrally buoyant, self-weight would create more sagging. The dynamic movement of the hull may induce a different type of bending in tethers. Fig. 4.22(d) and (e) show the phase difference in movement between the hull and the tether. When the hull reaches the maximum dynamic offset and starts moving in the opposite direction, a long tether may take some time to 'turn back'. When the pretension is large these effects would be small. But there is an important consequence. Any deviation of tethers from their upright positions would cause additional set-down of the hull. If there is a phase difference, more or less constant (Fig. 4.22(d) and (e)), the additional set-down would produce more tension in tethers in every response cycle. A slight change in draft may make a significant difference in tether tension because of relatively large diameter columns and associated water plane area. The additional set-down in this context goes against the 'air gap' criteria but it has one favourable effect. If it is found to be significant, a TLP might be designed with less pretension and consequently more deck payload.

The minimum tether tension limit state is losing its importance very recently and there is a trend in industry for designing TLPs with less pretension [4.15]. The additional set-down, if found significant may support the recent trend. DCATLP has been used to generate data sets for plotting the shapes of equivalent tethers at different time steps. Results of this type will be discussed later in Section 4.6.

4.4.2 Comparison of Results from DCATLP and LUSAS

The surge and heave motion of a particular node (node 90, see Fig. 4.9) are plotted in Figs. 4.23-4.49. The dynamic movements of a TLP hull come under 'large displacement, small strain' [4.4] category. So translational motions at any node on the hull practically represent the translational responses of the platform.

Figs. 4.23 and 4.24 present surge and heave responses of Model_2 under a sinusoidal

load of magnitude 40 MN and period 5 seconds. RMDC and RSDC stand for Rayleigh Mass and Stiffness Damping Coefficients (i.e. α_R and β_R) respectively. Fig. 4.25 shows the responses of Model_3 under the same load from DCATLP. The displacements are not steady because there is no form of damping included. The natural vibration part is mixed with the forced oscillation. The possible explanations are given in detail in Section 4.3.7 where a SDF system has been discussed. There is a remarkable similarity in nature and magnitude of surge response curves in Fig. 4.23 and 4.25. Please note that MYSTRO has rounded off 'Time (s)' along X axis in many figures to two decimal places which may create confusion. For example, '0.03 x E3' should be 0.025 x E3! The grids are equally spaced and it can be easily noticed. Unfortunately there is no 'user control' to rectify this confusion. FEA Ltd has been informed and this minor but confusing format error will not be there in the next upgrade.

The similarity in nature and magnitude of surge response of Model_2 and Model_3 in fact confirms the non-linear stiffness modelling in DCATLP. It also shows that an analysis is possible where a TLP can be successfully modelled without any kind of spring and the results closely follow what is expected. On the other hand, heave responses are different. The dynamic set-down increases when the hull gradually moves away from its upright position. To show this characteristics surge and heave are plotted together in Figs. 4.25, 4.28 and 4.31. The effect is more pronounced in Fig. 4.28. There are quite a few technicalities required for plotting these figures. The time step for this sinusoidal load analysis was 0.25 second in both LUSAS and DCATLP. Fig. 4.25 shows surge or heave by joining 1000 points (each representing a time station) by small straight lines. The points are visible in Fig. 4.25 if examined carefully. Fig. 4.23 or 4.24 has 250 points joined by straight lines. The PostScript driver from FEA Ltd. for converting picture files from MYSTRO is found to produce better quality output. LUSAS creates a very large size database for post-processing in MYSTRO, specially in the case of dynamic analyses. The size of the MYSTRO database for Model_2 is 65 megabytes when it is updated once in four successive time stations (total response time = 250 seconds, time step = 0.25 second). Only a few years back PCs used to have a hard disk of 20 megabytes size! This is one great disadvantage of using a general purpose powerful FE package that tends to write all possible information for graphical post-processing in its database. On the other hand, DCATLP 'opens' different output files for writing different types of results. The storage space is not a problem for DCATLP because it writes only what is necessary and in simple formats so that any graphics or spreadsheet software can read its results as 'text files' for drawing graphs later.

The spring stiffness values for Model_2 have already been discussed. The surge spring stiffness, T_0 / L_t for Model_2 is slightly less than the actual stiffness including set-down (see Eq.(4.13)). The surge stiffness for Model_3 does not have any explicit value because it depends on the global stiffness matrix in each increment. But Model_3 has slightly higher stiffness in surge or sway direction than the ideal spring value in Eq.(4.13). This is because of end-fixity of tethers which is described later in Section 4.5.6. So the surge response of Model_2 is expected to be slightly more than that of Model_3 in Figs. 4.23-4.49. Figs. 4.26 and 4.28 can explain it clearly if we focus our attention on the 'kinks' of the surge curves. But the resemblance in nature of these two surge curves is remarkable. There is another interesting aspect of the surge curves in Figs. 4.23, 4.25, 4.26, 4.28, 4.29 and 4.31. One surge response cycle in these figures takes around 101 seconds which is the estimated surge or sway natural period of Model_2 and it does not depend on the external loading frequency. The surge magnitude is gradually increasing with the forcing period in the wave frequency range. So one important conclusion can be drawn that in the absence of damping a TLP would oscillate in the horizontal plane with nearly equal surge /sway natural frequency and the motion magnitude would increase with the forcing period in the wave frequency range. But damping is significantly present in reality but its estimate is rather difficult.

The heave RAOs discussed in Chapter 3 are of the order of millimetres for waves of 1 metre amplitude. But the heave responses within Figs. 4.24-4.49 have considerably different magnitude because they include the initial stretch of tethers due to pretension.

$$\text{Initial stretch} = \frac{\text{Pretension}}{\text{Combined Stiffness}} = \frac{137.34\ \text{MN}}{813\ \text{MN/m}} = 0.169\ \text{m} \quad (4.32)$$

The complex heave response in Fig. 4.25 perhaps indicates the excitation in tethers because the forcing frequency is near the natural heave frequency of the platform. Please note that there is no damping in the system and the vertical tether natural frequencies may have an impact on the heave response. In Figs. 4.24, 4.27 and 4.30 the heave response period is very close to the forcing periods (5, 20 and 12.5 seconds respectively) although the force has been applied in the surge direction and only pretension is present in the vertical direction.

4.4.2.1 Analysis with damping included

Different other characteristics may be found in Figs. 4.23-31 that might be important in the theoretical study of MDF systems without damping. But they may not have much

significance in relation to a practical design of TLPs. Fig. 4.32 is the first graph that includes damping in the analysis. In general, the global damping matrix cannot be constructed from element damping matrices [4.5] such as the mass and stiffness matrices of the element assemblage. The purpose of including damping is to approximate the overall energy dissipation during the system response. In most practical analyses using direct integration, Rayleigh damping is assumed. A disadvantage of Rayleigh damping is that the higher modes are considerably more damped than the lower modes for which the Rayleigh constants have been selected [4.5]. The following equation relates the Rayleigh damping matrix with the global mass and stiffness matrices:

$$[B] = \alpha_R[M] + \beta_R[K] \tag{4.33}$$

α_R and β_R are to be determined from two given modal damping ratios that correspond to two unequal natural frequencies of vibration. The following equation is useful in selecting α_R and β_R or estimating damping ratios in other modes of vibration:

$$\alpha_R + \beta_R\omega_{n_i}^2 = 2\omega_{n_i}\xi_{d_i} \tag{4.34}$$

However, only two pairs of $(\xi_{d_1}, \omega_{n_1})$ and $(\xi_{d_2}, \omega_{n_2})$ determine α_R and β_R. When the damping ratios are known for more than two natural frequencies, average values of ξ_d can be used. It is possible to use Caughey series [4.8] for including more than two pairs of $(\xi_{d_i}, \omega_{n_i})$ to evaluate the damping coefficients but the damping matrix [B] will be, in general, a full matrix. The computation and time involved in the analysis are increased by a very significant amount if the damping matrix is not banded.

For Model_3 the global mass and stiffness matrices are reconstructed at each and every time step for including the effect of change in the tether inclination angle. So the damping matrix [B] would proportionally change with them. The variability would be small because the overall change is small since the hull exhibits rigid body like movements. But the magnitudes of α_R and β_R can be questioned. One practical solution is to calibrate them from experimental results instead of relating them to the theoretical modal damping ratios. This section describes α_R and β_R with 1% and 2% values only. Fortunately it has been found within these limited trials that the steady state response does not depend significantly on α_R and β_R. Several other combinations of α_R and β_R are possible but they would be meaningful only when they are supported by experiments. Marthinsen et al [4.22] have compared the predicted and measured responses of Snorre TLP. The design responses have been found to be 2 to 5 times higher than those in full scale. Marthinsen et al [4.22] think that this is mostly due to a larger damping in the real world than what could be justified at the

time of design.

4.4.2.2 Numerical results with damping included

Figs. 4.32 and 4.33 demonstrate the importance of damping in a dynamic system. They present the transient and nearly steady state surge and heave responses of Model_3. α_R and β_R are both 1% (i.e. [B] = 0.01 [M] + 0.01 [K]). Sometimes it is more convenient to express damping in the system as a fraction of critical modal damping. From Table 4.8 the surge and heave natural periods are substituted into Eq.(4.34) and ξ_{surge} and ξ_{heave} are found to be 8% and 1.87% of critical modal damping respectively. Fig. 4.33 shows a positive set-down because of the initial stretch in tethers. The heave motion is actually surge induced and small. It has been mentioned before that the MYSTRO database created by LUSAS for graphical post-processing is very large in size. So when Model_2 is analysed in LUSAS from 0 to 1000 seconds with α_R and β_R both as 1%, the MYSTRO database is created for first and last 250 seconds for saving the storage space. Figs. 4.34 and 4.35 are for the first 250 seconds. The agreement in the surge response of Model_2 and Model_3 is the same as expected. The heave response of Model_2 in Fig. 4.35 does not match with that of Model_3 in Fig. 4.33. So the doubt that tethers do not behave as springs in vertical direction is more or less confirmed. Figs. 4.32 and 4.33 are reproduced in Figs. 4.36 and 4.37 for 'close up' views of the last 250 seconds of the response time. The surge motion in Fig. 4.36 clearly shows that the natural vibration part has not yet vanished. The effect is also present but not so apparent in the heave response in Fig. 4.37. Figs. 4.38 and 4.39 are from MYSTRO and they are compared with Figs. 4.36 and 4.37. The damping level is now increased twice to observe its effect. As expected the transient state of response is short and Model_3 undergoes steady state vibration from 500 seconds onwards. The heave response in Fig. 4.41 is very similar to that in Fig. 4.33. Fig. 4.42 and 4.43 refer to the first 250 seconds of response of Model_2. Figs. 4.44 and 4.45 show the steady state surge and heave motions. Fig. 4.46 is for confirmation from LUSAS. Fig. 4.47 also presents a steady state heave response but different from that in Fig. 4.45. This difference is expected and some explanations are suggested in Fig. 4.22. Figs. 4.36 and 4.37 are for nearly steady state response. So for the sake of completeness Figs. 4.48 and 4.49 present the steady state solution with α_R and β_R both as 1%. The solution becomes steady after a long time (comparing with Figs. 4.44 and 4.45) because the damping level is low.

4.5. PROGRAM DCATLP

Program DCATLP has been briefly discussed before. This section describes in detail the main algorithm and matrices within the program. The development of DCATLP

has a background that explains some interesting aspects and problems involved in analysing TLP structures. Shin et al [4.32] provided numerical results of the extreme load effects (six components of force, moment and external pressure on a section of a platform) on a North Sea TLP. Their analysis throughout followed a reliability based methodology which employed the best state-of-the-art knowledge at that time. The probabilistic loading model had three main groups, - static, quasi-static and dynamic. There were a number of important simplifications. The set-down from the quasi-static environmental loading was treated as an increase in water level and combined with tide level variations. That was done because quasi-static and dynamic analyses were separate. A simplified space frame model of columns, pontoons and main deck girders was developed for their linear structural analysis. There were 146 beam elements and 133 nodes with 6 degrees of freedom. Tethers or risers were not included in their structural analysis. The most important simplification was with the boundary conditions. The TLP for their analysis had mooring flats inside the corner columns for supporting tethers. One of the four nodes in the space frame model representing these mooring flats was fixed in all three global directions. There were four other equally important nodes for transmitting lateral tension just above bellmouth (similar to Fig. 4.50(a)). One of them was restrained in two lateral directions (global X and Y) and another was fixed in the global Y direction to achieve a stable system. For any finite element analysis stability is important but when a TLP hull has six translational degrees of freedom restrained, the conclusions from the analysis can only be drawn by experts because in reality a TLP hull is free to move in the horizontal plane. The finite element analysis with these imposed boundary conditions may appear as a 'black art' to people without any prior experience with TLPs. The very recent trend in the commercial houses is to develop FE software as a standard design office tool [4.34]. Once set up, the program can be used by technicians for routine detail design in the same way CAD programs are used for drawing production. However, a TLP design would still demand some prerequisites and should not be confused with other standard design practices. But a 'black box' is always preferred than a 'black art'!

In Ref. [4.32] and [4.10] a brief description is also there about transfer of environmental loading onto their space frame model. The calculations of static, quasi-static and dynamic loading were separate. The deflections, rotations and member forces due to static loading were computed using the linear elastic theory. Quasi-static loading of wind, current and wave drift were superimposed individually. Dynamic loading came from a rigid body motion analysis (ABS/SPLASH program based on [4.27]). The rigid body motions were computed and combined with wave induced forces at the nodes of their space frame model.

Apparently it is clear that this type of analysis would involve manual calculations and / or important decisions that may vary with the configuration of the TLP. Forces from a rigid body motion program are required to be transferred to a space frame. If one program can calculate both motion and structural responses, the analysis would be automatic and independent (i.e. no dependency on the TLP configuration). In fact this objective forms the background of DCATLP. DCATLP attempts to solve the hydro-structural problem 'mechanically' without involving any transfer or important decision after the TLP configuration and design environmental parameters are given as input in a data file. The penalty lies in the number of equations in each time station which is far more than only six in a conventional rigid body motion analysis.

The author believes that there are a few other important aspects that need a different approach for clarification. In a TLP design, directional distributions of environmental conditions should be considered. The assumption of collinear wind, wave and current in an extreme storm may produce very conservative results with a much lower probability of occurrence than that of any one of the governing factors. So the environmental loading module should be in a position to handle external loads from any direction. It would be more realistic and appropriate if statistical parameters in connection with the extreme environment are included in the analysis. At present, DCATLP does not perform any probabilistic calculation but its loading module accepts external loads of any direction of action and superimposes them to form a right-hand-side column vector in a most general way.

The conventional steady offset calculation as a result of wind, current and steady wave drift forces from a quasi-static analysis is doubtful. Of course, there would be an offset under the action of quasi-static forces but that may not match with the calculated one where the effect of platform inertia is ignored. In reality, the platform moves under all kind of forces from different directions and the effect of inertia is always present. So a different treatment of external forces in the offset calculation may be questioned. This could be verified only if the calculation is done without neglecting the platform inertia and without differentiating forces as quasi-static or dynamic. This real-life simulation is only possible in time domain. DCATLP works with all kind of forces at any instant of time. One main intention here is to check the effect of inertia and any discrepancy therefrom.

The program can be broadly divided into three sections. The master module is to handle the time integration technique and various matrices generated by other modules.

The environmental loading part when it is called, returns a column vector with external loads acting at each and every node of the structure. The structural analysis module is to calculate the global mass and stiffness matrices and store them in two separate active column profiles. The 'skyline' or non-zero profile of the problem is determined before the time loop starts. Fig. 4.51 is the main flow chart for DCATLP. The following discussion would detail the calculation steps involved.

4.5.1 System Dependency

DCATLP is developed in Sun FORTRAN which is an enhanced FORTRAN 77 development system for Sun workstations. While compiling the program, the Level-3 Optimiser is used which does the local and global optimisation along with references and definitions for external variables. The optimised code also runs without any difficulty in the latest SPARC 514 computers working with Solaris 2.3 operating system. A few system dependent routines (e.g. time functions, subroutines for 'flushing' the buffer) are used in DCATLP which can be modified easily in case the program has to run in other systems.

4.5.2 Transformation Matrix

It is useful to first establish the element mass and stiffness matrices corresponding to the local element degrees of freedom in almost all finite element analyses. But the local axes system would vary with the member orientation. So a transformation matrix is required that can help transferring the contributions of mass or stiffness matrix from local to global co-ordinates. There are a number of textbooks available (e.g. [4.18]) with the derivation of this well known transformation matrix $[T_r]$ using vector algebra. For better explanation only the coefficients in the matrix are given here without any derivation. $[T_r]$ is actually formed by four identical submatrices:

$$[T_r] = \begin{bmatrix} [\hat{T}_r] & & & \\ & [\hat{T}_r] & & \\ & & [\hat{T}_r] & \\ & & & [\hat{T}_r] \end{bmatrix} \tag{4.35}$$

where the submatrix $[\hat{T}_r]$ is of the form:

$$[\hat{T}_r] = \begin{bmatrix} \hat{T}_r(1,1) & \hat{T}_r(1,2) & \hat{T}_r(1,3) \\ \hat{T}_r(2,1) & \hat{T}_r(2,2) & \hat{T}_r(2,3) \\ \hat{T}_r(3,1) & \hat{T}_r(3,2) & \hat{T}_r(3,3) \end{bmatrix} \tag{4.36}$$

The coefficients in $\left[\hat{T}_r\right]$ depend on the element orientation with the global axes. They can be easily found from the global direction cosines:

$$C_X = \frac{X_2 - X_1}{L} \tag{4.37a}$$

$$C_Y = \frac{Y_2 - Y_1}{L} \tag{4.37b}$$

$$C_Z = \frac{Z_2 - Z_1}{L} \tag{4.37c}$$

The coefficients in $\left[\hat{T}_r\right]$ can be defined in terms of direction cosines:

$$\hat{T}_r(1,1) = C_X \tag{4.38a}$$

$$\hat{T}_r(1,2) = C_Y \tag{4.38b}$$

$$\hat{T}_r(1,3) = C_Z \tag{4.38c}$$

$$\hat{T}_r(2,1) = \frac{-C_X C_Y}{\sqrt{C_X^2 + C_Z^2}} \tag{4.38d}$$

$$\hat{T}_r(2,2) = \sqrt{C_X^2 + C_Z^2} \tag{4.38e}$$

$$\hat{T}_r(2,3) = \frac{-C_Y C_Z}{\sqrt{C_X^2 + C_Z^2}} \tag{4.38f}$$

$$\hat{T}_r(3,1) = \frac{-C_Z}{\sqrt{C_X^2 + C_Z^2}} \tag{4.38g}$$

$$\hat{T}_r(3,2) = 0 \tag{4.38h}$$

$$\hat{T}_r(3,3) = \frac{C_X}{\sqrt{C_X^2 + C_Z^2}} \tag{4.38i}$$

These relations are valid when $C_Y \neq \pm 1$. Otherwise for the special case:

$$\left[\hat{T}_r\right] = \begin{bmatrix} 0 & C_Y & 0 \\ -C_Y & 0 & 0 \\ 0 & 0 & 1 \end{bmatrix} \text{ when } C_Y = \pm 1 \tag{4.39}$$

4.5.3 Consistent Mass Matrix

The element mass matrix can be formed in two ways. For a beam element the lumped mass formulation is popular. It is simpler to determine the mass matrix this way by assuming the mass of the bar in Fig. 4.52(a), cut in halves and concentrated at the

nodes in Fig. 4.52(b). In this case, there is no distribution of mass force involved. It also ignores the fact that the centroid of the half bar does not coincide with the node at the beam end. Fig. 4.52(c) is theoretically correct but it cannot be used in common finite element analysis where equations are formulated only at the nodes.

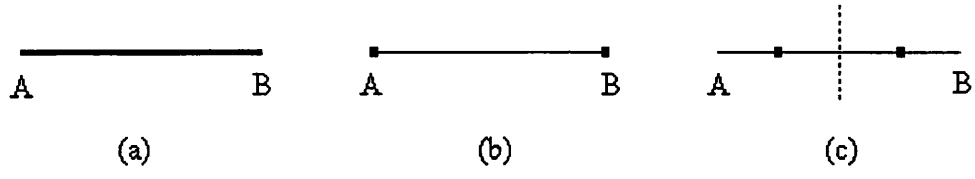

Fig. 4.52. Lumped Mass Formulation of a Beam Element

The difference would be significant when the element length is large. For small elements, however, the idealisation is acceptable. But the increase in beam element number would increase the total number of equations in each time step. This is one main reason for using consistent mass matrix formulation in DCATLP. It should be noted that a lumped mass matrix does not have any off-diagonal term and hence it is advantageous specially when the time integration scheme is 'explicit'. But DCATLP uses large step 'implicit' integration scheme for better accuracy. The derivation of the consistent beam element mass matrix of (12 x 12) size is complicated and beyond the scope of this thesis. The coefficients are simply reproduced in Fig. 4.53 from Ref. [4.29]. $\left[M^{e}_{pl}\right]$ in Fig. 4.53 includes rotatory-inertia effects but not the shear deformations. Archer [4.2] first derived the consistent mass matrix of (4 x 4) size including shear deformation effects. The expressions are too complex and it would be difficult to explain the relatively simple internal resisting force calculations in DCATLP if shear deformation effects are included. This is mainly because DCATLP does not perform any 'theoretically elegant non-linear analysis' (see [4.4]). A 'theoretically elegant non-linear analysis' with non-linear beams and corresponding tangent stiffness matrix formulation would be too far away from a straightforward rigid body modelling of TLPs. The author believes that it is not necessary because TLPs are 'weakly non-linear' structures [4.32].

4.5.4 Added Mass Matrix

Added mass of an element varies in different directions unlike its physical mass. For a vertical circular cylinder surge and sway added mass values are the same but its heave added mass would be different. For a rectangular pontoon the situation is even more

complicated. The author was not able to find any consistent added mass matrix in relevant publications. So a simplification was necessary to include added mass formulations in DCATLP. The simplification ignores rotatory-inertia effects and simply lump added mass at the end-nodes of a submerged element.

$$\left[M^e_{ag}\right] = \frac{1}{2}\rho V \begin{bmatrix} C_{aX} & & & & & & & & & & & \\ & C_{aY} & & & & & & & & & & \\ & & C_{aZ} & & & & & & & & & \\ & & & 0 & & & & & & & & \\ & & & & 0 & & & & & & & \\ & & & & & 0 & & & & & & \\ & & & & & & C_{aX} & & & & & \\ & & & & & & & C_{aY} & & & & \\ & & & & & & & & C_{aZ} & & & \\ & & & & & & & & & 0 & & \\ & & & & & & & & & & 0 & \\ & & & & & & & & & & & 0 \end{bmatrix}$$

Fig. 4.54. Simplified Diagonal Added Mass Matrix

These concentrated added masses at nodes are accounted for by adding them to the leading diagonal terms in the global consistent physical mass matrix whose arrangement is discussed in Section 4.5.7.

4.5.5 Element Stiffness Matrix

A book on finite element methods cannot be written without mentioning the beam element stiffness matrix. Any derivation or discussion in this line would be some unnecessary repetition of this well established concept. But one point is worth mentioning here that TLP members such as columns and pontoons do not invite any additional calculation when modelled as numerous beam elements in formulating their element stiffness matrices. Additional calculations may arise when the principal axes of the element cross section vary along the member length. But it only happens in case of irregular shaped bodies. Fig. 4.55 shows the well-known beam element stiffness matrix in local co-ordinates without shear deformation effects. Shear deformation effects are excluded from $\left[K^e_l\right]$ because they are not present in $\left[M^e_{pl}\right]$ (see Section 4.5.3).

4.5.6 Tether Connections

There are a number of ways to connect tethers to a TLP hull. Fig. 4.50(a) shows an

internal installation and support system adopted for the Hutton TLP. But the Jolliet design does not have mooring tunnels in the corner columns but rather has external porches near the bottom of the columns to transfer excess buoyancy loads to the tethers (Fig. 4.50(b)). For the ISSC TLP, the external installation and support system like Jolliet is assumed. For Model_3, node 114, 115, 116 and 117 (see Fig. 4.9) are the connecting points where equivalent tethers are attached to the column bases. Since these connecting nodes are flex joints in actual structures it is necessary to formulate internal hinges at these nodes in Model_3. These internal hinges in both vertical planes (i.e. global X-Z and Y-Z) would ensure the tether top-end movements. But the stiffness matrices for element 137, 138, 139 and 140 (see Fig. 4.10) have to be modified to introduce a hinge at one end of the elements. It should be noted that a hinge can be introduced by modifying the element stiffness matrix of any one of the two connecting elements (e.g. element 88 or 140). But the modification depends on the element orientation and its local axes definition. A more clear explanation is given in Fig. 4.56 to show the effect of a hinge at one end of a beam AB.

Fig. 4.56(a). Bending of AB without an End Hinge

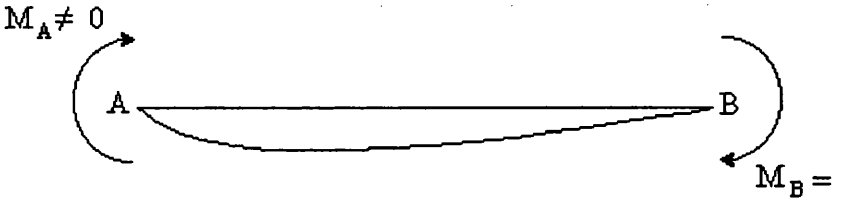

Fig. 4.56(b). Element AB with an End Hinge at B

If the translational and torsional degrees of freedom are not taken into account, the element stiffness matrix in Fig. 4.55 would reduce to the following:

$$\left[K_l^e\right] = \begin{bmatrix} \frac{4E_YI_y}{L} & 0 & \frac{2E_YI_y}{L} & 0 \\ 0 & \frac{4E_YI_z}{L} & 0 & \frac{2E_YI_z}{L} \\ \frac{2E_YI_y}{L} & 0 & \frac{4E_YI_y}{L} & 0 \\ 0 & \frac{2E_YI_z}{L} & 0 & \frac{4E_YI_z}{L} \end{bmatrix} \tag{4.40}$$

Wang [4.35] has given the modification necessary to introduce a hinge at one end of a beam including the derivation. For example, if node A of the element AB in Fig. 4.56 is the origin of its local x axis, $\left[K_l^e\right]$ is modified to the following for a hinge at node B:

$$\left[K_l^e\right] = \begin{bmatrix} \frac{3E_YI_y}{L} & 0 & 0 & 0 \\ 0 & \frac{3E_YI_z}{L} & 0 & 0 \\ 0 & 0 & 0 & 0 \\ 0 & 0 & 0 & 0 \end{bmatrix} \tag{4.41}$$

The analysis assumes the element AB as a prismatic member. In actual calculations in DCATLP other degrees of freedom are not ignored. The reduced stiffness matrix in Eq.(4.41) is shown for an illustration. In DCATLP, the corresponding (2 x 2) submatrices in the element stiffness matrix (Fig. 4.55) for bi-axial bending moments are modified according to Eq.(4.41).

Tethers also have flex joints at their sea-bed connections. But if internal hinges are introduced at nodes 154, 155, 156 and 157 in Fig. 4.9, we would in effect release the rotational degrees of freedom at these boundary nodes. But the structure would lose stability because there is no lateral stiffness. In that case the tethers may rotate through any angle under the action of any small lateral force. Perhaps there are a number of ways to tackle this problem. If the analysis is started with some form of lateral restraints and when the inertia forces and tether tensions are in action, the restraints can be gradually released. Another solution might be to put rotational springs with small stiffness values at boundaries (i.e. nodes 154-157). After all a real flex joint cannot have zero rotational stiffness! But the simplest and straight-forward solution is to assume nodes 154-157 as 'fixed' nodes. When the nodes are fixed the structure would have some lateral stiffness in surge or sway direction. So each equivalent tether would have one end hinged and the other end fixed. So the lateral stiffness of one equivalent tether is $3E_YI_z / L^3$ or $3E_YI_y / L^3$ [4.24] depending on surge or sway direction. Hence the total structural lateral stiffness of the platform is:

$$\text{Structural lateral stiffness} = 4 \times \frac{3 \times 208 \times 10^9 \times 0.1874}{(415)^3} = 6544.4 \text{ N/m} \quad (4.42)$$

From Eq.(4.14):

$$\text{Ideal horizontal spring stiffness} = 4 \times 82735 = 330940 \text{ N/m} \quad (4.43)$$

$$\frac{\text{Structural lateral stiffness}}{\text{Ideal horizontal spring stiffness}} = \frac{6544.4}{330940} = 0.019775 \quad (4.44)$$

Ideally a TLP does not have any structural lateral stiffness. The horizontal restoring force arises from the tension in inclined tethers. But for stability in the finite element analysis if the boundary nodes are 'fixed' the increase in stiffness would be less than 2% for the ISSC TLP. Please note that the actual stiffness is always larger than the ideal spring stiffness (see Eq.(4.13)). In the numerical examples in Section 4.6, nodes 154-157 are fixed. The slight increase in stiffness cannot have any significant effect in an inertia dominated dynamic analysis.

4.5.7 Skyline Method of Storage

The element mass and stiffness matrices are calculated for each element. The transformation matrix $[T_r]$ is then used to compute the global contributions:

$$\left[K_g^e\right] = [T_r]^T \left[K_l^e\right] [T_r] \quad (4.45)$$

$$\left[M_{pg}^e\right] = [T_r]^T \left[M_{pl}^e\right] [T_r] \quad (4.46)$$

The global mass and stiffness matrices, [M] and [K] are generated systematically from these $\left[M_{pg}^e\right]$ and $\left[K_g^e\right]$ respectively. It is straight-forward and easy to use [M] and [K] in their original square form in next stages of calculation. For small problems it might be acceptable but for considerably big ones like Model_3 the analysis would be highly inefficient. Moreover, quite a lot of memory space (i.e. RAM and swap space) might be necessary to execute such a problem where the global mass and stiffness matrices are stored in their original square form.

Actually it is not necessary to store the entire [M] and [K]. [M] is always symmetric and [K] is also symmetric in most cases. For the problem class of Model_3 [K] is symmetric. So it is sufficient to store only those coefficients above or below the principal diagonal. This reduces almost half the required storage space. Still larger savings in storage can be achieved if only the terms within a non-zero band are stored. In finite element formulations the maximum band-width of non-zero coefficients can usually be made small compared to the number of unknowns - often 10-20%, which reduces the storage from n(n+1)/2 to (0.1 to 0.2) n^2 for symmetric problems of (n x n)

size. It is possible to reduce the required storage and computational effort still further by storing the necessary parts of the upper triangular portion of [M] or [K] by columns. In this method it is necessary to store and compute only within the non-zero profile of the equations. A clear explanation is given in Fig. 4.57 by showing the differences in two storing methods. The non-zero profile method is also known as 'skyline' storage scheme because of its typical appearance as shown in Fig. 4.57.

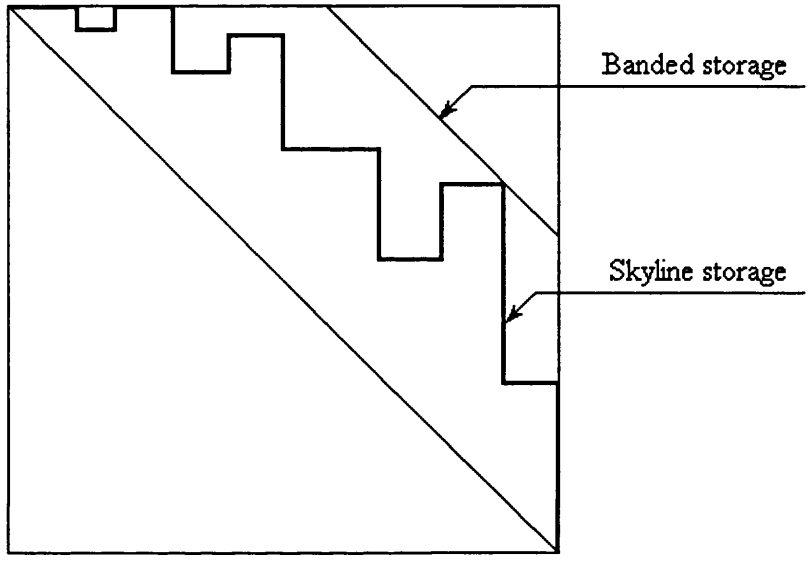

Fig. 4.57. Two Different Methods of Storing Global Mass or Stiffness Matrix

The skyline scheme has definite advantages over a banded storage. First, it always requires less storage unless the matrix is diagonal! Second, the storage requirements are not severely affected by a few very long columns and last, it is very easy to use vector dot product routines for triangular decomposition and forward reduction. The last fact is extremely important to modern vector oriented machines.

In DCATLP [M] and [K] are stored in two separate one-dimensional 'skyline' arrays. But it is sometimes essential to visualise the original reference position of each term in these profile columns. A transfer routine is there in the program for this purpose.

4.5.8 Solution of Equations

The effective stiffness matrix and modified force vector (described in Section 4.5.9.1) in the time integration scheme are formed from the contributions of global mass, damping, stiffness matrices and the external load vector. In fact, a set of differential equations are converted into a set of algebraic equations in this process.

4.5.8.1 Triangular decomposition

The first task is to construct the triangular decomposition of the effective stiffness matrix, $[K^*]$. In this process $[K^*]$ is written as a product of a lower triangular matrix with unit diagonals and an upper triangular matrix:

$$[K^*] = [K_L] \cdot [K_U] \tag{4.47a}$$

where

$$[K_L] = \begin{bmatrix} 1 & 0 & .. & 0 \\ K_{L_{21}} & 1 & .. & 0 \\ \vdots & & \ddots & \vdots \\ K_{L_{n1}} & K_{L_{n2}} & .. & 1 \end{bmatrix} \tag{4.47b}$$

and

$$[K_U] = \begin{bmatrix} K_{U_{11}} & K_{U_{12}} & .. & K_{U_{1n}} \\ 0 & K_{U_{22}} & .. & K_{U_{2n}} \\ \vdots & & \ddots & \vdots \\ 0 & 0 & .. & K_{U_{nn}} \end{bmatrix} \tag{4.47c}$$

This step is accomplished using a compact Crout method which is a variation of Gauss elimination.

In coefficient matrices resulting from a finite element problem some special properties are usually present. Often the effective stiffness matrix is symmetric ($K^*_{ij} = K^*_{ji}$) and it is easy to verify in this case that:

$$K_{U_{ij}} = K_{L_{ji}} \cdot K_{U_{ii}} \tag{4.48}$$

The Crout variation of Gauss elimination is used to successively reduce $[K^*]$ to upper triangular form. The lower triangular portion is not actually set to zero but is used to construct $[K_L]$. The upper and lower triangular matrices will replace the original matrix; and consequently it is not possible to retain the principal diagonal elements of both $[K_U]$ and $[K_L]$. Those of $[K_L]$ are understood since it is known by definition that they are all unity.

The decomposition algorithm is compact and the original matrix $[K^*]$ gets divided into three parts: part one being the region that is fully reduced, part two the region which is currently being reduced (called the active zone), and part three the region which contains the original unreduced coefficients. For a square matrix of (n x n) size the algorithm is briefly discussed below:

$$K_{U_{11}} = K^*_{11} \tag{4.49a}$$

$$K_{L_{11}} = 1 \tag{4.49b}$$

For each active zone j from 2 to n:

$$K_{L_{j1}} = K^*_{j1} / K_{U_{11}} \tag{4.50a}$$

$$K_{U_{1j}} = K^*_{1j} \tag{4.50b}$$

then for $i = 1,2,\cdots,j-1$:

$$K_{L_{ji}} = \left(K^*_{ji} - \sum_{m=1}^{i-1} K_{L_{jm}} K_{U_{mi}} \right) / K_{U_{ii}} \tag{4.51a}$$

$$K_{U_{ij}} = K^*_{ij} - \sum_{m=1}^{i-1} K_{L_{im}} K_{U_{mi}} \tag{4.51b}$$

and finally:

$$K_{L_{jj}} = 1 \tag{4.52a}$$

$$K_{U_{jj}} = K^*_{jj} - \sum_{m=1}^{j-1} K_{L_{jm}} K_{U_{mj}} \tag{4.52b}$$

4.5.8.2 Forward elimination and back substitution

For a linear problem, once the triangular decomposition of $[K^*]$ is done, several solutions for different right-hand-side column vectors (i.e. load vector) can be computed. This process is often called 'resolution' because it is not necessary to recompute $[K_L]$ and $[K_U]$. For every large coefficient matrix the decomposition process involves more computation than its corresponding resolution.

In the resolution process, solution to the original equations are obtained by solving the following pair of equations:

$$[K_L]\{G\} = \{W^*\} \tag{4.53a}$$

$$[K_U]\{X\} = \{G\} \tag{4.53b}$$

where $\{G\}$ is introduced to facilitate the separation [4.30]. The solution to Eq.(4.53) is trivial. For $i = 2,3,\cdots,n$:

$$G_1 = W^*_1 \tag{4.54a}$$

$$G_i = W^*_i - \sum_{j=1}^{i-1} K_{L_{ij}} G_j \tag{4.54b}$$

and for $i = n-1, n-2,\cdots,1$:

$$X_n = G_n / K_{U_{nn}} \tag{4.55a}$$

$$X_i = \left(G_i - \sum_{j=i+1}^{n} K_{U_{ij}} X_j \right) / K_{U_{ii}} \tag{4.55b}$$

Eq.(4.54) is called 'forward elimination' while Eq.(4.55) is called 'back substitution'. It is very easy to use vector dot product routines in forward reduction and back substitution. As mentioned before, the solution efficiency can be greatly enhanced if modern machines are used which are vector oriented.

4.5.8.3 Frontal methods versus active column profile

The frontal methods will be more efficient than band solution methods because the front width is smaller than the band width (when mid-side nodes are present). This statement is true for active column profile methods also. There is, however, more than a simple measure of front versus band or profile width that enters into the cost and time involved in solving equations. For the discussion here we restrict our comments to symmetric equations. The profile and band solution methods perform the triangular decomposition of the effective stiffness matrix by working from the first equation to the last. On the other hand, the frontal scheme works element by element (solution efficiency is a function of element order, not node order), forming only that part of the stiffness matrix belonging to the front. The other limitations are that the front stiffness must fit into the core and usually there is an extensive amount of transfer of coefficients before elimination. On the other hand, the active column profile solution method will require considerable amount of efforts to assemble the global effective stiffness matrix when many blocks are involved to store the total array. The issue is not clear as to which is the better method [4.37] and it is the choice of individual users to select between the two. There is no question that the active column profile is superior to conventional band solution methods.

4.5.8.4 Special considerations for Model_3

It has been mentioned before that the global stiffness matrix changes with the tether inclination angle. So a time-incremental-iterative approach cannot be avoided for Model_3 analysis. The modified Newton-Raphson algorithm is used to update the effective stiffness matrix in each time station. This updating frequency can be changed (e.g. once in two consecutive time stations) but it would increase the number of iterations in each time step. Although the triangular decomposition of $[K^*]$ is not necessary in the iterative loop but 'forward elimination' and 'back substitution' cannot be avoided. DCATLP uses the routines developed by Prof. R.L. Taylor [4.37]. They are highly efficient in the 'decomposition' as well as 'resolution' process. For a similar

problem a frontal method may involve more coding details and an extensive amount of coefficients movement before elimination.

There is another problem with the environmental forces. In many finite element problems the external forces at $t+\Delta t$ are known in advance and at the equation solving stage, displacements are calculated iteratively so that the internal restoring forces can match the external ones [4.17]. The environmental forces cannot be estimated independently because a TLP exhibits compliant characteristics. In DCATLP the external loading at $t+\Delta t$ is determined with a set of assumed values of TLP responses. The next cycle of iteration starts with the computed values of responses in the previous iteration cycle. So the structure and the external forces together 'decide' the dynamic equilibrium position at each and every time station. This in fact imposes some restriction on the selection of time increment value because convergence is expected from both sides.

4.5.9 Time Integration Scheme

The natural heave, roll and pitch periods of a TLP are usually less than 5 seconds because of high stiffness in the vertical direction. The explicit methods of time integration are avoided here because they only produce reasonable results at a very small time step for their dependence on the smallest natural period of the structure. Moreover, in the analysis of Model_3 the convergence at every time step is expected from both sides: the external as well as internal resisting forces because of their dependency on each other. As mentioned before, it puts further restriction on the time step selection. So a large step integration method for non-linear systems is necessary. LUSAS can perform implicit or explicit step-by-step dynamic analysis with various combinations of governing parameters. But to be consistent with DCATLP, Newmark-β integration scheme for linear systems is selected in LUSAS for analysing Model_2. The time integration algorithm used in DCATLP does not come straight from any publication. It is a variation of the original Newmark-β scheme. The algorithm is an effective combination of those proposed in Ref. [4.17], [4.6], [4.5] with two major modifications. The expressions for $[K^*]$ and $\{W^*\}$ in DCATLP have been derived from first principles. At present there are various algorithms available based on the finite difference equations originally proposed by Newmark [4.26] but still the author believes that the derivations given in Section 4.5.9.1 are not any reproduction of any published material. But some mathematical manipulations of finite difference equations are followed from Chan et al [4.9]

4.5.9.1 Effective stiffness matrix and modified load vector in DCATLP

It is perhaps better to state the original dynamic equilibrium equation before any derivation:

$$M]\{\ddot{X}\} + [B]\{\dot{X}\} + [K]\{X\} = \{W(t)\} \tag{4.56}$$

Various implicit methods have their origin in the following Taylor series:

$$X\}_{n+1} = \{X\}_n + \{\dot{X}\}_n \Delta t + \{\ddot{X}\}_n \frac{\Delta t^2}{2} + \{\dddot{X}\}_n \frac{\Delta t^3}{6} \cdots \tag{4.57}$$

where (n+1) and (n) are the time stations at time t = (n+1) Δt and nΔt respectively. Newmark assumed that the terms of power 3 and higher could be allowed for by a term involving two terms of power 2 and a factor β_N:

$$X\}_{n+1} = \{X\}_n + \Delta t\{\dot{X}\}_n + (\tfrac{1}{2} - \beta_N)\Delta t^2\{\ddot{X}\}_n + \beta_N \Delta t^2\{\ddot{X}\}_{n+1} \tag{4.58}$$

The other parameter δ_N introduced by Newmark is set to 0.5 here for avoiding numerical damping in the analysis. When δ_N is other than 0.5, numerical damping appears in the calculated responses [4.26] which might be confusing when interpreting the results with environmental damping present in the system. So the equation for velocity calculation with $\delta_N = 0.5$ is:

$$\dot{X}\}_{n+1} = \{\dot{X}\}_n + \frac{\Delta t}{2}(\{\ddot{X}\}_n + \{\ddot{X}\}_{n+1}) \tag{4.59}$$

Eq.(4.58) and (4.59) are the finite difference approximations proposed by Newmark. Now for the derivation of $\{K^*\}$ and $\{W^*\}$ we consider the dynamic equilibrium equations at time t = (n+1) Δt and nΔt respectively:

$$[M]\{\ddot{X}\}_{n+1} + [B]\{\dot{X}\}_{n+1} + [K]\{X\}_{n+1} = \{W\}_{n+1} \tag{4.60}$$

$$[M]\{\ddot{X}\}_n + [B]\{\dot{X}\}_n + [K]\{X\}_n = \{W\}_n \tag{4.61}$$

Multiplying Eq.(4.60) by $\beta_N \Delta t^2$ and Eq.(4.61) by $2(\tfrac{1}{2} - \beta_N)\Delta t^2$ and adding:

$$\begin{aligned}[M]\Delta t^2(\beta_N\{\ddot{X}\}_{n+1} + 2(\tfrac{1}{2} - \beta_N)\{\ddot{X}\}_n) + [B]\Delta t^2(\beta_N\{\dot{X}\}_{n+1} + 2(\tfrac{1}{2} - \beta_N)\{\dot{X}\}_n) \\ + [K]\Delta t^2(\beta_N\{X\}_{n+1} + 2(\tfrac{1}{2} - \beta_N)\{X\}_n) = \beta_N \Delta t^2\{W\}_{n+1} \\ + 2(\tfrac{1}{2} - \beta_N)\Delta t^2\{W\}_n\end{aligned} \tag{4.62}$$

From Eq.(4.58):

$$(\tfrac{1}{2} - \beta_N)\Delta t^2\{\ddot{X}\}_n + \beta_N \Delta t^2\{\ddot{X}\}_{n+1} = \{X\}_{n+1} - \{X\}_n - \Delta t\{\dot{X}\}_n \tag{4.63}$$

We will expand the term $\Delta t(\beta_N\{\dot{X}\}_{n+1} + 2(\tfrac{1}{2} - \beta_N)\{\dot{X}\}_n)$ as:

$$\frac{\Delta t}{2}\{\dot{X}\}_n + (\tfrac{1}{2} - \beta_N)\Delta t\{\dot{X}\}_n + \beta_N \Delta t(\{\dot{X}\}_{n+1} - \{\dot{X}\}_n)$$

$$= \frac{\Delta t}{2}\{\dot{X}\}_n + (\tfrac{1}{2} - \beta_N)\Delta t\{\dot{X}\}_n + \beta_N \frac{\Delta t^2}{2}(\{\ddot{X}\}_n + \{\ddot{X}\}_{n+1})$$

$$= \frac{1}{2}(\Delta t\{\dot{X}\}_n - 2\beta_N \Delta t\{\dot{X}\}_n + \Delta t\{\dot{X}\}_n + \frac{\Delta t^2}{2}\{\ddot{X}\}_n - \frac{\Delta t^2}{2}\{\ddot{X}\}_n$$

$$- \beta_N \Delta t^2\{\ddot{X}\}_n + 2\beta_N \Delta t^2\{\ddot{X}\}_n + \beta_N \Delta t^2\{\ddot{X}\}_{n+1})$$

$$= \frac{1}{2}(\{X\}_{n+1} - \{X\}_n + \Delta t\{\dot{X}\}_n(1 - 2\beta_N) - \frac{1}{2}\Delta t^2\{\ddot{X}\}_n(1 - 4\beta_N)) \qquad (4.64)$$

Using Eq.(4.64) and (4.63) in Eq.(4.62):

$$[M](\{X\}_{n+1} - \{X\}_n - \Delta t\{\dot{X}\}_n + (\tfrac{1}{2} - \beta_N)\Delta t^2\{\ddot{X}\}_n) +$$

$$\frac{\Delta t}{2}[B](\{X\}_{n+1} - \{X\}_n + \Delta t\{\dot{X}\}_n(1 - 2\beta_N) - \frac{1}{2}\Delta t^2\{\ddot{X}\}_n(1 - 4\beta_N)) +$$

$$[K]\Delta t^2(\beta_N\{X\}_{n+1} + 2(\tfrac{1}{2} - \beta_N)\{X\}_n) = \beta_N \Delta t^2\{W\}_{n+1}$$

$$+ 2(\tfrac{1}{2} - \beta_N)\Delta t^2\{W\}_n \qquad (4.65)$$

Rearranging Eq.(4.65):

$$([M] + \frac{\Delta t}{2}[B] + \beta_N \Delta t^2[K])\{X\}_{n+1} = \beta_N \Delta t^2\{W\}_{n+1} + 2(\tfrac{1}{2} - \beta_N)\Delta t^2\{W\}_n +$$

$$[M](\{X\}_n + \Delta t\{\dot{X}\}_n - (\tfrac{1}{2} - \beta_N)\Delta t^2\{\ddot{X}\}_n) - 2[K]\Delta t^2(\tfrac{1}{2} - \beta_N)\{X\}_n +$$

$$\frac{\Delta t}{2}[B](\{X\}_n - \Delta t\{\dot{X}\}_n(1 - 2\beta_N) + \frac{1}{2}\Delta t^2\{\ddot{X}\}_n(1 - 4\beta_N)) \qquad (4.66)$$

The right hand side of Eq.(4.66) can be simplified as:

$$([M] + \frac{\Delta t}{2}[B] + \beta_N \Delta t^2[K])\{X\}_{n+1} = \beta_N \Delta t^2\{W\}_{n+1} + 2(\tfrac{1}{2} - \beta_N)\Delta t^2([M]\ \ddot{X}\}_n +$$

$$[B]\ \dot{X}\}_n) + [M](\{X\}_n + \Delta t\{\dot{X}\}_n - (\tfrac{1}{2} - \beta_N)\Delta t^2\{\ddot{X}\}_n) +$$

$$[B](\frac{\Delta t}{2}\{X\}_n - \Delta t^2\{\dot{X}\}_n(\frac{1}{2} - \beta_N) + \frac{\Delta t^3}{4}\{\ddot{X}\}_n(1 - 4\beta_N)) \qquad (4.67)$$

$$([M] + \frac{\Delta t}{2}[B] + \beta_N \Delta t^2[K])\{X\}_{n+1} = \beta_N \Delta t^2\{W\}_{n+1} +$$

$$[M](\{X\}_n + \Delta t\{\dot{X}\}_n + (\tfrac{1}{2} - \beta_N)\Delta t^2\{\ddot{X}\}_n) +$$

$$[B](\frac{\Delta t}{2}\{X\}_n + \Delta t^2\{\dot{X}\}_n(\frac{1}{2} - \beta_N) + \frac{\Delta t^3}{4}\{\ddot{X}\}_n(1 - 4\beta_N)) \qquad (4.68)$$

Eq.(4.68) gives the relation between time station (n+1) and (n). It is quite easy to find similar relationship between (n) and (n-1) time station by replacing the subscript 'n+1' by 'n' and 'n' by 'n-1':

$$([M] + \frac{\Delta t}{2}[B] + \beta_N \Delta t^2[K])\{X\}_n = \beta_N \Delta t^2\{W\}_n +$$

$$[M](\{X\}_{n-1} + \Delta t\{\dot{X}\}_{n-1} + (\tfrac{1}{2} - \beta_N)\Delta t^2\{\ddot{X}\}_{n-1}) +$$

$$[B](\frac{\Delta t}{2}\{X\}_{n-1} + \Delta t^2\{\dot{X}\}_{n-1}(\frac{1}{2} - \beta_N) + \frac{\Delta t^3}{4}\{\ddot{X}\}_{n-1}(1 - 4\beta_N)) \qquad (4.69)$$

Defining $\delta\{X\} = \{X\}_{n+1} - \{X\}_n$ and subtracting Eq.(4.69) from Eq.(4.68):

$$([M] + \frac{\Delta t}{2}[B] + \beta_N \Delta t^2[K])\,\delta\{X\} = \beta_N \Delta t^2\{W\}_{n+1} - \beta_N \Delta t^2\{W\}_n +$$

$$[M](\{X\}_n + \Delta t\{\dot{X}\}_n + (\tfrac{1}{2} - \beta_N)\Delta t^2\{\ddot{X}\}_n) +$$

$$[B](\frac{\Delta t}{2}\{X\}_n + \Delta t^2\{\dot{X}\}_n(\frac{1}{2} - \beta_N) + \frac{\Delta t^3}{4}\{\ddot{X}\}_n(1 - 4\beta_N)) -$$

$$[M](\{X\}_{n-1} + \Delta t\{\dot{X}\}_{n-1} + (\tfrac{1}{2} - \beta_N)\Delta t^2\{\ddot{X}\}_{n-1}) -$$

$$[B](\frac{\Delta t}{2}\{X\}_{n-1} + \Delta t^2\{\dot{X}\}_{n-1}(\frac{1}{2} - \beta_N) + \frac{\Delta t^3}{4}\{\ddot{X}\}_{n-1}(1 - 4\beta_N)) \qquad (4.70)$$

Eq.(4.70) is very important in deriving $[K^*]$ and $\{W^*\}$. But it needs few mathematical manipulation specially on its right-hand-side. First, the terms with [M] on RHS of Eq.(4.70) can be simplified:

$$[M](\{X\}_n + \Delta t\{\dot{X}\}_n + (\tfrac{1}{2} - \beta_N)\Delta t^2\{\ddot{X}\}_n) -$$

$$[M](\{X\}_{n-1} + \Delta t\{\dot{X}\}_{n-1} + (\tfrac{1}{2} - \beta_N)\Delta t^2\{\ddot{X}\}_{n-1}) =$$

$$[M]((\{X\}_n - \{X\}_{n-1} - \Delta t\{\dot{X}\}_{n-1} - (\tfrac{1}{2} - \beta_N)\Delta t^2\{\ddot{X}\}_{n-1})$$

$$+ \Delta t\{\dot{X}\}_n + (\tfrac{1}{2} - \beta_N)\Delta t^2\{\ddot{X}\}_n) \qquad (4.71)$$

But from Eq.(4.58):

$$X\}_n - \{X\}_{n-1} - \Delta t\{\dot{X}\}_{n-1} - (\tfrac{1}{2} - \beta_N)\Delta t^2\{\ddot{X}\}_{n-1} = \beta_N\Delta t^2\{\ddot{X}\}_n \qquad (4.72)$$

That provides a compact expression for Eq.(4.71):

$$[M]((\{X\}_n - \{X\}_{n-1} - \Delta t\{\dot{X}\}_{n-1} - (\tfrac{1}{2} - \beta_N)\Delta t^2\{\ddot{X}\}_{n-1})$$

$$+ \Delta t\{\dot{X}\}_n + (\tfrac{1}{2} - \beta_N)\Delta t^2\{\ddot{X}\}_n) =$$

$$[M](\beta_N\Delta t^2\{\ddot{X}\}_n + \Delta t\{\dot{X}\}_n + (\tfrac{1}{2} - \beta_N)\Delta t^2\{\ddot{X}\}_n) \qquad (4.73)$$

The main aim of this manipulation is to eliminate the terms from (n-1) time station and that is very important and explained later. Now we concentrate on the terms with [B] on RHS of Eq.(4.70):

$$[B](\frac{\Delta t}{2}\{X\}_n + \Delta t^2\{\dot{X}\}_n(\frac{1}{2} - \beta_N) + \frac{\Delta t^3}{4}\{\ddot{X}\}_n(1 - 4\beta_N)) -$$

$$[B](\frac{\Delta t}{2}\{X\}_{n-1} + \Delta t^2\{\dot{X}\}_{n-1}(\frac{1}{2} - \beta_N) + \frac{\Delta t^3}{4}\{\ddot{X}\}_{n-1}(1 - 4\beta_N)) =$$

$$[B](\frac{\Delta t}{2}(\{X\}_n + \Delta t\{\dot{X}\}_n + \frac{\Delta t^2}{2}\{\ddot{X}\}_n) - \beta_N\Delta t^2(\{\dot{X}\}_n + \Delta t\{\ddot{X}\}_n)$$

$$-\frac{\Delta t}{2}(\{X\}_{n-1} + \Delta t\{\dot{X}\}_{n-1} + \frac{\Delta t^2}{2}\{\ddot{X}\}_{n-1}) + \beta_N\Delta t^2(\{\dot{X}\}_{n-1} + \Delta t\{\ddot{X}\}_{n-1})) \quad (4.74)$$

Interchanging few terms in Eq.(4.74):

$$[B](\frac{\Delta t}{2}(\{X\}_n + \Delta t\{\dot{X}\}_n + \frac{\Delta t^2}{2}\{\ddot{X}\}_n) - \beta_N\Delta t^2(\{\dot{X}\}_n + \Delta t\{\ddot{X}\}_n)$$

$$-\frac{\Delta t}{2}(\{X\}_{n-1} + \Delta t\{\dot{X}\}_{n-1} + \frac{\Delta t^2}{2}\{\ddot{X}\}_{n-1}) + \beta_N\Delta t^2(\{\dot{X}\}_{n-1} + \Delta t\{\ddot{X}\}_{n-1})) =$$

$$[B](\frac{\Delta t}{2}(\{X\}_n - \{X\}_{n-1} - \Delta t\{\dot{X}\}_{n-1}) - \beta_N\Delta t^2(\{\dot{X}\}_n + \Delta t\{\ddot{X}\}_n)$$

$$-\frac{\Delta t}{2}(\frac{\Delta t^2}{2}\{\ddot{X}\}_{n-1} - \Delta t\{\dot{X}\}_n - \frac{\Delta t^2}{2}\{\ddot{X}\}_n) + \beta_N\Delta t^2(\{\dot{X}\}_{n-1} + \Delta t\{\ddot{X}\}_{n-1})) \quad (4.75)$$

From Eq.(4.58):

$$X\}_n - \{X\}_{n-1} - \Delta t\{\dot{X}\}_{n-1} = \beta_N\Delta t^2\{\ddot{X}\}_n + \frac{\Delta t^2}{2}\{\ddot{X}\}_{n-1} - \beta_N\Delta t^2\{\ddot{X}\}_{n-1} \quad (4.76)$$

Utilising Eq.(4.76) into Eq.(4.75):

$$[B](\frac{\Delta t}{2}(\{X\}_n - \{X\}_{n-1} - \Delta t\{\dot{X}\}_{n-1}) - \beta_N\Delta t^2(\{\dot{X}\}_n + \Delta t\{\ddot{X}\}_n)$$

$$-\frac{\Delta t}{2}(\frac{\Delta t^2}{2}\{\ddot{X}\}_{n-1} - \Delta t\{\dot{X}\}_n - \frac{\Delta t^2}{2}\{\ddot{X}\}_n) + \beta_N\Delta t^2(\{\dot{X}\}_{n-1} + \Delta t\{\ddot{X}\}_{n-1})) =$$

$$[B](\frac{\Delta t}{2}(\beta_N\Delta t^2\{\ddot{X}\}_n + \frac{\Delta t^2}{2}\{\ddot{X}\}_{n-1} - \beta_N\Delta t^2\{\ddot{X}\}_{n-1}) - \beta_N\Delta t^2(\{\dot{X}\}_n + \Delta t\{\ddot{X}\}_n)$$

$$-\frac{\Delta t}{2}(\frac{\Delta t^2}{2}\{\ddot{X}\}_{n-1} - \Delta t\{\dot{X}\}_n - \frac{\Delta t^2}{2}\{\ddot{X}\}_n) + \beta_N\Delta t^2(\{\dot{X}\}_{n-1} + \Delta t\{\ddot{X}\}_{n-1})) =$$

$$[B](\frac{\Delta t^3}{4}\{\ddot{X}\}_n - \beta_N\frac{\Delta t^3}{2}\{\ddot{X}\}_n + \beta_N\frac{\Delta t^3}{2}\{\ddot{X}\}_{n-1} + \frac{\Delta t^2}{2}\{\dot{X}\}_n - \beta_N\Delta t^2\{\dot{X}\}_n$$

$$+ \beta_N\Delta t^2\{\dot{X}\}_{n-1}) \quad (4.77)$$

Adding and subtracting [B] $\beta_N\frac{\Delta t^3}{2}\{\ddot{X}\}_n$ in Eq.(4.77):

$$[B]\left(\frac{\Delta t^3}{4}\{\ddot{X}\}_n - \beta_N \frac{\Delta t^3}{2}\{\ddot{X}\}_n + \beta_N \frac{\Delta t^3}{2}\{\ddot{X}\}_{n-1} + \frac{\Delta t^2}{2}\{\dot{X}\}_n - \beta_N \Delta t^2 \{\dot{X}\}_n \right.$$

$$\left. + \beta_N \Delta t^2 \{\dot{X}\}_{n-1} \right) =$$

$$[B]\left(\beta_N \Delta t^2 (\{\dot{X}\}_{n-1} + \frac{\Delta t}{2}\{\ddot{X}\}_{n-1} + \frac{\Delta t}{2}\{\ddot{X}\}_n) + \frac{\Delta t^3}{4}\{\ddot{X}\}_n - \beta_N \Delta t^3 \{\ddot{X}\}_n \right.$$

$$\left. + \Delta t^2 \{\dot{X}\}_n (\frac{1}{2} - \beta_N) \right) \qquad (4.78)$$

But from Eq.(4.59):

$$\dot{X}\}_n = \{\dot{X}\}_{n-1} + \frac{\Delta t}{2}\{\ddot{X}\}_{n-1} + \frac{\Delta t}{2}\{\ddot{X}\}_n \qquad (4.79)$$

Putting Eq.(4.79) into Eq.(4.78):

$$[B]\left(\beta_N \Delta t^2 (\{\dot{X}\}_{n-1} + \frac{\Delta t}{2}\{\ddot{X}\}_{n-1} + \frac{\Delta t}{2}\{\ddot{X}\}_n) + \frac{\Delta t^3}{4}\{\ddot{X}\}_n - \beta_N \Delta t^3 \{\ddot{X}\}_n \right.$$

$$\left. + \Delta t^2 \{\dot{X}\}_n (\frac{1}{2} - \beta_N) \right) =$$

$$[B]\left(\beta_N \Delta t^2 \{\dot{X}\}_n + \frac{\Delta t^3}{4}\{\ddot{X}\}_n - \beta_N \Delta t^3 \{\ddot{X}\}_n + \Delta t^2 \{\dot{X}\}_n (\frac{1}{2} - \beta_N) \right) \qquad (4.80)$$

So the final form on the right-hand-side of Eq.(4.80) does not have any term from (n-1) time station. Eq.(4.73) and Eq.(4.80) are useful in rearranging Eq.(4.70):

$$([M] + \frac{\Delta t}{2}[B] + \beta_N \Delta t^2 [K])\delta\{X = \beta_N \Delta t^2 \{W\}_{n+1} - \beta_N \Delta t^2 \{W\}_n +$$

$$[M]\left(\beta_N \Delta t^2 \{\ddot{X}\}_n + \Delta t \{\dot{X}\}_n + (\tfrac{1}{2} - \beta_N)\Delta t^2 \{\ddot{X}\}_n \right) +$$

$$[B]\left(\beta_N \Delta t^2 \{\dot{X}\}_n + \frac{\Delta t^3}{4}\{\ddot{X}\}_n - \beta_N \Delta t^3 \{\ddot{X}\}_n + \Delta t^2 \{\dot{X}\}_n (\frac{1}{2} - \beta_N) \right) \qquad (4.81)$$

Now multiplying Eq.(4.61) by $\beta_N \Delta t^2$:

$$-\beta_N \Delta t^2 \{W\}_n + \beta_N \Delta t^2 [M]\{\ddot{X}\}_n + \beta_N \Delta t^2 [B]\{\dot{X}\}_n = -\beta_N \Delta t^2 [K]\{X\}_n \qquad (4.82)$$

So the final form of Eq.(4.81) is:

$$([M] + \frac{\Delta t}{2}[B] + \beta_N \Delta t^2 [K])\delta\{X = \beta_N \Delta t^2 (\{W\}_{n+1} - [K]\{X\}_n) +$$

$$[M]\left(\Delta t \{\dot{X}\}_n + (\tfrac{1}{2} - \beta_N)\Delta t^2 \{\ddot{X}\}_n \right) +$$

$$[B](\Delta t^3 \{\ddot{X}\}_n (\frac{1}{4} - \beta_N) + \Delta t^2 \{\dot{X}\}_n (\frac{1}{2} - \beta_N)) \qquad (4.83)$$

Eq.(4.83) has some special characteristics. It does not have any contribution from (n-1) time station. All the terms are related to the present time step except the external

load whose value is required at the immediate future time station. If the nature of external force is known (i.e. if it can be predicted beforehand), the solution of Eq.(4.83) would be straightforward. Otherwise, if it is dependent on structural displacement and velocity, it should be extrapolated and finally found through iterations.

Damping is very important to establish steady state responses but there is no need to store [B] as a separate matrix in the analysis. So [B] is eliminated by substituting Eq.(4.33) into Eq.(4.83):

$$([M](1 + \alpha_R\frac{\Delta t}{2}) + [K](\beta_N\Delta t^2 + \beta_R\frac{\Delta t}{2}))\,\delta\{X\} = \beta_N\Delta t^2\{W\}_{n+1} +$$

$$[M](\{\dot{X}\}_n(\Delta t + \alpha_R\frac{\Delta t^2}{2} - \alpha_R\beta_N\Delta t^2) + \{\ddot{X}\}_n(\frac{\Delta t^2}{2} - \beta_N\Delta t^2 + \alpha_R\frac{\Delta t^3}{4} - \alpha_R\beta_N\Delta t^3))$$

$$+ [K](-\beta_N\Delta t^2\{X\}_n + \beta_R\Delta t^3\{\ddot{X}\}_n(\frac{1}{4} - \beta_N) + \beta_R\Delta t^2\{\dot{X}\}_n(\frac{1}{2} - \beta_N)) \quad (4.84)$$

Now we define the effective stiffness matrix and modified load vector as:

$$\left[K^*\right] = [M](1 + \alpha_R\frac{\Delta t}{2}) + [K](\beta_N\Delta t^2 + \beta_R\frac{\Delta t}{2}) \quad (4.85a)$$

$$\left\{W^*\right\} = \beta_N\Delta t^2\{W\}_{n+1} +$$

$$[M](\{\dot{X}\}_n(\Delta t + \alpha_R\frac{\Delta t^2}{2} - \alpha_R\beta_N\Delta t^2) + \{\ddot{X}\}_n(\frac{\Delta t^2}{2} - \beta_N\Delta t^2 + \alpha_R\frac{\Delta t^3}{4} - \alpha_R\beta_N\Delta t^3))$$

$$+ [K](-\beta_N\Delta t^2\{X\}_n + \beta_R\Delta t^3\{\ddot{X}\}_n(\frac{1}{4} - \beta_N) + \beta_R\Delta t^2\{\dot{X}\}_n(\frac{1}{2} - \beta_N)) \quad (4.85b)$$

So Eq.(4.83) takes a very simple form for solving incremental displacement vector:

$$\left[K^*\right]\delta\{X\} = \left\{W^*\right\} \quad (4.86)$$

The flow chart in Fig. 4.51 is in a better position to explain the iterations involved. For Model_3 analysis, the widely known parameters, β_N and δ_N are set to 0.25 and 0.5 for highly accurate predictions within $O(\Delta t^3)$. One point should be noted here that [K], [M] and [K*] are never stored in a square matrix format for avoiding sheer waste of computational effort and storage. The algorithm deals with these three matrices in compacted column architecture. But the calculations, specially multiplications of matrices become complicated when only the non-zero coefficients of a large square matrix are stored in an one-dimensional array. So additional routines were necessary while developing DCATLP to maintain a general flow in the predictor-corrector algorithm while working in the compacted column storage mode.

4.5.9.2 Algorithm used by LUSAS for Model_2

Although LUSAS can perform 'theoretically elegant non-linear analysis' [4.4], only a linear standard Newmark-β integration scheme ($\beta_N = 0.25$, $\delta_N = 0.5$) has been used for analysing Model_2 in LUSAS. Both three and four point recurrence algorithms are available in LUSAS. They are multi-purpose schemes derived using a weighted residual approach [4.21]. The algorithms are very general and many commonly used schemes may be obtained by using the appropriate weighting functions. For the sake of completeness the Newmark constant-average-acceleration method used for Model_2 is briefly discussed below.

Initial Calculations :

1) Formation of global stiffness matrix [K], mass matrix [M] and damping matrix [B].
2) Initialisation of $X\}$, $\{\dot{X}\}$ and $\{\ddot{X}\}$.
3) Selection of time step size Δt, parameters β_N and δ_N

$$\delta_N \geq 0.50 \qquad \beta_N \geq 0.25(0.5+\delta_N)^2 \tag{4.87}$$

4) Calculation of integration constants:

$$C_0 = \frac{1}{\beta_N \Delta t^2};\ C_1 = \frac{\delta_N}{\beta_N \Delta t};\ C_2 = \frac{1}{\beta_N \Delta t};\ C_3 = \frac{1}{2\beta_N} - \ ;$$

$$C_4 = \frac{\delta_N}{\beta_N} - 1;\ C_5 = \frac{\Delta t}{2}\left(\frac{\delta_N}{\beta_N} - 2\right);\ C_6 = \Delta t(1 - \delta_N);\ C_7 = \delta_N \Delta t \tag{4.88}$$

5) Generation of effective stiffness matrix : $[K^*] = [K] + C_0[M] + C_1[B]$
6) Triangularisation of $[K^*]$: $[K^*] = [K_L]\cdot[K_U]$

For each time step:

1) Calculation of modified load vector at time station (n+1):

$$\{W^*\}_{n+1} = \{W^*\}_{n+1} + [M](C_0\{X\}_n + C_2\{\dot{X}\}_n + C_3\{\ddot{X}\}_n) + [B](C_1\{X\}_n + C_4\{\dot{X}\}_n + C_5\{\ddot{X}\}_n) \tag{4.89}$$

2) Solution for displacements at time station (n+1):

$$[K_L]\cdot[K_U]\cdot\{X\}_{n+1} = \{W^*\}_{n+1} \tag{4.90}$$

3) Calculation for accelerations and velocities at time station (n+1):

$$\ddot{X}\}_{n+1} = C_0(\{X\}_{n+1} - \{X\}_n) - C_2\{\dot{X}\}_n - C_3\{\ddot{X}\}_n \tag{4.91a}$$

$$\dot{X}\}_{n+1} = \{\dot{X}\}_n + C_6\{\ddot{X}\}_n + C_7\{\ddot{X}\}_{n+1} \tag{4.91b}$$

The algorithm is straightforward and the triangular decomposition of $[K^*]$ is required only once. This is a great advantage of a linear dynamic analysis. As explained earlier it is only possible for Model_2 because tethers are replaced by springs in each corner.

4.5.10 Internal Resisting Forces

The actual displacement of a TLP hull can be assumed as a superposition of two types of displacements. The hull under the action of environmental forces would have infinitesimal strains measured in a body-attached co-ordinate frame while this frame undergoes large rigid body translations and rotations. The rigid body displacements are of interest to a hydrodynamist but the strains are of more importance in the context of structural design of TLP components.

The small differences in displacements (translational and rotational) in two nodes of a 3-D beam element give rise to stresses. From the sectional properties of the element the internal resisting forces can be calculated. The computation procedure followed in DCATLP is only applicable for 'small strain' cases [4.4]. The calculation is done for each element in a specific group for all time stations. The groups are to be defined before the analysis starts. For example, a group may include all beam elements representing all corner columns. Otherwise, a group may consist of only few elements where higher values of internal forces are expected. This internal resisting force calculation is done only once in a time station and that is after achieving the required convergence. Let us consider a beam element AB at an arbitrary time station. In the first step six displacement values at node A and B (total twelve) are extracted from the converged global displacement vector $\{X\}$. The transformation matrix $[T_r]$ for element AB is then calculated based on the dynamic position of AB at that time station. $[T_r]$ is then used to find twelve displacement values in local co-ordinates at A and B from the following:

$$\{X_l^e\} = [T_r]\{X_g^e\} \tag{4.92}$$

Once displacement values are found in local co-ordinates, the internal resisting forces, $\{E\}$ can be simply calculated from the following:

$$\{E\} = [K_l^e]\{X_l^e\} \tag{4.93}$$

Calculating $\{E\}$ for many elements in different groups at each and every time station for searching the maximum values must be time consuming. But this time consuming search does a good job because it works automatically and it considers a very large set of time varying load cases on the platform. It is in fact calculating the internal forces in TLP components under the action of time varying environmental, inertia, damping and

restoring forces. This automatic, elaborate, element-by-element calculation is extremely difficult if not impossible, if the structural calculations have to depend on separate hydrodynamic analysis.

It is possible to avoid the matrix multiplication in Eq.(4.93). There are quite a few zero coefficients in $\left[K_l^e\right]$. So the analysis would be significantly faster if the results of the multiplication are programmed:

$$E(1) = \frac{E_Y A}{L}\left[X_l^e(1) - X_l^e(7)\right] \tag{4.94a}$$

$$E(2) = \frac{12E_Y I_z}{L^3}\left[X_l^e(2) - X_l^e(8)\right] + \frac{6E_Y I_z}{L^2}\left[X_l^e(6) + X_l^e(12)\right] \tag{4.94b}$$

$$E(3) = \frac{12E_Y I_y}{L^3}\left[X_l^e(3) - X_l^e(9)\right] - \frac{6E_Y I_y}{L^2}\left[X_l^e(5) + X_l^e(11)\right] \tag{4.94c}$$

$$E(4) = \frac{G_s J_x}{L}\left[X_l^e(4) - X_l^e(10)\right] \tag{4.94d}$$

$$E(5) = -\frac{6E_Y I_y}{L^2}\left[X_l^e(3) - X_l^e(9)\right] + \frac{4E_Y I_y}{L}\left[X_l^e(5) + \tfrac{1}{2}X_l^e(11)\right] \tag{4.94e}$$

$$E(6) = \frac{6E_Y I_z}{L^2}\left[X_l^e(2) - X_l^e(8)\right] + \frac{4E_Y I_z}{L}\left[X_l^e(6) + \tfrac{1}{2}X_l^e(12)\right] \tag{4.94f}$$

$$E(7) = -\frac{E_Y A}{L}\left[X_l^e(1) - X_l^e(7)\right] \tag{4.94g}$$

$$E(8) = -\frac{12E_Y I_z}{L^3}\left[X_l^e(2) - X_l^e(8)\right] - \frac{6E_Y I_z}{L^2}\left[X_l^e(6) + X_l^e(12)\right] \tag{4.94h}$$

$$E(9) = -\frac{12E_Y I_y}{L^3}\left[X_l^e(3) - X_l^e(9)\right] + \frac{6E_Y I_y}{L^2}\left[X_l^e(5) + X_l^e(11)\right] \tag{4.94i}$$

$$E(10) = -\frac{G_s J_x}{L}\left[X_l^e(4) - X_l^e(10)\right] \tag{4.94j}$$

$$E(11) = -\frac{6E_Y I_y}{L^2}\left[X_l^e(3) - X_l^e(9)\right] + \frac{4E_Y I_y}{L}\left[\tfrac{1}{2}X_l^e(5) + X_l^e(11)\right] \tag{4.94k}$$

$$E(12) = \frac{6E_Y I_z}{L^2}\left[X_l^e(2) - X_l^e(8)\right] + \frac{4E_Y I_z}{L}\left[\tfrac{1}{2}X_l^e(6) + X_l^e(12)\right] \tag{4.94l}$$

Eq.(4.94) appears to be much more complex than the simple straightforward presentation in Eq.(4.93). But the number of basic numerical operations is much less in Eq.(4.94). Eq.(4.94) highlights another aspect of internal force calculation. All these equations find the forces based on the differences in displacements in two nodes of an element. So the rigid body motion of the element does not affect the force calculation. But it should be kept in mind that rigid body motions do change stresses in structures in some non-linear theories (e.g. Cauchy stress changes due to a rigid body rotation of

the material but not 2nd Piola-Kirchhoff stress tensor [4.4]). The length of the element in Eq.(4.94) is the original unstretched length. It has been said before that the heave responses in this chapter include the initial stretch in tethers. This is important in this context because the initial stretch is necessary in the internal force calculation to reflect the tension fluctuation and its average magnitude.

This resisting force calculation depends on dynamic position and external nodal forces on elements. So it varies with time. DCATLP finds the maximum values of {E} in an element group at each time station and writes them to an output file in simple text format. The number of this type of output files is the same as the number of element groups. So at the end of a run each output file would contain the maximum values of {E} at each and every time station for a specific group of elements. Out of twelve coefficients of {E}, only six are necessary for further analysis. E(1) would indicate the axial tension or compression in the element and E(7) is not necessary. The other five required values are of shear forces in two vertical planes, bi-axial bending moments and torque. The maximum value of torque recorded by DCATLP in a specific element group at a particular time station may not correspond to the element where maximum axial tension or compression occurs. The six coefficients of {E} recorded may correspond to different elements in the same element group at the same time station. But different type of recording is also possible.

4.6 ENVIRONMENTAL LOADING AND RESPONSES

For numerical demonstration a regular wave of 18 m height and 17 seconds period is passed through Model_3. The selection of this wave height and period is based on the actual observations of peak storm events in the Hutton site in the period 1984-1988. But it should be kept in mind that the water depth for the ISSC TLP is three times more than that in the Hutton site. So it would be always a good idea to process the load effects in a reliability analysis instead of putting them straight into the design. The 18 m high wave propagates along the global X axis. Zero wave heading angle is purposely selected to eliminate the sway response of the platform. In Section 4.6.1 the dynamic relation between the platform surge and heave are shown with the help of Mathematica. It is difficult to interpret such results if sway motion is present along with surge and heave. One hour average wind speed at the reference height H_{wn} is taken as 30 m / s. The Department of Energy [4.14] recommended current profile in this numerical study has been discussed already in Chapter 2.

In Section 4.4 some numerical results are presented with two different Rayleigh damping levels. In one damping level α_R and β_R are both 1%. and in the other, they

are both 2%. It has been shown that the difference in response due to this change in damping is not significant. But the solution under the action of a sinusoidal load becomes steady after a long time when α_R and β_R are both 1%. For achieving quick convergence in connection with the steady state response, α_R and β_R are both 2% in Figs. 4.58-4.66 and Figs. 4.69-4.93. In Figs. 4.94 and 4.95 surge and heave responses for two different damping levels are compared. The difference is insignificant.

Figs. 4.58 and 4.59 show the total surge and heave force on the platform. The net resultant force in the heave direction includes the difference of platform weight and variable buoyancy. So it is not actually the total external force in Fig. 4.59. Figs. 4.60 and 4.61 present corresponding surge and heave responses. It is not computationally convenient to sum each component of environmental loading separately at all free nodes of the structure in each time step. But the very recent trend in industries [4.3] is to analyse different loading and response components separately in frequency domain. So in line with this recent trend environmental loading components are separated in DCATLP and plotted in Fig. 4.62 onwards. The wind force in Fig. 4.62 varies with time because of the relative velocity model in Eq.(2.64). The most important force component is shown in Fig. 4.63. The wave inertia includes the main wave drift component (see Chapter 2) because calculations are done considering the displaced dynamic position of the TLP. The drift is not much pronounced in Fig. 4.63 because MacCamy-Fuchs' theory is valid only up to SWL, not the free surface. But there are other closed-form drift and second order correction forces present in the analysis to take care of this discrepancy. The steady state offset of 40 m in Fig. 4.60 is largely due to the wave-current-motion interaction force in Fig. 4.64. The average magnitude of this interaction force in a wave cycle is quite large and the reason is further investigated in Figs. 4.65 and 4.66. The horizontal velocity along global X axis at node 90 (see Fig. 4.9) is given in Fig. 4.65. As discussed earlier velocity at node 90 can represent the rigid body velocity of the TLP hull. The maximum magnitude of velocity in Fig. 4.65 is around 1.7 m/s under the action of all components of environmental loading. The wave-current-motion interaction force is calculated in DCATLP from Eq.(2.66) in Chapter 2. It is interesting to note that the interaction force in Eq.(2.66) would attain its maximum magnitude when the hull moves against the wave and current flow. This is examined in Fig. 4.66. The wave and current flow are in the positive X direction. But when the structural velocity is negative the interaction force is greatly amplified. Please note that C_D for TLP components are kept constant in wave cycles. Perhaps that may not be true in reality and further research is required in this complex area of hydrodynamics. The steady potential and viscous drift force transfer functions are plotted in Figs. 4.67 and 4.68. The regular wave for this

numerical demonstration is of 17 seconds period. From Figs. 4.67 and 4.68 we can see that the steady drift forces at 17 s wave period are negligible for the ISSC TLP. So second order correction and steady drift forces are 'extracted' together as a group and plotted in Fig. 4.69. The difference between variable buoyancy and platform weight in Fig. 4.70 is the major component of tether tension. Figs. 4.71 and 4.72 present wave inertia and interaction force on Model_3 in the vertical direction.

It is not straightforward to estimate the pitch response of the platform from a finite element analysis. Translational motions at any node on a TLP hull approximately represent its rigid body translational motions. But when rotational movements are concerned, an average should be calculated from the platform geometry and translational motions at different nodes. This is because rotations in a finite element refer to that element only. The element rotation does not have any relation with the whole structure in general. The pitch response in Fig. 4.73 has been calculated from vertical motions of four nodes (66, 78, 90 and 102 in Fig. 4.9). The dynamic inclination angles of two pontoons (one joining node 66 and 78 and the other joining 102 and 90) are calculated at each time station from instantaneous vertical positions of four nodes. The pitch response in Fig. 4.73 is the average of these two inclination angles. A 'close up' view is also given in Fig. 4.74. The pitch response is in good agreement with the first order pitch transfer functions published in Ref. [4.31], [4.33].

The maximum pressure and internal resisting forces are important in the context of structural design and subsequent reliability study. The maximum hydrodynamic pressure on all four columns at each time station is plotted in Fig. 4.75. The maximum values (for all four columns) of axial compression, torsion, bi-axial bending moments and shear forces in local y and z directions are shown in Figs. 4.76-4.81. The peculiar nature of these curves are not important because they very much depend on the external forces acting on the structure. As explained earlier the maximum value of any internal force for an element group may 'shift' from one element to another within a wave cycle. The similar plots for pontoons and tethers are in Figs. 4.82-4.87 and Figs. 4.88-4.93 respectively. Please note that columns are always under compression in this numerical demonstration because of the action of deck weight and hydrodynamic pressure under the column bases. On the other hand, the tethers are always under tension. But the elements representing pontoons may be under tension or compression. So maximum values of tension as well as compression in pontoon elements are shown in Fig. 4.82. Zero compression indicates that all elements at that instant of time are under tension. For tether elements, the local y axis coincides with the global Y axis. This is only true for Model_3 mesh. There is no external sway force in this numerical

study. So the internal shear forces in the tether elements are very small in the global Y direction as expected. The bending moment about their local z axis is also very small whereas the bending moment about their local y (i.e. global Y in this case) axes is substantial. This bending moment actually comes from the end-fixity of four boundary nodes (i.e. 154-157) and should be interpreted very carefully.

It is quite natural to expect small values of shear force in the global Y direction for columns similar to the tether elements. But column elements are under compression and belong to a rigid frame work of the deck grillage and inter-connecting pontoons. So bending moments and shear forces are substantial and of the same order in both vertical planes.

Similar results can be reproduced for different damping levels. But slight change in damping does not have any significant influence on the responses. Figs. 4.94 and 4.95 compare surge and heave of Model_3 with both α_R and β_R as 1% and 2%. The deflection shape of an equivalent tether in the steady state motion is plotted in Fig. 4.96 for a complete wave cycle. It is interesting to notice the influence of end-fixity at the boundary nodes at the sea-bed level. The deflected shape looks like a deformed cantilever but an improved tether model with flex joints at the sea-bed should eliminate this minor discrepancy. Fig. 4.96 is drawn in scale and it is difficult to realise the dynamic set-down because the vertical axis in the graph covers 415 m. The tether is under high tension and the additional set-down effects as discussed in Section 4.4 are not quite apparent. The nodes along the equivalent tether are plotted as very small circles. The difference between two consecutive time stations in Fig. 4.96 is one second. The tether shapes in station I and XVIII are more or less identical because the next response cycle starts from station XVIII.

4.6.1 Interface with Mathematica

Mathematica from Wolfram Research is a powerful software for doing mathematics by computers. Mathematica can communicate at a high level with other programs and it is possible to set up a complete front end or control system in an external program which can call Mathematica as if it were a subroutine [4.36]. At present, Mathematica is used to read data in FORTRAN format generated by DCATLP and to send graphics to a generic PostScript output device. A three-dimensional graphical presentation is more significant in structural dynamics since the results become more visible and conclusions can be easily drawn. Fig. 4.97, a typical output from Mathematica is an ideal example because it actually represents the inverted pendulum like movement of a TLP which is beyond the scope of two-dimensional graphics.

4.7 CONCLUSIONS

One important conclusion in this study is about the spring models of tethers. The ideal horizontal spring stiffness, T_0 / L_t can provide reasonable estimates of the platform surge or sway response but tethers do not behave totally like springs in the vertical direction. Their behaviour in the vertical direction can only be understood from a hull-tether coupled analysis.

The importance of damping has also been demonstrated in this work. For steady state response calculation in time domain, damping in the system is essential. Otherwise the free vibration part in the transient state of response will not die out in the course of time. This may create confusion if the results are compared with frequency domain calculations.

DCATLP has been started with different initial conditions for verifications but the steady state response found is the same in all cases, as expected. The unsteady part depends on the initial conditions and if it is of interest (e.g. for estimating reactions of some impulsive loading) it is possible to start the analysis with specific values of offset, velocities and accelerations.

DCATLP can handle a large set of time varying load cases on a TLP. It also calculates the internal forces in TLP components under the action of time varying environmental, inertia, damping and restoring forces. This automatic, elaborate, element-by-element calculation is extremely difficult if not impossible, if the structural calculations have to depend on separate hydrodynamic analysis.

One discouraging aspect of the program is that calculations involved are far from simple. On a SPARC 514 machine DCATLP takes around 80 minutes CPU time to do all calculations for one thousand time stations. The real time spent is slightly more than 80 minutes when the machine is not shared by other users. But on an 'entry level' 486 PC it would take much more time to complete the same task. In this context perhaps we should remember that the computing world and associated hardware are improving dramatically. Not many years back people had to pay for using remote computers. Developing codes at that time was not easy. Nowadays there is a trend of purchasing a computer rather than a calculator! The big organisations have several computers and the cost of computation has practically come down to the electrical power consumption. In the fast changing world of parallel processing very complicated calculations are processed without any difficulty [4.19].

It should not be difficult to improve the capabilities of DCATLP. It can handle irregular and random waves without much modification. The environmental loading module can calculate forces from a number of regular waves and superimpose them together to form the right-hand-side external load vector. A random wave signal can be separated into a number of regular wave components through FFT (Fast Fourier Transformation). Standard FFT routines are available in the NAG library (from The Numerical Algorithms Group Ltd.). So it should not be a problem to handle site data in the immediate future extension of DCATLP.

4.8 REFERENCES

[4.1] Anonymous: "Heidrun Field Development Waiting for Go-ahead", Ocean Industry, pp. 53-56, July 1990.

[4.2] Archer, J.S.: "Consistent Mass Matrix for Distributed Mass Systems", Journal of the Structural Division, ASCE, Vol. 89, pp. 161-178, 1963.

[4.3] Banon, H., Jefferys, E.R., Toro, R.G. and De, R.S.: "Development of Reliability-Based Global Design Equations for TLPs", Proceedings of International Offshore Mechanics and Arctic Engineering Symposium, ASME, Vol. II, 1994.

[4.4] Bathe, K.J.: "Finite Element Procedures in Engineering Analysis", Prentice-Hall, 1982.

[4.5] Bathe, K.J. and Wilson, E.L.: "Numerical Methods in Finite Element Analysis", Prentice-Hall, 1976.

[4.6] Belytschko, T. and Schoeberle, D.F.: "On the Unconditional Stability of an Implicit Algorithm for Non-linear Structural Dynamics", Journal of Applied Mechanics, pp. 865-869, December 1975.

[4.7] Boom, de W.C. and Tan, S.G.: "The Wave Induced Motions of a Tension Leg Platform in Deep Water," OTC 4074, 13th Annual Offshore Technology Conference, Houston, pp. 89-98, 1981.

[4.8] Caughey, T.K.: "Classical Normal Modes in Damped Linear Systems", Journal of Applied Mechanics, Vol. 27, pp. 269-271, 1960.

[4.9] Chan, S.P., Cox, H.L. and Benfield, W.A.: "Transient Analysis of Forced Vibrations of Complex Structural-Mechanical Systems", Journal of the Royal Aeronautical Society, Vol. 66, pp. 457-460, July 1962.

[4.10] Chen, Y.N., Liu, D. and Shin, Y.S.: "Probabilistic Analyses of Environmental Loading and Motion of a Tension Leg Platform for Reliability-Based

Design", Centenary Conference, Marine Safety, University of Glasgow, Glasgow, September 1983.

[4.11] Conoco/ABS TLP Rule Case Committee: "Model Code for Structural Design of Tension Leg Platforms", New York, February 1984.

[4.12] Davies, K.B. and Mungall, J.C.H.: "Methods for Coupled Analysis of TLP's", OTC 6567, 23th Annual Offshore Technology Conference, Houston, pp. 57-68, 1991.

[4.13] Demirbilek, Z.: "Design Formulae for Offset, Set Down and Tether Loads of a Tension Leg Platform (TLP)", Ocean Engineering, Vol. 17, No. 5, pp. 517-523, 1990.

[4.14] Department of Energy: "Offshore Installations: Guidance on Design, Construction and Certification, Fourth Edition, 1990.

[4.15] Faulkner, D.: "Tension Buoyant Platforms Seminar - 25/26 May 1993", Departmental Memorandum on Attending the Seminar, Department of Naval Architecture and Ocean Engineering, University of Glasgow, Glasgow, 7 June 1993.

[4.16] Grant, R.G., Sircar, S. and Nikodym, L.A.: "A Systematic Procedure for Developing Optimum TLP Configurations", OTC 6570, 23th Annual Offshore Technology Conference, Houston, pp. 93-101, 1991.

[4.17] Hinton, E.: "NAFEMS Introduction to Non-linear Finite Element Analysis", NAFEMS, Glasgow, pp. 284-290, 1992.

[4.18] Holzer, S.M.: "Computer Analysis of Structures", Elsevier Science Publishing Company, 1985.

[4.19] Hunt, D.J.: "AMT DAP - a processor array in a workstation environment", Computer Systems Science and Engineering, Vol. 4, No. 2, 1989.

[4.20] Lee, J.S.: "Reliability Analysis of Continuous Structural Systems", Ph.D. Thesis (No. NAOE-89-43), Department of Naval Architecture and Ocean Engineering, University of Glasgow, Glasgow, 1989.

[4.21] LUSAS Theory Manual, Version 10.0, Finite Element Analysis Limited, 66 High Street, Surrey, 1990.

[4.22] Marthinsen, T. and Muren, J.: "Snorre TLP - Comparison of Predicted and Measured Response", BPP Seminar on Tensioned Buoyant Platforms, London, 1993.

[4.23] Mercier, J.A., Birell, N.D., Chivvis, J.C. and Hunter A.F.: "Tension Leg

Platforms - Progress and Prospects", SNAME Transactions, Vol. 99, pp. 249-279, 1991.

[4.24] Mukhopadhyay, M.: "Vibrations, Dynamics and Structural Systems", Oxford & IBH Publishing Company, Delhi, 1989.

[4.25] Mullarkey, T.P. and McNamara, J.K.: "Synthesis of First Order TLP Wave Load from Semi-analytical Solutions for Pontoons and Columns", Proceedings of International Offshore Mechanics and Arctic Engineering Symposium, ASME, Vol. 1, 1993.

[4.26] Newmark, N.: "A Method of Computation for Structural Dynamics", Journal of the Engineering Mechanics Division, Proceedings of ASCE, pp. 67-94, 1959.

[4.27] Paulling, J.R.: "Wave-Induced Forces and Motions of Tubular Structures", Proceedings of Eighth Symposium on Naval Hydrodynamics, Pasadena, ONR ACR179, 1970.

[4.28] Prince-Wright, R.: "Statistical Models of Environmental Data for Marine Structure Design", Ph.D. Thesis (No. NAOE-93-26), Department of Naval Architecture and Ocean Engineering, University of Glasgow, Glasgow, 1993.

[4.29] Przemieniecky, J.S.: "Theory of Matrix Structural Analysis", McGraw-Hill, 1968.

[4.30] Ralston, A.: "A First Course in Numerical Analyses", McGraw-Hill, 1965.

[4.31] Report of Committee I.2: "Case study of a Tension Leg Platform", Proceedings of the Ninth International Ship and Offshore Structures Congress, Registro Italiano Navale, Genova, Vol. 1, pp. I.2-48-55, 1985.

[4.32] Shin, Y.S., Xanthopoulos, E. and Unger, D.P.: "Extreme Value and Probability Density Function of Motion, Tether Tension and Load Effects on a North Sea Tension Leg Platform", Paper RCC(b) 16, 7 February 1983.

[4.33] Taylor, R.E. and Jefferys, E.R.: "Variability of Hydrodynamic Load Predictions for a Tension Leg Platform", Ocean Engineering, Vol. 13, No. 5, pp. 449-490, 1986.

[4.34] Turner, J.: "Chairman's Chat", LUSAS User Group Newsletter, No. 21, Summer 1994.

[4.35] Wang, C.K.: "Matrix Methods of Structural Analysis", International Textbook Company, Pennsylvania, 1966.

[4.36] Wolfram, S.: "Mathematica - A System for Doing Mathematics by

Computer", Second Edition, Addison-Wesley Publishing Co., California, 1991.

[4.37] Zienkiewicz, O.C.: "The Finite Element Method", Third Edition, McGraw-Hill, 1977.

Table 4.4. Design of Tethers for the ISSC TLP Based on Others in Service

TLP	Hutton	Jolliet	Snorre	Auger	Heidrun	ISSC	ISSC (EQ)
No. of tethers	16	12	16	12	12	12	4
Tether diameter (mm)	260	610	813	660	1110	1148.08	1988.54
Thickness (mm)	92.5	20.6	38.1	33	38	38.79	67.18
Diameter / thickness	2.81	29.61	21.34	20.00	29.21	29.60	29.60
Length (m)	150	512	310	840	350	415	415
Enclosed area (mm^2)	204	479	639	518	872	902	1562
Material area (mm^2)	48675	38144	92751	65003	127976	135173	405520
Material area per corner (mm^2)	194700	114432	371006	195008	383928	405520	405520
Pretension/tether (MN)	9.0743	3.6379	15.3281	8.8699	15.0000	11.4450	34.335
Pretension stress (MPa)	186.43	95.37	165.26	136.45	117.21	84.67	84.67
Pretension stress (ksi)	27.04	13.83	23.97	19.79	17.00	12.28	12.28

Table 4.6. Mass Distribution and the CG Position of the Hull

TLP Members	No.	Material Area (m^2)	Enclosed Area (m^2)	Length (m)	Density (lb/ft^3)	Density (kg/m^3)	Mass (kg)	Lever (m)	Moment (kg-m)
Pontoon	40	1.3446	78.75	6.9370	19.00	304.36	6650635.1	-32.75	-217808298.1
Column	40	1.8092	223.79	5.3250	15.26	244.45	11651884.5	-0.875	-10195398.9
Column Joint	8	2.7124	223.79	5.2500	24.78	396.94	3730891.6	-32.75	-122186698.6
Pontoon Joint	8	2.0169	78.75	8.4400	25.20	403.67	2146400.7	-32.75	-70294623.5
Deck	40	0.8844	56.25	21.5625	21.00	336.39	16320302.1	25.75	420247778.7
Total	136						40500113.9		-237240.4

CG Position w.r.t the base line (38 m above keel) = -0.00586 m

Table 4.7. Sectional Properties of TLP Components

TLP Members	No.	Shell Thickness (mm)	Flange (mm x mm)	Web (mm x mm)	No. of Stiffeners	Material Area (m^2)	Iz (m^4)	Iy (m^4)	Jx (m^4)
Pontoon	40	28	150 x 25	400 x 14	36	1.3446	12.9855	21.3466	19.2938
Column	40	25	189 x 19	300 x 15	60	1.8092	63.3078	63.3078	94.0194
Column Joint	8	37.5	189 x 28.5	300 x 22.5	60	2.7124	94.7180	94.7180	140.7160
Pontoon Joint	8	42	150 x 37.5	400 x 21	36	2.0169	19.4583	32.0016	28.9408
Deck	40	20	150 x 20	350 x 14	36	0.8844	7.8971	7.8971	8.4375
Tether	40	67.18	-	-	-	0.4055	0.1874	0.1874	0.3747
Total	176	-	-	-	-	-	-	-	-

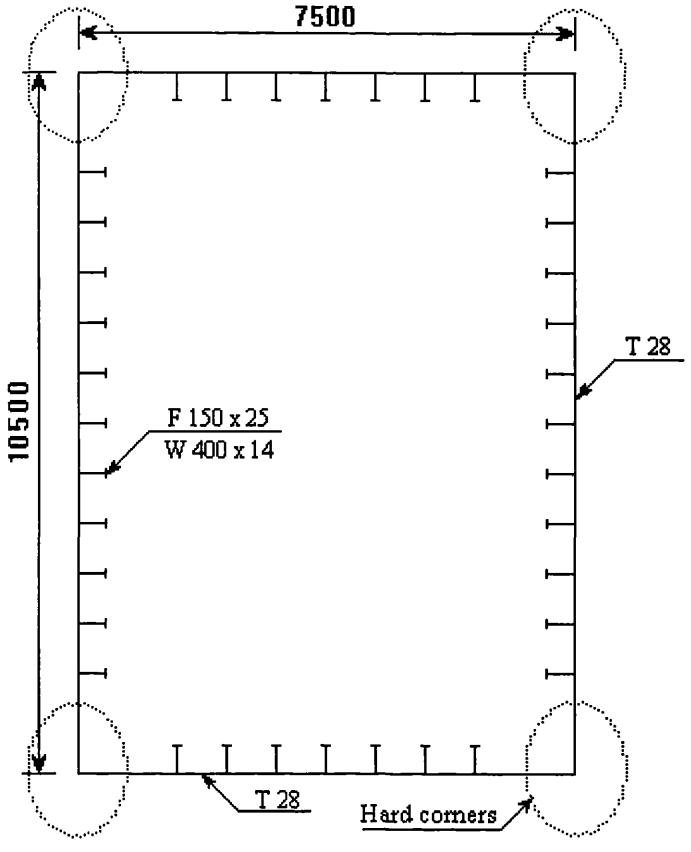

Fig. 4.1. Cross-section of the ISSC TLP Pontoons

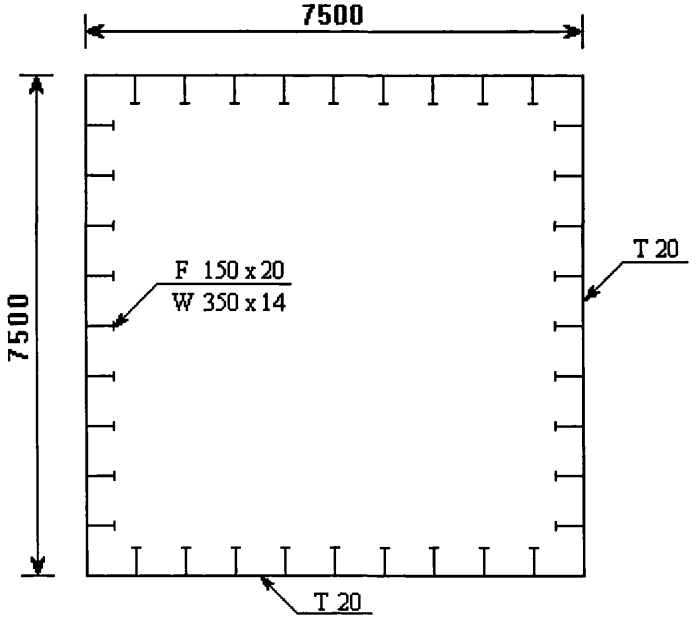

Fig. 4.2. Cross-section of the Deck Girders

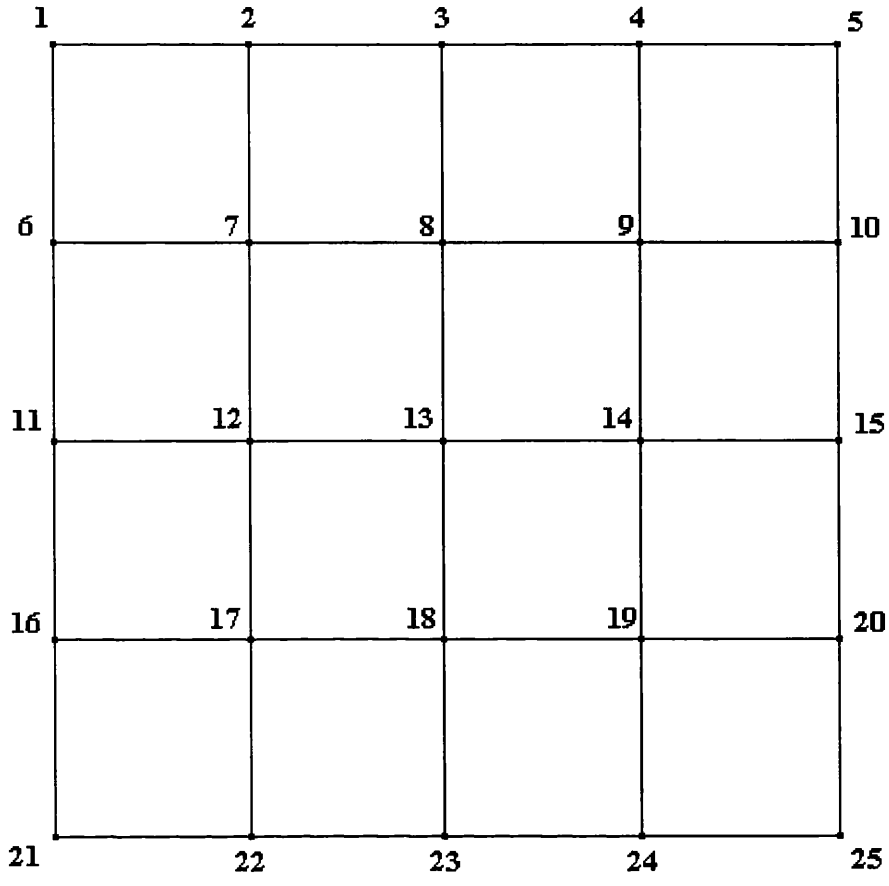

Fig. 4.3. Nodes on the Deck Grillage

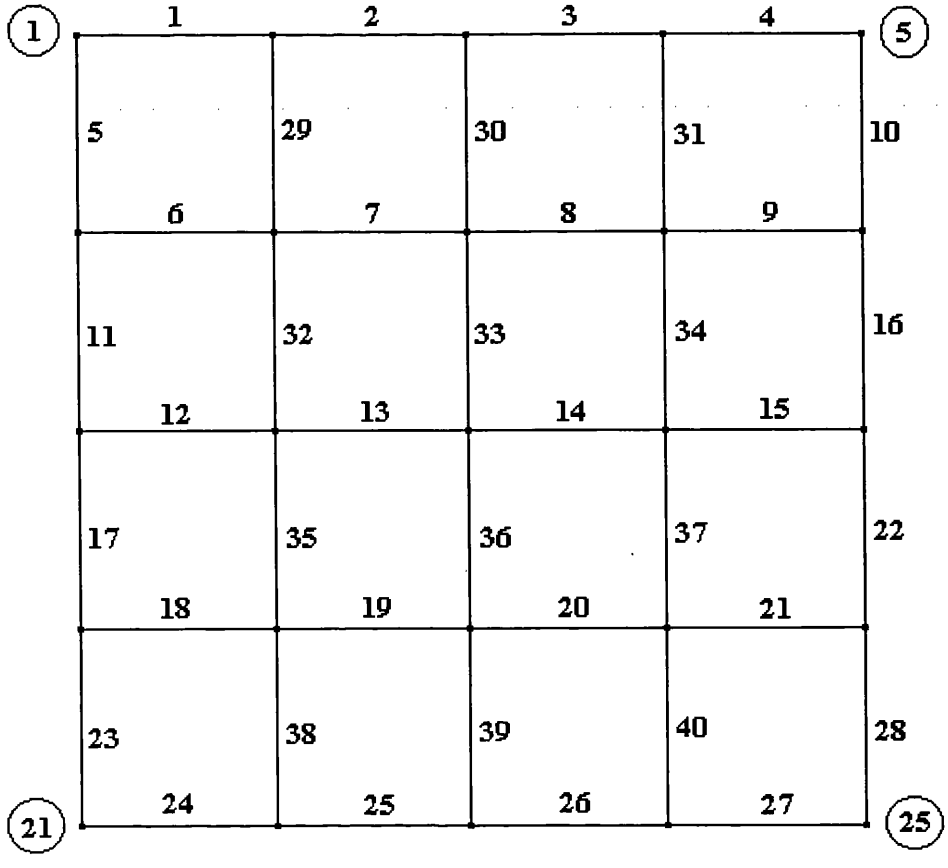

Fig. 4.4. Elements on the Deck Grillage

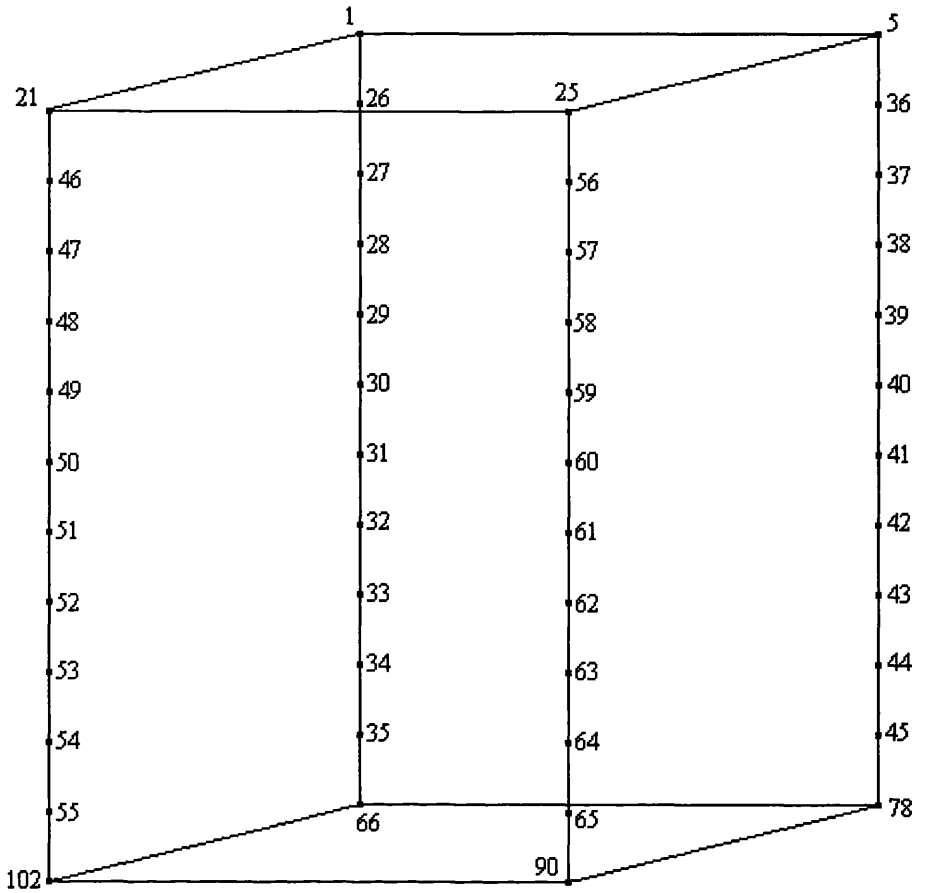

Fig. 4.5. Nodes on the TLP Columns

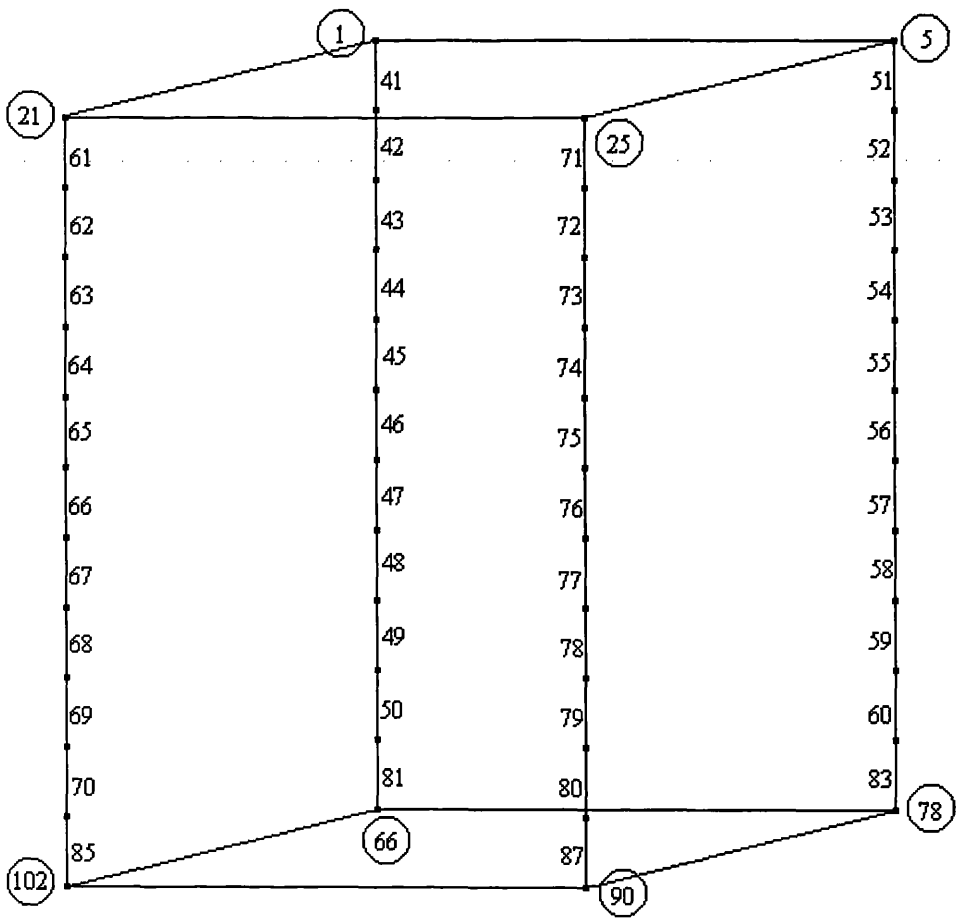

Fig. 4.6. Elements on the TLP Columns

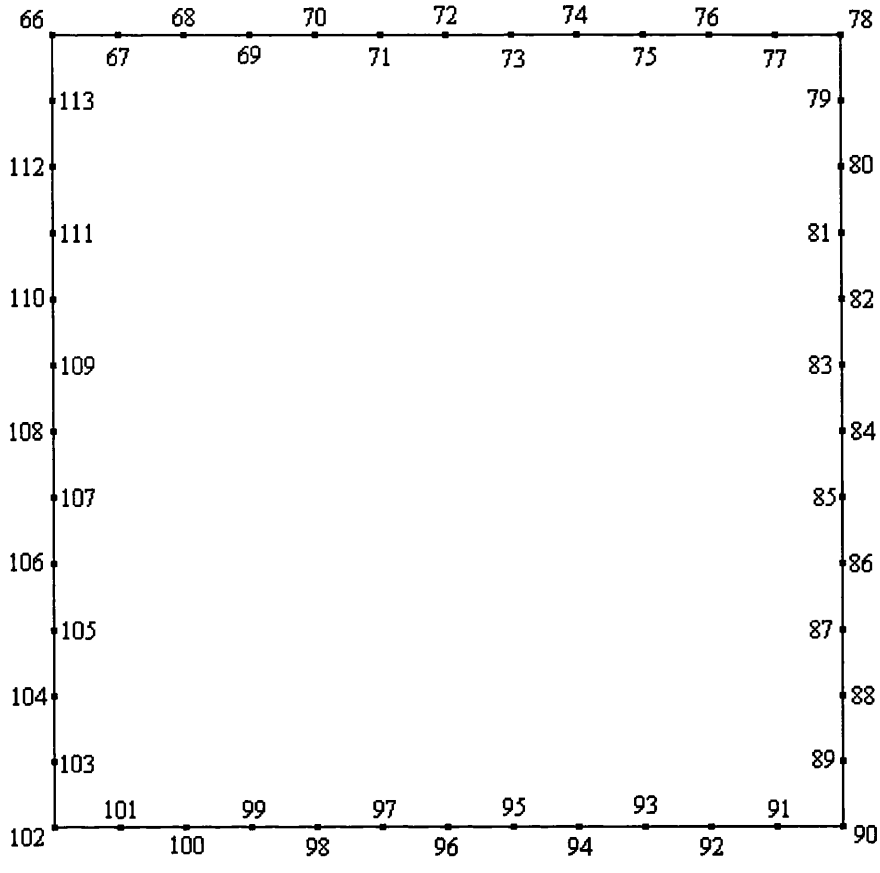

Fig. 4.7. Nodes at the Pontoon Level

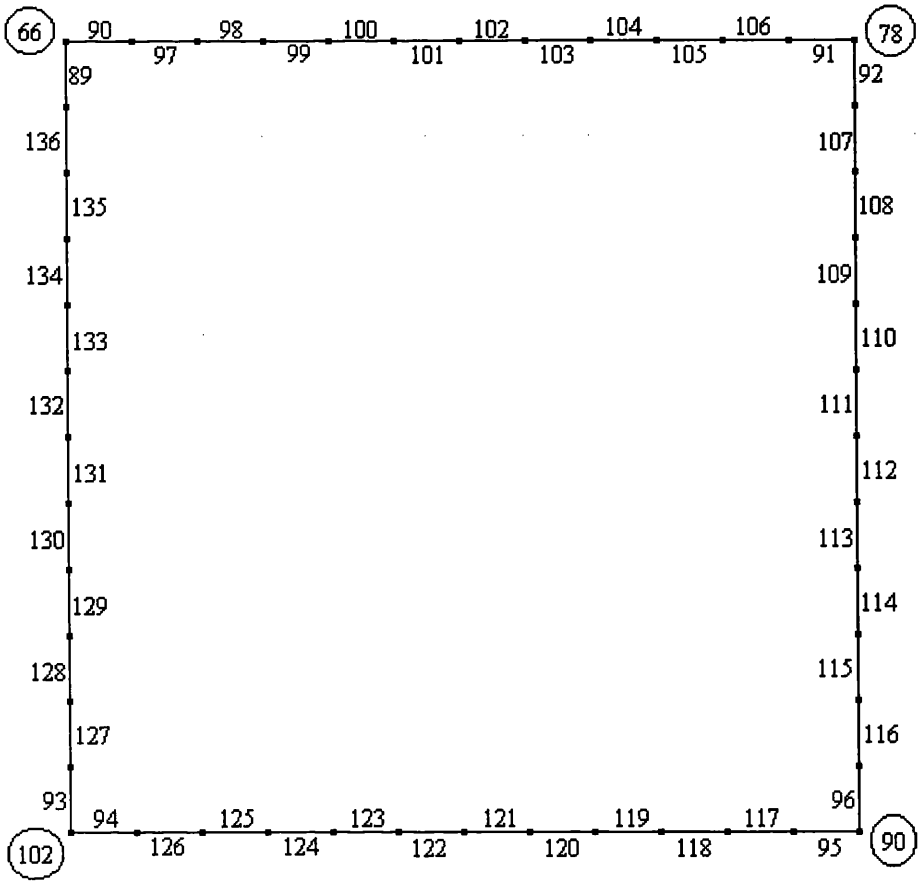

Fig. 4.8. Pontoon and Pontoon Joint Elements

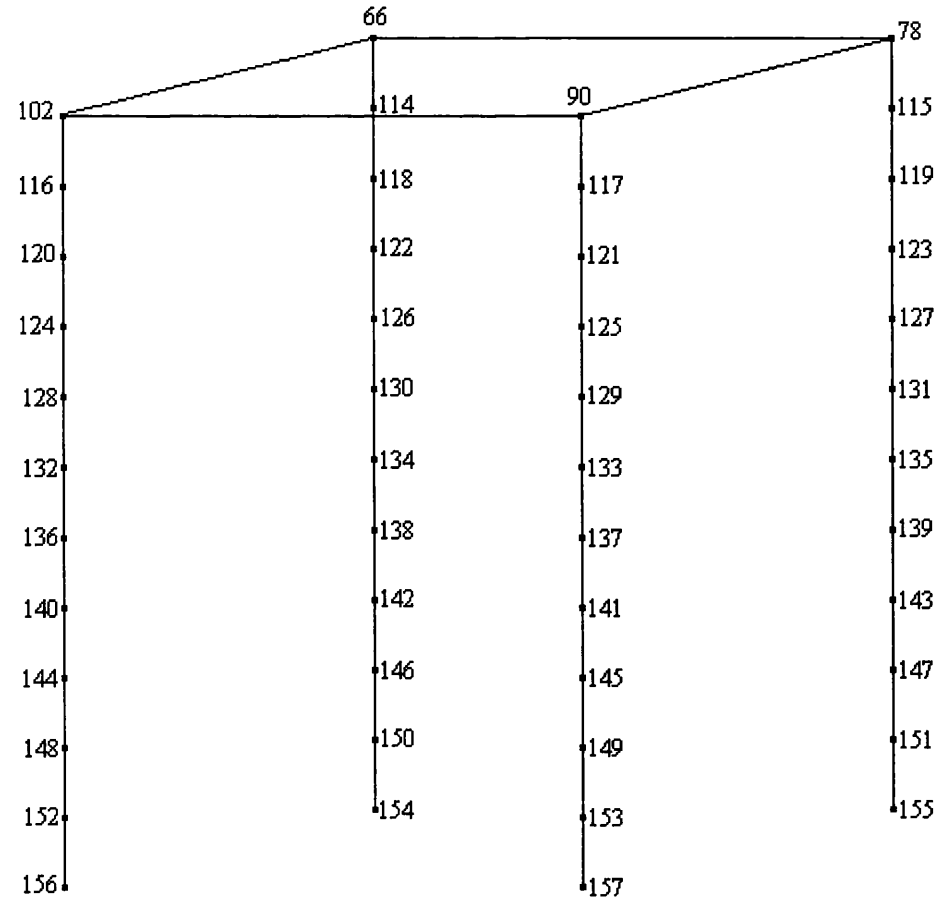

Fig. 4.9. Nodes along the Tethers

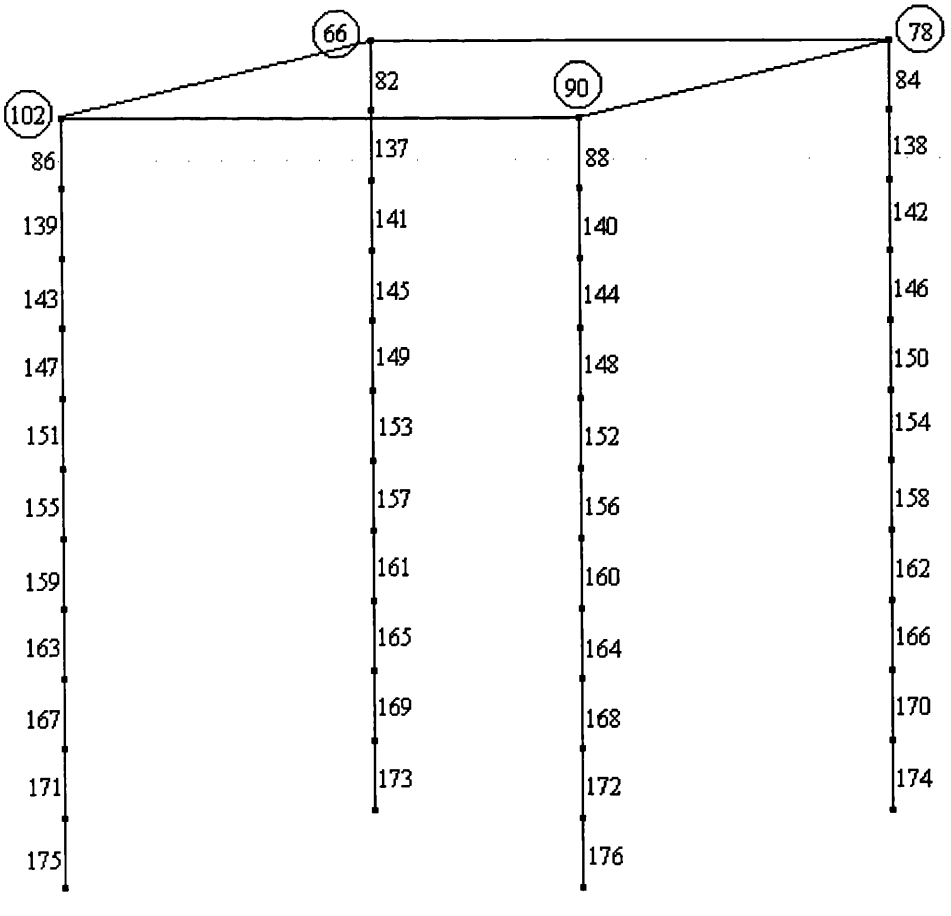

Fig. 4.10. Elements along the Tethers

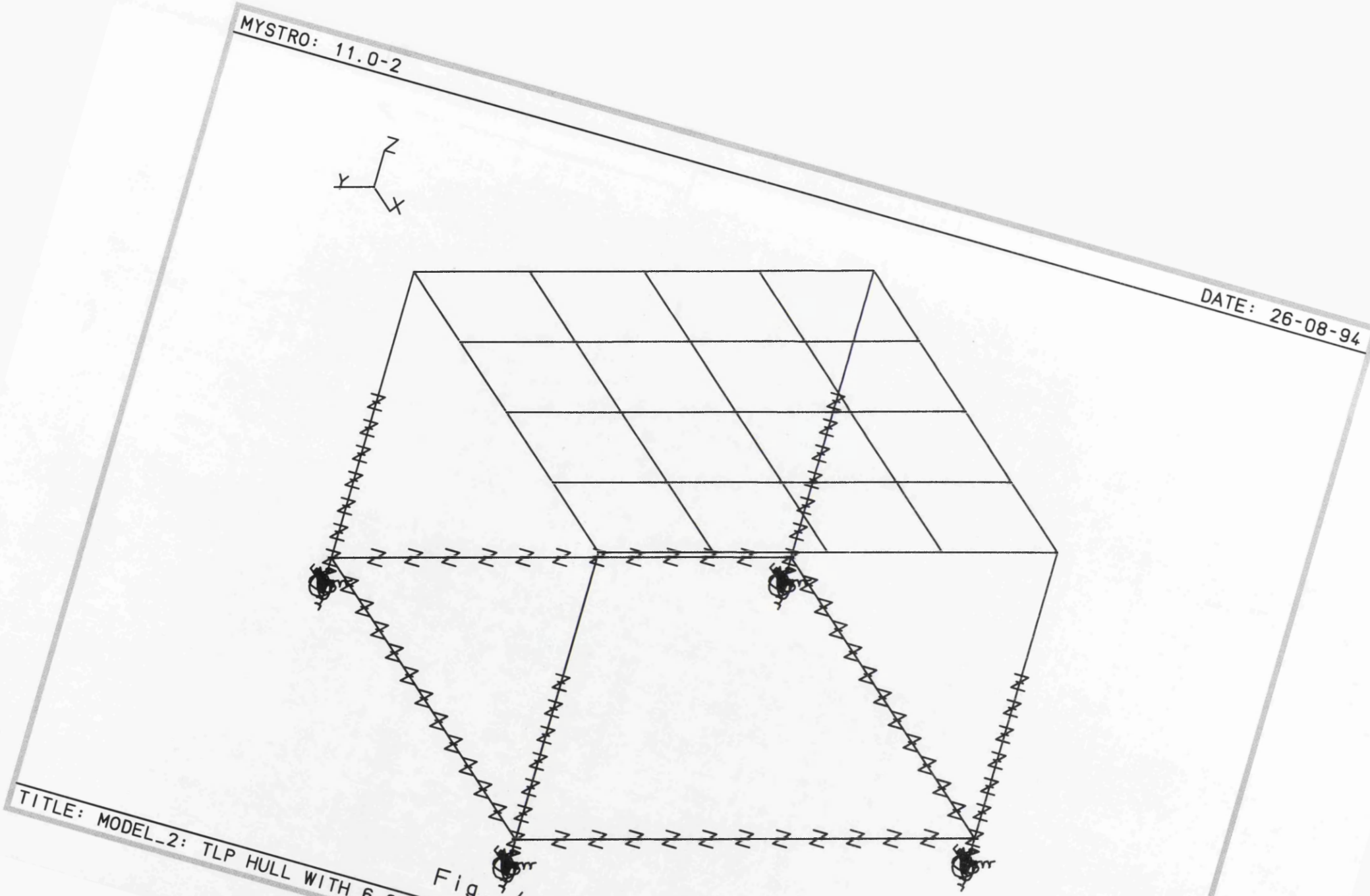

Fig. 4.12. Model_2 for LUSAS

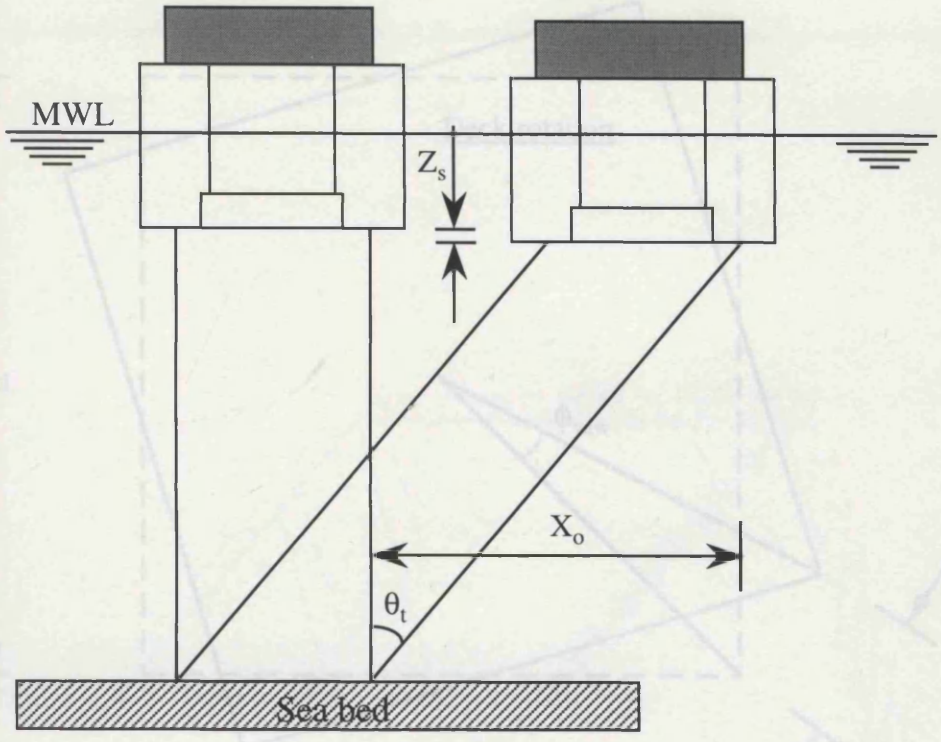

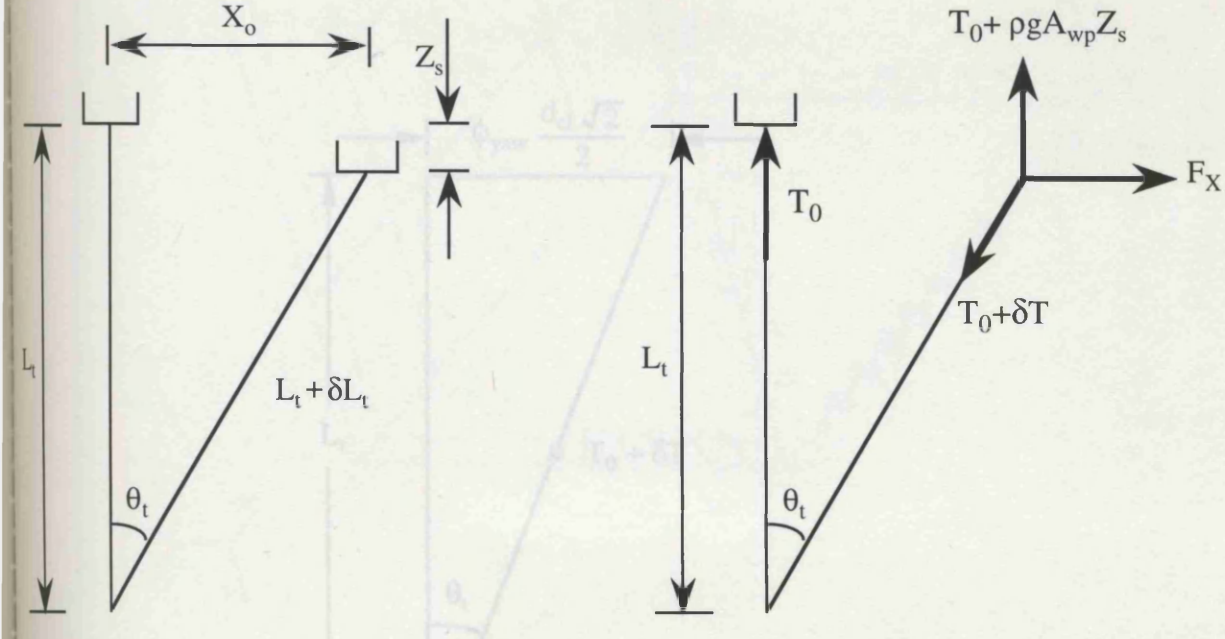

Fig. 4.13. Offset and Set-down of a TLP

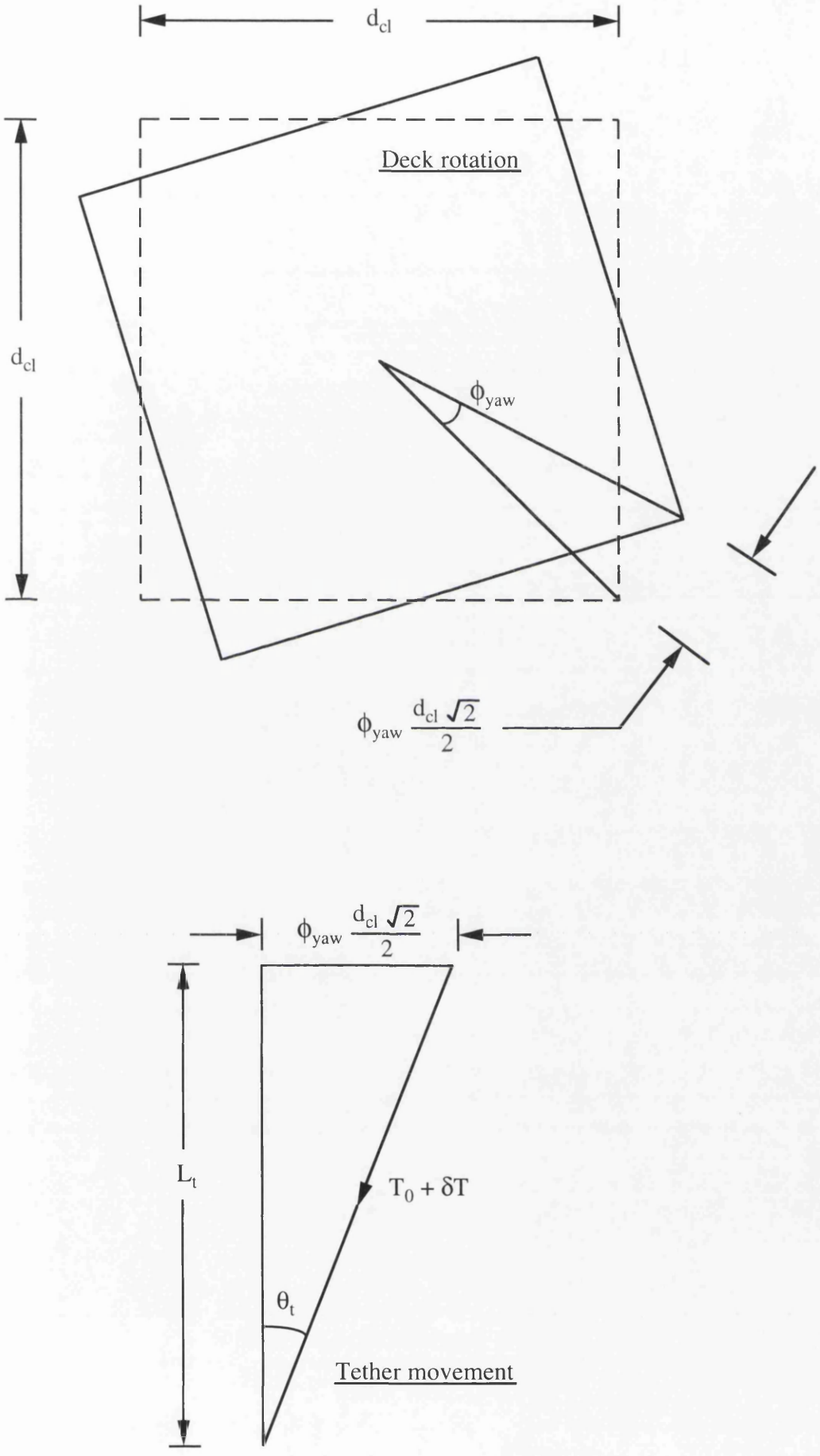

Fig. 4.14. Horizontal Motion from Yaw Rotation

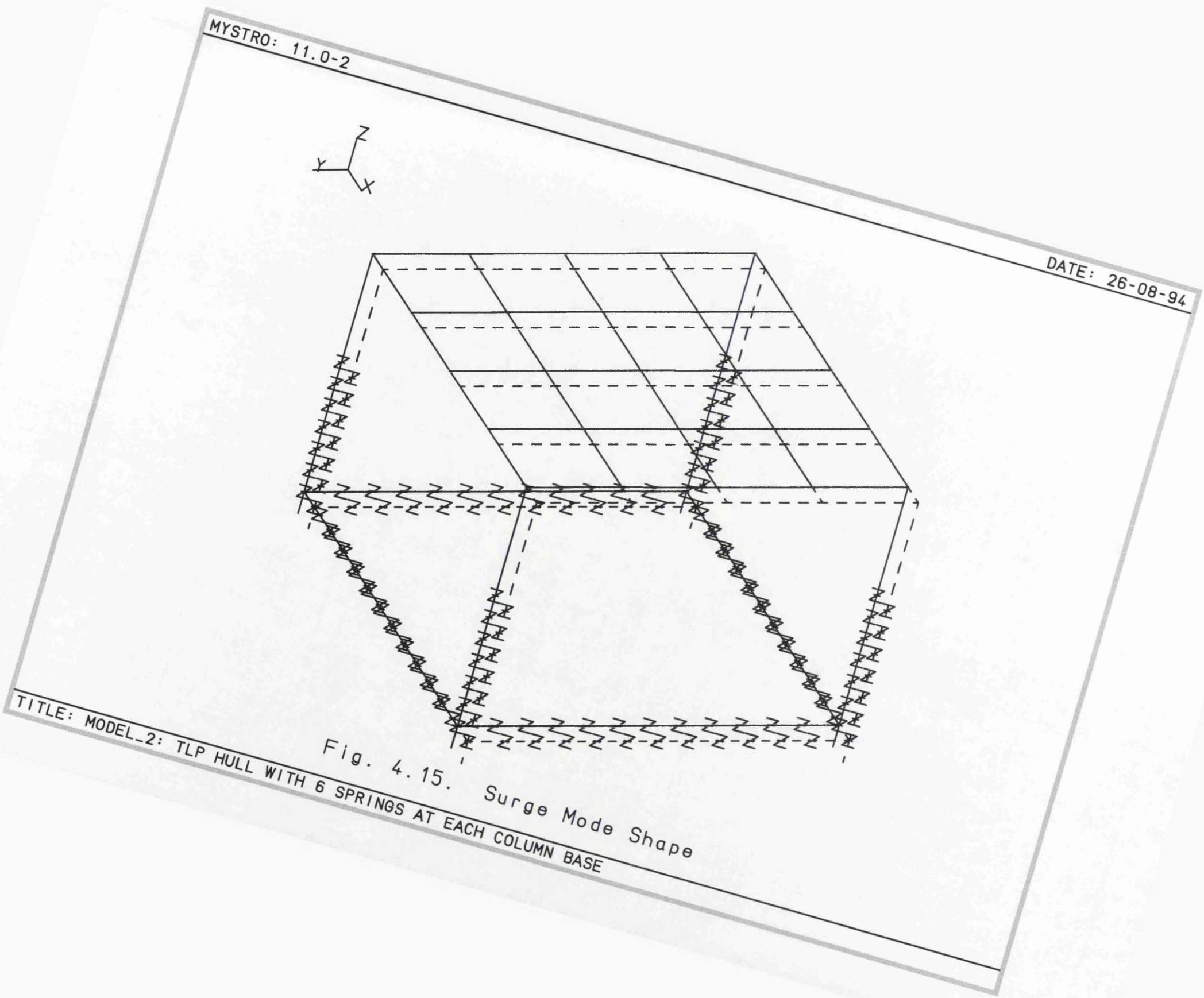

Fig. 4.15. Surge Mode Shape

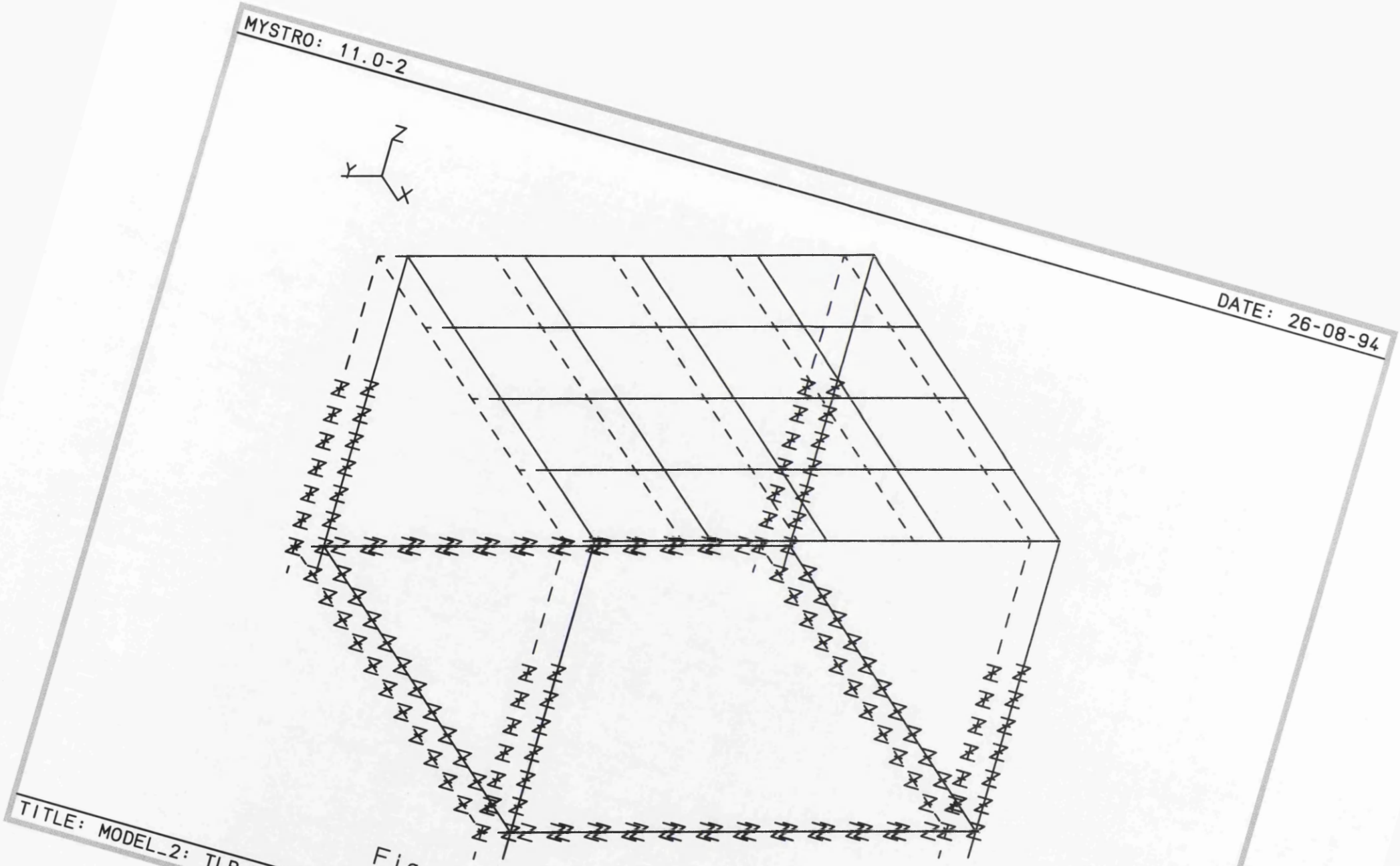

Fig. 4.16. Sway Mode Shape

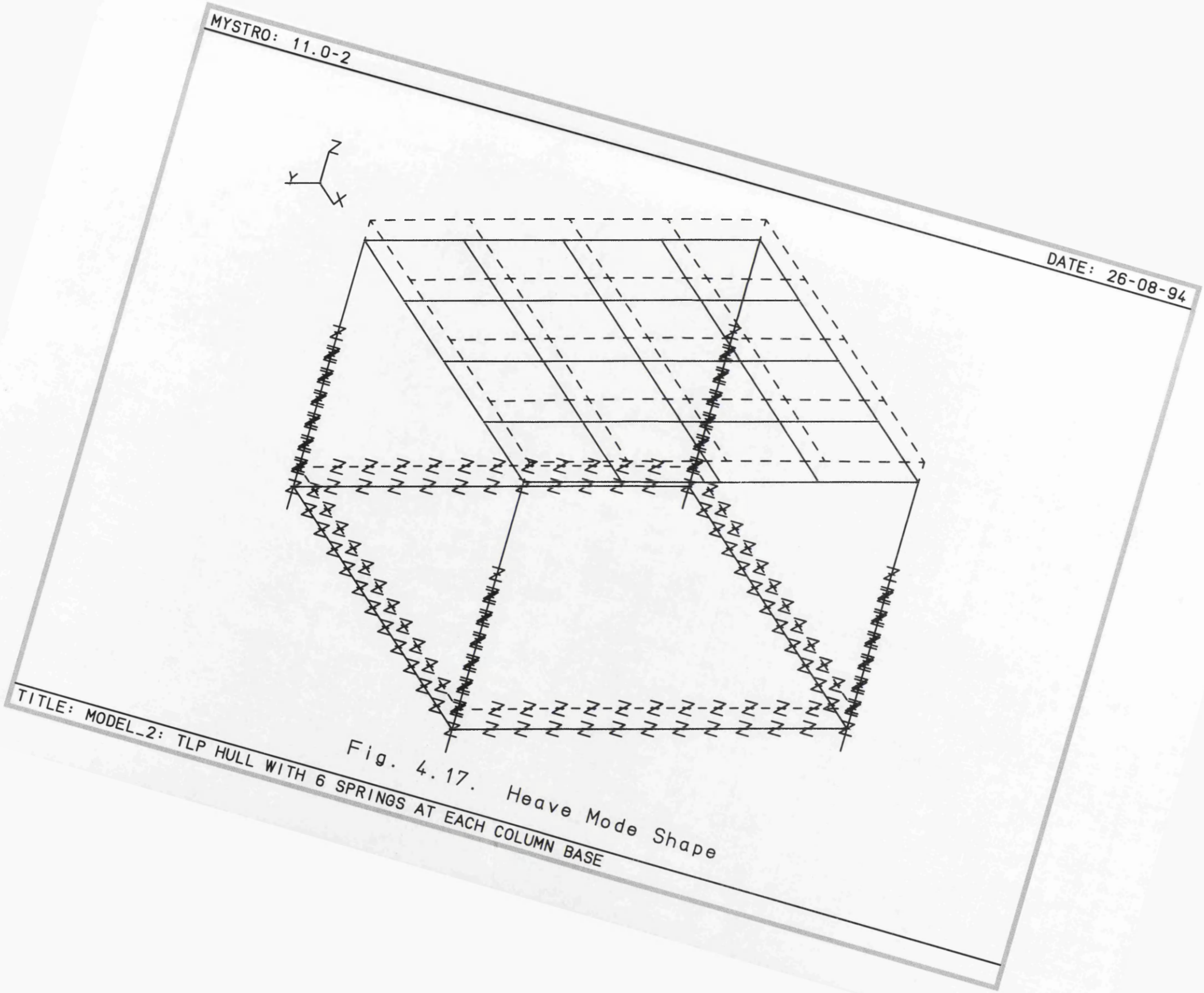

Fig. 4.17. Heave Mode Shape

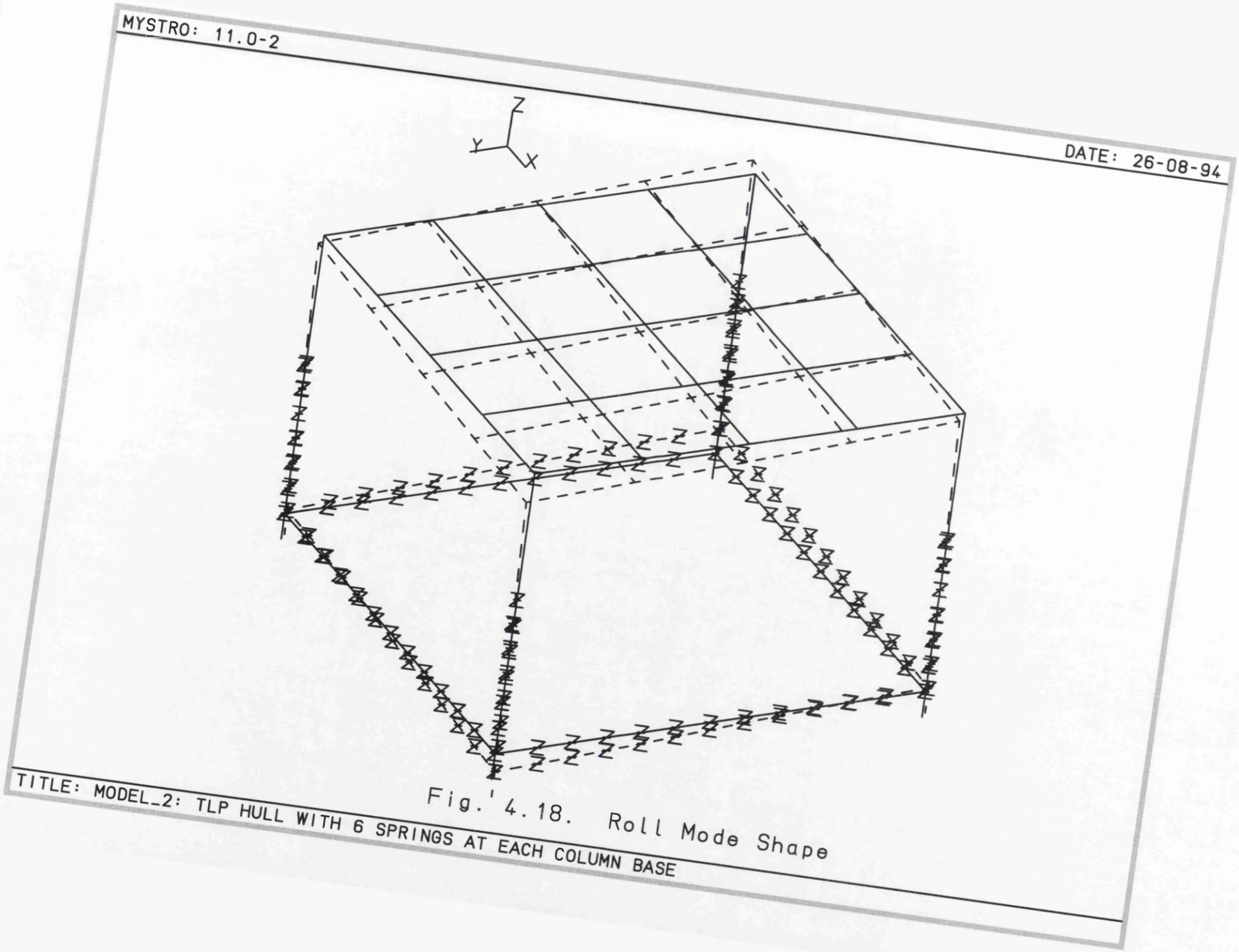

Fig. 4.18. Roll Mode Shape

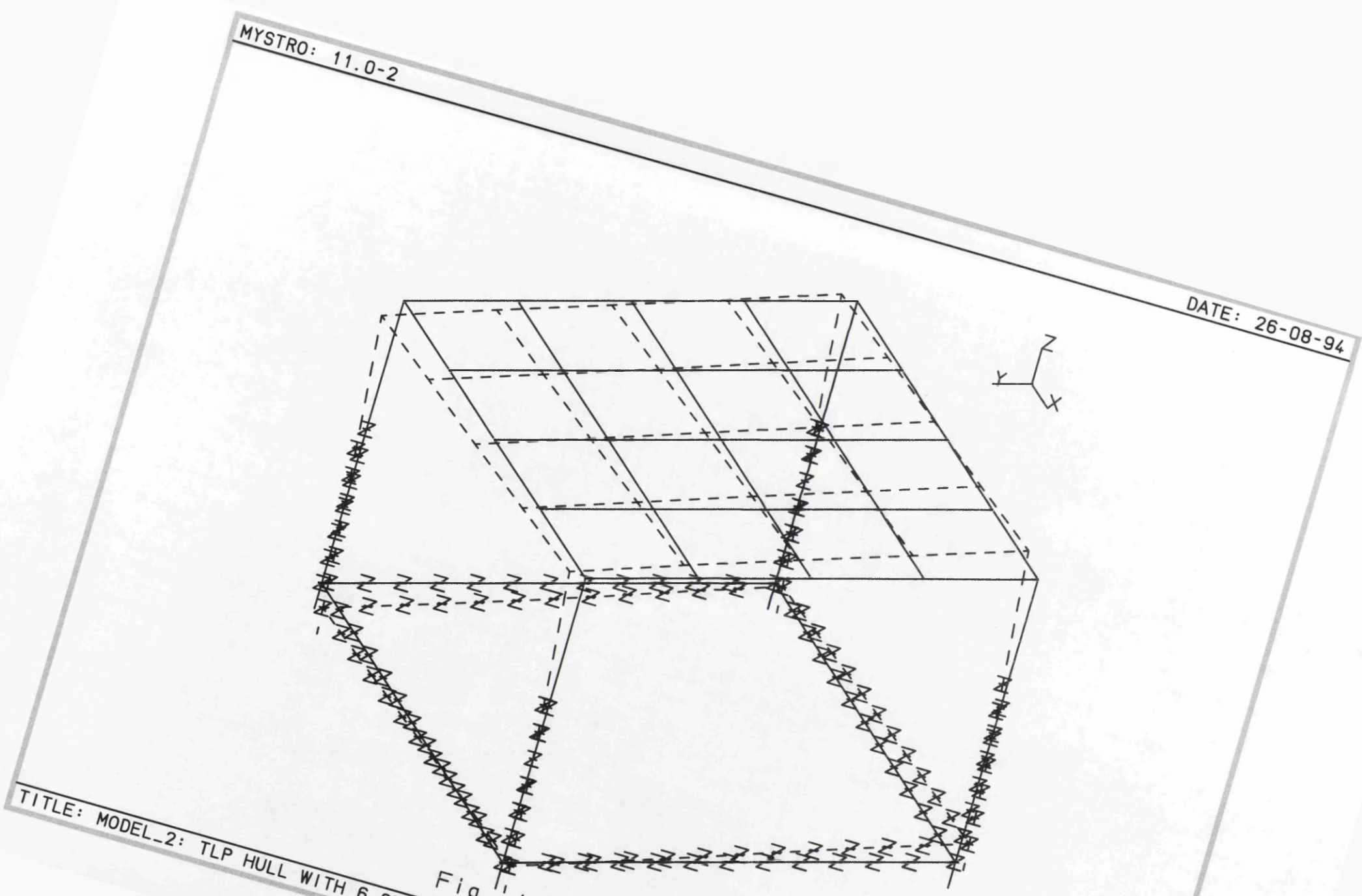

Fig. 4.19. Pitch Mode Shape

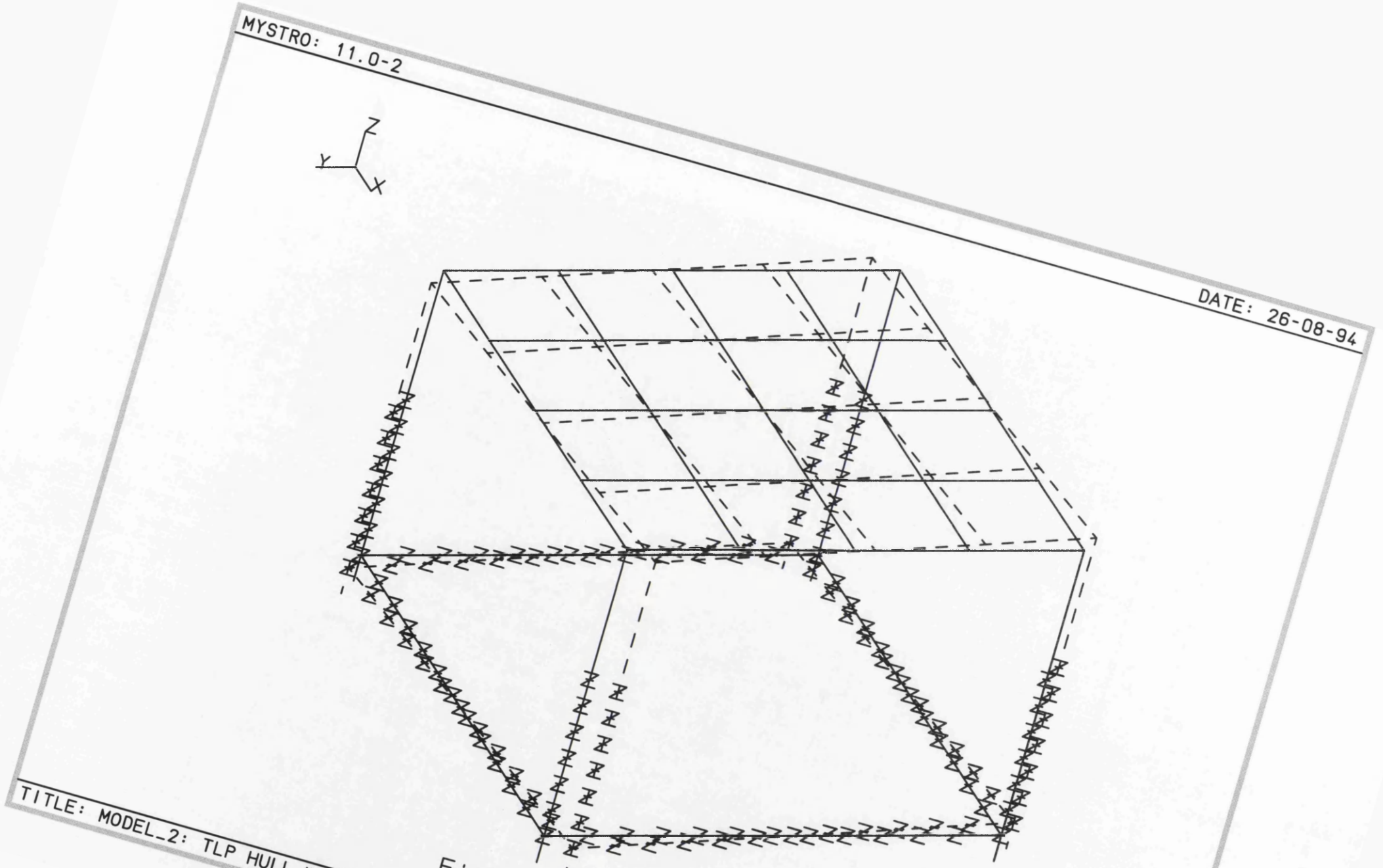

Fig. 4.20. Yaw Mode Shape

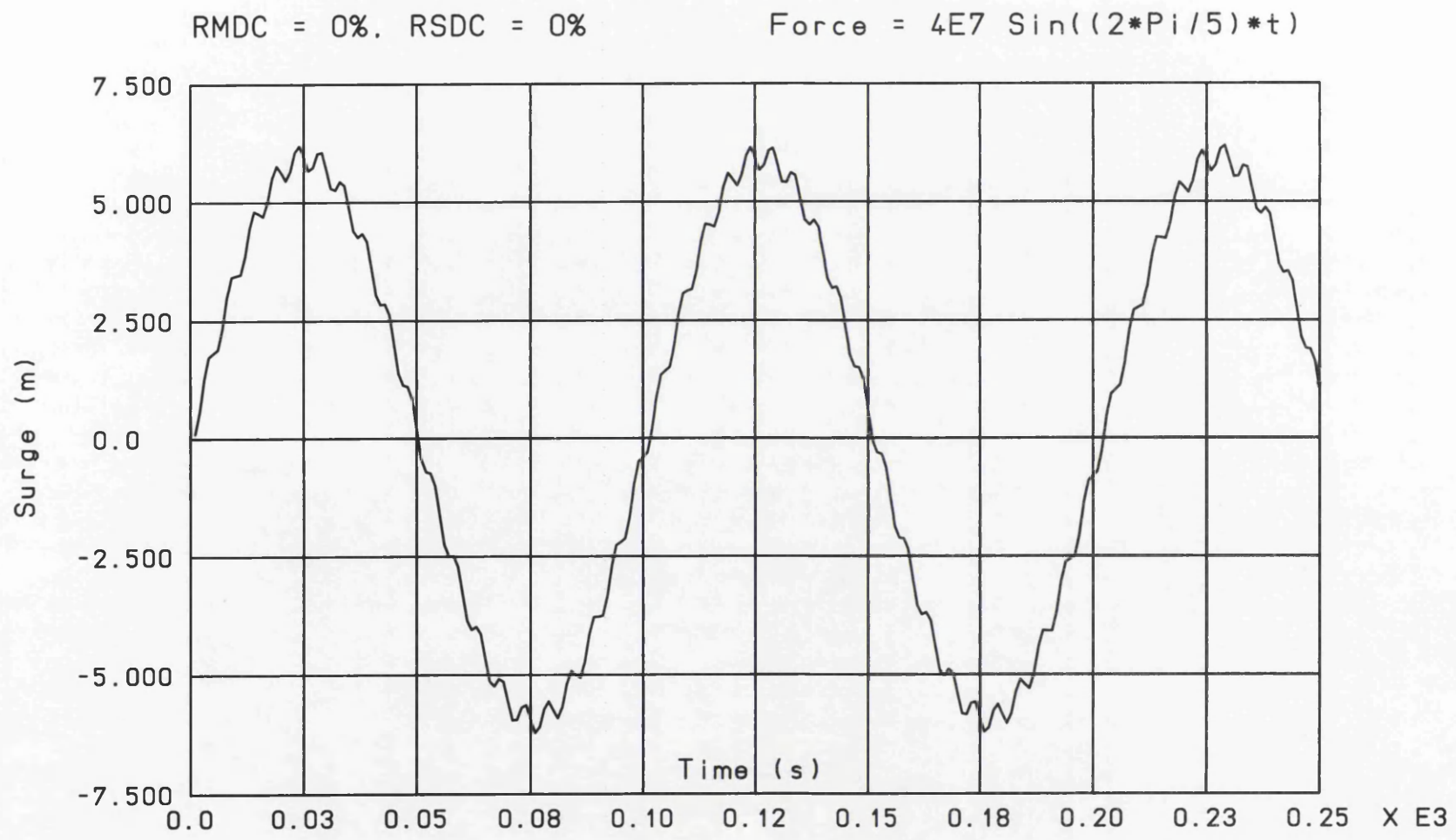

Fig. 4.23. Surge Response under Sinusoidal Load of 5.0 s Period

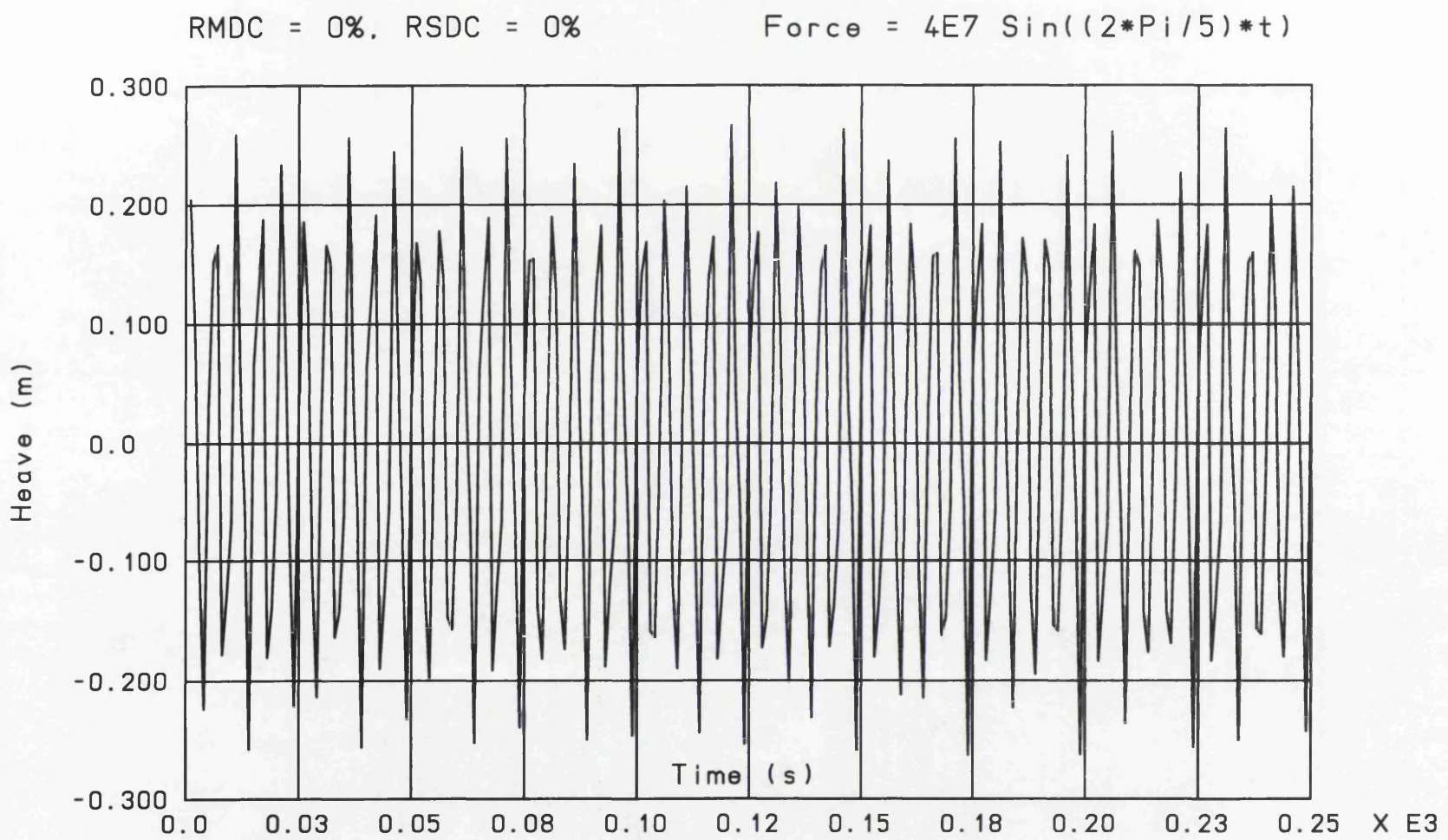

Fig. 4.24. Heave Response under Sinusoidal Load of 5.0 s Period

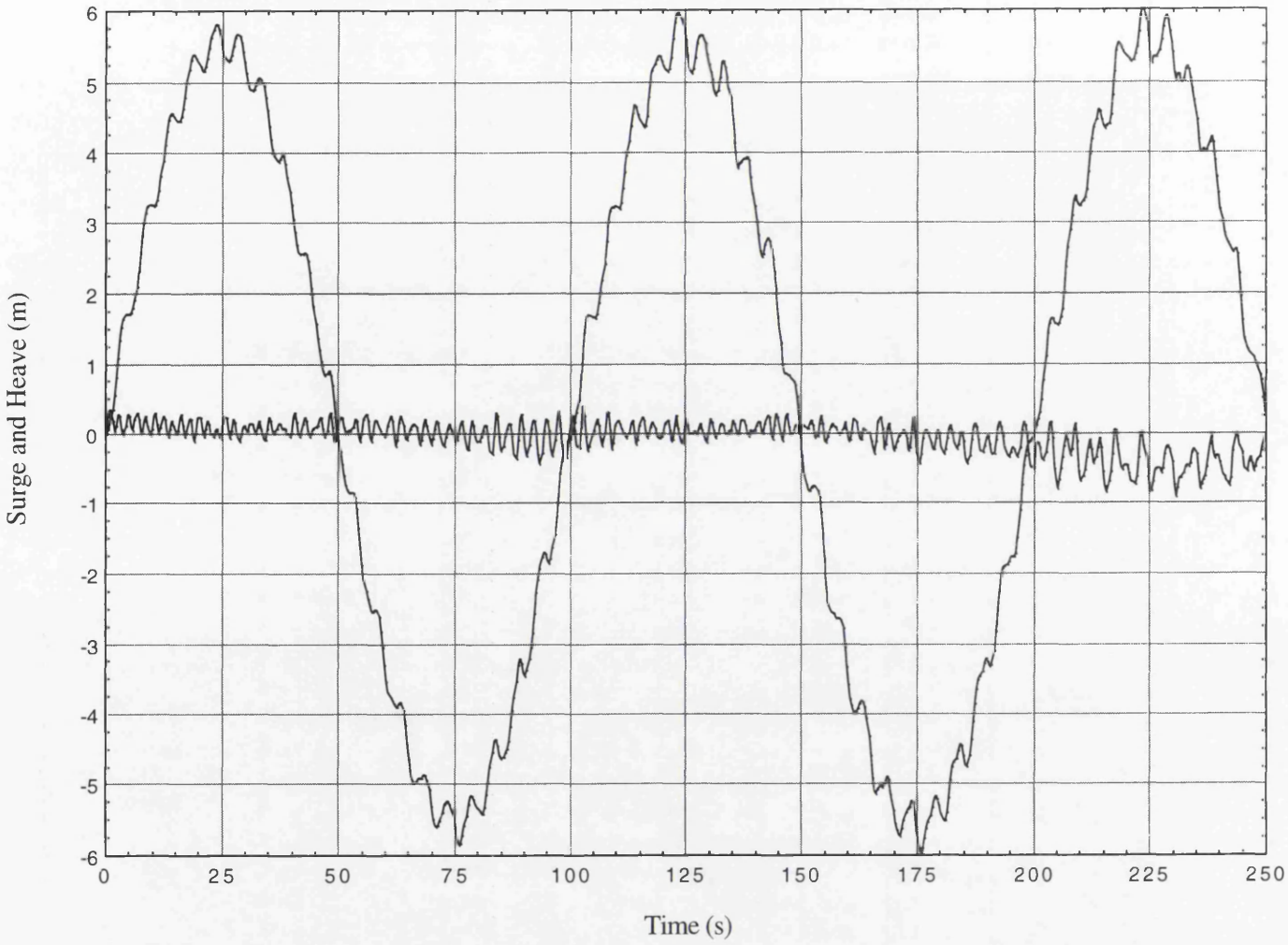

Fig. 4.25. Model_3 under Sinusoidal Load of 5 s Period

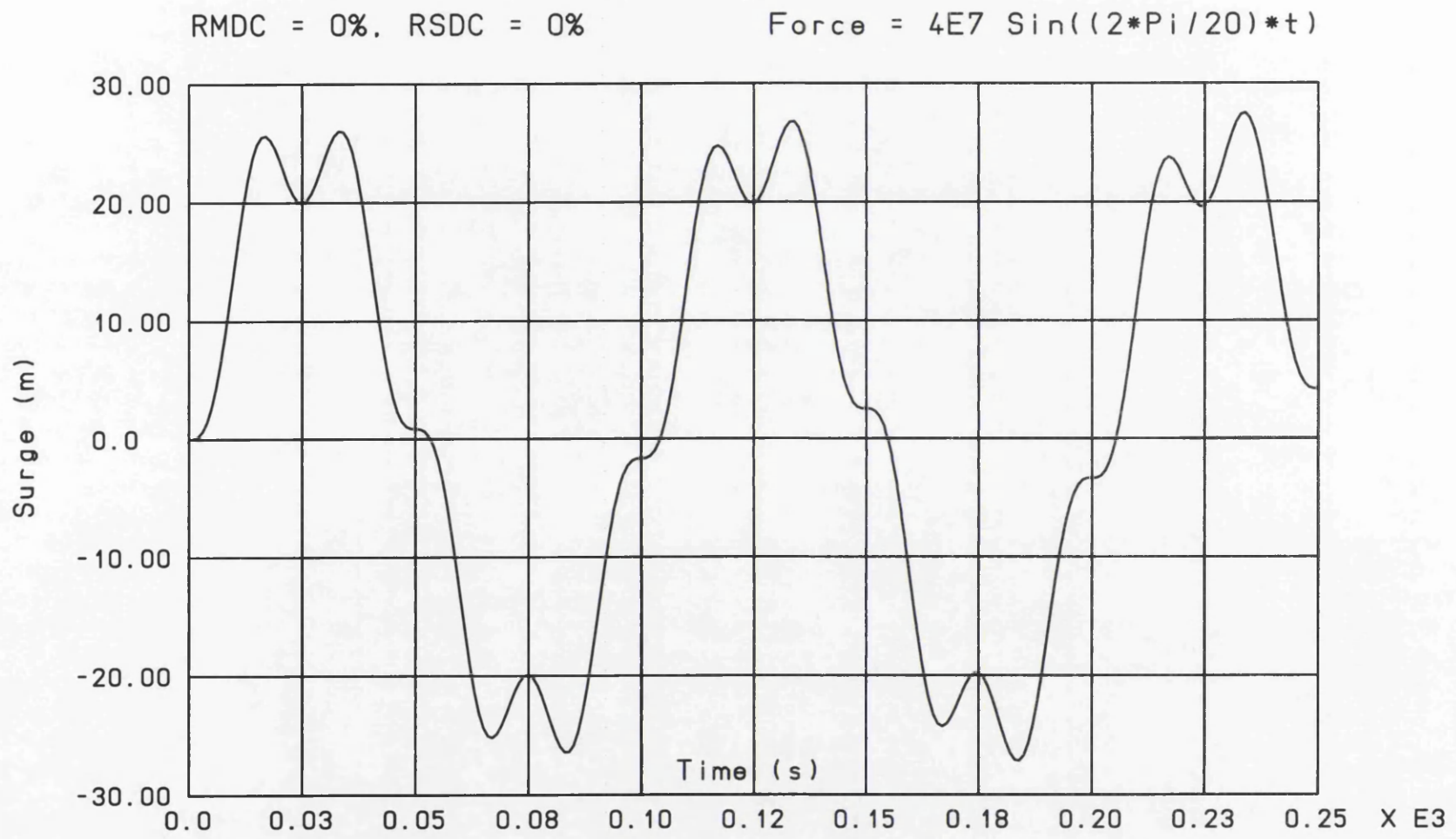

Fig. 4.26. Surge Response under Sinusoidal Load of 20.0 s Period

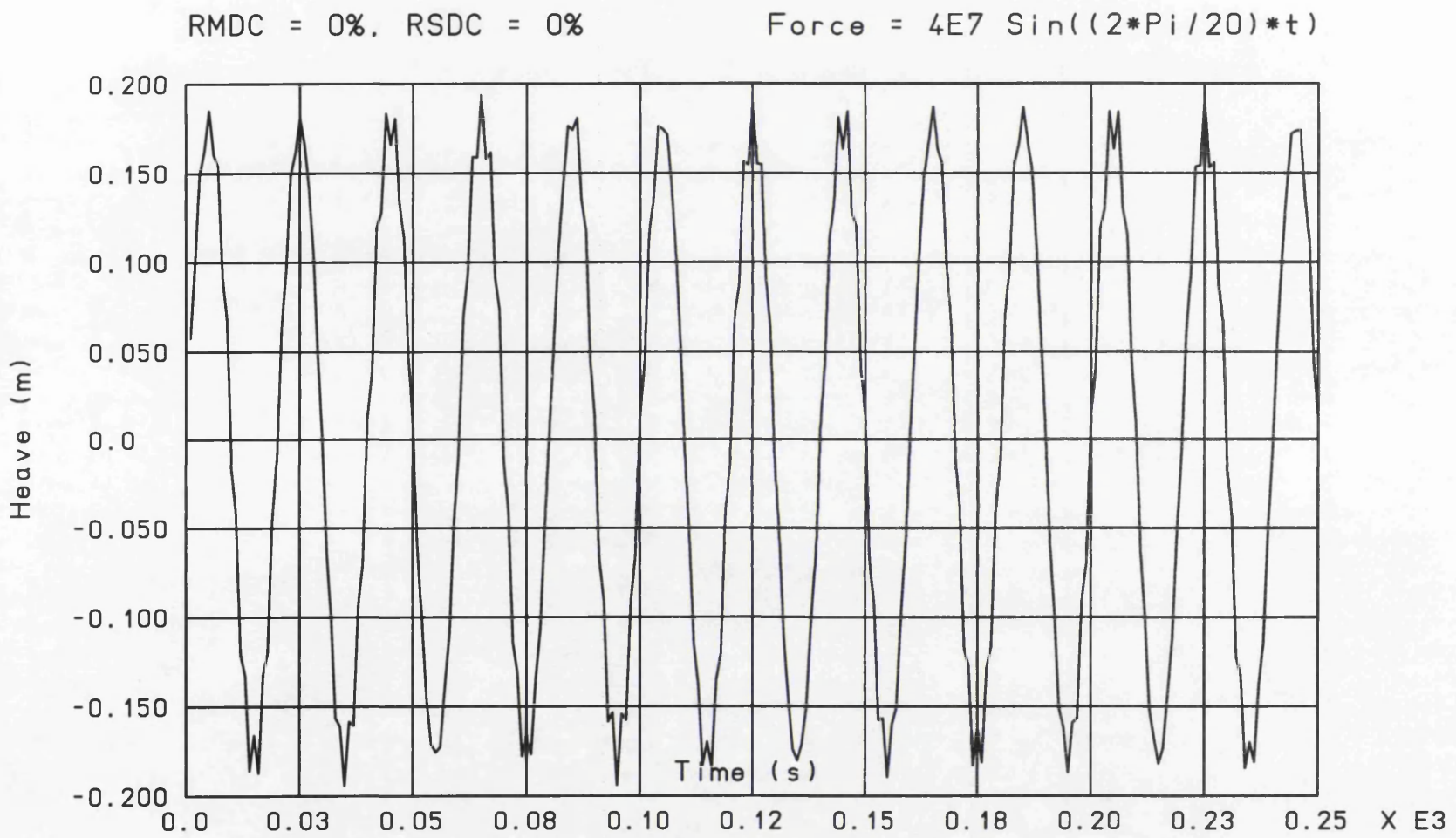

Fig. 4.27. Heave Response under Sinusoidal Load of 20.0 s Period

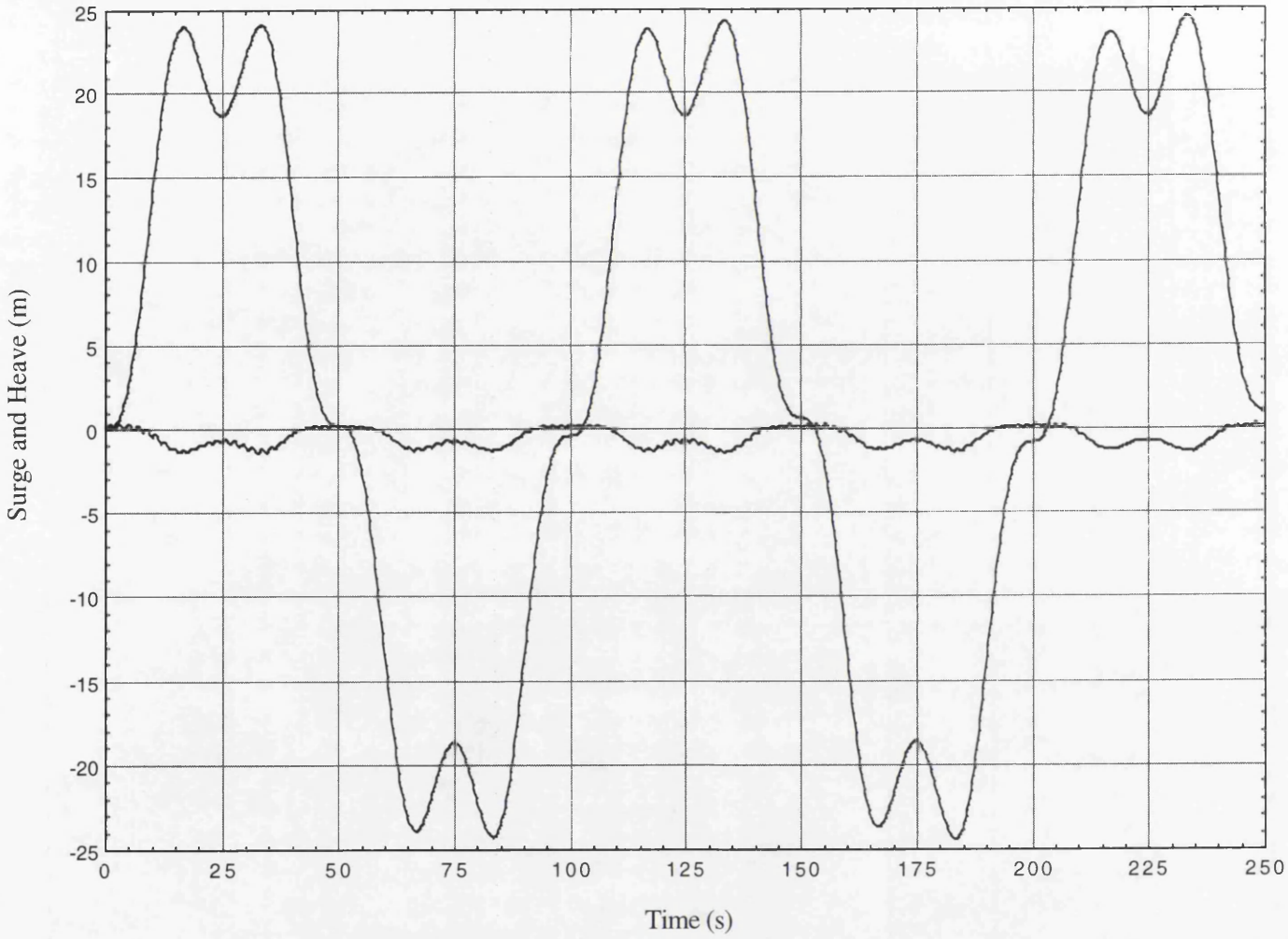

Fig. 4.28. Model_3 under Sinusoidal Load of 20 s Period

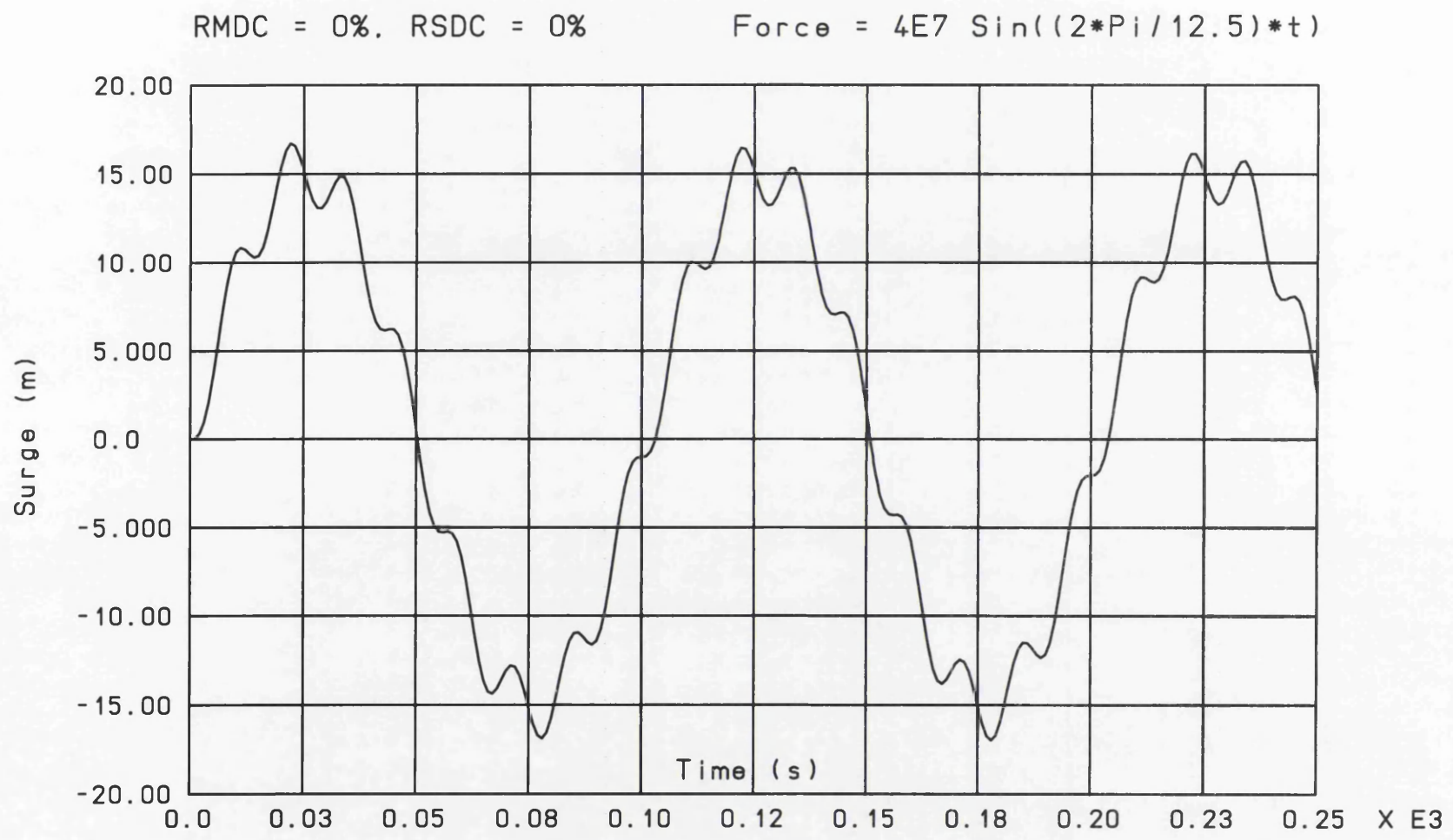

Fig. 4.29. Surge Response under Sinusoidal Load of 12.5 s Period

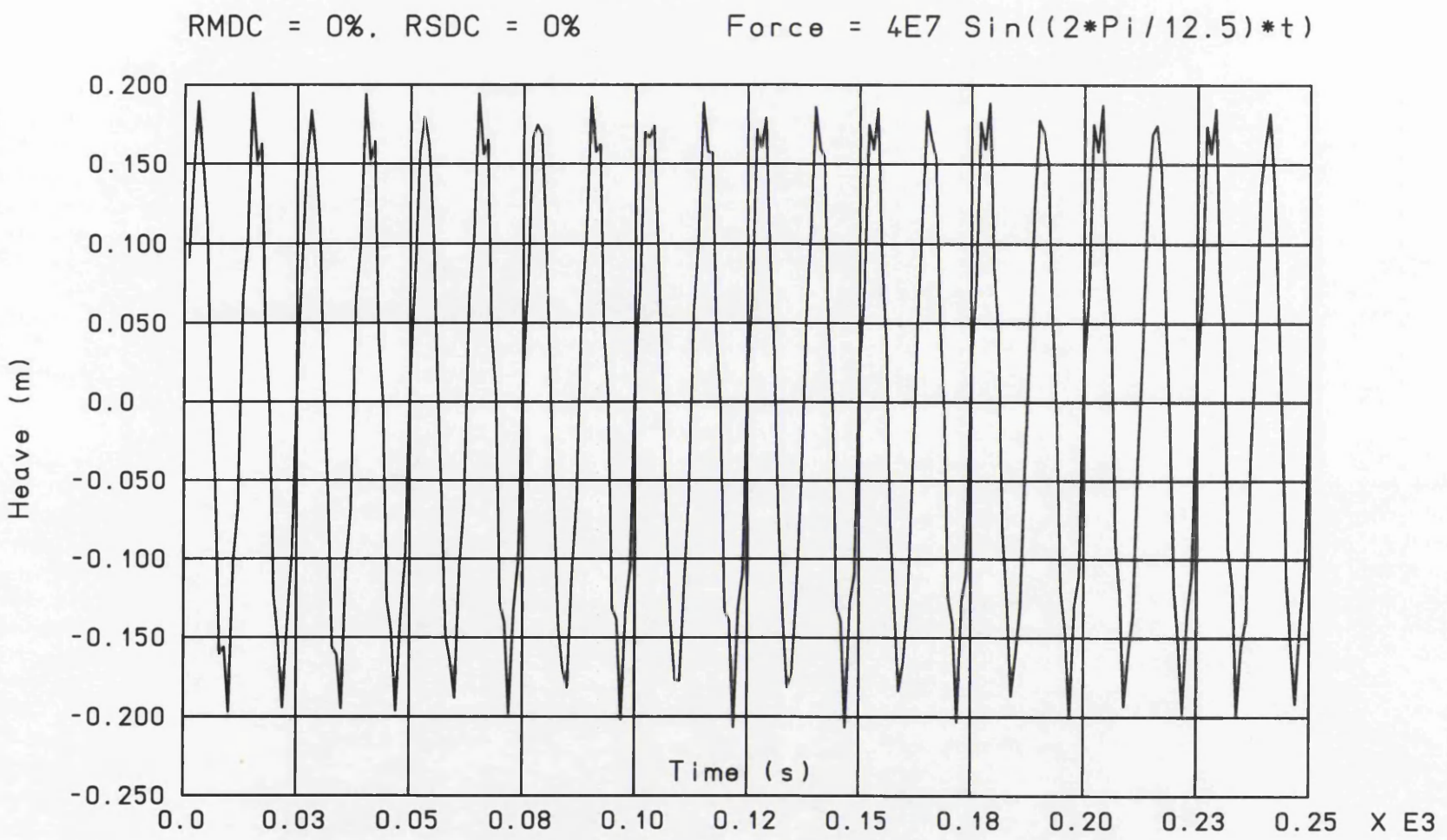

Fig. 4.30. Heave Response under Sinusoidal Load of 12.5 s Period

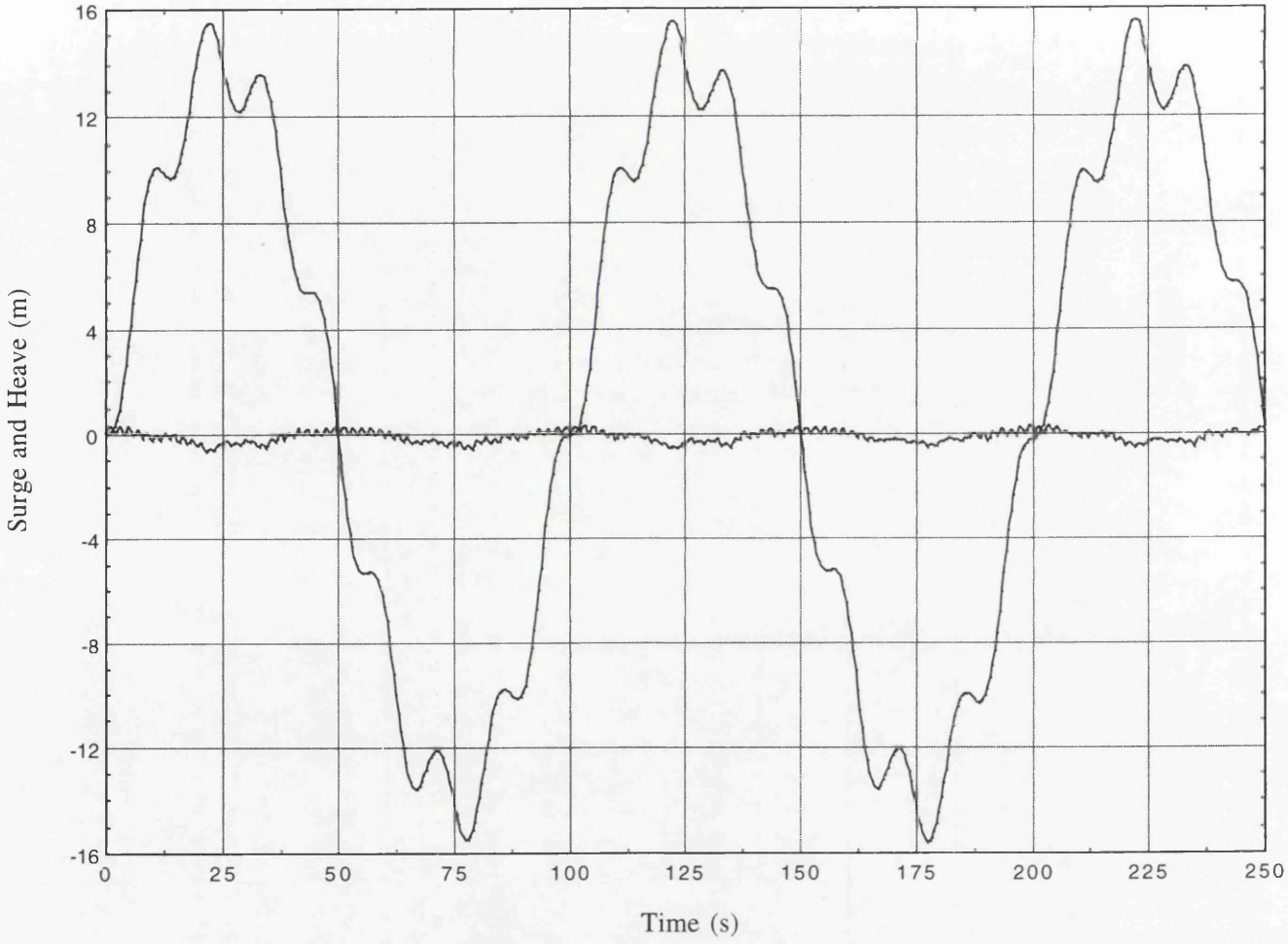

Fig. 4.31. Model_3 under Sinusoidal Load of 12.5 s Period

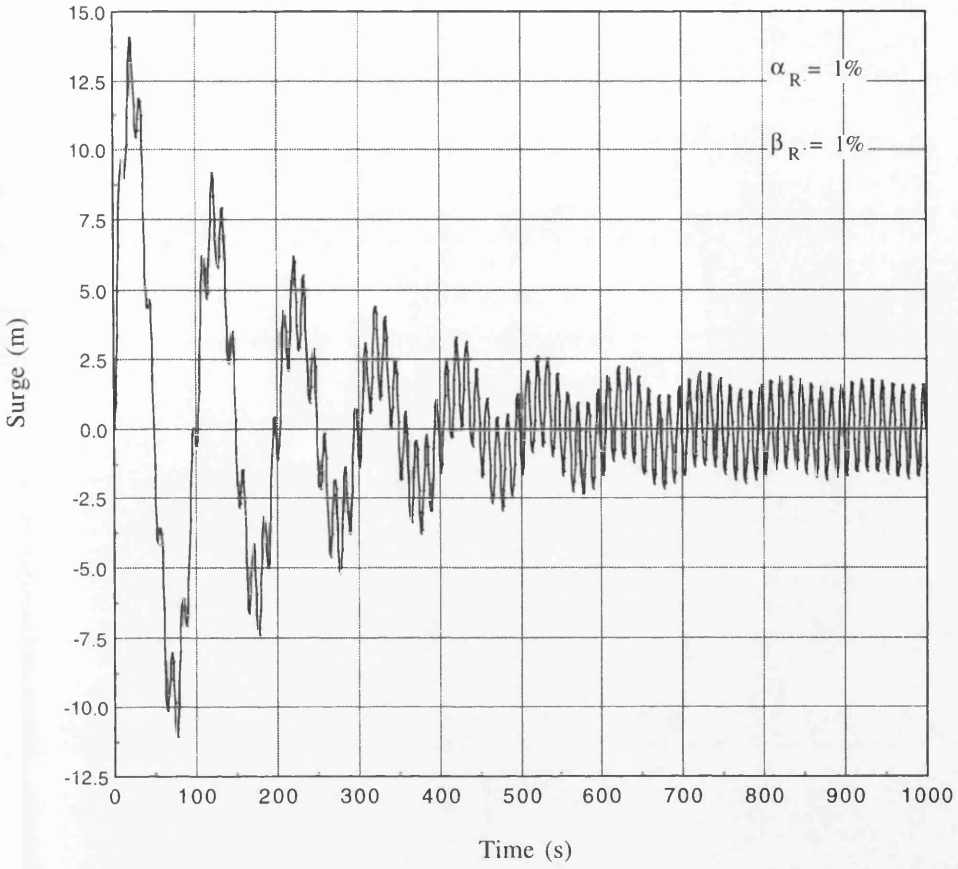

Fig. 4.32. Damped Surge Response of Model_3 under Sinusoidal Load of 12.5 s Period

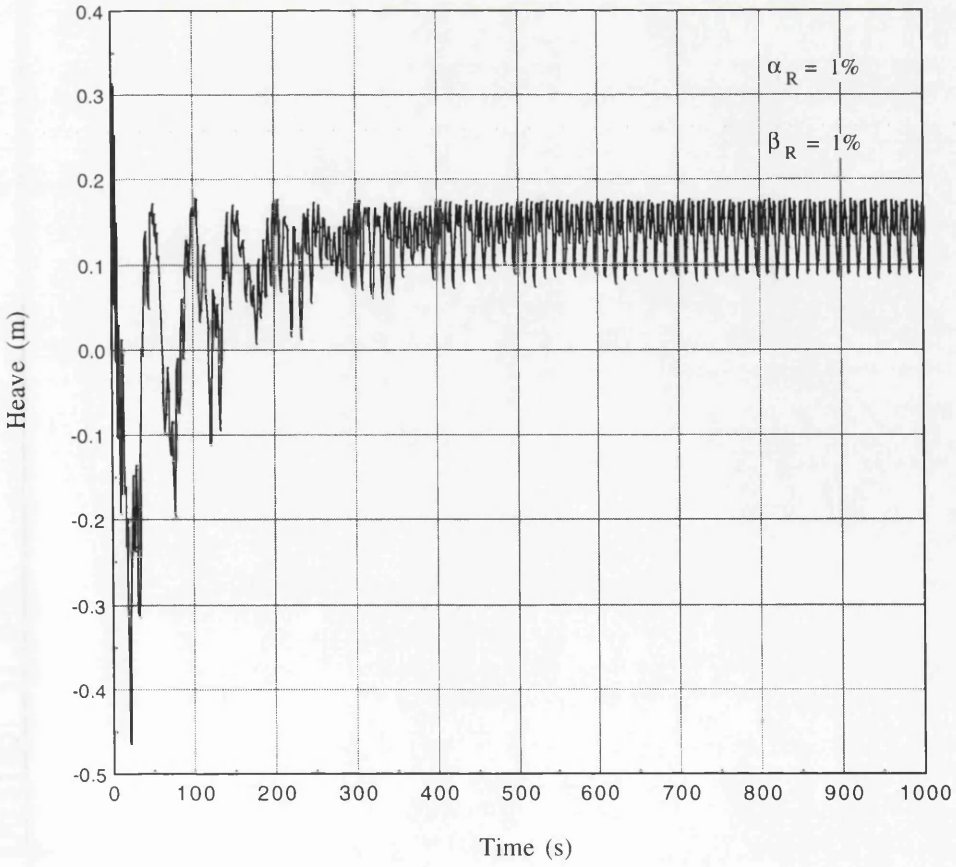

Fig. 4.33. Damped Heave Response of Model_3 under Sinusoidal Load of 12.5 s Period

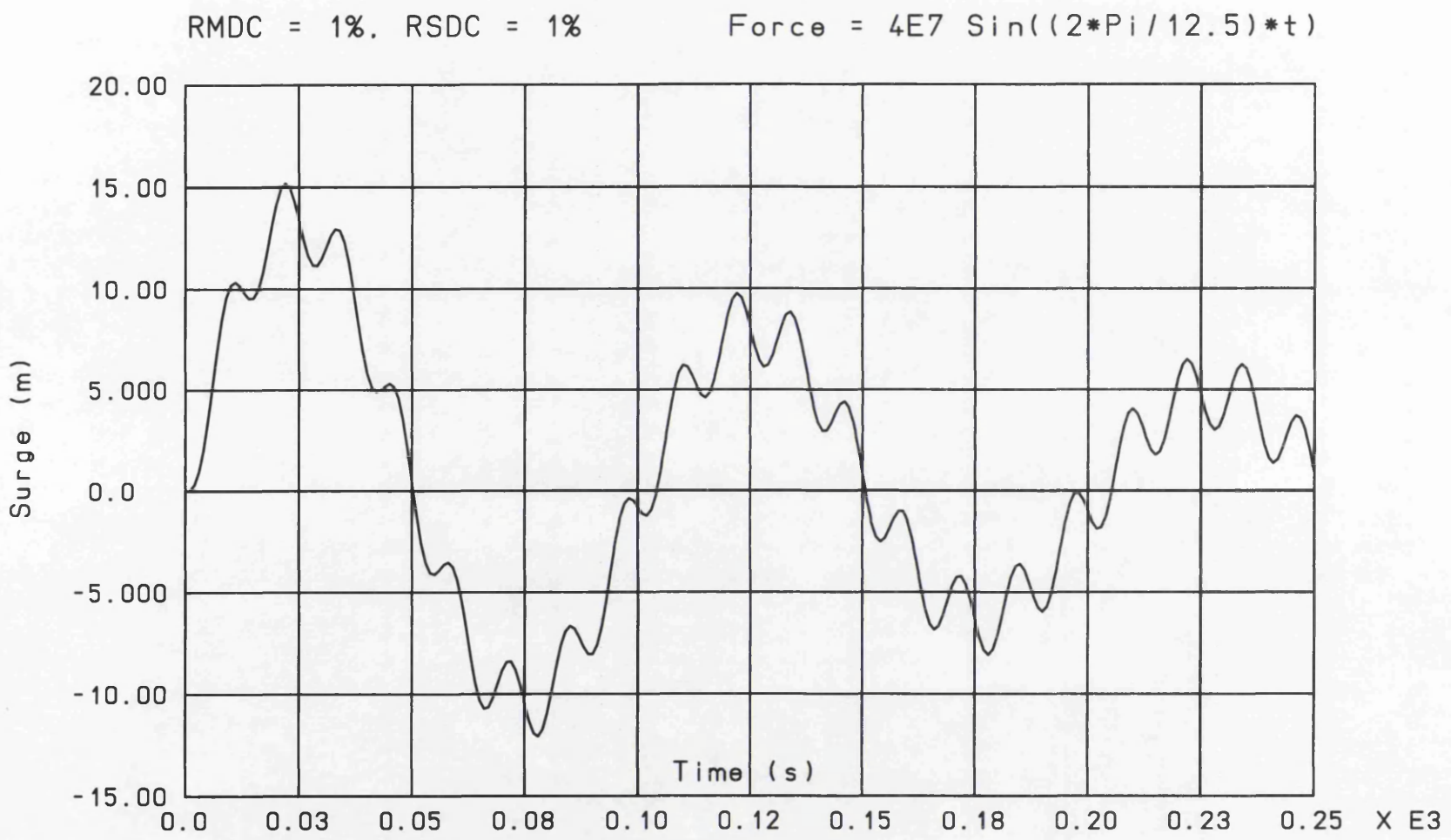

Fig. 4.34. Surge Response under Sinusoidal Load of 12.5 s Period

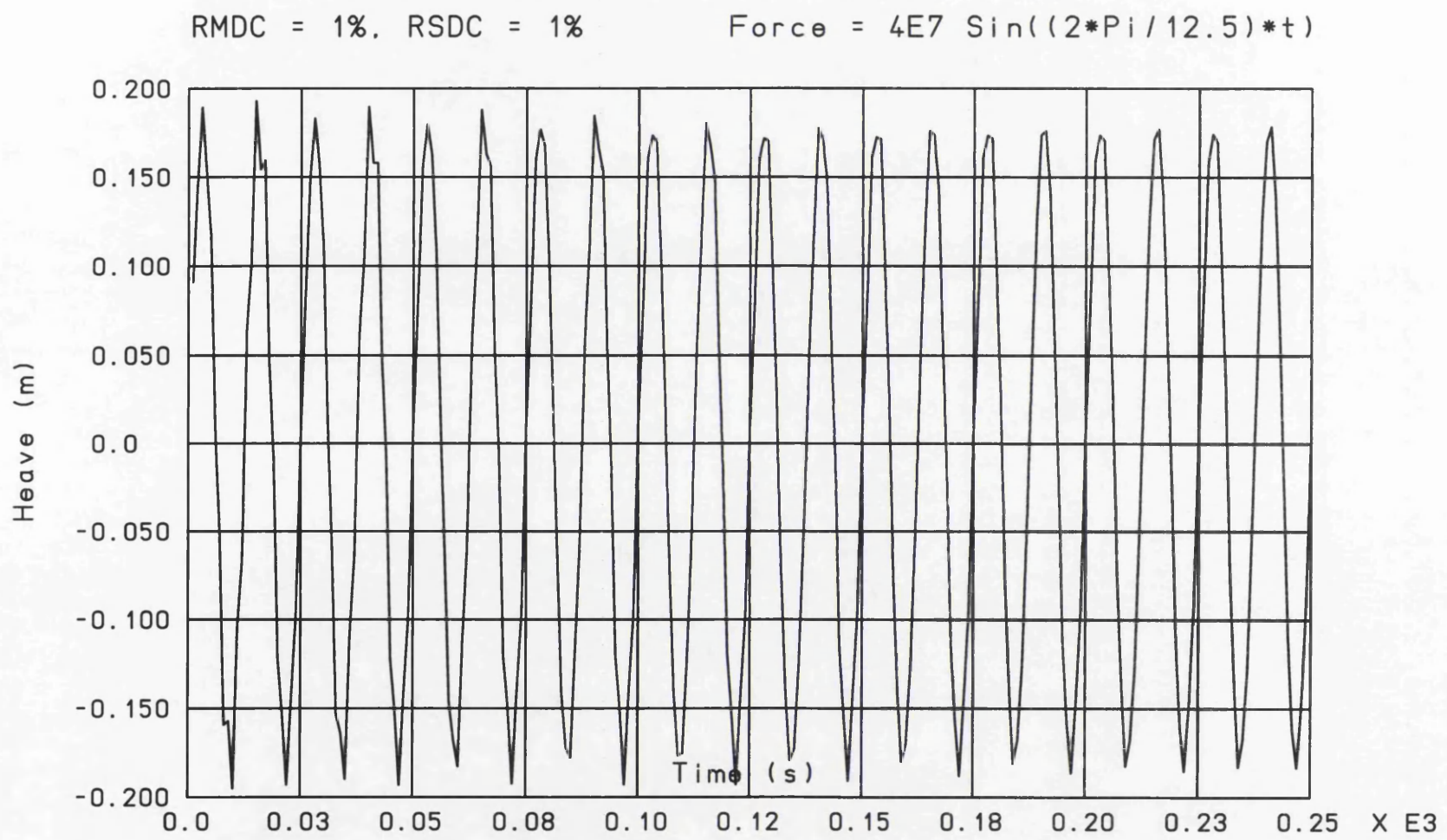

Fig. 4.35. Heave Response under Sinusoidal Load of 12.5 s Period

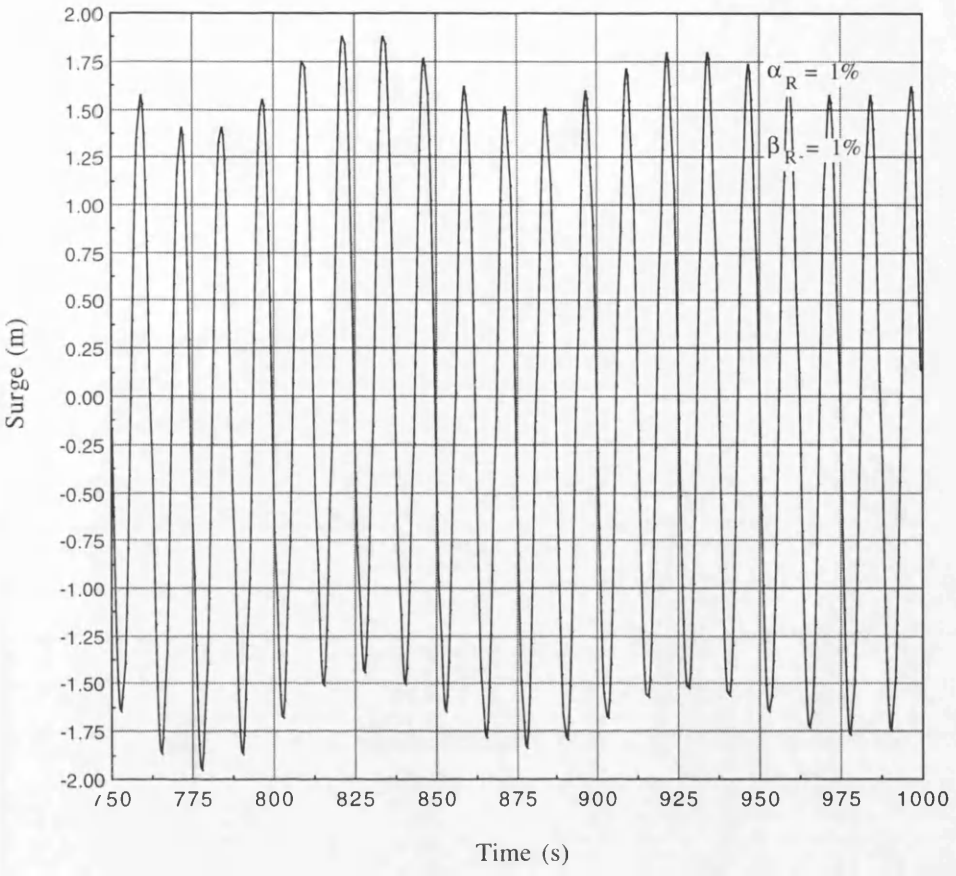

Fig. 4.36. Nearly Steady Surge Response of Model_3 under Sinusoidal Load of 12.5 s Period

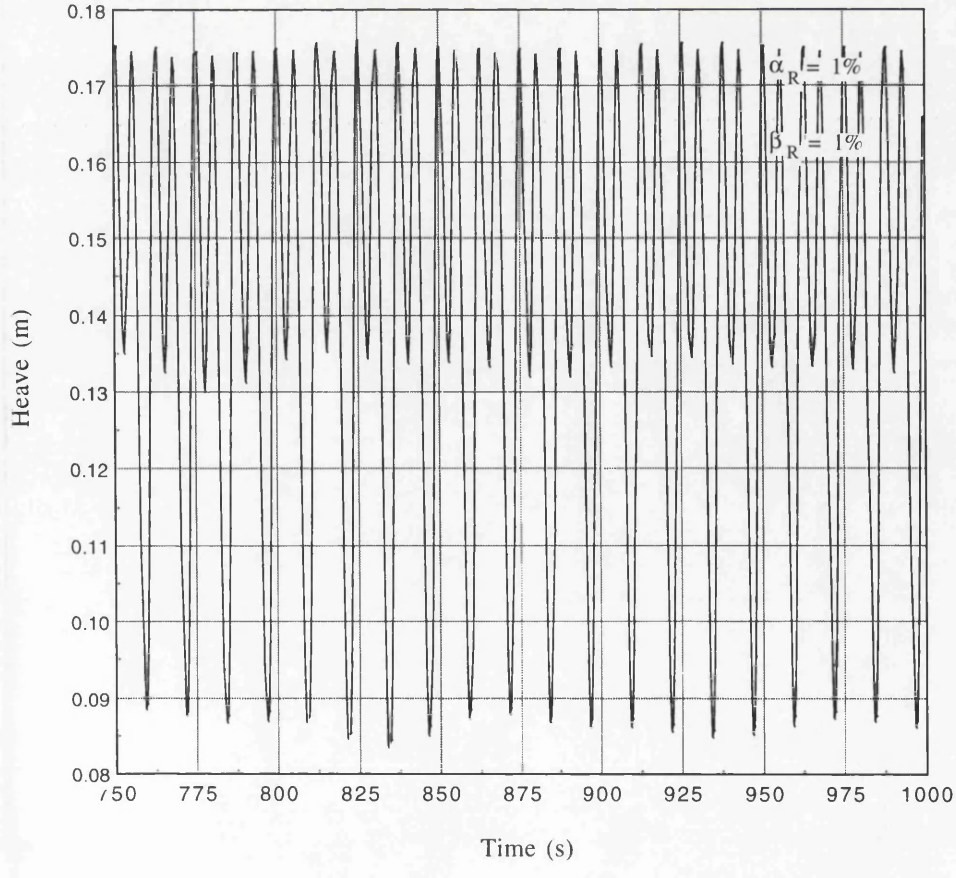

Fig. 4.37. Nearly Steady Heave Response of Model_3 under Sinusoidal Load of 12.5 s Period

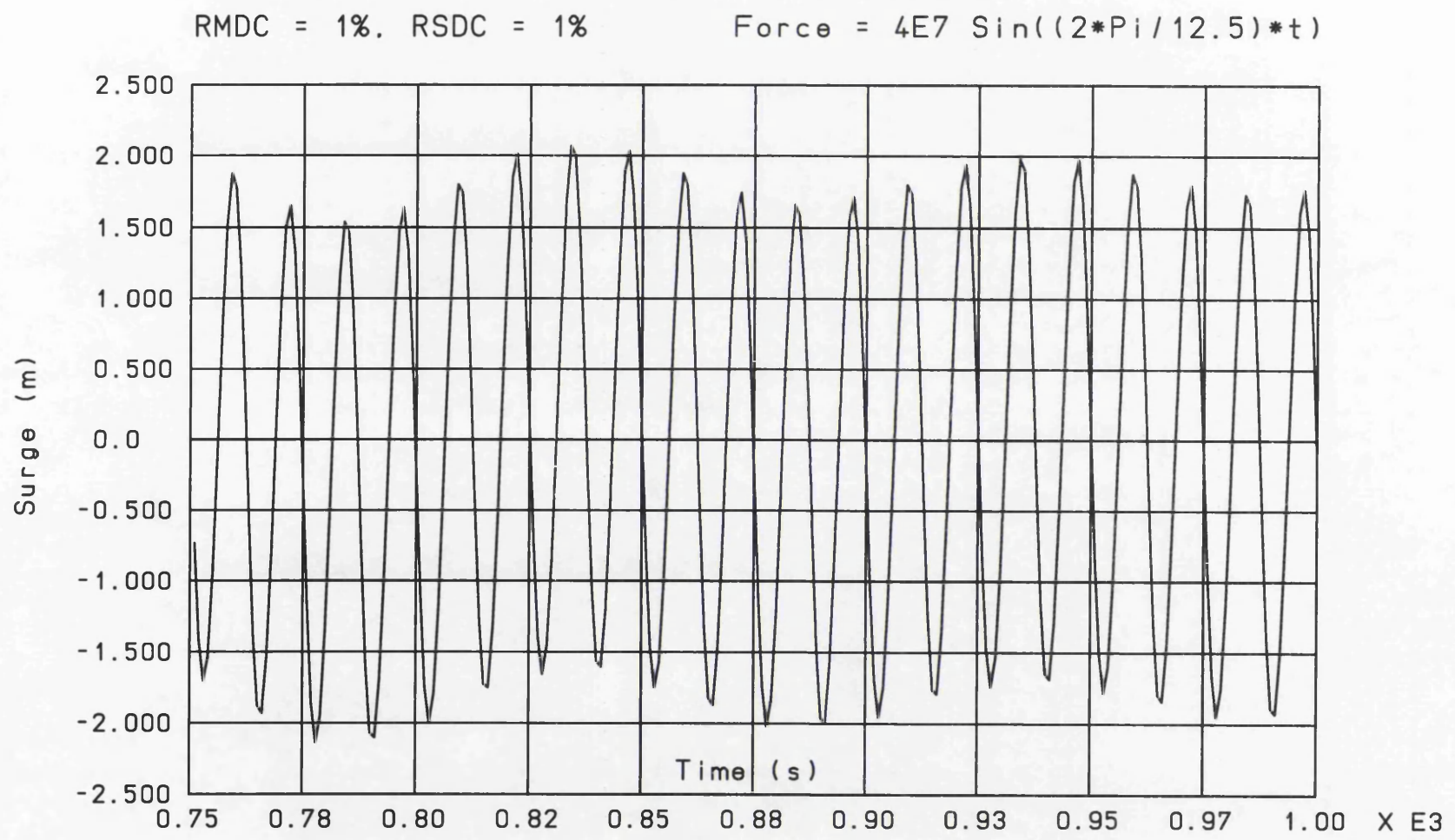

Fig. 4.38. Surge Response under Sinusoidal Load of 12.5 s Period

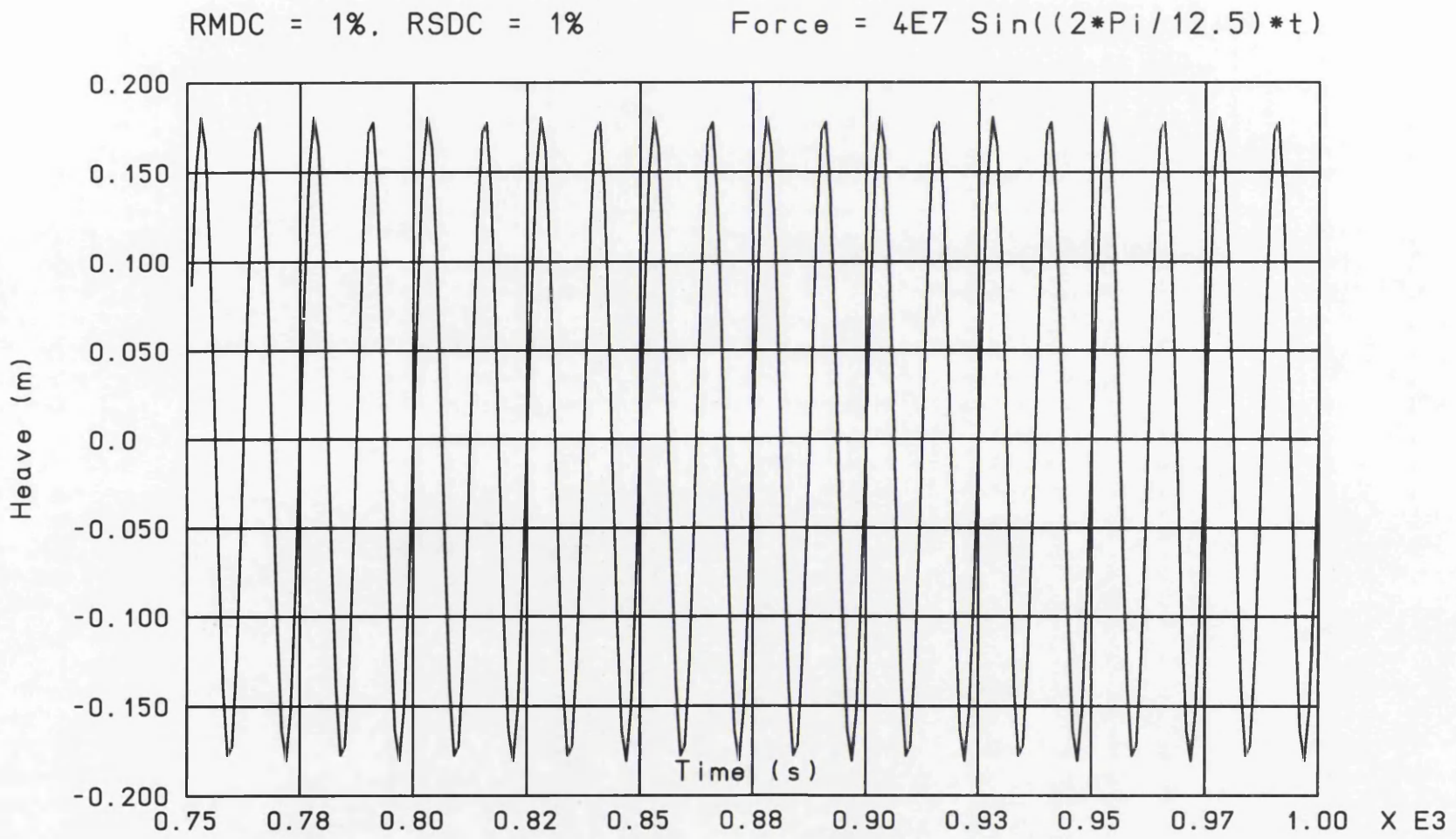

Fig. 4.39. Heave Response under Sinusoidal Load of 12.5 s Period

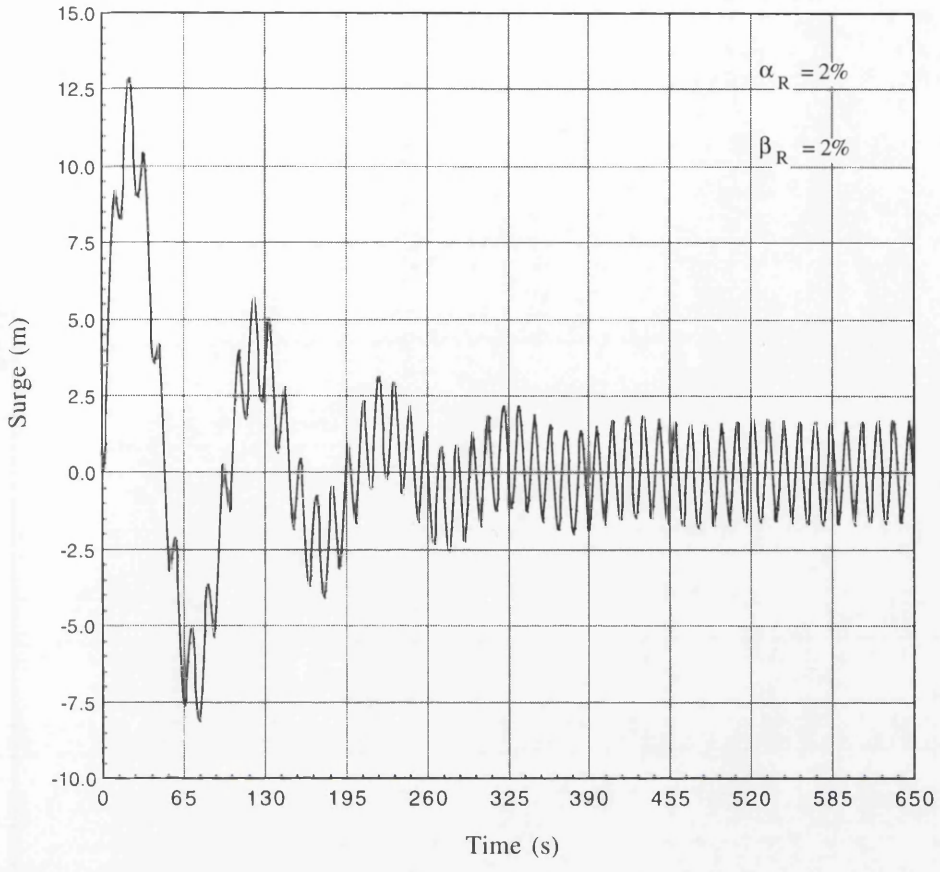

Fig. 4.40. Damped Surge Response of Model_3 under Sinusoidal Load of 12.5 s Period

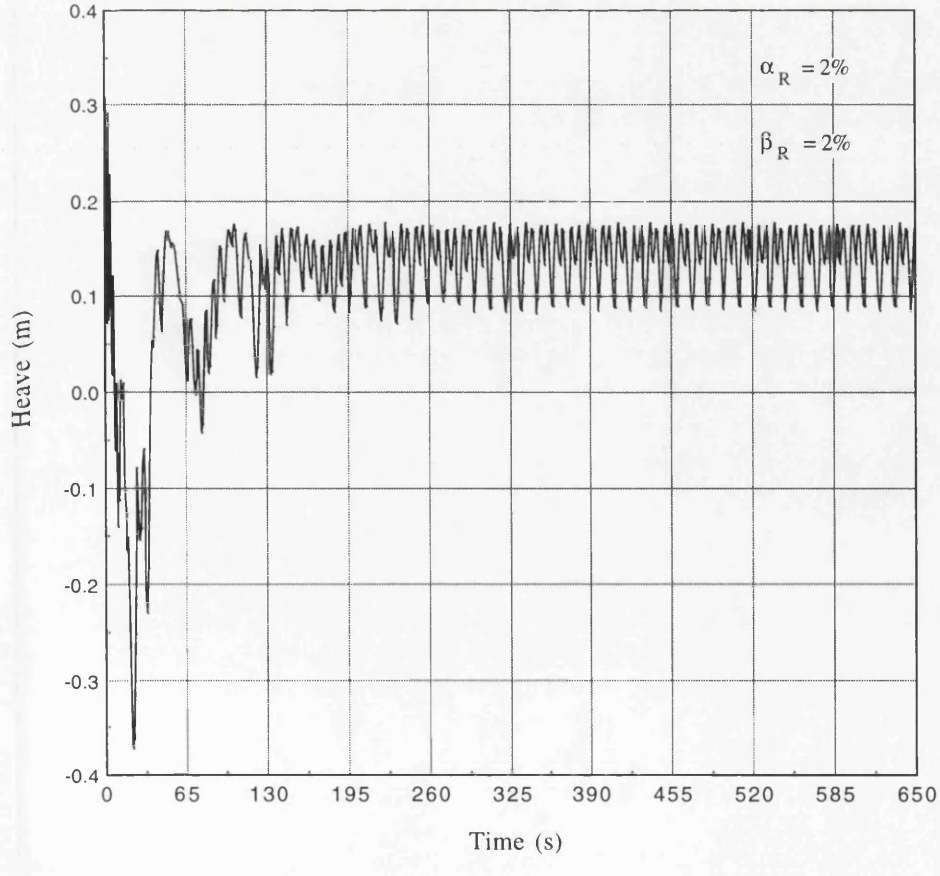

Fig. 4.41. Damped Heave Response of Model_3 under Sinusoidal Load of 12.5 s Period

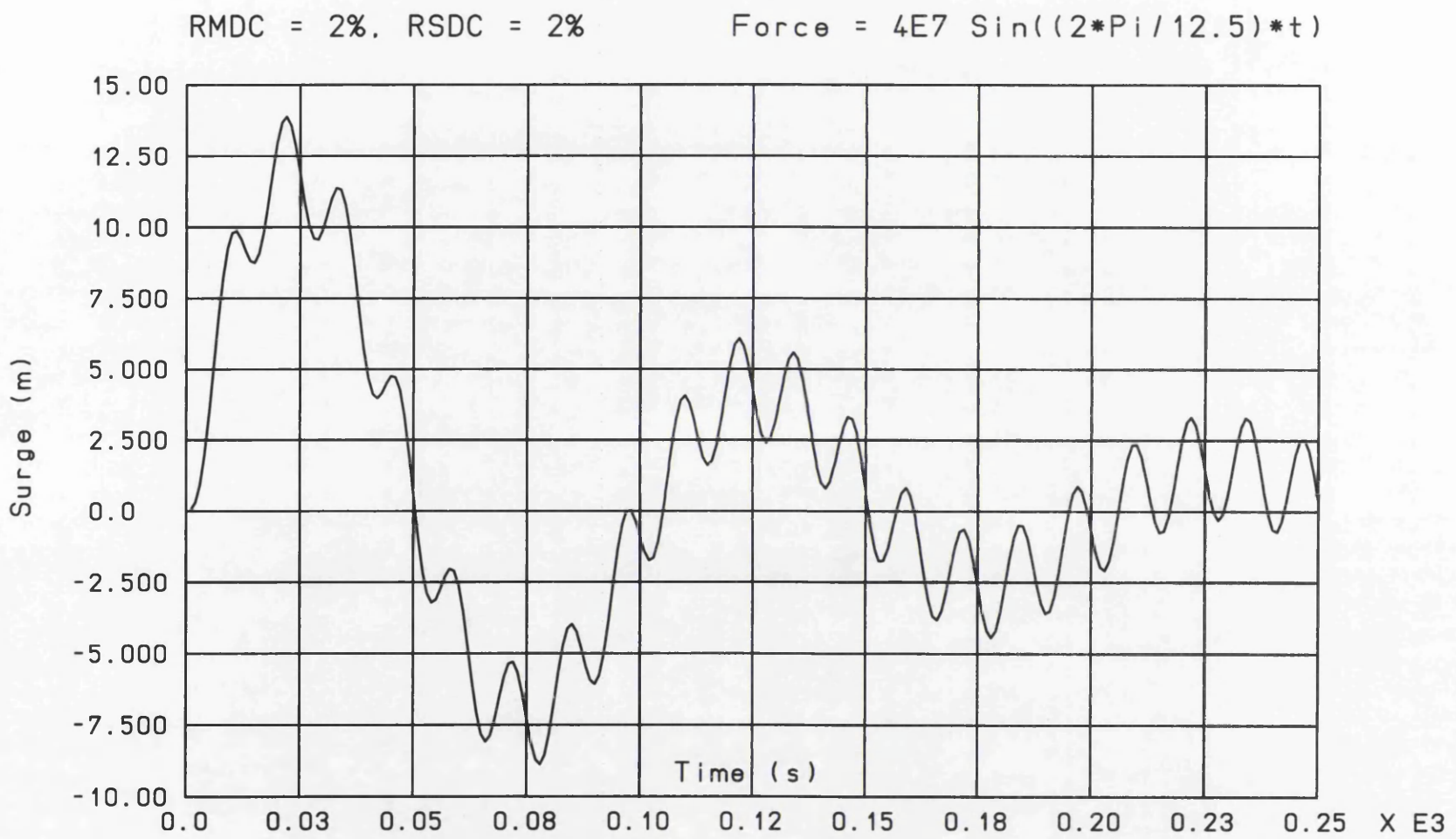

Fig. 4.42. Surge Response under Sinusoidal Load of 12.5 s Period

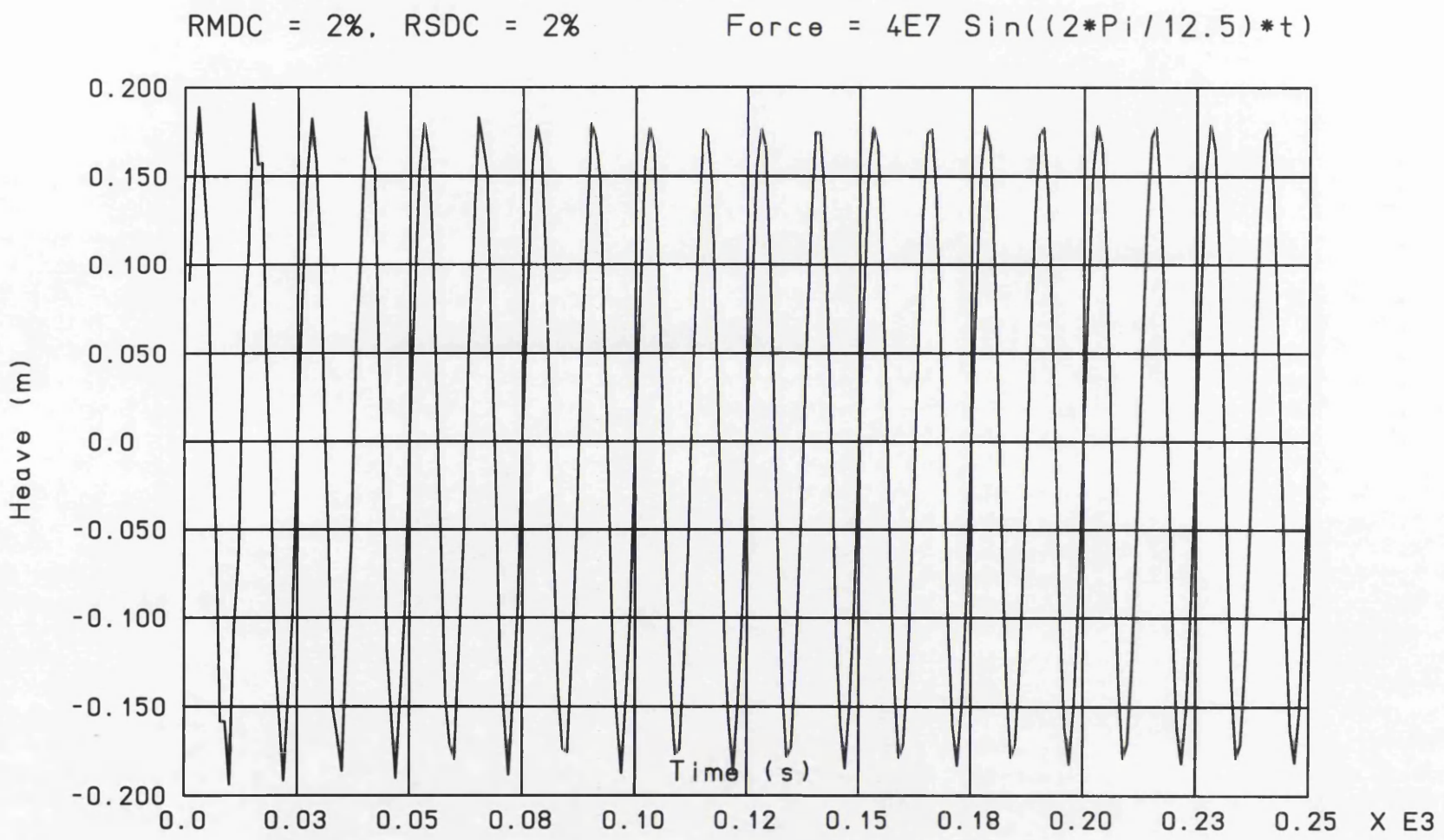

Fig. 4.43. Heave Response under Sinusoidal Load of 12.5 s Period

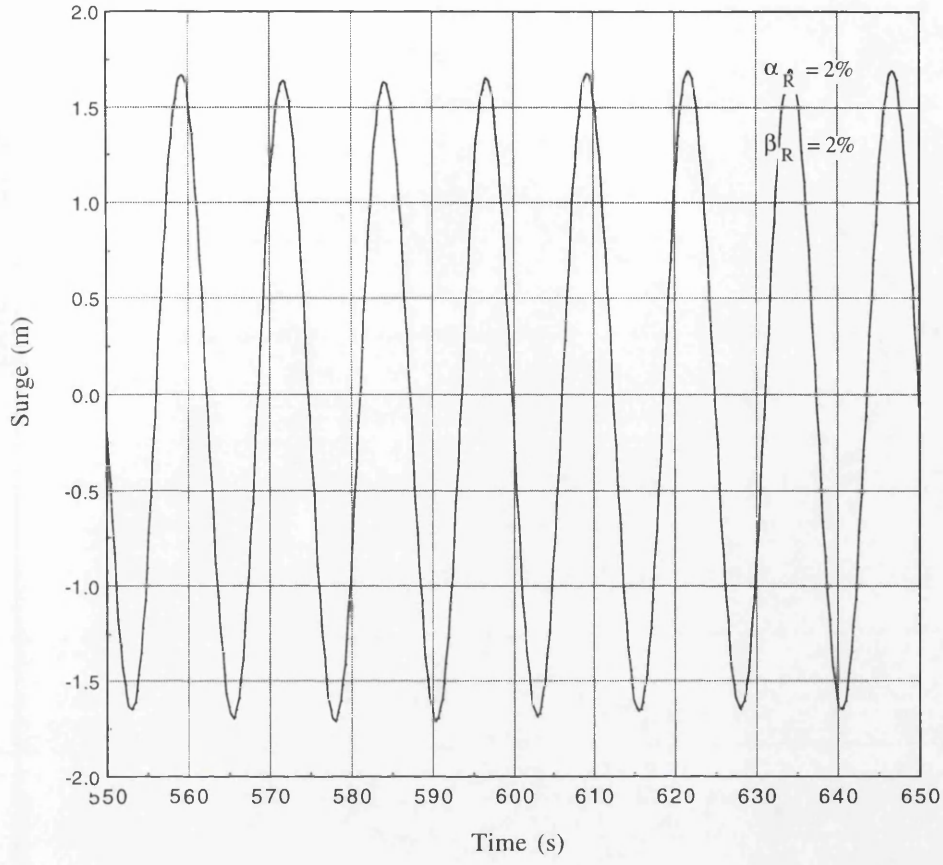

Fig. 4.44. Steady Surge Response of Model_3 under Sinusoidal Load of 12.5 s Period

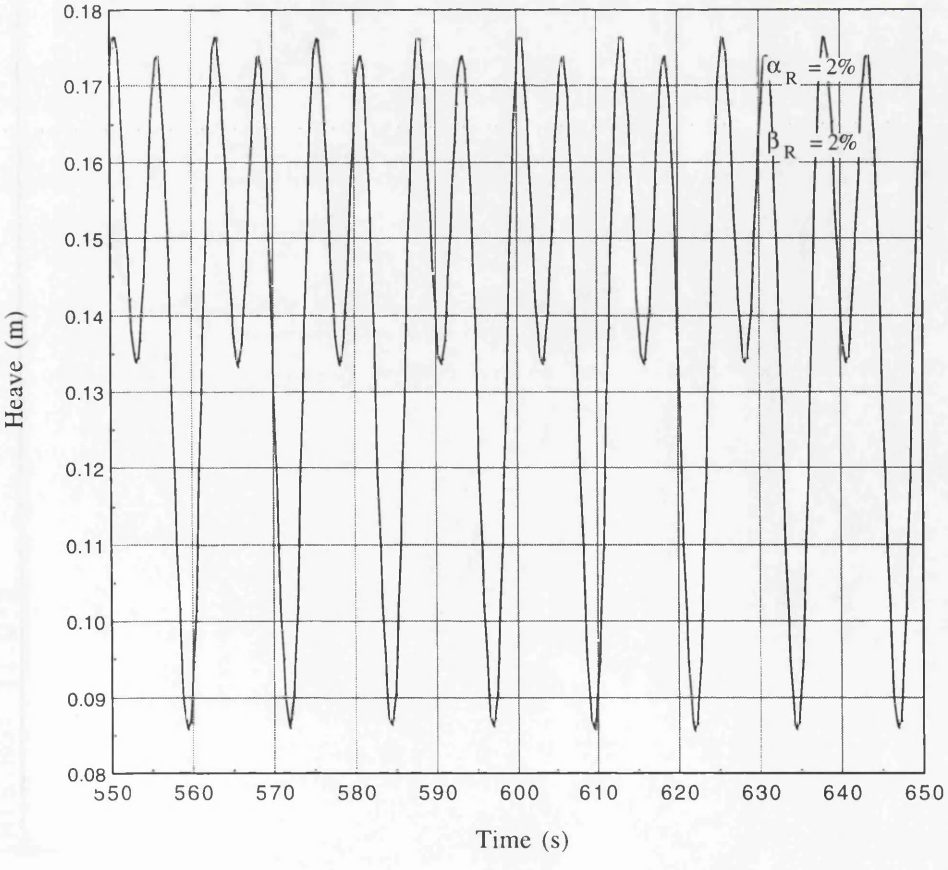

Fig. 4.45. Steady Heave Response of Model_3 under Sinusoidal Load of 12.5 s Period

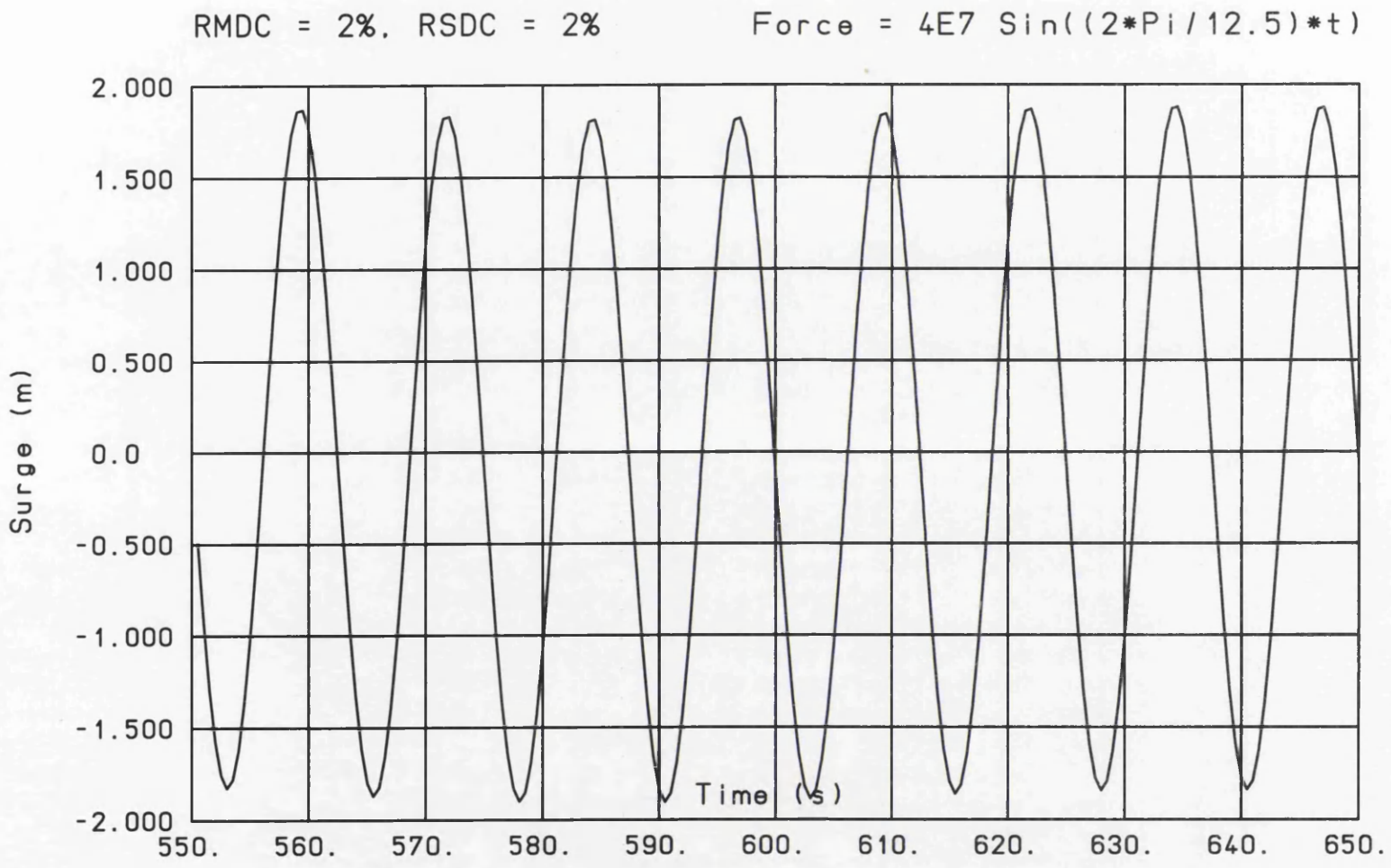

Fig. 4.46. Surge Response under Sinusoidal Load of 12.5 s Period

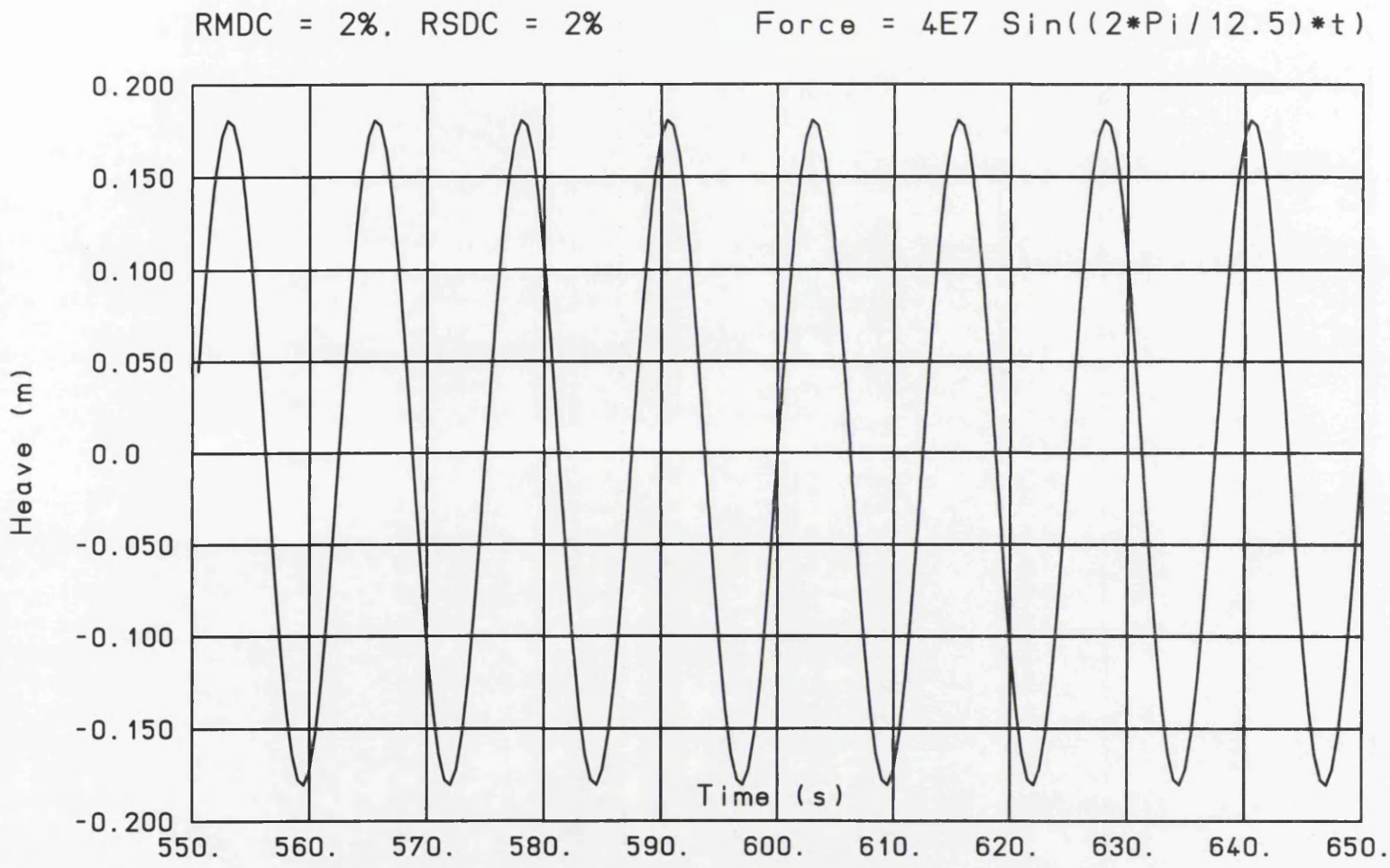

Fig. 4.47. Heave Response under Sinusoidal Load of 12.5 s Period

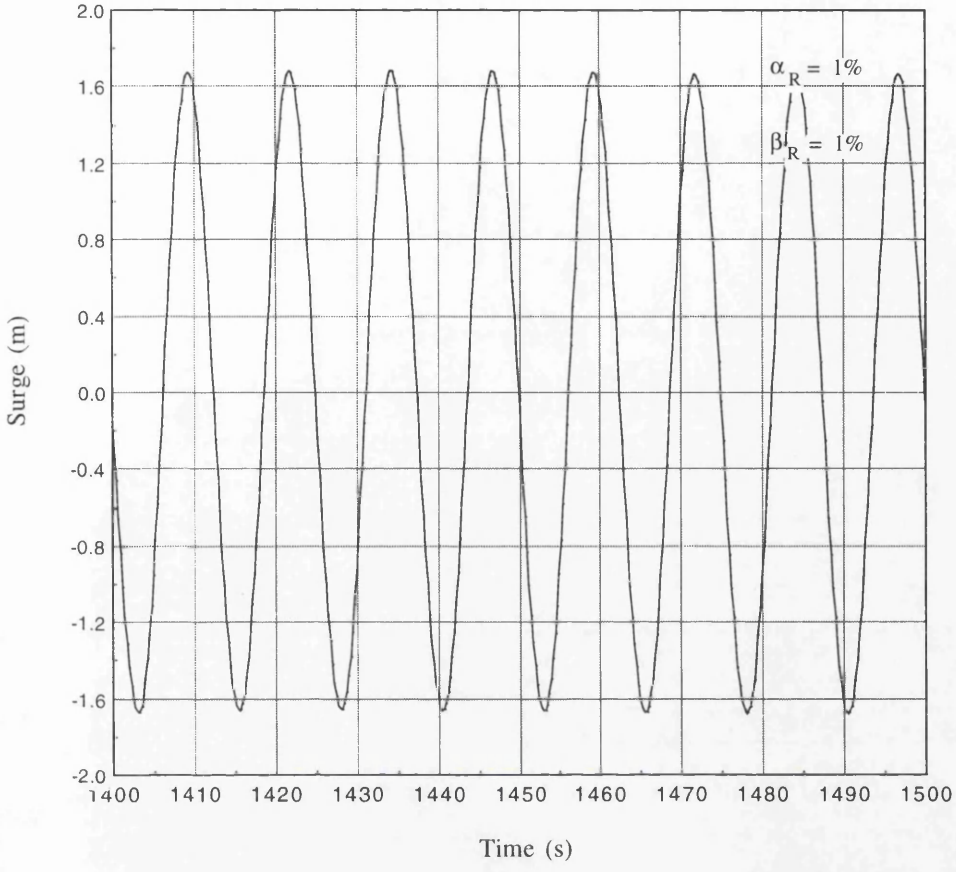

Fig. 4.48. Steady Surge Response of Model_3 under Sinusoidal Load of 12.5 s Period

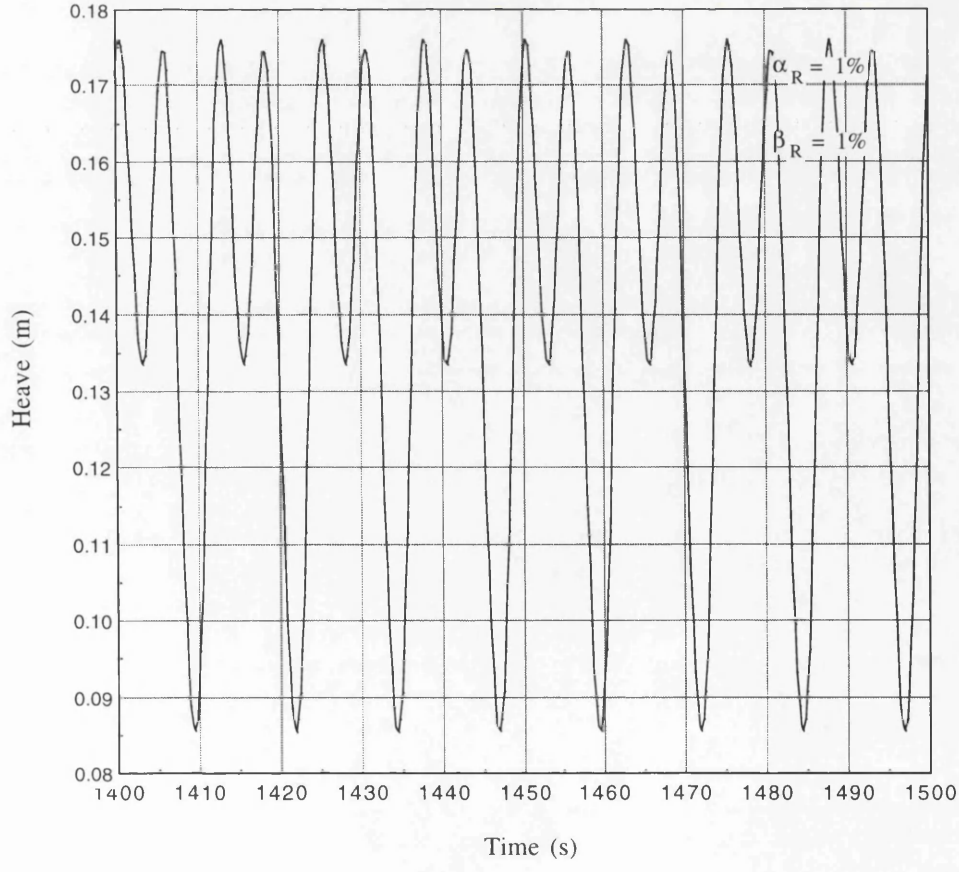

Fig. 4.49. Steady Heave Response of Model_3 under Sinusoidal Load of 12.5 s Period

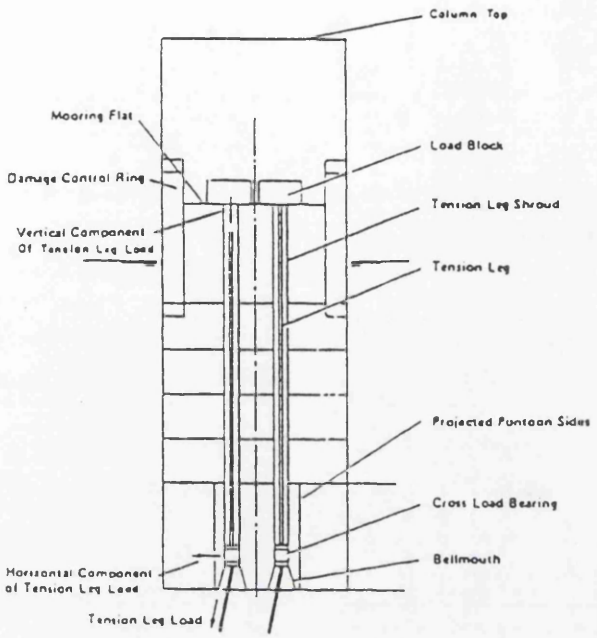

Fig. 4.50(a). Internal Tether Support System

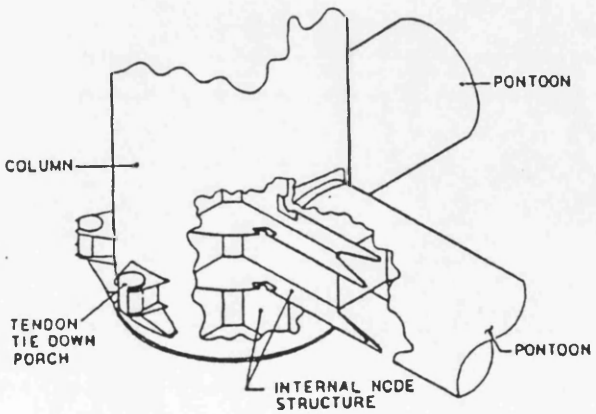

Fig. 4.50(b). External Tether Connections in Jolliet

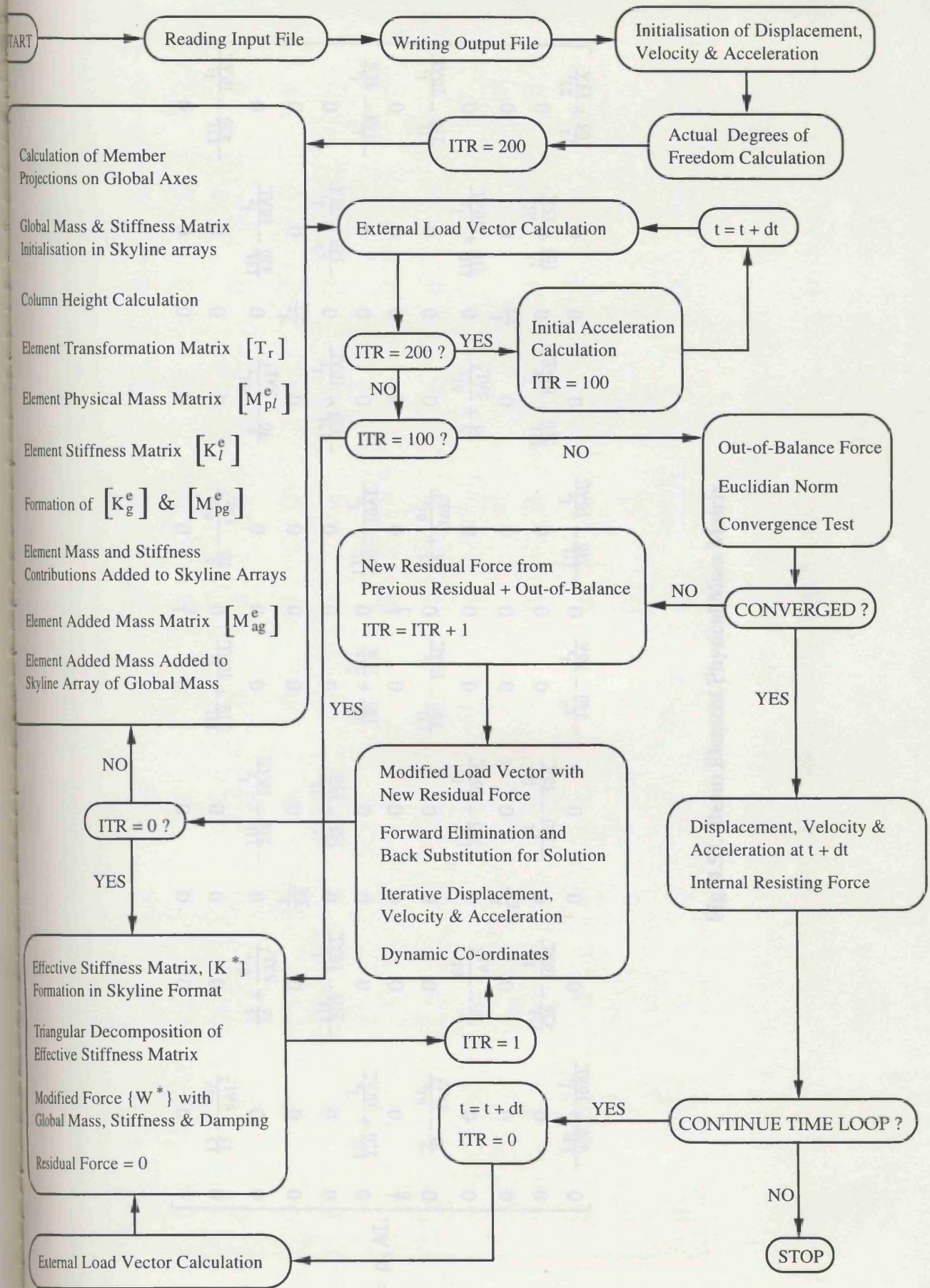

Fig. 4.51. Calculations Involved in Different Stages within DCATLP

$$\left[M_{pl}^{e}\right] = \rho_S AL \begin{bmatrix}
\frac{1}{3} & 0 & 0 & 0 & 0 & 0 & \frac{1}{6} & 0 & 0 & 0 & 0 & 0 \\
0 & \frac{13}{35}+\frac{6I_z}{5AL^2} & 0 & 0 & 0 & \frac{11L}{210}+\frac{I_z}{10AL} & 0 & \frac{9}{70}-\frac{6I_z}{5AL^2} & 0 & 0 & 0 & -\frac{13L}{420}+\frac{I_z}{10AL} \\
0 & 0 & \frac{13}{35}+\frac{6I_y}{5AL^2} & 0 & -\frac{11L}{210}-\frac{I_y}{10AL} & 0 & 0 & 0 & \frac{9}{70}-\frac{6I_y}{5AL^2} & 0 & \frac{13L}{420}-\frac{I_y}{10AL} & 0 \\
0 & 0 & 0 & \frac{J_x}{3A} & 0 & 0 & 0 & 0 & 0 & \frac{J_x}{6A} & 0 & 0 \\
0 & 0 & -\frac{11L}{210}-\frac{I_y}{10AL} & 0 & \frac{L^2}{105}+\frac{2I_y}{15A} & 0 & 0 & 0 & -\frac{13L}{420}+\frac{I_y}{10AL} & 0 & -\frac{L^2}{140}-\frac{I_y}{30A} & 0 \\
0 & \frac{11L}{210}+\frac{I_z}{10AL} & 0 & 0 & 0 & \frac{L^2}{105}+\frac{2I_z}{15A} & 0 & \frac{13L}{420}-\frac{I_z}{10AL} & 0 & 0 & 0 & -\frac{L^2}{140}-\frac{I_z}{30A} \\
\frac{1}{6} & 0 & 0 & 0 & 0 & 0 & \frac{1}{3} & 0 & 0 & 0 & 0 & 0 \\
0 & \frac{9}{70}-\frac{6I_z}{5AL^2} & 0 & 0 & 0 & \frac{13L}{420}-\frac{I_z}{10AL} & 0 & \frac{13}{35}+\frac{6I_z}{5AL^2} & 0 & 0 & 0 & -\frac{11L}{210}-\frac{I_z}{10AL} \\
0 & 0 & \frac{9}{70}-\frac{6I_y}{5AL^2} & 0 & -\frac{13L}{420}+\frac{I_y}{10AL} & 0 & 0 & 0 & \frac{13}{35}+\frac{6I_y}{5AL^2} & 0 & \frac{11L}{210}+\frac{I_y}{10AL} & 0 \\
0 & 0 & 0 & \frac{J_x}{6A} & 0 & 0 & 0 & 0 & 0 & \frac{J_x}{3A} & 0 & 0 \\
0 & 0 & \frac{13L}{420}-\frac{I_y}{10AL} & 0 & -\frac{L^2}{140}-\frac{I_y}{30A} & 0 & 0 & 0 & \frac{11L}{210}+\frac{I_y}{10AL} & 0 & \frac{L^2}{105}+\frac{2I_y}{15A} & 0 \\
0 & -\frac{13L}{420}+\frac{I_z}{10AL} & 0 & 0 & 0 & -\frac{L^2}{140}-\frac{I_z}{30A} & 0 & -\frac{11L}{210}-\frac{I_z}{10AL} & 0 & 0 & 0 & \frac{L^2}{105}+\frac{2I_z}{15A}
\end{bmatrix}$$

Fig. 4.53. Beam Element Physical Mass Matrix

$$
\left[K_l^e\right] = \begin{bmatrix}
\frac{E_Y A}{L} & 0 & 0 & 0 & 0 & 0 & \frac{-E_Y A}{L} & 0 & 0 & 0 & 0 & 0 \\
0 & \frac{12E_Y I_z}{L^3} & 0 & 0 & 0 & \frac{6E_Y I_z}{L^2} & 0 & \frac{-12E_Y I_z}{L^3} & 0 & 0 & 0 & \frac{6E_Y I_z}{L^2} \\
0 & 0 & \frac{12E_Y I_y}{L^3} & 0 & \frac{-6E_Y I_y}{L^2} & 0 & 0 & 0 & \frac{-12E_Y I_y}{L^3} & 0 & \frac{-6E_Y I_y}{L^2} & 0 \\
0 & 0 & 0 & \frac{G_s J_x}{L} & 0 & 0 & 0 & 0 & 0 & \frac{-G_s J_x}{L} & 0 & 0 \\
0 & 0 & \frac{-6E_Y I_y}{L^2} & 0 & \frac{4E_Y I_y}{L} & 0 & 0 & 0 & \frac{6E_Y I_y}{L^2} & 0 & \frac{2E_Y I_y}{L} & 0 \\
0 & \frac{6E_Y I_z}{L^2} & 0 & 0 & 0 & \frac{4E_Y I_z}{L} & 0 & \frac{-6E_Y I_z}{L^2} & 0 & 0 & 0 & \frac{2E_Y I_z}{L} \\
\frac{-E_Y A}{L} & 0 & 0 & 0 & 0 & 0 & \frac{E_Y A}{L} & 0 & 0 & 0 & 0 & 0 \\
0 & \frac{-12E_Y I_z}{L^3} & 0 & 0 & 0 & \frac{-6E_Y I_z}{L^2} & 0 & \frac{12E_Y I_z}{L^3} & 0 & 0 & 0 & \frac{-6E_Y I_z}{L^2} \\
0 & 0 & \frac{-12E_Y I_y}{L^3} & 0 & \frac{6E_Y I_y}{L^2} & 0 & 0 & 0 & \frac{12E_Y I_y}{L^3} & 0 & \frac{6E_Y I_y}{L^2} & 0 \\
0 & 0 & 0 & \frac{-G_s J_x}{L} & 0 & 0 & 0 & 0 & 0 & \frac{G_s J_x}{L} & 0 & 0 \\
0 & 0 & \frac{-6E_Y I_y}{L^2} & 0 & \frac{2E_Y I_y}{L} & 0 & 0 & 0 & \frac{6E_Y I_y}{L^2} & 0 & \frac{4E_Y I_y}{L} & 0 \\
0 & \frac{6E_Y I_z}{L^2} & 0 & 0 & 0 & \frac{2E_Y I_z}{L} & 0 & \frac{-6E_Y I_z}{L^2} & 0 & 0 & 0 & \frac{4E_Y I_z}{L}
\end{bmatrix}
$$

Fig. 4.55. Beam Element Stiffness Matrix

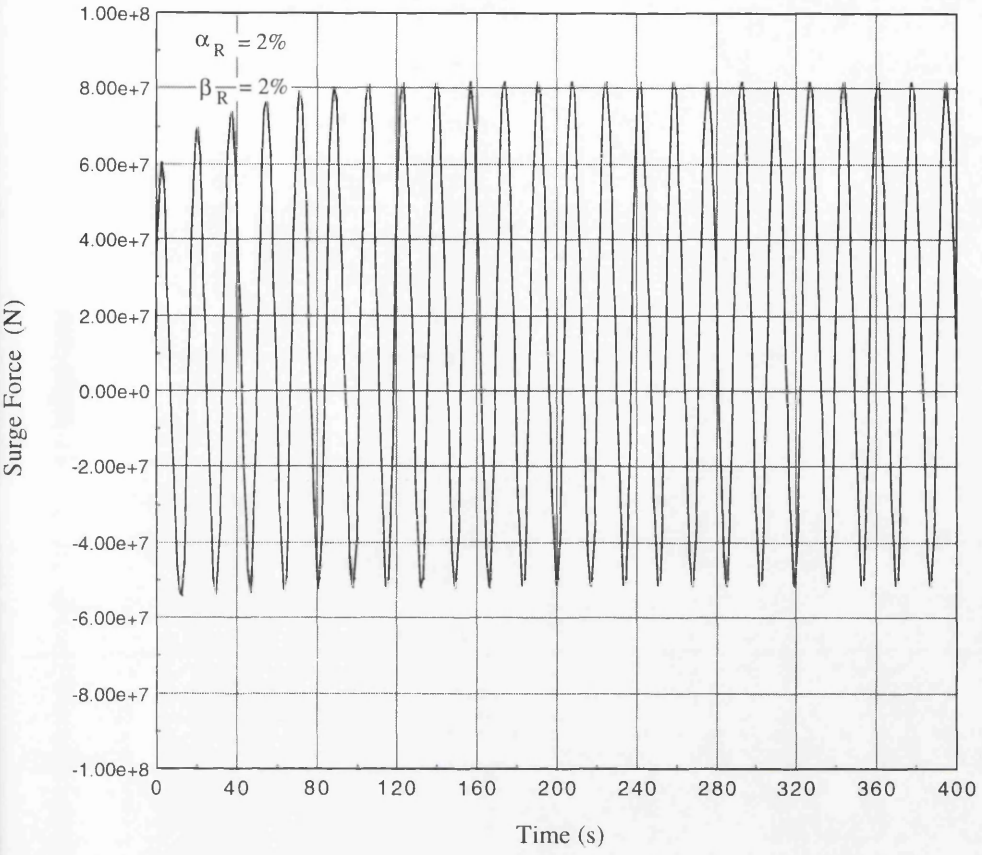

Fig. 4.58. Total Environmental Forces on Model_3 in the Surge Direction

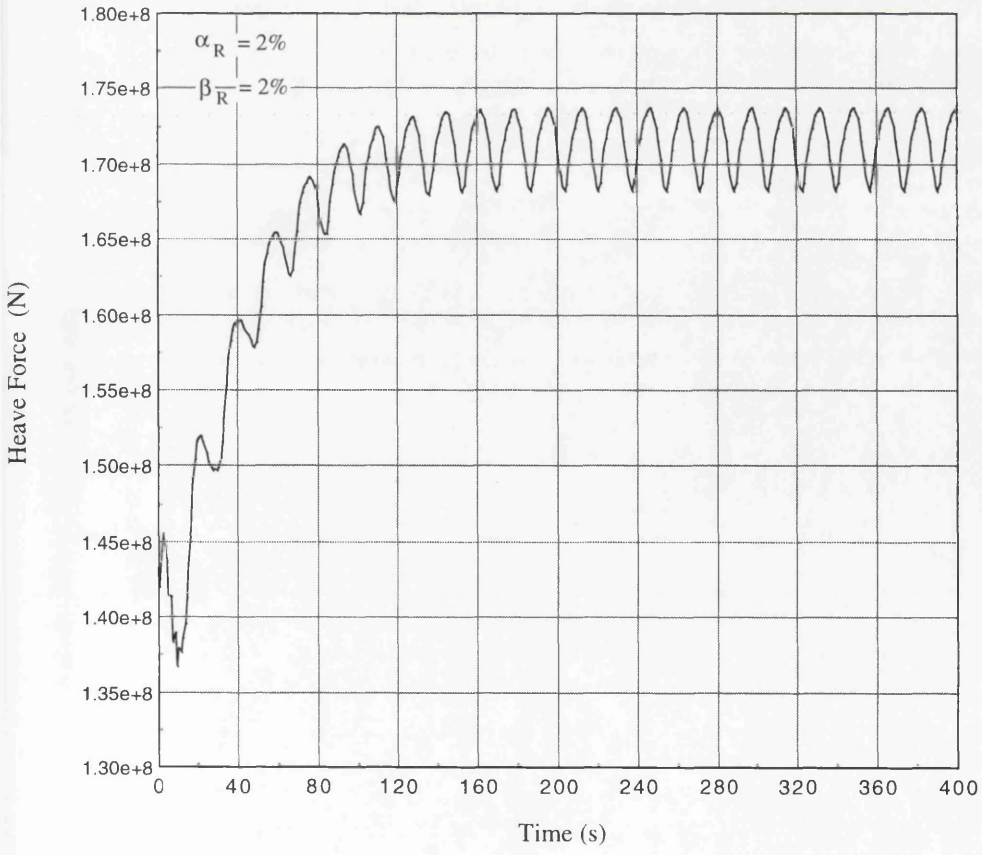

Fig. 4.59. Net Resultant Force on Model_3 in the Heave Direction

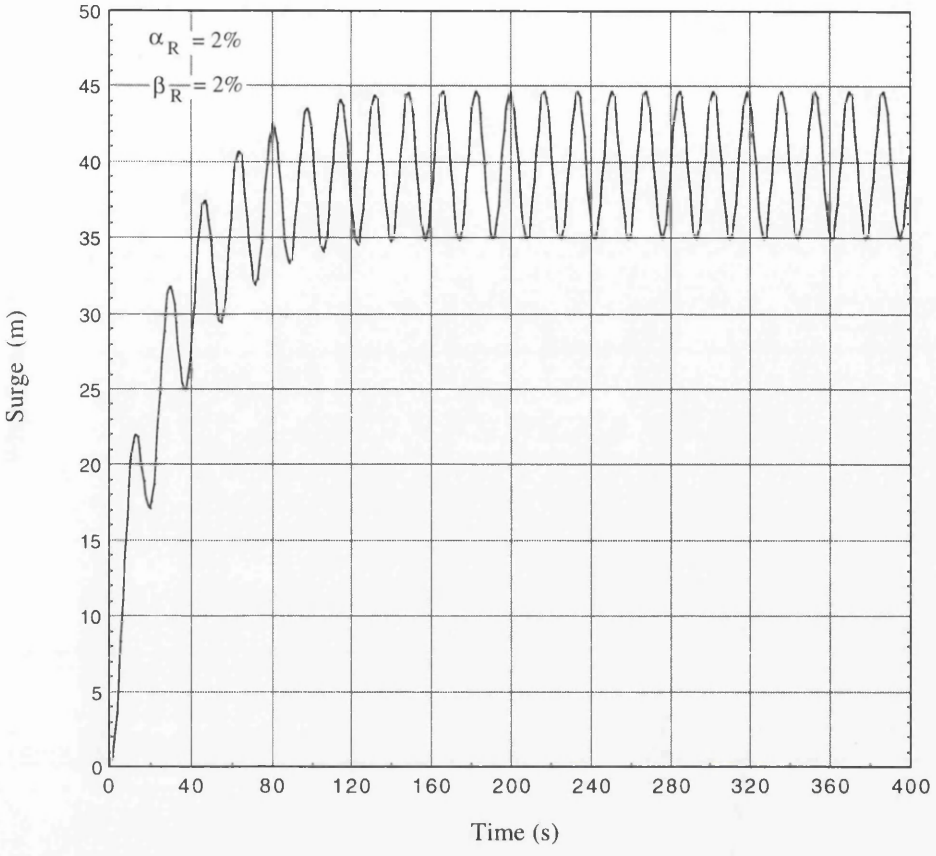

Fig. 4.60. Surge Response of Model_3 under All Environmental Forces

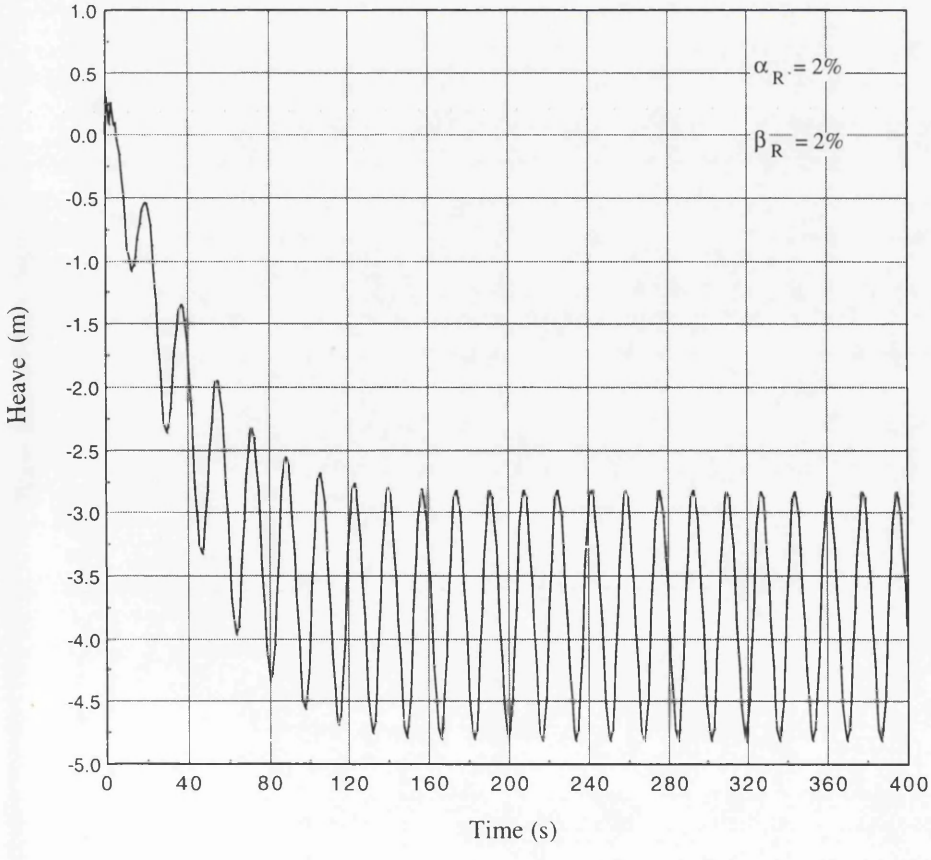

Fig. 4.61. Heave Response of Model_3 under All Environmental Forces

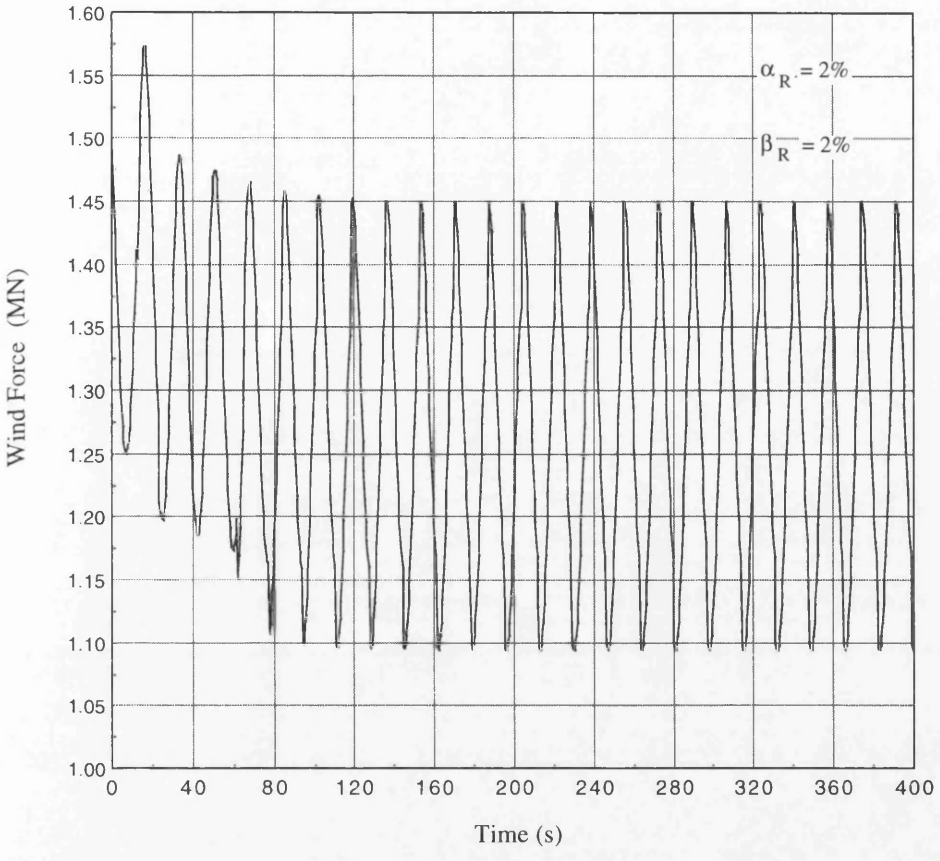

Fig. 4.62. Wind Force on Model_3

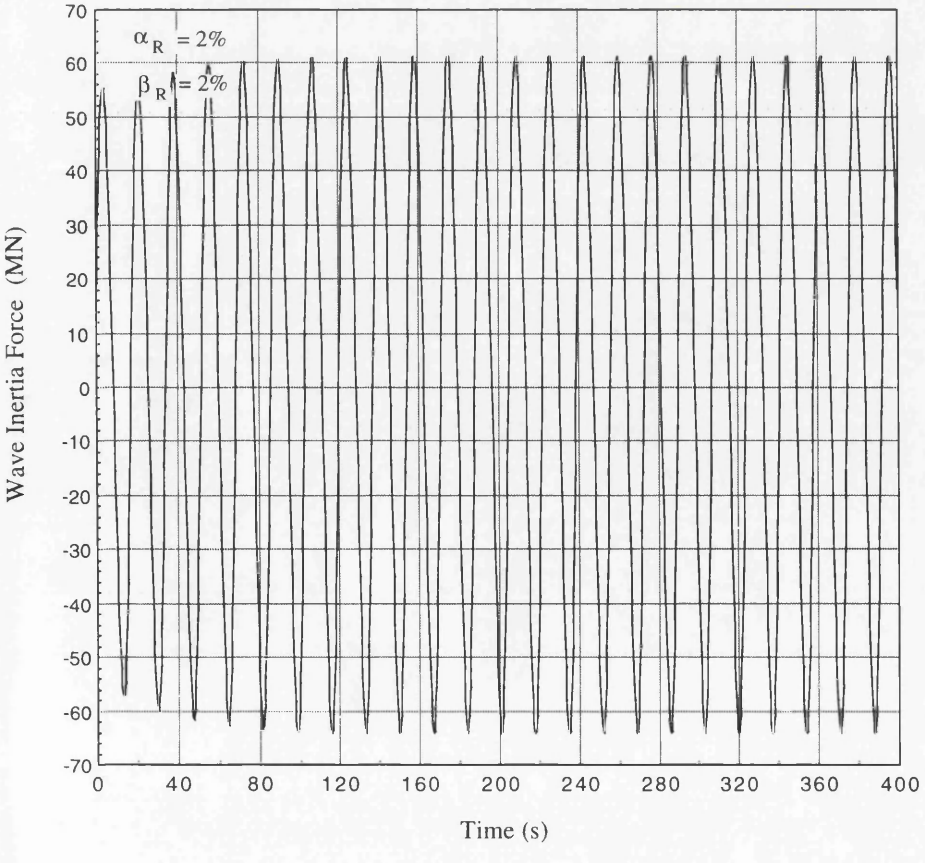

Fig. 4.63. Wave Inertia Force on Model_3 in the Surge Direction

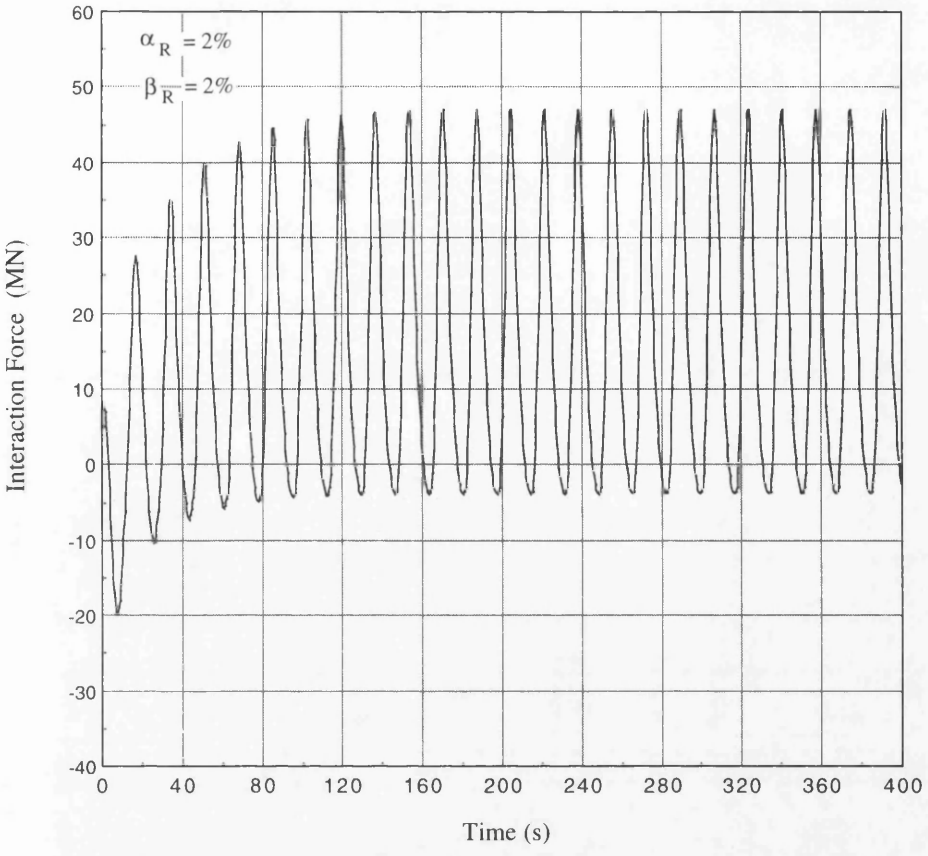

Fig. 4.64. Wave-Current-Motion Interaction Force on Model_3

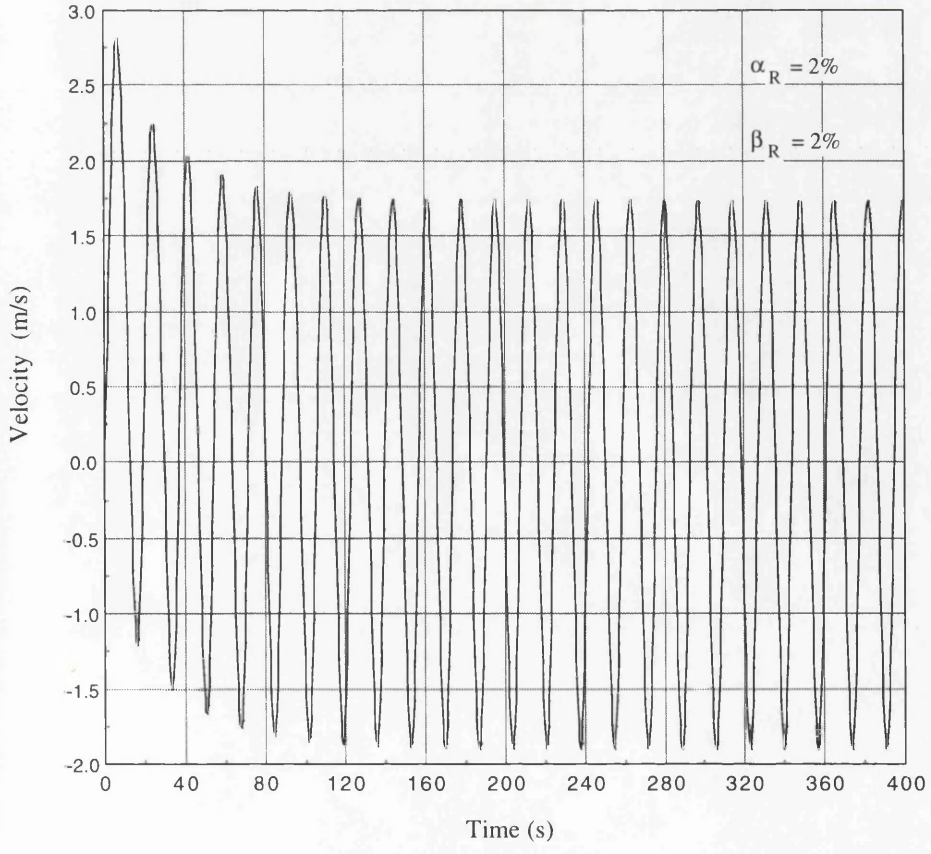

Fig. 4.65. Horizontal Velocity at Node 90 of Model_3

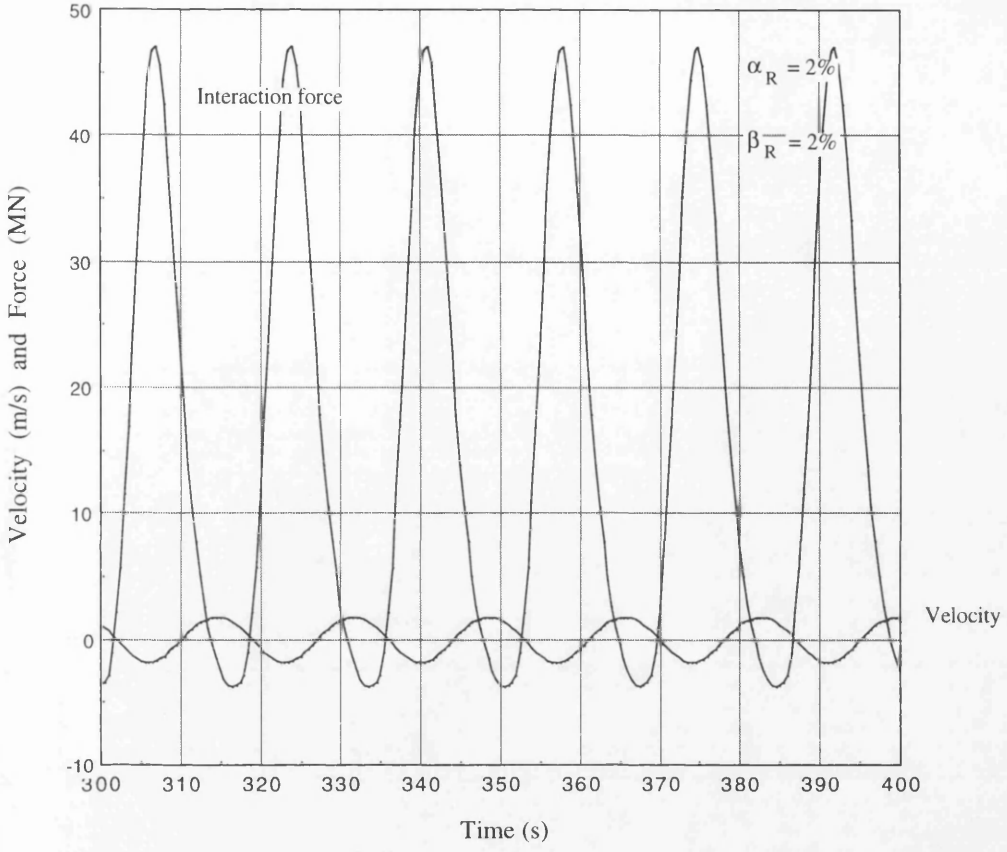

Fig. 4.66. Wave-Current-Motion Interaction Force and Structural Velocity

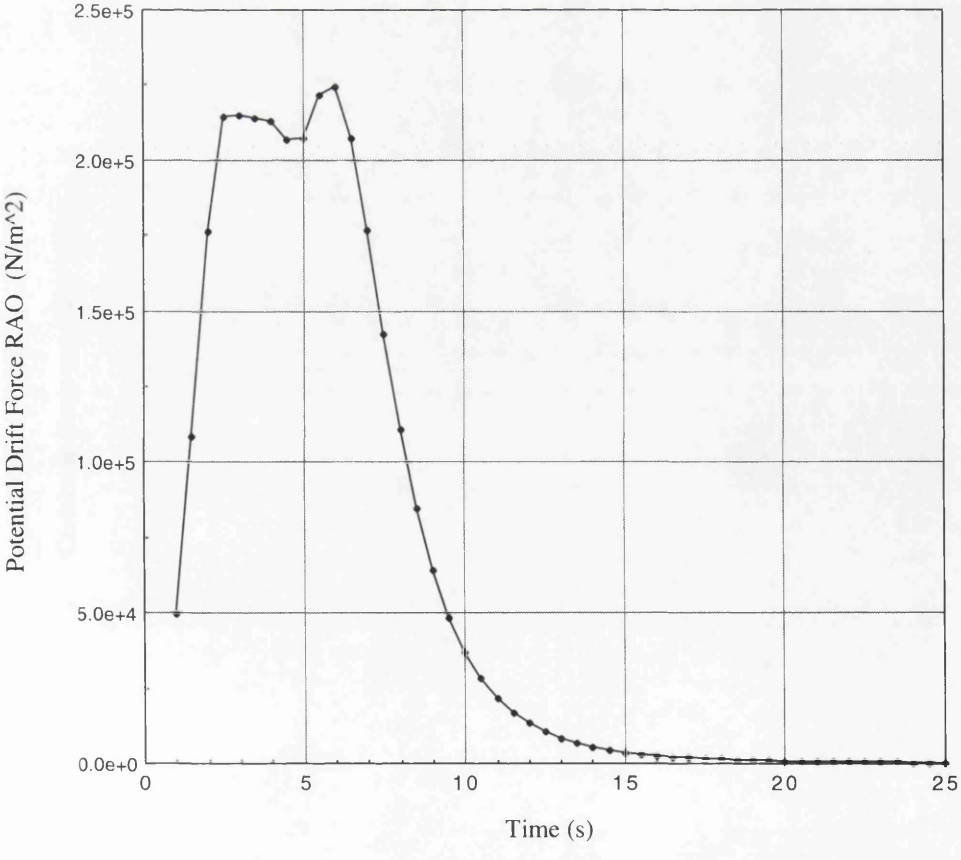

Fig. 4.67. Steady Potential Drift Force Transfer Function for Model_3

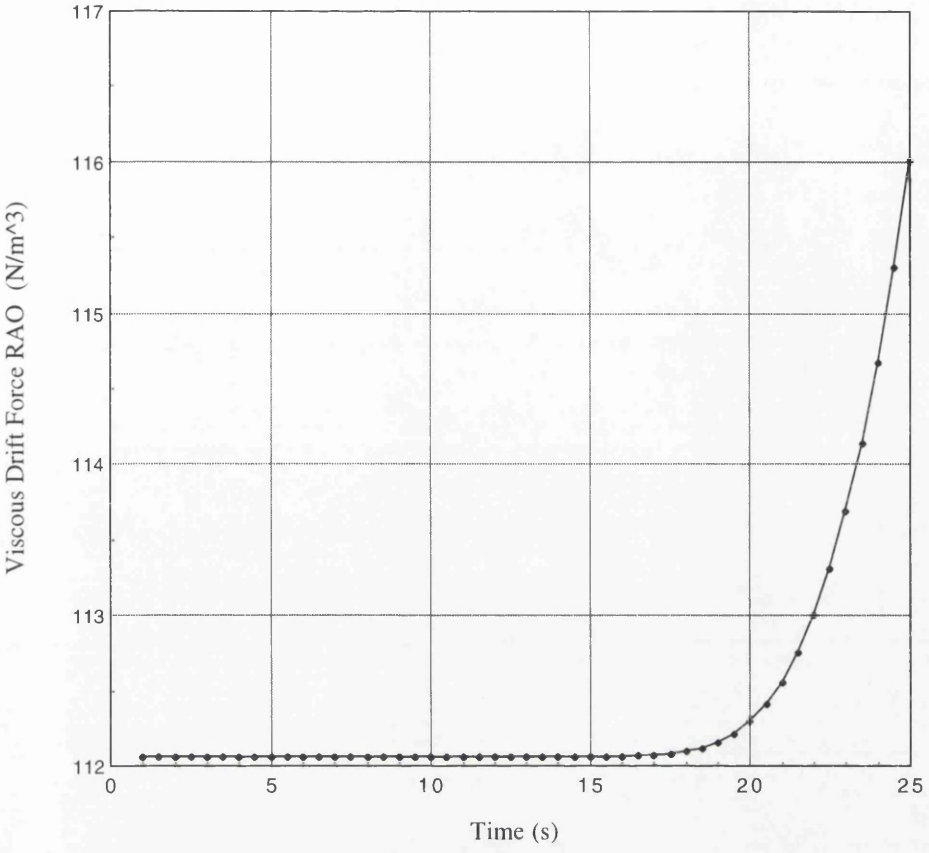

Fig. 4.68. Steady Viscous Drift Force Transfer Function for Model_3

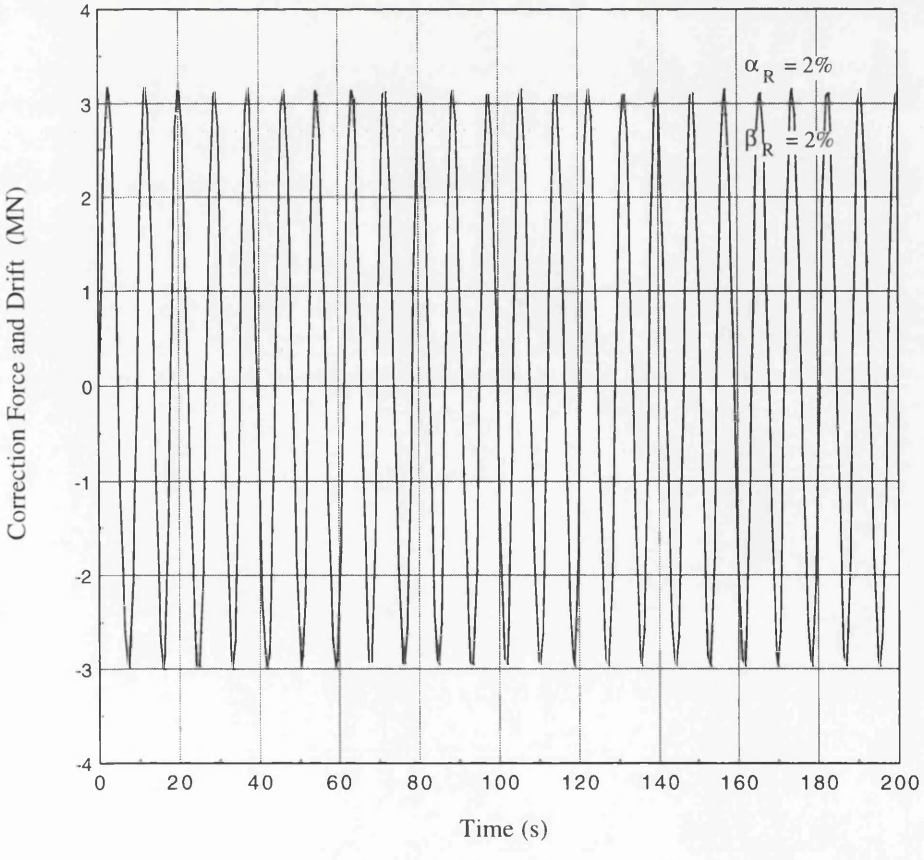

Fig. 4.69. Second Order Correction and Drift Forces on Model_3

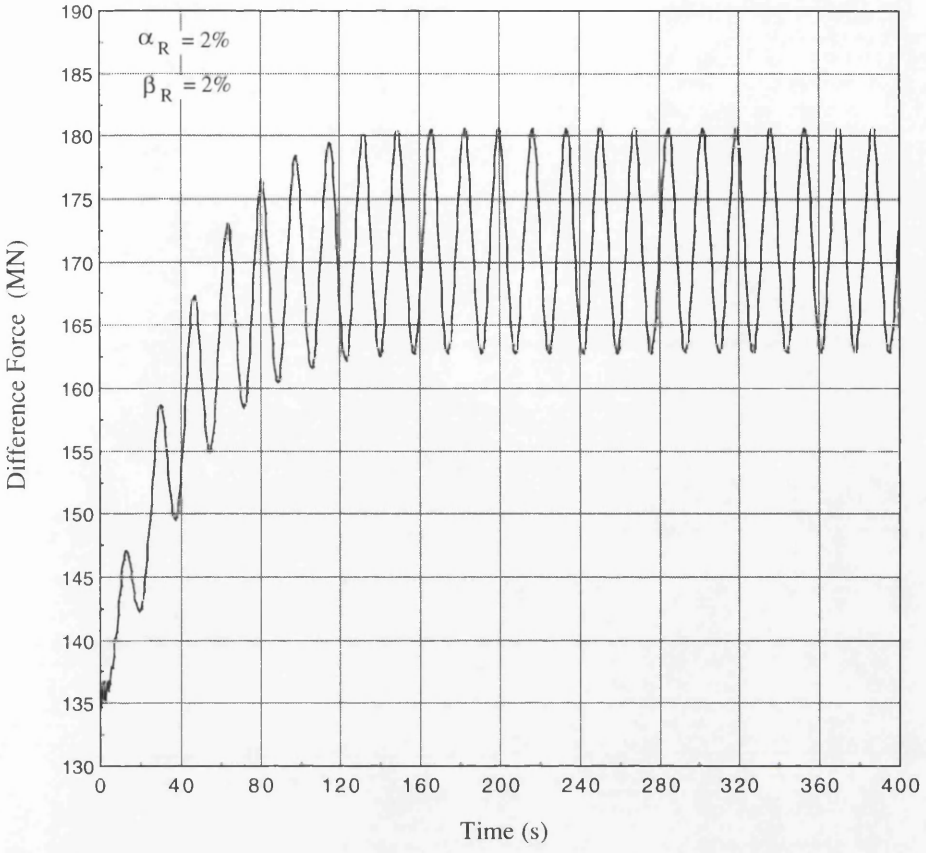

Fig. 4.70. Difference between Variable Buoyancy and Weight of Model_3

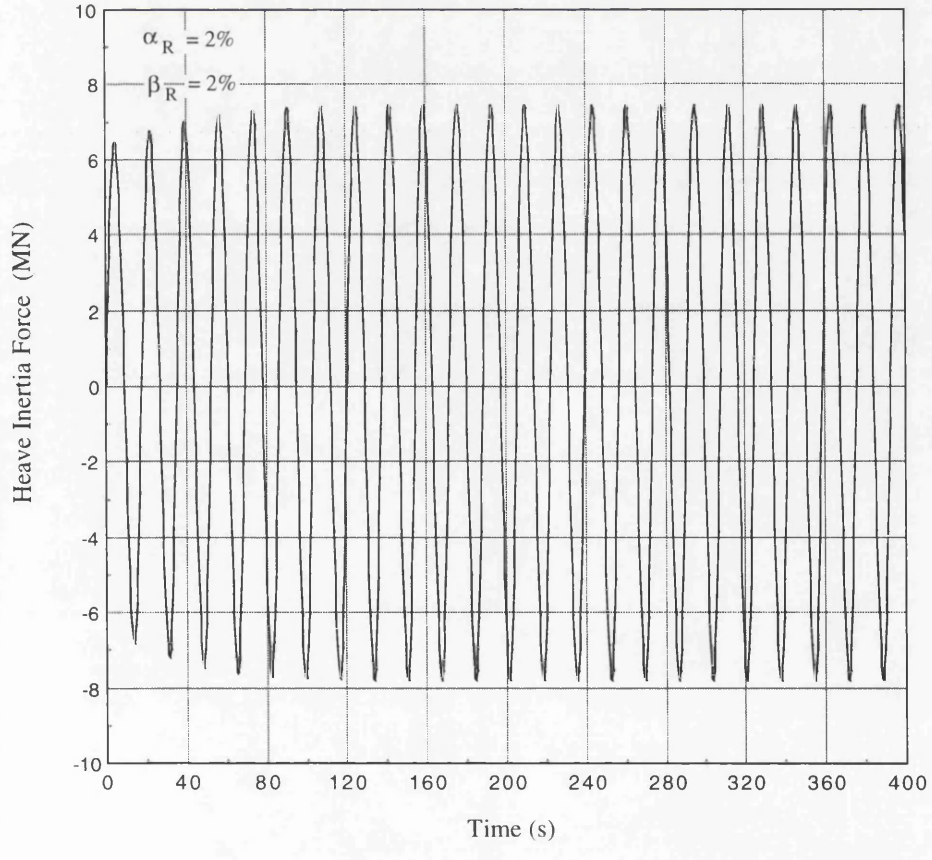

Fig. 4.71. Wave Inertia Force on Model_3 in the Heave Direction

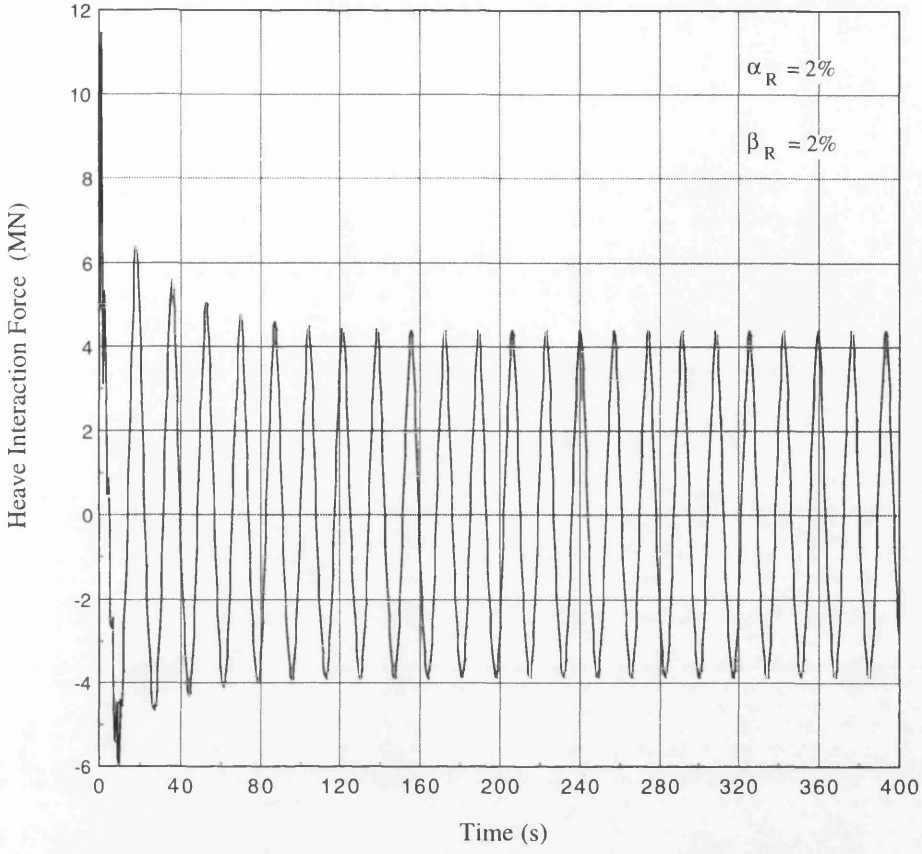

Fig. 4.72. Wave-Current-Motion Interaction Force on Model_3 in the Heave Direction

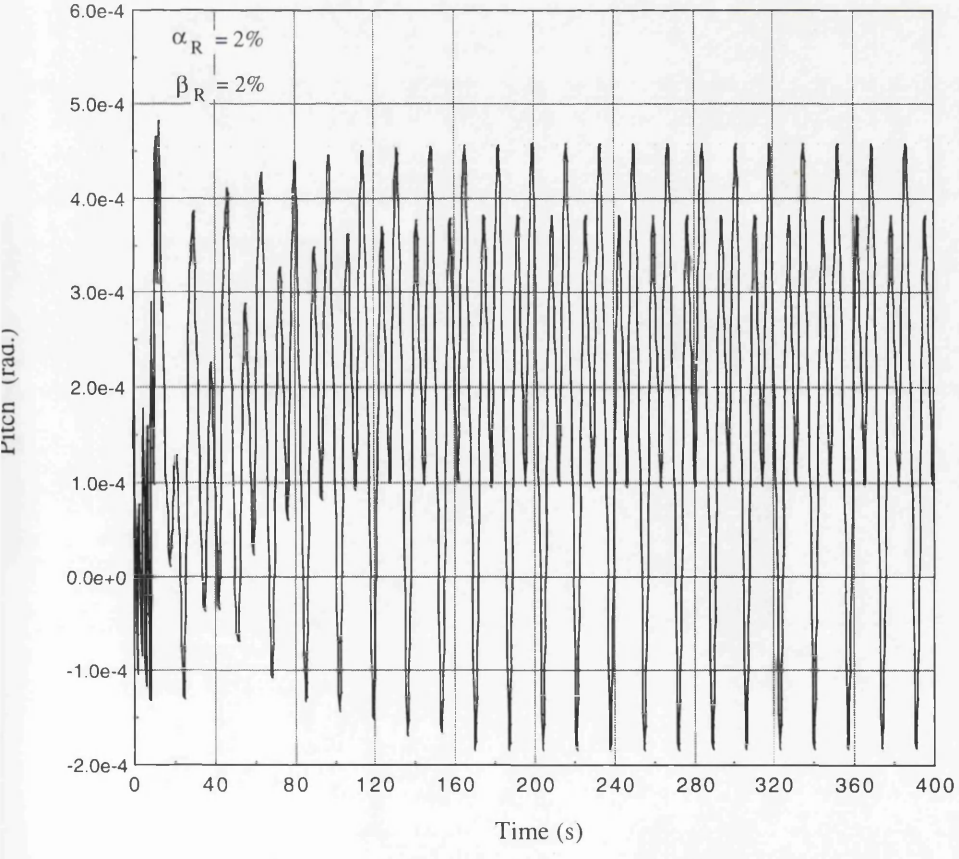

Fig. 4.73. Pitch Response of Model_3 under all Environmental Forces

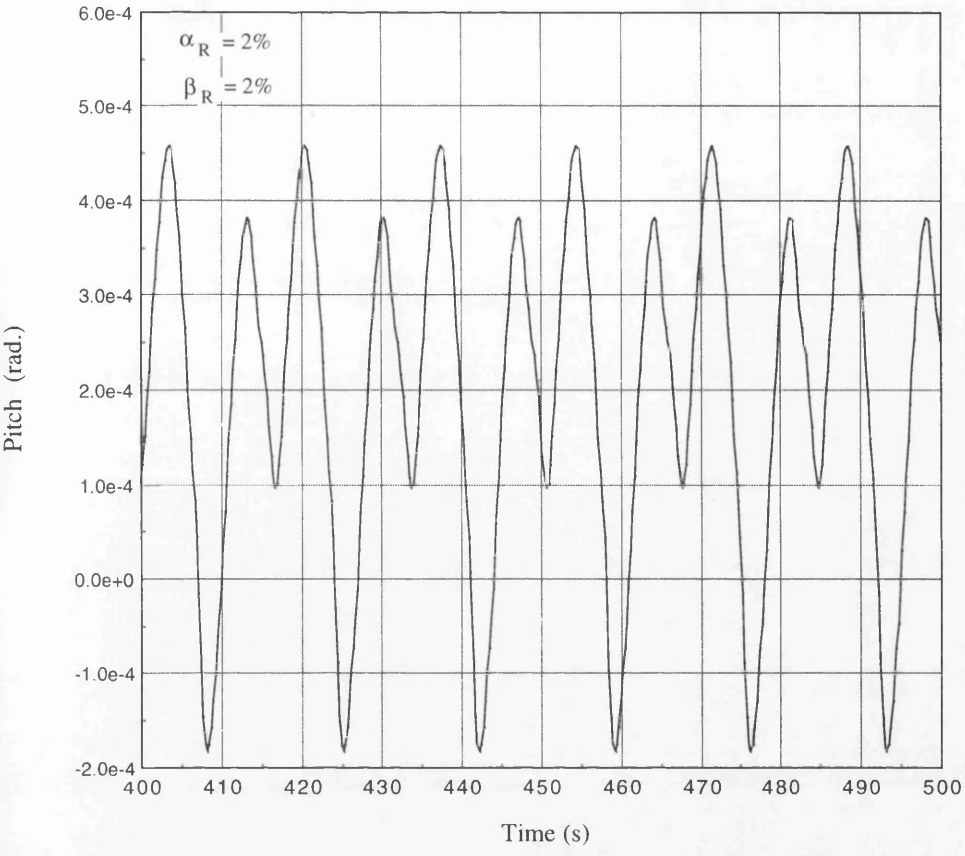

Fig. 4.74. Steady Pitch Response of Model_3 under all Environmental Forces

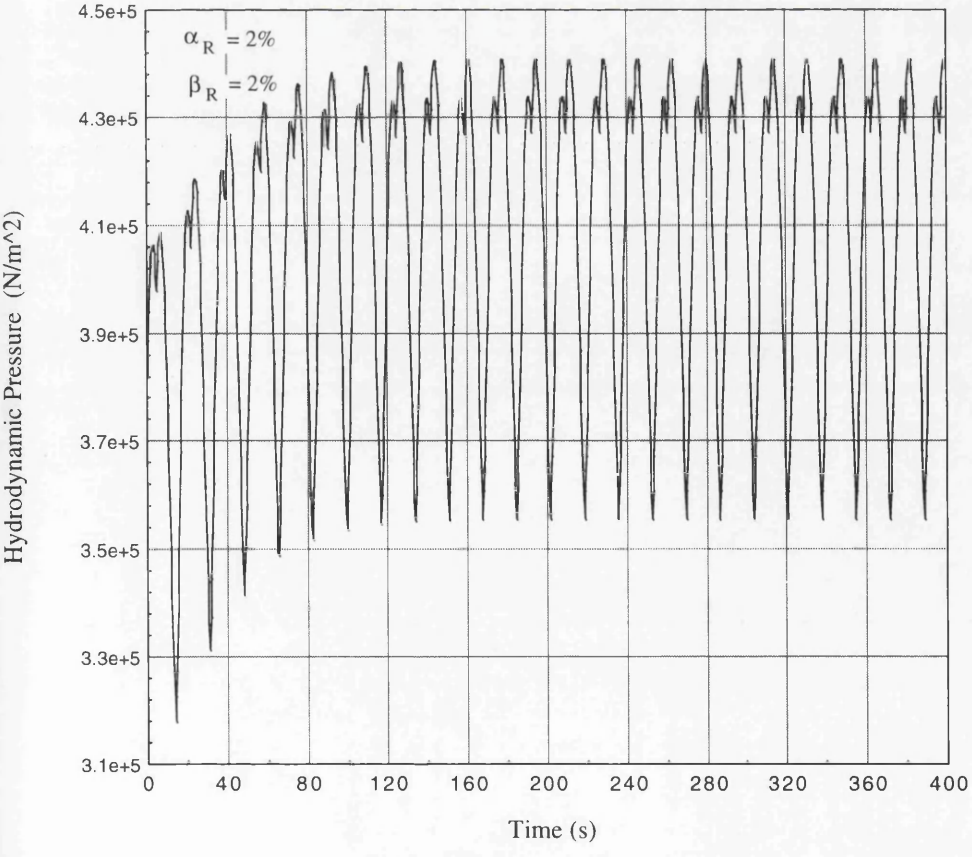

Fig. 4.75. Maximum Hydrodynamic Pressure on Columns of Model_3

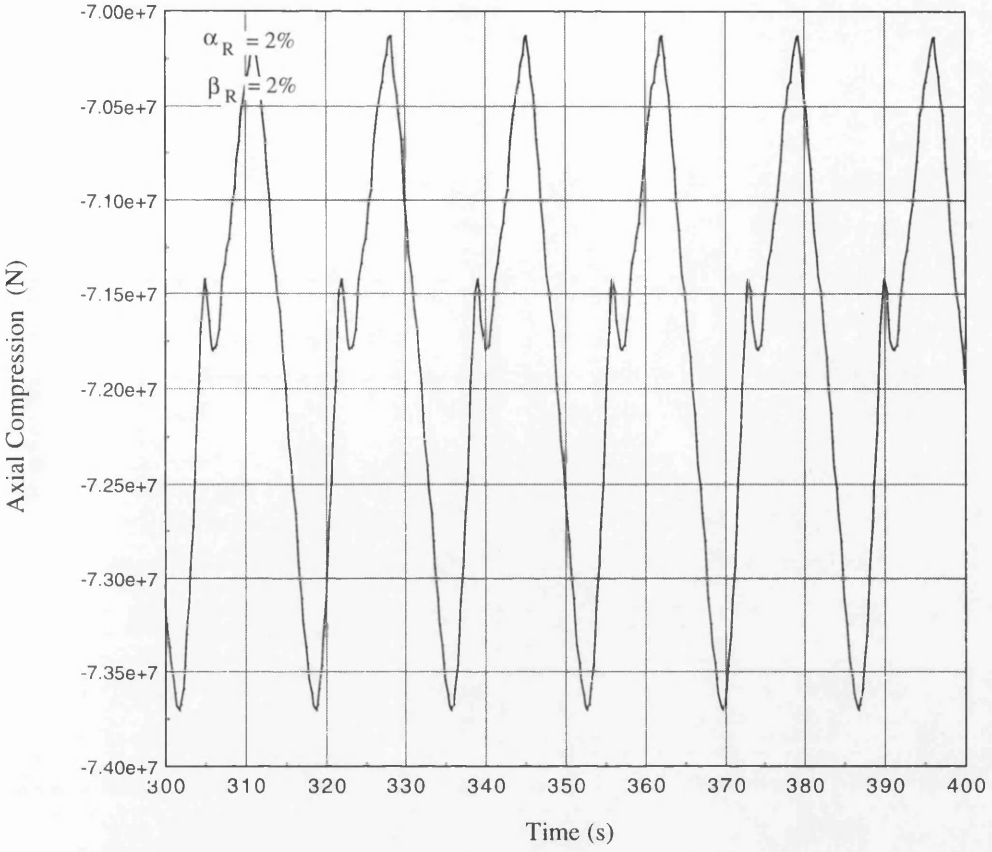

Fig. 4.76. Maximum Axial Compression in Model_3 Column Elements in Steady State Motion

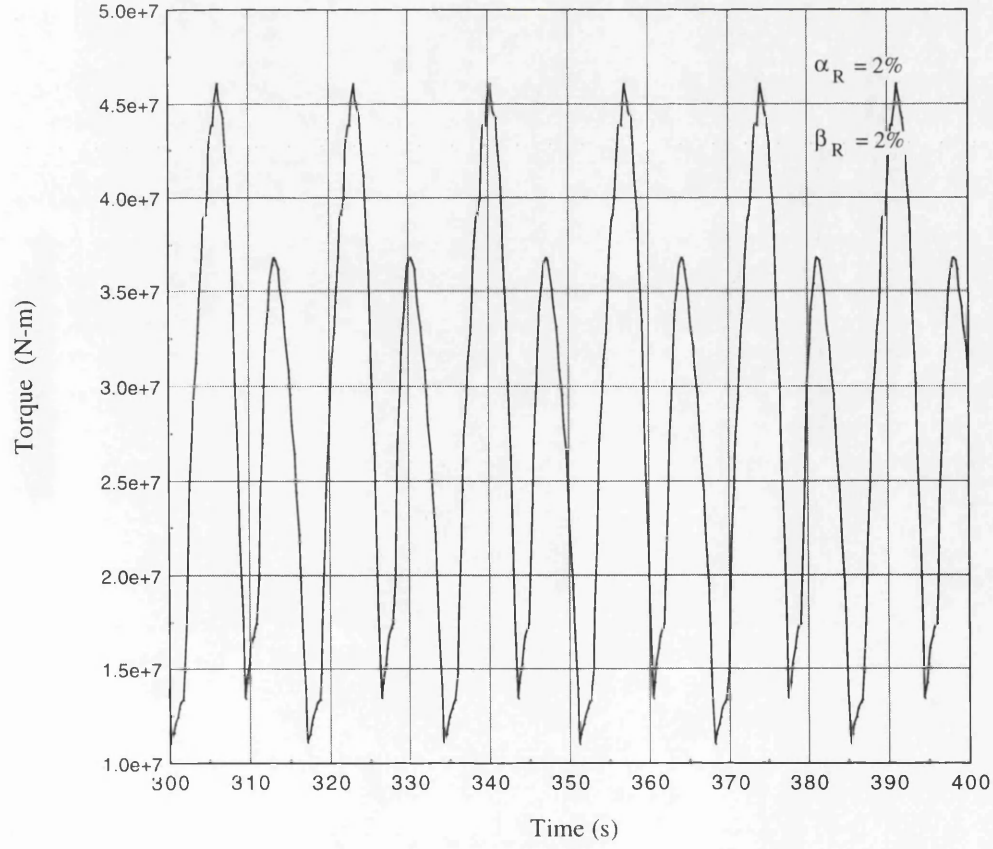

Fig. 4.77. Maximum Torsion in Model_3 Column Elements in Steady State Motion

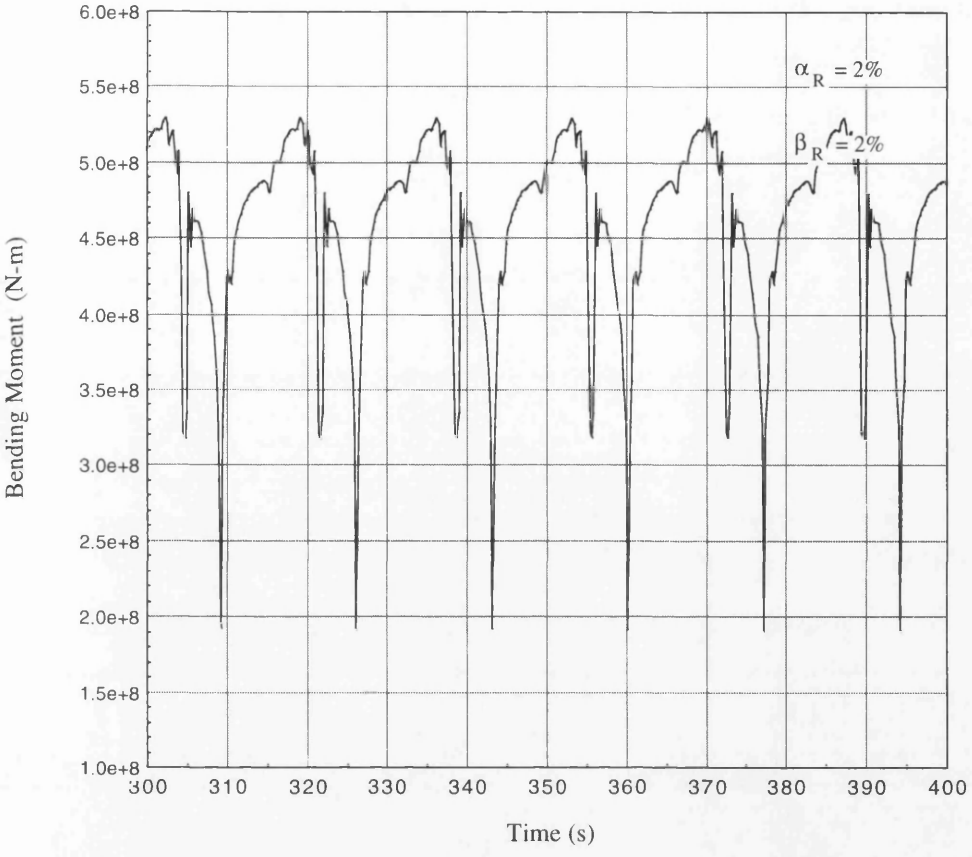

Fig. 4.78. Maximum Bending Moment about Local z Axis in Model_3 Column Elements

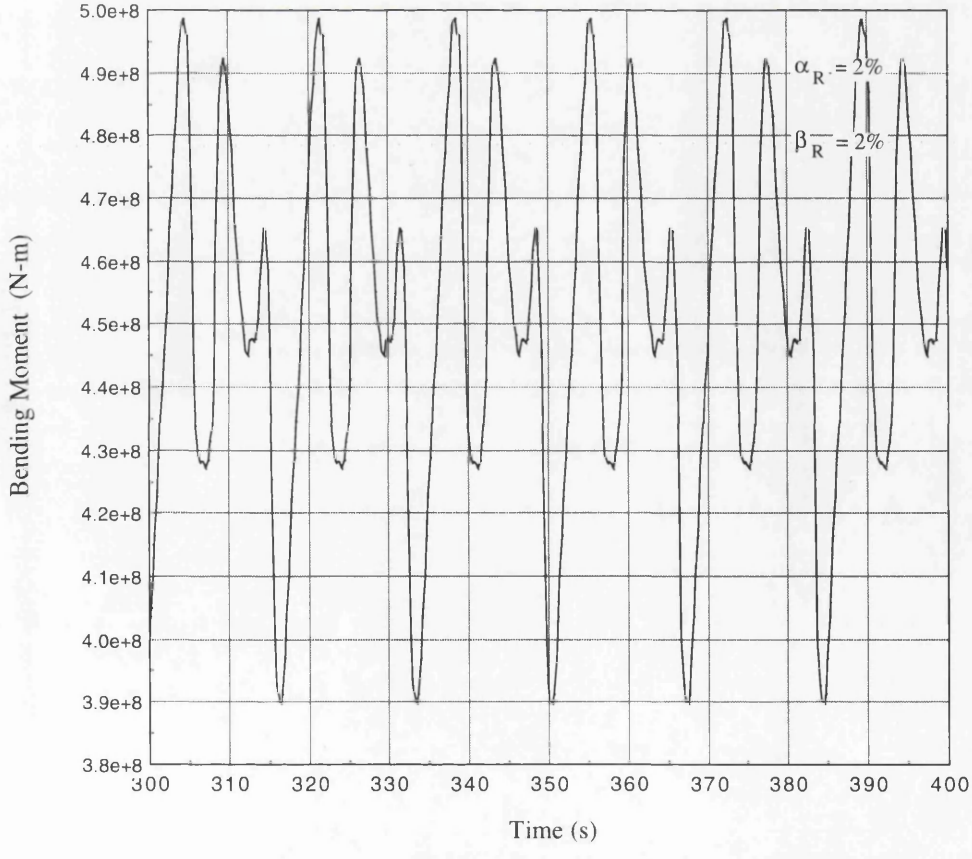

Fig. 4.79. Maximum Bending Moment about Local y Axis in Model_3 Column Elements

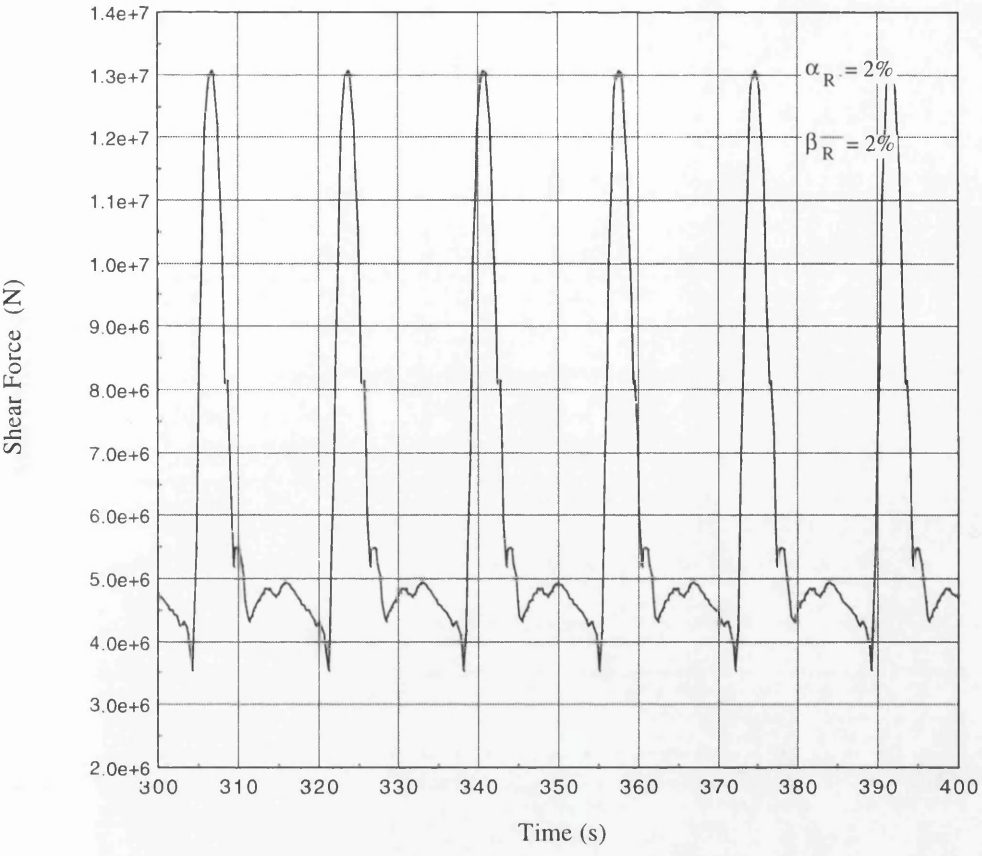

Fig. 4.80. Maximum Shear Force in Local y Direction in Model_3 Column Elements

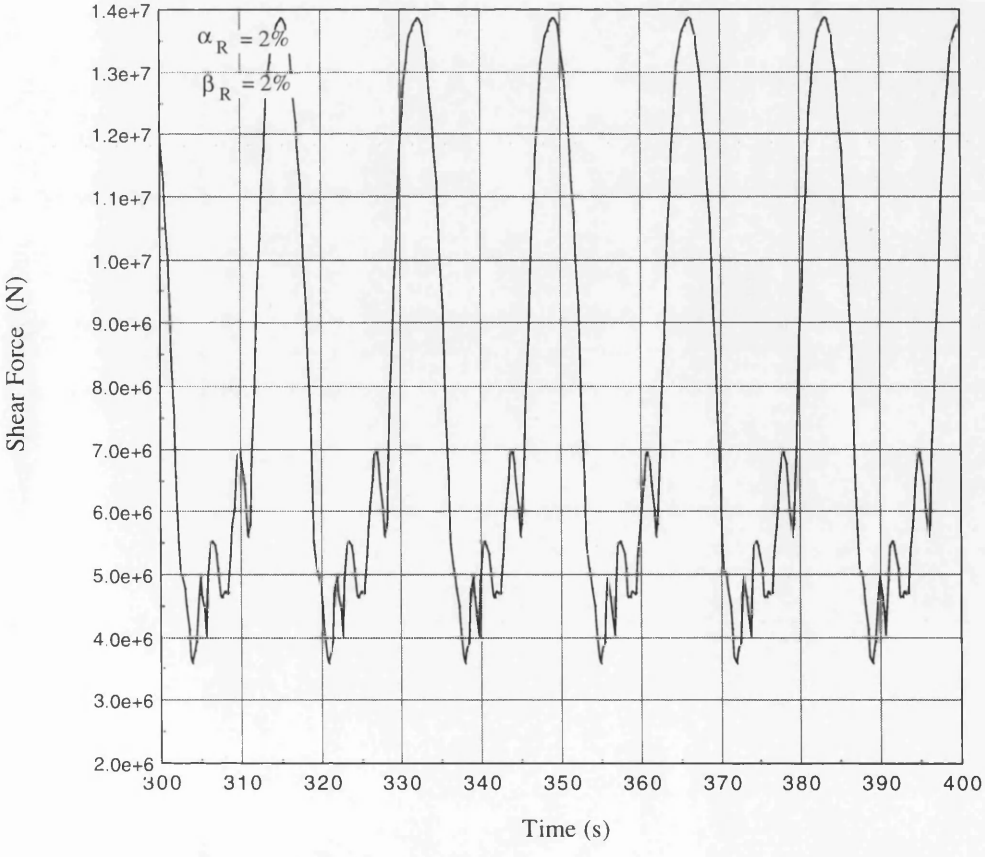

Fig. 4.81. Maximum Shear Force in Local z Direction in Model_3 Column Elements

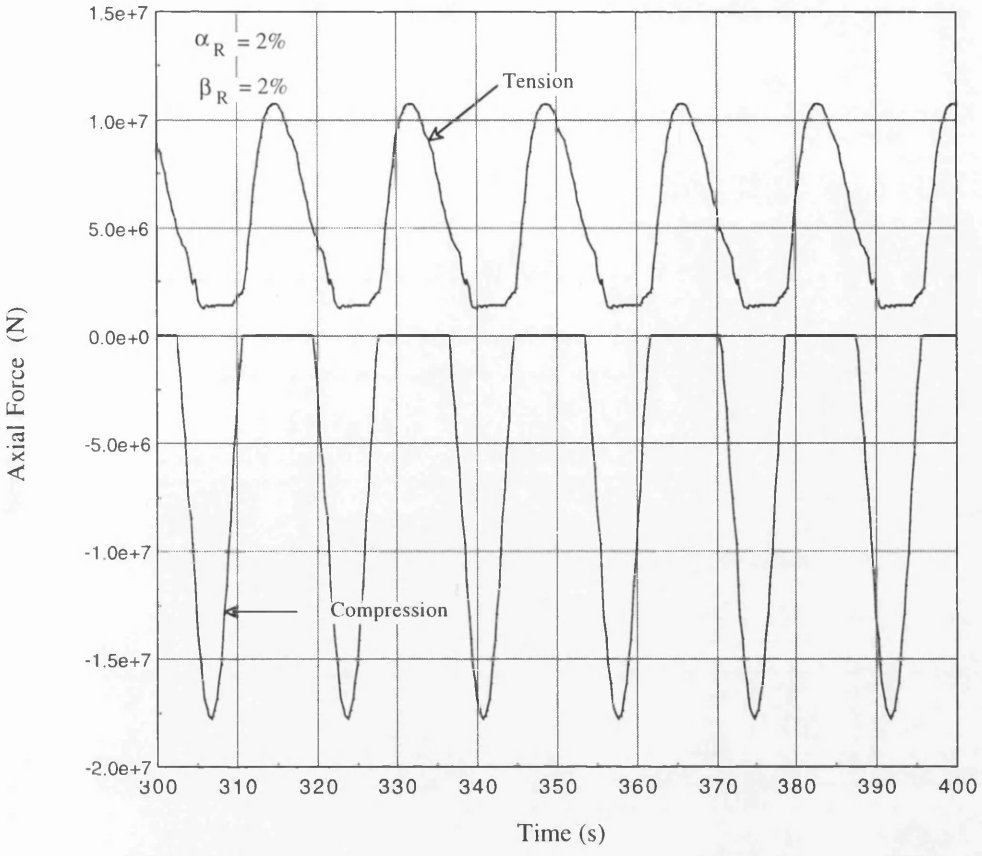

Fig. 4.82. Maximum Axial Tension and Compression in Model_3 Pontoon Elements

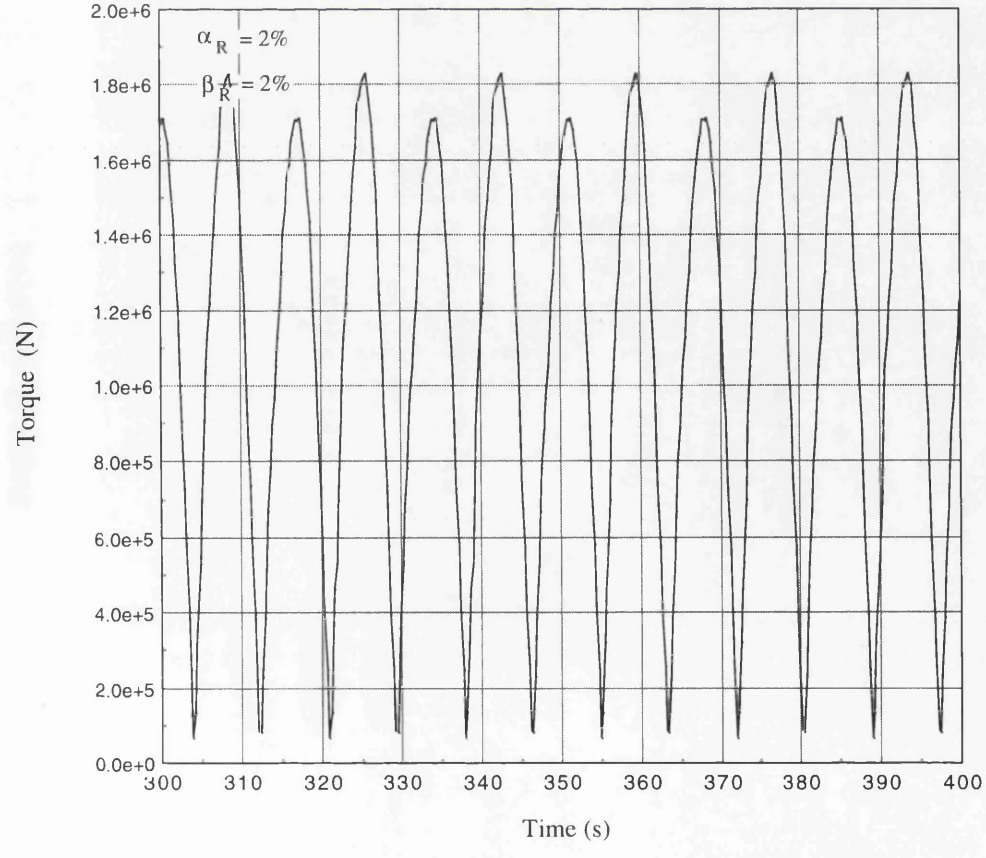

Fig. 4.83. Maximum Torsion in Model_3 Pontoon Elements in Steady State Motion

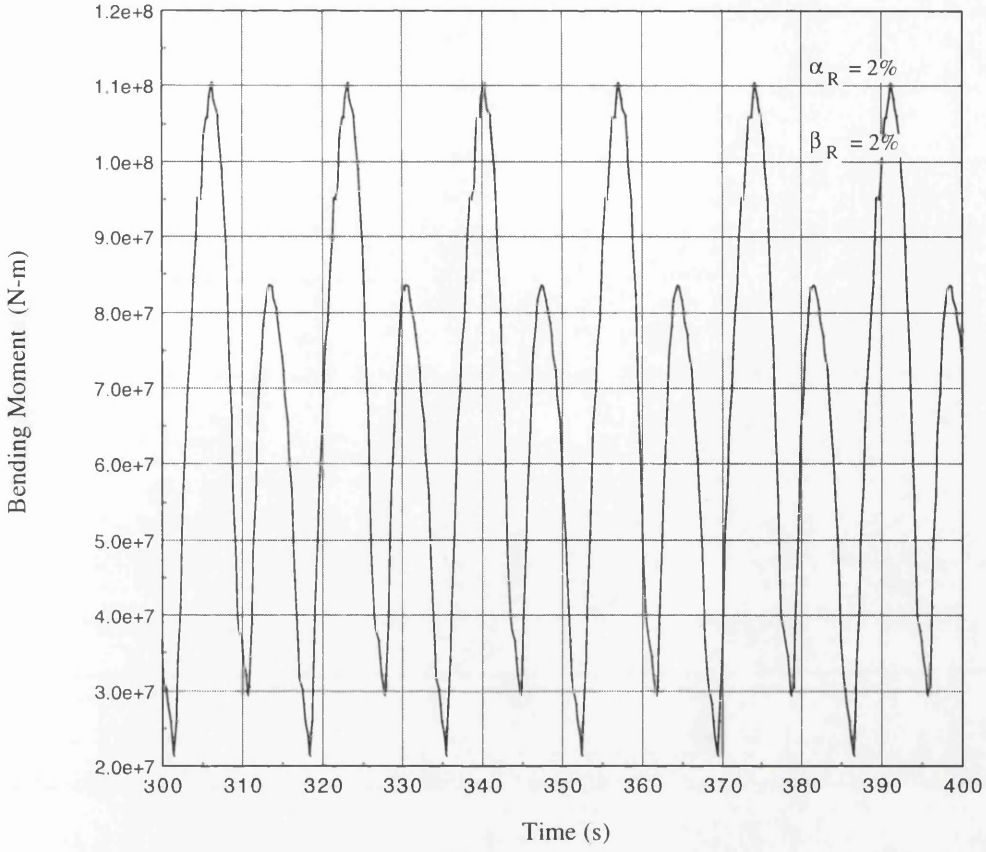

Fig. 4.84. Maximum Bending Moment about Local z Axis in Model_3 Pontoon Elements

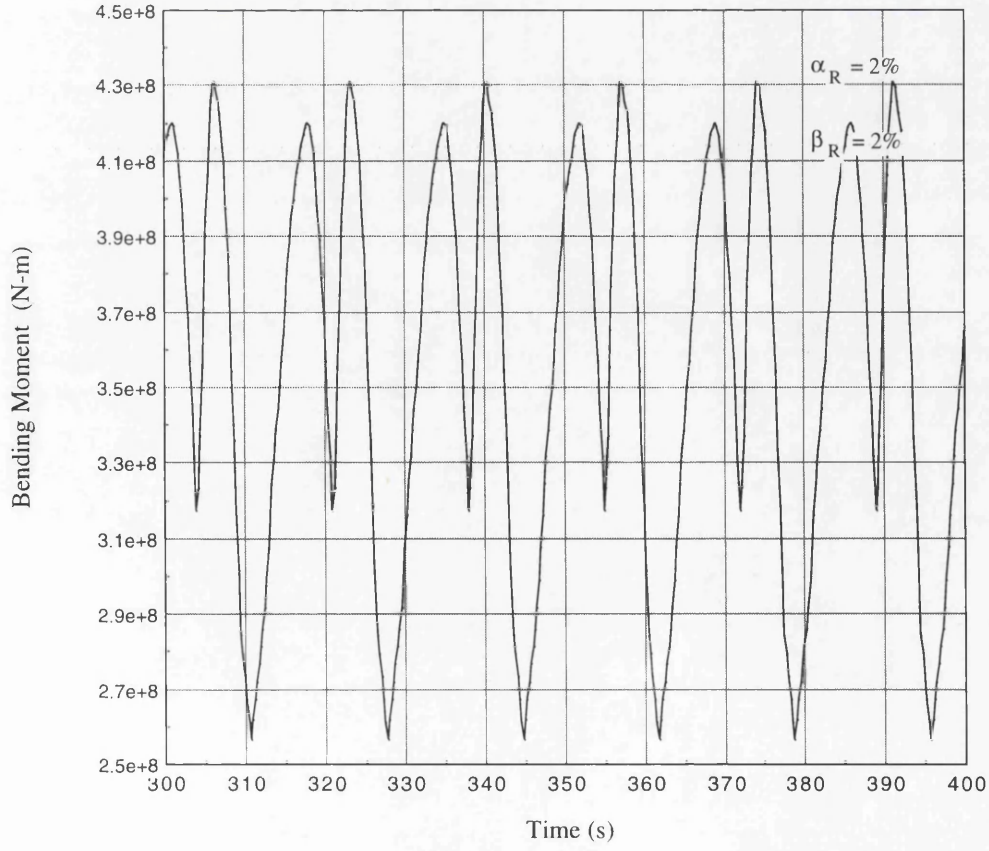

Fig. 4.85. Maximum Bending Moment about Local y Axis in Model_3 Pontoon Elements

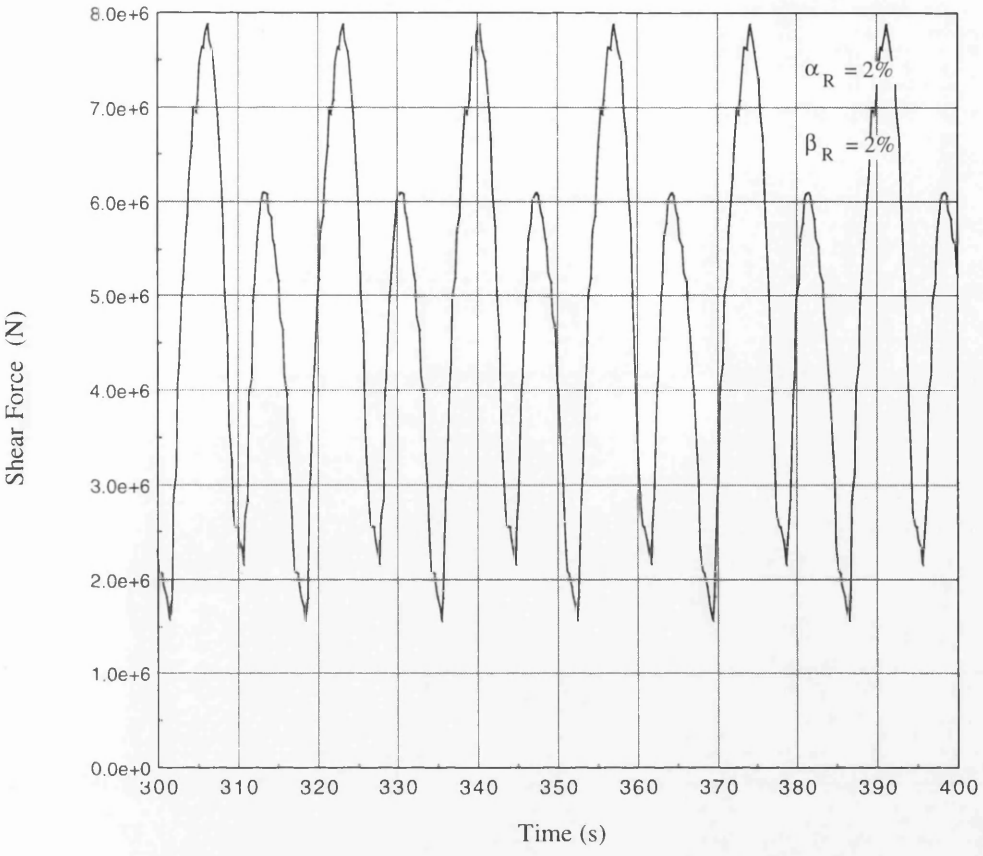

Fig. 4.86. Maximum Shear Force in Local y Direction in Model_3 Pontoon Elements

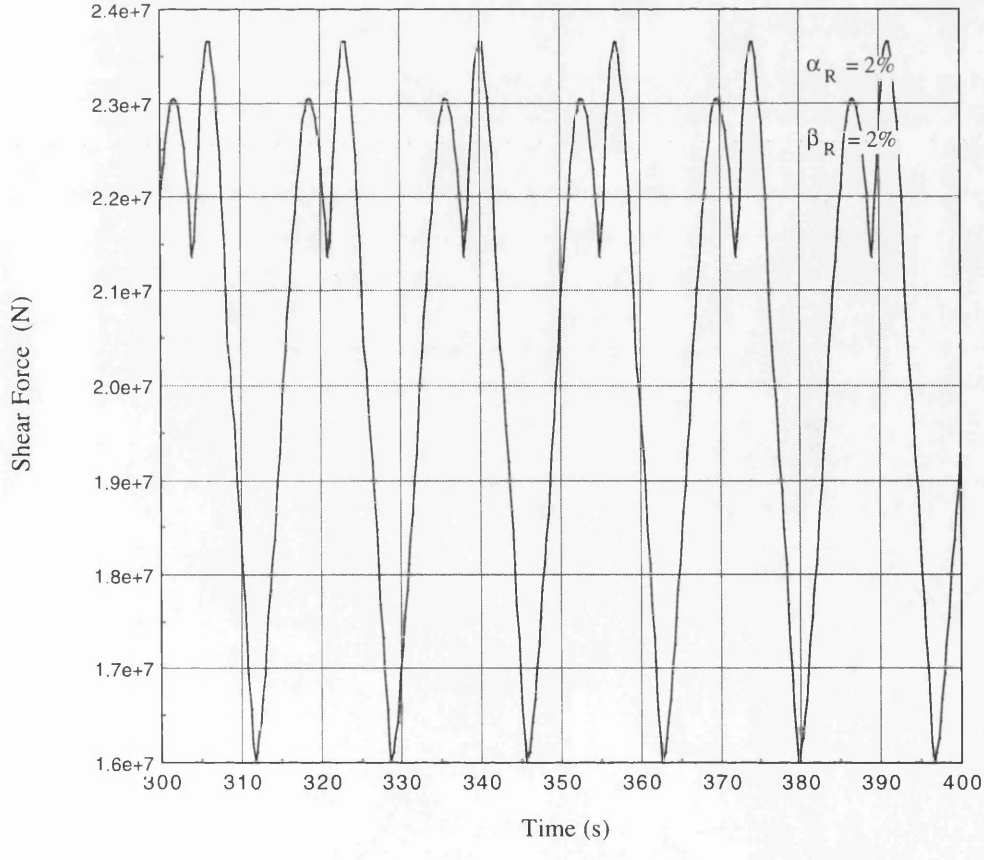

Fig. 4.87. Maximum Shear Force in Local z Direction in Model_3 Pontoon Elements

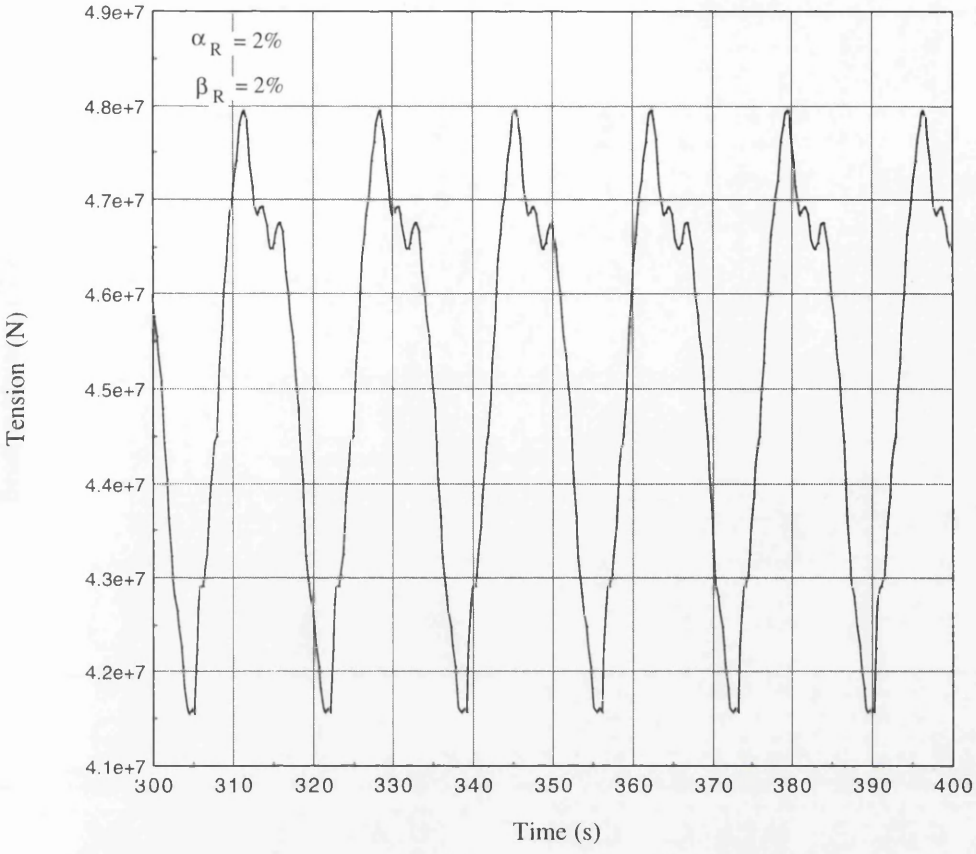

Fig. 4.88. Maximum Tension in Equivalent Tether Elements of Model_3

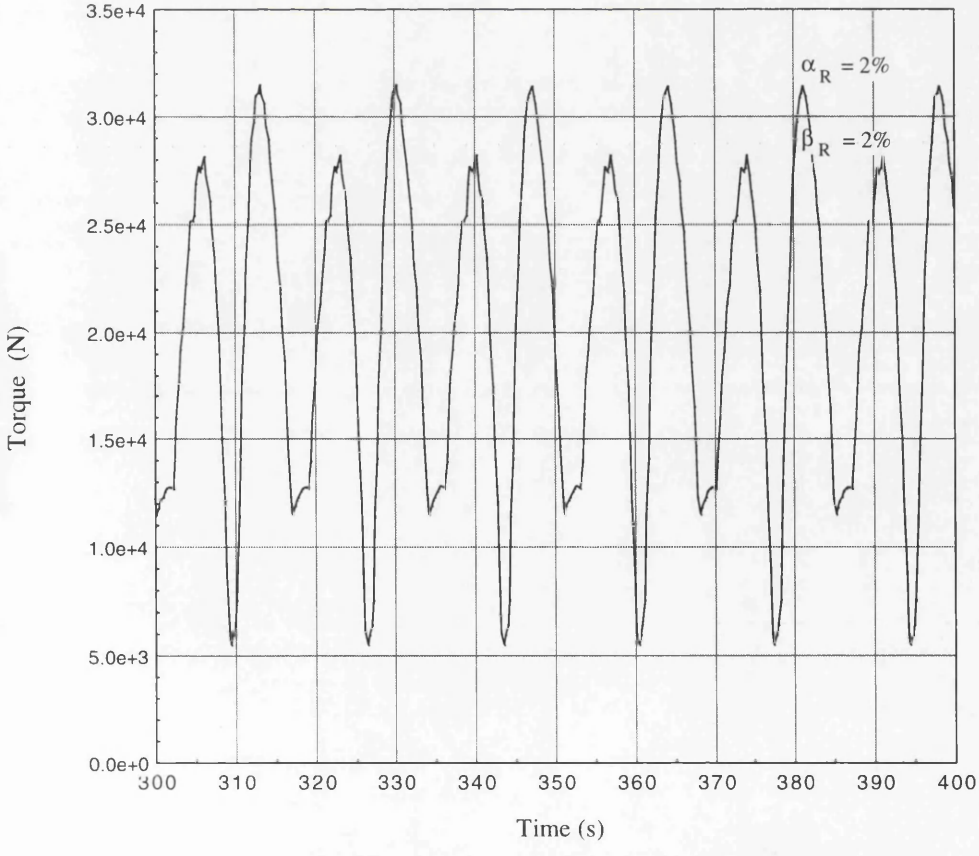

Fig. 4.89. Maximum Torsion in Equivalent Tether Elements of Model_3

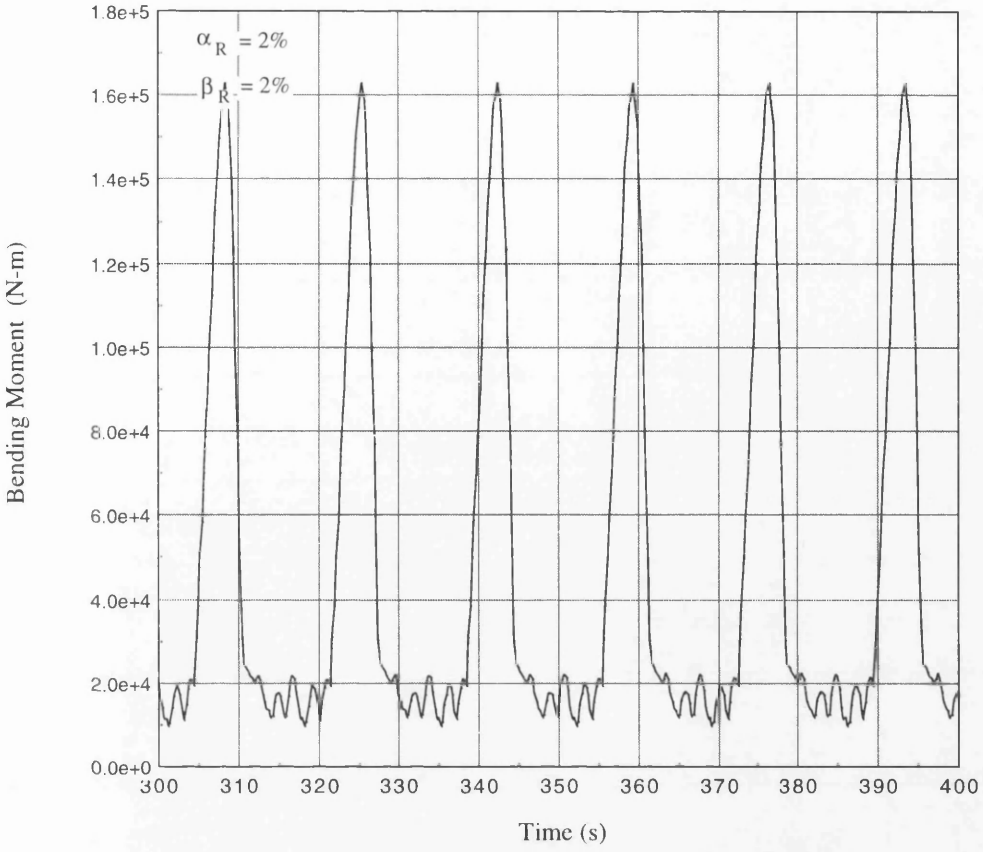

Fig. 4.90. Maximum Bending Moment about Local z Axis in Model_3 Equivalent Tethers

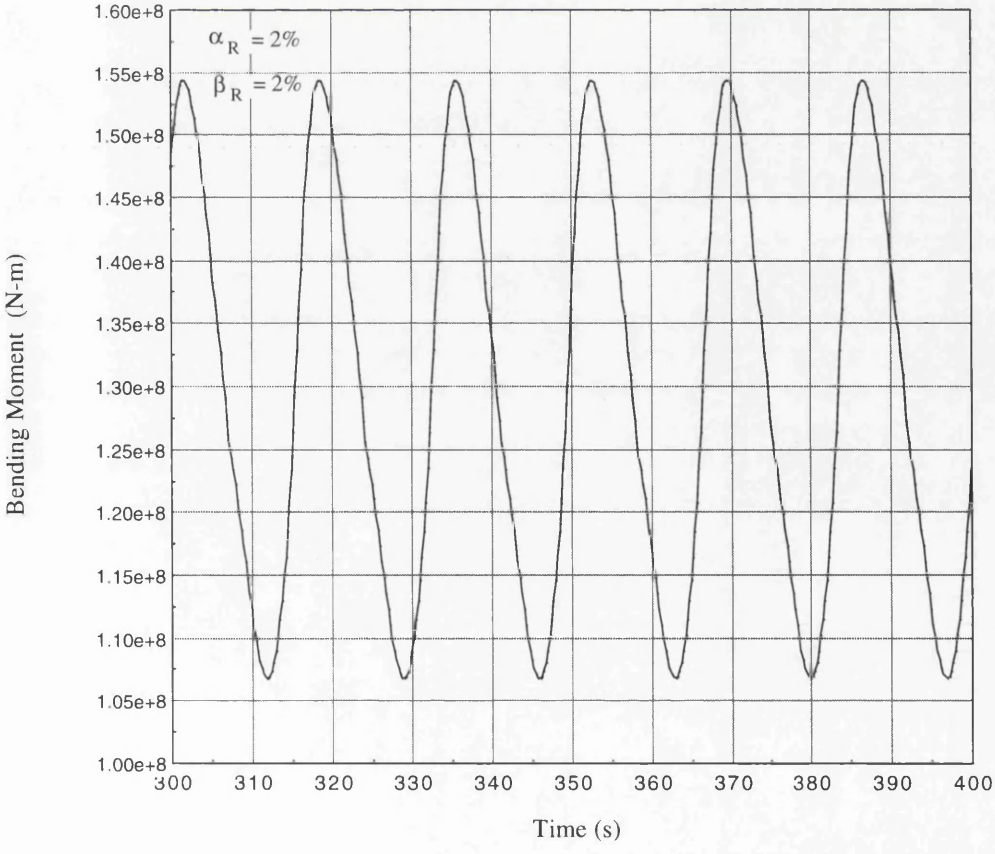

Fig. 4.91. Maximum Bending Moment about Local y Axis in Model_3 Equivalent Tethers

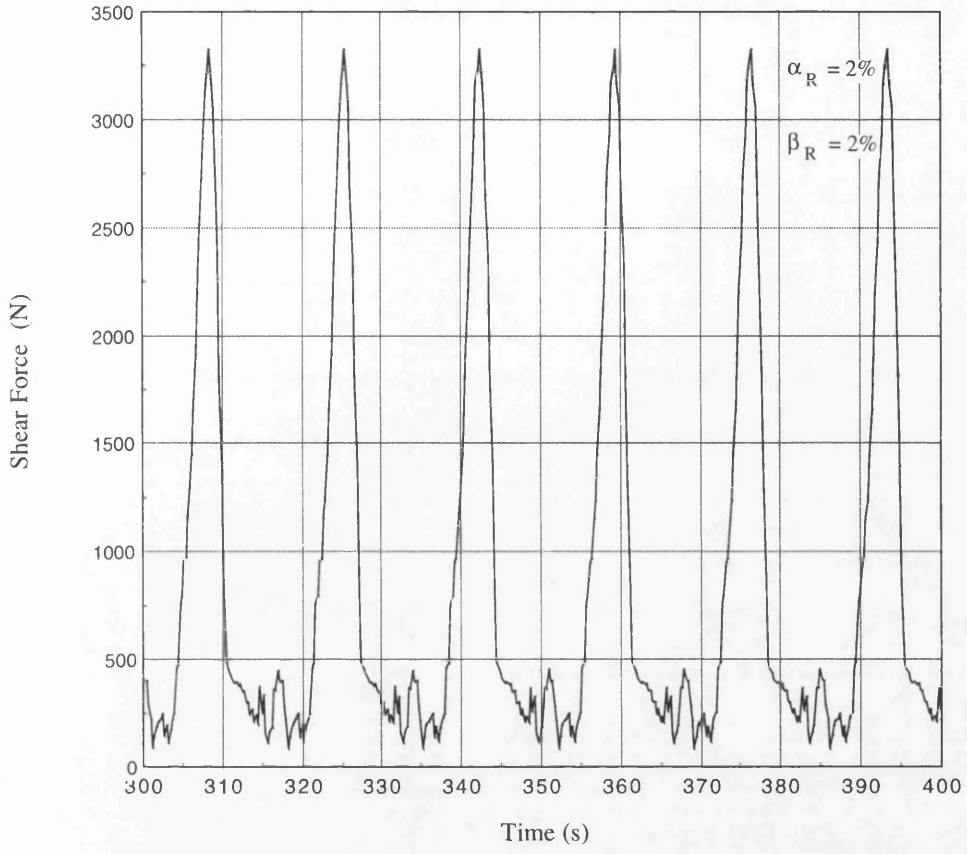

Fig. 4.92. Maximum Shear Force in Local y Direction in Model_3 Equivalent Tethers

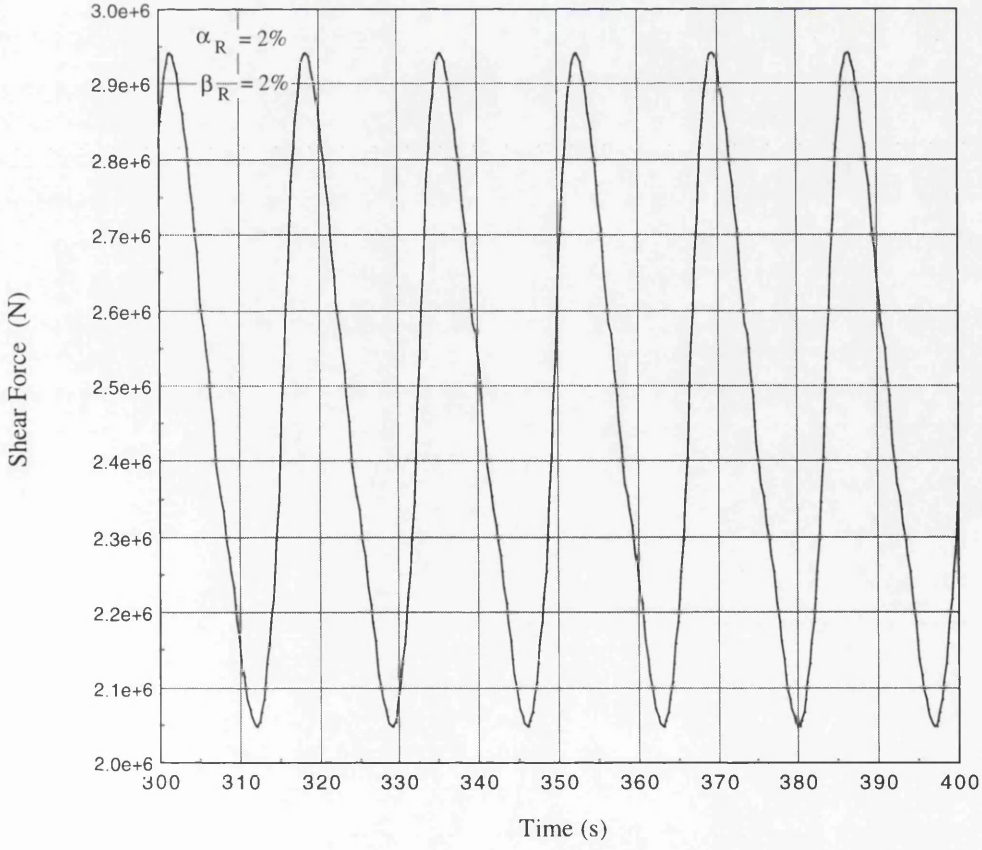

Fig. 4.93. Maximum Shear Force in Local z Direction in Model_3 Equivalent Tethers

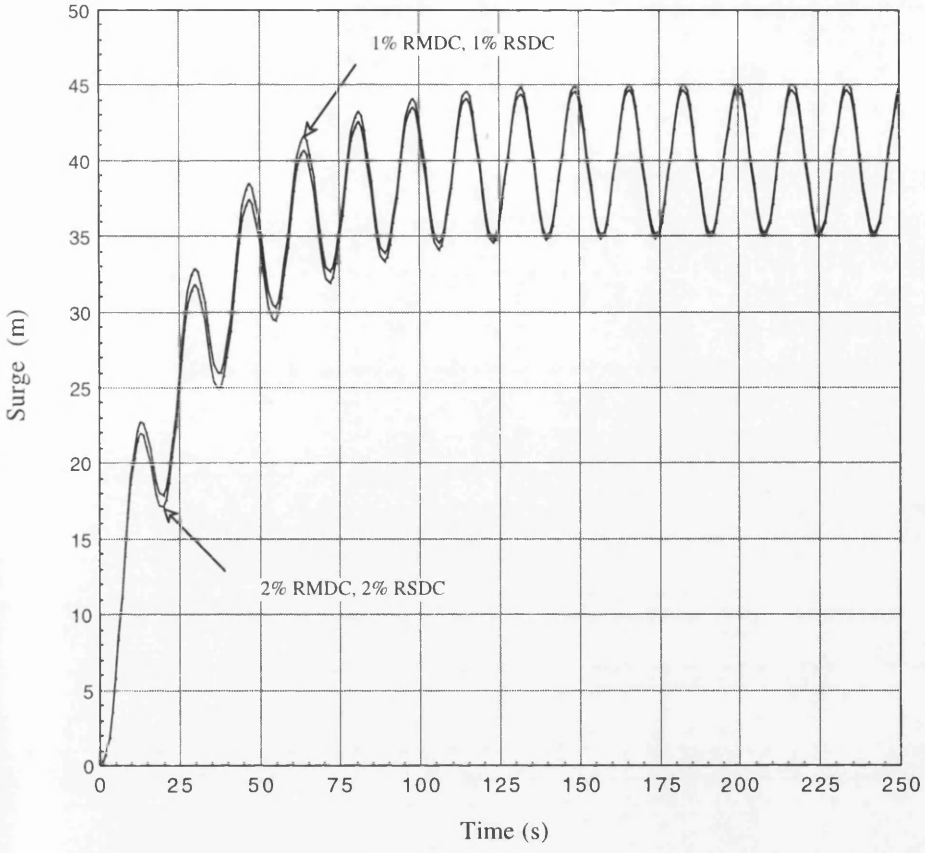

Fig. 4.94. Surge Response of Model_3 Compared with Different Damping Level

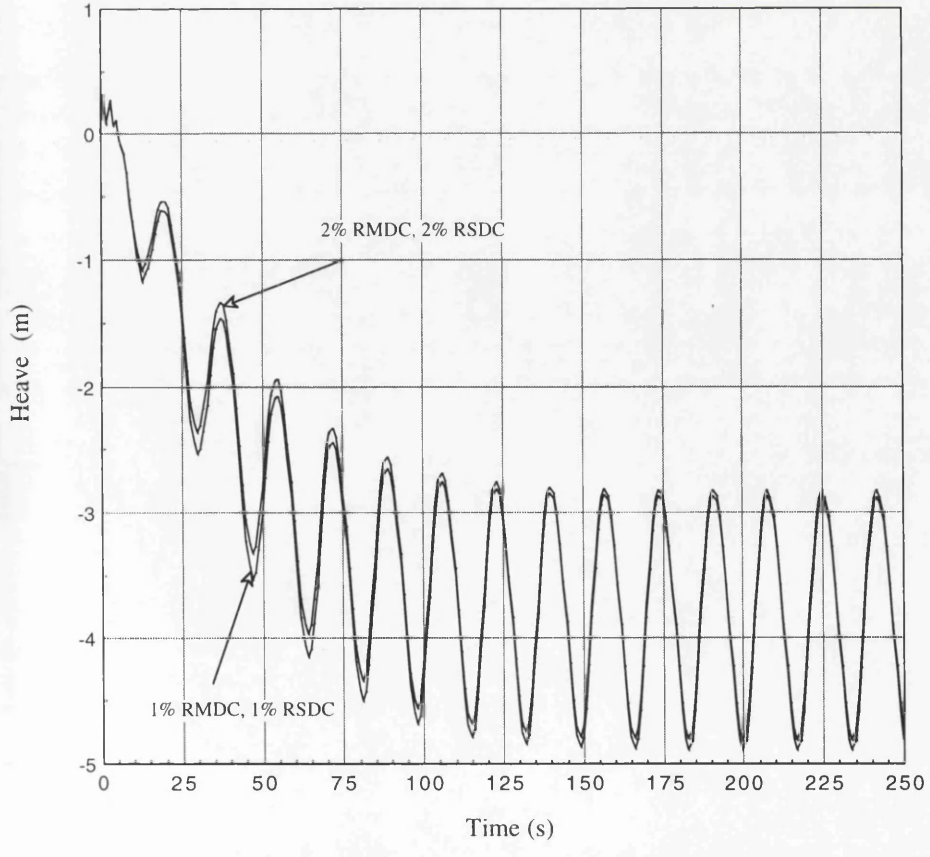

Fig. 4.95. Heave Response of Model_3 Compared with Different Damping Level

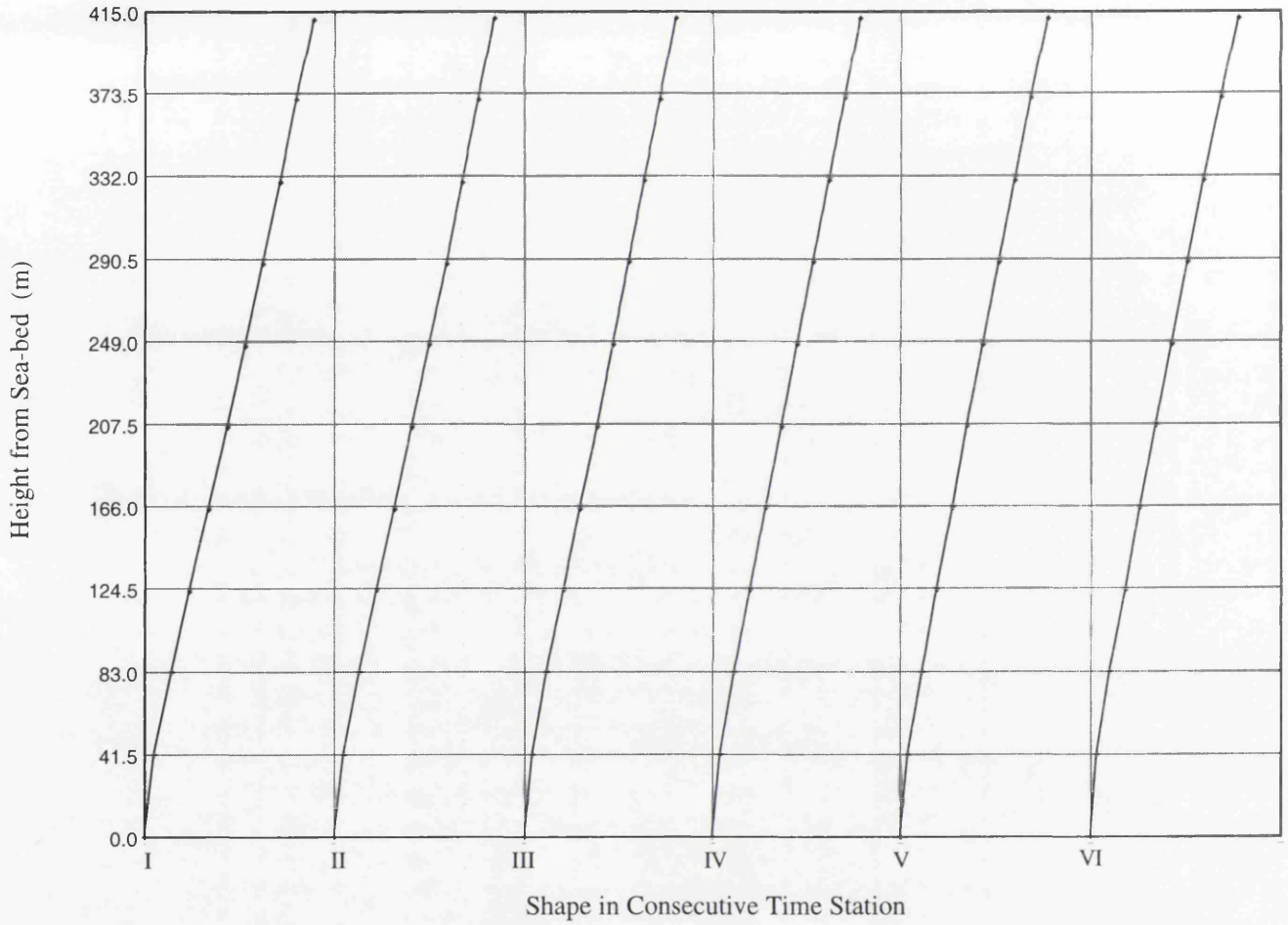

Fig. 4.96(a). Deflection Shape of One Equivalent Tether in Steady State Motion

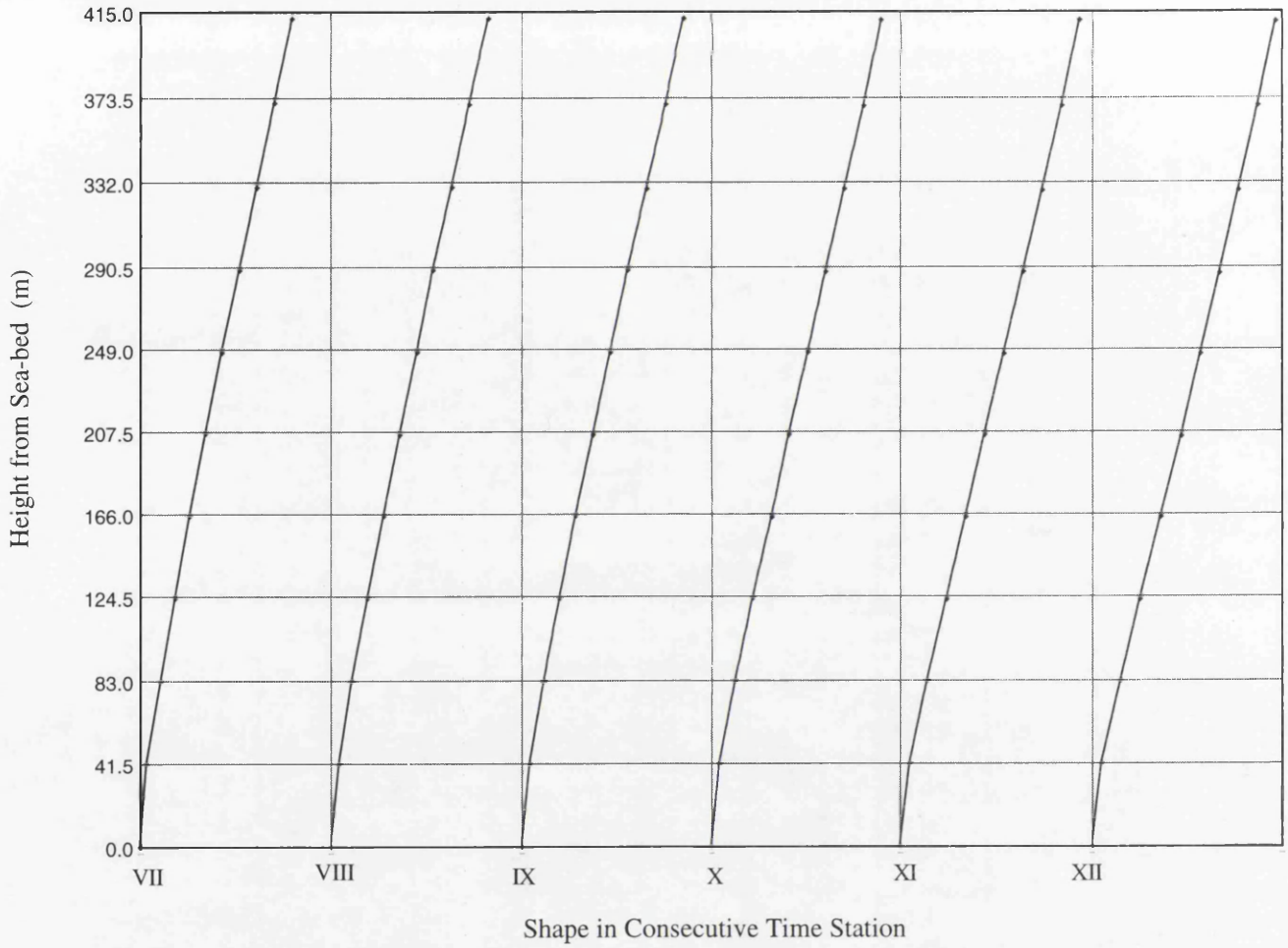

Fig. 4.96(b). Deflection Shape of One Equivalent Tether in Steady State Motion

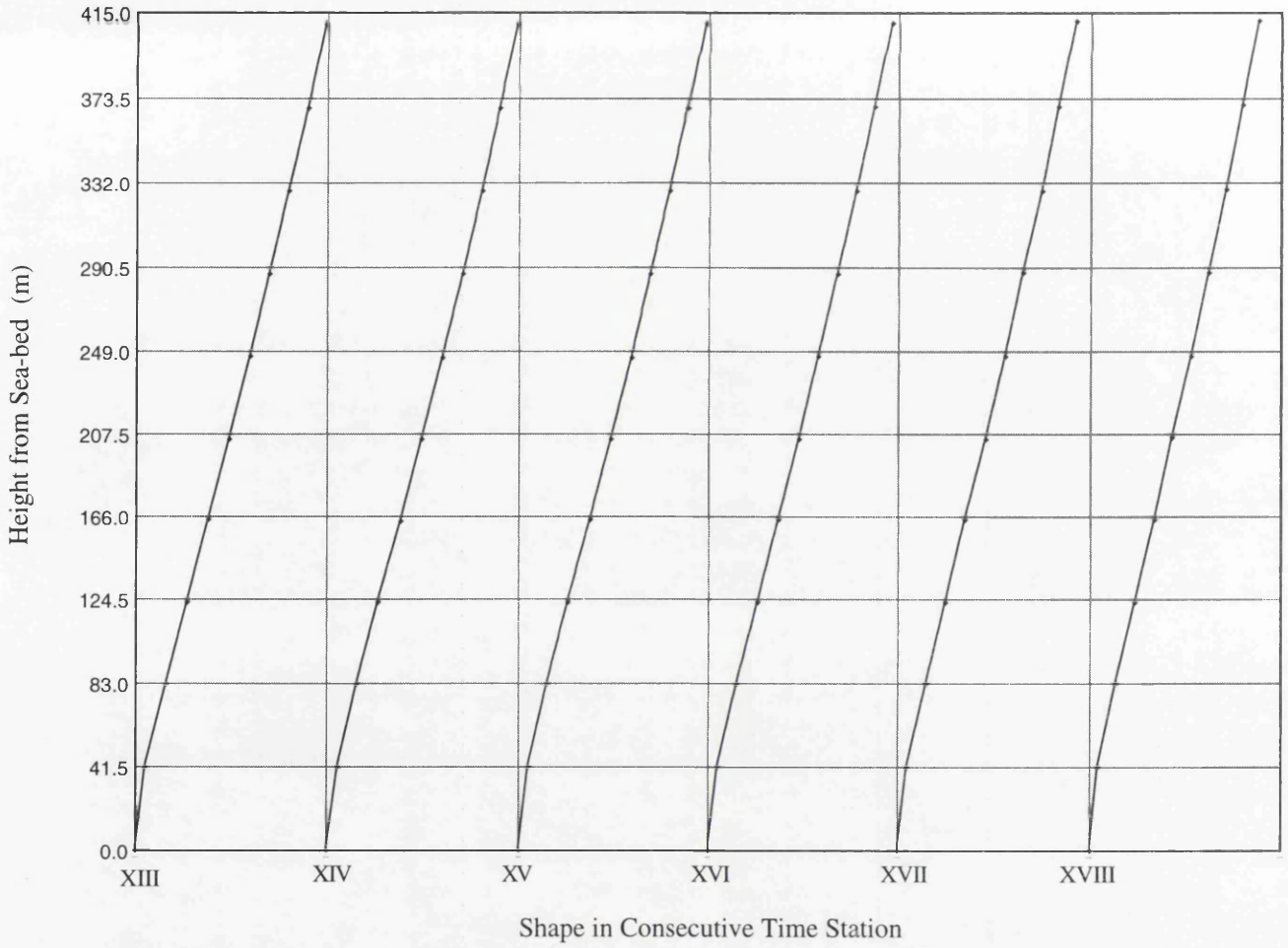

Fig. 4.96(c). Deflection Shape of One Equivalent Tether in Steady State Motion

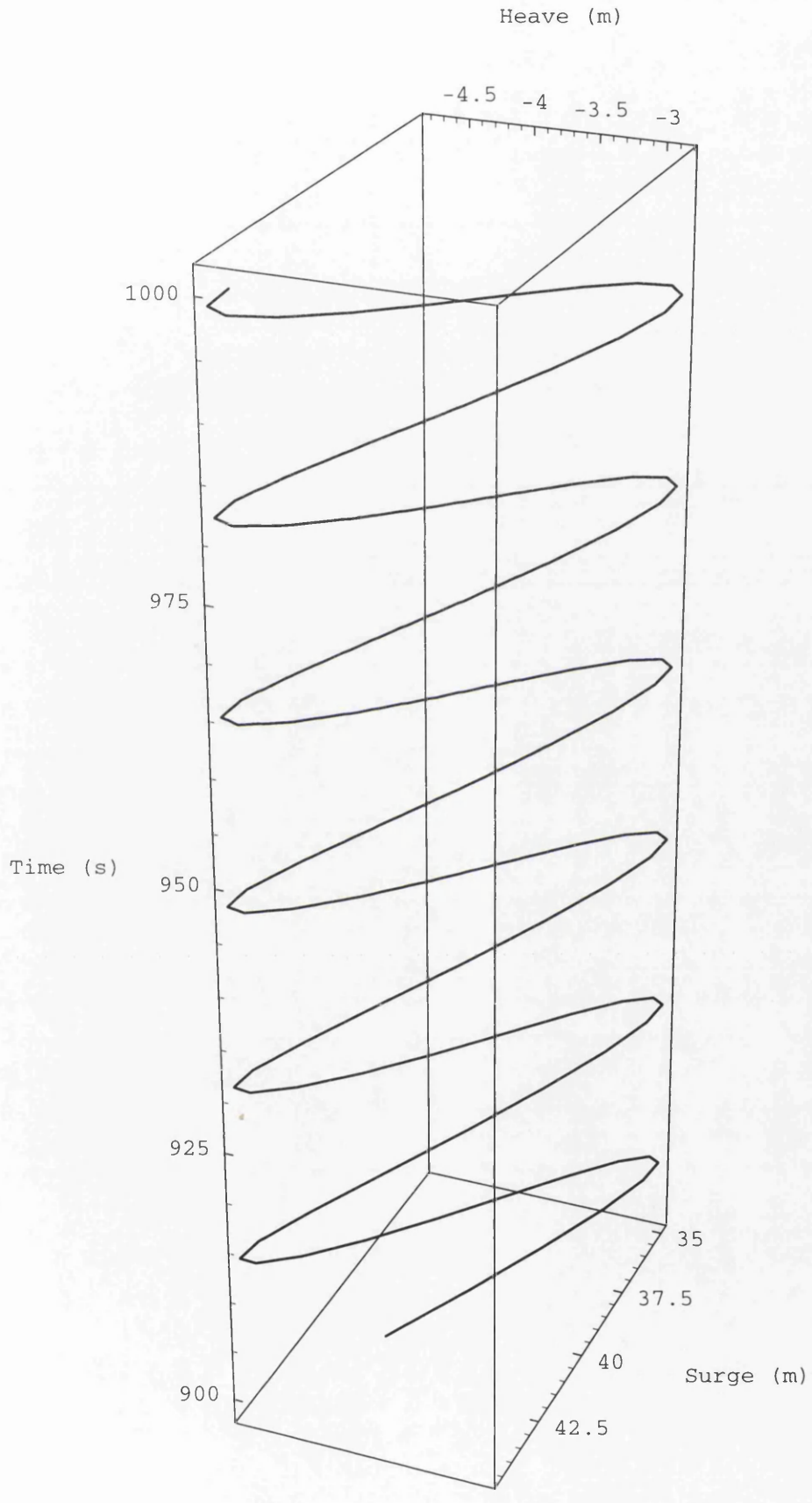

Fig. 4.97. Dynamic Relation Between Surge and Heave

CHAPTER 5

RELIABILITY ANALYSIS OF TLP COLUMNS

5.1 INTRODUCTION

This chapter presents some calculations necessary to utilise the results from dynamic analyses of TLPs done by the program DCATLP. DCATLP treats TLPs as coupled systems where the structural modelling involves 3-D beam and joint elements. But a TLP is a continuum structure rather than a framed one. Large diameter columns and pontoons of a TLP should be modelled with plate, shell and/or brick elements rather than 3-D beam elements. But an analysis involving plates, bricks or shells is often complex and time consuming, both to set up and run (see Chapter 6). Moreover, the calculations done by DCATLP with 3-D beam and joint elements are far from simple and the introduction of any other higher order element will bring additional complexities. Still it is also necessary to draw useful conclusions from the results produced by DCATLP so that they can help the design process.

There are two different ways to make use of the response results from DCATLP. The internal resisting forces calculated by DCATLP in elements of TLP members can be carefully used to define boundary loads with suitable support conditions in a local finite element analysis. The local analysis with the boundary loads from DCATLP would be of very general nature because the especial TLP characteristics would no longer be present. A local FE problem of such type can be solved by a general purpose software such as LUSAS, ABAQUS and others. The analysis may utilise powerful features of such packages by using higher order advanced elements in non-linear environments.

A reliability based assessment is another way to use DCATLP results in TLP design. This report shows an example where the design of the ISSC TLP [5.13], [5.15] corner columns is assessed based on probabilistic safety level measure in terms of a reliability or safety index, β which is directly related to the risk of buckling failure of the columns in the bay instability mode. The reliability index explicitly accounts for possible variability or uncertainty in the strength and load parameters. This chapter presents the calculations done by a program, BCCNNV (Beta Calculation of Correlated Non-Normal Variables). The source code is based on the well known Advanced First Order Second Moment (AFOSM) method where the expansion of the failure surface is carried at the 'design point'.

It has been explained earlier in Section 4.5.10 that DCATLP calculates internal resisting forces for each element in a specific group for all time stations. The groups are defined before the analysis starts. For example, a group may include all beam elements representing all corner columns. Otherwise, a group may consist of only a few elements where higher values of internal forces are expected. This internal resisting

force calculation is done only once in a time station and that is after achieving the required convergence. Figs. 4.75-4.81 (see also Ref. [5.4]), represent maximum axial compression, torsion, shear forces, bending moments and hydrodynamic pressure on columns of the ISSC TLP. The next section describes how these graphs can help us in calculating load effects appropriate for limit state functions defined according to API Bulletin 2U [5.2] and TLP Rule Case Committee Model Code [5.5].

5.2 LONGITUDINAL AND HOOP STRESSES

Figs. 4.75-4.81 are based on a particular load case which represents a peak storm event for the ISSC TLP. Instead of describing it as a load case it might be more appropriate if it is called a 'load set' because the environmental loading changes rapidly with time and DCATLP does account for this change. However, the load set in this context specifies wave height, period, wind and current speed at various water depths and corresponding heading angles. There might be several other worst combinations of the environmental parameters. In a reliability analysis, these possibilities are taken into account by assigning a coefficient of variation (COV) to the load effects. The strength variables of the structure such as thickness, yield stress etc. may have lower COV values because their distribution types and variations have been more or less established through extensive experiments in the past and do not in general involve as much uncertainty as in the case of environmental load effects. The distribution types and variations of environmental load effects are less known.

To calculate the mean longitudinal and hoop stresses for reliability calculations, the maximum values of forces, moments and pressure are selected from Figs. 4.75-4.81. These maximum values, shown in Table 5.1 are time independent and refer to the particular load set considered in Chapter 4. The selection of maximum time varying loads on the TLP columns in a peak storm event for calculating mean applied stresses may sound very conservative. According to the TLP Rule Case Committee [5.5], for practical purposes the mean of the load-effect variables refers to their extrema. But non-simultaneous occurrence of the load effect extreme values should be accounted for. But here simultaneous occurrence of load effects is assumed and appropriate small COV values can be later on assigned to the applied stresses calculated from the load effects. However, there are some other reasons behind this selection. We are interested in the ultimate buckling failure of TLP columns. Perhaps in other modes of failure (e.g. fatigue) the forces, moments and pressure values should not be selected from the extreme values. Secondly, we would like to avoid computations with other load sets for the selection of applied stresses.

The stresses in stiffened cylindrical shells will differ from the membrane stress in unstiffened shells because of the load sharing effects of the stiffeners. In this report, the stress calculation from load effects mainly follows the instructions in API Bulletin 2U [5.2]. However, two limit state functions for combined loading are taken from API and the RCC Model Code. The limit state functions are used in the reliability calculation where the total longitudinal and hoop stresses are given as input.

Table 5.1. Maximum Values of Forces, Moments and Hydrodynamic Pressure on ISSC TLP Columns

Description	Symbol	Magnitude
Axial compression	P_{af}	73.71 MN
Torsion	P_{tq}	46.02 MNm
Bending moment about local z axis	P_{bmz}	529.3 MNm
Bending moment about local y axis	P_{bmy}	498.8 MNm
Shear force in local y direction	P_{sfy}	13.06 MN
Shear force in local z direction	P_{sfz}	13.86 MN
Hydrodynamic pressure	p_d	0.4406 MPa

For axial and bending stresses, the effective cross-sectional area of the column is important. If the stringers are not spaced sufficiently close to make the shell fully effective then the effective area should be used instead of the actual cross-sectional area. The factor Q_a is a ratio of the effective area to the actual area:

$$Q_a = \frac{A_s + b_e t_s}{A_s + b_a t_s} \tag{5.1}$$

$$A = 2\pi R_{cl} t_s + N_s A_s \tag{5.2}$$

The total cross-sectional area of the column is given in Eq.(5.2).

$$f_a = \frac{P_{af}}{Q_a A} \tag{5.3}$$

The section provides calculations in detail wherever possible for future discussions. The ISSC TLP columns have been designed in Chapter 4 very close to an optimum model in Ref. [5.5]. The Rule Case Committee considered their model as an illustrative example for the purpose of demonstrating the applications of their new code. Table 4.1 presents ISSC TLP column design from their optimum model.

Some parameters for the ISSC TLP columns:

$$A_s = 189*19 + 300*15 = 8091\ \text{mm}^2 \tag{5.4a}$$

$$A = 2\pi*(8440 - 25/2)*25 + 60*8091\ \text{mm}^2 = 1.8092\ \text{m}^2 \tag{5.4b}$$

$$b_a = 2\pi R_{cl}/N_s = 2\pi*(8440 - 25/2)/60 = 882.5\ \text{mm} \tag{5.4c}$$

b_e comes from a lengthy calculation and here it shows that the shell between adjacent stringers is not fully effective:

$$b_e = 684.4\ \text{mm} \tag{5.5}$$

The factor Q_a in Eq.(5.1):

$$Q_a = \frac{8091 + 684.4*25}{8091 + 882.5*25} = 0.835767 \tag{5.6}$$

Applied stress due to axial compression in Eq.(5.3):

$$f_a = \frac{73.7054}{0.835767*1.8092} = 48.74\ \text{MN/m}^2\ (\text{or N/mm}^2) \tag{5.7}$$

Now it is necessary to combine bending moments about their local y and z axes:

$$\text{Combined moment} = P_{bm} = \sqrt{P_{bmy}^2 + P_{bmz}^2} \tag{5.8}$$

Similar to Eq.(5.8):

$$\text{Combined shear} = P_{sf} = \sqrt{P_{sfz}^2 + P_{sfy}^2} \tag{5.9}$$

From Ref. [5.2]:

$$f_b = \frac{P_{bm}}{Q_a \pi R_{cl}^2 t_e} \tag{5.10a}$$

$$t_e = t_s + A_s/b_a = 25 + 8091/882.5 = 34.2\ \text{mm} \tag{5.10b}$$

$$\Rightarrow f_b = \frac{\sqrt{529.247^2 + 498.77^2}*10^9}{0.835767*\pi*8427.5^2*34.2} = 114.14\ \text{N/mm}^2 \tag{5.10c}$$

The main contribution to the total hoop stress comes from hydrodynamic pressure:

$$f_\theta = \frac{p_d R_o}{t_s} K_{\theta L} \tag{5.11}$$

For the column configuration in Table 4.1, $K_{\theta L} = 1$.

$$\Rightarrow f_\theta = \frac{0.440643*8440}{25} = 148.76\ \text{N/mm}^2 \tag{5.12}$$

To calculate shear stress and torsional stress, the shear area of the column cross-

section is required. It is not easy to find the shear area of a ring and stringer stiffened circular shell. Instead of approximating to the shear area by using some empirical formulae, it is calculated here by a program, CSSP in the VAS suite from BSRA. CSSP uses the shear flow theory to calculate torsional properties of complicated cross-sections. It has limited graphics output facilities [5.3] but no Graphical User Interface (GUI). It is essential to prepare a data file by hand according to CSSP's specification. But one shortcut route was identified during the preparation of data files for CSSP. Just like any finite element software, CSSP requires *node co-ordinates* and *element topology*. In fact, the main effort goes in the preparation of these two sections. So a simple interface program has been written to extract *node co-ordinates* and *element topology* from an incomplete LUSAS data file for writing them in a different format for CSSP. The flow chart in Fig. 5.1 explains it more clearly.

The results from the shear flow analysis are shown in Table 5.2. Some parameters have been already calculated (i.e. Case 1) in Chapter 4 for finite element calculations. The shear deformation effects in bending were neglected for maintaining compatibility between element mass and stiffness matrices. But in this section shear areas are essential for calculating shear stresses. A_{sy} and A_{sz} from Case 3 are used because they are based on better assumptions (i.e. closer to the actual structure than for Case 2). The model in Case 3 of Table 5.2 is shown in Fig. 5.2. If examined carefully it can be seen that the model in Fig. 5.2 has flat plates between adjacent stringers instead of a circular shell.

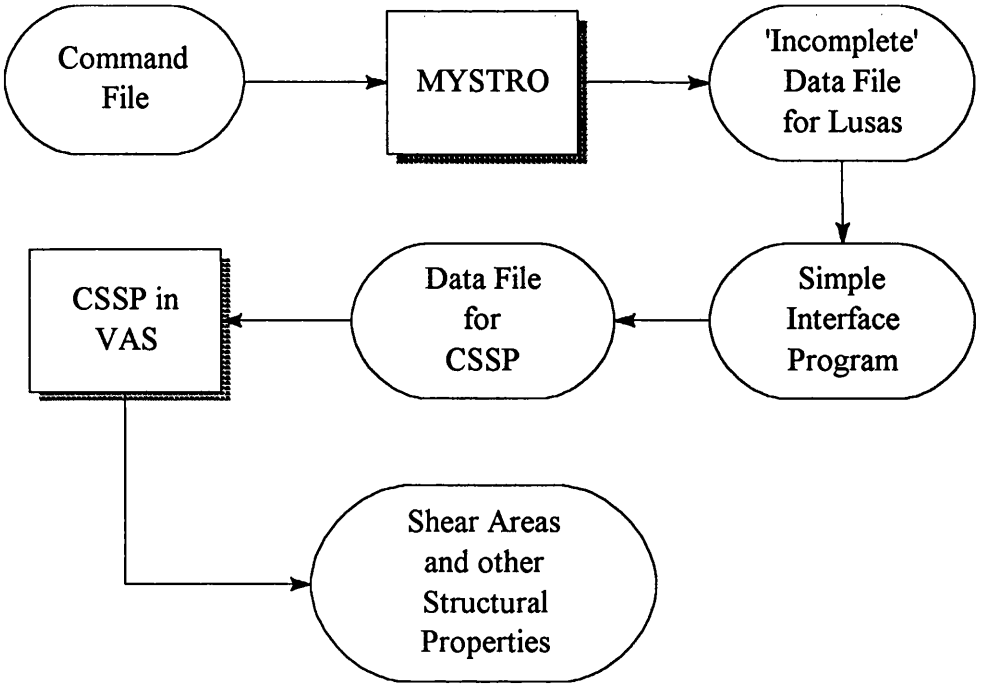

Fig. 5.1. Preparation of Data File for CSSP in VAS from BSRA

$$f_s = \frac{P_{sf}}{A_{sh}} = \frac{\sqrt{13.0589^2 + 13.8563^2}}{0.65261} = 29.18\ N/mm^2 \quad (5.13)$$

$$f_{tq} = \frac{P_{tq}R_o}{J_x} = \frac{46.017 * 8.44}{94.0194} = 4.13\ N/mm^2 \quad (5.14)$$

The total longitudinal and hoop stresses are calculated by summing the appropriate terms:

$$f_{long} = f_a + f_b = 48.74 + 114.14 = 162.88\ N/mm^2 \quad (5.15)$$

$$f_{hoop} = f_\theta + f_s + f_{tq} = 148.76 + 29.18 + 4.13 = 182.07\ N/mm^2 \quad (5.16)$$

The design variables together with their mean values, COVs and their distribution types are tabulated in Table 5.3. The distribution types and COVs are selected based on a similar study by Das et al [5.8]. The structural variables in Table 5.3 are random in nature but still their variations have been more or less established through many experiments. The variations in load effects in Table 5.1 are more difficult to verify. But as mentioned before, the longitudinal and hoop stresses in Table 5.3 may be assigned less COV values because they are calculated from the simultaneous occurrence of maximum load effects. But their COVs are varied from 5% to 20% to examine the change in reliability index.

Table 5.3. Design Variables for ISSC TLP Columns

Variables	No.	Distribution	Mean	COV (%)
Shell thickness	1	Normal	25 mm	3
Radius (R_{c1})	2	Normal	8427.5 mm	5
Ring frame spacing	3	Normal	2200 mm	2
Welding parameter	4	Normal	4.5	12
X_m (API Bulletin 2U) [5.7]	5	Lognormal	1.13	16.3
X_m (RCC Model Code) [5.7]	5	Lognormal	1.09	24.8
Young's modulus	6	Lognormal	208 kN/mm^2	5
Yield stress	7	Lognormal	391 N/mm^2	7
Longitudinal stress (f_{long})	8	Lognormal	162.88	5-20
Hoop stress (f_{hoop})	9	Lognormal	182.07	5-20

The mean bias and COV of model uncertainty factors in API and RCC Model Codes for combined loading have been evaluated by Das et al [5.8] from a population of 35

cylinders. For the RCC Code, the mean bias is less but the COV is more than those of API Bulletin 2U. The design variables are numbered for easy reference which might be useful in viewing Table 5.5 and 5.6.

5.3 THEORETICAL BACKGROUND OF BCCNNV

A concise summary of the theoretical background of reliability analysis is given here to explain the development of BCCNNV (Beta Calculation of Correlated Non-Normal Variables). The author would like to avoid much repetition because the Advanced First Order Second Moment methods have been discussed in great detail in many references (e.g. [5.1], [5.10] and [5.16]). But still some recapitulation of the underlying theory is required in this section to explain the author's understanding of the reliability index. The algorithm proposed by Rackwitz [5.12] is also discussed in brief since it forms the main module of BCCNNV. Some of the equations in the next sections will be used to explain the results presented in Section 5.5.

5.3.1 Linear Performance Functions

In a broader sense, the reliability of a structural system or any component may be defined as the probability of performing its intended function or mission. The level of performance will obviously depend on the properties of the system. The safety margin of the structure, Z_{sm} in this context can be defined in terms of a performance or state function $g(x_1, x_2, \cdots, x_n)$ where $x_1, x_2, \cdots, x_n$ are the basic state or design variables. In this context, the 'safe state' of the structure is defined as follows:

$$Z_{sm} = g(x_1, x_2, \cdots, x_n) > 0 \tag{5.17}$$

The 'failure state' is $Z_{sm} < 0$ whereas the boundary separating the safe and failure states is the 'limit state' defined by the equation $Z_{sm} = 0$. Geometrically, the limit state equation, $Z_{sm} = g(x_1, x_2, \cdots, x_n) = 0$ is an n-dimensional surface commonly known as the 'failure surface'. One basic definition of reliability index is the ratio of the mean and standard deviation of Z_{sm}:

$$\beta = \frac{\mu_{Z_{sm}}}{\sigma_{Z_{sm}}} \tag{5.18}$$

In the case of a linear performance function this definition does not cause any complexity especially when the design variables follow the Normal distribution. In this connection, let us define the reduced variates:

$$x_i' = \frac{x_i - \mu_{x_i}}{\sigma_{x_i}} \qquad i = 1, 2, \cdots, n \tag{5.19}$$

If the failure surface is portrayed in the space of the reduced variates, the safe state will be on one side (i.e. $g(x_1, x_2, \cdots\cdots, x_n) > 0$) with the failure state on the other side. The probability of failure, P_f is the volume integral of the joint Probability Density Function (PDF) of the design variables which is generally a formidable task. However, Shinozuka [5.14] and other researchers have shown that the point on the failure surface with minimum distance to the origin of the reduced variates is the most probable failure point. Thus, in some approximate sense [5.1], this minimum distance may be used as a measure of reliability and may be regarded as another definition of the reliability index, β.

The above two definitions of β coincide when the safety margin is expressed as a linear performance function such as:

$$g(\cdot) = C_0 + \sum_i C_i x_i \tag{5.20}$$

The failure surface will be a hyper-plane and its distance from the origin of the reduced variates will be equal to the ratio of the mean and standard deviation of the safety margin in Eq. (5.18), provided the design variables are uncorrelated and normally distributed. The reliability index in this case is:

$$\beta = \frac{C_0 + \sum_i C_i \mu_{x_i}}{\sqrt{\sum_i (C_i \sigma_{x_i})^2}} \tag{5.21}$$

5.3.2 Advanced First Order Second Moment (AFOSM) Methods

For non-linear performance functions, there is no unique distance from the failure surface to the origin of the reduced variates. The evaluation of the exact probability of failure will involve multiple numerical quadrature for the integration of the joint PDF of the design variables over the failure region (i.e. $g(x_1, x_2, \cdots\cdots, x_n) < 0$). For practical purposes approximation to the exact probability will be necessary. The tangent plane to the failure surface at the most probable failure point [5.14] with minimum distance to the origin of the reduced variates may then be used to approximate the actual failure surface. Depending on whether the exact non-linear failure surface is convex or concave toward the origin, this approximation will be on the safe side or unsafe side respectively. This approximation forms the background of AFOSM methods where the distance from the tangent plane at the failure point (i.e. $(x_1^*, x_2^*, \cdots\cdots, x_n^*)$) is used as the reliability index to represent the measure of reliability.

For first order approximations the Taylor series is useful. Expanding Eq. (5.17) in a

Taylor series and neglecting higher order terms:

$$Z_{sm} \approx g(x_1^*, x_2^*, \cdots, x_n^*) + \sum_{i=1}^{n}(x_i - x_i^*)\left(\frac{\delta g}{\delta x_i}\right)_* \tag{5.22}$$

where the partial derivatives are calculated at the unknown failure point, $(x_1^*, x_2^*, \cdots, x_n^*)$. The approximate mean value of the safety margin is:

$$\mu_{Z_{sm}} \approx \sum_{i=1}^{n}(\mu_{x_i} - x_i^*)\left(\frac{\delta g}{\delta x_i}\right)_* \tag{5.23}$$

and the standard deviation:

$$\sigma_{Z_{sm}} \approx \left[\sum_{i=1}^{n}\left\{\left(\frac{\delta g}{\delta x_i}\right)_* \sigma_{x_i}\right\}^2\right]^{1/2} \tag{5.24}$$

$\sigma_{Z_{sm}}$ may be expressed as a linear combination of the standard deviations of design variables:

$$\sigma_{Z_{sm}} \approx \sum_{i=1}^{n}\alpha_i\left(\frac{\delta g}{\delta x_i}\right)_* \sigma_{x_i} \tag{5.25}$$

where

$$\alpha_i = \frac{\left(\frac{\delta g}{\delta x_i}\right)_* \sigma_{x_i}}{\left[\sum_{j=1}^{n}\left\{\left(\frac{\delta g}{\delta x_j}\right)_* \sigma_{x_j}\right\}^2\right]^{1/2}} \tag{5.26}$$

α_i may be defined as the sensitivity factor since it reflects the relative influence of the *i*-th variable on the safety margin. Now the reliability index β can be calculated from the ratio of the mean and standard deviation of the safety margin:

$$\beta = \frac{\sum_{i=1}^{n}(\mu_{x_i} - x_i^*)\left(\frac{\delta g}{\delta x_i}\right)_*}{\sum_{i=1}^{n}\alpha_i\left(\frac{\delta g}{\delta x_i}\right)_* \sigma_{x_i}} \tag{5.27}$$

Eq. (5.27) yields a very important relationship, useful for iterative calculations:

$$\sum_{i=1}^{n}\left(\frac{\delta g}{\delta x_i}\right)_* (\mu_{x_i} - x_i^* - \alpha_i \beta \sigma_{x_i}) = 0 \tag{5.28}$$

The solution of Eq. (5.28) is:

$$x_i^* = \mu_{x_i} - \alpha_i \beta \sigma_{x_i} \quad \text{for all } i \tag{5.29}$$

5.3.3 The Rackwitz Algorithm

The algorithm proposed by Rackwitz [5.12] is essentially a β minimisation process. The algorithm is generally regarded as a powerful method with a fast rate of convergence. It involves the following steps:

(1) Guess a value of β

(2) Initially, set $x_i^* = \mu_{x_i}$ for all *i*

(3) Compute $\left(\frac{\delta g}{\delta x_i}\right)_*$ for all *i*

(4) Compute α_i for all *i*

(5) Compute the new failure point from $x_i^* = \mu_{x_i} - \alpha_i \beta \sigma_{x_i}$ for all *i*

(6) Repeat steps 3 to 5 until stable values of x_i^* are achieved

(7) Evaluate $Z_{sm} = g(x_1^*, x_2^*, \cdots, x_n^*)$

(8) Evaluate $\frac{\delta\beta}{\delta Z_{sm}}$ numerically and compute a better estimation of β from

$\beta_{new} = \beta_{previous} - Z_{sm} \frac{\delta\beta}{\delta Z_{sm}}$. Repeat steps 3 to 8 to achieve $Z_{sm} = 0$ within specific limits

(9) Compute the notional failure probability as $P_f = \Phi(-\beta)$

(10) Compute the partial safety factors as the ratio of x_i^* and μ_{x_i}.

5.3.4 Program BCCNNV

The Rackwitz Algorithm forms the basis of the program BCCNNV. BCCNNV has been written in a 'user friendly' way. It is a general purpose program and the user is supposed to provide his / her performance function in the form of a Fortran routine. The program guides the user to create necessary data files so that any prior knowledge regarding the source code is not necessary. There is already one program available in the Department which has been extensively used in the past. That program has helped in the verifications while developing BCCNNV. However, BCCNNV has some additional features:

1) Improved input data recording

2) Easily understandable output

3) Lognormal and Type I asymptotic distributions for non-normal variables.

4) Variables need not be uncorrelated

For statistically dependent random variables, BCCNNV transforms the original variates to a set of uncorrelated variables. Before the transformation if any non-normal variable is present, the equivalent normal distribution is found such that the cumulative probability as well as the probability density ordinate of the equivalent distribution are equal to those of the original non-normal distribution at the most probable failure point on the failure surface. Strictly speaking, the transformation (sometimes called *rotation of co-ordinates* [5.1]) is applicable only to normal or log-normal variables. But it provides a good estimate for correlated non-normal variates when compared with the *Rosenblatt transformation.* After the transformation, the Rackwitz algorithm is followed in BCCNNV. In some cases the performance function might be β-sensitive. Then it would be difficult to bring the unknown failure point on the failure surface through iterations because the performance function would change its sign from negative to positive or vice versa for a slight variation in β but never become zero! BCCNNV cleverly handles this typical problem in numerical modelling.

5.3.5 Classic Examples

The author has done a series of validation tests with the results from BCCNNV. This section will illustrate one well known example of nonlinear but simple performance function. This example has been illustrated in many places (e.g. [5.1], [5.6]) but in this section, for comparison the numerical values are taken from Ref. [5.1] and tabulated in Table 5.4.

Table 5.4. Three Classic Design Variables

Variables	No.	Distribution	Mean	COV (%)
Yield strength	1	Log-normal	40 ksi	12.5
Section modulus	2	Log-normal	50 in^3	5
Bending moment	3	Type I asymptotic	1000 in-kip	20

The fully plastic flexural capacity of a steel beam section may be given as x_1x_2 where x_1 and x_2 represent the yield strength of steel and the section modulus respectively. If the applied bending moment is x_3, the performance function may be defined as:

$$g(x_1, x_2, x_3) = x_1x_2 - x_3 \qquad (5.30)$$

It has been mentioned earlier that the user is supposed to provide the performance function as an external Fortran routine. It is also possible to link Pascal and C routines with BCCNNV but the task is simple and straight-forward in case of Fortran routines.

In this example the Fortran routine can be written as:

```
REAL*8 FUNCTION GF(N, A)
REAL*8 A(N)
GF = A(1)*A(2) - A(3)
RETURN
END
```

For complicated problems the routine might be a few thousand lines long! However, the three variables are first assumed as uncorrelated and the reliability index calculation is tabulated in Table 5.5. The results are slightly different from the hand calculations in Ref. [5.1] because BCCNNV does floating point calculations in double precision (i.e. up to sixteen decimal places). But the slight difference mainly comes from a simple approximation used in the hand calculations in Ref. [5.1] while estimating equivalent normal distributions. The iteration cycle for calculating the reliability index and corresponding failure point stops after reaching the convergence criteria which is a user defined small value representing the maximum difference between the new and previous x_i (expressed in percentage). BCCNNV calculates the ratio of the mean and standard deviation of the safety margin at the established failure point (see Eq. (5.18)) and compares it with the β value found through iterations. Both values of the reliability index are given in output (e.g. Tables 5.5, 5.6, 5.9, 5.10 etc.) for cross-verification.

To demonstrate a sample analysis with correlated variables, the yield strength and section modulus in the above example are assumed to be partially correlated with Γ_{12} = 0.40. But Γ_{13} and Γ_{23} are assumed as zero. When variables are no longer independent the correlation matrix $[\Gamma]$ should be given as input. But $[\Gamma]$ is symmetric and its leading diagonal has coefficients equal to unity. Therefore, BCCNNV asks for the coefficients above the leading diagonal only.

While dealing with correlated design variables in BCCNNV, it is necessary to find the eigenvalues and corresponding eigenvectors of the correlation matrix, $[\Gamma]$. It is worth noting that $[\Gamma]$ is real and symmetric and thus the eigenvectors are mutually orthogonal. Table 5.6 is an easily understandable output where the sensitivity factors of the transformed orthogonal variables, y_1, y_2 and y_3 are presented along with different parameters of the actual variables, x_1, x_2 and x_3. In Table 5.6, y_i corresponds to x_i and it is difficult to achieve this one-to-one correspondence in the correct order with almost all standard eigenvalue routines available in many Fortran and C libraries. This is mainly because the routines usually rearrange the eigenvalues in ascending order. The ascending order is important in many engineering problems such

as natural frequency calculations where the lowest eigenvalue is of main interest. But for correlated design variables the actual order is very important because the sensitivity of x_i is reflected through y_i. This unexpected problem is solved in BCCNNV in a roundabout way. The NAG Fortran Library [5.11] from The Numerical Algorithms Group Ltd. has various eigenvalue routines for different problems. BCCNNV uses a routine called F02AGF [5.11] which calculates all the eigenvalues and eigenvectors of a real unsymmetric matrix. For a real unsymmetric matrix, the eigenvalues and eigenvectors might be complex numbers with real and imaginary parts. Complex numbers cannot be 'easily' arranged in ascending or descending order (probably because there is no unique way for arranging them) and thus F02AGF returns the eigenvalues to BCCNNV without changing their order. BCCNNV ignores the imaginary parts of the eigenvalues and eigenvectors of $[\Gamma]$ because they would be zero since $[\Gamma]$ is real and symmetric! In fact, this is one way of cheating a standard routine for unsymmetric matrices by giving a symmetric matrix in disguise!

The hand calculations in Ref. [5.1] verify Tables 5.5 and 5.6. The sensitivity and partial safety factors in Table 5.6 are slightly different from those in Table 5.5. This is the effect of including $\Gamma_{12} = 0.40$ in this classic problem. The most probable failure point [5.14] and the corresponding reliability index calculated through iterations in Tables 5.5 and 5.6 are close but different.

5.4 SAFETY MARGINS FOR CYLINDRICAL STRUCTURES

In the 1970s, the stiffened cylinder buckling formulations that were used were derived from aircraft technology. This is hardly appropriate for the much less perfect welded steel structures used in offshore. In the early 1980s, Conoco and ABS along with many others conducted large scale tests of cylinders under axial, radial and combined loading for providing useful information on buckling loads and corresponding failure modes. Ref. [5.8] compares these experimental results with the strength formulations of various current codes. This section uses the safety margins developed and discussed in Refs. [5.7] and [5.8] from the interaction equations in API Bulletin 2U and RCC Model Code.

5.4.1 Performance Function from API Bulletin 2U

API Bulletin 2U defines the following interaction equation for axial compression, bending and hoop compression:

$$\left(\frac{f_{long}}{F_{xcB}}\right)^2 - \left[\frac{1.5\,(F_{xcB} + F_{hcB})}{\sigma_y} - 2.0\right]\left(\frac{f_{long}}{F_{xcB}}\right)\left(\frac{f_{hoop}}{F_{hcB}}\right) + \left(\frac{f_{hoop}}{F_{hcB}}\right)^2 = 1.0 \quad (5.31)$$

where f_{long} and f_{hoop} come from the applied load effects. In Eq. (5.31) they are not entirely independent of each other. Their values might be modified (for details see Ref. [5.2]) before inserting them into the above interaction equation. X_m has been introduced in Eq. (5.31) to define a suitable performance function in Ref. [5.8] for the safety margin:

$$g(\cdot) = 1.0 - \left(\frac{f_{long}}{F_{xcB}}\right)^2 + \left[\frac{1.5\,(F_{xcB}+F_{hcB})}{\sigma_y} - 2.0\right]\left(\frac{f_{long}}{F_{xcB}}\right)\left(\frac{f_{hoop}}{F_{hcB}\cdot X_m}\right) - \left(\frac{f_{hoop}}{F_{hcB}\cdot X_m}\right)^2 \tag{5.32}$$

5.4.2 Performance Function from RCC Model Code

The interaction equation in the RCC code is very similar to Eq. (5.32). In fact, API has developed Recommended Practice RP 2T for TLPs and two associated special Bulletins 2U for cylindrical shells and 2V for plane structures following earlier RCC work. Before coming to the RCC interaction equation for combined loading it is better to introduce the non-dimensionalised strength and load parameters:

$$\tilde{f}_{long} = \frac{f_{long}}{\sigma_y},\ \tilde{f}_{hoop} = \frac{f_{hoop}}{\sigma_y},\ \tilde{F}_{xcB} = \frac{F_{xcB}}{\sigma_y},\ \tilde{F}_{hcB} = \frac{F_{hcB}}{\sigma_y} \tag{5.33}$$

Based on these notations, the interaction equation is:

$$\left(\frac{\tilde{f}_{long}}{\tilde{F}_{xcB}}\right)^2 + \left[\frac{2\sqrt{\left(1-\tilde{F}_{xcB}^2\right)\left(1-\tilde{F}_{hcB}^2\right)}}{\tilde{F}_{xcB}\cdot\tilde{F}_{hcB}} - 1\right]\tilde{f}_{long}\cdot\tilde{f}_{hoop} + \left(\frac{\tilde{f}_{hoop}}{\tilde{F}_{hcB}}\right)^2 = 1.0 \tag{5.34}$$

The performance function for the safety margin includes the model uncertainty factor. Rearranging Eq. (5.34), g(·) takes the following form [5.8]:

$$g(\cdot) = 1.0 - \left(\frac{\tilde{f}_{long}}{\tilde{F}_{xcB}}\right)^2 - \left[\frac{2\sqrt{\left(1-\tilde{F}_{xcB}^2\right)\left(1-\tilde{F}_{hcB}^2\right)}}{\tilde{F}_{xcB}\cdot\tilde{F}_{hcB}} - 1\right]\frac{\tilde{f}_{long}\cdot\tilde{f}_{hoop}}{X_m} - \left(\frac{\tilde{f}_{hoop}}{\tilde{F}_{hcB}\cdot X_m}\right)^2 \tag{5.35}$$

5.5 NUMERICAL RESULTS ON ISSC TLP COLUMNS

The author has done a series of verification tests with the results from BCCNNV. Table 5.7 checks deterministically the ISSC TLP column design. The value of g(·) has

been calculated from Eqs. (5.32) and (5.35) after ignoring X_m. The positive sign of $g(\cdot)$ in Table 5.7 (in the absence of X_m) indicates that the design is on the safe side of the failure surface although X_m plays a dominant role as we shall see later. The ultimate longitudinal (i.e. axial) strength values for the TLP columns found from API and RCC are almost identical. This similarity between RCC and API follows from the latter being mainly derived from the former [5.9].

Table 5.7. Deterministic Calculations from API and RCC Model Code

Results	Unit	Symbol	API [5.2]	RCC [5.5]
Elastic buckling stress	N/mm^2	F_{xeB}	6467.62	6436.35
Inelastic buckling stress	N/mm^2	F_{xcB}	386.57	386.55
Ultimate longitudinal load	MN	P_{cB}	584.50	596.82
Average longitudinal stress	N/mm^2	F_{xca}	323.08	329.51
Ultimate hoop pressure	N/mm^2	p_{cB}	1.0732	1.2748
Ultimate hoop stress	N/mm^2	F_{hcB}	362.33	391.00
$g(\cdot)$	-	-	0.6528	0.7328

Table 5.8 presents another verification test. As discussed before, COVs of stresses are varied from 5% to 20%. Table 5.8 has only three possible sets of stress COVs. The first three cases in Table 5.8 deal with the safety margin (i.e. Eq. (5.32)) from API Bulletin 2U. The next three cases involve the RCC Model Code. Case 1 and 2, and similarly Case 4 and 5 study the effects of single precision and double precision calculations. It is insignificant here but may change results dramatically in other cases (e.g. in finite element calculations). Case 3 and 6 are the results from the old program (i.e. not BCCNNV) already available in the Department. The results are almost the same but BCCNNV and the existing program use identical failure surface subroutines [5.7]. However, the failure surface routines have been checked and revised by the author.

Tables 5.9 and 5.10 provide hardcopies of typical output from BCCNNV. The variable numbers are explained in Table 5.3. The partial safety factors are calculated after establishing the most probable failure point through iterations. Tables 5.9 and 5.10 with 10% COV for both longitudinal and hoop stress should reflect a general impression about the design. The target safety index is 3.72 (corresponding to a notional probability of failure of 0^{-4} during the lifetime of the structure) in the RCC Model Code. In Table 5.9, the probability of failure is 0.2 x 0^{-4} corresponding to β =

4.1035. Therefore, the design of ISSC TLP columns may be considered as adequately safe with a possibility of further optimisation and minimisation of structural weight. The model uncertainly factor plays a vital role in this study. It has the maximum sensitivity factor of 0.786 and its partial safety factor is 1.7. The hoop stress is the next most sensitive one with a partial safety factor of 1.22.

Table 5.10 where the safety margin is defined from the RCC Model Code, presents a different picture. The reliability index calculated does not reach the target specified by the Rule Case Committee [5.5]. The ring frame spacing has the minimum sensitivity. The model uncertainty factor is again the most sensitive one with a sensitivity factor equal to 0.89474. The next sensitive design variable is again hoop stress. It has been said before that the mean bias and COV of the model uncertainty factor come from a population of 35 cylinders [5.8]. After observing the high sensitivity factor of X_m the author took interest to see the change in β value by decreasing the high COV of X_m. This is of course a hypothetical observation and should not be used in any practical design purpose. But the result of varying X_m's COV is quite interesting. When its COV is assumed as 20%, β is 4.022 (i.e. $P_f = 0.288 \times 0^{-4}$). If its COV is reduced to 15%, β becomes 4.908 (i.e. $P_f = 0.46 \times 0^{-6}$). The mean value and COV of the other variables are not changed.

The original aim of this study was to see the effect of varying the COVs of applied stresses while keeping other variables unaltered. Refer to Tables 5.11 and 5.12, each one of them has 256 β values. The calculations for each β value are similar to those shown in Tables 5.9 and 5.10. To understand the nature of the variations, two special plotting methods are used here. Figs. 5.3 and 5.5 are 3-D surface plots showing the importance of hoop stress in both API and RCC codes. Mathematica [5.17] has special tools for calculating contours from 3-D surfaces. Figs. 5.4 and 5.6 are the plan views of Figs. 5.3 and 5.5. The reliability index is constant on any line in Figs. 5.4 and 5.6. So the lines (iso-beta lines !) are showing the β variation explicitly. It is quite surprising that there is no variation in β due to the change in COV of the longitudinal stress according to the RCC Model Code. However, β changes rapidly in Fig. 5.4 (i.e. API formulations) when the COV of f_{long} is increased beyond 14% but the change depends on f_{hoop}'s COV as well.

But these results can not be used to draw general conclusions. They are valid for the numerical values of the design variables considered. But the results in Figs. 5.4 and 5.6 are unexpected because they do not show any significant influence of the applied longitudinal stress although its mean value is close to that of the applied hoop stress.

This is investigated further. The obvious suspect is X_m because of its high sensitivity factor compared to others. It is possible that the effect of some variables have been suppressed because X_m is so dominant. This might be a shortfall of the underlying assumption that the design variables are independent.

To understand the nature of variation in the absence of X_m, its mean and COV are set to 1.0 and 0.0 respectively. Tables 5.13 and 5.14 are similar to Tables 5.11 and 5.12 but they ignore X_m. The reliability index now varies over a wide range. If Tables 5.12 and 5.13 are compared, we shall see that the difference in β decreases with an increase in the COV of longitudinal and / or hoop stress. Here the difference in β refers to the difference in β values in Tables 5.12 and 5.13 for identical longitudinal and hoop stress COVs (e.g. 9.534-3.553=5.981 for 5% f_{long} and f_{hoop}). It is also true if Tables 5.11 and 5.14 are compared. The higher β values in the absence of X_m perhaps indicate the conservative nature of API and RCC codes. It is therefore the reliability study where this conservatism can be focused and a level of uniform safety can be achieved in various codes. The data in Tables 5.13 and 5.14 are plotted in Figs. 5.7-5.10. Figs. 5.8 and 5.10 truly reflect the original nature of the interaction equations (see Eqs. (5.31) and (5.34)). A 'ridge' on the surface in both Figs. 5.7 and 5.9 is one interesting aspect. The nature of both surfaces is also strongly similar.

Tables 5.15 and 5.16 present output similar to those in Tables 5.9 and 5.10. But the model uncertainty factor has been ignored in Tables 5.15 and 5.16 to examine the sensitivity of other variables in the absence of X_m. The first thing to note is that the number of iterations has increased considerably in both tables. The starting value of β has been changed but that change could not influence the number of iterations required. The maximum sensitive variable in both Tables 5.15 and 5.16 is longitudinal stress! The sensitivity factors of other variables are appreciable. The applied hoop stress has negligible sensitivity in Table 5.16 from the RCC code but that can be explained. The deterministic calculations in Table 5.1 show that the ultimate hoop stress is equal to the yield stress according to RCC. This prediction indicates that there would be no buckling of the ISSC TLP columns before yielding under hoop stress only (i.e. single load action). The ultimate hoop load calculated is also very high. So minor variations in design variables most probably cannot change the ultimate hoop stress prediction of RCC which is equal to the yield stress. The applied hoop stress is included in the performance function after non-dimensionalising it with the ultimate hoop stress. Therefore, it might be the reason why the hoop stress is not predominant any more in the absence of X_m according to RCC.

It is due to the position of X_m in the performance function (i.e. Eq.(5.35)) formulated according to the interaction equation of the RCC code which is causing unacceptable trend in Fig. 5.6. It is necessary to check the calibration of the deterministic model and probably this may require two model uncertainty factors to be used for longitudinal stress and hoop stress.

5.6 CONCLUSIONS

The analysis technique described in this chapter depends on all partial derivatives calculated at each iteration. The number crunching involved is not simple and thus almost nothing can be taken as general conclusions with certainty!

⊗

First of all, let us distinguish the difference between the interaction equations and the performance functions. The interaction equations (i.e. Eqs. (5.31) and (5.34)) come straight from the API and RCC codes. They are formulated mainly for deterministic analyses. The performance functions are defined in Ref. [5.7] from these interaction equations after inserting the model uncertainty factor. Figs. 5.8 and 5.10 show that the change in COV for longitudinal stress or hoop stress almost 'equally' affects the reliability index and that is in the absence of X_m. This is also clearly visible in the symmetric surface plots in Figs. 5.7 and 5.9. But the situation changes when X_m is included in the analysis. The effect of changing the applied longitudinal stress COV disappears as indicated in Fig. 5.6. Fig. 5.6 is not acceptable because it fails to show any effect of f_{long} which is the most sensitive in the absence of X_m. It might be suggested that the performance functions should be reconfigured so that the modification can capture the effect of changes made in the value of f_{long}. The other possible solution is to introduce correlation coefficients among variables so that X_m is no longer an independent variable, playing the most dominant role suppressing others. But the problem lies in the selection of suitable Γ_{ij} and the author does not have enough background for this type of selection. BCCNNV can be used as a 'black box' once $[\Gamma]$ is ready. The additional input required for the ISSC TLP columns to convert the analysis status from 'uncorrelated' to 'correlated' are explained clearly in Fig. 5.11.

The ISSC TLP columns are designed from a parametric study conducted by RCC [5.5]. It is a pure coincidence that the radius and other factors were very close. So the preliminary design of the ISSC TLP columns was a clever design indeed because it closely followed the optimum cylinder model established by RCC. Through deterministic as well as probabilistic checks, it can be concluded that the proposed design of the ISSC TLP columns is adequately safe.

However, the ultimate goal of this work is not to design the ISSC TLP columns. Rather it is aimed at setting up an integrated design track for TLPs. The integrated design process would share more information among hydrodynamics, structural engineering and associated reliability aspects. In practice, a design problem is handled by a number of groups of people. Often they share as little as one or two vital pieces of information (e.g. the maximum stress or load value) to link up their work. Instead of

sharing a little information, if they share a dynamic database which might be complicated to set up at first, but this would certainly improve the whole scenario.

		Design Variables in Table 5.3								
		1	2	3	4	5	6	7	8	9
V	1	1.0	Γ_{12}	Γ_{13}	Γ_{14}	Γ_{15}	Γ_{16}	Γ_{17}	Γ_{18}	Γ_{19}
a	2		1.0	Γ_{23}	Γ_{24}	Γ_{25}	Γ_{26}	Γ_{27}	Γ_{28}	Γ_{29}
r	3			1.0	Γ_{34}	Γ_{35}	Γ_{36}	Γ_{37}	Γ_{38}	Γ_{39}
i	4				1.0	Γ_{45}	Γ_{46}	Γ_{47}	Γ_{48}	Γ_{49}
a	5					1.0	Γ_{56}	Γ_{57}	Γ_{58}	Γ_{59}
b	6						1.0	Γ_{67}	Γ_{68}	Γ_{69}
l	7			Symmetric				1.0	Γ_{78}	Γ_{79}
e	8								1.0	Γ_{89}
s	9									1.0

Fig. 5.11. Required Input for the Correlation Matrix

5.7 REFERENCES

[5.1] Ang, A. H-S. and Tang, W.H.: "Probability Concepts in Engineering Planning and Design", Vol. II, John Wiley & Sons, 1984.

[5.2] API Bulletin 2U: "Bulletin on Stability Design of Cylindrical Shells", American Petroleum Institute, Washington, May 1987.

[5.3] Catley, D.: "VAS User Manual: The BSRA Vibration Analysis Suite of Programs", The British Ship Research Association, Wallsend, 1983.

[5.4] Chatterjee, P.C. and Das, P.K.: "Hydro-Structural Response of ISSC TLP", Technical Report - NAOE-94-31, University of Glasgow, 1994.

[5.5] Conoco/ABS TLP Rule Case Committee: "Model Code for Structural Design of Tension Leg Platforms", New York, February 1984.

[5.6] Das, P.K.: "A Tutorial on Reliability Based Design", Comett / UETP Course on Advanced Design for Ships and Offshore Floating Systems, September 1992.

[5.7] Das, P.K., Faulkner, D. and Guedes da Silva, A.: "Limit State Formulations and Modelling for Reliability Based Analyses of Orthogonally Stiffened

Cylindrical Shell Structural Components", Technical Report - NAOE-91-26, University of Glasgow, 1991.

[5.8] Das, P.K., Faulkner, D. and Zimmer, R.A.: "Efficient Reliability Based Design of Ring and Stringer Stiffened Cylinders Under Combined Loads", Proc. of BOSS Conference, London, pp. 180-193, 1992.

[5.9] Faulkner, D.: "Efficient Design of Orthogonally Stiffened Cylinders", BPP Seminar on Tensioned Buoyant Platforms, London, May 1993.

[5.10] Melchers, R.E.: "Structural Reliability Analysis and Prediction", Ellis Horwood Limited, Chichester, 1987.

[5.11] Numerical Algorithms Group Limited: "NAG Fortran Library Manual", Mark 14, Oxford, April 1990.

[5.12] Rackwitz, R.: "Practical Probabilistic Approach to Design", Bulletin 112, Comite European du Beton, Paris, 1976.

[5.13] Report of Committee I.2: "Case study of a Tension Leg Platform", Proceedings of the Ninth International Ship and Offshore Structures Congress, Registro Italiano Navale, Genova, Vol. 1, pp. I.2-48-55, 1985.

[5.14] Shinozuka, M.: "Basic Analysis of Structural Safety", Journal of Structural Division, ASCE, Vol. 3, 109, March 1983.

[5.15] Taylor, R.E. and Jefferys, E.R.: "Variability of Hydrodynamic Load Predictions for a Tension Leg Platform", Ocean Engineering, Vol. 13, No. 5, pp. 449-490, 1986.

[5.16] Thoft-Christensen, P.: "Structural Reliability Theory and Its Applications", Springer-Verlag, Germany, 1982.

[5.17] Wolfram, S.: "Mathematica - A System for Doing Mathematics by Computer", Second Edition, Addison-Wesley Publishing Co., California, 1991.

Table 5.2. Sectional Properties of ISSC TLP Columns

Case	Idealisation	Material Area (m^2)	Iz (m^4)	Iy (m^4)	Jx (m^4)	Shear Area about Local y Axis (m^2)	Shear Area about Local z Axis (m^2)
1	1) Stringers lumped at their CG but curved shell panel maintained	1.809	63.31	63.31	94.02	-	-
2	1) Stringers lumped at their connecting points to the shell. 2) Flat plate joining adjacent stringers for representing curved shell panel	1.809	64.14	64.14	93.72	0.6616	0.6616
3	1) Stringer flanges lumped at the end of webs 2) Flat plate joining adjacent stringers for representing curved shell panel	1.809	63.27	63.27	93.72	0.6526	0.6526

Table 5.5. Reliability Index Calculation in a Classic Problem of Three Uncorrelated Nonnormal Variables

ITERATION NO. = 1

VARIABLE X(i)	FAILURE POINT	EQUIV. MEAN	EQUIV. SD	SENSITIVITY FACTOR	NEW FAILURE POINT
1	4.0000E+01	3.9690E+01	4.9806E+00	7.5579E-01	2.7738E+01
2	5.0000E+01	4.9938E+01	2.4984E+00	3.0330E-01	4.7532E+01
3	1.0000E+03	9.6612E+02	1.9122E+02	-5.8033E-01	1.3185E+03

BETA CALCULATED IN ITERATION NO. 1 = 3.17495

ITERATION NO. = 2

VARIABLE X(i)	FAILURE POINT	EQUIV. MEAN	EQUIV. SD	SENSITIVITY FACTOR	NEW FAILURE POINT
1	2.7738E+01	3.7677E+01	3.4539E+00	4.5996E-01	3.3224E+01
2	4.7532E+01	4.9879E+01	2.3751E+00	1.8458E-01	4.8650E+01
3	1.3185E+03	8.6159E+02	3.1000E+02	-8.6854E-01	1.6163E+03

BETA CALCULATED IN ITERATION NO. 2 = 2.80321

ITERATION NO. = 3

VARIABLE X(i)	FAILURE POINT	EQUIV. MEAN	EQUIV. SD	SENSITIVITY FACTOR	NEW FAILURE POINT
1	3.3224E+01	3.9133E+01	4.1369E+00	4.3054E-01	3.4248E+01
2	4.8650E+01	4.9921E+01	2.4310E+00	1.7278E-01	4.8769E+01
3	1.6163E+03	6.6396E+02	4.1411E+02	-8.8588E-01	1.6702E+03

BETA CALCULATED IN ITERATION NO. 3 = 2.74295

ITERATION NO. = 4

VARIABLE X(i)	FAILURE POINT	EQUIV. MEAN	EQUIV. SD	SENSITIVITY FACTOR	NEW FAILURE POINT
1	3.4248E+01	3.9299E+01	4.2644E+00	4.2772E-01	3.4298E+01
2	4.8769E+01	4.9924E+01	2.4369E+00	1.7165E-01	4.8777E+01
3	1.6702E+03	6.2284E+02	4.3151E+02	-8.8746E-01	1.6729E+03

BETA CALCULATED IN ITERATION NO. 4 = 2.74217

ITERATION NO. = 5

VARIABLE X(i)	FAILURE POINT	EQUIV. MEAN	EQUIV. SD	SENSITIVITY FACTOR	NEW FAILURE POINT
1	3.4298E+01	3.9307E+01	4.2706E+00	4.2759E-01	3.4299E+01
2	4.8777E+01	4.9924E+01	2.4373E+00	1.7159E-01	4.8777E+01
3	1.6729E+03	6.2072E+02	4.3238E+02	-8.8754E-01	1.6730E+03

BETA CALCULATED IN ITERATION NO. 5 = 2.74217

Table 5.5. (Continued)

```
BETA FROM BASIC DEFINITION =  2.74217

BETA THROUGH ITERATION     =  2.74217

PROBABILITY OF FAILURE     =  0.30517D-02


        -- PARTIAL SAFETY FACTORS --

        VARIABLE                PSF
            1                 1.1662
            2                 1.0251
            3                 1.6730
```

Table 5.6. Reliability Index Calculation in a Classic Problem of Three Correlated Nonnormal Variables

ITERATION NO. = 1

VARIABLE NO.	ASSUMED X(i)	CORRPD. Y(i)	EQUIVALENT MEAN OF X(i)	EQUIVALENT SD OF X(i)	PART. DIFF. W.R.T. Y(i)	SENSITIVITY FACTOR	NEW Y(i)
1	4.0000E+01	6.1690E-02	3.9690E+01	4.9806E+00	2.4676E+02	0.8146E+00	-2.8703E+00
2	5.0000E+01	2.6356E-02	4.9938E+01	2.4984E+00	1.0542E+02	0.2278E+00	-5.2554E-01
3	1.0000E+03	1.7716E-01	9.6612E+02	1.9122E+02	-1.9122E+02	-0.5335E+00	1.5887E+00

BETA CALCULATED IN ITERATION NO. 1 = 2.97809

ITERATION NO. = 2

VARIABLE NO.	ASSUMED X(i)	CORRPD. Y(i)	EQUIVALENT MEAN OF X(i)	EQUIVALENT SD OF X(i)	PART. DIFF. W.R.T. Y(i)	SENSITIVITY FACTOR	NEW Y(i)
1	2.7730E+01	-3.2618E+00	3.7674E+01	3.4529E+00	1.5655E+02	0.5298E+00	-1.7155E+00
2	4.5795E+01	-8.1103E-01	4.9761E+01	2.2883E+00	6.6973E+01	0.1484E+00	-3.1452E-01
3	1.2699E+03	1.3125E+00	8.8673E+02	2.9196E+02	-2.9196E+02	-0.8350E+00	2.2852E+00

BETA CALCULATED IN ITERATION NO. 2 = 2.73659

ITERATION NO. = 3

VARIABLE NO.	ASSUMED X(i)	CORRPD. Y(i)	EQUIVALENT MEAN OF X(i)	EQUIVALENT SD OF X(i)	PART. DIFF. W.R.T. Y(i)	SENSITIVITY FACTOR	NEW Y(i)
1	3.2718E+01	-1.8071E+00	3.9039E+01	4.0739E+00	1.9163E+02	0.4946E+00	-1.5600E+00
2	4.7494E+01	-3.8716E-01	4.9877E+01	2.3732E+00	8.1930E+01	0.1384E+00	-2.8583E-01
3	1.5539E+03	2.1452E+00	7.1002E+02	3.9339E+02	-3.9339E+02	-0.8580E+00	2.2874E+00

BETA CALCULATED IN ITERATION NO. 3 = 2.66580

ITERATION NO. = 4

VARIABLE NO.	ASSUMED X(i)	CORRPD. Y(i)	EQUIVALENT MEAN OF X(i)	EQUIVALENT SD OF X(i)	PART. DIFF. W.R.T. Y(i)	SENSITIVITY FACTOR	NEW Y(i)
1	3.3722E+01	-1.5628E+00	3.9218E+01	4.1989E+00	1.9854E+02	0.4907E+00	-1.5469E+00
2	4.7739E+01	-2.8826E-01	4.9888E+01	2.3854E+00	8.4874E+01	0.1373E+00	-2.8340E-01
3	1.6098E+03	2.2841E+00	6.6884E+02	4.1198E+02	-4.1198E+02	-0.8605E+00	2.2928E+00

BETA CALCULATED IN ITERATION NO. 4 = 2.66455

ITERATION NO. = 5

VARIABLE NO.	ASSUMED X(i)	CORRPD. Y(i)	EQUIVALENT MEAN OF X(i)	EQUIVALENT SD OF X(i)	PART. DIFF. W.R.T. Y(i)	SENSITIVITY FACTOR	NEW Y(i)
1	3.3784E+01	-1.5469E+00	3.9228E+01	4.2066E+00	1.9898E+02	0.4904E+00	-1.5462E+00
2	4.7757E+01	-2.8341E-01	4.9889E+01	2.3864E+00	8.5061E+01	0.1372E+00	-2.8327E-01
3	1.6134E+03	2.2927E+00	6.6616E+02	4.1315E+02	-4.1315E+02	-0.8606E+00	2.2931E+00

BETA CALCULATED IN ITERATION NO. 5 = 2.66455

BETA FROM BASIC DEFINITION = 2.66455

BETA THROUGH ITERATION = 2.66455

PROBABILITY OF FAILURE = 0.38546D-02

-- PARTIAL SAFETY FACTORS & FAILURE POINT --

X(i)	PSF	FAILURE POINT
1	1.1839	3.3786E+01
2	1.0469	4.7758E+01
3	1.6136	1.6136E+03

Table 5.8. Verification Test for BCCNNV

	Case 1	Case 2	Case 3	Case 4	Case 5	Case 6
Fortran file	afosm.f	afosm_dp.f	rely1.for	afosm.f	afosm_dp.f	relyrcc.for
Failure suboutine	api_g.f	api_g_dp.f	-	rcc_g.f	rcc_g_dp.f	-
Data file	issc_api	issc_api	issc_api_das	issc_rcc	issc_rcc	issc_rcc_das
EXE file	afosm_api	afosm_api_dp	rely1	afosm_rcc	afosm_rcc_dp	relyrcc
Location	cent/drpt5	cent/drpt5	eng/drpt5	cent/drpt5	cent/drpt5	eng/drpt5
Long. COV	10	10	10	10	10	10
Hoop COV	10	10	10	10	10	10
β	4.10350	4.10350	4.103	3.38411	3.38408	3.384
Long. COV	5	5	5	5	5	5
Hoop COV	5	5	5	5	5	5
β	4.51575	4.51578	4.516	3.55320	3.55322	3.554
Long. COV	20	20	20	20	20	20
Hoop COV	20	20	20	20	20	20
β	3.19543	3.19551	3.195	2.91193	2.91192	2.911

Table 5.9. Reliability Index Calculation with 10% COV for Longitudinal and Hoop Stresses According to API Code

ITERATION NO. = 1

VARIABLE X(i)	FAILURE POINT	EQUIV. MEAN	EQUIV. SD	SENSITIVITY FACTOR	NEW FAILURE POINT
1	2.5000E+01	2.5000E+01	7.5000E-01	-4.8417E-03	2.5015E+01
2	8.4275E+03	8.4275E+03	4.2138E+02	-2.8882E-01	8.9360E+03
3	2.2000E+03	2.2000E+03	4.4000E+01	-2.2573E-01	2.2415E+03
4	4.5000E+00	4.5000E+00	5.4000E-01	-1.5488E-01	4.8494E+00
5	1.1300E+00	1.1152E+00	1.8298E-01	5.6303E-01	6.8473E-01
6	2.0800E+02	2.0774E+02	1.0394E+01	2.1357E-01	1.9847E+02
7	3.9100E+02	3.9004E+02	2.7337E+01	2.9862E-01	3.5594E+02
8	1.6288E+02	1.6207E+02	1.6247E+01	-5.1310E-01	1.9690E+02
9	1.8207E+02	1.8116E+02	1.8162E+01	-3.5576E-01	2.0816E+02

BETA CALCULATED IN ITERATION NO. 1 = 4.17812

ITERATION NO. = 2

VARIABLE X(i)	FAILURE POINT	EQUIV. MEAN	EQUIV. SD	SENSITIVITY FACTOR	NEW FAILURE POINT
1	2.5015E+01	2.5000E+01	7.5000E-01	-5.4948E-02	2.5171E+01
2	8.9360E+03	8.4275E+03	4.2138E+02	-1.6118E-01	8.7099E+03
3	2.2415E+03	2.2000E+03	4.4000E+01	-2.1216E-01	2.2388E+03
4	4.8494E+00	4.5000E+00	5.4000E-01	-8.8186E-02	4.6980E+00
5	6.8473E-01	1.0188E+00	1.1088E-01	7.5270E-01	6.7175E-01
6	1.9847E+02	2.0753E+02	9.9171E+00	1.4693E-01	2.0147E+02
7	3.5594E+02	3.8851E+02	2.4885E+01	2.5709E-01	3.6191E+02
8	1.9690E+02	1.5857E+02	1.9641E+01	-1.9774E-01	1.7472E+02
9	2.0816E+02	1.7925E+02	2.0764E+01	-4.7421E-01	2.2019E+02

BETA CALCULATED IN ITERATION NO. 2 = 4.15795

ITERATION NO. = 3

VARIABLE X(i)	FAILURE POINT	EQUIV. MEAN	EQUIV. SD	SENSITIVITY FACTOR	NEW FAILURE POINT
1	2.5171E+01	2.5000E+01	7.5000E-01	-7.1204E-02	2.5219E+01
2	8.7099E+03	8.4275E+03	4.2138E+02	-1.1271E-01	8.6225E+03
3	2.2388E+03	2.2000E+03	4.4000E+01	-2.0036E-01	2.2362E+03
4	4.6980E+00	4.5000E+00	5.4000E-01	-5.5362E-02	4.6228E+00
5	6.7175E-01	1.0123E+00	1.0878E-01	7.8108E-01	6.6342E-01
6	2.0147E+02	2.0764E+02	1.0067E+01	1.1236E-01	2.0300E+02
7	3.6191E+02	3.8901E+02	2.5303E+01	2.5258E-01	3.6276E+02
8	1.7472E+02	1.6159E+02	1.7429E+01	-1.0302E-01	1.6896E+02
9	2.2019E+02	1.7724E+02	2.1964E+01	-4.9184E-01	2.2160E+02

BETA CALCULATED IN ITERATION NO. 3 = 4.10633

ITERATION NO. = 4

VARIABLE X(i)	FAILURE POINT	EQUIV. MEAN	EQUIV. SD	SENSITIVITY FACTOR	NEW FAILURE POINT
1	2.5219E+01	2.5000E+01	7.5000E-01	-7.4292E-02	2.5229E+01
2	8.6225E+03	8.4275E+03	4.2138E+02	-1.0125E-01	8.6026E+03
3	2.2362E+03	2.2000E+03	4.4000E+01	-1.9737E-01	2.2356E+03

Table 5.9. (Continued)

4	4.6228E+00	4.5000E+00	5.4000E-01	-4.7376E-02	4.6050E+00
5	6.6342E-01	1.0080E+00	1.0743E-01	7.8566E-01	6.6169E-01
6	2.0300E+02	2.0769E+02	1.0144E+01	1.0432E-01	2.0334E+02
7	3.6276E+02	3.8907E+02	2.5362E+01	2.5172E-01	3.6287E+02
8	1.6896E+02	1.6193E+02	1.6854E+01	-8.2519E-02	1.6763E+02
9	2.2160E+02	1.7696E+02	2.2105E+01	-4.9469E-01	2.2183E+02

BETA CALCULATED IN ITERATION NO. 4 = 4.10350

BETA FROM BASIC DEFINITION = 4.10350

BETA THROUGH ITERATION = 4.10350

PROBABILITY OF FAILURE = 0.20348D-04

-- PARTIAL SAFETY FACTORS --

VARIABLE	PSF
1	1.0091
2	1.0208
3	1.0162
4	1.0233
5	1.7077
6	1.0229
7	1.0775
8	1.0292
9	1.2184

Table 5.10. Reliability Index Calculation with 10% COV for Longitudinal and Hoop Stresses According to RCC Model Code

ITERATION NO. = 1

VARIABLE X(i)	FAILURE POINT	EQUIV. MEAN	EQUIV. SD	SENSITIVITY FACTOR	NEW FAILURE POINT
1	2.5000E+01	2.5000E+01	7.5000E-01	9.5291E-02	2.4785E+01
2	8.4275E+03	8.4275E+03	4.2138E+02	-2.0047E-01	8.6821E+03
3	2.2000E+03	2.2000E+03	4.4000E+01	-2.8421E-03	2.2004E+03
4	4.5000E+00	4.5000E+00	5.4000E-01	-1.0234E-01	4.6665E+00
5	1.0900E+00	1.0575E+00	2.6630E-01	6.9074E-01	5.0316E-01
6	2.0800E+02	2.0774E+02	1.0394E+01	1.1502E-01	2.0414E+02
7	3.9100E+02	3.9004E+02	2.7337E+01	3.6712E-01	3.5980E+02
8	1.6288E+02	1.6207E+02	1.6247E+01	-4.8038E-01	1.8559E+02
9	1.8207E+02	1.8116E+02	1.8162E+01	-2.9044E-01	1.9706E+02

BETA CALCULATED IN ITERATION NO. 1 = 3.01351

ITERATION NO. = 2

VARIABLE X(i)	FAILURE POINT	EQUIV. MEAN	EQUIV. SD	SENSITIVITY FACTOR	NEW FAILURE POINT
1	2.4785E+01	2.5000E+01	7.5000E-01	2.0054E-02	2.4949E+01
2	8.6821E+03	8.4275E+03	4.2138E+02	-4.0540E-02	8.4854E+03
3	2.2004E+03	2.2000E+03	4.4000E+01	-5.5137E-04	2.2001E+03
4	4.6665E+00	4.5000E+00	5.4000E-01	-2.0769E-02	4.5380E+00
5	5.0316E-01	8.7710E-01	1.2293E-01	8.9141E-01	5.0555E-01
6	2.0414E+02	2.0771E+02	1.0201E+01	2.4020E-02	2.0688E+02
7	3.5980E+02	3.8884E+02	2.5155E+01	2.4907E-01	3.6760E+02
8	1.8559E+02	1.6044E+02	1.8513E+01	-4.0046E-02	1.6296E+02
9	1.9706E+02	1.8049E+02	1.9657E+01	-3.7243E-01	2.0531E+02

BETA CALCULATED IN ITERATION NO. 2 = 3.39078

ITERATION NO. = 3

VARIABLE X(i)	FAILURE POINT	EQUIV. MEAN	EQUIV. SD	SENSITIVITY FACTOR	NEW FAILURE POINT
1	2.4949E+01	2.5000E+01	7.5000E-01	1.2597E-02	2.4968E+01
2	8.4854E+03	8.4275E+03	4.2138E+02	-2.6086E-02	8.4647E+03
3	2.2001E+03	2.2000E+03	4.4000E+01	-3.7203E-04	2.2001E+03
4	4.5380E+00	4.5000E+00	5.4000E-01	-1.2907E-02	4.5236E+00
5	5.0555E-01	8.7887E-01	1.2351E-01	8.9474E-01	5.0490E-01
6	2.0688E+02	2.0774E+02	1.0337E+01	1.5031E-02	2.0721E+02
7	3.6760E+02	3.8939E+02	2.5700E+01	2.4194E-01	3.6835E+02
8	1.6296E+02	1.6207E+02	1.6255E+01	-1.0012E-02	1.6262E+02
9	2.0531E+02	1.7962E+02	2.0480E+01	-3.7360E-01	2.0552E+02

BETA CALCULATED IN ITERATION NO. 3 = 3.38408

BETA FROM BASIC DEFINITION = 3.38408

BETA THROUGH ITERATION = 3.38408

PROBABILITY OF FAILURE = 0.35709D-03

Table 5.10. (Continued)

-- PARTIAL SAFETY FACTORS --

VARIABLE	PSF
1	1.0013
2	1.0044
3	1.0000
4	1.0052
5	2.1589
6	1.0038
7	1.0615
8	1.0016
9	1.1288

Table 5.11. Variation in Reliability Index According to API Performance Function

Long. Stress COV (%)	Hoop Stress COV (%)															
	5	6	7	8	9	10	11	12	13	14	15	16	17	18	19	20
5	4.516	4.448	4.372	4.289	4.201	4.109	4.015	3.919	3.824	3.729	3.635	3.543	3.453	3.366	3.282	3.201
6	4.515	4.447	4.371	4.288	4.200	4.108	4.014	3.919	3.823	3.728	3.635	3.543	3.453	3.366	3.282	3.201
7	4.514	4.446	4.370	4.287	4.199	4.107	4.014	3.918	3.823	3.728	3.634	3.543	3.453	3.366	3.282	3.201
8	4.512	4.445	4.369	4.286	4.198	4.107	4.013	3.918	3.822	3.728	3.634	3.542	3.453	3.366	3.282	3.200
9	4.512	4.444	4.368	4.286	4.198	4.106	4.012	3.917	3.822	3.727	3.634	3.542	3.453	3.366	3.282	3.200
10	4.507	4.439	4.364	4.282	4.195	4.104	4.012	3.917	3.822	3.727	3.634	3.542	3.452	3.366	3.281	3.200
11	4.505	4.438	4.362	4.280	4.193	4.102	4.009	3.914	3.819	3.727	3.634	3.542	3.453	3.366	3.282	3.200
12	4.505	4.437	4.361	4.279	4.192	4.101	4.008	3.913	3.818	3.724	3.631	3.540	3.453	3.366	3.282	3.200
13	4.514	4.443	4.365	4.281	4.192	4.100	4.007	3.912	3.817	3.723	3.630	3.539	3.450	3.364	3.280	3.201
14	4.584	4.469	4.360	4.275	4.187	4.096	4.003	3.909	3.817	3.723	3.630	3.539	3.450	3.363	3.280	3.199
15	4.562	4.517	4.454	4.277	4.185	4.093	4.004	3.909	3.814	3.720	3.630	3.538	3.449	3.363	3.279	3.198
16	4.248	4.247	4.245	4.355	4.190	4.094	3.998	3.906	3.812	3.720	3.627	3.536	3.450	3.363	3.279	3.198
17	4.054	4.055	4.052	4.051	4.051	4.049	3.996	3.903	3.810	3.718	3.625	3.536	3.447	3.361	3.280	3.198
18	3.876	3.876	3.874	3.874	3.872	3.873	3.870	3.870	3.807	3.715	3.624	3.534	3.446	3.361	3.277	3.197
19	3.710	3.710	3.710	3.710	3.708	3.709	3.707	3.709	3.706	3.833	3.623	3.534	3.447	3.359	3.278	3.197
20	3.561	3.561	3.559	3.559	3.559	3.559	3.557	3.558	3.557	3.555	3.555	3.530	3.445	3.359	3.277	3.196

Table 5.12. Variation in Reliability Index According to RCC Performance Function

		Hoop Stress COV (%)															
		5	6	7	8	9	10	11	12	13	14	15	16	17	18	19	20
Long. Stress COV (%)	5	3.553	3.527	3.497	3.463	3.426	3.384	3.341	3.297	3.250	3.203	3.155	3.106	3.057	3.008	2.959	2.910
	6	3.553	3.527	3.497	3.463	3.426	3.384	3.341	3.297	3.250	3.203	3.155	3.106	3.057	3.008	2.959	2.910
	7	3.554	3.527	3.497	3.463	3.424	3.384	3.341	3.297	3.250	3.203	3.155	3.106	3.057	3.008	2.959	2.911
	8	3.554	3.528	3.498	3.462	3.424	3.384	3.341	3.297	3.250	3.203	3.155	3.106	3.057	3.008	2.959	2.911
	9	3.555	3.529	3.496	3.462	3.424	3.384	3.341	3.297	3.251	3.203	3.155	3.106	3.057	3.008	2.959	2.911
	10	3.554	3.527	3.496	3.462	3.424	3.384	3.341	3.297	3.251	3.203	3.155	3.106	3.057	3.008	2.959	2.911
	11	3.554	3.527	3.496	3.462	3.425	3.384	3.342	3.297	3.251	3.203	3.155	3.106	3.057	3.008	2.959	2.911
	12	3.554	3.527	3.497	3.462	3.425	3.384	3.342	3.297	3.251	3.203	3.155	3.106	3.057	3.008	2.959	2.911
	13	3.554	3.527	3.497	3.462	3.425	3.384	3.342	3.297	3.251	3.203	3.155	3.106	3.057	3.008	2.959	2.911
	14	3.554	3.528	3.497	3.462	3.425	3.385	3.342	3.297	3.251	3.204	3.155	3.106	3.057	3.008	2.959	2.911
	15	3.555	3.528	3.497	3.463	3.425	3.385	3.342	3.297	3.251	3.204	3.155	3.107	3.058	3.008	2.960	2.911
	16	3.556	3.529	3.498	3.464	3.426	3.385	3.343	3.298	3.252	3.204	3.156	3.107	3.058	3.009	2.960	2.911
	17	3.555	3.528	3.497	3.463	3.425	3.385	3.344	3.299	3.252	3.205	3.156	3.107	3.058	3.009	2.960	2.912
	18	3.555	3.528	3.497	3.463	3.427	3.386	3.343	3.298	3.252	3.204	3.155	3.108	3.059	3.010	2.961	2.912
	19	3.555	3.528	3.497	3.463	3.425	3.385	3.342	3.298	3.251	3.205	3.157	3.108	3.058	3.009	2.960	2.911
	20	3.556	3.529	3.498	3.463	3.426	3.385	3.342	3.298	3.251	3.204	3.156	3.107	3.059	3.010	2.961	2.912

Table 5.13. Variation in Reliability Index Ignoring Model Uncertainty Factor (RCC)

Long. Stress COV (%)	Hoop Stress COV (%) 5	6	7	8	9	10	11	12	13	14	15	16	17	18	19	20
5	9.534	9.245	8.731	8.186	7.662	7.170	6.723	6.318	5.956	5.625	5.327	5.058	4.815	4.593	4.392	4.208
6	6.862	8.949	8.702	8.178	7.656	7.171	6.723	6.318	5.953	5.627	5.328	5.059	4.815	4.594	4.392	4.208
7	8.396	8.385	8.370	8.160	7.652	7.167	6.724	6.318	5.953	5.623	5.326	5.060	4.815	4.594	4.392	4.208
8	7.831	7.828	7.821	7.810	7.641	7.166	6.721	6.316	5.953	5.623	5.326	5.058	4.817	4.594	4.393	4.208
9	7.303	7.301	7.296	7.295	7.288	7.161	6.717	6.317	5.952	5.624	5.326	5.058	4.814	4.596	4.393	4.209
10	6.820	6.815	6.814	6.815	6.811	6.810	7.012	6.315	5.953	5.623	5.327	5.058	4.815	4.593	4.392	4.210
11	6.378	6.379	6.376	6.375	6.376	6.374	6.373	6.371	5.951	5.625	5.326	5.059	4.815	4.594	4.392	4.208
12	5.982	5.982	5.983	5.981	5.981	5.982	5.980	5.979	5.978	5.623	5.326	5.058	4.816	4.594	4.392	4.208
13	5.627	5.628	5.628	5.629	5.627	5.627	5.628	5.627	5.626	5.626	5.328	5.058	4.815	4.596	4.393	4.208
14	5.309	5.309	5.309	5.310	5.311	5.309	5.309	5.310	5.309	5.309	5.311	5.058	4.815	4.594	4.392	4.209
15	5.023	5.023	5.023	5.024	5.024	5.026	5.023	5.024	5.025	5.024	5.026	5.024	4.815	4.594	4.393	4.208
16	4.766	4.766	4.766	4.766	4.766	4.767	4.768	4.766	4.766	4.767	4.766	4.768	4.766	4.594	4.393	4.209
17	4.533	4.533	4.533	4.533	4.533	4.533	4.534	4.536	4.533	4.533	4.534	4.534	4.535	4.536	4.393	4.210
18	4.322	4.322	4.322	4.322	4.322	4.322	4.323	4.323	4.325	4.322	4.323	4.323	4.323	4.324	4.324	4.323
19	4.130	4.130	4.130	4.130	4.130	4.130	4.131	4.131	4.132	4.131	4.131	4.131	4.132	4.131	4.132	4.132
20	3.955	3.955	3.955	3.955	3.955	3.955	3.956	3.956	3.956	3.957	3.956	3.956	3.956	3.957	3.956	3.957

Table 5.14. Variation in Reliability Index Ignoring Model Uncertainty Factor (API)

Long. Stress COV (%)	Hoop Stress COV (%)															
	5	6	7	8	9	10	11	12	13	14	15	16	17	18	19	20
5	7.352	7.248	6.991	6.615	6.235	5.865	5.520	5.205	4.920	4.658	4.421	4.205	4.009	3.830	3.667	3.518
6	7.084	7.019	6.882	6.575	6.213	5.855	5.514	5.200	4.914	4.657	4.419	4.204	4.008	3.830	3.667	3.517
7	6.779	6.733	6.667	6.503	6.180	5.836	5.506	5.195	4.910	4.651	4.419	4.203	4.007	3.829	3.666	3.517
8	6.452	6.422	6.379	6.314	6.129	5.811	5.491	5.189	4.906	4.648	4.413	4.203	4.007	3.829	3.666	3.517
9	6.113	6.097	6.070	6.033	5.976	5.775	5.474	5.177	4.897	4.644	4.410	4.197	4.003	3.828	3.665	3.516
10	5.781	5.770	5.756	5.733	5.704	5.653	5.447	5.163	4.891	4.638	4.408	4.195	4.002	3.825	3.665	3.516
11	5.467	5.456	5.447	5.436	5.417	5.390	5.352	5.141	4.881	4.633	4.402	4.193	4.000	3.823	3.662	3.516
12	5.169	5.165	5.155	5.147	5.135	5.123	5.102	5.069	4.863	4.625	4.398	4.188	3.998	3.822	3.661	3.513
13	4.892	4.890	4.883	4.877	4.871	4.861	4.848	4.836	4.810	4.610	4.392	4.186	3.994	3.821	3.659	3.512
14	4.639	4.637	4.635	4.628	4.623	4.619	4.610	4.600	4.587	4.569	4.380	4.177	3.992	3.817	3.659	3.511
15	4.406	4.405	4.403	4.402	4.395	4.392	4.388	4.381	4.373	4.362	4.351	4.170	3.984	3.813	3.655	3.508
16	4.194	4.193	4.192	4.191	4.186	4.183	4.180	4.178	4.171	4.165	4.156	4.146	3.980	3.809	3.652	3.507
17	4.000	3.999	3.998	3.997	3.997	3.992	3.990	3.988	3.983	3.980	3.975	3.968	3.959	3.805	3.649	3.505
18	3.823	3.822	3.822	3.821	3.820	3.820	3.815	3.813	3.812	3.808	3.806	3.801	3.796	3.788	3.646	3.502
19	3.661	3.660	3.660	3.659	3.658	3.658	3.655	3.653	3.652	3.651	3.647	3.646	3.642	3.638	3.631	3.499
20	3.512	3.512	3.511	3.511	3.510	3.510	3.510	3.506	3.505	3.504	3.504	3.500	3.500	3.496	3.492	3.489

Table 5.15. Reliability Index Calculation with 10% COV for Longitudinal and Hoop Stresses Ignoring Model Uncertainty Factor (API)

ITERATION NO. = 1

VARIABLE X(i)	FAILURE POINT	EQUIV. MEAN	EQUIV. SD	SENSITIVITY FACTOR	NEW FAILURE POINT
1	2.5000E+01	2.5000E+01	7.5000E-01	-3.5304E-02	2.5160E+01
2	8.4275E+03	8.4275E+03	4.2138E+02	-3.2877E-01	9.2630E+03
3	2.2000E+03	2.2000E+03	4.4000E+01	-3.0345E-01	2.2805E+03
4	4.5000E+00	4.5000E+00	5.4000E-01	-1.7395E-01	5.0665E+00
5	1.0000E+00	1.0000E+00	0.0000E+00	0.0000E+00	1.0000E+00
6	2.0800E+02	2.0774E+02	1.0394E+01	2.5253E-01	1.9191E+02
7	3.9100E+02	3.9004E+02	2.7337E+01	3.7643E-01	3.2799E+02
8	1.6288E+02	1.6207E+02	1.6247E+01	-5.3301E-01	2.1430E+02
9	1.8207E+02	1.8116E+02	1.8162E+01	-5.2797E-01	2.3899E+02

BETA CALCULATED IN ITERATION NO. 1 = 6.03068

ITERATION NO. = 2

VARIABLE X(i)	FAILURE POINT	EQUIV. MEAN	EQUIV. SD	SENSITIVITY FACTOR	NEW FAILURE POINT
1	2.5160E+01	2.5000E+01	7.5000E-01	-4.6570E-03	2.5020E+01
2	9.2630E+03	8.4275E+03	4.2138E+02	-3.2457E-01	9.2033E+03
3	2.2805E+03	2.2000E+03	4.4000E+01	-2.7395E-01	2.2684E+03
4	5.0665E+00	4.5000E+00	5.4000E-01	-1.8984E-01	5.0815E+00
5	1.0000E+00	1.0000E+00	0.0000E+00	0.0000E+00	1.0000E+00
6	1.9191E+02	2.0712E+02	9.5896E+00	2.7722E-01	1.9204E+02
7	3.2799E+02	3.8482E+02	2.2931E+01	3.5404E-01	3.3877E+02
8	2.1430E+02	1.5444E+02	2.1376E+01	-5.4013E-01	2.1994E+02
9	2.3899E+02	1.7279E+02	2.3840E+01	-5.3815E-01	2.4557E+02

BETA CALCULATED IN ITERATION NO. 2 = 5.67285

ITERATION NO. = 3

VARIABLE X(i)	FAILURE POINT	EQUIV. MEAN	EQUIV. SD	SENSITIVITY FACTOR	NEW FAILURE POINT
1	2.5020E+01	2.5000E+01	7.5000E-01	-3.2407E-03	2.5014E+01
2	9.2033E+03	8.4275E+03	4.2138E+02	-3.3463E-01	9.2274E+03
3	2.2684E+03	2.2000E+03	4.4000E+01	-2.7236E-01	2.2680E+03
4	5.0815E+00	4.5000E+00	5.4000E-01	-2.0159E-01	5.1175E+00
5	1.0000E+00	1.0000E+00	0.0000E+00	0.0000E+00	1.0000E+00
6	1.9204E+02	2.0713E+02	9.5960E+00	2.7975E-01	1.9190E+02
7	3.3877E+02	3.8652E+02	2.3685E+01	3.4619E-01	3.4000E+02
8	2.1994E+02	1.5279E+02	2.1939E+01	-5.4938E-01	2.2116E+02
9	2.4557E+02	1.7088E+02	2.4496E+01	-5.2275E-01	2.4352E+02

BETA CALCULATED IN ITERATION NO. 3 = 5.67285

ITERATION NO. = 4

VARIABLE X(i)	FAILURE POINT	EQUIV. MEAN	EQUIV. SD	SENSITIVITY FACTOR	NEW FAILURE POINT
1	2.5014E+01	2.5000E+01	7.5000E-01	2.1190E-03	2.4991E+01
2	9.2274E+03	8.4275E+03	4.2138E+02	-3.3966E-01	9.2385E+03
3	2.2680E+03	2.2000E+03	4.4000E+01	-2.6778E-01	2.2668E+03

Table 5.15. (Continued)

4	5.1175E+00	4.5000E+00	5.4000E-01	-2.0751E-01	5.1349E+00
5	1.0000E+00	1.0000E+00	0.0000E+00	0.0000E+00	1.0000E+00
6	1.9190E+02	2.0712E+02	9.5892E+00	2.8289E-01	1.9175E+02
7	3.4000E+02	3.8669E+02	2.3771E+01	3.4036E-01	3.4084E+02
8	2.2116E+02	1.5241E+02	2.2061E+01	-5.6169E-01	2.2263E+02
9	2.4352E+02	1.7149E+02	2.4291E+01	-5.0842E-01	2.4147E+02

BETA CALCULATED IN ITERATION NO. 4 = 5.66623

ITERATION NO. = 5

VARIABLE X(i)	FAILURE POINT	EQUIV. MEAN	EQUIV. SD	SENSITIVITY FACTOR	NEW FAILURE POINT
1	2.4991E+01	2.5000E+01	7.5000E-01	6.8217E-03	2.4971E+01
2	9.2385E+03	8.4275E+03	4.2138E+02	-3.4412E-01	9.2491E+03
3	2.2668E+03	2.2000E+03	4.4000E+01	-2.6357E-01	2.2657E+03
4	5.1349E+00	4.5000E+00	5.4000E-01	-2.1226E-01	5.1495E+00
5	1.0000E+00	1.0000E+00	0.0000E+00	0.0000E+00	1.0000E+00
6	1.9175E+02	2.0711E+02	9.5815E+00	2.8513E-01	1.9163E+02
7	3.4084E+02	3.8680E+02	2.3830E+01	3.3548E-01	3.4150E+02
8	2.2263E+02	1.5195E+02	2.2207E+01	-5.7397E-01	2.2418E+02
9	2.4147E+02	1.7209E+02	2.4087E+01	-4.9367E-01	2.3947E+02

BETA CALCULATED IN ITERATION NO. 5 = 5.66623

ITERATION NO. = 6

VARIABLE X(i)	FAILURE POINT	EQUIV. MEAN	EQUIV. SD	SENSITIVITY FACTOR	NEW FAILURE POINT
1	2.4971E+01	2.5000E+01	7.5000E-01	1.1421E-02	2.4951E+01
2	9.2491E+03	8.4275E+03	4.2138E+02	-3.4812E-01	9.2587E+03
3	2.2657E+03	2.2000E+03	4.4000E+01	-2.5930E-01	2.2646E+03
4	5.1495E+00	4.5000E+00	5.4000E-01	-2.1653E-01	5.1625E+00
5	1.0000E+00	1.0000E+00	0.0000E+00	0.0000E+00	1.0000E+00
6	1.9163E+02	2.0710E+02	9.5754E+00	2.8708E-01	1.9152E+02
7	3.4150E+02	3.8689E+02	2.3876E+01	3.3083E-01	3.4213E+02
8	2.2418E+02	1.5145E+02	2.2362E+01	-5.8576E-01	2.2567E+02
9	2.3947E+02	1.7266E+02	2.3887E+01	-4.7915E-01	2.3751E+02

BETA CALCULATED IN ITERATION NO. 6 = 5.66623

ITERATION NO. = 7

VARIABLE X(i)	FAILURE POINT	EQUIV. MEAN	EQUIV. SD	SENSITIVITY FACTOR	NEW FAILURE POINT
1	2.4951E+01	2.5000E+01	7.5000E-01	1.5823E-02	2.4933E+01
2	9.2587E+03	8.4275E+03	4.2138E+02	-3.5174E-01	9.2663E+03
3	2.2646E+03	2.2000E+03	4.4000E+01	-2.5508E-01	2.2635E+03
4	5.1625E+00	4.5000E+00	5.4000E-01	-2.2049E-01	5.1738E+00
5	1.0000E+00	1.0000E+00	0.0000E+00	0.0000E+00	1.0000E+00
6	1.9152E+02	2.0709E+02	9.5702E+00	2.8879E-01	1.9145E+02
7	3.4213E+02	3.8697E+02	2.3920E+01	3.2632E-01	3.4280E+02
8	2.2567E+02	1.5096E+02	2.2511E+01	-5.9681E-01	2.2699E+02
9	2.3751E+02	1.7319E+02	2.3692E+01	-4.6506E-01	2.3555E+02

BETA CALCULATED IN ITERATION NO. 7 = 5.65917

Table 5.15. (Continued)

ITERATION NO. = 8

VARIABLE X(i)	FAILURE POINT	EQUIV. MEAN	EQUIV. SD	SENSITIVITY FACTOR	NEW FAILURE POINT
1	2.4933E+01	2.5000E+01	7.5000E-01	1.9920E-02	2.4915E+01
2	9.2663E+03	8.4275E+03	4.2138E+02	-3.5498E-01	9.2740E+03
3	2.2635E+03	2.2000E+03	4.4000E+01	-2.5103E-01	2.2625E+03
4	5.1738E+00	4.5000E+00	5.4000E-01	-2.2408E-01	5.1848E+00
5	1.0000E+00	1.0000E+00	0.0000E+00	0.0000E+00	1.0000E+00
6	1.9145E+02	2.0708E+02	9.5665E+00	2.9023E-01	1.9137E+02
7	3.4280E+02	3.8706E+02	2.3967E+01	3.2205E-01	3.4338E+02
8	2.2699E+02	1.5052E+02	2.2643E+01	-6.0694E-01	2.2830E+02
9	2.3555E+02	1.7372E+02	2.3496E+01	-4.5171E-01	2.3378E+02

BETA CALCULATED IN ITERATION NO. 8 = 5.65917

ITERATION NO. = 9

VARIABLE X(i)	FAILURE POINT	EQUIV. MEAN	EQUIV. SD	SENSITIVITY FACTOR	NEW FAILURE POINT
1	2.4915E+01	2.5000E+01	7.5000E-01	2.3755E-02	2.4899E+01
2	9.2740E+03	8.4275E+03	4.2138E+02	-3.5784E-01	9.2808E+03
3	2.2625E+03	2.2000E+03	4.4000E+01	-2.4714E-01	2.2615E+03
4	5.1848E+00	4.5000E+00	5.4000E-01	-2.2738E-01	5.1948E+00
5	1.0000E+00	1.0000E+00	0.0000E+00	0.0000E+00	1.0000E+00
6	1.9137E+02	2.0708E+02	9.5626E+00	2.9148E-01	1.9130E+02
7	3.4338E+02	3.8714E+02	2.4007E+01	3.1799E-01	3.4393E+02
8	2.2830E+02	1.5008E+02	2.2773E+01	-6.1613E-01	2.2948E+02
9	2.3378E+02	1.7417E+02	2.3320E+01	-4.3922E-01	2.3214E+02

BETA CALCULATED IN ITERATION NO. 9 = 5.65917

ITERATION NO. = 10

VARIABLE X(i)	FAILURE POINT	EQUIV. MEAN	EQUIV. SD	SENSITIVITY FACTOR	NEW FAILURE POINT
1	2.4899E+01	2.5000E+01	7.5000E-01	2.7263E-02	2.4884E+01
2	9.2808E+03	8.4275E+03	4.2138E+02	-3.6035E-01	9.2868E+03
3	2.2615E+03	2.2000E+03	4.4000E+01	-2.4350E-01	2.2606E+03
4	5.1948E+00	4.5000E+00	5.4000E-01	-2.3035E-01	5.2039E+00
5	1.0000E+00	1.0000E+00	0.0000E+00	0.0000E+00	1.0000E+00
6	1.9130E+02	2.0707E+02	9.5592E+00	2.9255E-01	1.9125E+02
7	3.4393E+02	3.8721E+02	2.4046E+01	3.1421E-01	3.4445E+02
8	2.2948E+02	1.4967E+02	2.2891E+01	-6.2435E-01	2.3055E+02
9	2.3214E+02	1.7459E+02	2.3156E+01	-4.2771E-01	2.3064E+02

BETA CALCULATED IN ITERATION NO.10 = 5.65917

ITERATION NO. = 11

VARIABLE X(i)	FAILURE POINT	EQUIV. MEAN	EQUIV. SD	SENSITIVITY FACTOR	NEW FAILURE POINT
1	2.4884E+01	2.5000E+01	7.5000E-01	3.0425E-02	2.4871E+01
2	9.2868E+03	8.4275E+03	4.2138E+02	-3.6251E-01	9.2911E+03
3	2.2606E+03	2.2000E+03	4.4000E+01	-2.4014E-01	2.2597E+03
4	5.2039E+00	4.5000E+00	5.4000E-01	-2.3299E-01	5.2113E+00
5	1.0000E+00	1.0000E+00	0.0000E+00	0.0000E+00	1.0000E+00

Table 5.15. (Continued)

6	1.9125E+02	2.0707E+02	9.5563E+00	2.9344E-01	1.9121E+02
7	3.4445E+02	3.8727E+02	2.4082E+01	3.1074E-01	3.4496E+02
8	2.3055E+02	1.4930E+02	2.2998E+01	-6.3160E-01	2.3141E+02
9	2.3064E+02	1.7495E+02	2.3006E+01	-4.1727E-01	2.2923E+02

BETA CALCULATED IN ITERATION NO.11 = 5.65335

ITERATION NO. = 12

VARIABLE X(i)	FAILURE POINT	EQUIV. MEAN	EQUIV. SD	SENSITIVITY FACTOR	NEW FAILURE POINT
1	2.4871E+01	2.5000E+01	7.5000E-01	3.3166E-02	2.4859E+01
2	9.2911E+03	8.4275E+03	4.2138E+02	-3.6434E-01	9.2954E+03
3	2.2597E+03	2.2000E+03	4.4000E+01	-2.3718E-01	2.2590E+03
4	5.2113E+00	4.5000E+00	5.4000E-01	-2.3525E-01	5.2182E+00
5	1.0000E+00	1.0000E+00	0.0000E+00	0.0000E+00	1.0000E+00
6	1.9121E+02	2.0706E+02	9.5548E+00	2.9413E-01	1.9118E+02
7	3.4496E+02	3.8733E+02	2.4118E+01	3.0771E-01	3.4538E+02
8	2.3141E+02	1.4899E+02	2.3084E+01	-6.3784E-01	2.3223E+02
9	2.2923E+02	1.7529E+02	2.2866E+01	-4.0807E-01	2.2804E+02

BETA CALCULATED IN ITERATION NO.12 = 5.65335

ITERATION NO. = 13

VARIABLE X(i)	FAILURE POINT	EQUIV. MEAN	EQUIV. SD	SENSITIVITY FACTOR	NEW FAILURE POINT
1	2.4859E+01	2.5000E+01	7.5000E-01	3.5580E-02	2.4849E+01
2	9.2954E+03	8.4275E+03	4.2138E+02	-3.6587E-01	9.2991E+03
3	2.2590E+03	2.2000E+03	4.4000E+01	-2.3453E-01	2.2583E+03
4	5.2182E+00	4.5000E+00	5.4000E-01	-2.3721E-01	5.2242E+00
5	1.0000E+00	1.0000E+00	0.0000E+00	0.0000E+00	1.0000E+00
6	1.9118E+02	2.0706E+02	9.5529E+00	2.9472E-01	1.9115E+02
7	3.4538E+02	3.8738E+02	2.4147E+01	3.0501E-01	3.4575E+02
8	2.3223E+02	1.4870E+02	2.3165E+01	-6.4319E-01	2.3293E+02
9	2.2804E+02	1.7557E+02	2.2747E+01	-4.0002E-01	2.2701E+02

BETA CALCULATED IN ITERATION NO.13 = 5.65335

BETA FROM BASIC DEFINITION = 5.65335

BETA THROUGH ITERATION = 5.65335

PROBABILITY OF FAILURE = 0.78674D-08

-- PARTIAL SAFETY FACTORS --

VARIABLE	PSF
1	1.0061
2	1.1034
3	1.0265
4	1.1609
5	1.0000
6	1.0882
7	1.1309
8	1.4301
9	1.2468

Table 5.16. Reliability Index Calculation with 10% COV for Longitudinal and Hoop Stresses Ignoring Model Uncertainty Factor (RCC)

ITERATION NO. = 1

VARIABLE X(i)	FAILURE POINT	EQUIV. MEAN	EQUIV. SD	SENSITIVITY FACTOR	NEW FAILURE POINT
1	2.5000E+01	2.5000E+01	7.5000E-01	1.2471E-01	2.4300E+01
2	8.4275E+03	8.4275E+03	4.2138E+02	-2.6237E-01	9.2554E+03
3	2.2000E+03	2.2000E+03	4.4000E+01	-3.7196E-03	2.2012E+03
4	4.5000E+00	4.5000E+00	5.4000E-01	-1.3394E-01	5.0417E+00
5	1.0000E+00	1.0000E+00	0.0000E+00	0.0000E+00	1.0000E+00
6	2.0800E+02	2.0774E+02	1.0394E+01	1.5052E-01	1.9602E+02
7	3.9100E+02	3.9004E+02	2.7337E+01	5.3135E-01	2.8127E+02
8	1.6288E+02	1.6207E+02	1.6247E+01	-5.9645E-01	2.3464E+02
9	1.8207E+02	1.8116E+02	1.8162E+01	-4.8673E-01	2.4736E+02

BETA CALCULATED IN ITERATION NO. 1 = 7.48879

ITERATION NO. = 2

VARIABLE X(i)	FAILURE POINT	EQUIV. MEAN	EQUIV. SD	SENSITIVITY FACTOR	NEW FAILURE POINT
1	2.4300E+01	2.5000E+01	7.5000E-01	1.3256E-01	2.4294E+01
2	9.2554E+03	8.4275E+03	4.2138E+02	-2.4317E-01	9.1556E+03
3	2.2012E+03	2.2000E+03	4.4000E+01	-3.1021E-03	2.2010E+03
4	5.0417E+00	4.5000E+00	5.4000E-01	-1.1902E-01	4.9567E+00
5	1.0000E+00	1.0000E+00	0.0000E+00	0.0000E+00	1.0000E+00
6	1.9602E+02	2.0740E+02	9.7951E+00	1.5369E-01	1.9671E+02
7	2.8127E+02	3.7323E+02	1.9665E+01	5.2722E-01	2.9956E+02
8	2.3464E+02	1.4782E+02	2.3406E+01	-6.4268E-01	2.5471E+02
9	2.4736E+02	1.7032E+02	2.4675E+01	-4.4102E-01	2.4765E+02

BETA CALCULATED IN ITERATION NO. 2 = 7.10582

ITERATION NO. = 3

VARIABLE X(i)	FAILURE POINT	EQUIV. MEAN	EQUIV. SD	SENSITIVITY FACTOR	NEW FAILURE POINT
1	2.4294E+01	2.5000E+01	7.5000E-01	1.4179E-01	2.4256E+01
2	9.1556E+03	8.4275E+03	4.2138E+02	-2.6478E-01	9.2085E+03
3	2.2010E+03	2.2000E+03	4.4000E+01	-3.3631E-03	2.2010E+03
4	4.9567E+00	4.5000E+00	5.4000E-01	-1.3310E-01	5.0031E+00
5	1.0000E+00	1.0000E+00	0.0000E+00	0.0000E+00	1.0000E+00
6	1.9671E+02	2.0744E+02	9.8292E+00	1.6566E-01	1.9604E+02
7	2.9956E+02	3.7863E+02	2.0944E+01	4.9272E-01	3.0639E+02
8	2.5471E+02	1.3956E+02	2.5408E+01	-7.0580E-01	2.6509E+02
9	2.4765E+02	1.7023E+02	2.4703E+01	-3.5169E-01	2.3105E+02

BETA CALCULATED IN ITERATION NO. 3 = 7.00011

ITERATION NO. = 4

VARIABLE X(i)	FAILURE POINT	EQUIV. MEAN	EQUIV. SD	SENSITIVITY FACTOR	NEW FAILURE POINT
1	2.4256E+01	2.5000E+01	7.5000E-01	1.5018E-01	2.4224E+01
2	9.2085E+03	8.4275E+03	4.2138E+02	-2.8016E-01	9.2408E+03
3	2.2010E+03	2.2000E+03	4.4000E+01	-3.4830E-03	2.2011E+03

Table 5.16. (Continued)

4	5.0031E+00	4.5000E+00	5.4000E-01	-1.4559E-01	5.0416E+00
5	1.0000E+00	1.0000E+00	0.0000E+00	0.0000E+00	1.0000E+00
6	1.9604E+02	2.0740E+02	9.7961E+00	1.7708E-01	1.9545E+02
7	3.0639E+02	3.8035E+02	2.1421E+01	4.4600E-01	3.1453E+02
8	2.6509E+02	1.3466E+02	2.6443E+01	-7.6606E-01	2.7421E+02
9	2.3105E+02	1.7485E+02	2.3048E+01	-2.4623E-01	2.1395E+02

BETA CALCULATED IN ITERATION NO. 4 = 6.88936

ITERATION NO. = 5

VARIABLE X(i)	FAILURE POINT	EQUIV. MEAN	EQUIV. SD	SENSITIVITY FACTOR	NEW FAILURE POINT
1	2.4224E+01	2.5000E+01	7.5000E-01	1.5473E-01	2.4208E+01
2	9.2408E+03	8.4275E+03	4.2138E+02	-2.8923E-01	9.2597E+03
3	2.2011E+03	2.2000E+03	4.4000E+01	-3.5330E-03	2.2011E+03
4	5.0416E+00	4.5000E+00	5.4000E-01	-1.5543E-01	5.0731E+00
5	1.0000E+00	1.0000E+00	0.0000E+00	0.0000E+00	1.0000E+00
6	1.9545E+02	2.0737E+02	9.7666E+00	1.8431E-01	1.9508E+02
7	3.1453E+02	3.8221E+02	2.1990E+01	4.0347E-01	3.2163E+02
8	2.7421E+02	1.3001E+02	2.7353E+01	-8.0342E-01	2.8007E+02
9	2.1395E+02	1.7836E+02	2.1342E+01	-1.6122E-01	2.0186E+02

BETA CALCULATED IN ITERATION NO. 5 = 6.82813

ITERATION NO. = 6

VARIABLE X(i)	FAILURE POINT	EQUIV. MEAN	EQUIV. SD	SENSITIVITY FACTOR	NEW FAILURE POINT
1	2.4208E+01	2.5000E+01	7.5000E-01	1.5678E-01	2.4199E+01
2	9.2597E+03	8.4275E+03	4.2138E+02	-2.9393E-01	9.2710E+03
3	2.2011E+03	2.2000E+03	4.4000E+01	-3.5474E-03	2.2011E+03
4	5.0731E+00	4.5000E+00	5.4000E-01	-1.6231E-01	5.0969E+00
5	1.0000E+00	1.0000E+00	0.0000E+00	0.0000E+00	1.0000E+00
6	1.9508E+02	2.0735E+02	9.7478E+00	1.8847E-01	1.9483E+02
7	3.2163E+02	3.8366E+02	2.2487E+01	3.7656E-01	3.2599E+02
8	2.8007E+02	1.2687E+02	2.7937E+01	-8.2003E-01	2.8289E+02
9	2.0186E+02	1.8003E+02	2.0136E+01	-1.1358E-01	1.9560E+02

BETA CALCULATED IN ITERATION NO. 6 = 6.81026

ITERATION NO. = 7

VARIABLE X(i)	FAILURE POINT	EQUIV. MEAN	EQUIV. SD	SENSITIVITY FACTOR	NEW FAILURE POINT
1	2.4199E+01	2.5000E+01	7.5000E-01	1.5783E-01	2.4194E+01
2	9.2710E+03	8.4275E+03	4.2138E+02	-2.9649E-01	9.2783E+03
3	2.2011E+03	2.2000E+03	4.4000E+01	-3.5520E-03	2.2011E+03
4	5.0969E+00	4.5000E+00	5.4000E-01	-1.6655E-01	5.1125E+00
5	1.0000E+00	1.0000E+00	0.0000E+00	0.0000E+00	1.0000E+00
6	1.9483E+02	2.0733E+02	9.7357E+00	1.9088E-01	1.9468E+02
7	3.2599E+02	3.8447E+02	2.2792E+01	3.6307E-01	3.2812E+02
8	2.8289E+02	1.2531E+02	2.8219E+01	-8.2621E-01	2.8409E+02
9	1.9560E+02	1.8061E+02	1.9512E+01	-9.2530E-02	1.9290E+02

BETA CALCULATED IN ITERATION NO. 7 = 6.81026

Table 5.16. (Continued)

ITERATION NO. = 8

VARIABLE X(i)	FAILURE POINT	EQUIV. MEAN	EQUIV. SD	SENSITIVITY FACTOR	NEW FAILURE POINT
1	2.4194E+01	2.5000E+01	7.5000E-01	1.5841E-01	2.4191E+01
2	9.2783E+03	8.4275E+03	4.2138E+02	-2.9785E-01	9.2822E+03
3	2.2011E+03	2.2000E+03	4.4000E+01	-3.5536E-03	2.2011E+03
4	5.1125E+00	4.5000E+00	5.4000E-01	-1.6886E-01	5.1210E+00
5	1.0000E+00	1.0000E+00	0.0000E+00	0.0000E+00	1.0000E+00
6	1.9468E+02	2.0732E+02	9.7277E+00	1.9222E-01	1.9459E+02
7	3.2812E+02	3.8485E+02	2.2940E+01	3.5691E-01	3.2909E+02
8	2.8409E+02	1.2464E+02	2.8339E+01	-8.2842E-01	2.8452E+02
9	1.9290E+02	1.8079E+02	1.9242E+01	-8.4024E-02	1.9181E+02

BETA CALCULATED IN ITERATION NO. 8 = 6.81026

BETA FROM BASIC DEFINITION = 6.81026

BETA THROUGH ITERATION = 6.81026

PROBABILITY OF FAILURE = 0.48710D-11

-- PARTIAL SAFETY FACTORS --

VARIABLE	PSF
1	1.0334
2	1.1014
3	1.0005
4	1.1380
5	1.0000
6	1.0689
7	1.1881
8	1.7468
9	1.0535

MYSTRO: 11.0-2 DATE: 18-12-94

Elements = 120

Nodes = 120

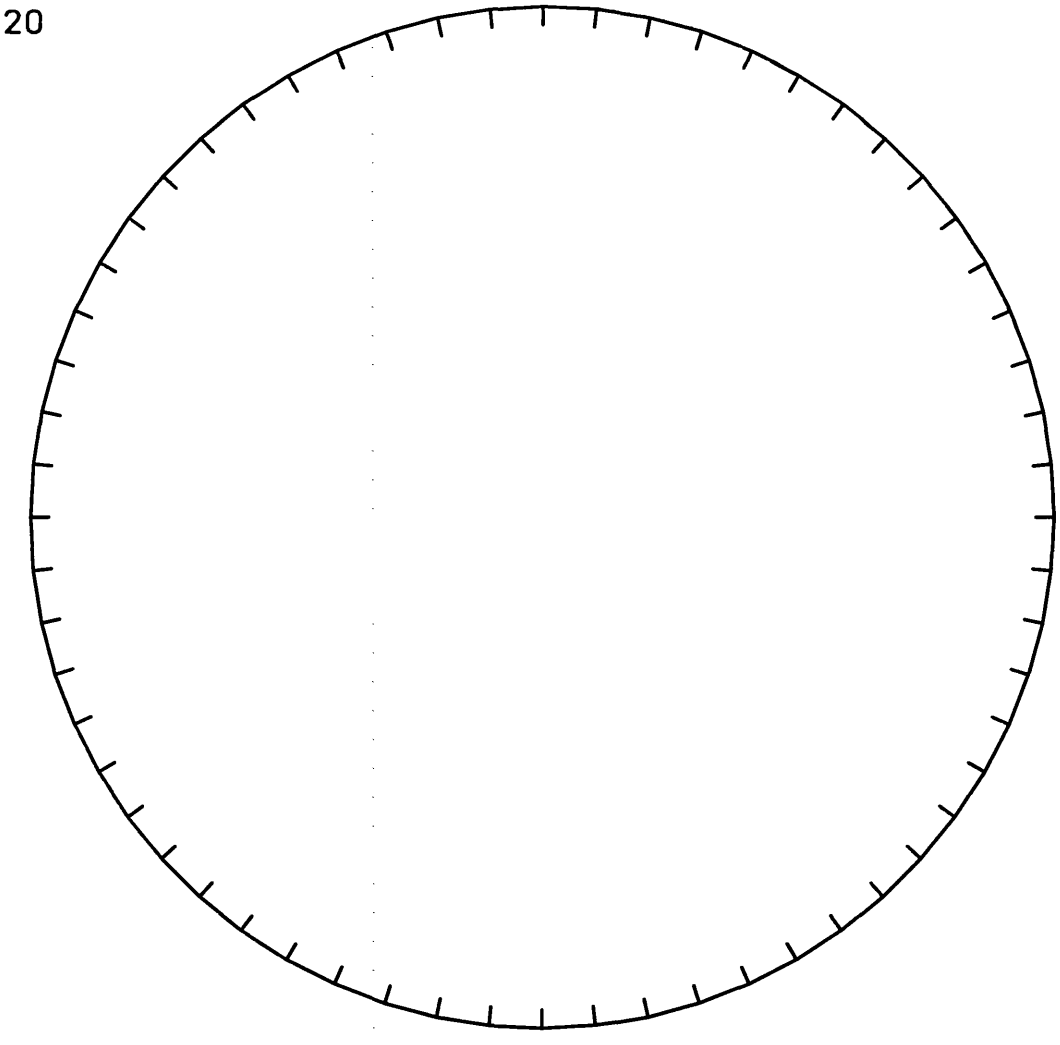

Fig. 5.2. The Model for Case 3 in Table 5.2

TITLE: Model for Program CSSP in VAS

Fig. 5.3. Reliability Index Variation According to API Formulations

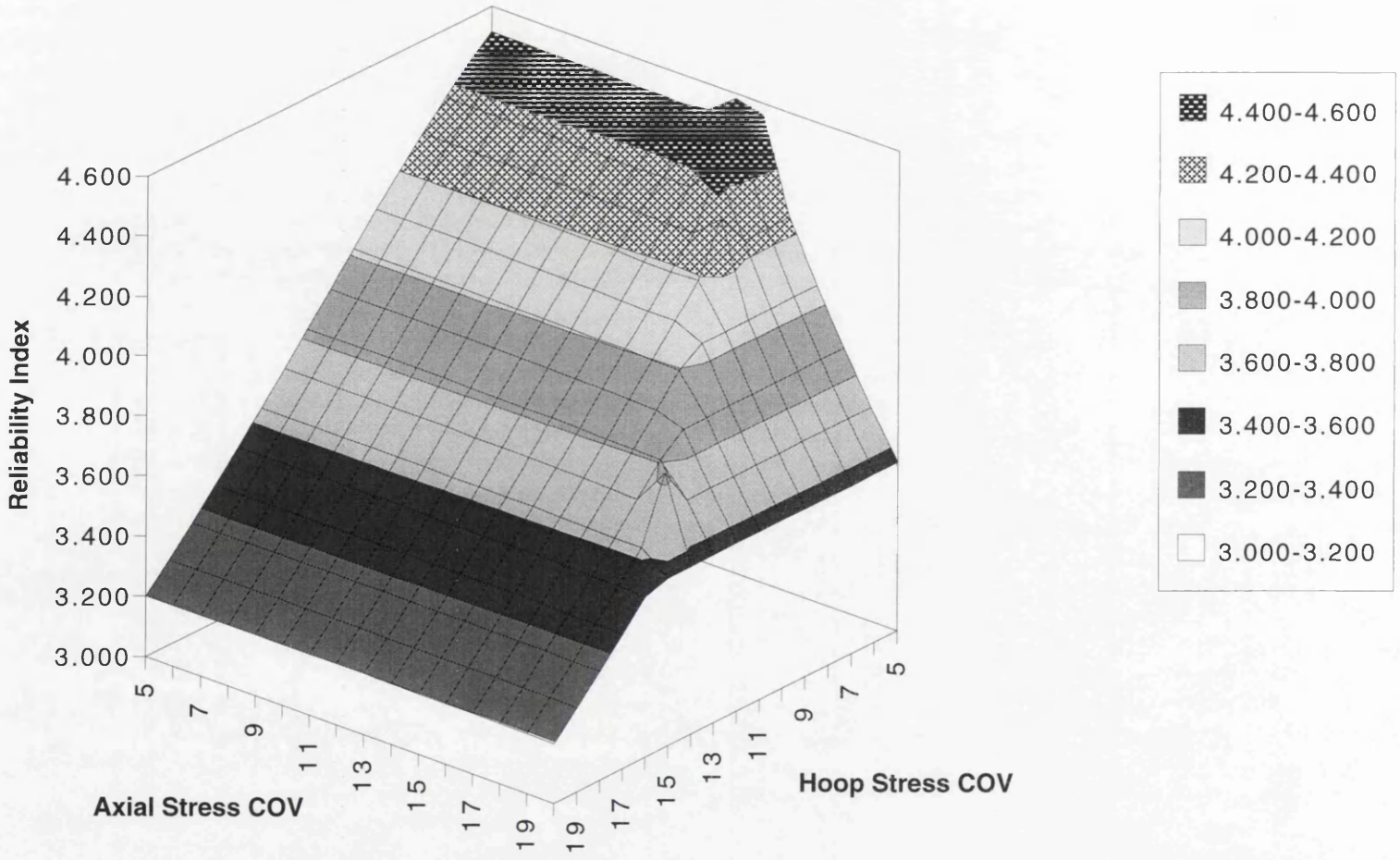

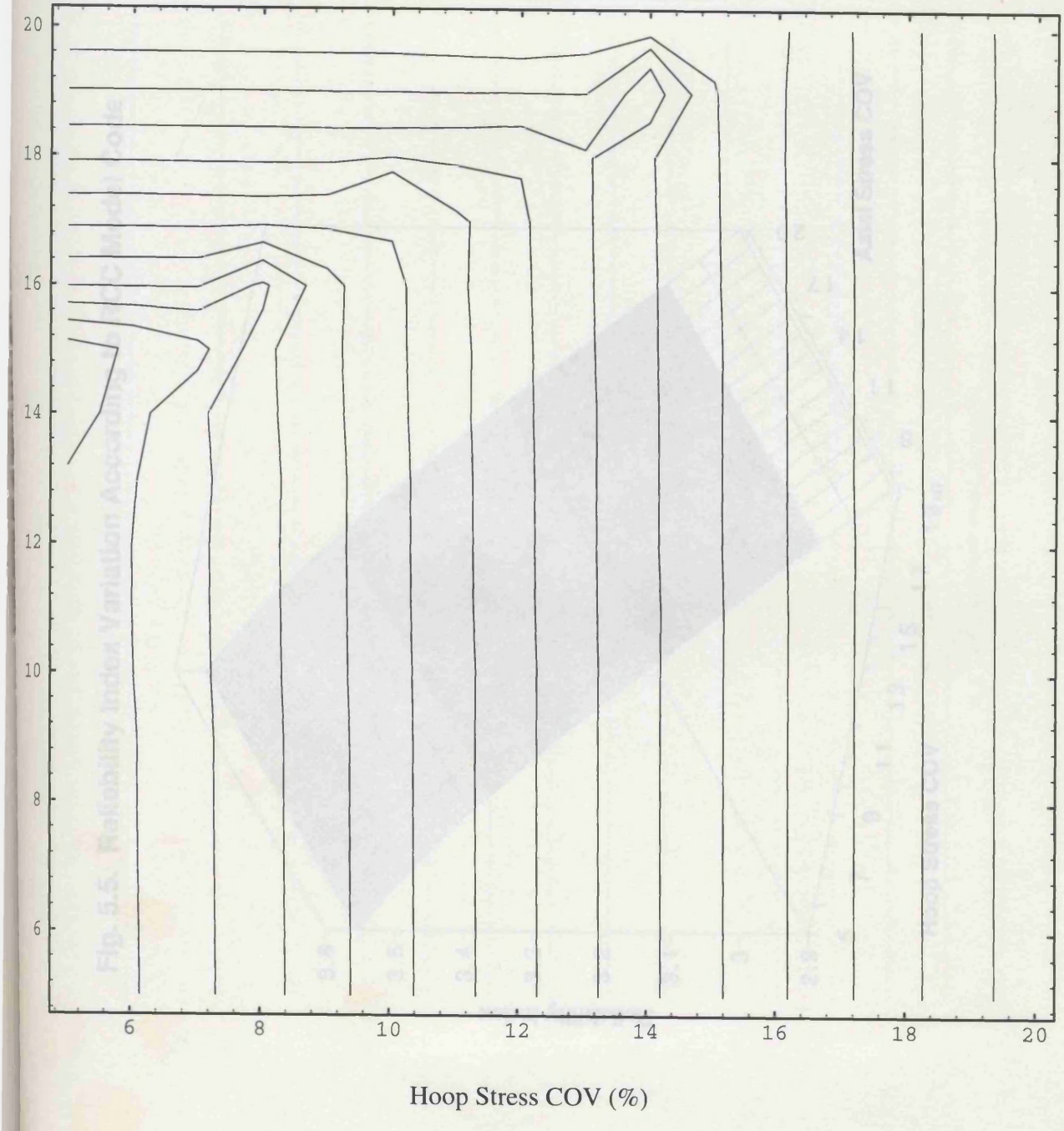

Fig. 5.4. Contour Plot of Reliability Index Variation According to API Code

Fig. 5.5. Reliability Index Variation According to RCC Model Code

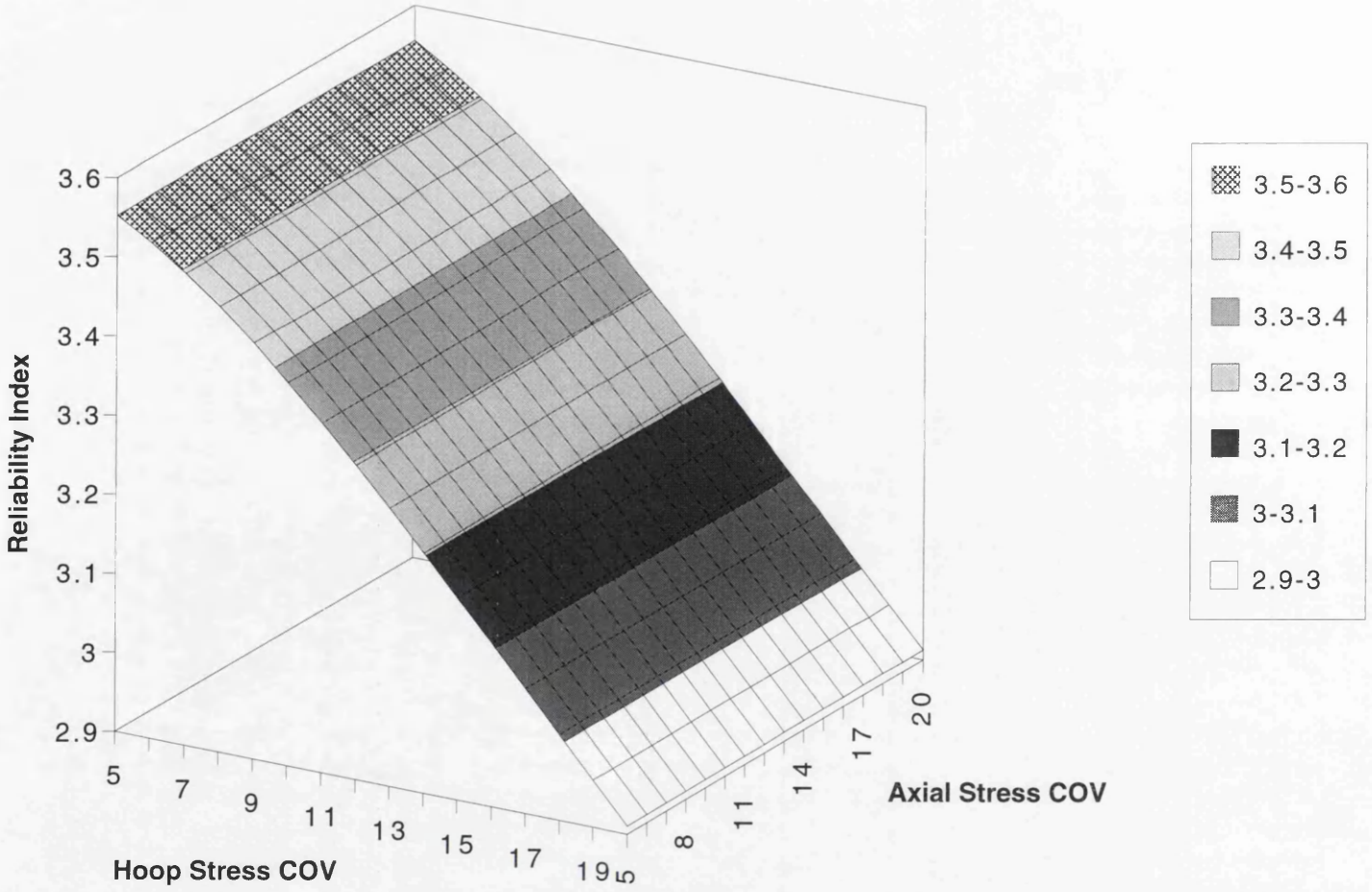

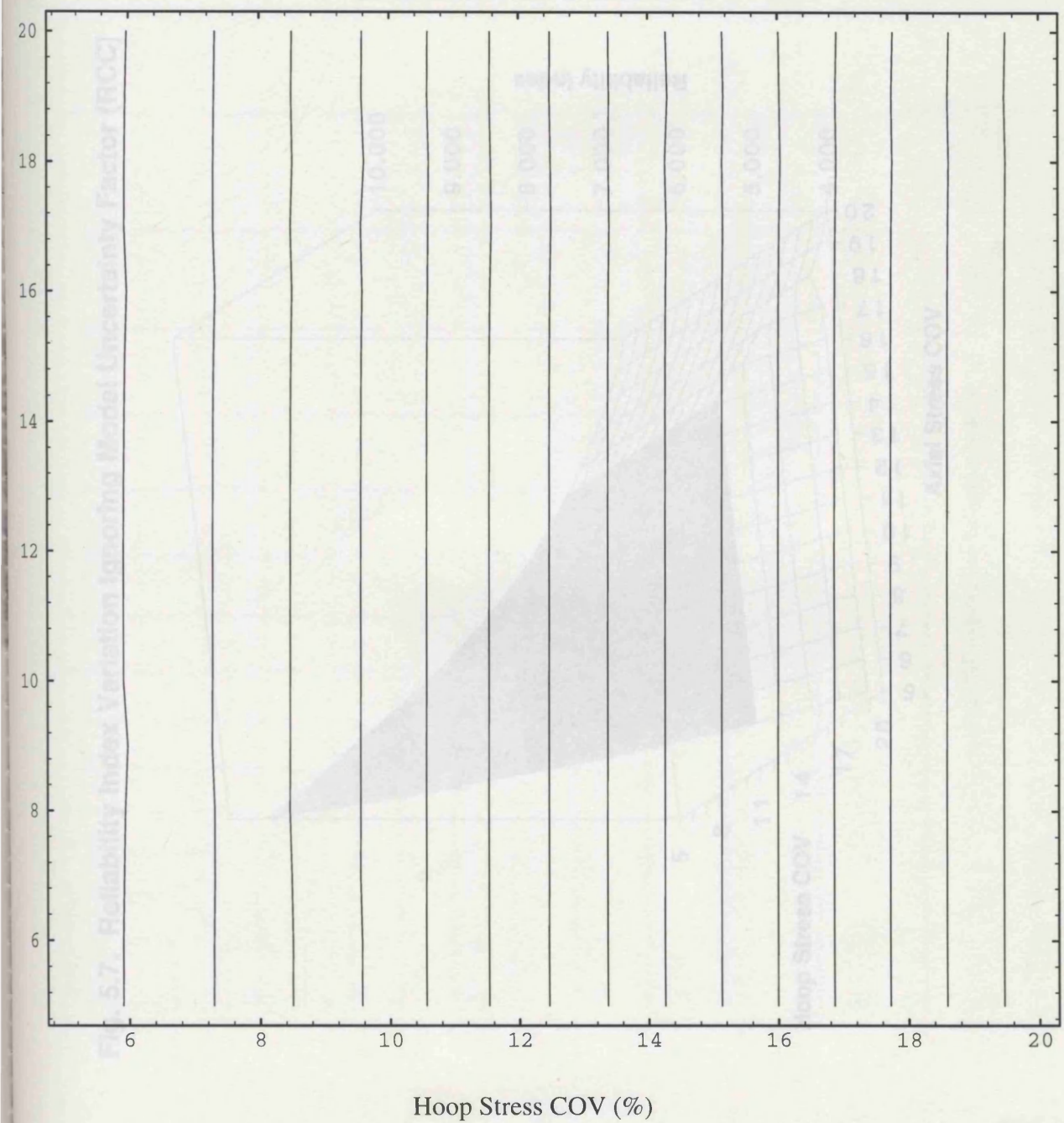

Fig. 5.6. Contour Plot of Reliability Index Variation According to RCC Code

Fig. 5.7. Reliability Index Variation Ignoring Model Uncertainty Factor (RCC)

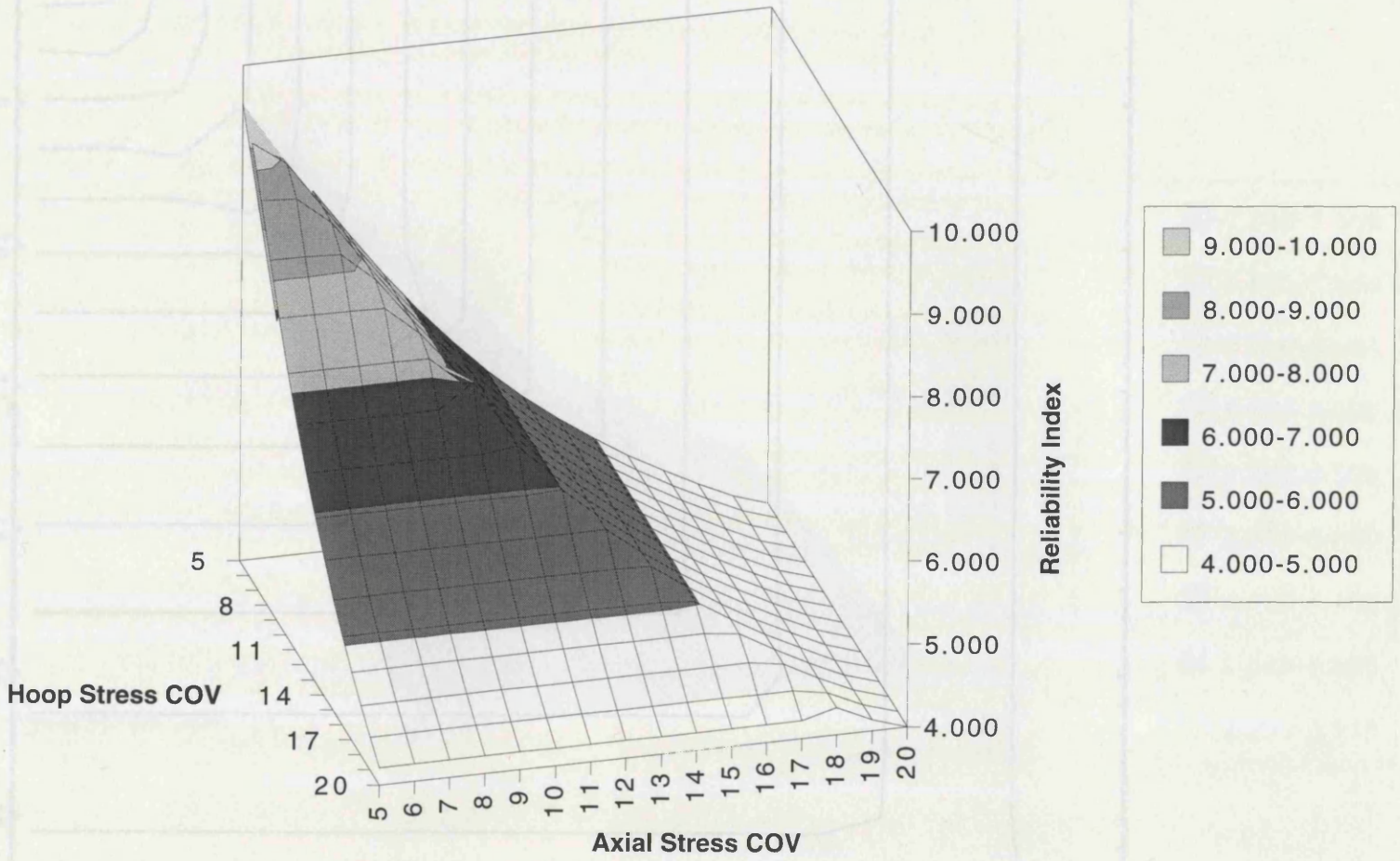

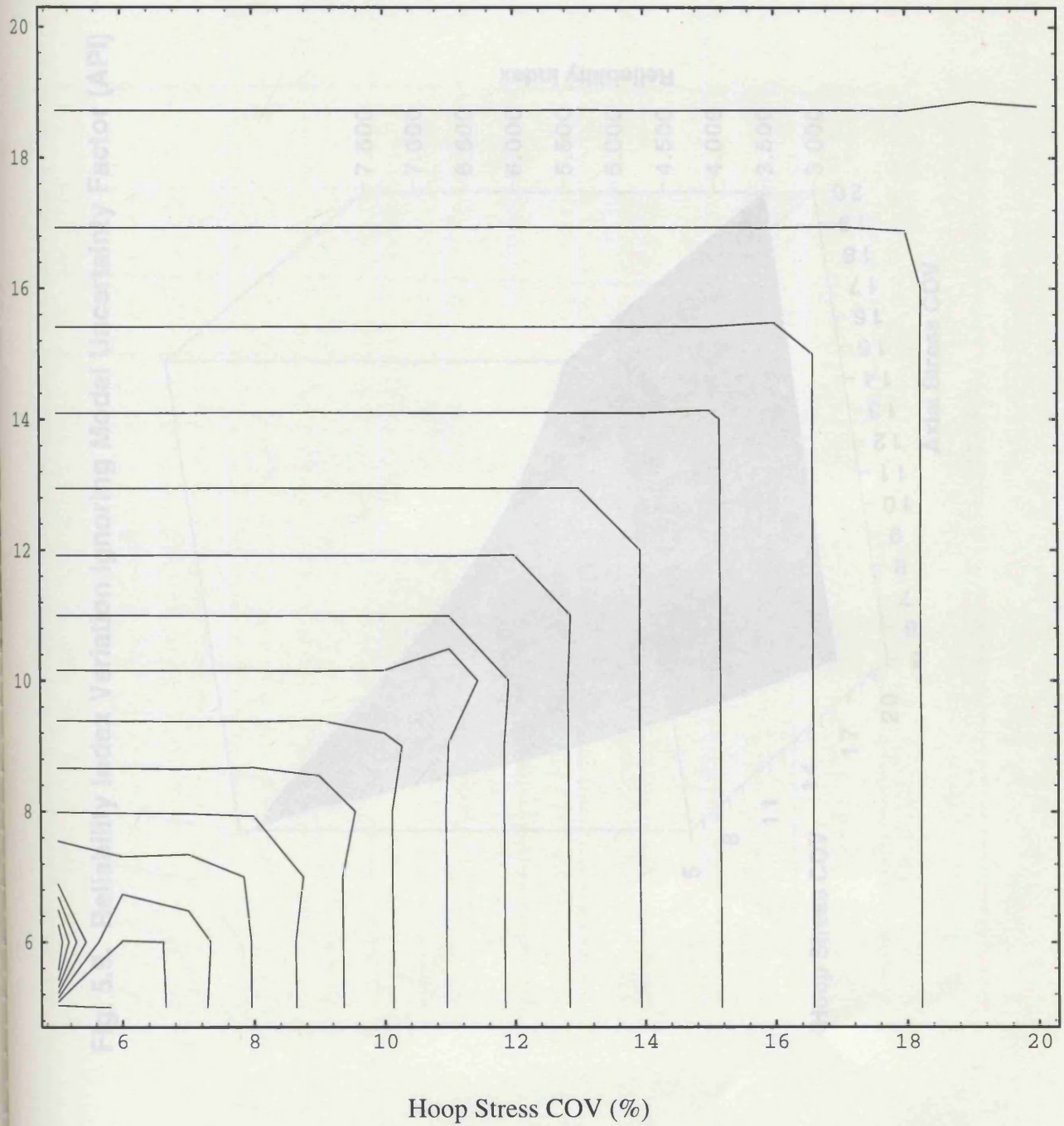

Fig. 5.8. Contour Plot of Reliability Index Ignoring Model Uncertainty Factor (RCC)

Fig. 5.9. Reliability Index Variation Ignoring Model Uncertainty Factor (API)

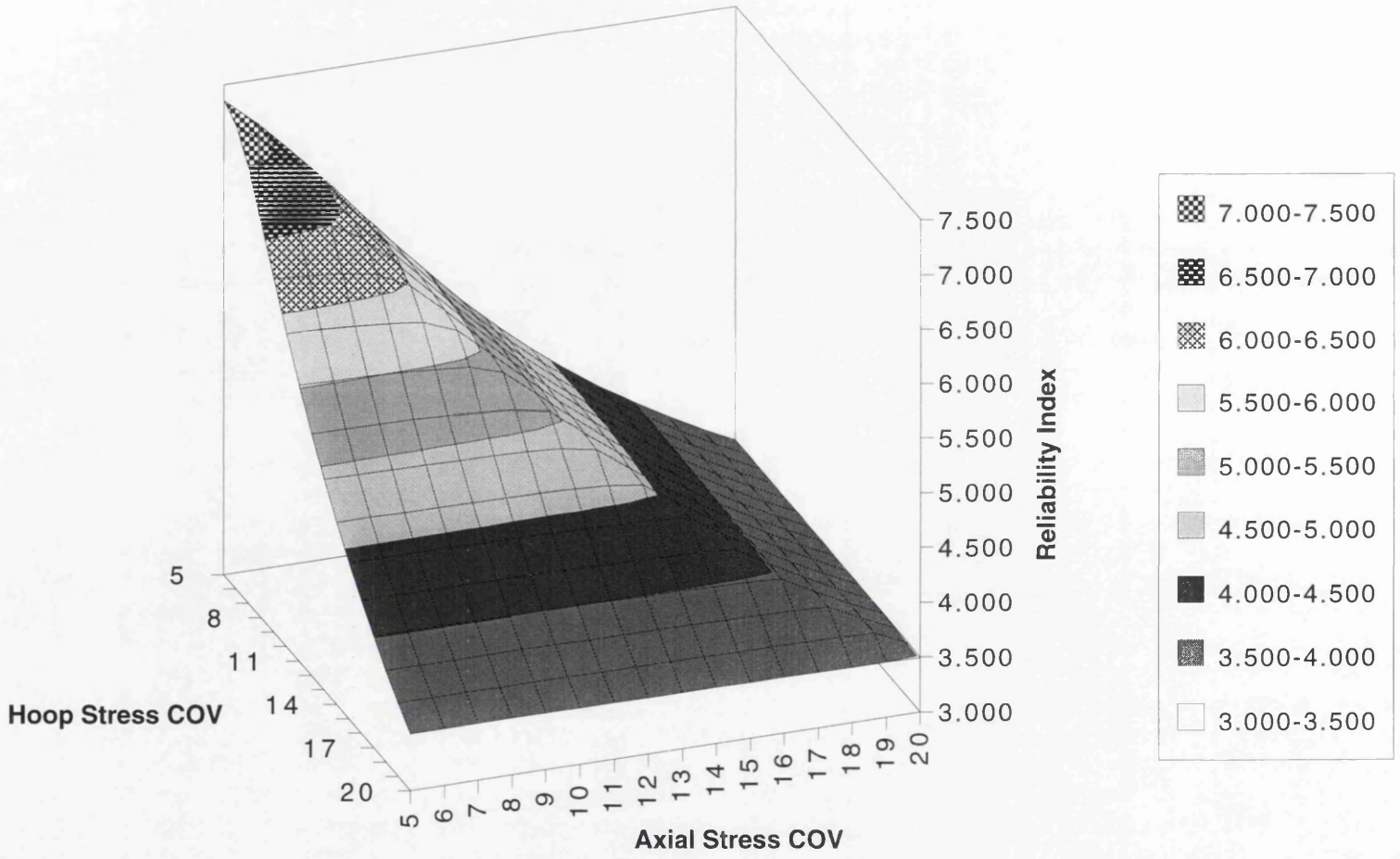

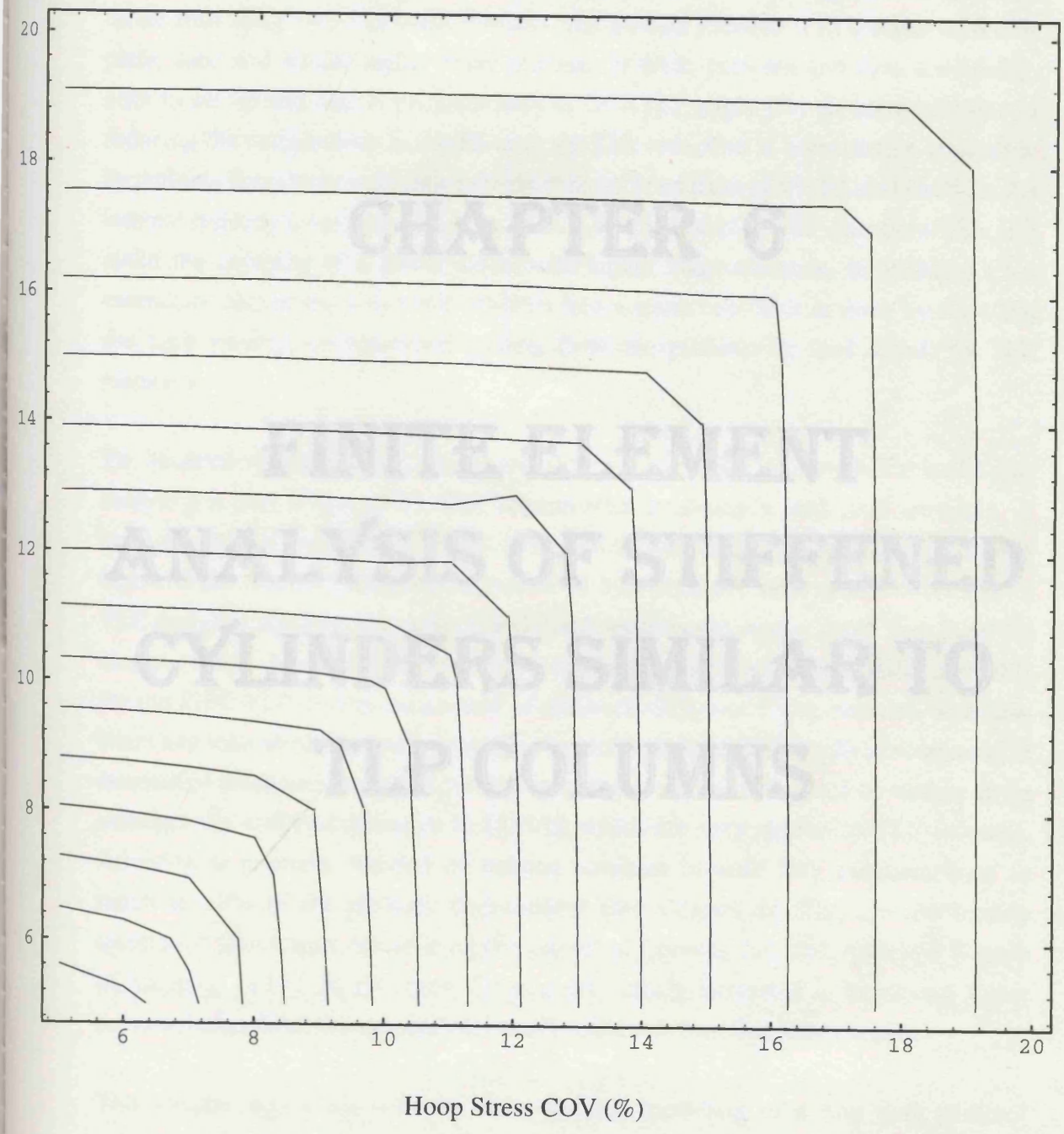

Fig. 5.10. Contour Plot of Reliability Index Ignoring Model Uncertainty Factor (API)

CHAPTER 6

FINITE ELEMENT ANALYSIS OF STIFFENED CYLINDERS SIMILAR TO TLP COLUMNS

6.1 INTRODUCTION

In Chapter 3 and mainly in Chapter 4 I have idealised a TLP as a 3-D space frame with joint elements to find structural and motion responses. In fact, a TLP is a continuum structure with large diameter columns and rectangular or circular pontoons. A modelling with plate, shell and/or brick elements would be more appropriate for TLPs rather than using only 3-D beam elements. But a Finite Element (FE) analysis involving plate, shell and similar higher order elements is often complex and time consuming, both to set up and run. A program such as DCATLP might play an important role in reducing the complexities in the FE analysis. This reduction in computation is possible by defining boundary loads with suitable support conditions in a local analysis from the internal resisting forces calculated by DCATLP in elements of TLP members. This will avoid the necessity of a global model with higher order elements. In addition, I am essentially converting a dynamic problem into a static one. This is done by replacing the time varying environmental loading from the problem by load effects in TLP members.

To illustrate this point, we may consider the load effect values in Table 5.1 for analysing a part of one ISSC TLP column after modelling it with shell elements. A local analysis of the ISSC TLP columns with the load effects from Table 5.1 would demonstrate that a 'seamless integration' of hydrodynamic and structural aspects in TLP design is possible. However, it is difficult to compare the results of such local FE analysis simply because there is no experimental data or similar information available for the ISSC TLP. But in the context of structural design of TLPs, research with only beam and joint elements may be regarded as incomplete because it may not capture the continuum characteristics of TLP structures. It was therefore decided to analyse three orthogonally stiffened cylinders in LUSAS which are very similar to TLP columns. Attention is primarily focused on column members because they can contribute as much as 70% of the platform displacement (see Chapter 1). The cylinder models mentioned above were tested in a joint project of Conoco, Inc. and American Bureau of Shipping [6.15]. At that time, Conoco was mainly interested in improving Jolliet column design from the experimental results obtained from that joint project.

This chapter also deals with the finite element modelling of a ring only stiffened cylinder under external pressure. The experimental results are available from the study of Seleim et al [6.14]. This is included here because the author was interested in understanding some aspects of shell buckling with a relatively simple problem. The ring only stiffened cylinder modelling has given the author more background to analyse orthogonally stiffened cylinders under combined loads.

It is important to emphasise once again that the main aim is to develop computational tools or utilise well established software to find new routes which can help a TLP designer in taking decisions without the need for understanding the complex nature of underlying hydrodynamic and structural phenomena. The work presented, therefore in this chapter concentrates on identifying acceptable external loads on cylindrical structures, typical in TLPs, through FE modelling. Buckling patterns and associated failure modes do not come under the aims of this study.

6.2 SHELL BUCKLING

Buckling is a mysterious phenomenon that transforms objects with symmetrical beauty into junk. Bushnell [6.6] believes that most of the failures did not occur because of a lack of analysis capability. There were computer programs that, given appropriate input, would yield accurate predictions. But the structures failed because very few had sufficient familiarity with buckling phenomena to identify proper numerical tests that would warn of impending disaster.

To understand shell buckling, it is important to know the difference between membrane and bending stiffness. The membrane stiffness of a thin shell is in general, several orders of magnitude greater than the bending stiffness. In fact, it can absorb a great deal of membrane strain energy without deforming too much. It must deform much more in order to absorb an equivalent amount of bending strain energy. If the shell is loaded in such a way that most of its strain energy is in the form of membrane compression and if there is a way that this stored-up membrane energy can be converted into bending energy, the shell may fail rather dramatically in a process called 'buckling', as it exchanges its membrane energy for bending energy. Very large deflections are generally required for this type of strain energy conversion.

6.3 RING STIFFENED CYLINDERS UNDER EXTERNAL PRESSURE

Seleim et al [6.14] carried out buckling experiments with ten ring only stiffened cylinders machined from aluminium alloy. Their objective was to see the change in buckling behaviour as the stiffening pattern on an otherwise constant shell progresses from many equally spaced weak rings to a few heavy rings. In other words, the size, spacing and number of rings were varied so that the weight of all ten models remained constant at 6.57 kg. All the models had the same internal diameter of 254 mm, overall length of 920 mm and wall thickness of 2 mm. The test specimens were machined from 1 inch thick aluminium tubes to reduce the initial geometric imperfections. Stiffened shells may have rings placed either externally or internally depending on their function in practical applications. The models in the work of Seleim et al [6.14] utilised exterior

rings for convenience and ease of machining. Out of ten models, two (i.e. Model 3 and 10) were identical. They were built with a special interest to see whether the experimental results could be reproduced closely. The author has selected the geometry of their Model 3 or 10 to gain experience in the eigenvalue buckling problems.

6.4 EIGENVALUE BUCKLING ANALYSIS

Eigenvalue buckling analysis is a technique that can be applied to relatively 'stiff' structures to estimate the maximum load that can be supported prior to structural instability or collapse. The basic assumptions for this type of analysis are that the linear stiffness matrix does not change prior to buckling and that the stress stiffness matrix is simply a multiple of its initial value. Accordingly, the technique can only be used to predict the load level at which a structure becomes unstable, provided the pre-buckling displacements have negligible influence on the structural response.

It is beyond the scope of this thesis to discuss the theoretical background of eigenvalue buckling analysis. However, the governing equation is given below:

$$([K] + \{\lambda_b\}[K_\sigma])\{\Phi_b\} = 0 \qquad (6.1)$$

where $\{\lambda_b\}$ are the eigenvalues which are used as multipliers to evaluate the buckling loads and $\{\Phi_b\}$ are the eigenvectors which contain the associated buckling mode shapes. In most structural problems the lowest mode (i.e. the mode shape corresponding to the smallest eigenvalue) is the only one of interest. Hence, the critical buckling load is calculated by multiplying the smallest eigenvalue from $\{\lambda_b\}$ with the initially applied load vector.

6.4.1 Subspace Iteration Technique

LUSAS [6.11] as well as ABAQUS [6.2] use the subspace iteration technique for eigenvalue buckling analysis. It is simple to extract several modes simultaneously, although the lowest mode might be of interest. Efficient evaluation of the lowest eigenvalues and corresponding eigenvectors is achieved by performing simultaneous inverse iteration using a set of iteration vectors [6.3], [6.4]. The method is actually a projection of the problem matrices onto the subspace formed by the iteration vectors. This produces a reduced eigen-problem which can be solved using Jacobi iteration. The eigenvectors of the reduced problem are then transformed back to the full space to form new iteration vectors. The process is repeated until the iteration vectors converge on the lowest eigenvectors of the full problem.

6.4.2 Sturm Sequence Check

The subspace algorithm is very stable but does not necessarily converge to the lowest eigenvalues. Therefore, the Sturm sequence check has been incorporated in LUSAS. This is an extremely stable procedure [6.11] which indicates the number of eigenvalues below a given eigenvalue. It is utilised to test for missing values, i.e. if p eigenvalues have been found and the Sturm sequence check indicates that r>p eigenvalues exist below the highest eigenvalue, (r-p) eigenvalues have been missed. In that case, the analysis must be repeated with a different number of starting iteration vectors and/or different convergence tolerance.

6.5 FINITE ELEMENT EXPERIMENTS WITH LUSAS

LUSAS finite element system is equipped with a powerful Graphical User Interface (GUI) known as MYSTRO. MYSTRO can be used as pre-processing and post-processing interactive system. The finite element solver, LUSAS accepts data input through a datafile which is based on a series of self descriptive data sections. The data input is flexible and completely free-format. Powerful data generation facilities are available in MYSTRO to reduce the time spent preparing data to a minimum. LUSAS also performs a pre-analysis data check to diagnose and warn of erroneous or improbable data before a full analysis is undertaken. A superelement facility also exists in LUSAS which allows large finite element models to be divided into smaller, more manageable components which are then added together to form the complete structure.

The superelement facility is not utilised in this study. Rather, the author was primarily concerned to ensure adequate swap space so that a large finite element model can be analysed in one run. LUSAS creates three scratch files (i.e. problem, frontal and shape) during an analysis. These scratch files may be very large in size depending on the problem type. Some of the models discussed later in this chapter require more than 700 Megabytes of scratch space to be analysed. To avoid any hardware limitation, a SPARC 514 computer is used in this study which is equipped with a scratch disk of 1.6 GB size. The author is grateful to the Glasgow Marine Technology Centre for giving him access to this rare facility.

6.5.1 QSL8 Elements

The LUSAS element library contains over 100 element types, enabling a wide range of engineering applications to be efficiently modelled. For modelling the ring stiffened cylinder [6.14] two types of shell elements are used in this study. QSL8 (8-noded

Quadrilateral Semi-Loof) is a thin doubly curved isoparametric element formed by applying Kirchhoff constraints to a three dimensional degenerated thick shell elements. QSL8 can accommodate varying thickness and anisotropic and composite material properties. The formulation takes account of both membrane and flexural deformations. Transverse shear deformations are excluded as required by thin shell theory.

The application of symmetry and/or anti-symmetry is very important in reducing the problem size. Let us consider a Cartesian co-ordinate system of X, Y and Z axes for a FE problem with three translational and three rotational degrees of freedom per node. The symmetry about a plane where X=constant would imply restraining the translation along X and rotations about Y and Z. But the in-plane degrees of freedom (i.e. rotation about X and translations along Y and Z) should be kept free. The anti-symmetric boundary conditions are just opposite [6.1]. The in-plane degrees of freedom are restrained and out-of-plane degrees of freedom are kept free. This is a general principle to be followed in applying symmetric boundary conditions. But it requires three translational and three rotational degrees of freedom per node.

QSL8 elements have only three translational degrees of freedom at corner nodes. The midside nodes include two loof rotations besides three translations. There are example problems with QSL8 in Ref. [6.12] where symmetric boundary conditions have been employed. However, QSL8 is not used in this study to utilise symmetry for avoiding any unforeseeable problem with boundary conditions.

6.5.2 QTS8 Elements

QTS8 (8-noded Quadrilateral Thick Shell) belongs to a family of thick shell elements in the LUSAS element library for the analysis of arbitrarily curved shell geometries, including multiple branched junctions. QTS8 elements can account for varying thickness. The formulation of QTS8 takes account of membrane, shear and flexural deformations. One interesting property of QTS8 is that it can be used to model thin shells as well. To model thin shell, QTS8 uses an incompatible strain field to define transverse shear. The assumed strain field prevents the 'shear locking' when the elements are thin.

It is advised in Ref. [6.10] to use 5 degrees of freedom for QTS8 elements, wherever possible, while dealing with smooth shell surface. But 6 degrees of freedom relating to global axes (i.e. three translations and three rotations) can be enforced using a data section called 'Nodal Freedom'. This option is essential to model symmetric sections

with the boundary conditions discussed in Section 6.5.1. However, enforcing 6 nodal freedoms in QTS8 elements might cause singularities if appropriate rotations are not restrained. This topic is discussed later with examples.

6.6 NUMERICAL AND EXPERIMENTAL RESULTS ON RING ONLY STIFFENED CYLINDERS UNDER EXTERNAL PRESSURE

As indicated earlier, Model 3 and 10 were identical in the experiments of Seleim et al [6.14]. Their Model 3 failed at 2.837 MPa with three circumferential waves extending over the entire length of the cylinder. Although Model 10 was identical, its experimental buckling pressure differs by 6% from the results of Model 3. Model 10 failed at 3.124 MPa.

A major problem in experimental buckling analyses is to estimate the ideal critical buckling pressure of the perfect structure using experimental data obtained from a geometrically imperfect structure. Seleim et al [6.14] have used the Southwell method to estimate the ideal critical buckling pressure from their experimental data because the method is consistent and easy to apply.

Table 6.1. Experimental Results [6.14] and Analytical Predictions [6.13] in MPa

Models [6.14]	Experiment	Southwell Plot	ABAQUS [6.13]
3	2.837	2.963	2.914
10	3.124	3.171	2.914

Table 6.1 includes analytical predictions of Morandi [6.13] using ABAQUS. He has tried both 4 and 8-noded shell elements. His results show that there is no difference in the critical buckling pressure prediction if the mesh is refined while using 8-noded shell elements (known as S8R in ABAQUS element library).

6.6.1 Numerical Results from LUSAS

Four FE models are created in LUSAS to compare results presented in Table 6.1. The numerical models are named after the elements used. QSL8_F and QTS8_F are the full or complete models ('F' in their names stands for 'Full') of the aluminium cylinder [6.14], as shown in Fig. 6.1. From Fig. 6.1 it would be quite easy to visualise the actual configuration of the cylinder. As discussed before, symmetric boundary conditions are used only with QTS8 elements. QTS8_S1 and QTS8_S2 are sections of the aluminium cylinder where symmetry is applied.

One difficulty with the eigenvalue buckling analysis is that several eigenvalues might be clustered near the critical load [6.6]. In some cases, it might be required to judge whether the calculated mode shape is at all feasible. In the subspace iteration method, it is simple to extract several eigenpairs simultaneously. It was therefore decided to find the lowest four eigenvectors and associated eigenvalues for QSL8_F and QTS8_F. The first (i.e. the lowest one) and second buckling mode shapes extracted for both QTS8_F and QSL8_F are identical and shown in Fig. 6.2. The first and second mode shapes are identical too but they have a phase difference along the circumference. Actually the second mode shape can be found by rotating the first mode shape about the cylinder axis. Fig. 6.2 does not show any hidden surface of the cylinder so that three circumferencial waves can be viewed clearly. The circumferencial waves are found over the entire length of the cylinder. The critical buckling load calculated for QSL8_F is 2.595 MPa. The buckling load for QTS8_F is 3.223 MPa which is significantly different from that of QSL8_F, although there is no difference in terms of mesh discretisation. This in fact shows the influence of element type selection in a FE analysis.

In the context of engineering design the mode shapes above the lowest one are not important. However, it might be interesting to view the higher mode shapes and associated axial and circumferencial waves. The third mode shape of QSL8_F in Fig. 6.3 shows four circumferencial waves over the length of the cylinder. The fourth one in Fig. 6.4 shows the changes along the length. Figs. 6.3 and 6.4 are included here to show the global deformation of QSL8_F.

QSL8_F and QTS8_F had an important role in identifying the minimum number of circumferencial waves occurring over the length of the cylinder. Since the minimum number is three, theoretically, $\frac{1}{12}$ of the cylinder can be now modelled with symmetry on one side and anti-symmetry on the other side (see [6.13]). But the lowest buckling mode shape of such a small model may not be the desirable one in all cases. A different mode shape might occur depending on the nature of the finite element used and its sensitivity to the end-effects. Therefore, it was decided to model 1/3 of the cylinder with symmetry on both sides. Please note that computational time and storage requirements are unimportant in this study since a high speed multi-processor SPARC 514 machine with a large scratch disk is used.

The mesh of QTS8_S1 is shown in Fig. 6.5. Fig. 6.6 presents the symmetric boundary conditions in QTS8_S1. The singularity problem with QTS8 elements has been

mentioned in Section 6.5.2. To avoid that, six nodal freedoms are enforced to only those nodes where boundary conditions are required. The symmetry conditions in Fig. 6.6 do not match with the global axes. So a local co-ordinate system was defined in MYSTRO which was applied on two sides of the section (i.e. QTS8_S1) so that appropriate boundary conditions can take place on both sides. The arrows in Fig. 6.6 indicate that the degrees of freedom in those directions are restrained.

The first and lowest buckling mode shape found for QTS8_S1 is the one we are looking for. It is shown in Fig. 6.7. So far as the mesh discretisation is concerned, there is no difference among QSL8_F, QTS8_F and QTS8_S1. Naturally no difference is expected in the results of QTS8_S1 from those of QTS8_F. The critical buckling load found for QTS8_S1 is almost identical to that of QTS8_F. In other words, it indicates that the symmetric boundary conditions imposed in QTS8_S1 are working all right.

With one-dimensionally discretised models, convergence with increasing nodal point density is not too important because one can generally afford to provide more than enough nodes to be on the safe side. With two-dimensionally discretised models such as the aluminium cylinder in this study, limitations of budget for computer runs and limitations of computer core and auxiliary mass storage capacity often dictate the use of models with rather sparse nodal point distributions. The quality of the solutions is questionable because the sparsely discretised models behave differently from the actual continuum and the size or even the sign of the error is rarely known [6.6].

In the light of the above, it is necessary to refine the mesh of QTS8_S1 to see if there is any appreciable change in the results. Since there is no practical limitation regarding computer runs and storage space, as mentioned before, QTS8_S2 is made four times larger than QTS8_S1 in size. This is done by dividing each element in QTS8_S1 into four for QTS8_S2 (Fig. 6.8). In other words, the element aspect ratio is identical in QTS8_S1 and QTS8_S2. Please note that the element aspect ratio here refers to the ratio of the element length and width. However, quadruple nodal density could not affect the results and the critical buckling load found for QTS8_S2 is almost identical to that of QTS8_S1. This is not surprising because similar results were found by Morandi [6.13] while using ABAQUS. The general conclusion is that the particular cylinder geometry under consideration is not sensitive to mesh discretisation. We shall see later that this is not the case with orthogonally stiffened cylinders from Conoco/ABS experiments.

Fig. 6.9 presents the Von Mises equivalent stress distribution contour on QTS8_S2. It is difficult to understand the contour plots unless they are in colour. To avoid problems as far as possible, 600 dpi greyscale printing technology is used for the contour plots in this chapter. As observed in the experiments [6.14], higher stresses are found at mid-bay location (see Fig. 6.9). The first (i.e. lowest) buckling mode shape of QTS8_S2 is essentially similar to that in Fig. 6.7.

Table 6.2. Buckling Loads of LUSAS Models for the Aluminium Cylinder [6.14]

FE Model Name	No. of Nodes	No. of Elements	No. of Equations	Buckling Load (MPa)
QSL8_F	6288	2064	27216	2.59450
QTS8_F	6288	2064	32880	3.22317
QTS8_S1	2186	688	11659	3.22307
QTS8_S2	8496	2752	44132	3.24585

Table 6.2 summarises the four models. The critical buckling loads in Table 6.2 refer to the lowest mode shape only. The buckling loads are shown up to six significant digits to indicate that the difference in results is really small for QTS8 models. QSL8_F has under-estimated the buckling load but QTS8 models performed well being very close to the experimental collapse pressure.

6.7 ORTHOGONALLY STIFFENED CYLINDERS UNDER COMBINED LOADING

A series of 66 large scale steel cylinders were tested to failure to develop data for limit state buckling formulations in a test program jointly administered by Conoco and ABS [6.15]. The tests were essentially grouped into 14 basic geometries. Each geometry group of four or more cylinders was subjected to four basic loading conditions ranging from axial compression alone to external pressure alone. The geometry group '2-2' is selected from their study for FE analysis in LUSAS. Various FE models are created in LUSAS for this geometry group depending on the loading type and mesh discretisation. In order to distinguish them, each model is named based on its purpose and properties. The original code [6.15] designating the applied load on the geometry group 2-2 is shown in Table 6.3.

The problem of buckling of thin monocoque cylindrical shells under axial compression has received far more attention than most problems in structural mechanics because of

the extra-ordinary discrepancy between test and theory which remained unexplained for so many years. The design recommendation of Brush and Almroth [6.5] for cylinders subjected to axial compression is around 20% of the theoretical buckling stress, based on the distribution of test data. The discrepancy arises from the extreme sensitivity of the critical load to initial geometric imperfections.

Table 6.3. Different Loading on Four Models in Geometry Group 2-2 [6.15]

Models	Loading
2-2A	Axial compression alone, $N_\theta = 0$
2-2B	External hydrostatic pressure, $N_x = 0.5\ N_\theta$
2-2C	External radial pressure, $N_x = 0$
2-2D	Combined loading, $N_x = 1.8\ N_\theta$

However, ring and stringer stiffened cylinders are not that imperfection sensitive like monocoque cylindrical shells [6.6]. But Model 2-2A is not included in this study because it would be essential to model its initial imperfections. Incorporation of imperfections and residual stresses in non-linear FE analysis does not fall within the objectives of the present study. All four models in group 2-2 were stress relieved. So the question of residual stress disappears from the problem. Three other models (i.e. 2-2B, 2-2C and 2-2D) are considered here for analytical modelling without any initial imperfection. The main assumption is that external pressure would trigger the buckling and consequently the milder nature of imperfection sensitivity of orthogonally stiffened cylinders can be ignored.

It can be proved that hydrostatic pressure on a circular cylinder (closed end) creates axial stress which is 50% of the hoop stress. Therefore, the combined loading on 2-2B was called hydrostatic pressure loading in the original test. Otherwise, 2-2B and 2-2D are in the same category with different proportion of axial compression and external radial pressure.

6.8 FE MODELLING IN MYSTRO

We have discussed before that powerful data generation facilities are available in MYSTRO to reduce the time spent preparing data to a minimum. The first phase of model preparation in MYSTRO is very similar to creating drawings in CAD packages by defining points, lines, surfaces and volumes. In the second phase, different properties such as thickness, elastic/plastic modulus etc. are assigned to the features (i.e. points, lines, surfaces and volumes). The mesh can be defined by the user or s/he

can rely on MYSTRO to discretise the geometry. After defining the external loading and the type of analysis the user may 'ask' MYSTRO to tabulate the model as a datafile so that the FE solver can start the analysis.

MYSTRO is a fully interactive system and the user may communicate with MYSTRO in four different ways:

1) Selecting actions from the menu bar
2) Selecting actions from the menu panel
3) Entering commands in the command window
4) Replaying a command file

The author particularly preferred the option of replaying a command file in MYSTRO. MYSTRO contains a parametric command language facility based on the syntax of the C language, for use in command files. Besides this parametric language, it is possible to capture valid MYSTRO commands from a session and these commands can be used to form a command file for future use. This facility can help the user to generate similar but slightly different complex models in just a few minutes! An example of a command file to illustrate different activities in MYSTRO is given later.

6.9 MESH DISCRETISATION

Four FE models are created for each cylinder, i.e. 2-2B, 2-2C and 2-2D. It is essential to distinguish them clearly so that they can be understood without any confusion. Initial imperfections are not considered in this study. But mean thicknesses of shell, rings and stringers are used which are slightly different for each cylinder. Besides ignoring initial imperfections, there is another important simplification. From material tests, it was found [6.15] that steel used in 2-2B, 2-2C and 2-2D are orthotropic in nature. But Young's moduli in longitudinal and transverse directions are very close for each one of them. Therefore in LUSAS, the FE models are defined isotropic with an average of Young's moduli in longitudinal and transverse directions for each cylinder. However, please note that this average Young's modulus used is different for 2-2B, 2-2C and 2-2D.

As mentioned before, 2-2B, 2-2C and 2-2D belong to the same geometry group with identical radius and bay lengths. In theory, thicknesses were supposed to be identical too. But in practice, the mean values were slightly different. This leads to a situation where the same FE mesh can be used for each cylinder with different material properties and thicknesses. A general mesh study is carried out with four different types of mesh for each cylinder. The mesh types are 'F', 'S1', 'S2' and 'S3'. 'F'

indicates the full cylinder but 'S1', 'S2' and 'S3' stand for three different symmetric sections. When simply F_2-2 is mentioned, it would imply the mesh of F_2-2B, F_2-2C and F_2-2D as well. However, the model F_2-2B would refer to the mesh type 'F' with material and geometric properties of the cylinder 2-2B. The author expects that this terminology will not create any confusion.

Fig. 6.11 presents a typical panel of F_2-2 with the shell in between two stringers. 14 surfaces are defined in MYSTRO where no. 12-14 are for the stringer at side, no. 1-8 for end and middle ring portions and no. 9-11 for middle and end bay shell plates. The dotted lines in Fig. 6.11 shows the mesh discretisation for the type 'F'. The full cylinder model with coarse mesh had an important purpose. F_2-2B, F_2-2C and F_2-2D are used to observe the global deformation shape in the eigenvalue buckling analysis.

It has been observed by many researchers that the performance depends on the element aspect ratio (i.e. element length to width) where plate and shell elements are involved. As a general guideline, Catley [6.7] suggested to keep the aspect ratio below 2.5. In many cases best performance is observed when the elements are almost square in dimension although it may not be feasible in many places since the computational efforts would increase dramatically. It is worth noting that Ref. [6.11] does not mention any scope of improvement in performance regarding QTS8 element size. However, the author was interested in a mesh study with a general guideline of Catley [6.7] and Hinton [6.9].

Table 6.4. Mesh Divisions in one panel of S1_2-2, S2_2-2 and S3_2-2

Division of Shell, Rings and Stringer in a Panel	S1_2-2	S2_2-2	S3_2-2
Shell along circumference	3	4	6
Shell/stringer in middle bay along cylinder length	5	8	14
Shell/stringer in end bays along cylinder length	4	6	10
Width of stringer	2	2	2

The three cylinders under study in 2-2 geometry group had 18 panels. For symmetric FE sections three panels are used. The reason is discussed later in Section 6.10. Each panel in symmetric sections (i.e. mesh type 'S1' etc.) is slightly different from the panel with 14 surfaces in Fig. 6.11. For appropriate boundary conditions, the stringer is placed just at the middle of cylindrical shell as shown in Fig. 6.12. Physically we are defining a panel with the stringer at the middle instead of placing it at the side. The

panel in Fig. 6.12 requires 25 surfaces for defining all components. The definition of one panel is enough because MYSTRO can generate any other identical panel by copying the original with a suitable transformation dataset.

Table 6.4 provides information on how the mesh types 'S1', 'S2' and 'S3' are generated from the panel in Fig. 6.12. The type 'S1' is quite close to the full mesh, 'F'. The element aspect ratios in S1_2-2 are shown in Table 6.5a. Please note that the length of QTS8 elements in Tables 6.5 refers to the longer dimension which might be straight or curved. S2_2-2 is a relatively fine mesh. But the aspect ratio of nearly equal to 1.0 is achieved in S3_2-2 at the cost of increasing number of elements dramatically. This rise in element number may or may not create any significant difference in performance as we shall see later. Figs. 6.13-6.15 provide visual presentation of the three mesh types.

Table 6.5a. Element Aspect Ratios in S1_2-2

Surface No.	Total	Length	Width	Aspect Ratio	Elements
10, 24	2	45.72	33.30	1.37	30
9, 23, 11, 25	4	40.43	33.30	1.21	48
1, 15, 3, 17, 4, 18, 5, 19	8	33.30	15.72	2.12	48
2, 16, 6, 20, 7, 21, 8, 22	8	33.30	15.72	2.12	24
13	1	45.72	15.72	2.91	10
12, 14	2	40.43	15.72	2.57	16
Total No. of Elements/Panel					176

Table 6.5b. Element Aspect Ratios in S2_2-2

Surface No.	Total	Length	Width	Aspect Ratio	Elements
10, 24	2	28.58	24.98	1.14	64
9, 23, 11, 25	4	26.96	24.98	1.08	96
1, 15, 3, 17, 4, 18, 5, 19	8	24.98	15.72	1.59	64
2, 16, 6, 20, 7, 21, 8, 22	8	24.98	15.72	1.59	32
13	1	28.58	15.72	1.82	16
12, 14	2	26.96	15.72	1.72	24
Total No. of Elements/Panel					296

Table 6.5c. Element Aspect Ratios in S3_2-2

Surface No.	Total	Length	Width	Aspect Ratio	Elements
10, 24	2	16.33	16.65	1.02	168
9, 23, 11, 25	4	16.17	16.65	1.03	240
1, 15, 3, 17, 4, 18, 5, 19	8	16.65	15.72	1.06	96
2, 16, 6, 20, 7, 21, 8, 22	8	16.65	15.72	1.06	48
13	1	16.33	15.72	1.04	28
12, 14	2	16.17	15.72	1.03	40
Total No. of Elements/Panel					620

6.10 EIGENVALUE BUCKLING RESULTS OF FE MODELS FOR ORTHOGONALLY STIFFENED CYLINDERS

The 'F' type mesh was created to understand the nature of global deformation. For the ring stiffened aluminium cylinder, we have seen that the number of circumferencial waves in the lowest mode shape would determine the size of the symmetric sections (i.e. type 'S1' etc.). For ring and stringer stiffened cylinders, circumferencial waves tend to occur within consecutive stringers. Fig. 6.16 is an ideal example. There is a special technique to plot such a figure in MYSTRO by combining a model file with the corresponding result files. The facility offers a 'feature-wise' selection for drawing undeformed and deformed mesh. An area of interest in the mesh can be selected through this facility. This way the user gains more control when element and node numbers are quite large. Fig. 6.16 has been drawn after removing the surfaces defining the rings to indicate clearly the circumferencial waves between stringers. Please note that there is an exaggeration factor involved in drawing the deformed mesh. Similar deformation patterns are observed in the case of F_2-2D under combined loading as shown in Fig. 6.17. Clearly, the size of the symmetric sections can be made independent of the circumferencial wave number since deformations are found locally distributed between stringers. It was decided to consider three panels in the mesh type 'S1', 'S2' and 'S3'.

6.10.1 Actual Findings in Conoco/ABS Experiments [6.15]

Before presenting the results from LUSAS, actual experimental results are briefly discussed in this section. 2-2B, 2-2C and 2-2D were 45 inches diameter cylinders of 21.6 inches length. In each cylinder, two middle rings were placed 9.0 inches apart. But the length of both end bays was 6.3 inches. The design thickness of shell and stringers was 14 ga. (i.e. 0.0747"). The cylinders were typical buckling models.

In actual experiments, deformation started at low pressures in individual panels in either an alternating in-out or a reverse bending action [6.15]. This later transformed into a bay instability mode where the shell and stringers simultaneously bowed in two or three panel wide waves. Considerable load and deformation increases generally ensued prior to reaching the maximum condition. All three cylinders failed in the middle bays.

In the experiments, initial instability loads and maximum loads were recorded. The maximum load was the one that the cylinder could sustain. This was characterised by a decrease in load caused by the continuing deflection of the cylinder. Generally this was a gradual fall-off in load for the pressure loaded cases. However, the initial instability load was not so uniquely defined. It was considered to be the load where one of the following first occurred:

a) Audible or distinct 'snap' to new position at any shell panel.
b) Sudden tripping of a stringer(s).
c) Significant departure from linearity in the axial shortening curves.
d) Abrupt change or significant deflection in the incremental radial movement curves.
e) Sudden severe flaking or other signs of inception of more rapid movement.

The magnitudes of initial buckling loads for 2-2B, 2-2C and 2-2D were recorded in Ref. [6.15] but not the specific reasons behind those records. The buckling histories mainly give accounts of deformations occurred within initial instability and maximum loads. It is worth noting that a number of buckles took place before reaching the maximum loads in all three cases. Table 6.6 reproduces the actual experimental results:

Table 6.6 Experimental Buckling Results of 2-2B, 2-2C and 2-2D

Cylinder Name	Initial Instability		Maximum Load	
	Axial (kips)	Pressure (psi)	Axial (kips)	Pressure (psi)
2-2B	75.4	47.0	145.7	91.2
2-2C	0.0	63.2	0.0	110.1
2-2D	223.3	39.0	286.8	50.1

6.10.2 Eigenvalue Buckling Results from LUSAS

Before comparing the results obtained from LUSAS, the buckling loads are normalised for quick reference and understanding. In each case, the maximum load is normalised to a load factor of 10. Please note that the ratio between axial compression load and radial pressure was maintained in all cases throughout the experiments. There is a purpose behind setting the maximum load in each case to a load factor of 10. In a non-linear analysis, as discussed later, that could help in visualising the load steps, starting load etc.

Table 6.7. Eigenvalue Buckling Predictions Compared with Experimental Results

Cylinder 2-2B:

Finite Element Models					Experimental Loads	
Eigenvalue	F_2-2B	S1_2-2B	S2_2-2B	S3_2-2B	Instability	Maximum
Buckling	5.109	5.309	6.488	7.327	5.175	10

Cylinder 2-2C:

Finite Element Models					Experimental Loads	
Eigenvalue	F_2-2C	S1_2-2C	S2_2-2C	S3_2-2C	Instability	Maximum
Buckling	4.636	4.724	5.900	6.692	5.74	10

Cylinder 2-2D:

Finite Element Models					Experimental Loads	
Eigenvalue	F_2-2D	S1_2-2D	S2_2-2D	S3_2-2D	Instability	Maximum
Buckling	7.224	7.650	9.175	10.280	7.786	10

Table 6.7 compares computerised analytical predictions with actual experimental results. Unlike the ring stiffened aluminium cylinder in Section 6.6.1, the results depend very much on the mesh discretisation. The buckling mode shapes such as the one in Fig. 6.18 clearly show that the deformations mainly occur in the middle bay. It is

important to note that the eigenvalue buckling analysis results should be compared with the initial instability loads recorded in the experiments. This is because an eigenvalue buckling analysis is essentially a linear analysis based on the initial shape of the structure. It is valid when the pre-buckling displacements have negligible influence on the structural response. The analytical predictions in Table 6.7 should not be correlated with the maximum loads attained in the experiments after a number of buckles and substantial deformations.

In the light of the above, the mesh type 'S1' has performed well in combined loading cases whereas S2_2-2C is very close to the corresponding initial instability load. The fine mesh type 'S3' is over-estimating the buckling load in all cases when compared to the experimental instability loads. Increasing the nodal point density might cause a softening action, allowing the mesh to deform smoothly and that could raise the estimate of the buckling load. Fig 6.19 presents the subspace iteration results for all four FE models of 2-2C. The convergence was practically achieved in first five iterations although the analyses were carried up to a stable position.

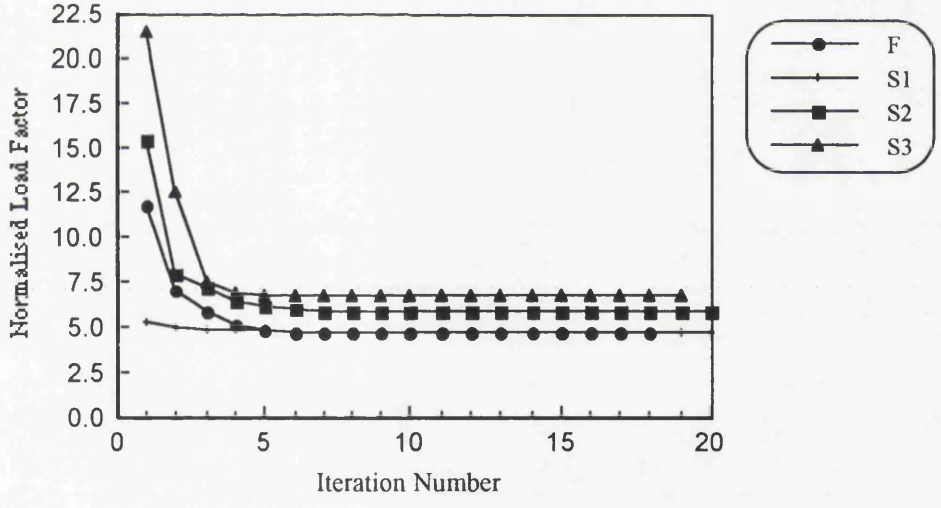

Fig. 6.19. Convergence in Subspace Iteration for FE Models of 2-2C

In multi-axial situations, the concept of an 'equivalent' stress and strain is used. A popular effective stress measure is the Von Mises equivalent stress which provides a yield surface in the form of a circular cylinder in principal stress space. For principal stresses falling inside the yield surface the behaviour is elastic and when stresses reach the yield surface plasticity begins. The average yield stress for the steel used in 2-2B, 2-2C and 2-2D is around 380 MPa. The Von Mises equivalent stress (i.e. SE in LUSAS) contour plots in Figs. 6.20-6.22 show that the maximum buckling stresses are appreciably lower than their corresponding yield stress values. They also reflect that the experimental cylinders were typical buckling models. However, please note that

there is no material non-linearity involved in the eigenvalue buckling analysis. The equivalent stress contour plots were very similar for all 12 FE models showing maximum stresses occurring mainly in the middle bays. The mesh type 'S3' is only selected in Figs. 6.20-6.22 to avoid repetitions of similar figures. Another reason is that the contour plots are better on fine meshes.

6.11 GEOMETRICALLY AND MATERIALLY NON-LINEAR ANALYSIS

We have already discussed that the three cylinders under study had strong links with typical TLP column structures. The ASTM A606 hot rolled steel used for these cylinders was selected on the basis that it is representative of a 50 ksi yield strength steel plate. Please note that 50 ksi steel plates were used later in the fabrication of the Jolliet TLWP. This material exhibits a slightly rounded stress strain curve with a sharp yield plateau. The eigenvalue analysis results have already indicated that the buckling stresses are significantly lower than the material yield stress. Therefore the slightly rounded stress strain curve is simplified to a bi-linear curve (i.e. elastic and perfectly plastic) for non-linear computational modelling. In fact, geometric non-linearity is the important issue for these buckling problems, not material non-linearity. It has been mentioned before that the initial imperfections are ignored in this study for simplicity and milder sensitivity of stringer stiffened [6.6] cylinders. However, it is very important to include geometric non-linearity even if the analysis starts with the perfect structure because the stiffness matrices can then be formed based on the deformed shape in different load steps.

6.11.1 Non-linear Analysis Controls in LUSAS

A LUSAS datafile has several data sections depending on the nature of the problem. There are 42 parameters in the 'Nonlinear Control' section although all of them may not be necessary in most of the problems. The required parameters are to be specified by the user to guide the solution procedure. There is another way to modify the computational procedure by specifying relevant option number in the 'Options' data section. LUSAS offers around 250 options to guide the FE solver to meet the requirements in especial situations.

The theoretical background behind the line search method, the arc length method etc. in non-linear analyses is mathematically rigorous and complex. The lack of clear understanding might lead the user to select a wrong or unnecessary parameter/option in a LUSAS analysis.

The load levels in LUSAS can be controlled in a number of ways. With the constant load level incremental and iterative procedure, the load is applied in specified fixed increments and the chosen iterative algorithm is utilised to obtain convergence of the solution at each load level. The loading remains constant in the iteration process. The constant load level methods fail when the solution reaches the 'limit' points. These are the points where either displacement or load reversals occur, resulting in a singular or near singular stiffness matrix.

One of the two arc length algorithms implemented in LUSAS follows the one proposed by Crisfield [6.8]. The salient characteristic of arc length methods is that the load level does not remain constant during each load increment. The load level is modified during the iteration procedure so that convergence near limit points may be achieved. A further benefit of the arc length constraint is in stabilising the iterative process. This is of particular importance when using the Modified Newton iteration. The arc length methods may therefore improve the efficiency of the solution, even when no limit points are involved.

6.11.2 Practical Difficulties

The main aim of carrying out non-linear analyses in this chapter was to study the structural behaviour after the initiation of buckling. It is always advisable to use the arc length control near structural collapse so that the load level can be automatically adjusted when limit points are encountered. The author started his non-linear analyses with the arc length control option but it ended off with a real frustrating experience. The arc length algorithms in LUSAS are guided by the minimum pivot occurring in the structure. When the minimum pivot calculated becomes negative at some load level, it indicates the existence of a bifurcation point. At a bifurcation point on the solution path, may proceed along several paths, one stable and the others unstable.

It is worth noting that the initial instability loads found in the experiments with 2-2B and 2-2C were 52% and 57% of the maximum loads attained (see Table 6.7). Therefore one should not be surprised to find a number of bifurcation points on the solution paths of the FE models under consideration. The problem with the arc length solution starts when the first bifurcation point is encountered. The solution oscillates about this point with no further progress being made. The output is a jagged load deflection curve.

The author does not have well-founded experience in this type of numerical problems. He decided to avoid the arc length control since he was interested to go beyond the

initiation of buckling. The constant load level procedure was the second alternative. All the results presented in the next section come from the constant load level non-linear analyses. One immediate consequence of avoiding the arc length control is that the solution procedure has to be 're-started' several times with a modified incremental-iterative scheme to capture the structural response beyond the initiation of buckling.

Very recently, it has been discovered by the author that the solution difficulty with the arc length procedure in LUSAS near a bifurcation point can be tackled by using one of those 250 options mentioned earlier. The actual problem lies in the selection of the correct root of a quadratic equation (see Ref. [6.8]) where one root will take the solution forward and the other backward! Option 164 allows the solution to continue on the fundamental path and overcomes any oscillation near a bifurcation point. This is done by controlling the arc length procedure by the current stiffness parameter instead of the minimum pivot. The current stiffness parameter is a scalar quantity designed to characterise the overall structural stiffness at various stages of a non-linear solution.

The author will continue working on this problem. However, no such result using Option 164 together with the arc length procedure is presented in this thesis.

6.11.3 Numerical Results

MYSTRO contains a parametric command language facility based on the syntax of the C language. Table 6.8 presents a typical command file 'replayed' in MYSTRO to create a datafile called nl_s1_b.dat. It is the non-linear analysis datafile of the FE model, S1_2-2B. The command file in Table 6.8 has a number of comment cards starting with '!'. They are included to illustrate each and every step involved in developing a computational model in a GUI like MYSTRO. The non-linear control section in the datafile or in the restart file is subsequently modified depending on the nature of the solution path.

The output from a non-linear analysis can be several times larger than what can be extracted from a linear analysis. Fig. 6.23 shows the locations of some sampling points (the word 'sampling' is not used in any statistical sense) on S1_2-2B and S1_2-2D under combined loading. The node numbers on S1_2-2C under external pressure are slightly different but the mesh configuration is identical. Please note that some points are specifically chosen on the stringers and rings in Fig. 6.23 to compare the nature of load deflection and stress strain curves at these points with those on the shell plate.

Only the mesh type 'S1' is used in the non-linear analysis because of the problems

discussed in Section 6.11.2. It is of course possible to do similar analysis with the other mesh types 'S2' and 'S3'. They are avoided mainly because several attempts are required to complete one problem with the constant load level procedure. Moreover, the fine mesh type 'S3' was not very helpful in the eigenvalue buckling analysis and 'S2' is quite close to 'S1'. Therefore, it is expected that the conclusions drawn from the non-linear analyses of 'S1' mesh would not be seriously affected if further computations are carried out with 'S2' and 'S3'.

Figs. 6.24-6.28 present the results of analysing S1_2-2B. The solution failed to converge at the 13th. load increment. The maximum load factor attained is 5.4 which is very close to the eigenvalue result (i.e. 5.3) of S1_2-2B. In actual experiments with the cylinder 2-2B, initial instability was recorded at a load factor of 5.175. Please note that the computational models and the experimental structures are never identical. From a designer's view point, the initial instability is very important because the actual structure should be safeguarded from any type of instability. However, the FE model failed to show the post-buckling behaviour observed in the experiment. Nevertheless, it produced quite reasonable results so far as the design of similar structure is concerned. At least one can spot the load level from where the structure starts becoming unstable. The load displacement plots at nodes 1324 and 761 in the middle bay are identical because of the axisymmetric shell buckling. The number 11 and 12 in Figs. 6.24 and 6.25 refer to the load increment steps. It is interesting to note that unstable nature of displacement can be noticed even in nodes on stringers and rings. The stress strain curves in Figs. 6.26 and 6.27 also present the initiation of unstable structural behaviour.

Similar set of results from the non-linear analysis of S1_2-2D is presented in Figs. 6.29-6.34. The analysis failed to converge at the 9th. load increment. The maximum load factor attained is 8.2 which is close to the eigenvalue result (i.e. 7.65) of S1_2-2D. In actual experiments with the cylinder 2-2D, initial instability was recorded at a load factor of 7.786. Still we could not reach the experimental maximum load factor of 10. It might be because of the constant load level procedure used in the analysis which usually fails to follow the solution path near structural collapse. The equivalent loads are never shown in any figure in this chapter because the pressure load would cover the entire drawing and it would be difficult to examine anything else. However, the displacement contour plot in Fig. 6.34 demands some explanation based on the assignment of loading. The equivalent axial compression load is assigned to the bottom ring. To be precise, the line of action of the axial compression coincides with the

curved line joining the shell and the bottom ring. The top ring is fixed. In view of this boundary condition, the displacement pattern can now be understood quite clearly.

The node numbering on S1_2-2C is slightly different but the mesh discretisation is identical to that of S1_2-2B and S1_2-2D. Nodes 959, 1319, 806 and 1099 are in the same position on the mesh as nodes 957, 1324, 800 and 1104 in Fig. 6.23 respectively. The nature of load displacement curves are quite interesting. Nodes on the shell plate (i.e. 806 and 1319) are showing a displacement reversal although the stress values do not change appreciably at these points. However, there are nodes where the resultant displacements are larger than those at 806 and 1319 (see Fig. 6.39). The analysis failed to converge at the 17th. load increment. The maximum load factor attained is 8.21. In actual experiments with the cylinder 2-2C, initial instability was recorded at a load factor of 5.74. This is the only one model where the analysis could go beyond the initial instability. But please note that there is no axial compression present in 2-2C. The equivalent stress values in Fig. 6.40 are much higher than others discussed before. This might be due to the fact that the analysis could go quite far beyond the initial instability.

6.12 CONCLUSIONS

There are references on non-linear FE analysis where the readers are discouraged to take attempts to solve numerical problems if they are not well acquainted with the theoretical background. But the author has learnt something different. He thinks that it is extremely difficult to understand the theories alone unless someone works with the numerical problems.

The main objective was to carry out a detail FE analysis of a part of a TLP structure with the help of the results from a 3-D beam element based global analysis. Although the ISSC TLP structure is not analysed in this chapter since no experimental data is available, it is still possible to generate computational models for any TLP column similar to the cylinders considered here. In fact, the command files already created can be used to analyse other cylindrical structures with slight modifications.

The computerised analytical predictions presented are in good agreement with the experimental results. LUSAS is a general-purpose FE package. But it could adequately handle the buckling problems and the results can be used in design to avoid structural instabilities.

6.13 REFERENCES

[6.1] ABAQUS Standard User's Manual, Version 5.3, Hibbitt, Karlsson & Sorensen, Inc., Pawtucket, US, 1993.

[6.2] ABAQUS Theory Manual, Version 5.3, Hibbitt, Karlsson & Sorensen, Inc., Pawtucket, US, 1993.

[6.3] Bathe, K.J.: "Finite Element Procedures in Engineering Analysis", Prentice-Hall, 1982.

[6.4] Bathe, K.J. and Wilson, E.L.: "Numerical Methods in Finite Element Analysis", Prentice-Hall, 1976.

[6.5] Brush, D.O. and Almroth, B.O.: "Buckling of Bars, Plates and Shells", McGraw-Hill Book Company, New York, 1975.

[6.6] Bushnell, D.: "Computerized Buckling Analysis of Shells", Martinus Nijhoff Publishers, Dordrecht, 1985.

[6.7] Catley, D.: "VAS User Manual: The BSRA Vibration Analysis Suite of Programs", The British Ship Research Association, Wallsend, 1983.

[6.8] Crisfield, M.A.: "A Fast Incremental/Iterative Solution Procedure that Handles Snap-through", Computers and Structures, Vol. 13, pp 55-62, 1981.

[6.9] Hinton, E.: "NAFEMS Introduction to Non-linear Finite Element Analysis", NAFEMS, Glasgow, pp. 284-290, 1992.

[6.10] LUSAS Finite Element Library, Version 11.0, Finite Element Analysis Limited, 66 High Street, Surrey, 1993.

[6.11] LUSAS Theory Manual, Version 10.0, Finite Element Analysis Limited, 66 High Street, Surrey, 1990.

[6.12] LUSAS Utility Manual, Version 11.0, Finite Element Analysis Limited, 66 High Street, Surrey, 1993.

[6.13] Morandi, A.C.: "Computer Aided Reliability Based Design of Ring-Stiffened Cylindrical Shells Under External Pressure", Ph.D. Thesis, Department of Naval Architecture and Ocean Engineering, University of Glasgow, Glasgow, 1994.

[6.14] Seleim, S.S. and Roorda, J.: "Buckling Behaviour of Ring-Stiffened Cylinders; Experimental Study", Thin-Walled Structures, Vol. 4, pp 203-222, 1986.

[6.15] Vojta, J.F. and Miller, C.D.: "Buckling Tests on Ring and Stringer Stiffened

Cylinder Models Subject to Combined Loads", Main Research Report, CBI Industries Inc., Vol. I, April 1983.

Table 6.8. A MYSTRO Command File Illustrating Different Steps in Non-linear FE Modelling of Orthogonally Stiffened Cylinders

```
! 'S1' type mesh of 2-2B, 176 elements per panel

! Defining transformation datasets
DEFINE TRANSFORMATION TRANSLATION ITSET=1 X=0 Y=161.73 Z=0
DEFINE TRANSFORMATION TRANSLATION ITSET=2 X=0 Y=390.33 Z=0
DEFINE TRANSFORMATION TRANSLATION ITSET=3 X=0 Y=552.06 Z=0
DEFINE TRANSFORMATION XZ_ANGLE ITSET=4 THETA=10 X0=0 Y0=0 Z0=0
DEFINE TRANSFORMATION TRANSLATION ITSET=5 X=0 Y=228.60 Z=0
DEFINE TRANSFORMATION XZ_ANGLE ITSET=6 THETA=20 X0=0 Y0=0 Z0=0

! Tolerance
SET TOLERANCE MERGE MGTOL=  3.00000
SET TOLERANCE EQUIVALENCE EQTOL=  3.00000
SET LABEL POINTS
SET LABEL LINES
SET LABEL SURFACES

! Defining points, lines and surfaces
DEFINE POINT PN=1 X=572.48 Y=0 Z=0
DEFINE POINT PN=2 X=541.02 Y=0 Z=0
DEFINE POINT PN=3 X=525.78 Y=0 Z=0

DEFINE LINE ARC_MINOR BY_SWEEPING LN=1 PN=1 ITSET=4
DEFINE LINE ARC_MINOR BY_SWEEPING LN=2 PN=2 ITSET=4
DEFINE LINE ARC_MINOR BY_SWEEPING LN=3 PN=3 ITSET=4

DEFINE SURFACE BY_JOINING SN=1 FN1=L1 FN2=L2
DEFINE SURFACE BY_JOINING SN=2 FN1=L2 FN2=L3

COPY SURFACE SN=1 SNINC=* NTIMES=1 ITSET=1
COPY SURFACE SN=1 SNINC=* NTIMES=1 ITSET=2
COPY SURFACE SN=1 SNINC=* NTIMES=1 ITSET=3
COPY SURFACE SN=2 SNINC=* NTIMES=1 ITSET=1
COPY SURFACE SN=2 SNINC=* NTIMES=1 ITSET=2
COPY SURFACE SN=2 SNINC=* NTIMES=1 ITSET=3

ERASE
TRANSFORM ROTATE ALPHA=45 GAMMA=-110
DRAW POINT PN=ACTIVE COLOUR=100.000.000 SYMBOL=1 SIZE=5.0
DRAW LINE LN=ACTIVE COLOUR=100.100.000 LTYPE=0
DRAW SURFACE SN=ACTIVE COLOUR=000.100.000 LTYPE=0
DRAW SURFACE AXES SN=ACTIVE VECMAX=6.0 SIZE=5.0 COLOUR=000.100.000

DEFINE SURFACE CYLINDER BY_JOINING SN=* FN1=L1 FN2=L8
DEFINE SURFACE CYLINDER BY_JOINING SN=* FN1=L8 FN2=L12
DEFINE SURFACE CYLINDER BY_JOINING SN=* FN1=L12 FN2=L16
DEFINE SURFACE BY_POINTS SN=* PN=6;4;12;14
DEFINE SURFACE BY_POINTS SN=* PN=14;12;18;20
DEFINE SURFACE BY_POINTS SN=* PN=20;18;24;26
COPY SURFACE SN=1T11 SNINC=* NTIMES=1 ITSET=4

ERASE
DRAW SURFACE SN=ACTIVE COLOUR=000.100.000 LTYPE=0
```

```
DRAW SURFACE AXES SN=ACTIVE VECMAX=6.0 SIZE=5.0 COLOUR=000.100.100
FILE PAUSE

! Mesh discretisation
DEFINE MESH BY_NAME IMSH=* FEATYP=Surface LNAME=qts8 MSHTYP=3 NDIVX=2
NDIVY=3
DEFINE MESH BY_NAME IMSH=* FEATYP=Surface LNAME=qts8 MSHTYP=3 NDIVX=1
NDIVY=3
DEFINE MESH BY_NAME IMSH=* FEATYP=Surface LNAME=qts8 MSHTYP=3 NDIVX=4
NDIVY=3
DEFINE MESH BY_NAME IMSH=* FEATYP=Surface LNAME=qts8 MSHTYP=3 NDIVX=5
NDIVY=3
DEFINE MESH BY_NAME IMSH=* FEATYP=Surface LNAME=qts8 MSHTYP=3 NDIVX=2
NDIVY=4
DEFINE MESH BY_NAME IMSH=* FEATYP=Surface LNAME=qts8 MSHTYP=3 NDIVX=2
NDIVY=5

DEFINE EQUIVALENCE IEQV=* EQTOL=3.0
ASSIGN EQUIVALENCE FEATYP=Point PN=ALL IEQV=1
ASSIGN EQUIVALENCE FEATYP=Line LN=ALL IEQV=1
ASSIGN EQUIVALENCE FEATYP=Surface SN=ALL IEQV=1

! Assigning mesh to the surfaces
ASSIGN MESH FEATYP=Surface SN=1;3;4;5 IMSH=1
ASSIGN MESH FEATYP=Surface SN=2;6;7;8 IMSH=2
ASSIGN MESH FEATYP=Surface SN=9;11 IMSH=3
ASSIGN MESH FEATYP=Surface SN=10 IMSH=4
ASSIGN MESH FEATYP=Surface SN=12;14 IMSH=5
ASSIGN MESH FEATYP=Surface SN=13 IMSH=6

ASSIGN MESH FEATYP=Surface SN=15;17;18;19 IMSH=1
ASSIGN MESH FEATYP=Surface SN=16;20;21;22 IMSH=2
ASSIGN MESH FEATYP=Surface SN=23;25 IMSH=3
ASSIGN MESH FEATYP=Surface SN=24 IMSH=4

ERASE
DRAW MESH COLOUR=100.100.100 LTYPE=0
FILE PAUSE

! Thickness of shell, stringers and rings
! IGMP=1 for shell and IGMP=3 for stringer
DEFINE GEOMETRY IGMP=1 LGTPF=7 E=0 T=1.96088
DEFINE GEOMETRY IGMP=2 LGTPF=7 E=0 T=3.4163
DEFINE GEOMETRY IGMP=3 LGTPF=7 E=0 T=1.93802

ASSIGN GEOMETRY FEATYP=Surface SN=1;2;5;8 IGMP=2
ASSIGN GEOMETRY FEATYP=Surface SN=3;4;6;7;9T11 IGMP=1
ASSIGN GEOMETRY FEATYP=Surface SN=12;13;14 IGMP=3

ASSIGN GEOMETRY FEATYP=Surface SN=15;16;19;22 IGMP=2
ASSIGN GEOMETRY FEATYP=Surface SN=17;18;20;21;23T25 IGMP=1

! Non-linear material
DEFINE MATERIAL IMAT=1 MATTYP=1 LPTPF=1 E=209566 NU=0.3
ASSIGN MATERIAL FEATYP=Surface SN=ALL IMAT=1

DEFINE MATERIAL IMAT=2 MATTYP=2 LPTPF=72 HF=0.0 SIGYO=365.46
ASSIGN MATERIAL_PLASTIC FEATYP=Surface SN=ALL IPLAS=2
```

```
DEFINE MATERIAL IMAT=3 MATTYP=3 LPTPF=70 CI=0 LI=1
ASSIGN MATERIAL_TENSION FEATYP=Surface SN=ALL ITENS=3


! Support conditions, fixed = '1'
! Bottom ring
DEFINE SUPPORTS ISUP=1 U=1 V=1 W=1 THX=0 THY=0 THZ=0
ASSIGN SUPPORT FEATYP=Surface SN=5;8;19;22 ISUP=1 LCID=1

! Top ring under load
DEFINE SUPPORTS ISUP=2 U=1 V=0 W=1 THX=0 THY=0 THZ=0
ASSIGN SUPPORT FEATYP=Surface SN=1;2;15;16 ISUP=2 LCID=1

ERASE
DRAW POINT PN=ACTIVE COLOUR=100.000.000 SYMBOL=1 SIZE=5.0
DRAW LINE LN=ACTIVE COLOUR=100.100.000 LTYPE=0

! Axial Compression
DEFINE LOADING ILDG=1 LTPF="Concentrated Load" PY=292.044
ASSIGN LOADING FEATYP=Line LN=1;50 ILDG=1 LCID=1 FACTOR=1.0
DEFINE LOADING ILDG=2 LTPF="Concentrated Load" PY=-292.044
ASSIGN LOADING FEATYP=Point PN=1;4 ILDG=2 LCID=1 FACTOR=1.0

! External pressure
DEFINE LOADING ILDG=3 LTPF="Uniformly Dist. Load" WZ=-0.06288
ASSIGN LOADING FEATYP=Surface SN=9;10;11 ILDG=3 LCID=1 FACTOR=1.0
ASSIGN LOADING FEATYP=Surface SN=23;24;25 ILDG=3 LCID=1 FACTOR=1.0

DRAW LOADING ILDG=ALL VECMAX=6.0 VECMIN=0.0 SIZE=5.0 COLOUR=000.100.100

! Copying the first panel to generate other two panels
COPY SURFACE SN=ALL SNINC=* NTIMES=2 ITSET=6

! Adjusting load at point number 1
ASSIGN LOADING FEATYP=Point PN=1 ILDG=2 LCID=1 FACTOR=-1.0

! Defining local co-ordinates for symmetric support conditions
DEFINE LOCAL_COORDINATE CARTESIAN XZ_ANGLE LCN=* THETA=60
ASSIGN LOCAL_COORDINATE FEATYP=Line ...
LN=253;257;285;261;273;289;265;277;293;269;281 LCN=1

! Symmetric support conditions
! Top ring side under load
DEFINE SUPPORTS ISUP=3 U=1 V=0 W=1 THX=1 THY=1 THZ=0
ASSIGN SUPPORT FEATYP=Line LN=4;6 ISUP=3 LCID=1
ASSIGN SUPPORT FEATYP=Line LN=253;257 ISUP=3 LCID=1

! Side shell and middle rings with x and y freedom
DEFINE SUPPORTS ISUP=4 U=0 V=0 W=1 THX=1 THY=1 THZ=0
ASSIGN SUPPORT FEATYP=Line LN=32;10;22;34;14;26;36;18;30 ISUP=4 LCID=1
ASSIGN SUPPORT FEATYP=Line LN=285;261;273;289;277;265;293;269;281 ...
ISUP=4 LCID=1

! Bottom ring side- fixed
DEFINE SUPPORTS ISUP=5 U=1 V=1 W=1 THX=1 THY=1 THZ=0
ASSIGN SUPPORT FEATYP=Line LN=30;18 ISUP=5 LCID=1
ASSIGN SUPPORT FEATYP=Line LN=269;281 ISUP=5 LCID=1
```

```
ERASE
DRAW MESH COLOUR=100.100.100 LTYPE=0
DRAW SUPPORT ISUP=ALL VECMAX=6.0 SIZE=5.0 COLOUR=020.100.050
DRAW LOADING ILDG=ALL VECMAX=6.0 VECMIN=0.0 SIZE=5.0 COLOUR=000.100.100

! Total Lagrangian geometric non-linearity
SET OPTIONS 87

! Non-linear control section to start with
DEFINE CONTROL ICTRL=1 ITYPE1=1 ITYPE2=0 SLAMDA=0.2 ISURFC=0 ITD=4
TLAMDX=15 MAXINC=15 INCPLT=1
ASSIGN CONTROL ICTRL=1 LCID=1

! Creating the datafile
TABULATE nl_s1_b
```

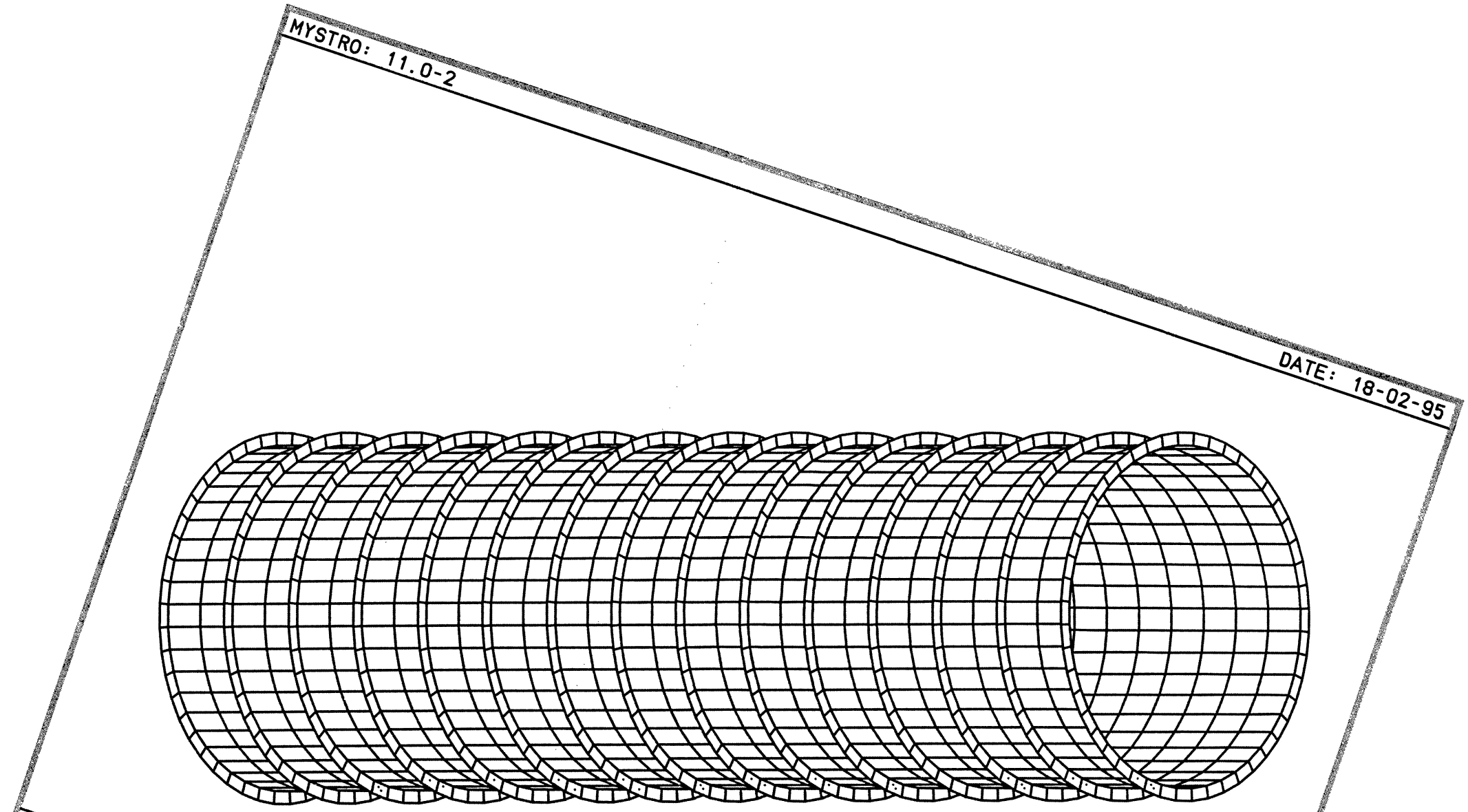

Fig. 6.1. Finite Element Mesh of QSL8_F and QTS8_F

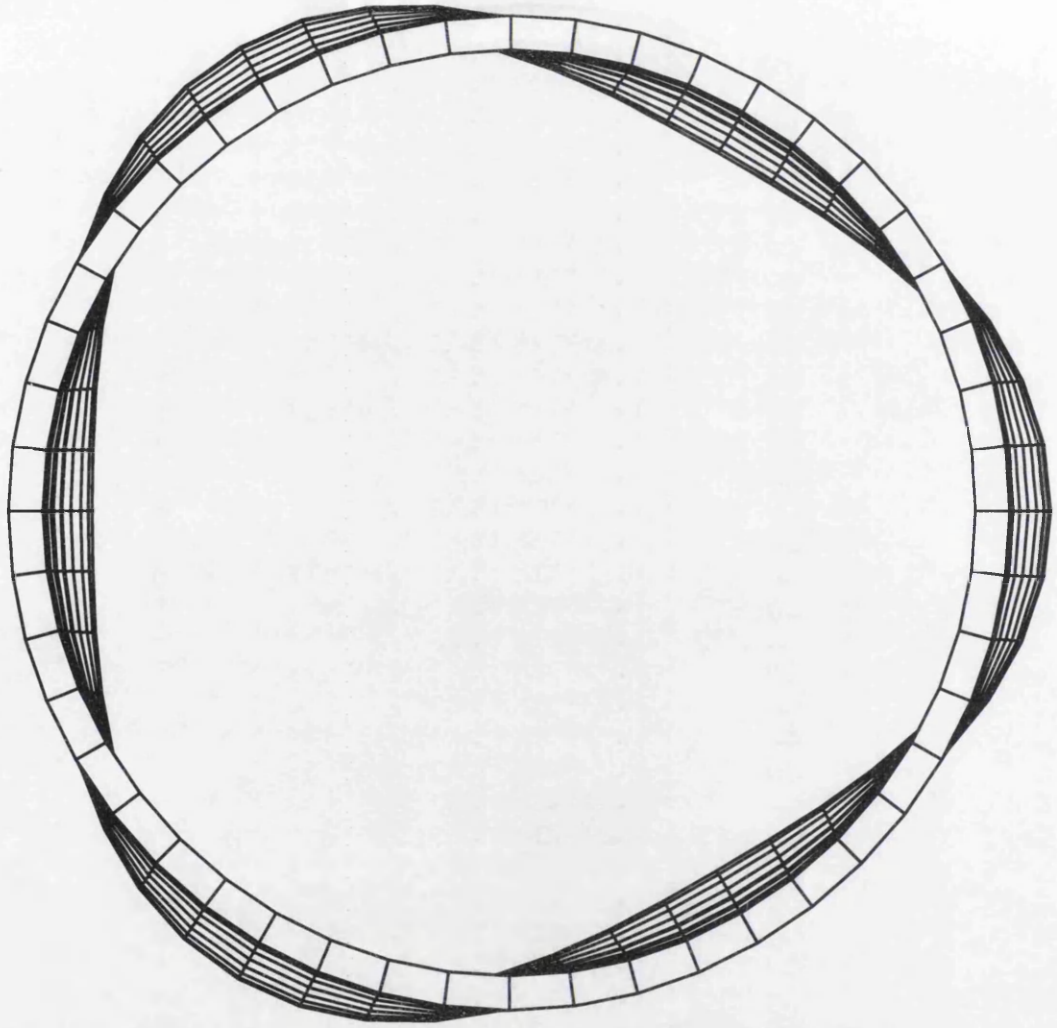

Fig. 6.2. First and Second Buckling Mode Shapes of QSL8_F and QTS8_F

MYSTRO: 11.0-2 DATE: 18-02-95

Buckling Load = 3.314 MPa

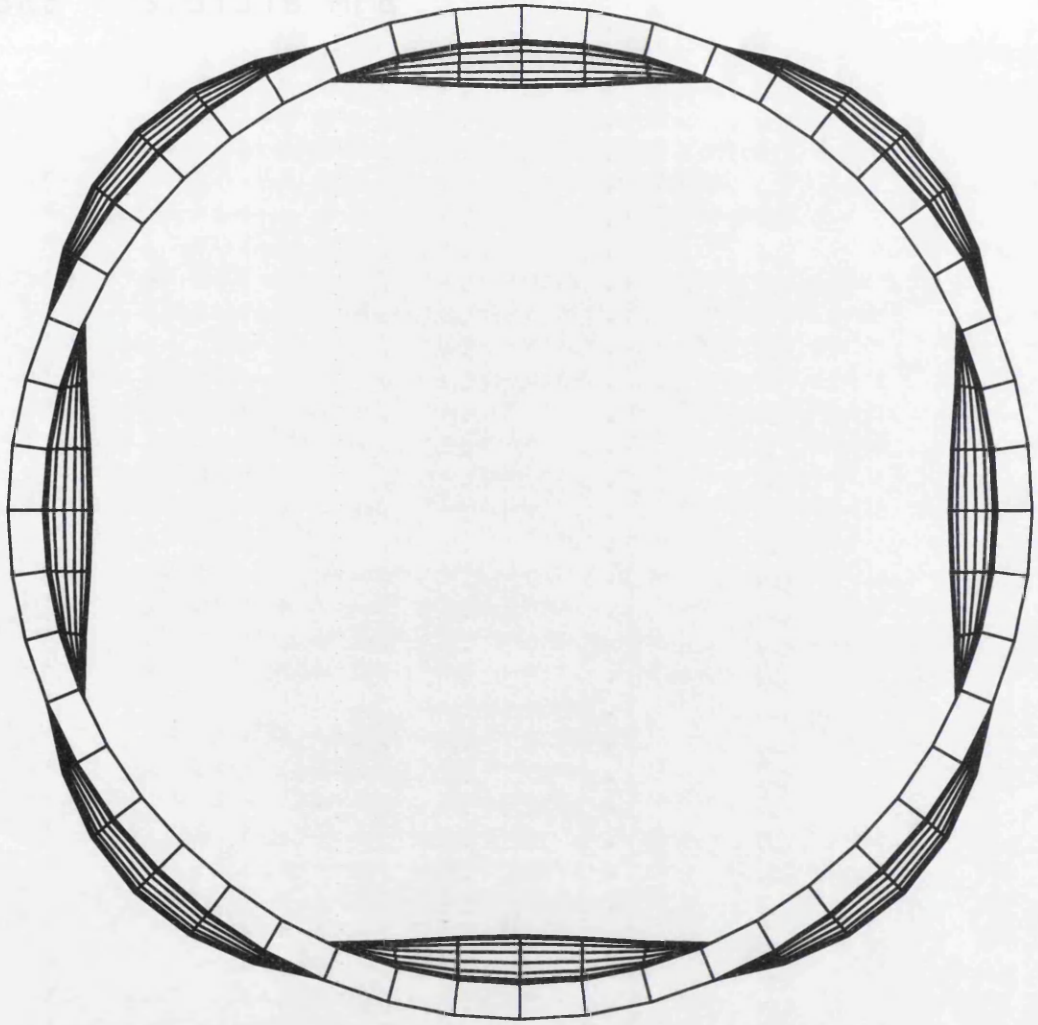

Fig. 6.3. Third Buckling Mode Shape of QSL8_F

TITLE: RING STIFFENED ALUMINIUM CYLINDER

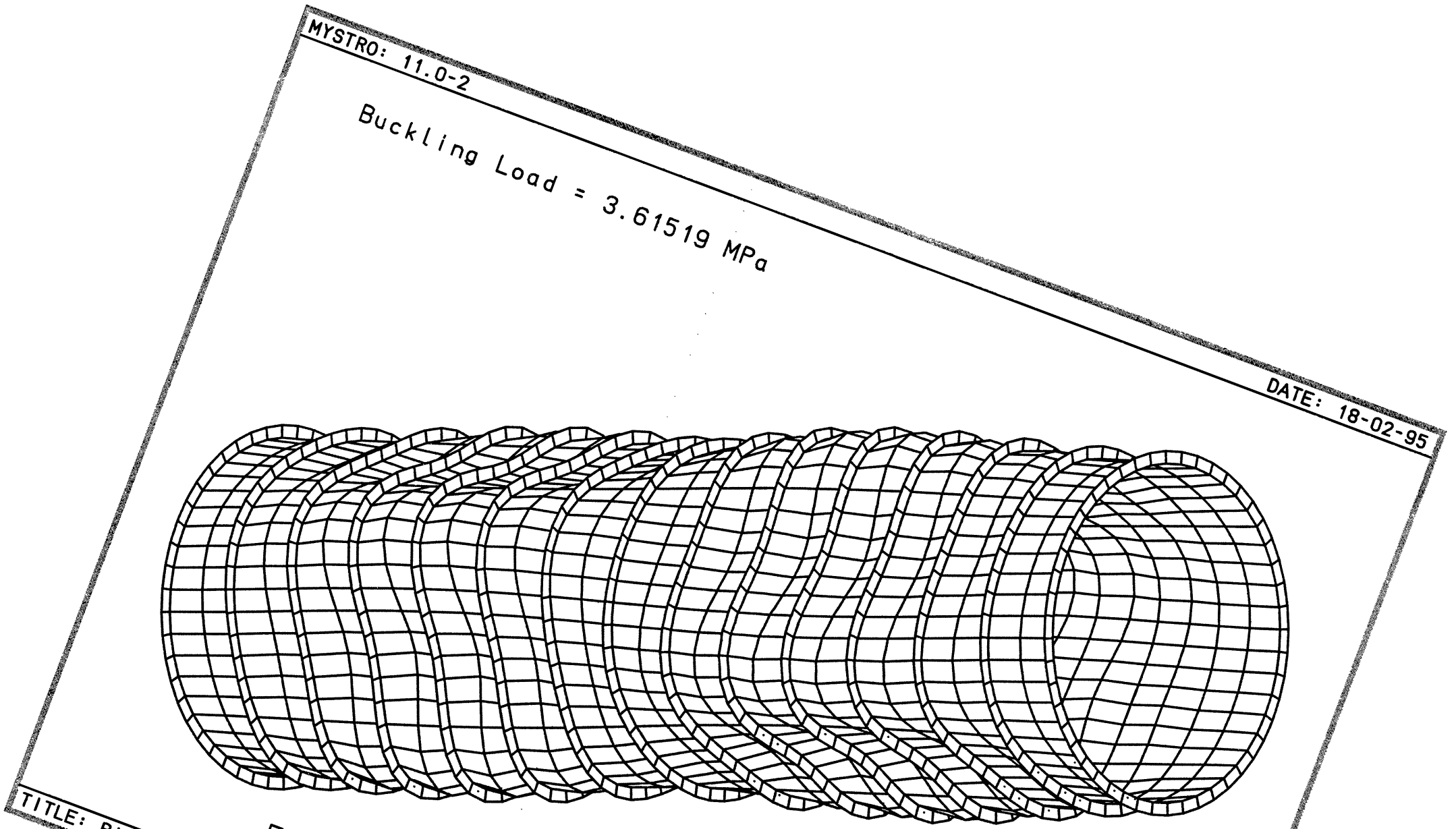

Fig. 6.4. Fourth Buckling Mode Shape of QSL8_F

MYSTRO: 11.0-2

DATE: 18-02-95

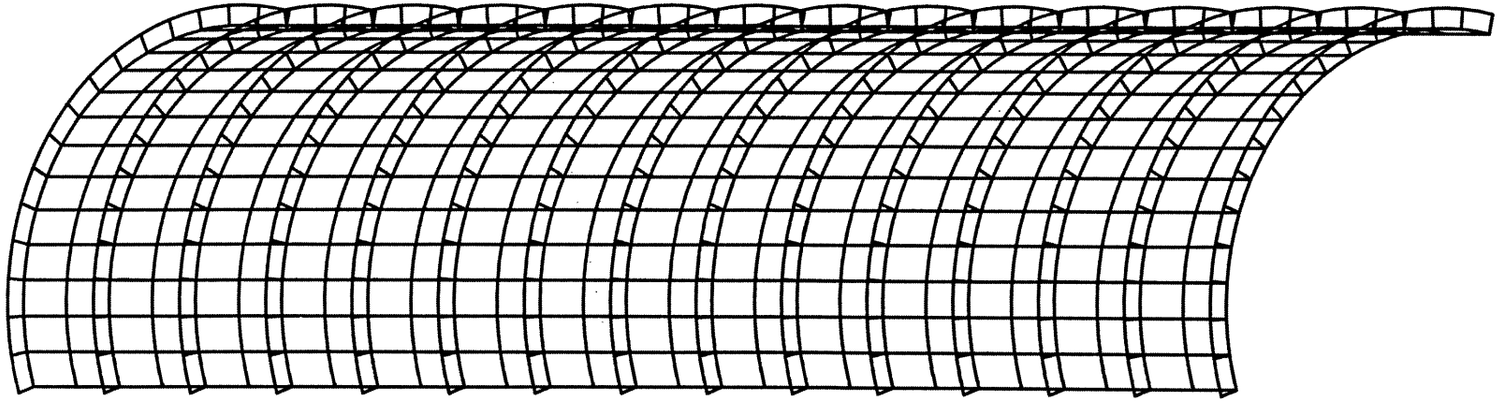

Fig. 6.5. FE Mesh of QTS8_S1 (1/3 of the Cylinder)

TITLE: RING STIFFENED ALUMINIUM CYLINDER

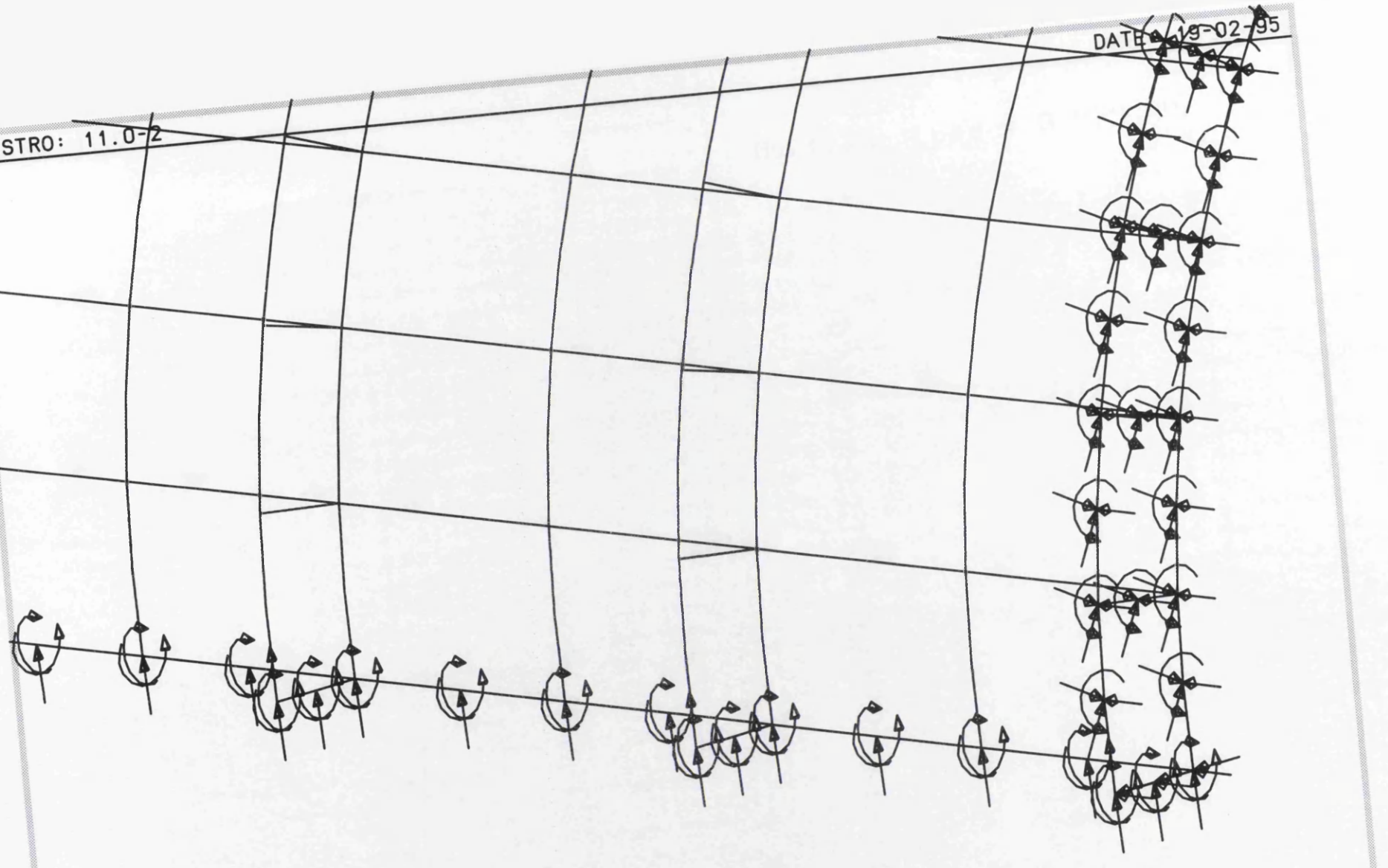

Fig. 6.6. Symmetric Boundary Conditions in QTS8_S1

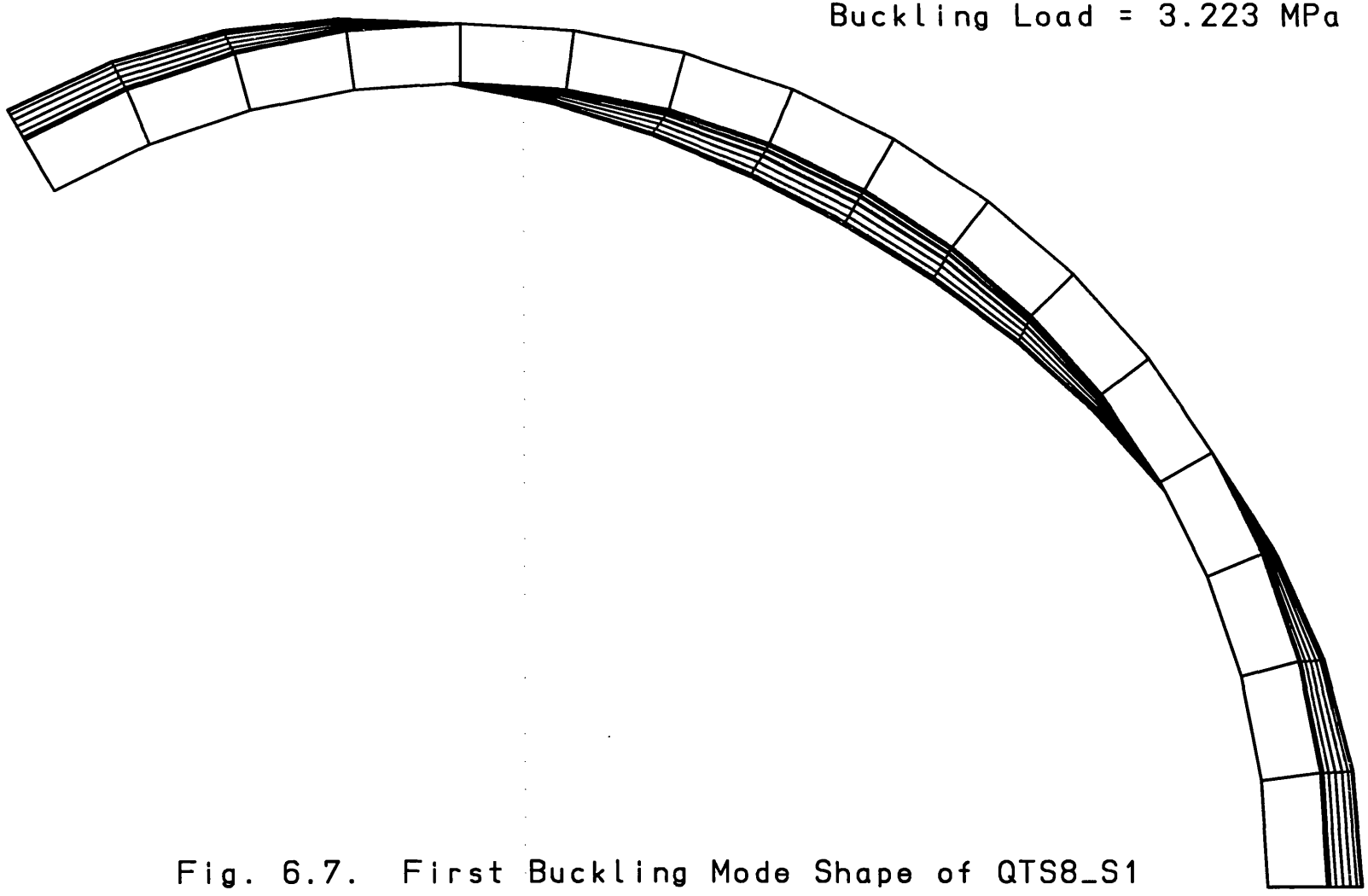

Fig. 6.7. First Buckling Mode Shape of QTS8_S1

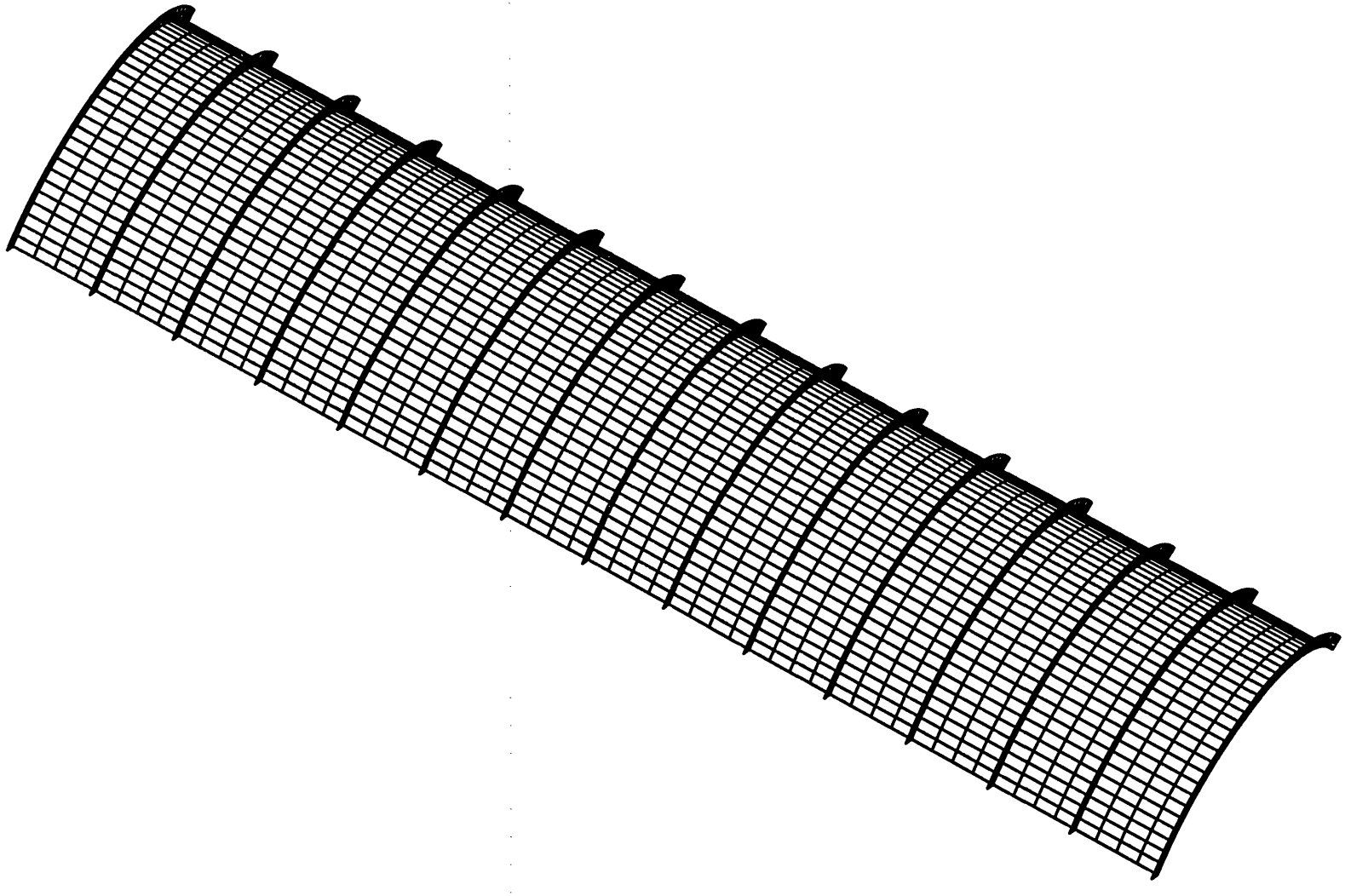

Fig. 6.8. FE Mesh of QTS8_S2 (1/3 of the Cylinder)

TITLE: RING STIFFENED ALUMINIUM CYLINDER

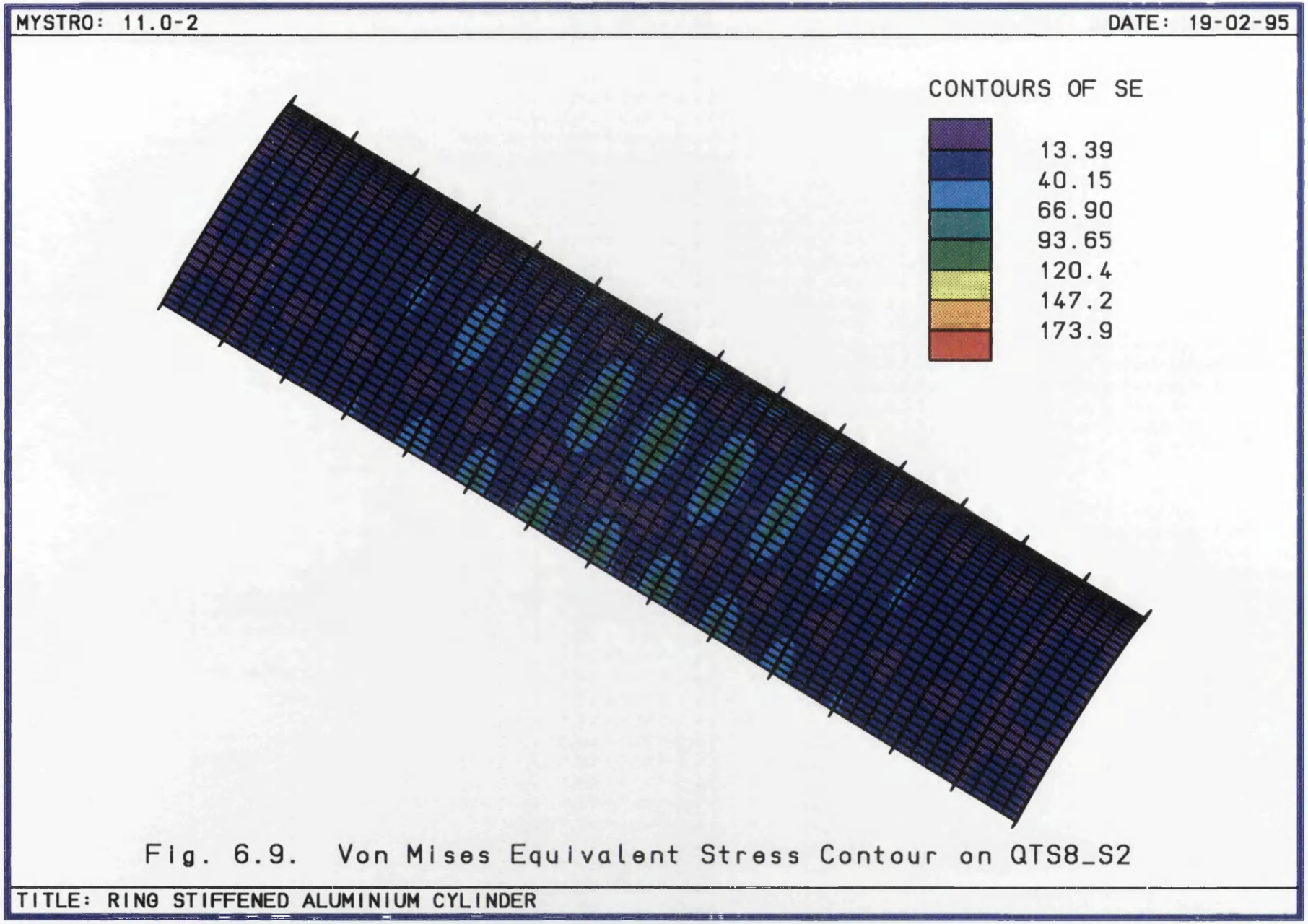

Fig. 6.9. Von Mises Equivalent Stress Contour on QTS8_S2

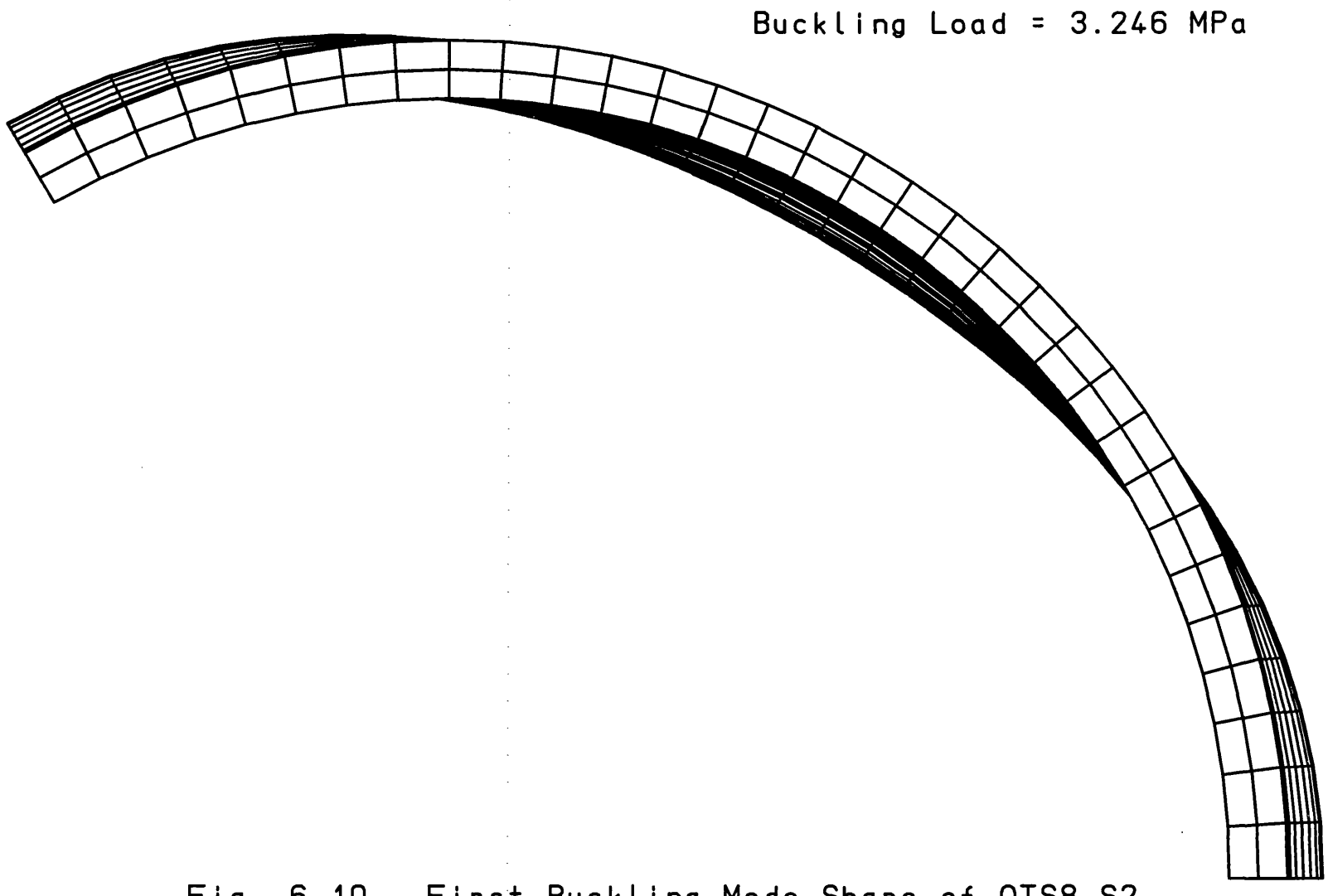

Fig. 6.10. First Buckling Mode Shape of QTS8_S2

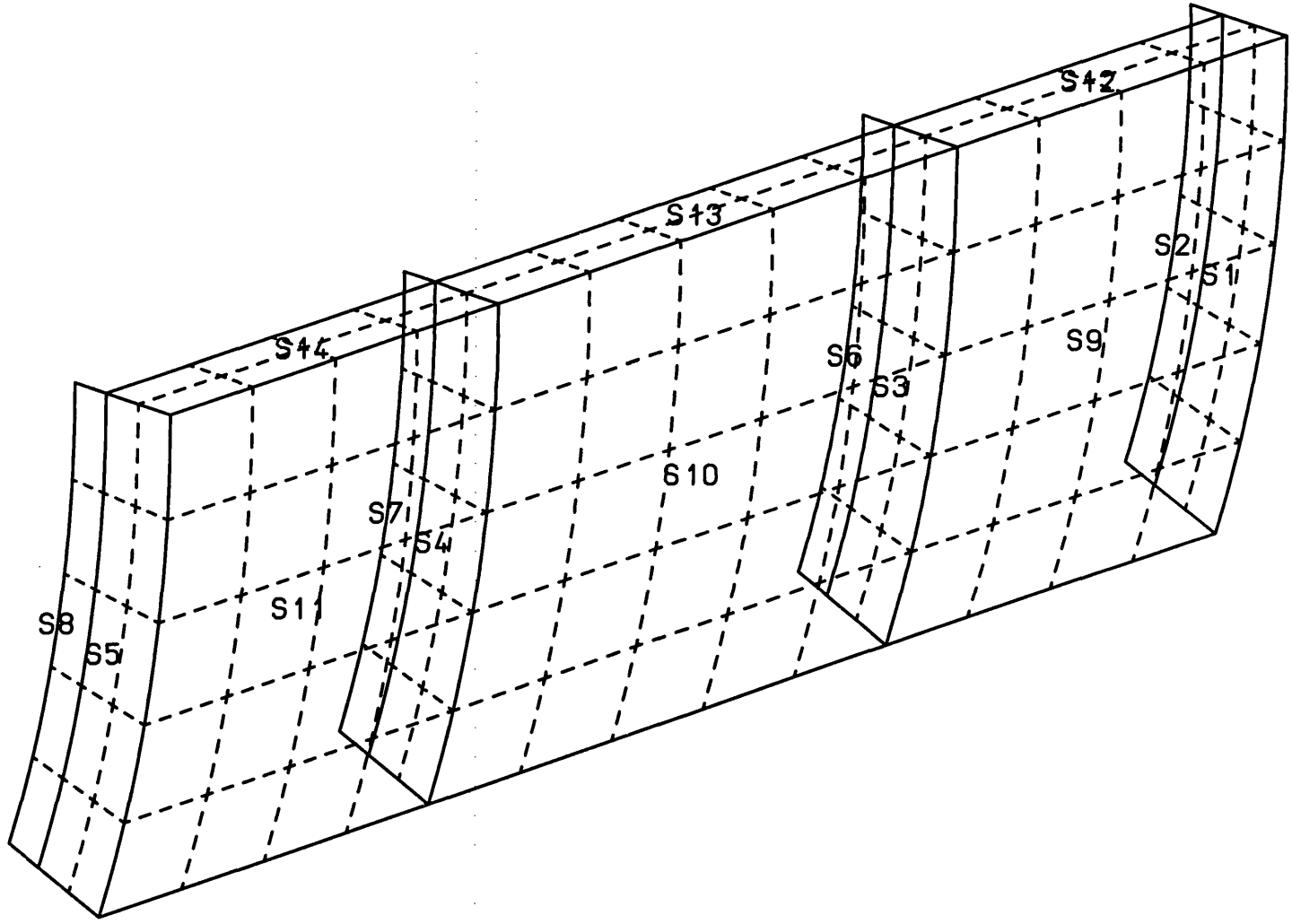

Fig. 6.11. 14 Surfaces Defined in One Panel of F_2-2

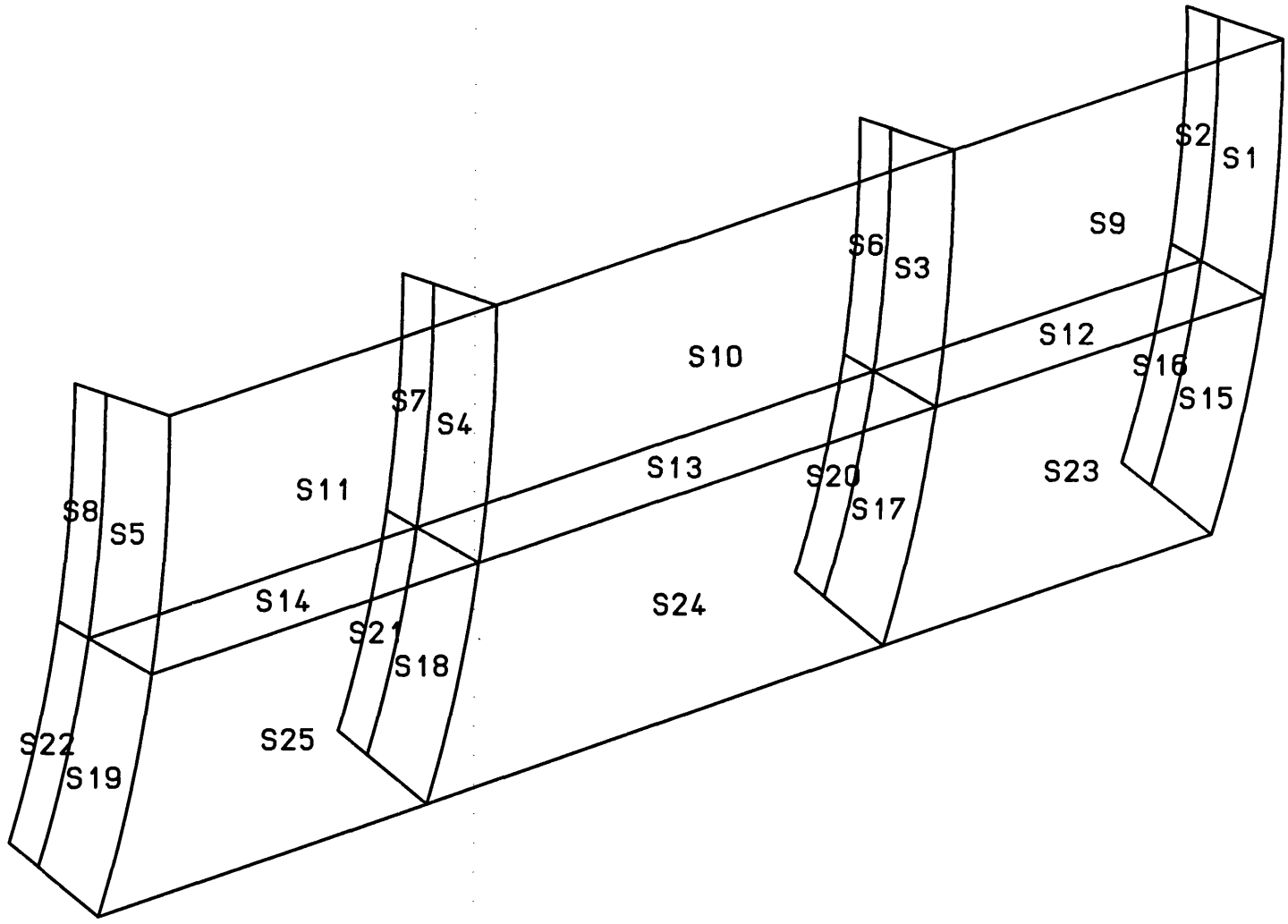

Fig. 6.12. 25 Surfaces Defined in One Panel of S1_2-2, S2_2-2 and S3_2-2

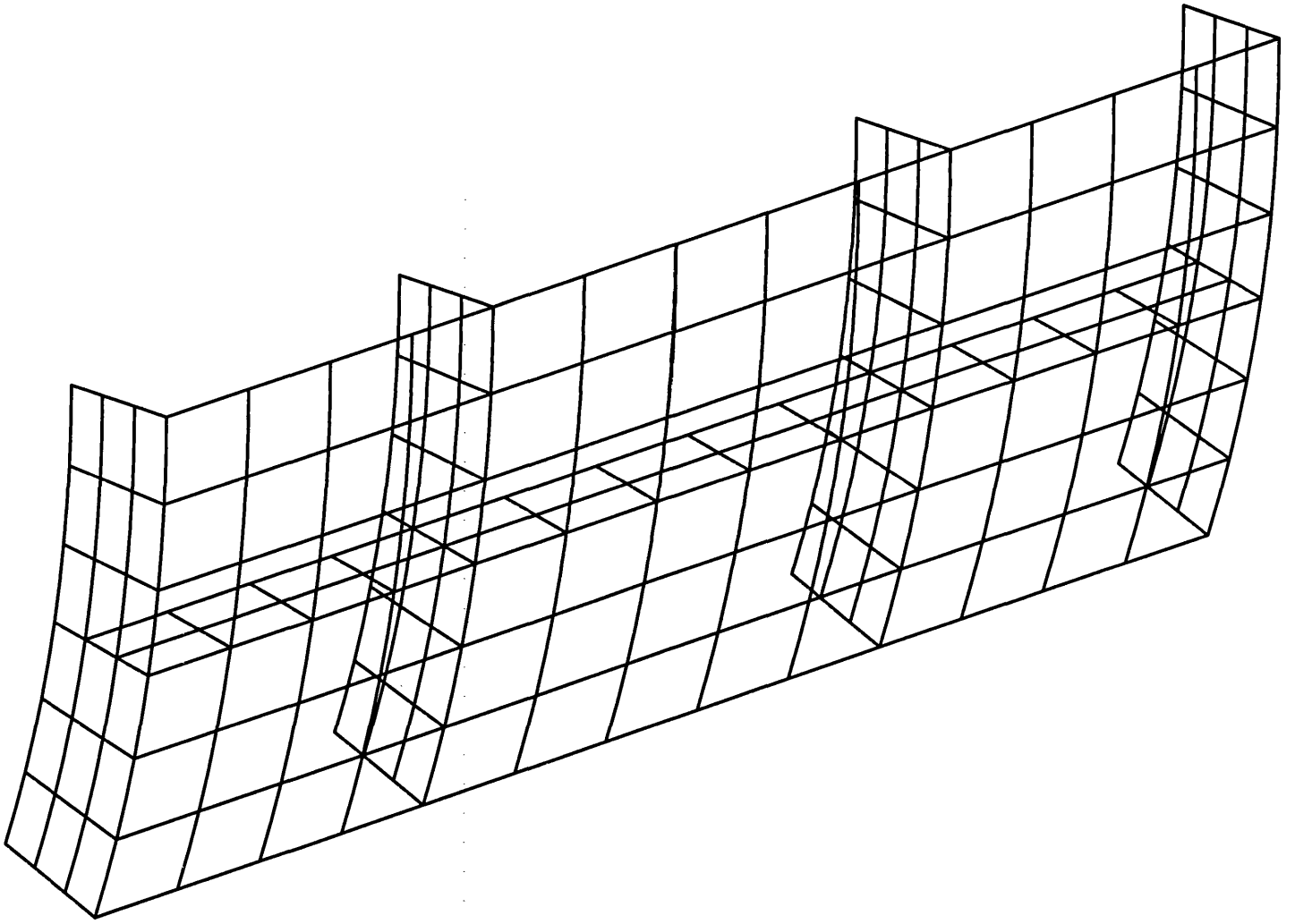

Fig. 6.13. FE Mesh of One Panel in S1_2-2

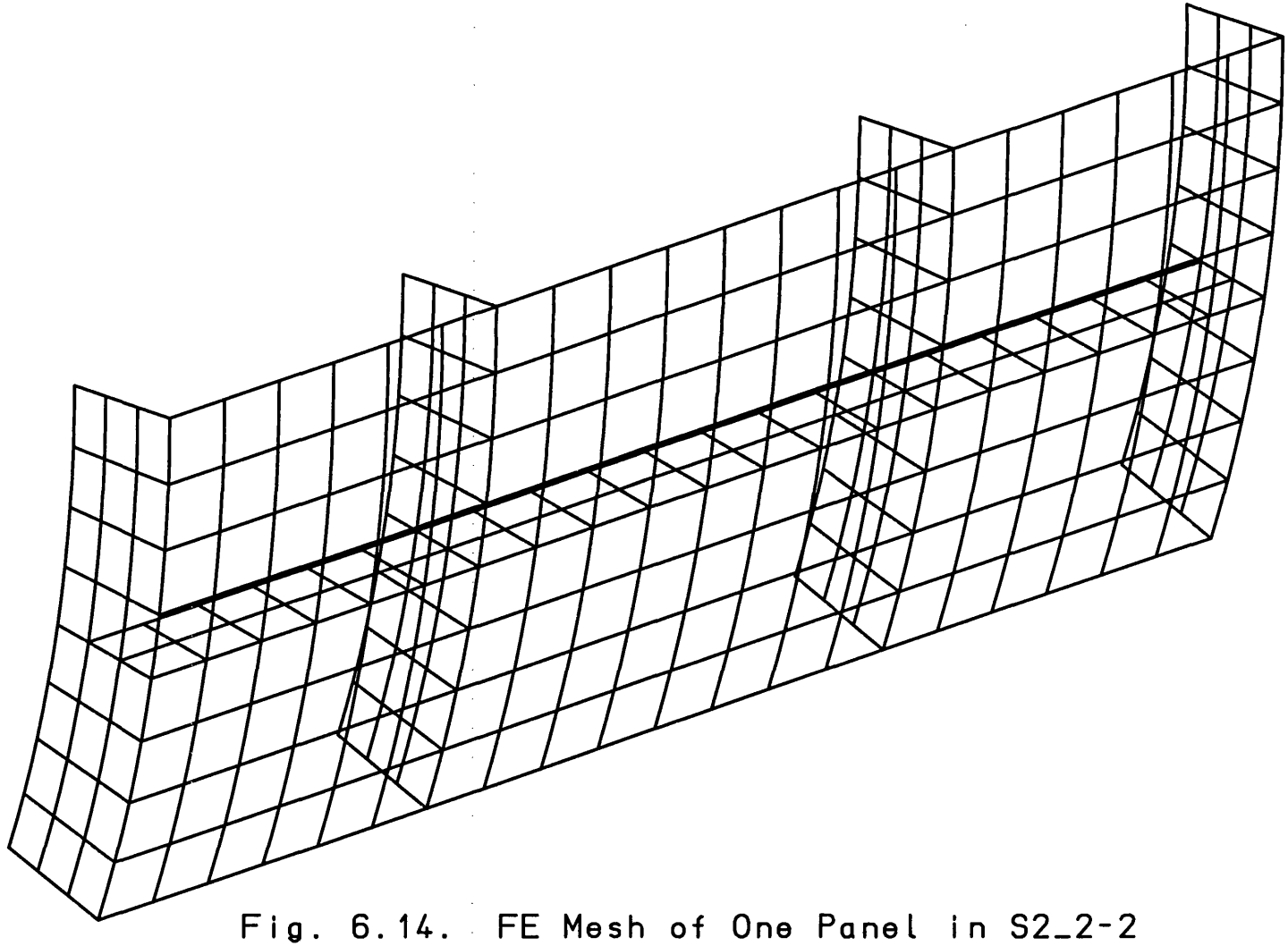

Fig. 6.14. FE Mesh of One Panel in S2_2-2

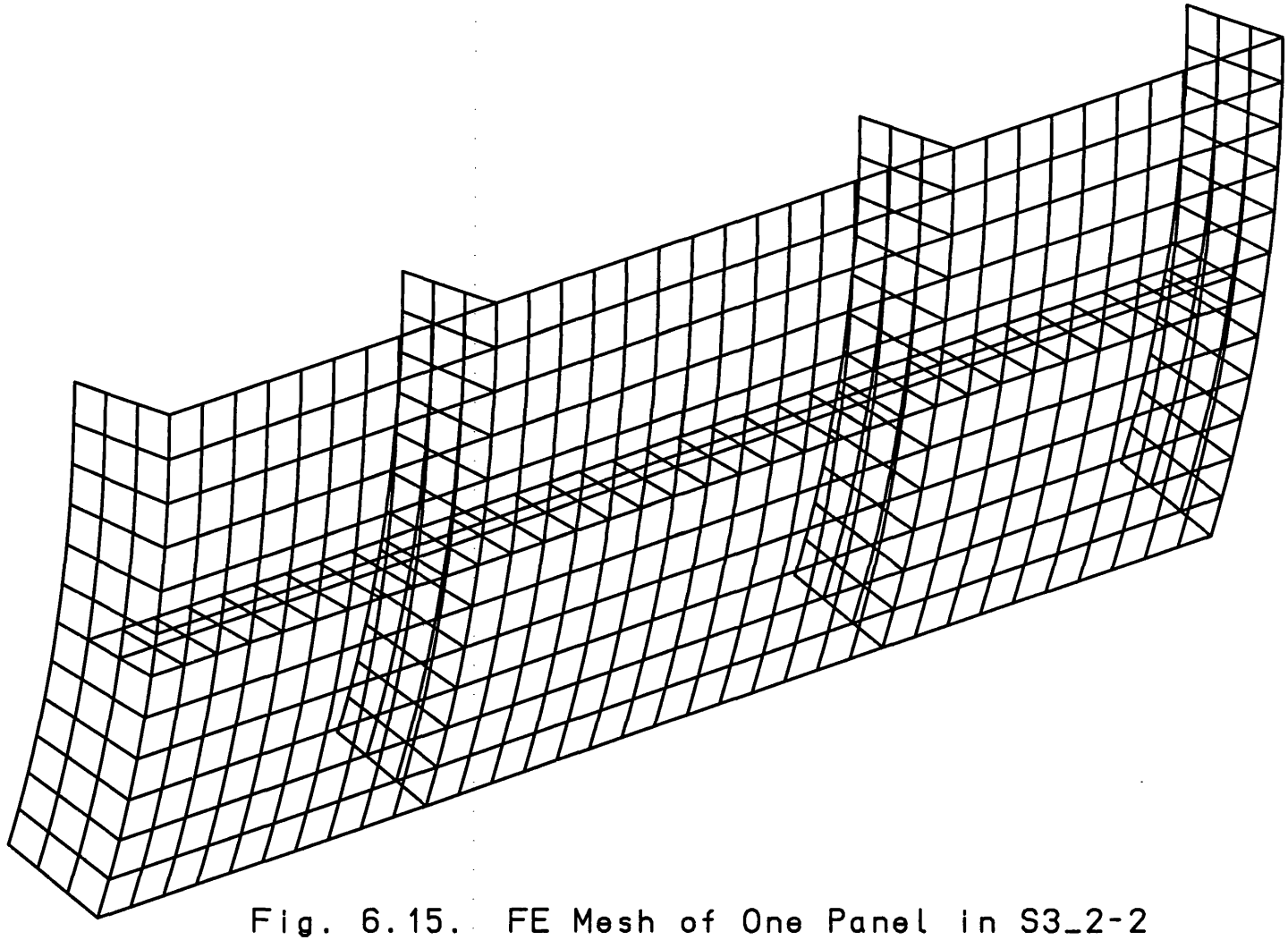

Fig. 6.15. FE Mesh of One Panel in S3_2-2

MYSTRO: 11.0-2 DATE: 20-02-95

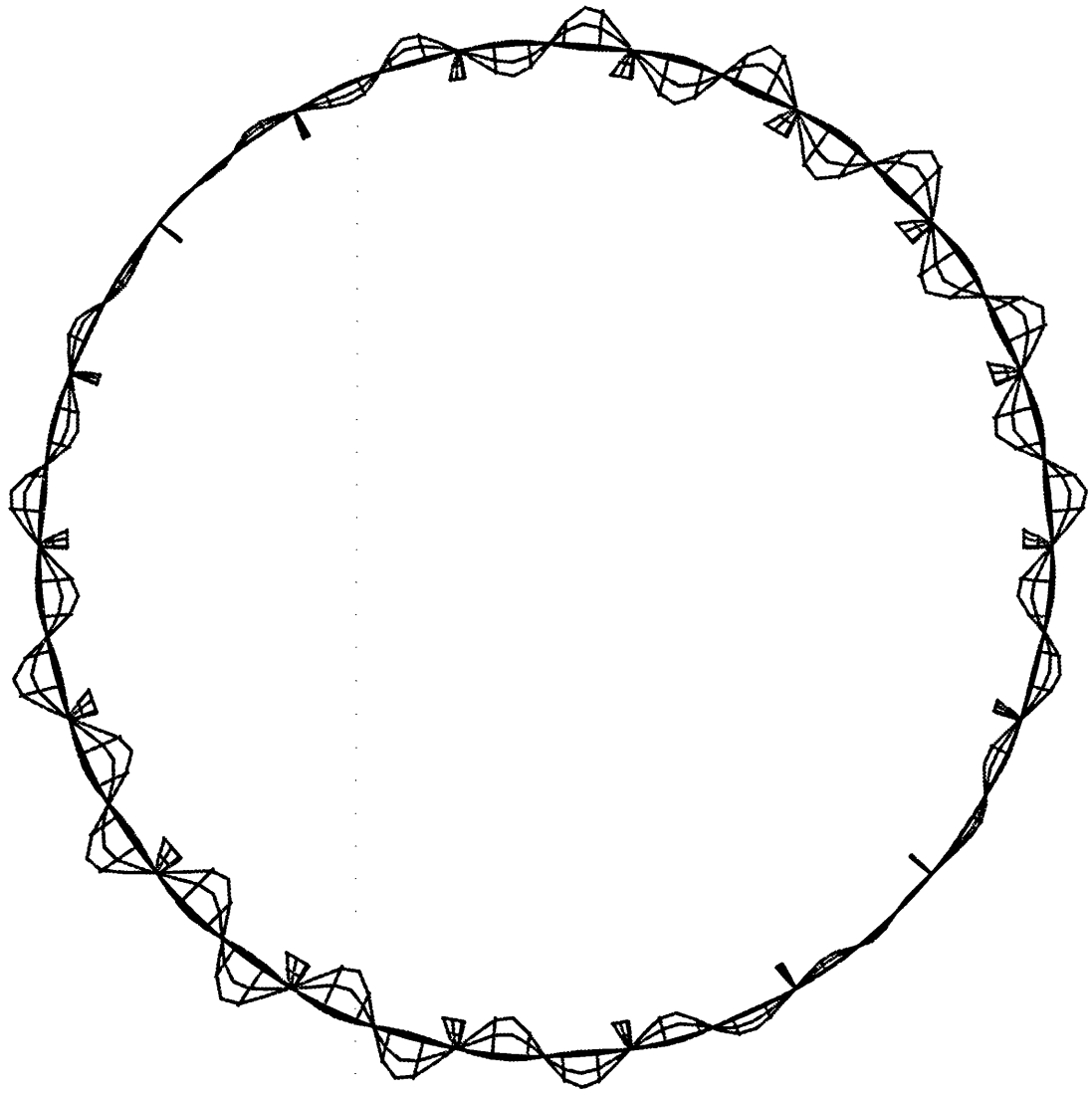

Fig. 6.16. Buckling Mode Shape of F_2-2C under External Radial Pressure

TITLE: 2-2 SERIES OF CONOCO/ABS TEST CYLINDERS

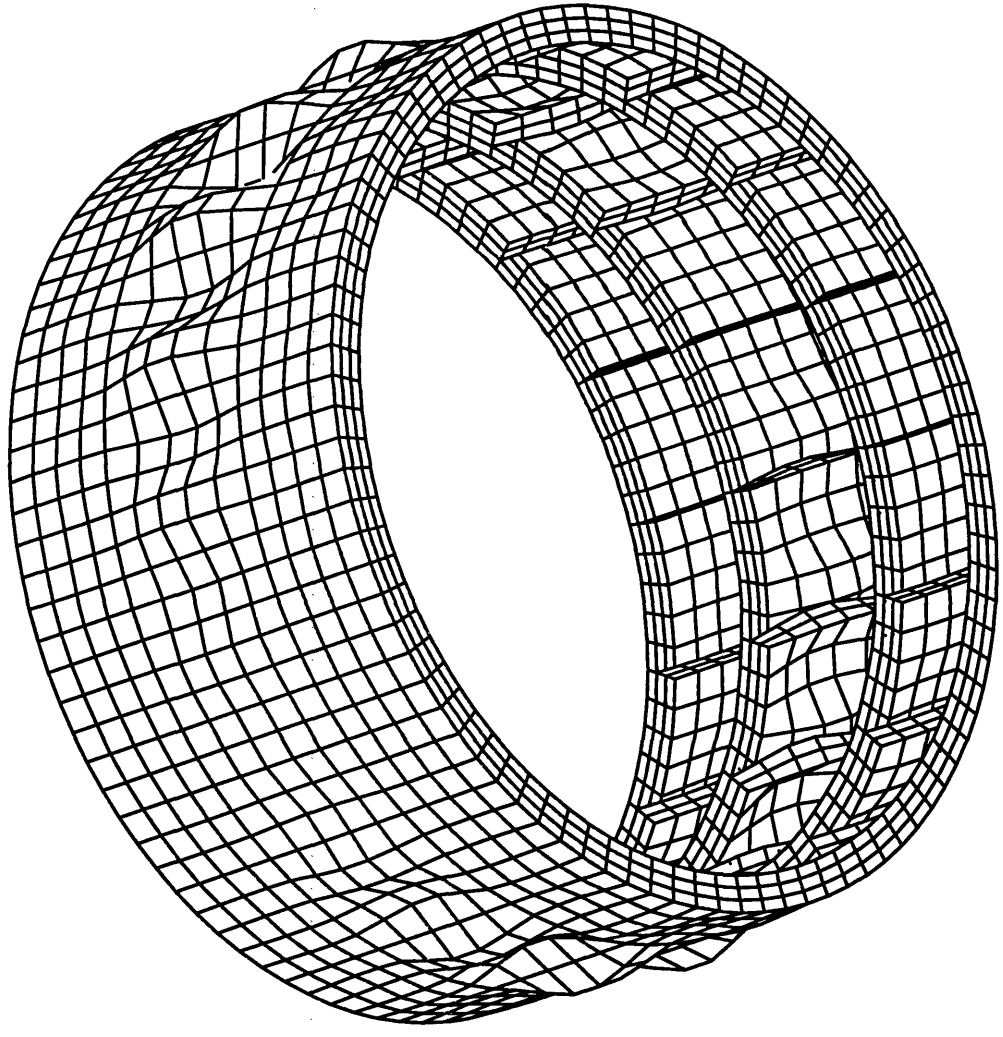

Fig. 6.17. Buckling Mode Shape of F_2-2D under Combined loading

MYSTRO: 11.0-2 DATE: 20-02-95

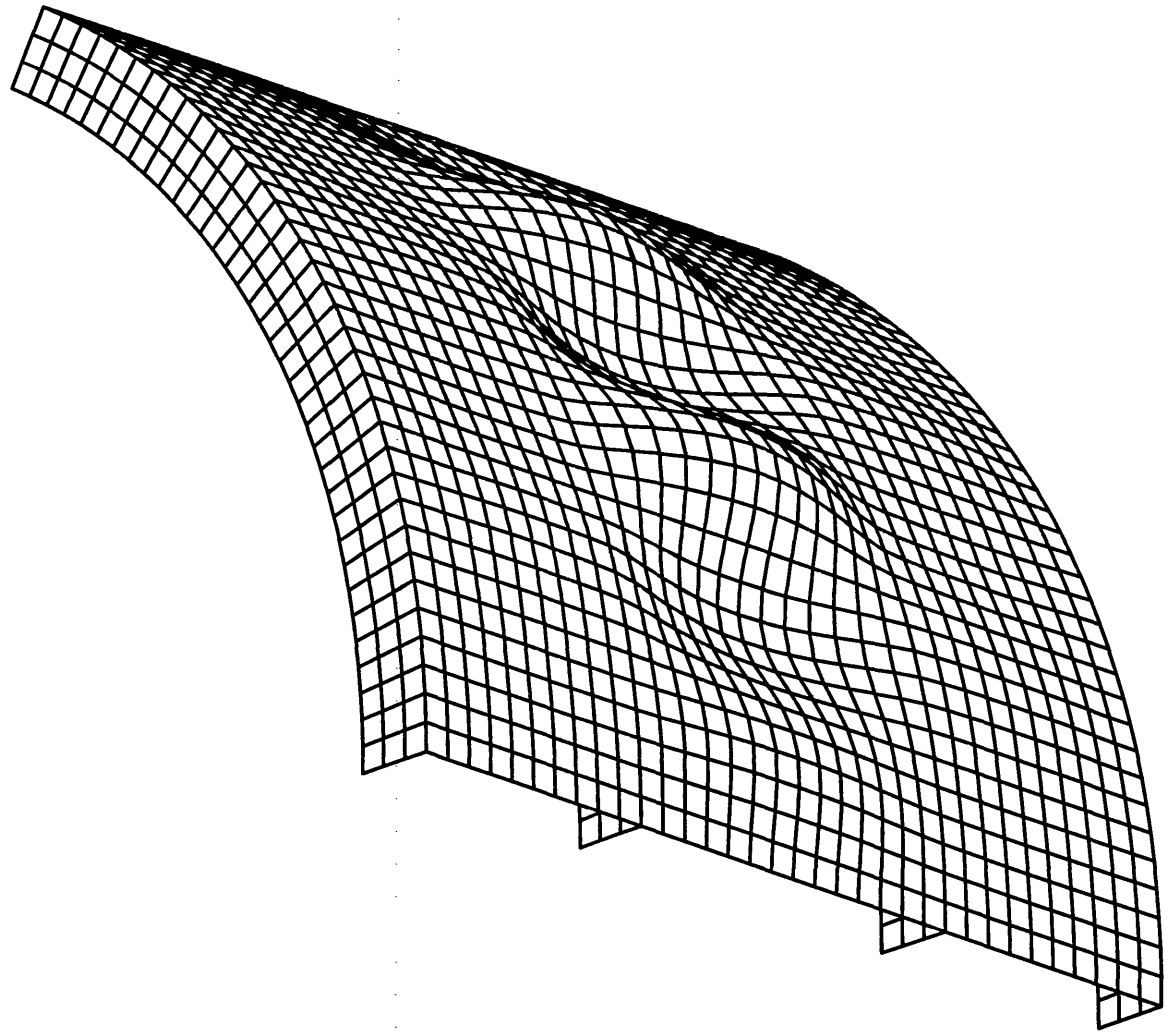

Fig. 6.18. Buckling Mode Shape of S3_2-2B under Hydrostatic Loading

TITLE: 2-2 SERIES OF CONOCO/ABS TEST CYLINDERS

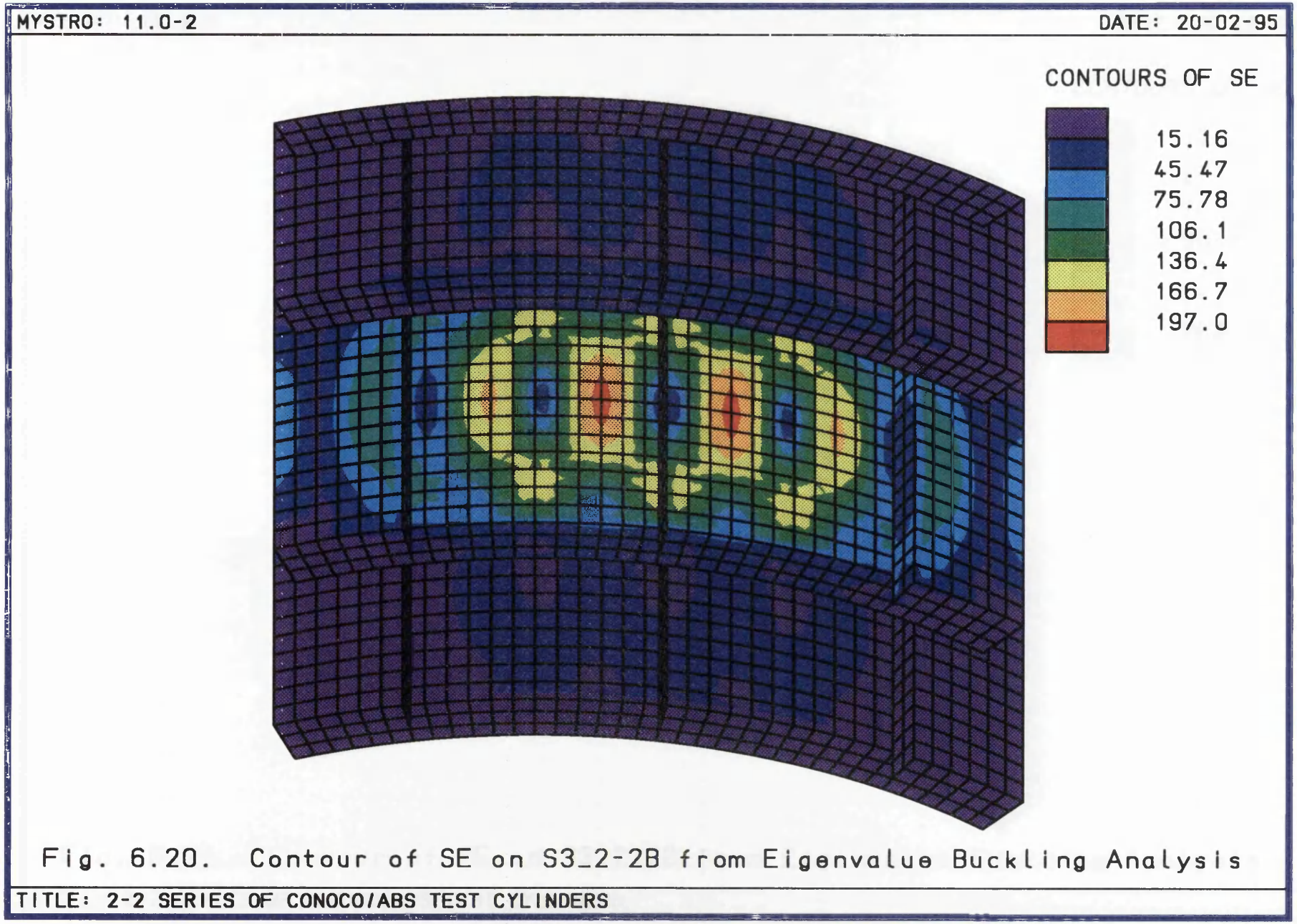

Fig. 6.20. Contour of SE on S3_2-2B from Eigenvalue Buckling Analysis

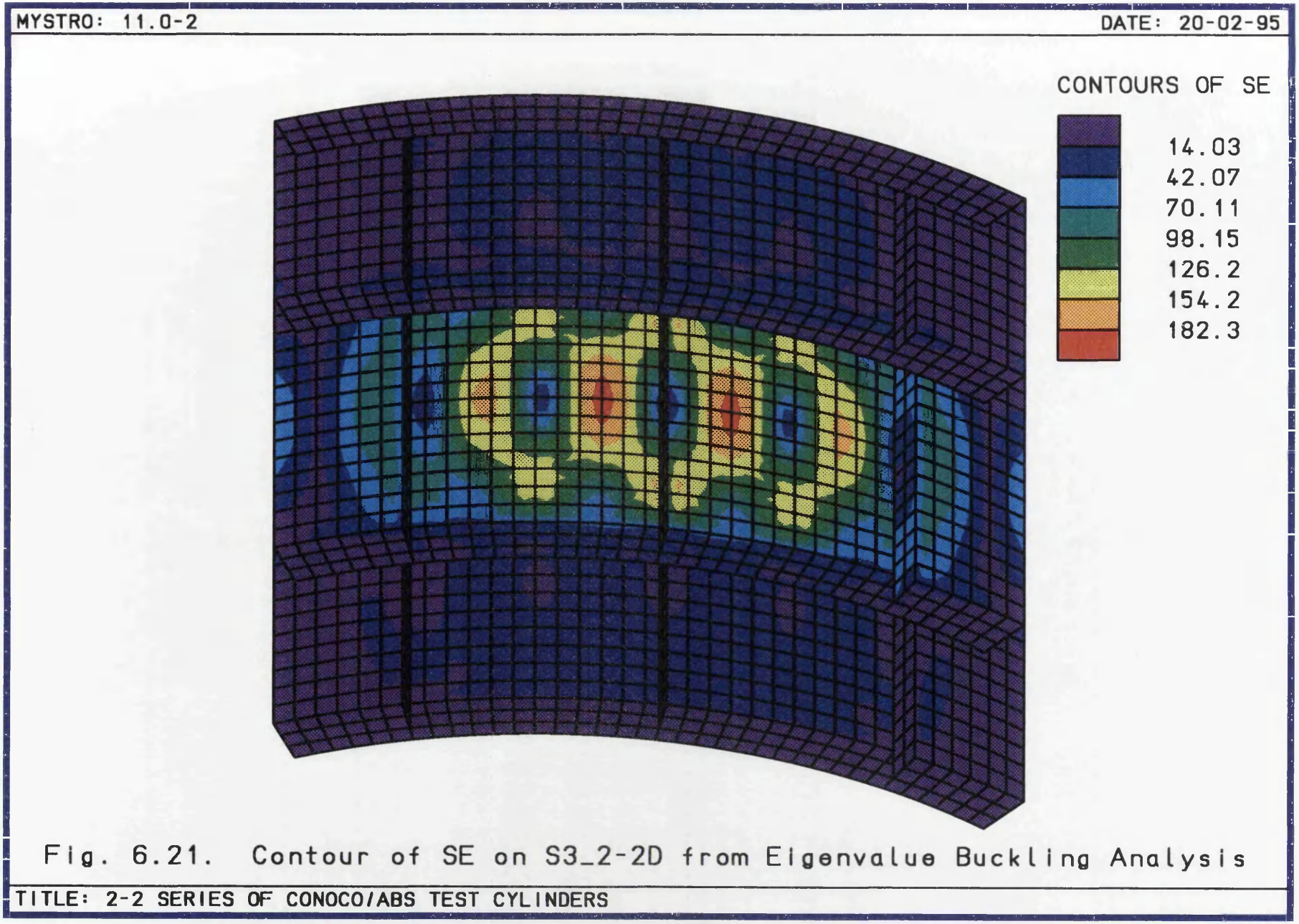

Fig. 6.21. Contour of SE on S3_2-2D from Eigenvalue Buckling Analysis

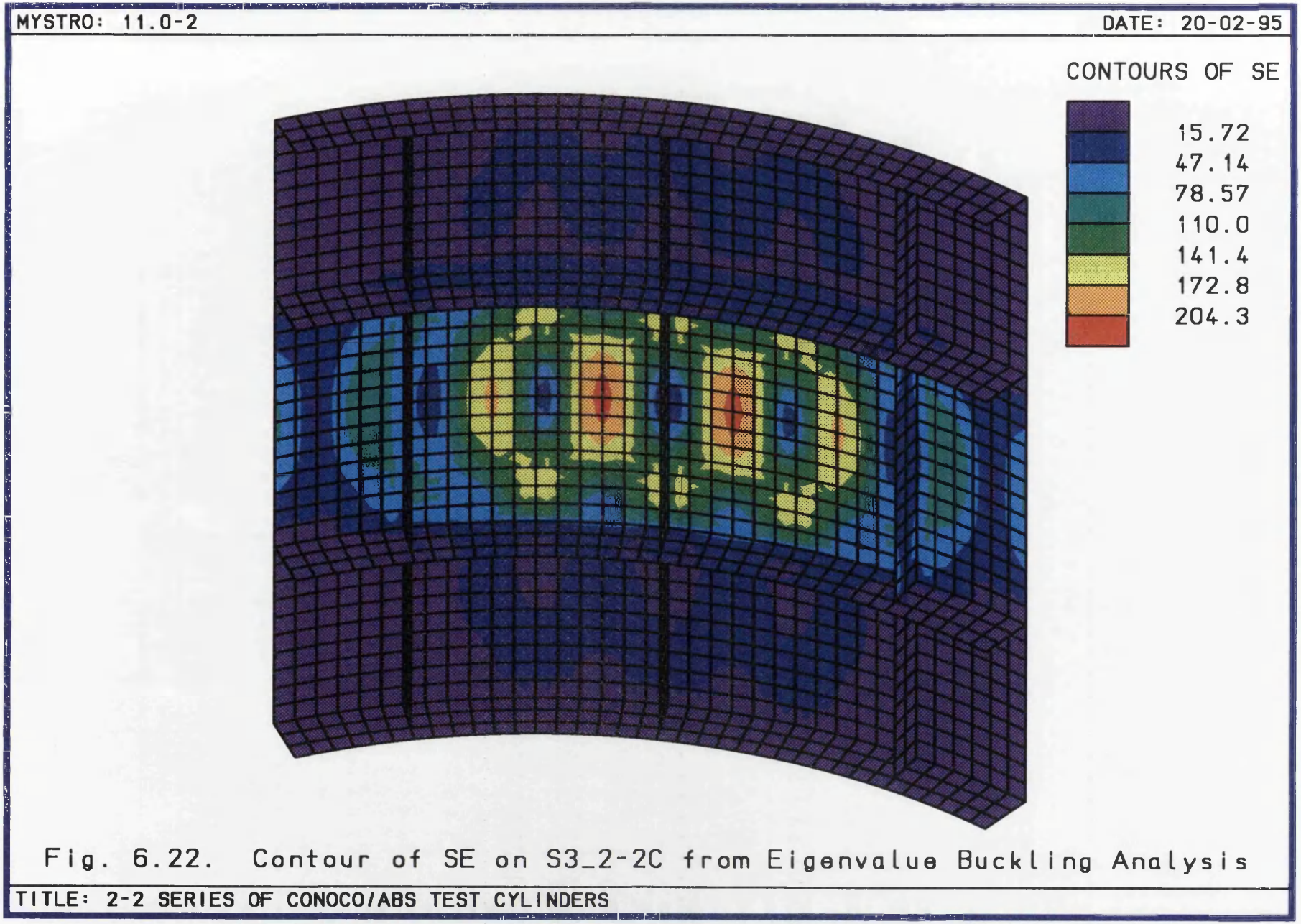

Fig. 6.22. Contour of SE on S3_2-2C from Eigenvalue Buckling Analysis

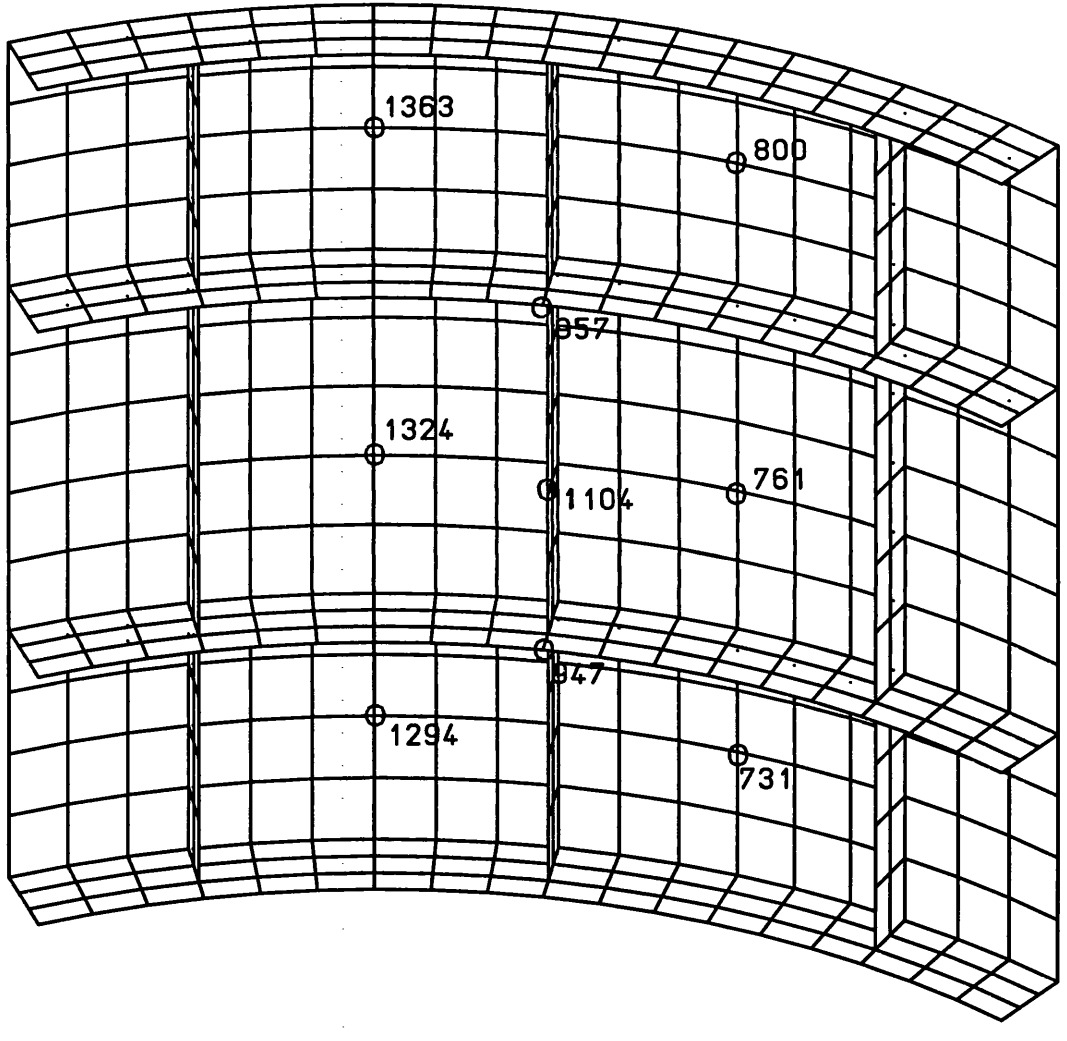

Fig. 6.23. Sampling Points on S1_2-2B and S1_2-2D for Non-linear Analysis

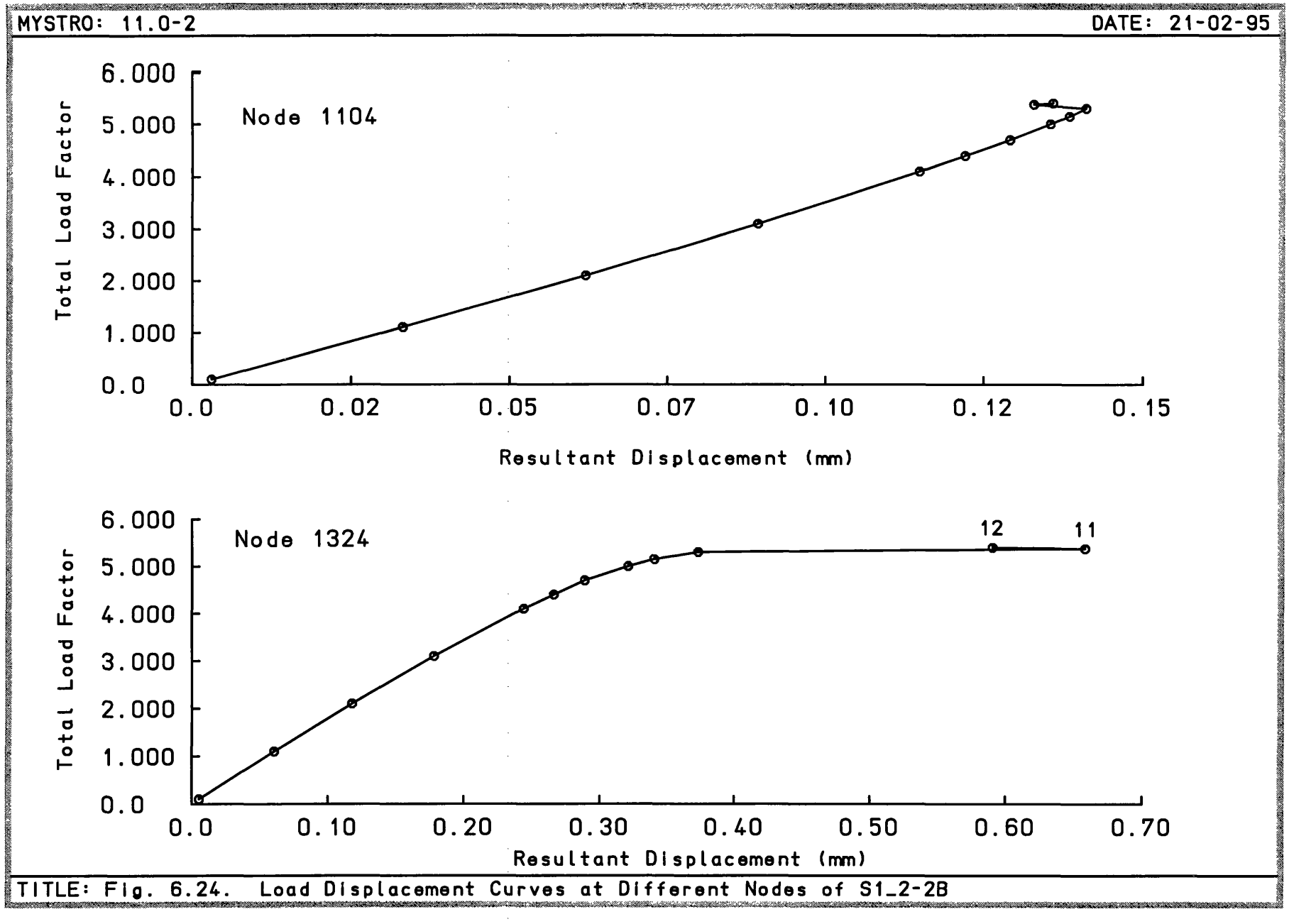
MYSTRO: 11.0-2
DATE: 21-02-95
Node 1104
Total Load Factor
6.000
5.000
4.000
3.000
2.000
1.000
0.0
0.0
0.02
0.05
0.07
0.10
0.12
0.15
Resultant Displacement (mm)
Node 1324
12
11
Total Load Factor
6.000
5.000
4.000
3.000
2.000
1.000
0.0
0.0
0.10
0.20
0.30
0.40
0.50
0.60
0.70
Resultant Displacement (mm)
TITLE: Fig. 6.24. Load Displacement Curves at Different Nodes of S1_2-2B

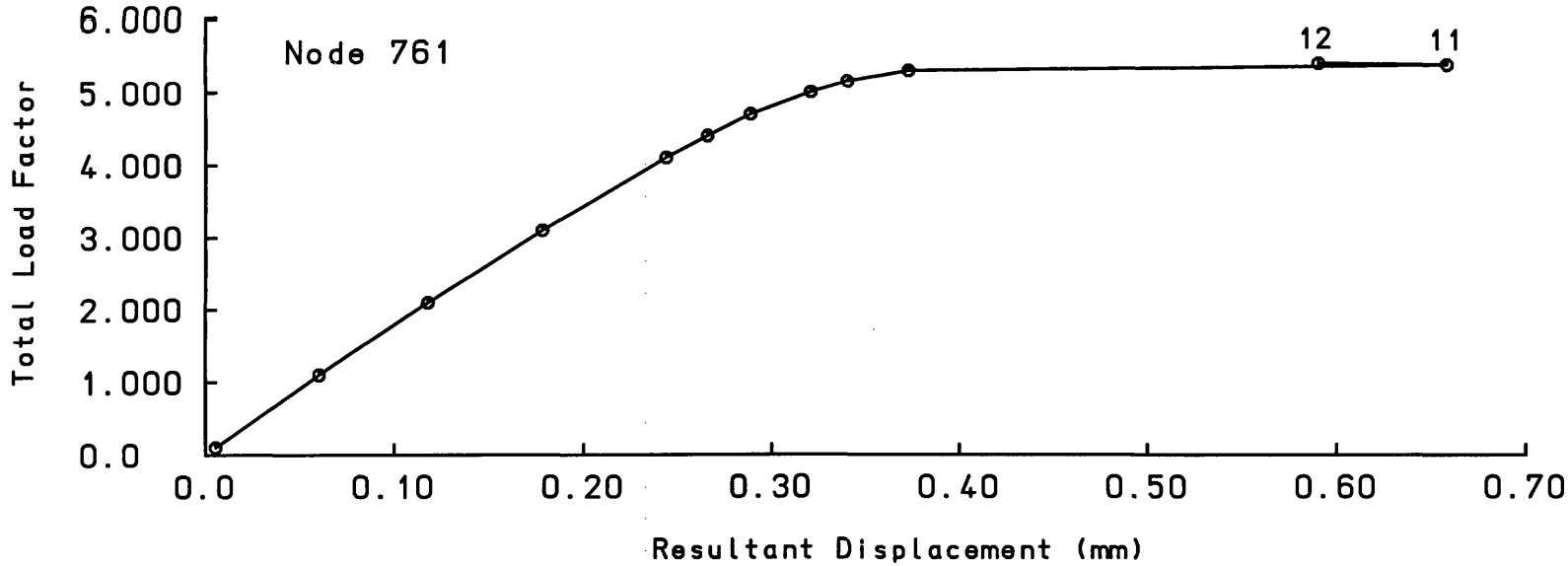

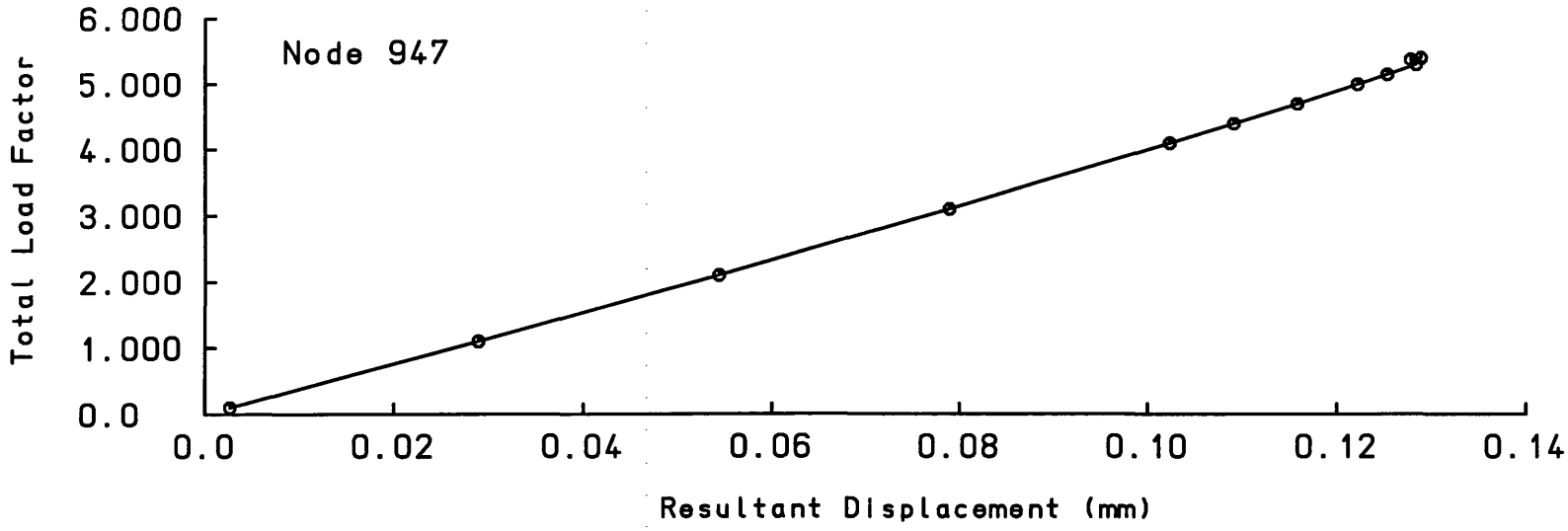

TITLE: Fig. 6.25. Load Displacement Curves at Different Nodes of S1_2-2B

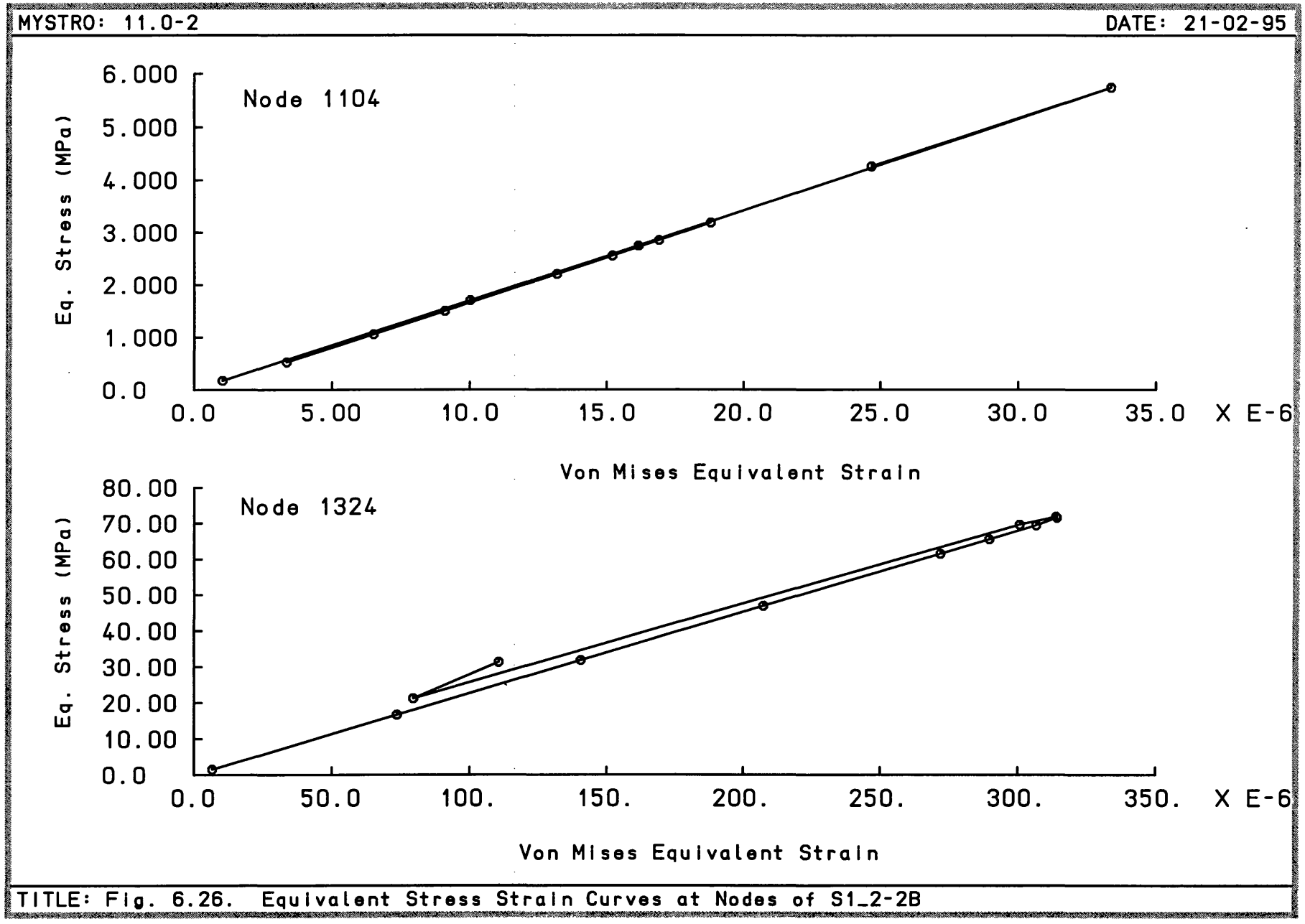

TITLE: Fig. 6.26. Equivalent Stress Strain Curves at Nodes of S1_2-2B

MYSTRO: 11.0-2 DATE: 21-02-95

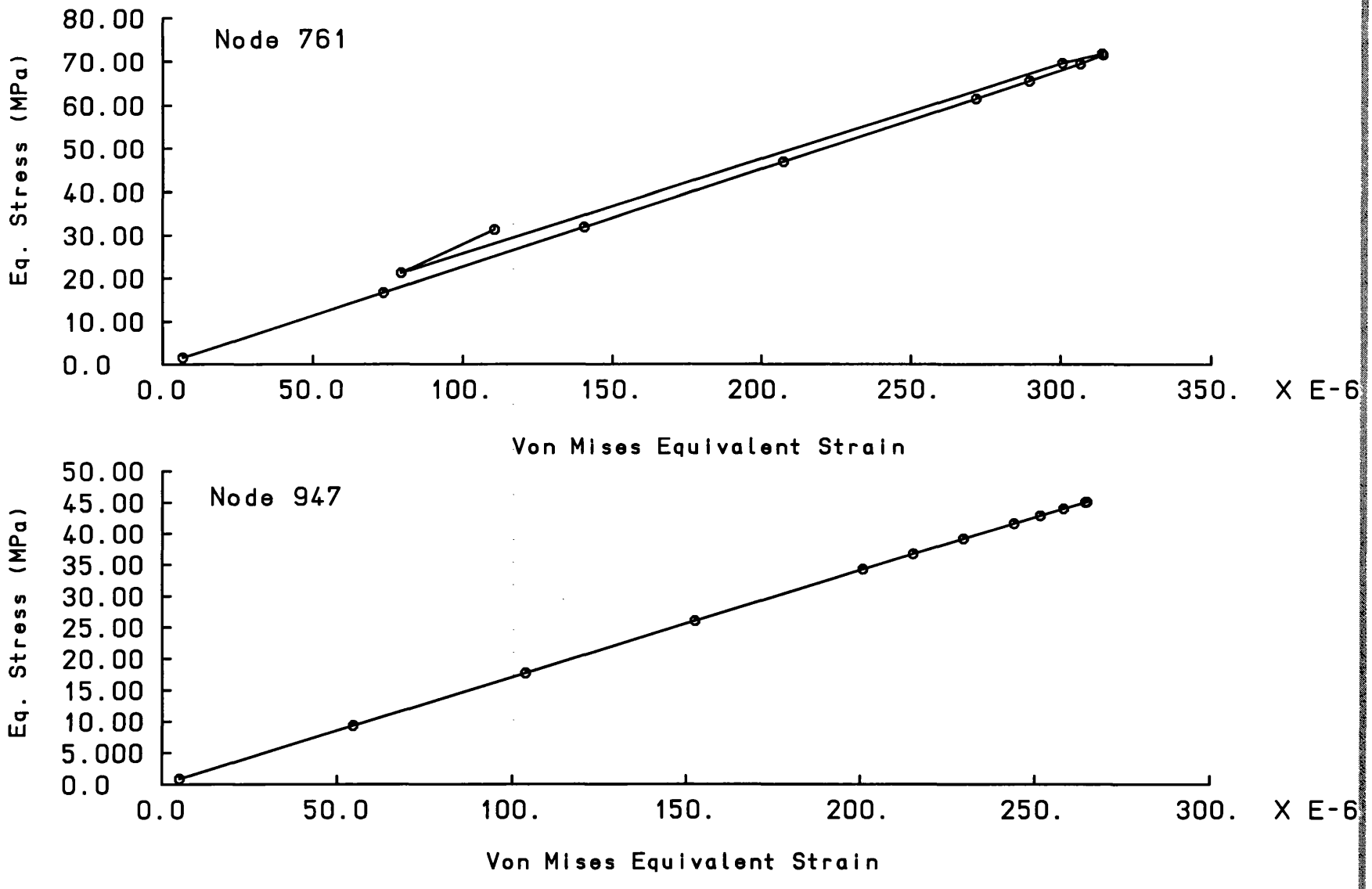

TITLE: Fig. 6.27. Equivalent Stress Strain Curves at Nodes of S1_2-2B

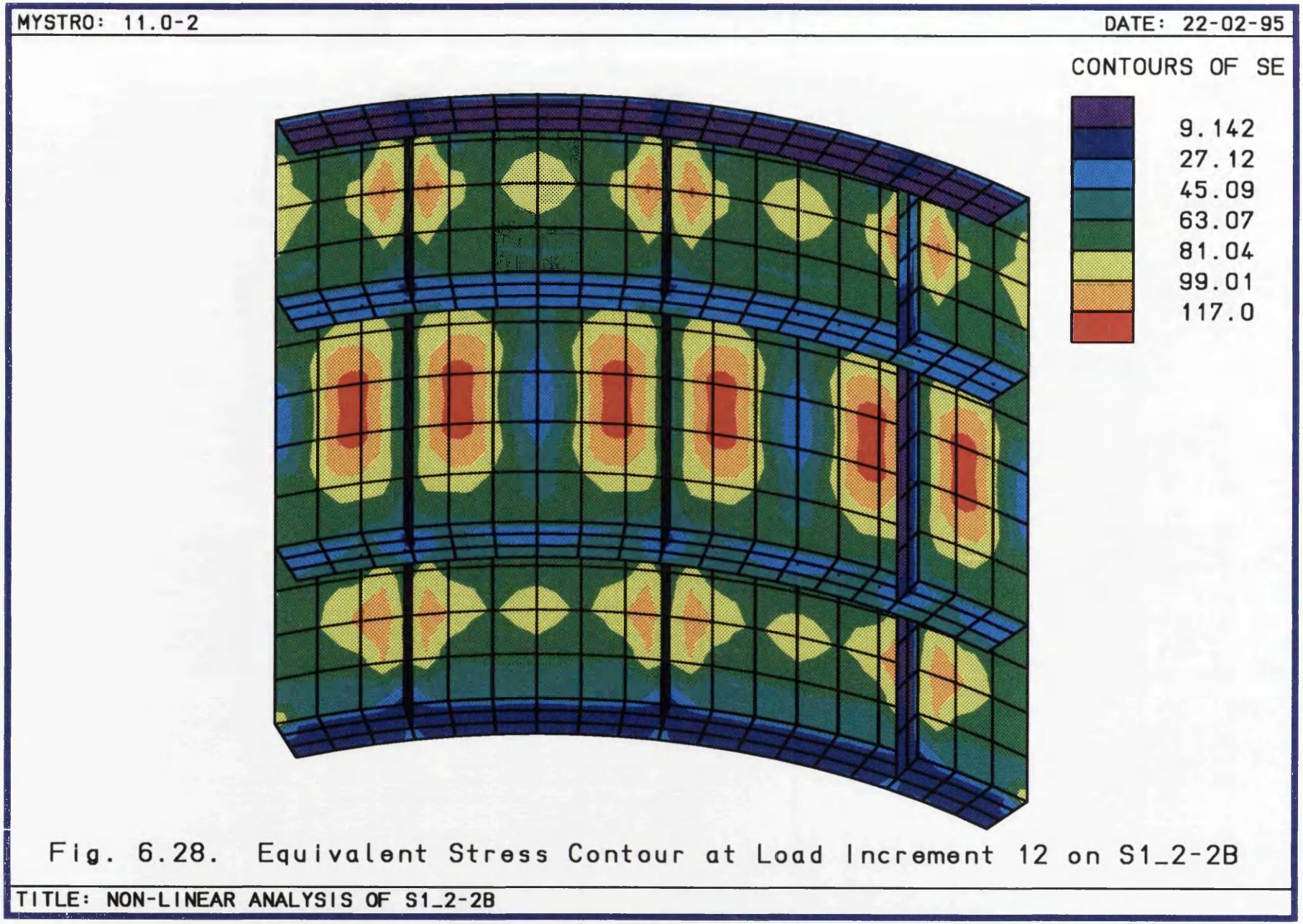

Fig. 6.28. Equivalent Stress Contour at Load Increment 12 on S1_2-2B

MYSTRO: 11.0-2 DATE: 22-02-95

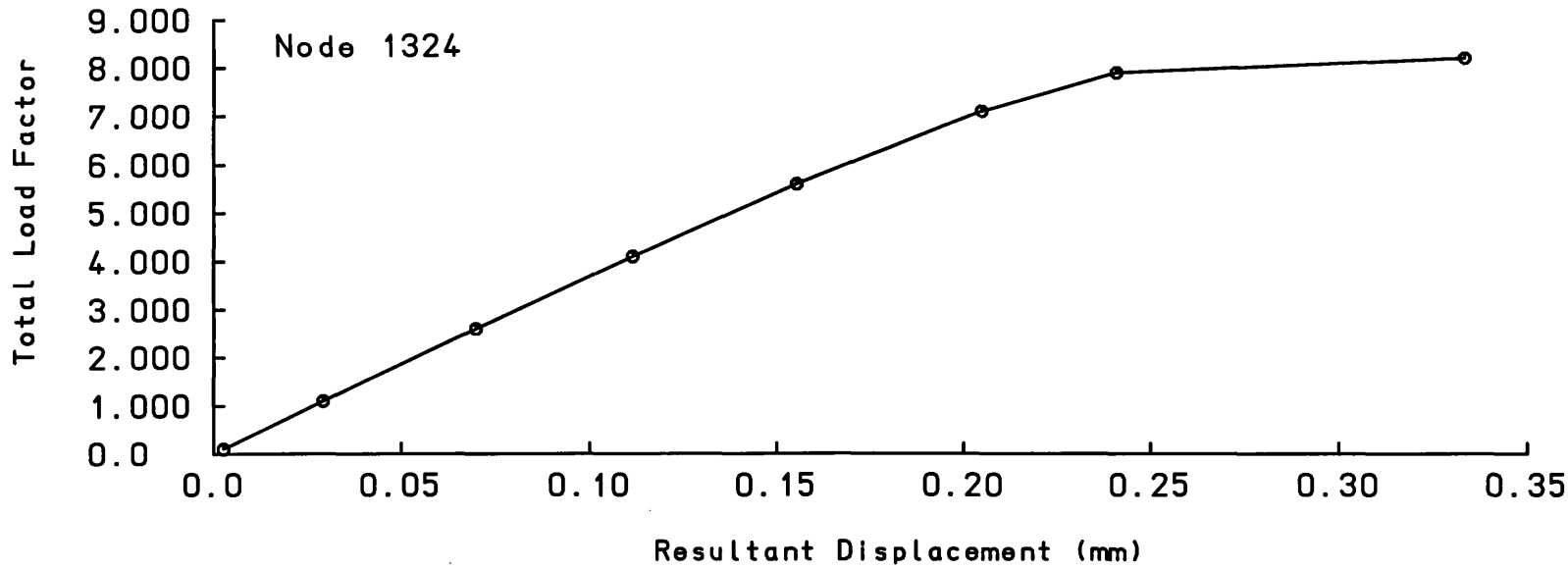

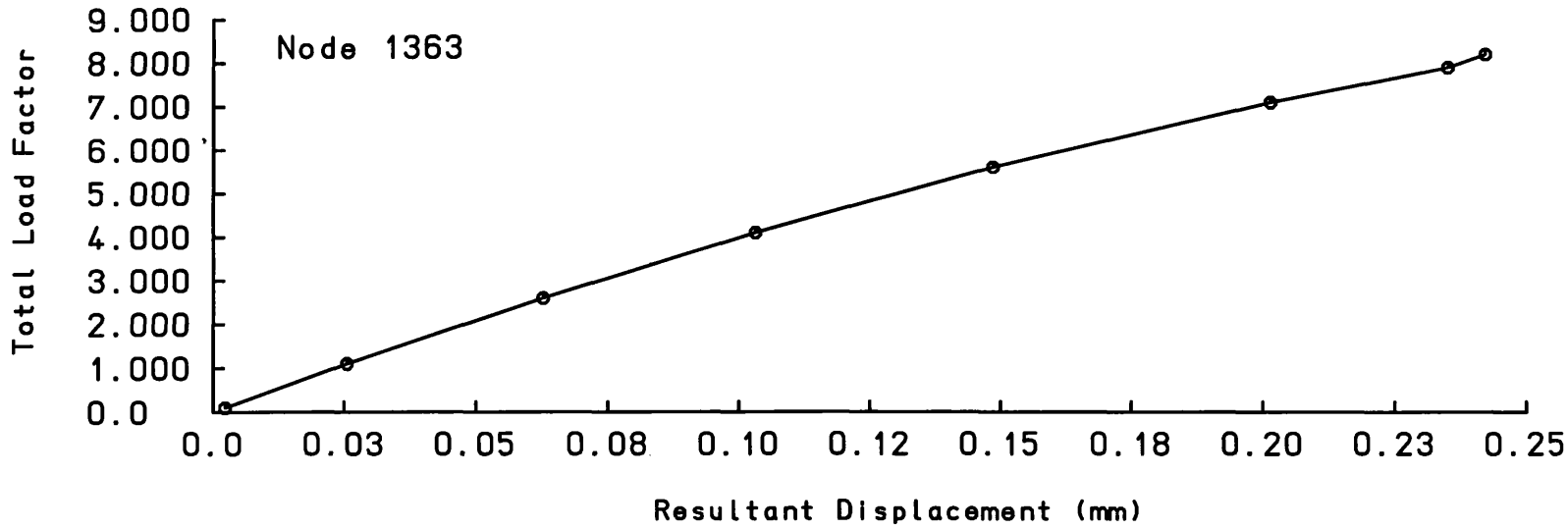

TITLE: Fig. 6.29. Load Displacement Curves at Different Nodes of S1_2-2D

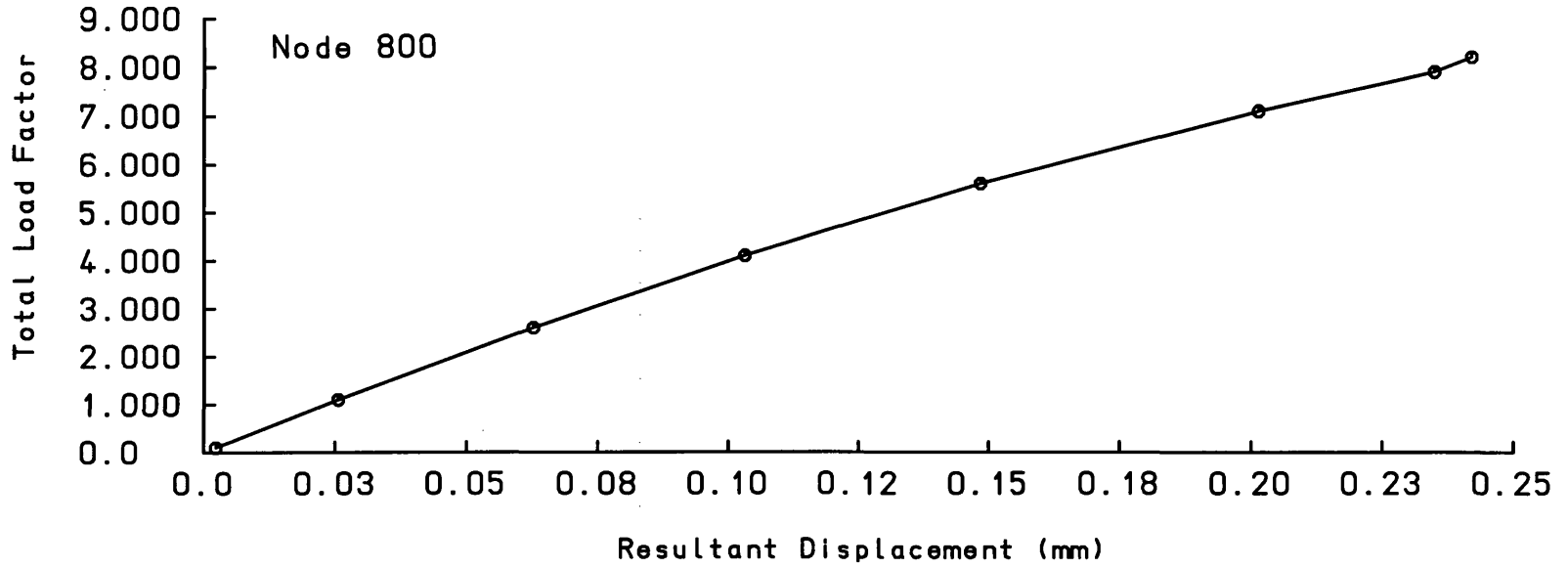

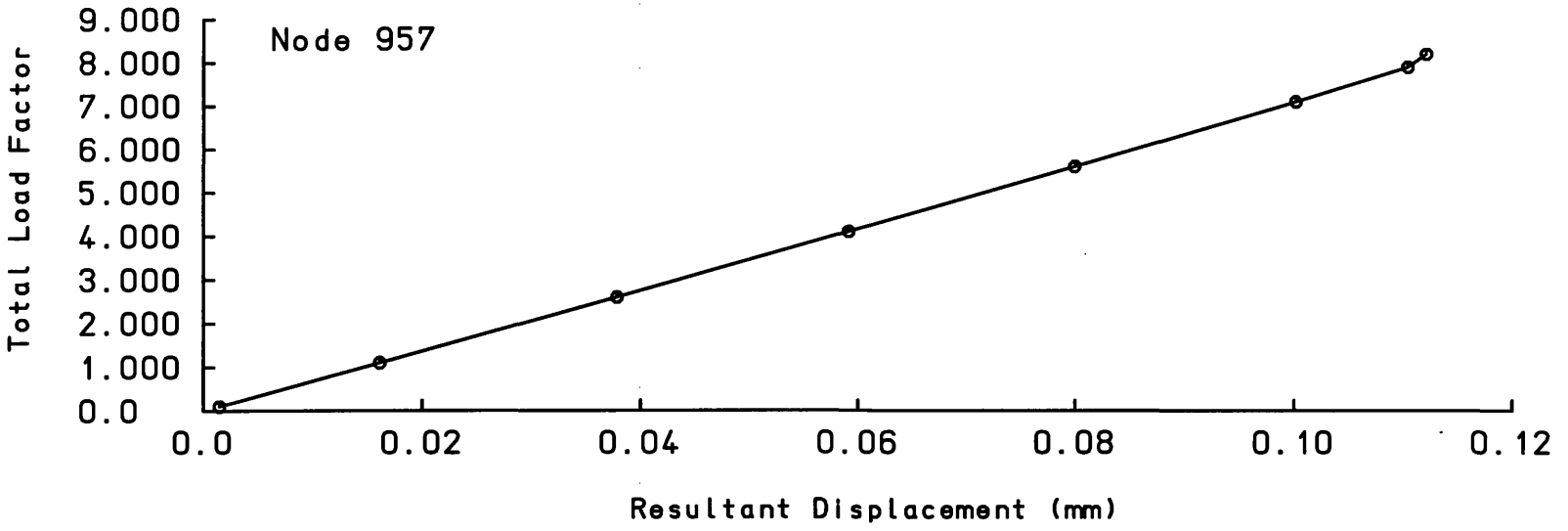

TITLE: Fig. 6.30. Load Displacement Curves at Different Nodes of S1_2-2D

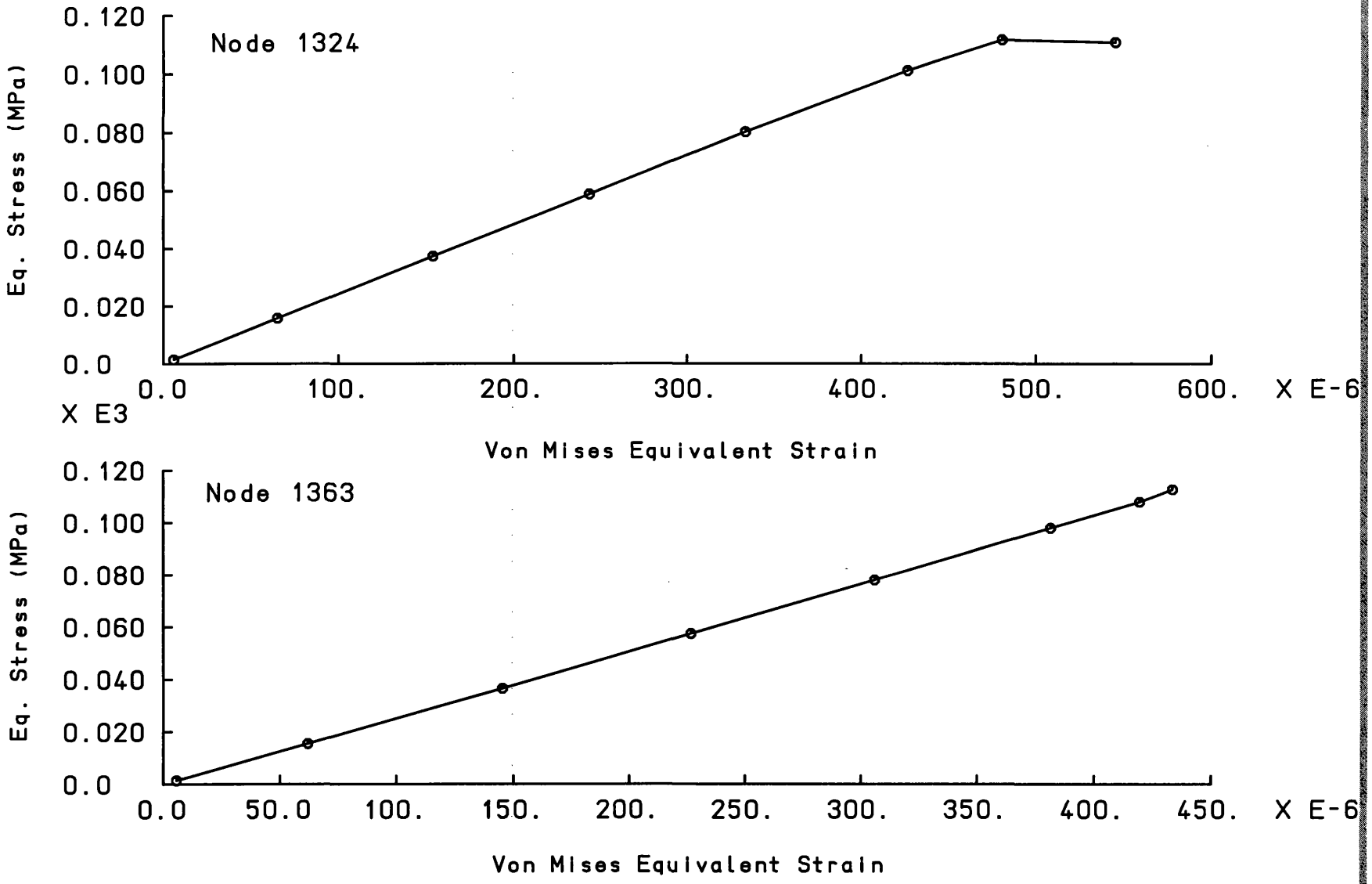

TITLE: Fig. 6.31. Equivalent Stress Strain Curves at Nodes of S1_2-2D

MYSTRO: 11.0-2 DATE: 22-02-95

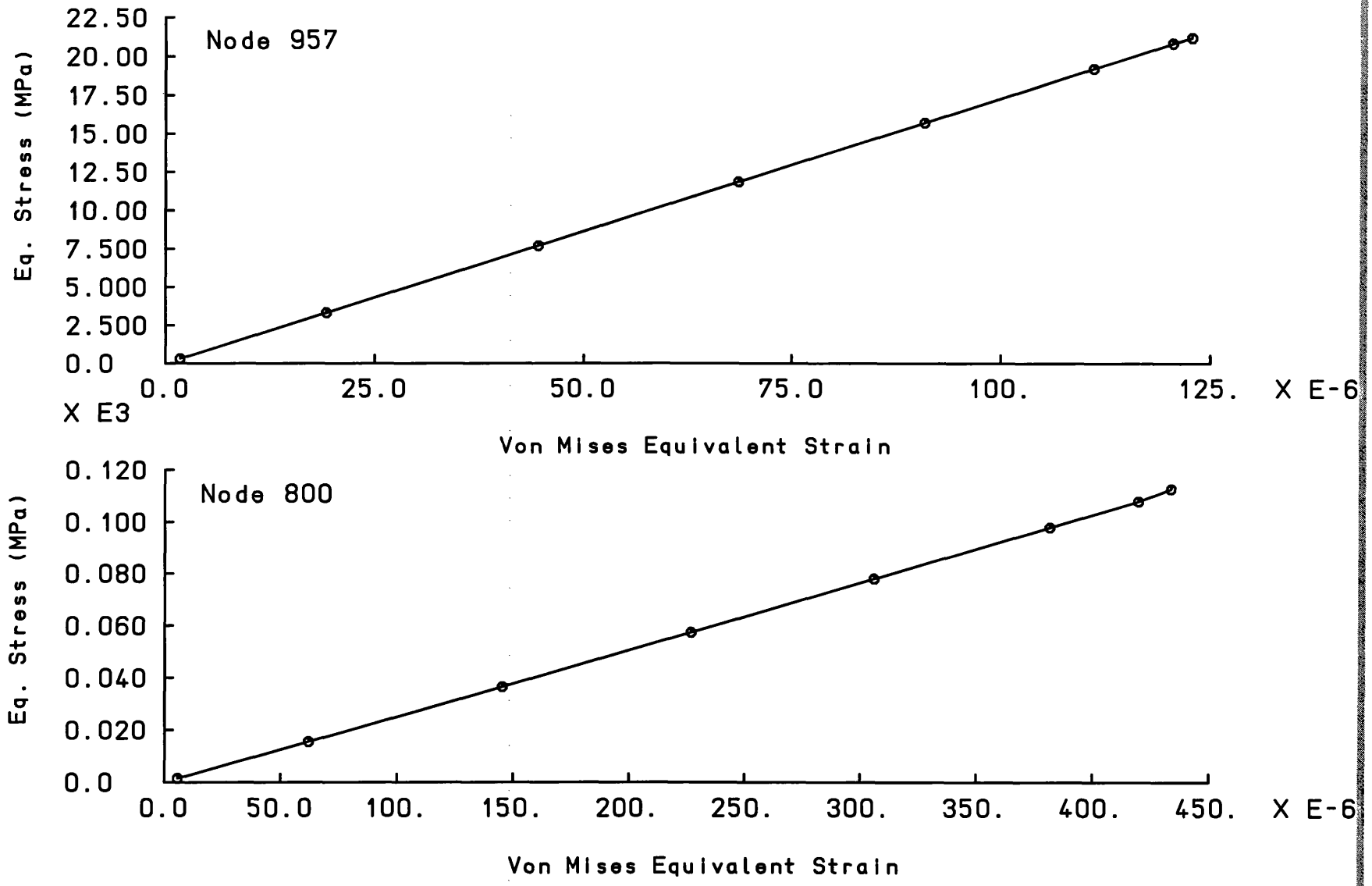

TITLE: Fig. 6.32. Equivalent Stress Strain Curves at Nodes of S1_2-2D

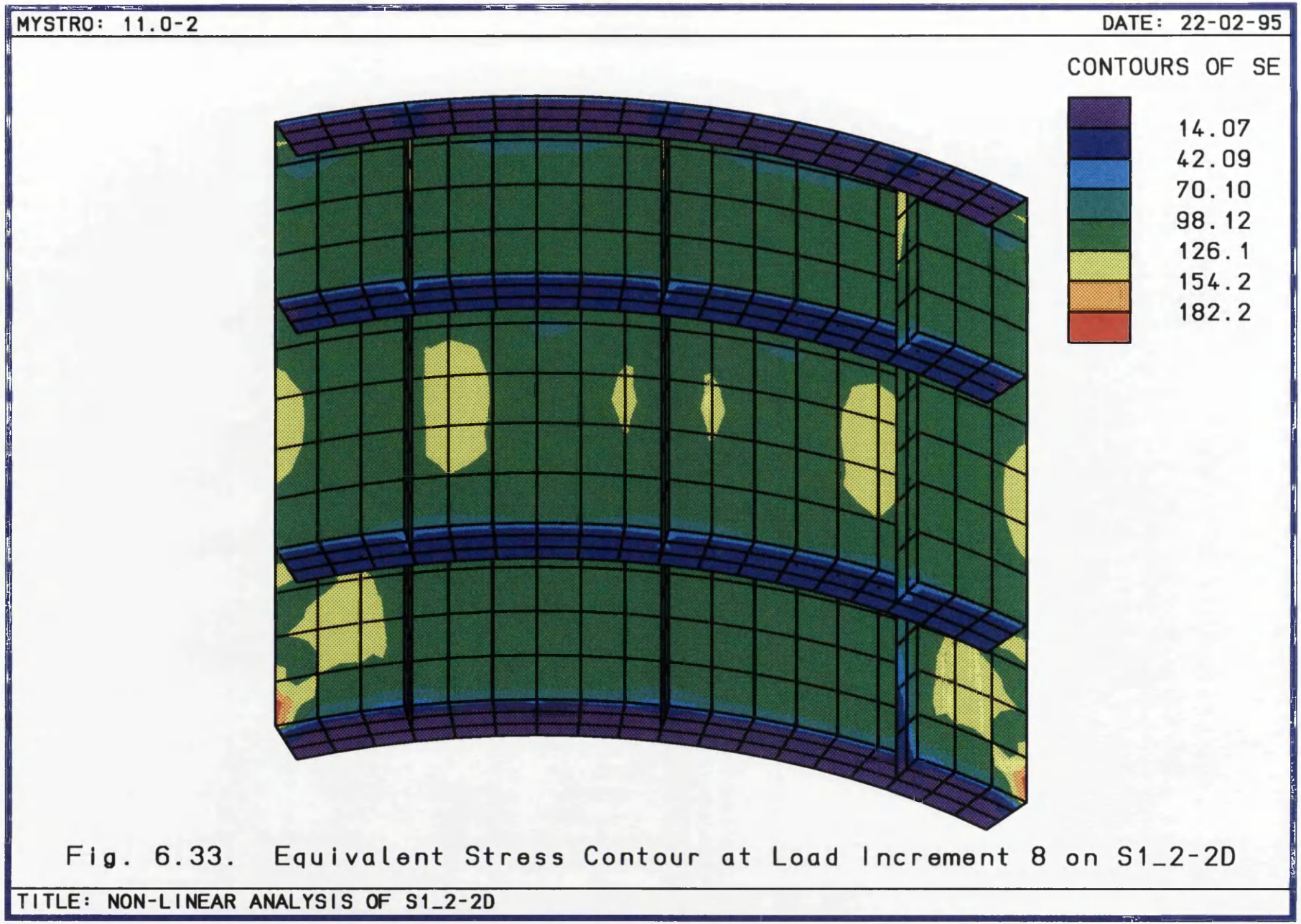

Fig. 6.33. Equivalent Stress Contour at Load Increment 8 on S1_2-2D

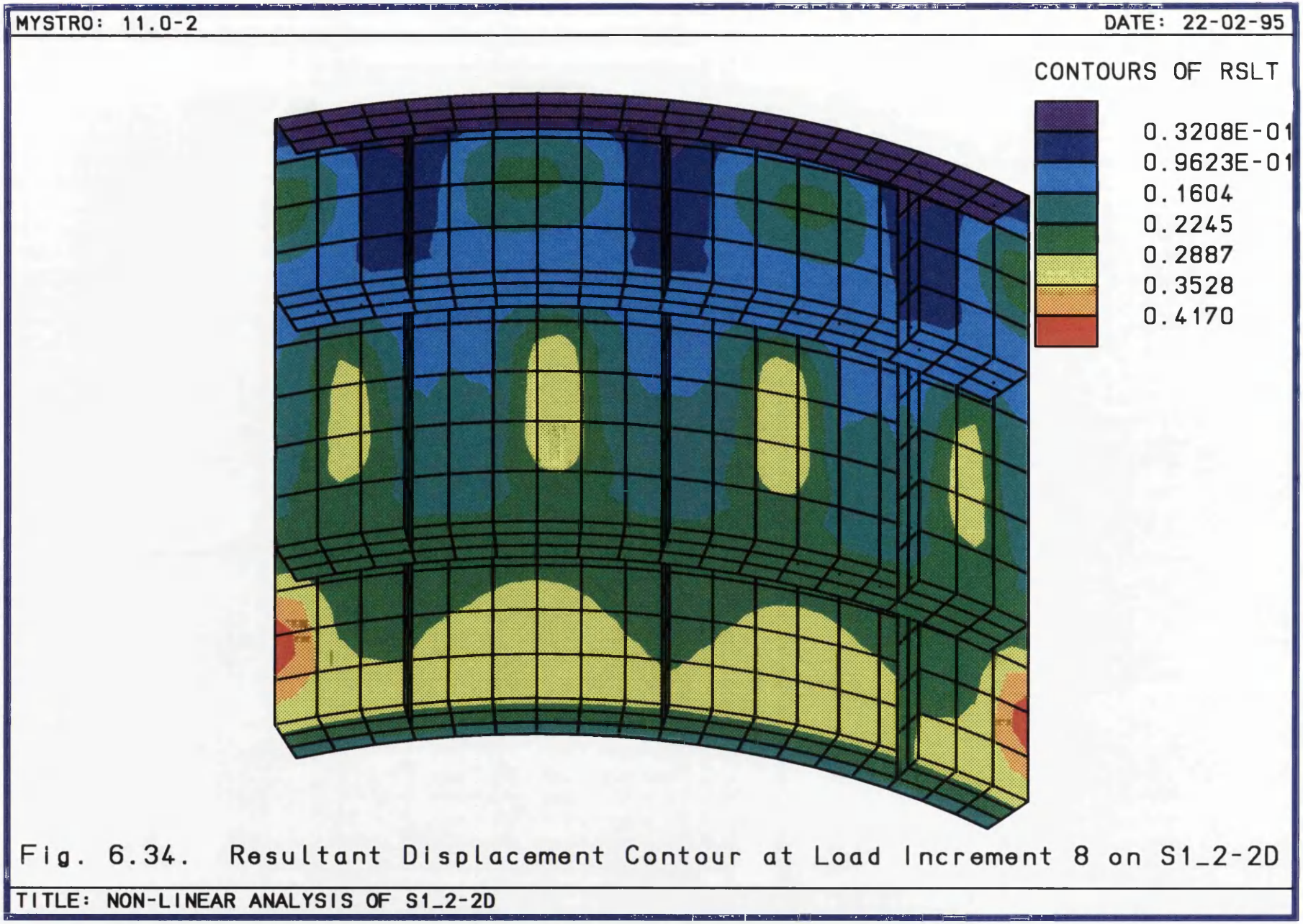

Fig. 6.34. Resultant Displacement Contour at Load Increment 8 on S1_2-2D

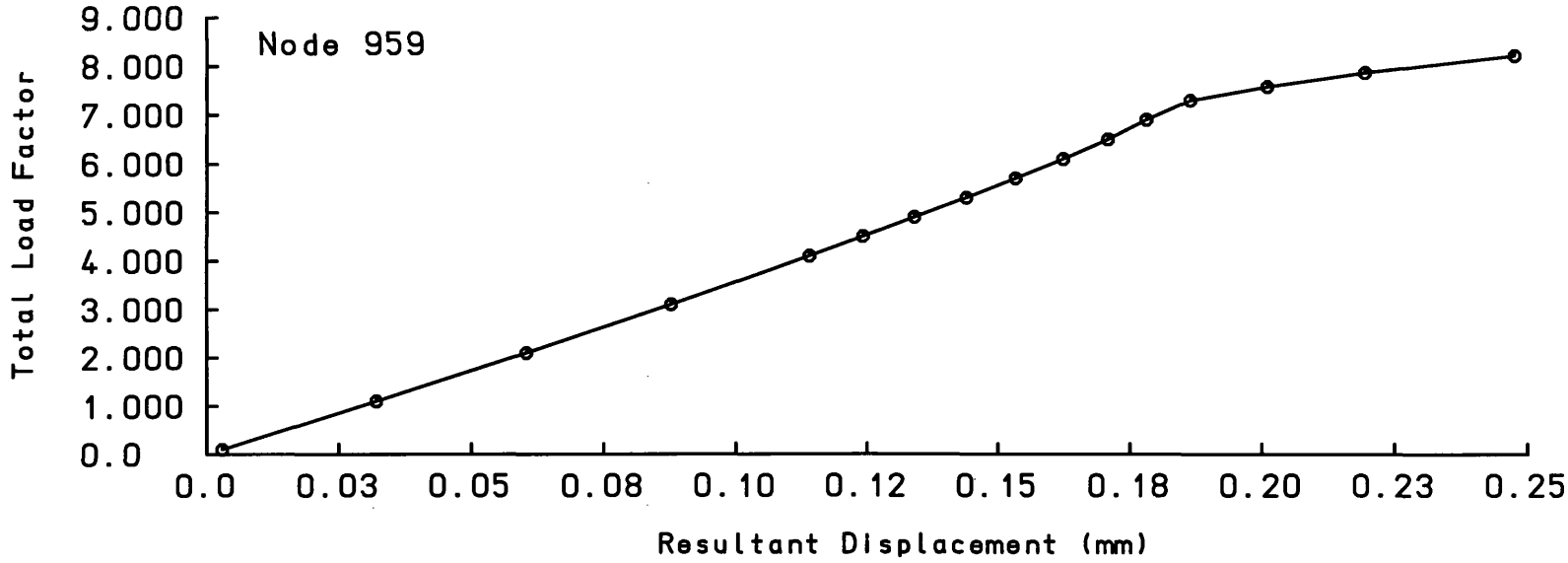

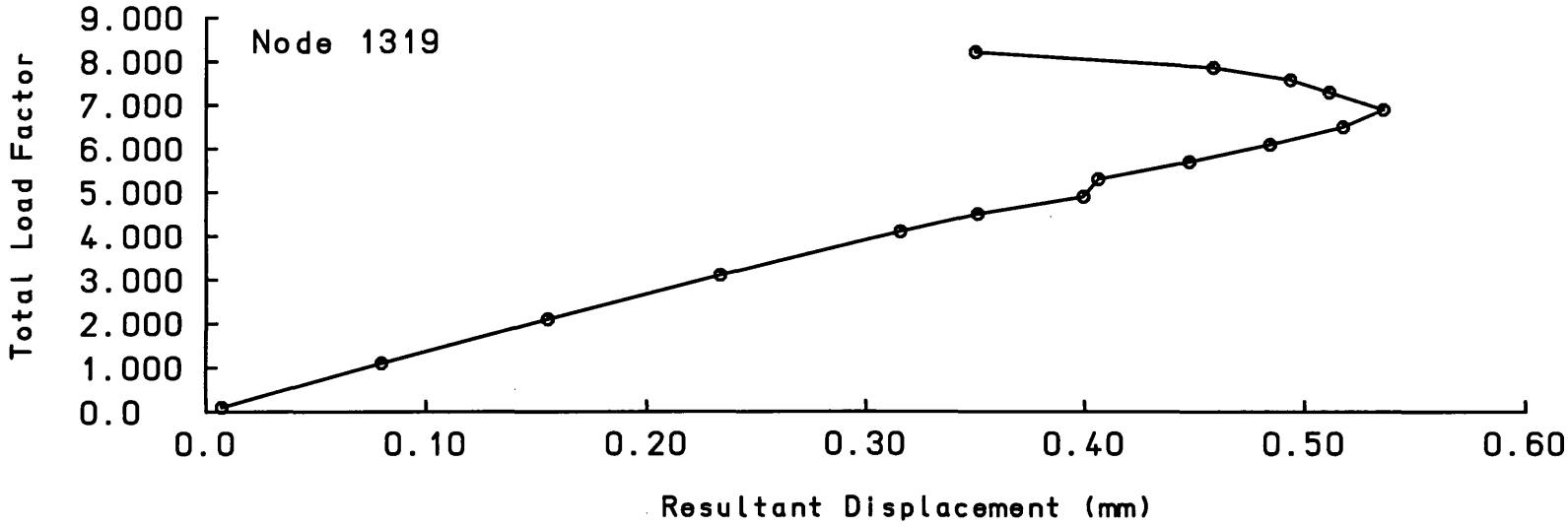

TITLE: Fig. 6.35. Load Displacement Curves at Different Nodes of S1_2-2C

MYSTRO: 11.0-2 DATE: 22-02-95

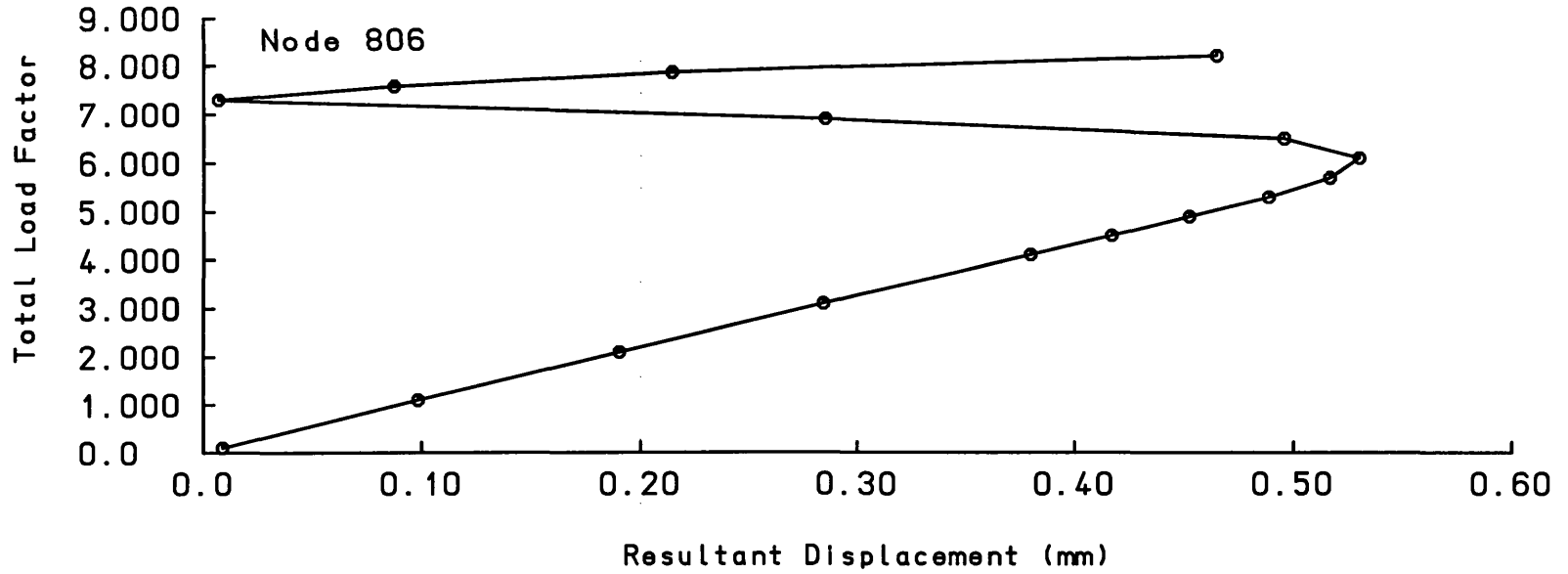

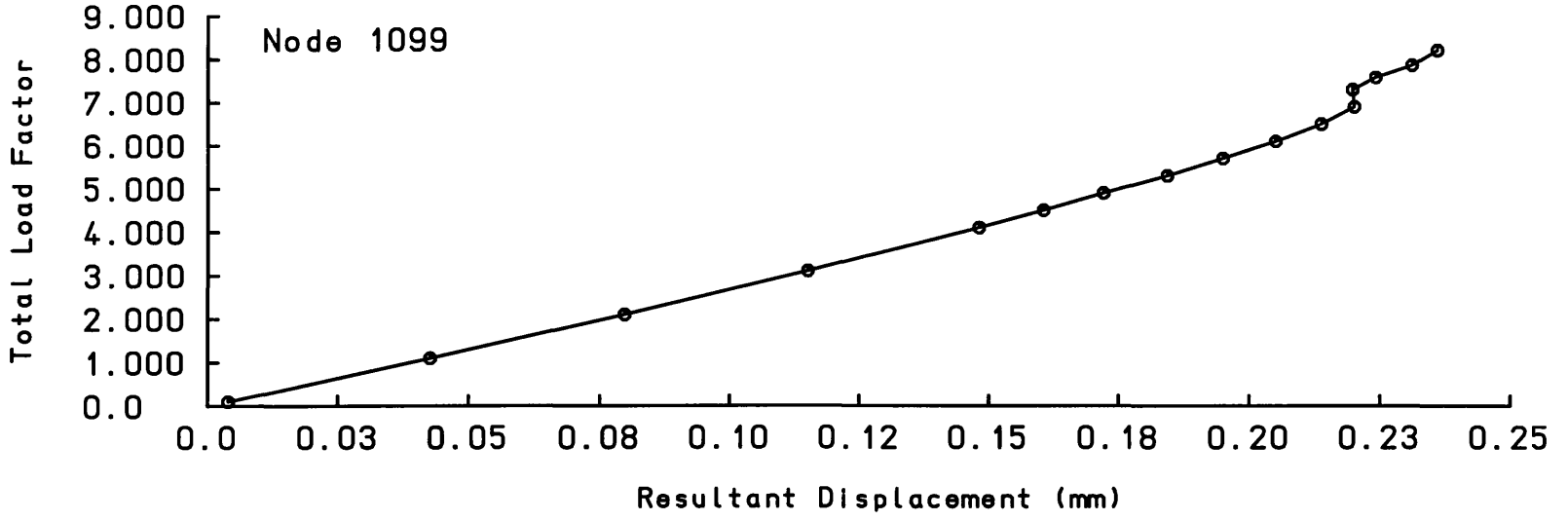

TITLE: Fig. 6.36. Load Displacement Curves at Different Nodes of S1_2-2C

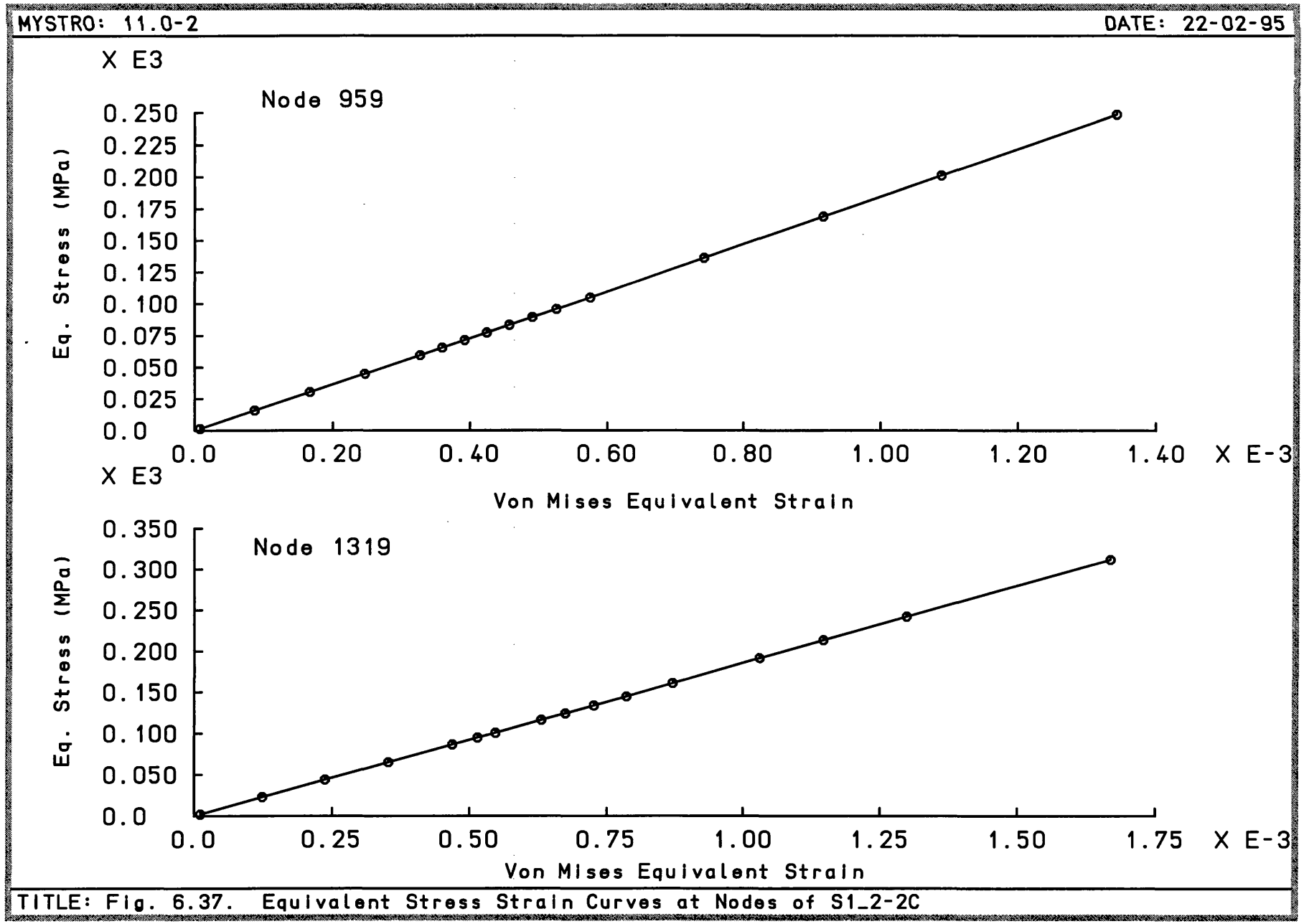
MYSTRO: 11.0-2
DATE: 22-02-95
X E3
Node 959
Eq. Stress (MPa)
0.250
0.225
0.200
0.175
0.150
0.125
0.100
0.075
0.050
0.025
0.0
0.0
0.20
0.40
0.60
0.80
1.00
1.20
1.40
X E-3
Von Mises Equivalent Strain
X E3
Node 1319
Eq. Stress (MPa)
0.350
0.300
0.250
0.200
0.150
0.100
0.050
0.0
0.0
0.25
0.50
0.75
1.00
1.25
1.50
1.75
X E-3
Von Mises Equivalent Strain
TITLE: Fig. 6.37. Equivalent Stress Strain Curves at Nodes of S1_2-2C

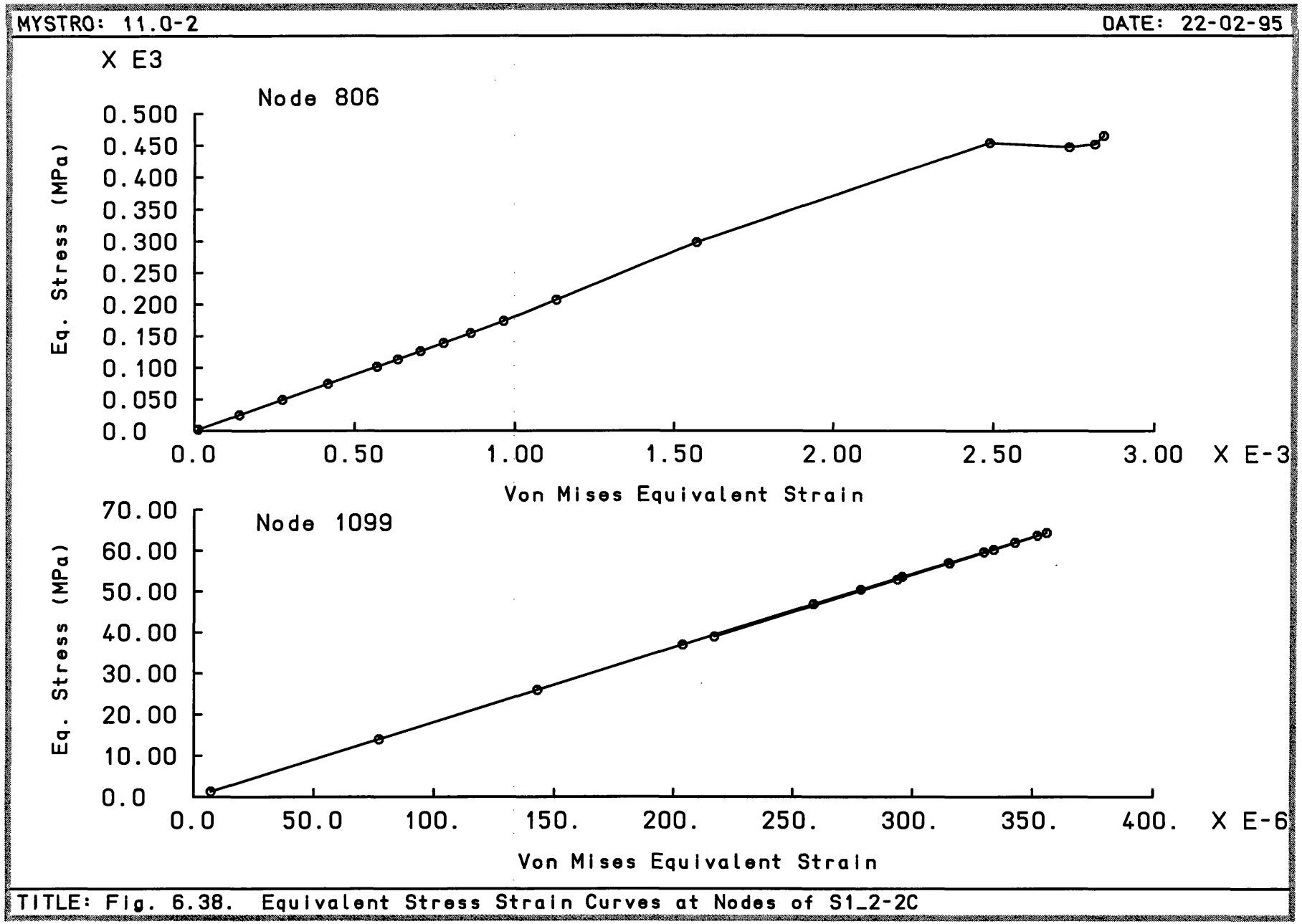

TITLE: Fig. 6.38. Equivalent Stress Strain Curves at Nodes of S1_2-2C

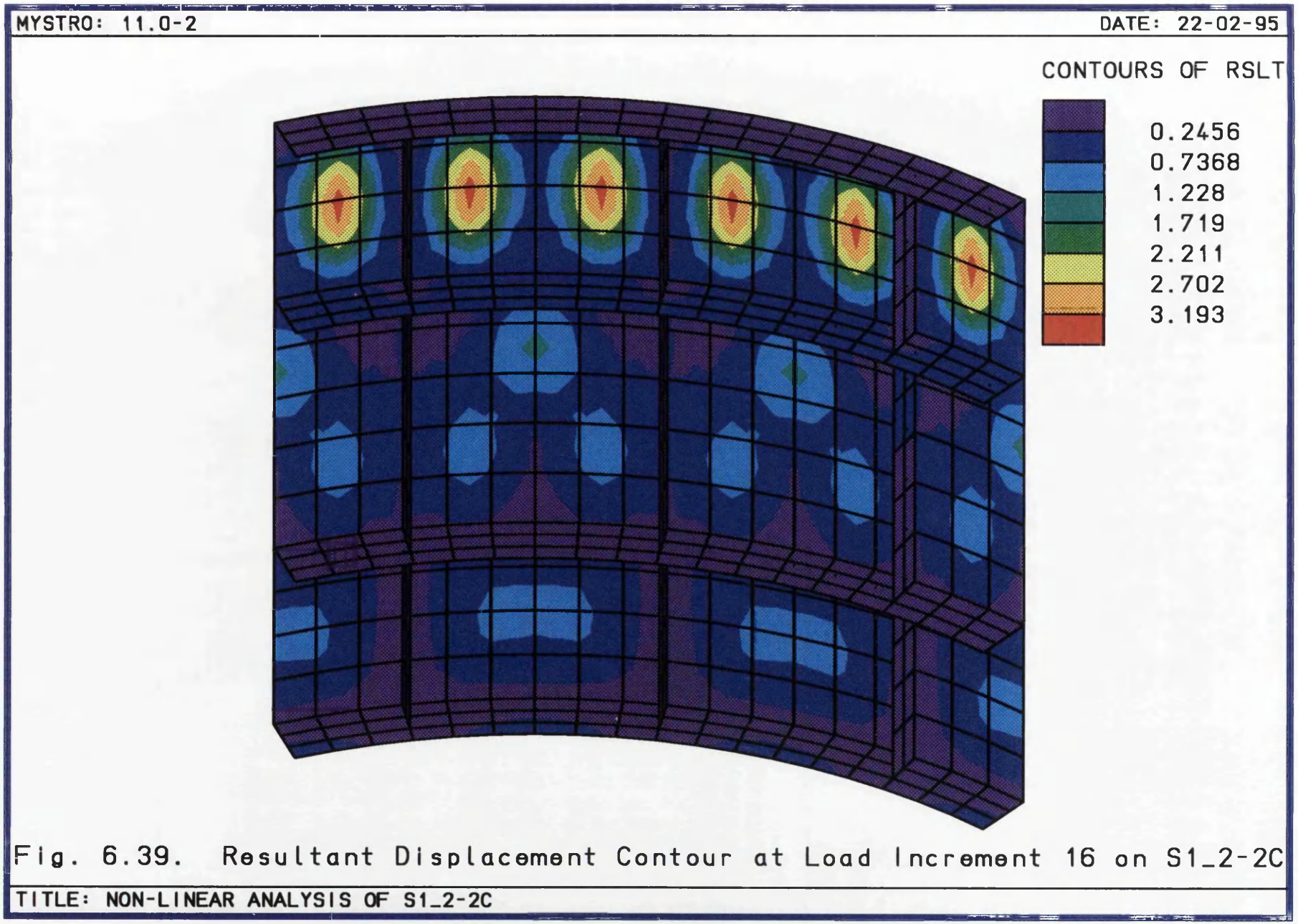

Fig. 6.39. Resultant Displacement Contour at Load Increment 16 on S1_2-2C

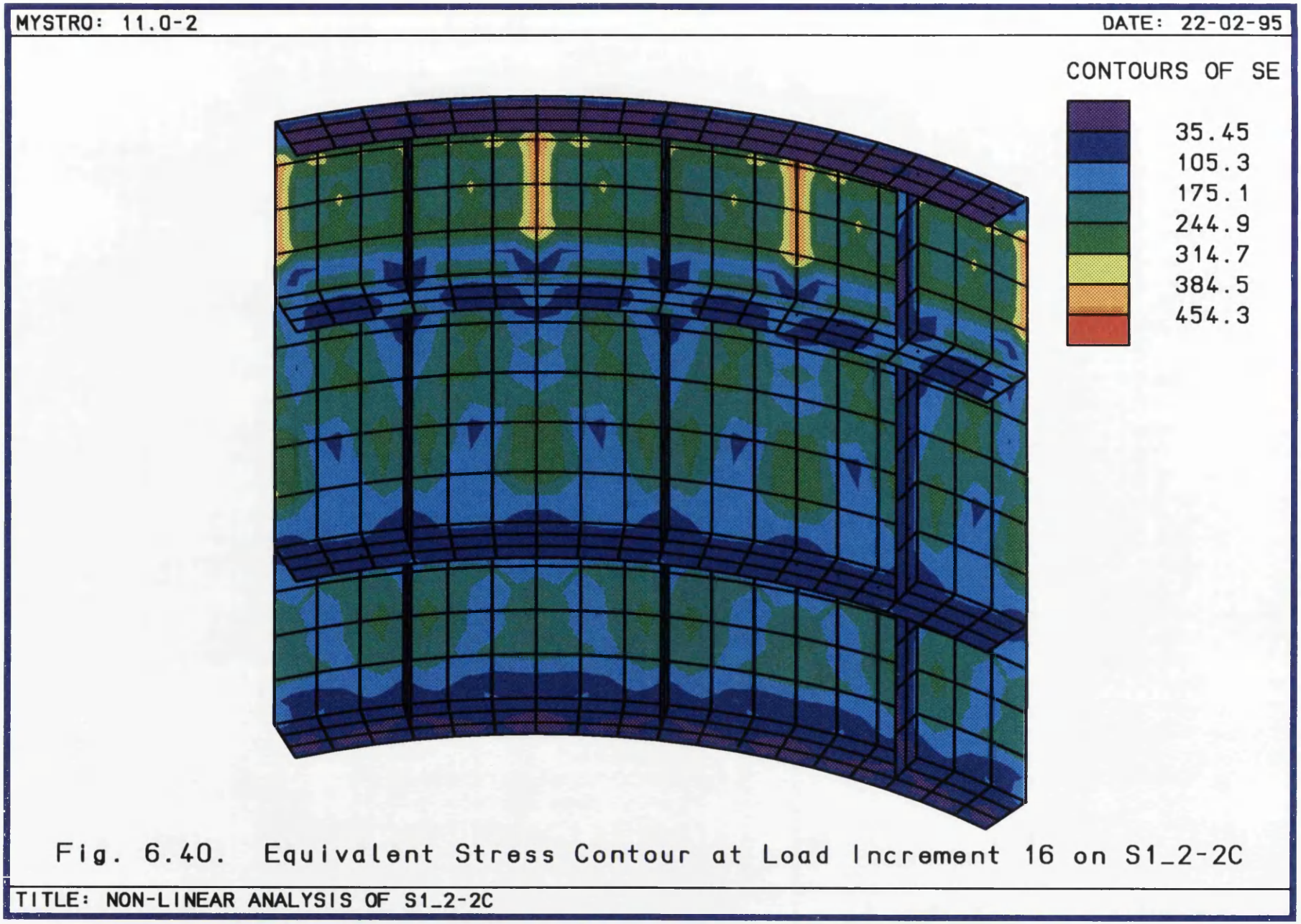

Fig. 6.40. Equivalent Stress Contour at Load Increment 16 on S1_2-2C

CHAPTER 7

CONCLUSIONS AND FUTURE WORK

7.1 GENERAL

For almost all ship hull forms, prescriptive rules exist from major classification societies. These empirical formula based rules have served for decades to define minimum requirements for the structural design of ships. There have been classic examples of structural failure when new ship designs fell outside the scope of the experience on which such prescriptive rules were based. But for TLP structures, such an experience base does not exist at all. TLPs designed to date are for quite different missions and therefore have different dimensions and other features. It is essential therefore to start analyses using engineering first principles.

The following section will summarise what the author has learnt through his research work detailed in earlier chapters. He started his work without any theoretical or practical experience with TLPs. It was also necessary for him to learn how to plan various stages of a long-term research work. One obvious choice was to proceed from the simplest computational methods. It was found that simple hand calculations demonstrated by other researchers could be of great help in understanding the global behaviour of TLP structures.

The research was aimed at setting up an integrated design track for TLPs. In practice, various groups of people are involved in designing and constructing TLPs and similar structures. Sometimes they might share as little as one or two vital pieces of information (e.g. the maximum stress or load value) to tie up their work. But an integrated design process would share more information among hydrodynamics, structural engineering and associated reliability aspects. One possible solution is to create a common database of information. An interactive database might be difficult to set up at first, but that can certainly improve the situation. However, different stages of the design process have to programmed such that the developed modules can read from or write to the common database.

Another objective was to explore new and existing avenues where attention can be gradually shifted from the ocean environment to final strength checking and reliability aspects.

7.2 MAIN CONCLUSIONS

In earlier chapters, some immediate conclusions have been drawn to point out the results of the computational efforts involved. But this section will discuss the main conclusions separately without any technical details.

(a) Importance of Numerical Modelling

While going through a number of references, the author has noticed that the readers are often discouraged to take attempts to solve numerical problems if they are not well acquainted with the theoretical background. This is particularly true when non-linear FE analyses are involved. But the author has a different view point in this respect. He thinks that it is extremely difficult to understand the theories alone unless someone works with the numerical problems.

(b) Equivalent Loads in the Ocean Environment

Even today, apart from concentrated and uniformly distributed loads, only a few standard types can be handled adequately by general purpose finite element software. The author has tried to combine some existing computational methods and techniques of structural mechanics to simplify the task of transferring complicated member loads to the corresponding nodes of beam elements. In the process, some closed-form expressions are formulated which can be very helpful to anyone who does not want to get into the complexity of the interaction of waves with the structure. The added advantage is that the closed-form expressions are analytically integrated and simplified. So there is no need for any numerical integration which is usually computationally expensive. The beam elements are not subdivided if the closed-form expressions are used and thereby the computer run time and storage requirements can be considerably decreased.

(c) Equivalent Loads for Arbitrarily Oriented Beams in Space

In the case of a beam, arbitrarily oriented in space, equivalent loads can only be found through numerical integration. But the computation procedure proposed in Chapter 2 will achieve a reasonable solution depending on the size and number of divisions along the element length. The method can also deal with any other form of member loads in addition to forces from ocean waves. It can be easily programmed and stored as a separate module which can be utilised later in the main analysis.

(d) Dynamic or Quasi-Static ?

It is important to remember that compliant offshore structures like TLPs are inertia dominated and any attempt to analyse them quasi-statically might produce erroneous answers unless platform inertia forces are properly adjusted with external environmental forces. Patel et al [7.2] have found that typical inertia forces can be 15 times greater than the tether forces for a TLP in 120 m of water. The author has gained similar experience while developing DCATLP.

(e) Rigid Body Response Calculations

One useful feature of rigid body response programs such as RBRA is that they can quickly and efficiently generate force and response RAOs. The RAOs can be utilised in frequency domain analysis with sea spectra to calculate response statistics. However, a rigid body response program is not quite helpful in structural design. Maximum magnitudes of the environmental and platform inertia forces can be transferred to a separate space frame model with various simplifications and assumptions [7.5] for structural analysis. In fact, DCATLP has been developed to give answers to these problems.

(f) Dynamic Coupled Analysis

DCATLP can execute a large set of time varying load cases on a TLP. It works with all kinds of forces (i.e. static, quasi-static, dynamic) at any instant of time. It also calculates the internal forces in TLP components under the action of time varying environmental, inertia, damping and restoring forces. This automatic, elaborate, element-by-element calculation is extremely difficult if not impossible, if the structural calculations have to depend on separate hydrodynamic analysis.

(g) Tether Stiffness

One important conclusion in this study is about the spring models of tethers. The ideal horizontal spring stiffness, can provide reasonable estimates of the platform surge or sway response but tethers do not behave totally like springs in the vertical direction. Their behaviour in the vertical direction can only be understood from a hull-tether coupled analysis.

(h) Damping

The importance of damping has been demonstrated in this work. For steady state response calculation in time domain, damping in the system is essential. Otherwise the free vibration part in the transient state of response will not die out in the course of time. This may create confusion if the results are compared with frequency domain calculations.

(i) Practical Applications

Various modules of the programs developed in this research work have been checked and verified by a general purpose FE software called LUSAS. The configurations of company specific TLPs in service are avoided in this work to comply with the academic license of LUSAS. However, the analysis procedure set out for Model_2 of

the ISSC TLP has been followed recently [7.3] to calculate natural frequencies and forced response of the Snorre TLP. The results found are in good agreement with the experimental results.

Program RBRA has been successfully used in a research work [7.4] for modelling multi-variate environmental data. In fact, RBRA is a collection of subroutines which can be easily linked to a different program to do some useful analysis with sea spectra.

However, DCATLP still remains an academic exercise. It was important for the author to get some feed back from industries. It is worth noting that a detailed report on DCATLP [7.1] has been reviewed and appreciated by experts in Conoco and Shell.

(j) Analysis of TLP columns

TLPs are column stabilised structures. The columns may contribute 70% of the platform displacement. In general, TLP columns are constructed of large cross-section thin stiffened shells which will always fail by inelastic buckling at applied stress levels lower than the yield stress, often appreciably lower. In such cases a working stress basis for design is clearly inappropriate and is potentially unconservative. Therefore it was necessary to verify the proposed design of the ISSC TLP columns through deterministic as well as probabilistic checks. Similar column structure design can be verified quickly if the step-by-step computation procedure detailed in Chapter 5 is followed.

(k) Model Uncertainty Factor

The modelling uncertainty factor dominated quite strongly in the demonstrations in Chapter 5 to obtain the failure probabilities at the expense of more 'physical' variables such as dimensions and material properties. While formulating a performance function from an interaction equation, care must be taken to include model uncertainty factor(s). Otherwise, the significance of other design variables might be lost. If the correlation coefficients among variables are taken into account, improved solutions can be achieved.

(l) Local FE Analysis

It has been widely recognised that component structures can only be assessed using 3-D and 2-D finite element analysis techniques on a routine basis. The main objective in Chapter 6 was to carry out a detail FE analysis of a part of a TLP structure with the help of the results from a 3-D beam element based global analysis. The application of

the subspace iteration technique used in the eigenvalue buckling analysis is found to be easy and straight-forward. It is helpful to get an initial 'feel' for the structure. However, the buckling load calculated in this process might vary with the mesh discretisation in some cases as seen in Chapter 6. It would be therefore a wise decision to verify a column design through rigorous non-linear FE analysis.

7.3 USEFUL FEATURES OF THIS RESEARCH WORK

The author would like to close this thesis with the hope that it may provide one corner stone in the hydro-structural analysis and its application to the design of TLPs in the future. A few useful features of this research work that the author would like to claim as his contributions are noted below for quick reference:

(a) Offset Calculation

There are simplified formulae available in several publications for estimating offset and set-down of a TLP under the action of quasi-static environmental forces. But in most cases, a few factors are ignored to keep these formulae simple and straight-forward. In Section 4.3.3, an offset calculation method is proposed which accounts for set-down, tether inclination angle, change in tether tension and the stretch in tethers as well. This method is expected to be useful in future.

(b) Closed-form Expressions for Equivalent Nodal Loads

Analytical diffraction forces from the MacCamy and Fuchs' theory and inertia and drag forces from the Morison equation have been separately integrated with the shape functions of the Bernoulli-Euler beam to generate closed-form expressions in Chapter 2 for equivalent nodal loads, suitable for beam element based FE analyses. The general step-by-step procedure for similar calculations with member loads which do not follow any standard pattern in the case of an arbitrarily oriented beam in space can be useful too.

(c) Hydro-Structural Analysis

The ultimate aim of developing DCATLP is to provide calculation methods and computational tools for a 'seamless integration' of hydrodynamic and structural aspects in a TLP design. The author is not aware of the existence of any other program like DCATLP or similar calculation procedures available in the public domain.

(d) Failure Probability from Internal Resisting Forces

A step-by-step calculation procedure is presented in Chapter 5 to find failure probabilities of TLP column structures after assigning appropriate coefficients of variation to the strength and load variables. The calculation of longitudinal and hoop stresses from maximum axial compression, torsion, shear forces, bending moments and hydrodynamic pressure is also shown. This component reliability analysis procedure might be useful to provide information as criteria for decision making in the design stages.

(e) From Global Dynamic Analysis to Non-linear Local Analysis

The internal resisting forces in TLP members calculated by a hydro-structural analysis program can be carefully used to define boundary loads with suitable support conditions in a local FE analysis. The local analysis would be of general nature without any especial characteristics of TLPs. This way a general purpose FE software can be introduced in a TLP design.

7.4 FUTURE WORK

(a) Irregular and Random Waves

It is not difficult to improve the capabilities of DCATLP. It can work with irregular and random waves without much modifications. The environmental loading module can calculate forces from a number of regular waves and superimpose them together to form the right-hand-side external load vector. A random wave signal can be separated into a number of regular wave components through FFT (Fast Fourier Transformation). Standard FFT routines are available in various subroutine libraries (e.g. NAG library from The Numerical Algorithms Group Ltd. [7.6]). It is expected that DCATLP could take site data into account in the immediate future extension.

(b) Correlation Coefficients in the Reliability Based Design

The selection of appropriate correlation coefficients among design variables in a TLP column design is difficult. But BCCNNV can be used as a 'black box' once the correlation coefficients are ready. This is an important future work to see the influence of the model uncertainty factor when it is correlated to other design variables.

(c) Geometrically and Materially Non-linear Buckling Analysis

This is one of the most difficult areas in the structural analysis. The attempts taken with the help of LUSAS in Chapter 6 can be certainly improved if the arc length control is implemented in the analysis. Perhaps it will provide more information on

post-buckling deformations. The author is interested in pursuing these studies in future.

7.5 REFERENCES

[7.1] Chatterjee, P.C. and Das, P.K.: "Hydro-Structural Response of ISSC TLP", Departmental Report (No. NAOE-94-31),. Department of Naval Architecture and Ocean Engineering, University of Glasgow, Glasgow, 1994.

[7.2] Patel, M.H. and Witz, J.A.: "Compliant Offshore Structures", Butterworth-Heinemann Publication, 1991.

[7.3] Phelps, A.: "Finite Element Modelling of a Tension Leg Platform (TLP) Structure", Final Year Project Thesis (No. NAOE-95-10), Department of Naval Architecture and Ocean Engineering, University of Glasgow, Glasgow, 1995.

[7.4] Prince-Wright, R.: "Statistical Models of Environmental Data for Marine Structure Design", Ph.D. Thesis (No. NAOE-93-26), Department of Naval Architecture and Ocean Engineering, University of Glasgow, Glasgow, 1993.

[7.5] Shin, Y.S., Xanthopoulos, E. and Unger, D.P.: "Extreme Value and Probability Density Function of Motion, Tether Tension and Load Effects on a North Sea Tension Leg Platform", Paper RCC(b) 16, 7 February 1983.

[7.6] The NAG Fortran Library Manual, Mark 14, The Numerical Algorithms Group Limited, Oxford, UK, April 1990.